FUNCTIONAL NANOMATERIALS FOR CANCER DIAGNOSTICS AND THERAPY

EDITED BY: Wansong Chen, Xiaoli Wei and Jianhua Zhang

PUBLISHED IN: Frontiers in Chemistry, Frontiers in Nanotechnology and Frontiers in Bioengineering and Biotechnology

frontiers Research Topics

frontiers

ISSN 1664-8714
ISBN 978-2-88966-776-5
DOI 10.3389/978-2-88966-776-5

About Frontiers

Frontiers is more than just an open-access publisher of scholarly articles: it is a pioneering approach to the world of academia, radically improving the way scholarly research is managed. The grand vision of Frontiers is a world where all people have an equal opportunity to seek, share and generate knowledge. Frontiers provides immediate and permanent online open access to all its publications, but this alone is not enough to realize our grand goals.

Frontiers Journal Series

The Frontiers Journal Series is a multi-tier and interdisciplinary set of open-access, online journals, promising a paradigm shift from the current review, selection and dissemination processes in academic publishing. All Frontiers journals are driven by researchers for researchers; therefore, they constitute a service to the scholarly community. At the same time, the Frontiers Journal Series operates on a revolutionary invention, the tiered publishing system, initially addressing specific communities of scholars, and gradually climbing up to broader public understanding, thus serving the interests of the lay society, too.

Dedication to Quality

Each Frontiers article is a landmark of the highest quality, thanks to genuinely collaborative interactions between authors and review editors, who include some of the world's best academicians. Research must be certified by peers before entering a stream of knowledge that may eventually reach the public - and shape society; therefore, Frontiers only applies the most rigorous and unbiased reviews.
Frontiers revolutionizes research publishing by freely delivering the most outstanding research, evaluated with no bias from both the academic and social point of view. By applying the most advanced information technologies, Frontiers is catapulting scholarly publishing into a new generation.

What are Frontiers Research Topics?

Frontiers Research Topics are very popular trademarks of the Frontiers Journals Series: they are collections of at least ten articles, all centered on a particular subject. With their unique mix of varied contributions from Original Research to Review Articles, Frontiers Research Topics unify the most influential researchers, the latest key findings and historical advances in a hot research area! Find out more on how to host your own Frontiers Research Topic or contribute to one as an author by contacting the Frontiers Editorial Office: frontiersin.org/about/contact

FUNCTIONAL NANOMATERIALS FOR CANCER DIAGNOSTICS AND THERAPY

Topic Editors:
Wansong Chen, Central South University, China
Xiaoli Wei, University of California, San Diego, United States
Jianhua Zhang, Tianjin University, China

Citation: Chen, W., Wei, X., Zhang, J., eds. (2021). Functional Nanomaterials for Cancer Diagnostics and Therapy. Lausanne: Frontiers Media SA.
doi: 10.3389/978-2-88966-776-5

Table of Contents

frontiers in Chemistry

EDITORIAL
published: 24 March 2021
doi: 10.3389/fchem.2021.670410

Editorial: Functional Nanomaterials for Cancer Diagnostics and Therapy

Wansong Chen[1], *Jianhua Zhang*[2*] *and Xiaoli Wei*[3*]

[1] College of Chemistry and Chemical Engineering, Central South University, Changsha, China, [2] Department of Polymer Science and Engineering, School of Chemical Engineering and Technology, Tianjin University, Tianjin, China, [3] Department of Pharmacology, School of Basic Medical Sciences, Fudan University, Shanghai, China

Keywords: nanomaterials, diagnostics, drug delivery, bioimaging, cancer therapy

Editorial on the Research Topic

Functional Nanomaterials for Cancer Diagnostics and Therapy

Efficient cancer therapy has been the research focus in biomedicine field for decades. Available therapeutic modalities for cancer treatment in clinic include surgery, chemotherapy, and radiotherapy. Surgery is difficult to completely remove tumors from normal tissues, and residual tumor cells are readily to relapse and result in treatment failure. In this regard, chemotherapy and radiotherapy are usually required to eradicate residual tumor cells after tumor resection by surgery. However, both chemotherapy and radiotherapy are challenged by serious side effects because of their off-target damage to normal tissues. Moreover, tumor cells are likely to activate anti-apoptotic signaling pathways to resist treatment. Very recently, immunotherapy has been demonstrated an promising way in fabricating long-term antitumor immunity to fight against cancer recurrence and metastasis, but only present efficacy to a subset of patients. In light of the above mentioned issues, it is imperative to develop more efficient and safe strategies for cancer treatment.

The interdisciplinary research of material chemistry and biomedicine provides more opportunities to overcome these challenges. Enormous endeavors have been devoted in the past decades from the following aspects.

(1) To improve the efficacy of chemotherapy or radiotherapy, intelligent drug nanocarriers have been designed and constructed to increase drug retention in tumors. Drugs are released from nanocarriers in response to specific tumor microenvironment, such as low pH or high glutathione level. Moreover, external stimuli (i.e., light, ultrasound, or magnetic field) have also been employed for drug controlled release.

(2) Phototherapeutic platforms have been developed based on some semiconducting materials or photosensitive agents, which can generate local hyperthermia or reactive oxygen species (ROS) under light irradiation. Since visible light hardly penetrates human tissues, near infrared (NIR) light with much deeper tissue penetrating depth has been widely investigated for phototherapy in recent years. In addition to light, ultrasound with extraordinary tumor penetrability has also been employed for generating ROS in tumors, which is termed as sonodynamic therapy.

(3) Tumor therapy drugs have been combined with imaging agents, such as upconversion nanoparticles, quantum dots, or fluorescence dyes. Under the guidance of imaging agents, both tumor location and drug delivery process can be facilely monitored, providing possibilities to achieve personal medicine and tumor theranostics.

(4) Besides, some nanomaterials themselves can be designed with therapeutic functions, such as radioprotection, anti-inflammation, or immune activation for tumor vaccines.

In this topic, we present original research and review articles with focus on functional nanomaterials for cancer diagnostics and therapy. In the direction of functional nanocarriers,

OPEN ACCESS

Edited by:
Jie He,
University of Connecticut, United States

Reviewed by:
Shaoyi Zhang,
Colgate Palmolive, United States

****Correspondence:***
Jianhua Zhang
jhuazhang@tju.edu.cn
Xiaoli Wei
weixiaoli06@gmail.com

Specialty section:
This article was submitted to Nanoscience, a section of the journal Frontiers in Chemistry

Received: *21 February 2021*
Accepted: *01 March 2021*
Published: *24 March 2021*

Citation:
Chen W, Zhang J and Wei X (2021) Editorial: Functional Nanomaterials for Cancer Diagnostics and Therapy. Front. Chem. 9:670410. doi: 10.3389/fchem.2021.670410

Wang et al. reported a covalent organic framework nanomaterials as carriers for DOX loading, showing high drug loading capacity and pH-/redox-sensitive release in tumor cells. Howaili et al. synthesized a plasmonic nanogel composed of Au nanoparticles and polymer-based hydrogel nanoparticles. Such plasmonic nanogel was employed as drug carrier for curcumin delivery and dual pH-/photo-responsive release. In addition, Zhao et al. investigated the potential of black phosphorus quantum dots as carriers of Chinese herbal medicine for lymphoma therapy. Lin et al. synthesized a new kind of polymer nanocarriers with minimal cytotoxicity and high stability. The polymer nanocarriers improved antioxidant activity of curcumin, showing great potential as protection agent in caner radiotherapy. Gupta et al. developed solid lipid nanoparticles as carriers to improve the solubility, stability, and bioavailability of curcumin.

In the direction of phototherapy/sonodynamic therapy, Feng et al. developed a multifunctional nanosystem with bovine serum albumin as "mother ships" material. The nanosystem was demonstrated to be selectively accumulated within tumors, disrupt extracellular matrix for tumor penetration, and generate ROS to induce tumor cell apoptosis. This work offer a new avenue for improving photodynamic therapy via reprogramming tumor microenvironment. To improve tumor hypoxic environment, Huang et al. designed an oxygen-sufficient nanoplatform with polymer-perfluorocarbon nanoparticles as oxygen carriers. The nanoplatform not only improved the ROS generating efficiency of sonodynamic process, but also overcame tumor drug resistance to enhance therapeutic outcomes. As a Food and Drug Administration (FDA)-approved NIR photosensitizer, indocyanine green (ICG) has been widely used in oncology. Sevieri et al. summarized the applications and perspectives of ICG nanoparticles, offering insights for its further biomedical applications. Zhang et al. reviewed the progress of photodynamic therapy with internal light sources from the aspects of chemiluminescence, bioluminescence, and Cerenkov radiation, all of which circumvent the limitation of light penetration in body. Jia et al. coated Fe_3O_4 with mesoporous silica and polydopamine for drug delivery and synergistic photothermal/chemodynamic therapy.

In the direction of cancer diagnostics and theranostics, Yu et al. reviewed the recent progress of rare-earth-doped nanoparticles for tumor fluorescence imaging and theranostics in the second near infrared window (NIR-II, 1,000–1,700 nm). Hong et al. reported theranostic platform based on upconversion nanoparticles, which can accumulated in the mitochondria of tumor cells. Under NIR light irradiation, such nanoplatform emitted fluorescence signal for imaging-guidance and produced ROS for tumor killing. Tang et al. reviewed the advances of noble metal nanoclusters (Au and Ag) in biosensing, bioimaging, and cancer therapy.

Besides, Shang et al. studied antitumor activity and tumor-killing mechanism of zirconia nanoparticles (ZrO_2), providing a promising alternative to traditional chemotherapy drugs for tumor treatment. When camouflaged with platelet membrane (PLT), the obtained PLT@ZrO_2 nanoparticles successfully escaped from immune recognition and targeted tumor cells, thereby achieving prolonged blood circulation time and tumor targeting delivery Shang et al.. Seré et al. reported a nanovaccine based on ovalbumin-conjugated mesoporous silica nanoparticles, which was attractive as a replacement of dendritic cell-based vaccines.

We hope this Research Topic will provide researchers information to understand the advanced strategies of functional nanoplatforms in cancer diagnostics and therapy, inspiring new ideas for future research directions and research activities.

AUTHOR CONTRIBUTIONS

All authors listed have made a substantial, direct and intellectual contribution to the work, and approved it for publication.

FUNDING

This work was supported by the National Natural Science Foundation of China (No. 21807117) and Natural Science Foundation of Tianjin City (No. 19JCYBJC17200).

Conflict of Interest: The authors declare that the research was conducted in the absence of any commercial or financial relationships that could be construed as a potential conflict of interest.

frontiers in Chemistry

ORIGINAL RESEARCH
published: 05 December 2019
doi: 10.3389/fchem.2019.00853

Programmable Ce6 Delivery via Cyclopamine Based Tumor Microenvironment Modulating Nano-System for Enhanced Photodynamic Therapy in Breast Cancer

Chan Feng[1], Lv Chen[1], Yonglin Lu[1], Jie Liu[1], Shujing Liang[1], Yun Lin[1], Yongyong Li[2] and Chunyan Dong[1]**

[1] Cancer Center, Shanghai East Hospital, Tongji University, Shanghai, China, [2] The Institute for Biomedical Engineering & Nano Science (iNANO), School of Medicine, Tongji University, Shanghai, China

OPEN ACCESS

Edited by:
Wansong Chen,
Central South University, China

Reviewed by:
Na Kong,
Zhejiang University, China
Zhongmin Tang,
Shenzhen University, China

***Correspondence:**
Yongyong Li
yongyong_li@tongji.edu.cn
Chunyan Dong
cy_dong@tongji.edu.cn

Specialty section:
This article was submitted to Nanoscience, a section of the journal Frontiers in Chemistry

Received: *13 November 2019*
Accepted: *25 November 2019*
Published: *05 December 2019*

Citation:
Feng C, Chen L, Lu Y, Liu J, Liang S, Lin Y, Li Y and Dong C (2019) Programmable Ce6 Delivery via Cyclopamine Based Tumor Microenvironment Modulating Nano-System for Enhanced Photodynamic Therapy in Breast Cancer. Front. Chem. 7:853. doi: 10.3389/fchem.2019.00853

Photodynamic therapy (PDT) has shown great promise in breast cancer treatment. However, simplex target ligand modification or stimuli release cannot meet the requirement of effective drug delivery to solid tumor tissue. To overcome continuous bio-barriers existing in the tumor microenvironment, multi-stage response drug delivery was desirable. Herein, we developed a unique tumor microenvironment tailored nanoplatform for chlorin e6 (Ce6) delivery. We chose bovine serum albumin (BSA) as "mother ships" material for effective tumor periphery resident, cyclopamine (CYC) as extracellular matrix (ECM) inhibitor and synergistic anti-tumor agent, and diselenide containing amphiphilic hyaluronic acid-chlorin e6 polymers (HA-SeSe-Ce6) synthesized as "small bombs" for internal tissue destruction. The above three distinct function compositions were integrated into an independent CYC and HA-SeSe-Ce6 co-delivery albumin nano-system (ABN@HA-SeSe-Ce6/CYC). The obtained nano-system presents good biocompatible, long circulation and effective tumor accumulation. After entering tumor microenvironment, CYC gradually releases to disrupt the ECM barrier to open the way for further penetration of HA-SeSe-Ce6. Subsequently, targeted tumor cell internalization and intracellular redox response release of Ce6 would achieve. Moreover, CYC could also make up the deficiency of Ce6 in hypoxia area, owing to its anti-tumor effect. Improved therapeutic efficacy was verified in a breast cancer cell line and tumor-bearing mice model.

Keywords: chlorin e6, cyclopamine, photodynamic therapy, drug delivery, breast cancer

INTRODUCTION

Among various emerging therapies, photodynamic therapy (PDT) is a promising non-invasive therapeutic method for superficial tumors, such as breast cancer (Agostinis et al., 2011; Wang D. et al., 2018). One of the most widely used photosensitizers is chlorin e6 (Ce6) (Du et al., 2016; Feng et al., 2019). However, the poor water solubility of photosensitizers hinders their clinical application. In addition, off-target activation

of photosensitizers leads to serious side effects (Liu et al., 2017). Therefore, improved delivery of hydrophobic photosensitizers leveraging nanoscale system is desirable. In the past decades, although the various sophisticated chemical design and multi-functional nanoscale systems have developed, cancer nanomedicine still facing challenges for enhancing clinical benefits. Just target ligand modified and stimuli release no longer meet the requirement of effective drug delivery to solid tumor tissue. Despite nanoscale substances preferentially accumulate in tumor tissue than in normal tissue due to permeability and retention effect (EPR effect), abnormal tumor microenvironment with heterogeneous structure often leads to the perivascular area and tumor periphery resident of nanoparticles (Overchuk and Zheng, 2018). Therefore, the design of tumor microenvironment tailored multi-stage photosensitizers delivery is essential.

Due to the lack of mature vessels inside the tumor, it is unable to maintain adequate perfusion of internal tumor tissues (Niu et al., 2018). In addition, tightly packed tumor cells, dense extracellular matrix (ECM) and high interstitial fluid pressure, leading to growth-induced stress, act as biological barriers that further restrict nanoparticle infiltration into the tumor parenchyma after extravasation from vessels (Yang and Gao, 2017; Wang S. et al., 2018). For this dilemma, one of the promising strategies is reducing ECM to open the way for nanoparticles penetration. Cancer-associated fibroblasts (CAFs) play an indispensable role in the formation of ECM, owing to abnormal activation of Hedgehog (Hh) signaling pathway. This pathway is initiated by binding tumor cell-derived Hh ligands to patched 1 (Ptch 1) receptor in CAFs membrane, subsequently, the inhibition of smoothened (SMO) protein is relieved, which triggers activation of the glioma-associated oncogene transcription factor (Gli1-2), leading to downstream genes expression and abundant ECM production (Zhang et al., 2018). Cyclopamine (CYC), a kind of hydrophobic steroid alkaloid, can target the SMO receptor on cancer cells and CAFs to inhibit Hh signaling pathway (Che et al., 2013; Feng et al., 2018). Therefore, CYC is a superexcellent candidate to disrupt the ECM barrier in the tumor microenvironment, as well as an effective anticancer agent.

After collapsing the ECM barrier, further diffusion to deeper tumor sites and tumor intracellular smart drug release would be the other two indispensable drug delivery stage. For the former, it was reported that "Cluster Bomb" design could benefit for high-performance tumor suppression (Lei et al., 2017). That is, smaller components, which fall off from the nanoparticles stranded in the tumor periphery, will be easier to infiltrate to deeper tumor tissue. As for the latter stage, these smaller "bomb" components would be better to modify tumor target ligands for effective tumor cells internalization and equip with sensitive linkages for tumor intracellular triggered drug release. Hyaluronic acid (HA), a natural anionic hydrophilic polysaccharide targeting differentiation 44 (CD44) on the cancer cell membrane, is a promising target ligand candidate due to its desirable biocompatibility, biodegradability, non-immunogenicity, and easy functionalization (Choi et al., 2011; Xia et al., 2018a; Feng et al., 2019). In addition, the diselenide bond has particular advantages owing to its high sensitivity to redox condition and singlet oxygen ($^1O_2$), which makes PDT positive drug release theoretically possible (Xia et al., 2016, 2018b; Sun et al., 2017). Herein, a tumor microenvironment tailored multi-stage delivery system based on CYC loaded albumin nanoformulation and was designed for improved PDT therapy in breast cancer treatment (**Scheme 1**). In our previous study, CYC loaded bovine serum albumin (BSA) nanoparticles showed effective and enduring tumor tissue accumulation and extracellular retention which increase binding of CYC and SMO membrane receptors (Feng et al., 2018). Therefore, we chose BSA as "mother ships" material to load CYC and HA-SeSe-Ce6 via heat-mediate assembling to form co-delivery albumin nanosystem (ABN@HA-SeSe-Ce6/CYC). When nanosystem accumulates in the tumor, CYC will release to inhibit ECM barriers and exert a synergetic anti-cancer effect. Moreover, HA-SeSe-Ce6 as smaller "bomb" component will release and further infiltrate to deeper tumor tissue. In the redox condition of tumor intracellular or existence of $^1O_2$, diselenide bonds would cleave and lead to Ce6 release (Feng et al., 2019). The improved PDT anticancer effects via tumor microenvironment tailored multi-stage delivery was investigated in breast cancer cell line and breast cancer-bearing mice.

MATERIALS AND METHODS

Materials

Chlorin e6 was obtained from J&K Scientific, Ltd. Cyclopamine was obtained from Hitsan Biotechnology Co., Ltd. (Shanghai, China). Bovine serum albumin, 2-(N-morpholino) ethanesulfonic acid (MES), C4H12N2Se2·2HCl, EDC·HCl, and NHS were obtained from Sigma-Aldrich (Shanghai) Trading Co., Ltd. Hyaluronic acid was purchased from Ruixi biotechnology Co., Ltd.

Synthesis of HA-Sese-Ce6 Polymers

Five milligrams of HA and 2.5 mg C4H12N2Se2·2HCl were dispersed in 5 ml PBS (pH 7.4). Thirty microliters of EDC·HCl (50 mg/ml) and 20 μl NHS were added to above mixture and stirred at room temperature for 4 h. Ten milligrams of Ce6 was dispersed in 500 μl DMSO, then pipetted 225 μl Ce6 solution and added dropwise to above mixture liquid and stirred for another 4 h. The solution was collected and transferred to centrifugal ultrafiltration tube (10 kDa mol. Cutoff, Pall Corporation, USA) and centrifuged at 6,000 rpm for 15 min. free Ce6, HA, C4H12N2Se$_2$·2HCl, and PBS were removed by washing three times with HyPure water. Then, HA-sese-Ce6 solution was 10 times concentrated.

Preparation of ABN@HA-Sese-Ce6/CYC NPs

Two milligrams of SDS was added to the above HA-sese-Ce6 solution and stirred for 1 h. Two milligrams or milliliters of BSA solution was prepared by adding 5 mg BSA powder to 2.5 ml MES buffer (50 mM, pH = 6.0). Two hundred microliters of CYC ethanol solution (10 mg/ml) and 200 μl HA-sese-Ce6 solution (containing Ce6 2 mg) was slowly added to the BSA solution, respectively. Subsequently, the mixture solution was heated in

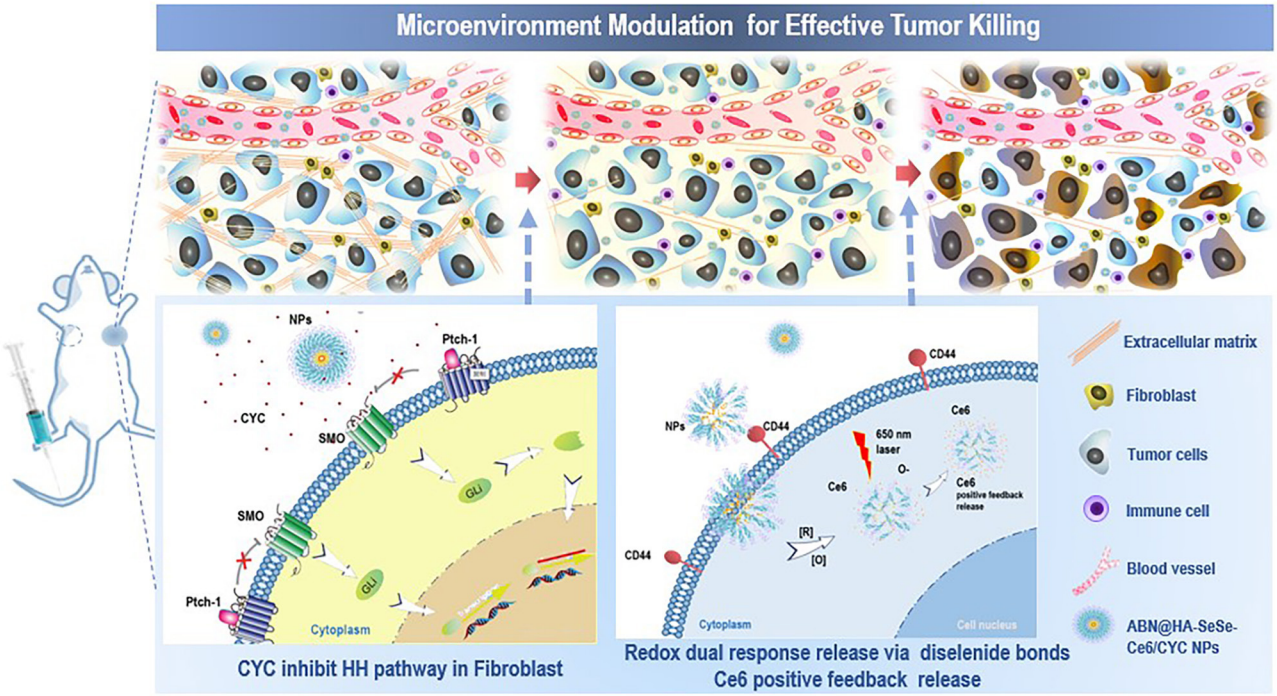

SCHEME 1 | Schematic illustration of tumor microenvironment modulation effect of ABN@HA-SeSe-Ce6/CYC NPs for enhanced PDT. After intravenous injection, NPs will accumulate in tumor periphery and release CYC to disrupt ECM via inhibiting HH pathway in CAFs. Due to the alleviation of solid stress, gradually dissociated ABN@HA-SeSe-Ce6/CYC NPs and smaller HA-SeSe-Ce6 molecules released from the main body will further infiltrate to deeper tumor tissue. Then after targeted tumor cell internalization via recognization of CD44+with HA, diselenide linkages of HA-SeSe-Ce6 molecules will further cleavage to release Ce6 in intracellular redox condition or singlet oxygen ($^1O_2$) existence. In addition, dead tumor cells lead to more immune cells infiltration.

a silicone oil bath at 70°C and stirred at 800 rpm for 50 s. and the assembly process was stopped by immersing in ice water immediately. The solution was transferred to 100 kda mol. Cutoff centrifugal ultrafiltration tube and centrifuged at 4,500 rpm at 25°C for 20 min. It was washed trice with HyPure water to remove MES, free CYC, and free Ce6.

Characterization of Nanoparticles

The morphology of nanoparticles was measured by high-resolution transmission electron microscopy (FEI Tccnai G2 F20 S-Twin). Twenty microliters solution of nanoparticles (2 mg/ml) was dripped on carbon-coated copper grid, after 1 min, excess liquid was removed by filter paper. Then add 10 μl 1% uranyl acetate for another 30 s. The TEM samples were dried in the shade at room temperature. The size of nanoparticles was detected by Nano-ZS 90 Nanosizer (Malvern Instruments, UK). Ultraviolet-visible (UV) spectra was recorded by UV spectrophotometer (Varian).

In vitro Drug Release Behavior of ABN@HA-Sese-Ce6/CYC NPs

Two milliliters solution of nanoparticles (containing 5 mg CYC) in dialysis tube was immerged in 50 ml PBS buffer. At predetermined time points, 1 ml of the buffer solution was taken out to measure CYC concentration, and then add 1 ml fresh PBS buffer to keep the volume of solution. The CYC content was measured by LC-MS (the mobile phase: acetonitrile: 0.1% formic acid 80:20 solution, flow rate 0.35 ml/min). Ten milliliters solution of nanoparticles (containing 6 mg Ce6) was individually transferred to 5 dialysis tubes, and then immerged in 50 ml PBS, 10 mM GSH, 100 mM GSH, 1 mM H_2O_2, 10 mM H_2O_2 solution, respectively. At predetermined time points, 1 ml buffer solution was taken out to measure Ce6 concentration via UV spectrophotometer at 404 nm. Two milliliters solution of nanoparticles (containing 1 mg Ce6) was exposed to 650 nm (20 mW/cm^2) for 10 min, then immerged in PBS solution to measure Ce6 concentration at different time points.

Singlet Oxygen ($^1O_2$) Measurement

Take out the buffer solution from groups treated with 10 mM GSH and 10 mM H_2O_2 described in method 2.5, and add $^1O_2$ detecting reagent SOSG to the solution (final concentration: 1 μM). Then, the above solutions were exposed to 650 nm laser for 90, 180, 270, 360, and 450 s. The fluorescence was measured by Hitachi F2500 luminescence spectrometer (emission spectra: 490–700 nm, excitation wavelength: 488 nm).

In vitro Cytotoxicity Test

In 37°C incubator with 5% carbon dioxide, the mouse breast cancer cell line 4T1 cells were cultured in DMEM medium containing 10% FBS. 1×10^4 cells/well 4T1 cells

were seeded in 96 wells plate and incubated for 12 h. Then add free Ce6, ABN@HA-sese-Ce6 and ABN@HA-sese-Ce6/CYC solutions containing different Ce6 concentrations (0.25, 0.5, 1.2 μM), respectively. The same volume of serum-free DMEM was added as control treatment. The half of above cells were exposed to 650 nm laser (20 mW/cm^2) for 5 min, while the other cells were still cultured in the dark. Twenty-four hours later, 10 μl CCK-8 solution was added to every well. After 3 h incubation, the absorbance of each well was detected by the plate reader at 450 nm.

Targeted Cellular Uptake Assay

1×10^5 cells/ well 4T1 cells were seeded in confocal dishes. After 24 incubation, cells were treated individually with free Ce6 and ABN@HA-sese-Ce6/CYC for 2, 6, and 10 h. Remove the medium of each well and wash with PBS for three times. Then, cells were stained with DAPI for 15 min and washed with PBS. The prepared samples were detected by confocal laser scanning microscope (Leica TCS SP5II, Germany).

Tumor Models

The animal experiments in this study were carried out according to Tongji University Animal Ethics Guidelines. The animal experiment protocol was approved by Tongji University Animal Ethics Committee.

Five-week-old female BALA/c mice were injected with 5×10^5 4T1 cells (subcutaneous route). When tumor tissue reached ∼500 mm^3, tumor tissues were excised and cut into 1 mm^3 tissue blocks. The tissue block was planted in the left mammary fat pad of 5-week-old female BALA/c mice. When the tumor growth large enough, tumor models were further treated.

In vivo Fluorescence Imaging

The breast cancer bearing mice were pretreated with tail vein injection of ABN@CYC (CYC 20 mg/kg) for three time every 2 days. Then the pretreated mice were injected with ABN@HA-sese-Ce6/CYC NPs. At the same time, the mice without pretreatment were inject free Ce6 and ABN@HA-sese-Ce6 (equivalent Ce6 concentration) as control. At predetermined time points, *in vivo* fluorescence imaging was carried out by a Night OWL LB 983 *in vivo* imaging system.

Photodynamic Therapy in Animals

Plant tumor tissue block in the left mammary fat pad of 5-week-old female BALA/c mice to build animal model. After 7 days, mice were treated individually with PBS, free CYC, free Ce6, ABN@HA-sese-Ce6 and ABN@HA-sese-Ce6/CYC NPs for 7 times (CYC 20 mg/kg, Ce6 2.5 mg/kg, every 2 days). Began with third injection, the mice were exposed to a 650 nm laser (20 mW/cm^2) for 30 min under anesthesia after each injection. The survival time of five groups of mice was recorded. Mice with tumors exceeding ethical requirements (>2 cm) were euthanized (equivalent to endpoint of observation), and the animals were euthanized using carbon dioxide asphyxia. Excised tumor weight of every group was also measured. Tumor volume and mice body weight were recorded every 2 days, the calculation formula was as following:

$$Tumor\ volume = (Length \times Width \times Width)/2$$

The major organs (heart, liver, spleen, lung, and kidney) and tumors were excised from mice of different groups. The collected tissues were immerged in 4% paraformaldehyde overnight. Then the tissues were dehydrated in graded ethanol solution and embedded in paraffin. The paraffin sections were prepared for hematoxylin and eosin (HE) and terminal deoxynucleotidyl transferase dUTP nick end labeling (TUNEL) staining. In addition, tumor microenvironment fibronectin and immune cells distribution were performed by immunofluorescence through tumor tissue frozen section, and detected by confocal laser imaging microscope.

Statistical Analysis

All values of this study are presented as mean ± SD. The statistical significance of the data was determined by one-way single factorial analysis of variance (ANOVA). Significant differences are expressed as $^*p \leq 0.05$, $^{**} \leq 0.01$, $^{***} \leq 0.001$.

RESULTS AND DISCUSSION

Nanoparticles Synthetic Strategy and Characterization

The ABN@HA-sese-Ce6/CYC delivery system is consist of three functional parts. Firstly, BSA was chosen as main drug carrier material to integrate every part via transient heat triggered assembling. Then, hydrophobic small molecule CYC acted as tumor microenvironment modulator. At last, we assign the diselenide containing amphiphilic hyaluronic acid-chlorin e6 polymers (HA-SeSe-Ce6) as redox response "small bomb" of delivery system. To avoid its self-assembling, we pretreated HA-SeSe-Ce6 with some SDS to make it stretch. The assembling process is driven by the BSA hydrophobic sites exposure and hydrophobic nucleation effects of hydrophobic agents (Ce6 and CYC). The hydrophobic interaction finally promotes to the formation of ABN@HA-sese-Ce6/CYC with compact assembly. The strategy was shown in **Scheme 2**. The ABN@HA-sese-Ce6 was prepared as control. The morphology of ABN@HA-sese-Ce6/CYC NPs and ABN@HA-sese-Ce6 NPs were measured by transmission electron microscopy (TEM). As shown in **Figure 1**, nanoparticles are a spherical shape with a narrow distribution. The average size of ABN@HA-sese-Ce6/CYC NPs was 35 nm, slightly larger than ABN@HA-sese-Ce6 NPs (28 nm).

Drug Release Behavior of ABN@HA-Sese-Ce6/CYC NPs *in vitro*

The CYC release behavior was measured in PBS (pH 7.4) at 37°C. As shown in **Figure 2A**, the CYC cumulative release ratio increased in the first 8 h and reached about 30%, then slowed down. Due to the existence of diselenide bonds between the Ce6

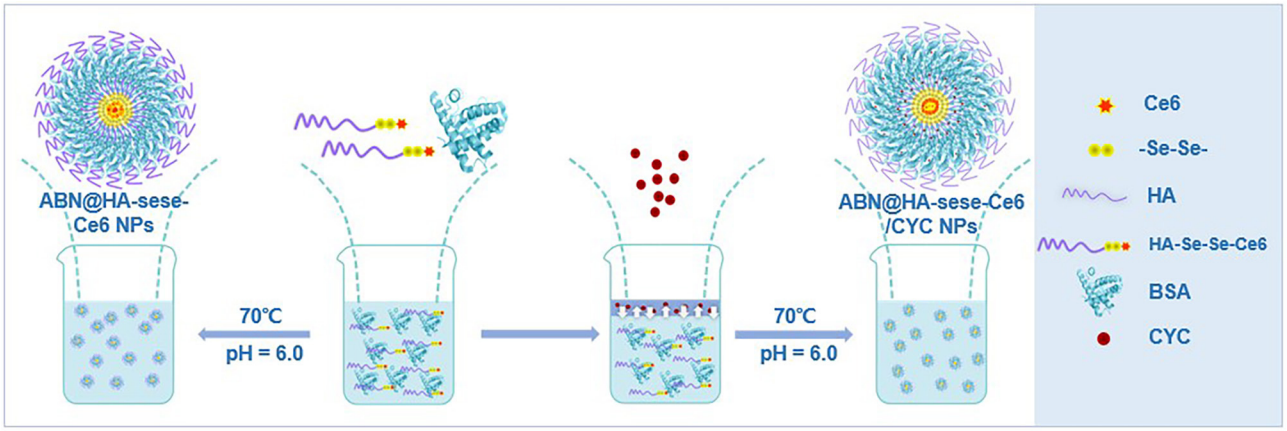

SCHEME 2 | The schematic process of ABN@HA-sese-Ce6/CYC NPs and ABN@HA-sese-Ce6 NPs preparation. HA-sese-Ce6 molecules and BSA were added to MES solution and mix well. Then slowly add CYC ethanol solution to the mixture to form temporary binary solution. Subsequently, the hydrophobic sites on BSA was exposed at 70°C, which facilitate the process of assembling with CYC and HA-sese-Ce6 and form compact ABN@HA-sese-Ce6/CYC NPs. Besides, ABN@HA-sese-Ce6 NPs can be prepared in same way via heating HA-sese-Ce6 molecules and BSA mixture solution for 50 s.

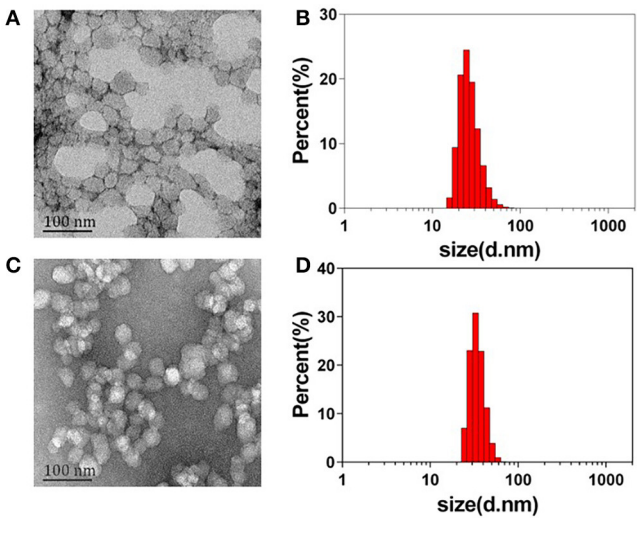

FIGURE 1 | The morphology and size distribution of nanoparticles. **(A)** The TEM image of ABN@HA-sese-Ce6 NPs; **(B)** Hydrate particle size of ABN@HA-sese-Ce6 NPs; **(C)** TEM image of ABN@HA-sese-Ce6/CYC NPs; **(D)** Hydrate particle size of ABN@HA-sese-Ce6/CYC NPs.

and HA, it was easier for CYC to release from NPs than Ce6 in PBS, which provided the benefit for CYC to inhibit EMC first. As shown in **Figure 2B**, there was a small quantity of Ce6 release in PBS solution, which could be explained by mixed free Ce6 physical adsorption. In theory, diselenide bonds will cleavage to promote Ce6 release while nanoparticles exposed in redox conditions. To investigate the redox-sensitive release of Ce6, we measured Ce6 release behavior in GSH and H_2O_2 solutions with different concentration at 37°C. As shown in **Figure 2B**, Ce6 cumulative release presented GSH concentration-dependent. In 100 mM GSH group, the higher plateau of Ce6 cumulative release (44%) was observed in 12 h, while Ce6 cumulative release only reached 28% in 12 h in 10 mM GSH group. Overall, GSH treated group showed the obviously increased release of Ce6, compared with the PBS group.

Similar to GSH treated group, Ce6 cumulative release also presented H_2O_2 concentration-dependent increase. The results of H_2O_2 treated group were shown in **Figure 2D**, in 10 mM H_2O_2 group, Ce6 cumulative release reached a plateau at 55% in 12 h, while 1 mM H_2O_2 group reached a plateau at 43% in 12 h. In addition, it was found that more Ce6 cumulative release treated with H_2O_2 than GSH, suggesting more sensitivity of diselenide in oxidizing condition. $^1O_2$ would be generated from Ce6 under 650 nm laser, which theoretically breaks part of diselenide bonds to further promote Ce6 release. Therefore, we also investigate the sensitivity of NPs when they exposed to the laser. The results in **Figure 2C** verified it, and we can find that more Ce6 release in 650 nm laser-treated group, compared with the control group. Finally, we further measured $^1O_2$ generation of released Ce6 in GSH and H_2O_2 treated group respectively to indirectly confirm redox triggered Ce6 release (**Figures 2E,F**).

In vitro Cytotoxicity and Targeted Cellular Uptake Assay

We evaluated the *in vitro* phototoxicity and dark cytotoxicity of NPs in mice breast cancer 4T1 cell line. As shown in **Figure 3A**, ABN@HA-sese-Ce6 NPs had better concentration-dependent phototoxicity than free Ce6, while ABN@HA-sese-Ce6/CYC had the most phototoxicity against 4T1 cell line with <10% cell viability at low Ce6 concentration (2 μM). In the condition without laser exposure, ABN@HA-sese-Ce6 and free ce6 exhibited no significant toxicity (**Figure 3B**). As expected, ABN@HA-sese-Ce6/CYC NPs was effective at all concentrations, the concentration-dependent dark toxicity was owing to CYC (the CYC concentration was 10 times of Ce6

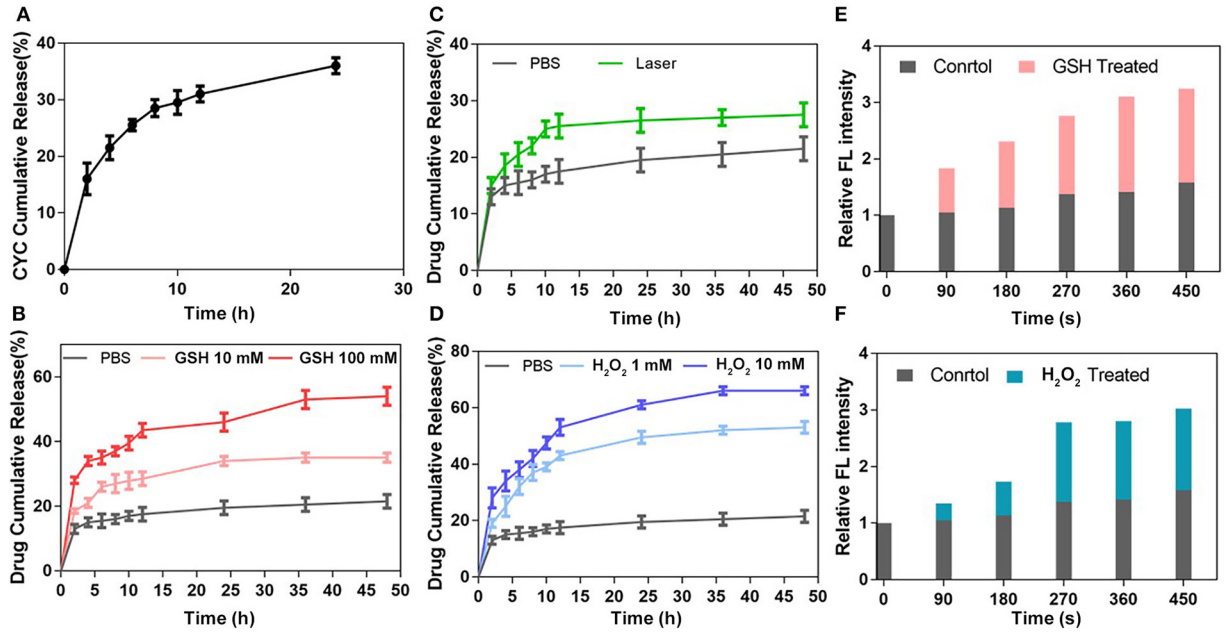

FIGURE 2 | Drug release behavior of ABN@HA-sese-Ce6/CYC NPs. **(A)** The Ce6 release of ABN@HA-sese-Ce6/CYC NPs in PBS, 10 mM GSH, 100 Mm GSH, respectively. **(B)** The Ce6 release of ABN@HA-sese-Ce6/CYC NPs in PBS, 1 mM H_2O_2, 10 mM H_2O_2. **(C)** The Ce6 release of ABN@HA-sese-Ce6/CYC NPs when treated with 650 nm laser (20 mW/cm^2). Without the laser treatment group as a control. **(D)** The CYC release of ABN@HA-sese-Ce6/CYC NPs in PBS. **(E)** Singlet oxygen generated by the released Ce6 of ABN@HA-sese-Ce6/CYC NPs in 10 mM GSH treated group when exposed to 650 nm laser (20 mW/cm^2). PBS group as a control. **(F)** Singlet oxygen generated by the released Ce6 of ABN@HA-sese-Ce6/CYC NPs in 1 mM H_2O_2 treated group when exposed to 650 nm laser (20 mW/cm^2). PBS group as a control.

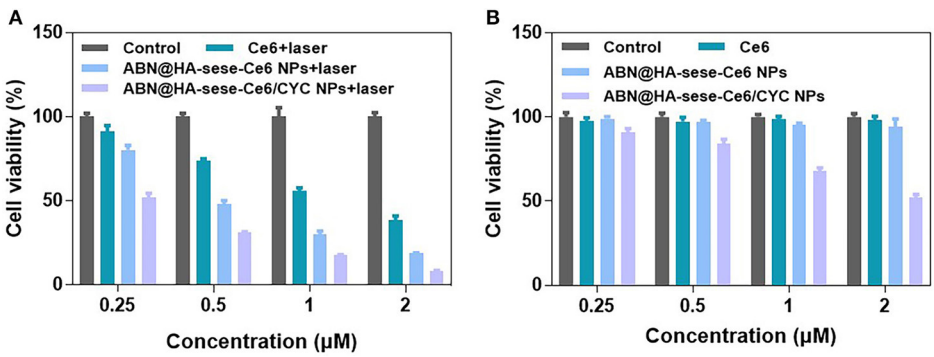

FIGURE 3 | Cytotoxicity assay in 4T1 breast cancer cells. **(A)** Phototoxicity of Ce6, BSA@HA-sese-Ce6, and BSA@HA-sese-Ce6@CYC (equivalent concentration 0.25–2 μM Ce6). Fresh DMEM medium with laser as a control group; **(B)** Dark toxicity of above-treated groups. Fresh DMEM medium as a control group.

concentration). Therefore, HH pathway inhibitor CYC provided complementation in cancer inhibition.

To further confirm the targeted anti-cancer effect, we investigate the targeting cancer internalization of NPs by CLSM. 4T1 cells were seeded in confocal dishes and treated with free Ce6 and ABN@HA-sese-Ce6/CYC NPs, respectively. After 2, 6, 10 h, cells were stained with DAPI and observed by CLSM. As shown in **Figure 4**, the cells treated with ABN@HA-sese-Ce6/CYC NPs exhibited stronger fluorescence than free Ce6 treated group in every time point, especially in 6 h (**Figures 4C,D**). These results verified the targeting effect of HA in CD44+ overexpressed 4T1 cell line.

In vivo Tumor Accumulation of ABN@HA-Sese-Ce6/CYC NPs

To investigate the CYC effect for improving tumor accumulation, the breast cancer-bearing mice were pretreated with ABN@CYC for 3 times every 2 days. Then the pretreated mice were injected via tail vein with ABN@HA-sese-Ce6/CYC NPs. At the same time, 4T1 breast cancer-bearing mice without pretreatment were injected with free Ce6 and ABN@HA-sese-Ce6 (equivalent Ce6 concentration) as control. At 1, 2, 4, 6 h after injection, *in vivo* fluorescence imaging was performed. In free Ce6 group, fluorescence signal was observed in part of tumor in fist 1 h, meanwhile, the lung, liver, kidney,

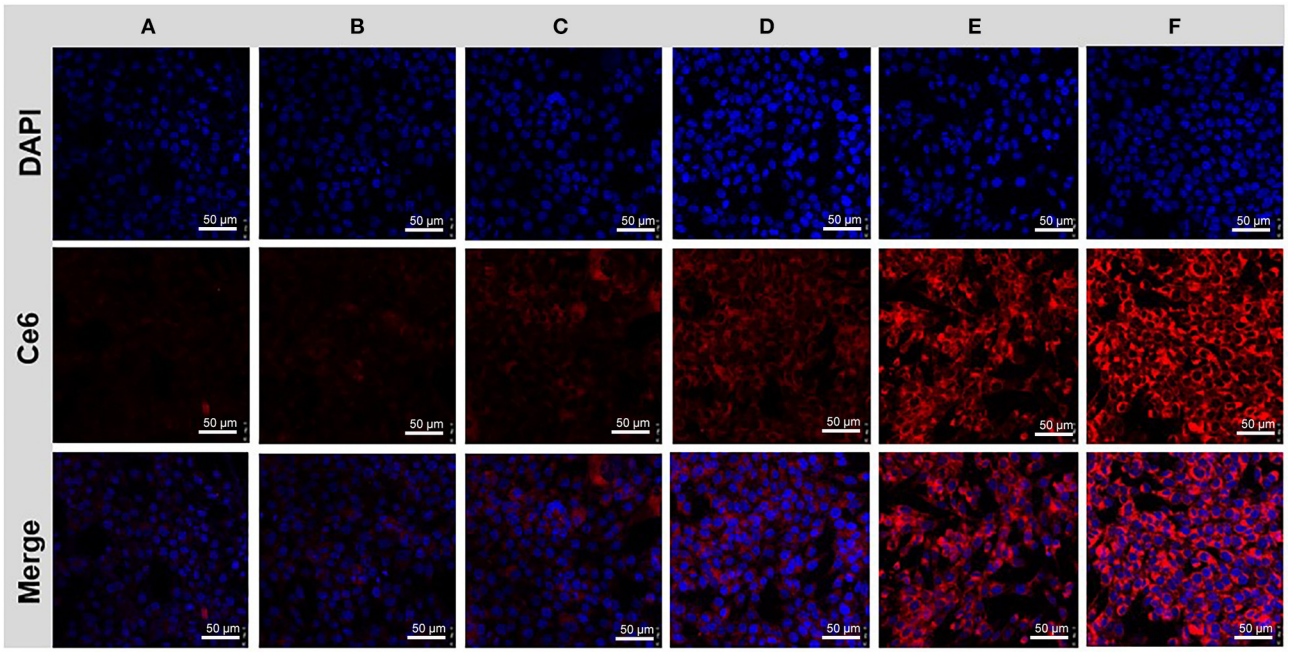

FIGURE 4 | Cancer cell uptake assay. Cells treated with free Ce6 for 2 h **(A)**, 6 h **(C)**, 10 h **(E)**; and BSA@HA-sese-Ce6@CYC for 2 h **(B)**, 6 h **(D)**, 10 h **(F)**.

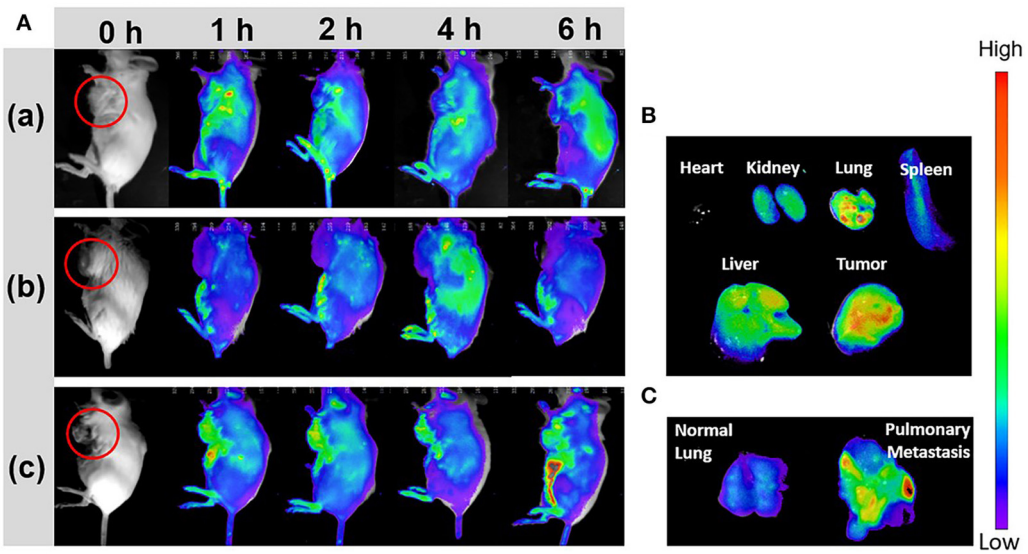

FIGURE 5 | *In vivo* fluorescence imaging. **(A)** 4T1 breast cancer bearing mice were imaged in 1, 2, 4, 6 h after i.v. injection with free Ce6 (a), ABN@Ce6 NPs (b), and ABN@HA-sese-Ce6/CYC NPs (c). **(B)** Florescence images of excised heart, kidney, lung, spleen, liver, and tumor in ABN@HA-sese-Ce6/CYC NPs treated group. **(C)** Florescence images of normal lung and pulmonary metastasis after injection with ABN@HA-sese-Ce6/CYC NPs.

and bladder accumulations were also obvious (**Figure 5A**a). After 1 h, the fluorescence in tumor tissue was weakened and others organ accumulation was enhanced. In ABN@HA-sese-Ce6 group, there was no obvious tumor accumulation until 4 h, and the fluorescence was just limited to peripheral area of tumor (**Figure 5A**b). As shown in **Figure 5A**c, the most strong and enduring tumor fluorescence signal was exhibited in ABN@HA-sese-ce6/CYC NPs treatment group, compared with ABN@HA-sese-Ce6 and free Ce6 group without pretreatment. The results confirmed the significant effect of CYC for enhancing tumor accumulation. Moreover, we also excised heart, kidney, lung, spleen, liver, and tumor from the

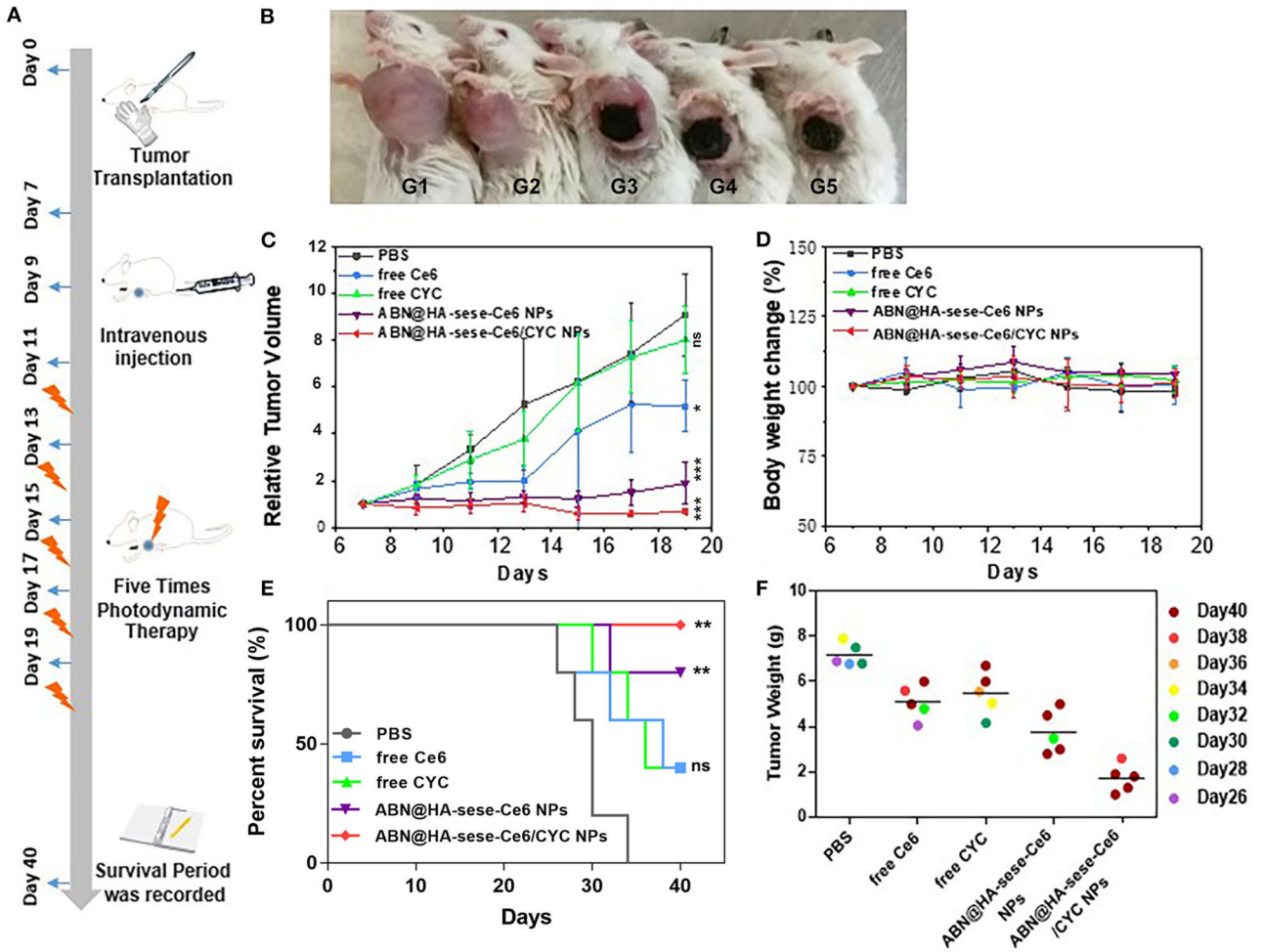

FIGURE 6 | Anti-tumor effects in breast cancer bearing mice model. **(A)** Schematic illustration of animal experiments. **(B)** Photos of tumor bearing mice in different treatment group (from left to right: PBS, free CYC, free Ce6, ABN@HA-sese-Ce6 NPs, ABN@HA-sese-Ce6/CYC NPs treatment group). **(C)** Tumor volume curve of mice treated with PBS, free Ce6, free CYC, ABN@HA-sese-Ce6 NPs, ABN@HA-sese-Ce6/CYC NPs ($n = 5$). The data are mean ± SD, $^{*}p < 0.05$, $^{**} < 0.01$, $^{***} < 0.001$ vs. PBS group. **(D)** Body weight change curve of mice in above groups. **(E)** The survival curve of mice in different groups. $^{*}p < 0.05$, $^{**} < 0.01$, $^{***} < 0.001$ vs. PBS group ($n = 5$). **(F)** Excised tumor weight of mice in above treatment groups when natural death or on Day 40 (endpoint).

mouse at 6 h in ABN@HA-sese-ce6/CYC NPs group. As shown in **Figure 5B**, the strong fluorescence was observed in tumor and liver, suggesting significant targeted tumor accumulation and liver clearance. Besides, accumulation in pulmonary metastasis was also remarkable. After ABN@HA-sese-ce6/CYC treatment, it was found that stronger fluorescence accumulation in pulmonary metastasis than normal lung (**Figure 5C**).

In vivo Anti-tumor Effects and ECM Modulation Evaluation

In vivo anti-cancer therapeutic experiment was carried on in the 4T1 orthotopic mammary fat pad tumor bearing mice. As schematic illustration shown in **Figure 6A**, we termed the day when we planted the tumor blocks in mice as Day 0. From Day 7 to Day 19, tumor bearing mice were treated with PBS, free CYC, free Ce6, ABN@HA-sese-Ce6, and ABN@HA-sese-Ce6/CYC NPs for 7 times, respectively. From Day 11 to Day 19, mice were exposed to 650 nm laser for 30 min after every injection (20 mW/cm^2, at 1 h after injection via tail vein).

As shown in **Figures 6B,C**, there was a remarkable difference between different treated groups. Compared with PBS control group, free CYC group exhibited minimal anti-tumor effect, free Ce6 showed much more remarkable anti-tumor effect. By contrast, ABN@HA-sese-Ce6 and ABN@HA-sese-Ce6/CYC NPs had strong anti-tumor effect, especially ABN@HA-sese-Ce6/CYC NPs reduced the tumor volume obviously. Besides, remarkable necrosis and escharosis were observed in three Ce6 treated groups (**Figure 6B**). Consistent with tumor volume change curve, the tumor weight of ABN@HA-sese-Ce6/CYC NPs treated group were also lightest among all groups (**Figure 6F**).

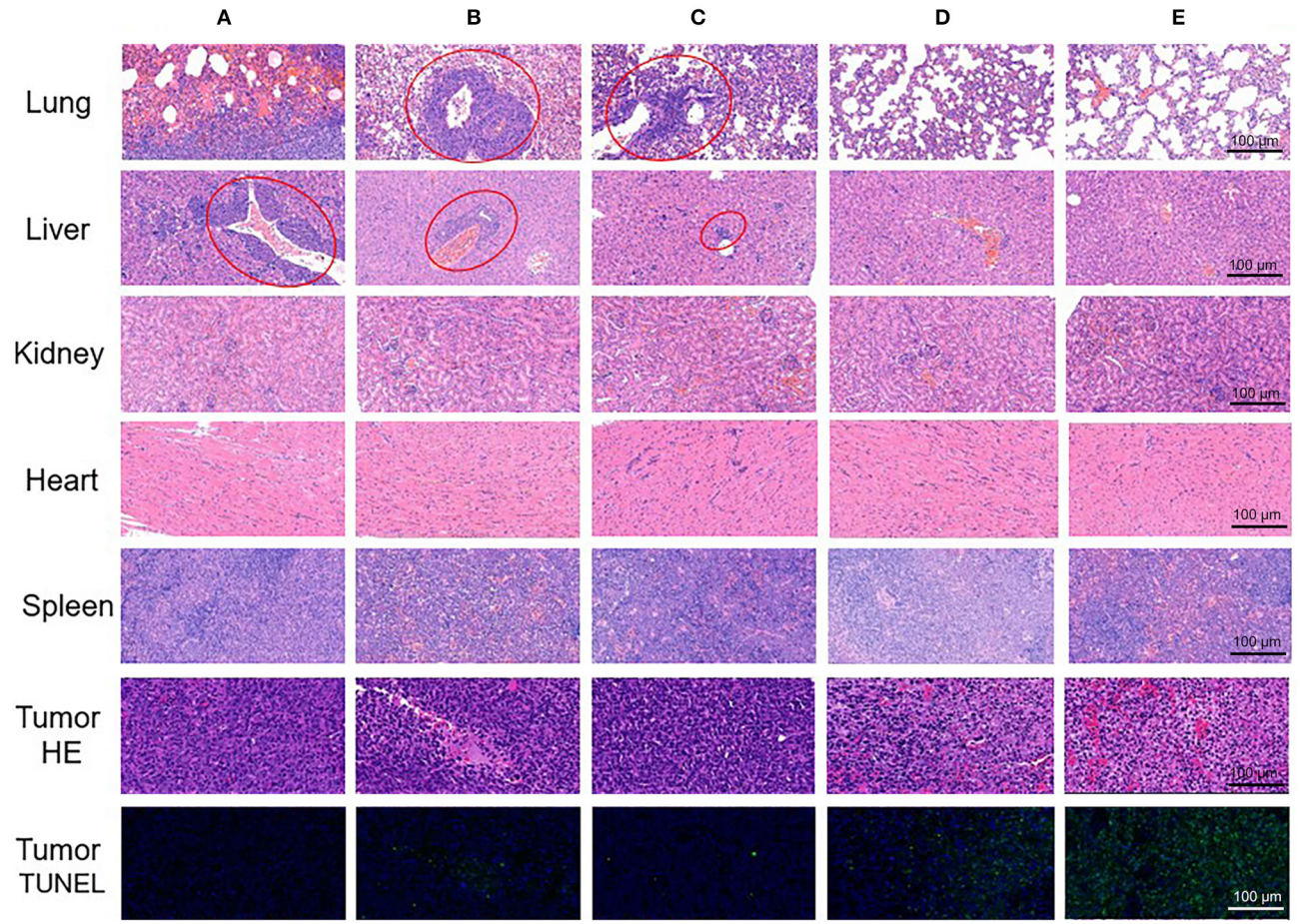

FIGURE 7 | The pathological slices of excised tumor and organs (lung, liver, kidney, heart, spleen) in control group **(A)**, free Ce6 group **(B)**, free CYC group **(C)**, ABN@HA-sese-Ce6 NPs group **(D)**, and ABN@HA-sese-Ce6/CYC NPs group **(E)**. Red circles represent tumor metastasis.

Moreover, survival period of mice was recorded until Day 40, and the mice of ABN@HA-sese-Ce6/CYC NPs were all survival (**Figure 6E**). During the process of therapy, there was no significant body weight change of mice in every treatment group (**Figure 6D**).

To further confirm anti-tumor and metastasis inhibition effects in histological level, we excised tumors and organs from treated mice, and prepared pathological slices. As TUNEL staining and HE staining of tumors shown in **Figure 7**, the most numbers of necrotic and apoptosis cells were found in ABN@HA-sese-Ce6/CYC treated group, which was consistent with above animal experiment results. Besides, it's worth noting that obvious liver metastasis and pulmonary consolidation due to tumor metastasis can be observed, except ABN@HA-sese-Ce6 and ABN@HA-sese-Ce6/CYC group. Compared with ABN@HA-sese-Ce6 group with scattered metastasis focuses, there was no significant metastasis found in ABN@HA-sese-Ce6/CYC group, suggesting the good metastasis inhibition effect of ABN@HA-sese-Ce6/CYC NPs.

Moreover, the ECM modulation effect was also investigated. We excised tumor tissues from the mice (PBS, free CYC, ABN@HA-sese-Ce6/CYC treated groups), and prepared tissue sections. The Fibronectin of tumor tissue was label by red fluorescence. Compared with PBS control group, weaken red fluorescence was observed in free CYC and ABN@HA-sese-Ce6/CYC treated groups, while the ABN@HA-sese-Ce6/CYC group exhibited the weakest fibronectin fluorescence (**Figure 8**). It was confirmed that CYC can inhibit the fibronectin expression in tumor tissues, and ABN@HA-sese-Ce6/CYC improve the effects of CYC in some degree.

CONCLUSION

In this study, we developed a programmable Ce6 delivery nano-system to promote PDT therapy. Redox response, laser triggered Ce6 release and tumor cells targeted internalization was confirmed *in vitro*. Improved tumor accumulation via EMC inhibition of ABN@HA-sese-Ce6/CYC was confirmed in 4T1 tumor bearing mice. Moreover, enhanced anti-tumor effect, obvious metastasis inhibition as well as extended survival period

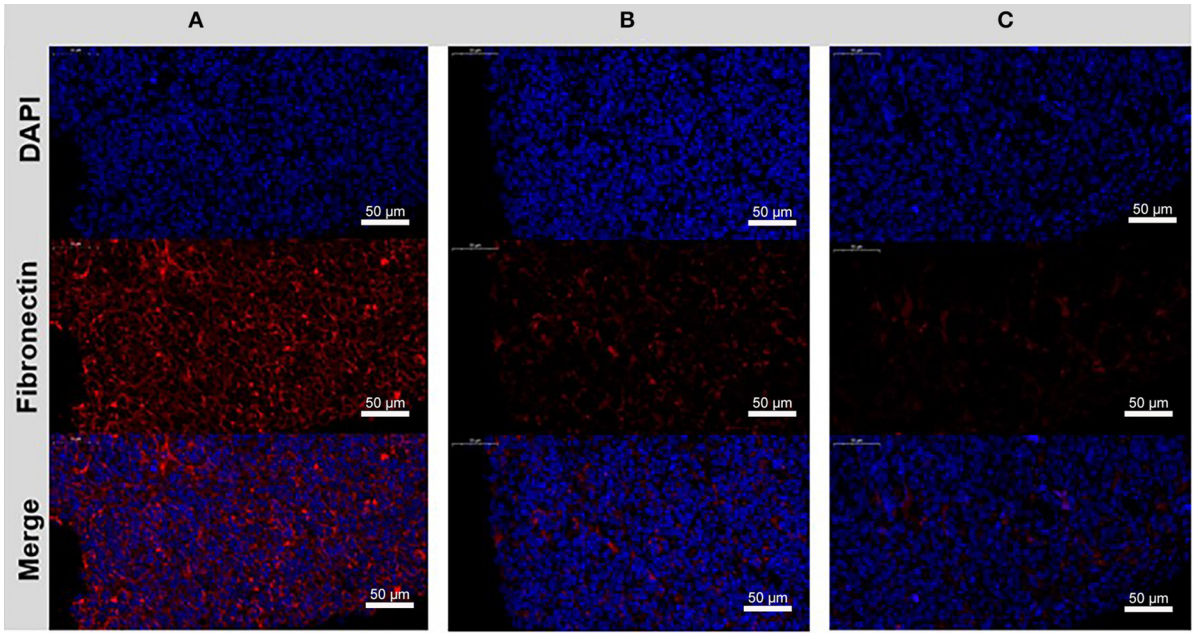

FIGURE 8 | The disrupting effect of CYC treatment to fibronectin in the tumor ECM. Immunofluorescence images of control group **(A)**, free CYC treatment group **(B)**, ABN@HA-sese-Ce6/CYC NPs treatment group **(C)** after 4 times i.v. injection. Blue, nuclei. Red, Fibronectin.

were observed in animal experiments. Therefore, this Ce6 delivery nano-system with improved tumor targeted delivery via tumor microenvironment modulation, smart drug release and promoted therapeutic efficacy, which provided a promising drug delivery strategy for overcome continuous bio-barriers in anti-tumor delivery.

DATA AVAILABILITY STATEMENT

All datasets generated for this study are included in the article/supplementary material.

ETHICS STATEMENT

The animal study was reviewed and approved by Tongji University Animal Ethics Guidelines.

AUTHOR CONTRIBUTIONS

CF, CD, and YLi designed the experiments. CF, LC, YLu, and JL carried out the experiments. SL and YLin helped analyzing the experimental results. CF wrote the manuscript.

FUNDING

This work was supported by National Natural Science Foundation of China Regional Project (81860547), National Natural Science Foundation of China Project (81573008), Key Cross-cutting Projects of Central Universities (kx0150720173382), Pilot Talent Training Program of Shanghai East Hospital (No. 201701), Research project of Shanghai Association for Science and Technology (16441901004), and Pudong new area Health and Family Planning Committee Joint Project (PW2017D-10).

REFERENCES

Agostinis, P., Berg, K., Cengel, K. A., Foster, T. H., Girotti, A. W., Gollnick, S. O., et al. (2011). Photodynamic therapy of cancer: an update. *CA Cancer J. Clin.* 61, 250–281. doi: 10.3322/caac.20114

Che, J., Zhang, F. Z., Zhao, C. Q., Hu, X. D., and Fan, S. J. (2013). Cyclopamine is a novel hedgehog signaling inhibitor with significant anti-proliferative, anti-invasive and anti-estrogenic potency in human breast cancer cells. *Oncol. Lett.* 5, 1417–1421. doi: 10.3892/ol.2013.1195

Choi, K. Y., Yoon, H. Y., Kim, J.-H., Bae, S. M., Park, R.-W., Kang, Y. M., et al. (2011). Smart nanocarrier based on PEGylated hyaluronic acid for cancer therapy. *ACS Nano* 5, 8591–8599. doi: 10.1021/nn202070n

Du, D., Wang, K., Wen, Y., Li, Y., and Li, Y. Y. (2016). Photodynamic graphene quantum dot: reduction condition regulated photoactivity and size dependent efficacy. *ACS Appl. Mater. Interfaces* 8, 3287–3294. doi: 10.1021/acsami.5b11154

Feng, C., Wang, K., Lin, Y., Song, Z., Lu, Y., Liu, J., et al. (2018). Extracellular retention of a cyclopamine nanoformulation leveraging larger size and more negative charge for improved breast cancer treatment. *J. Mater. Chem. B* 6, 1834–1843. doi: 10.1039/C7TB02777J

Feng, C., Zhu, D., Chen, L., Lu, Y., Liu, J., Kim, N. Y., et al. (2019). Targeted delivery of chlorin e6 via redox sensitive diselenide-containing micelles for improved photodynamic therapy in cluster of differentiation 44-Overexpressing breast Cancer. *Front Pharmacol.* 10:369. doi: 10.3389/fphar.2019.00369

Lei, Q., Wang, S.-B., Hu, J.-J., Lin, Y.-X., Zhu, C.-H., Rong, L., et al. (2017). Stimuli-responsive "Cluster Bomb" for programmed tumor therapy. *ACS Nano* 11, 7201–7214. doi: 10.1021/acsnano.7b03088

Liu, Y., Ma, K., Jiao, T., Xing, R., Shen, G., and Yan, X. (2017). Water-insoluble photosensitizer nanocolloids stabilized by supramolecular interfacial assembly towards photodynamic therapy. *Sci. Rep.* 7:42978. doi: 10.1038/srep42978

Niu, Y., Zhu, J., Li, Y., Shi, H., Gong, Y., Li, R., et al. (2018). Size shrinkable drug delivery nanosystems and priming the tumor microenvironment for deep intratumoral penetration of nanoparticles. *J. Control Release* 277, 35–47. doi: 10.1016/j.jconrel.2018.03.012

Overchuk, M., and Zheng, G. (2018). Overcoming obstacles in the tumor microenvironment: recent advancements in nanoparticle delivery for cancer theranostics. *Biomaterials* 156, 217–237. doi: 10.1016/j.biomaterials.2017.10.024

Sun, C., Ji, S., Li, F., and Xu, H. (2017). Diselenide-containing hyperbranched polymer with light-induced cytotoxicity. *ACS Appl. Mater. Interfaces* 9, 12924–12929. doi: 10.1021/acsami.7b02367

Wang, D., Shi, R., Zhou, J., Shi, S., Wu, H., Xu, P., et al. (2018). Photo-enhanced singlet oxygen generation of prussian blue-based nanocatalyst for augmented photodynamic therapy. *iScience* 9, 14–26. doi: 10.1016/j.isci.2018.10.005

Wang, S., Yu, G., Wang, Z., Jacobson, O., Tian, R., Lin, L. S., et al. (2018). Hierarchical tumor microenvironment-responsive nanomedicine for programmed delivery of chemotherapeutics. *Adv Mater.* 30:e1803926. doi: 10.1002/adma.201803926

Xia, J., Du, Y., Huang, L., Chaurasiya, B., Tu, J., Webster, T. J., et al. (2018a). Redox-responsive micelles from disulfide bond-bridged hyaluronic acid-tocopherol succinate for the treatment of melanoma. *Nanomedicine* 14, 713–723. doi: 10.1016/j.nano.2017.12.017

Xia, J., Ji, S., and Xu, H. J. P. C. (2016). Diselenide covalent chemistry at the interface: stabilizing an asymmetric diselenide-containing polymer via micelle formation. *Polymer Chem.* 7, 6708–6713. doi: 10.1039/C6PY01610C

Xia, J., Li, T., Lu, C., and Xu, H. J. M. (2018b). Selenium-containing polymers: perspectives toward diverse applications in both adaptive and biomedical materials. *Macromolecules* 51, 7435–7455. doi: 10.1021/acs.macromol.8b01597

Yang, S., and Gao, H. (2017). Nanoparticles for modulating tumor microenvironment to improve drug delivery and tumor therapy. *Pharmacol. Res.* 126, 97–108. doi: 10.1016/j.phrs.2017.05.004

Zhang, B., Wang, H., Jiang, T., Jin, K., Luo, Z., Shi, W., et al. (2018). Cyclopamine treatment disrupts extracellular matrix and alleviates solid stress to improve nanomedicine delivery for pancreatic cancer. *J. Drug Target.* 26, 913–919. doi: 10.1080/1061186X.2018.1452243

Conflict of Interest: The authors declare that the research was conducted in the absence of any commercial or financial relationships that could be construed as a potential conflict of interest.

frontiers in Chemistry

CORRECTION
published: 27 November 2020
doi: 10.3389/fchem.2020.608312

Corrigendum: Programmable Ce6 Delivery via Cyclopamine Based Tumor Microenvironment Modulating Nano-System for Enhanced Photodynamic Therapy in Breast Cancer

Chan Feng[1], Lv Chen[1], Yonglin Lu[1], Jie Liu[1], Shujing Liang[1], Yun Lin[1], Yongyong Li[2] and Chunyan Dong[1]**

[1] Cancer Center, Shanghai East Hospital, Tongji University, Shanghai, China, [2] The Institute for Biomedical Engineering & Nano Science (iNANO), School of Medicine, Tongji University, Shanghai, China

Keywords: chlorin e6, cyclopamine, photodynamic therapy, drug delivery, breast cancer

OPEN ACCESS

Edited by:
Wansong Chen,
Central South University, China

Reviewed by:
Yevgeny Brudno,
University of North Carolina at Chapel Hill, United States

****Correspondence:***
Yongyong Li
yongyong_li@tongji.edu.cn
Chunyan Dong
cy_dong@tongji.edu.cn

Specialty section:
This article was submitted to Nanoscience, a section of the journal Frontiers in Chemistry

Received: *20 September 2020*
Accepted: *30 October 2020*
Published: *27 November 2020*

Citation:
Feng C, Chen L, Lu Y, Liu J, Liang S, Lin Y, Li Y and Dong C (2020) Corrigendum: Programmable Ce6 Delivery via Cyclopamine Based Tumor Microenvironment Modulating Nano-System for Enhanced Photodynamic Therapy in Breast Cancer. Front. Chem. 8:608312. doi: 10.3389/fchem.2020.608312

A Corrigendum on

Programmable Ce6 Delivery via Cyclopamine Based Tumor Microenvironment Modulating Nano-System for Enhanced Photodynamic Therapy in Breast Cancer
by Feng, C., Chen, L., Lu, Y., Liu, J., Liang, S., Lin, Y., et al. (2019). Front. Chem. 7:853. doi: 10.3389/fchem.2019.00853

In the original article, there was a mistake in ****Figure 6E**** as published. ****We made a data processing error of PBS survival curve in Figure 6E**.** The corrected ****Figure 6**** appears below.

In the original article, there was an error. ****There is no detail description of operations involving ethical aspects of experimental animals****.

A correction has been made to *****Materials and Methods****, *****Photodynamic Therapy in animals****, *****Paragraph 1****:

****Plant tumor tissue block in the left mammary fat pad of 5-week-old female BALA/c mice to build animal model. After 7 days, mice were treated individually with PBS, free CYC, free Ce6, ABN@HA-sese-Ce6 and ABN@HA-sese-Ce6/CYC NPs for 7 times (CYC 20 mg/kg, Ce6 2.5 mg/kg, every 2 days). Began with third injection, the mice were exposed to a 650 nm laser (20 mW/cm^2) for 30 min under anesthesia after each injection. The survival time of five groups of mice was recorded. Mice with tumors exceeding ethical requirements (>2 cm) were euthanized (equivalent to endpoint of observation), and the animals were euthanized using carbon dioxide asphyxia. Excised tumor weight of every group was also measured. Tumor volume and mice body weight were recorded every 2 days, the calculation formula was as following:****

The authors apologize for this error and state that this does not change the scientific conclusions of the article in any way. The original article has been updated.

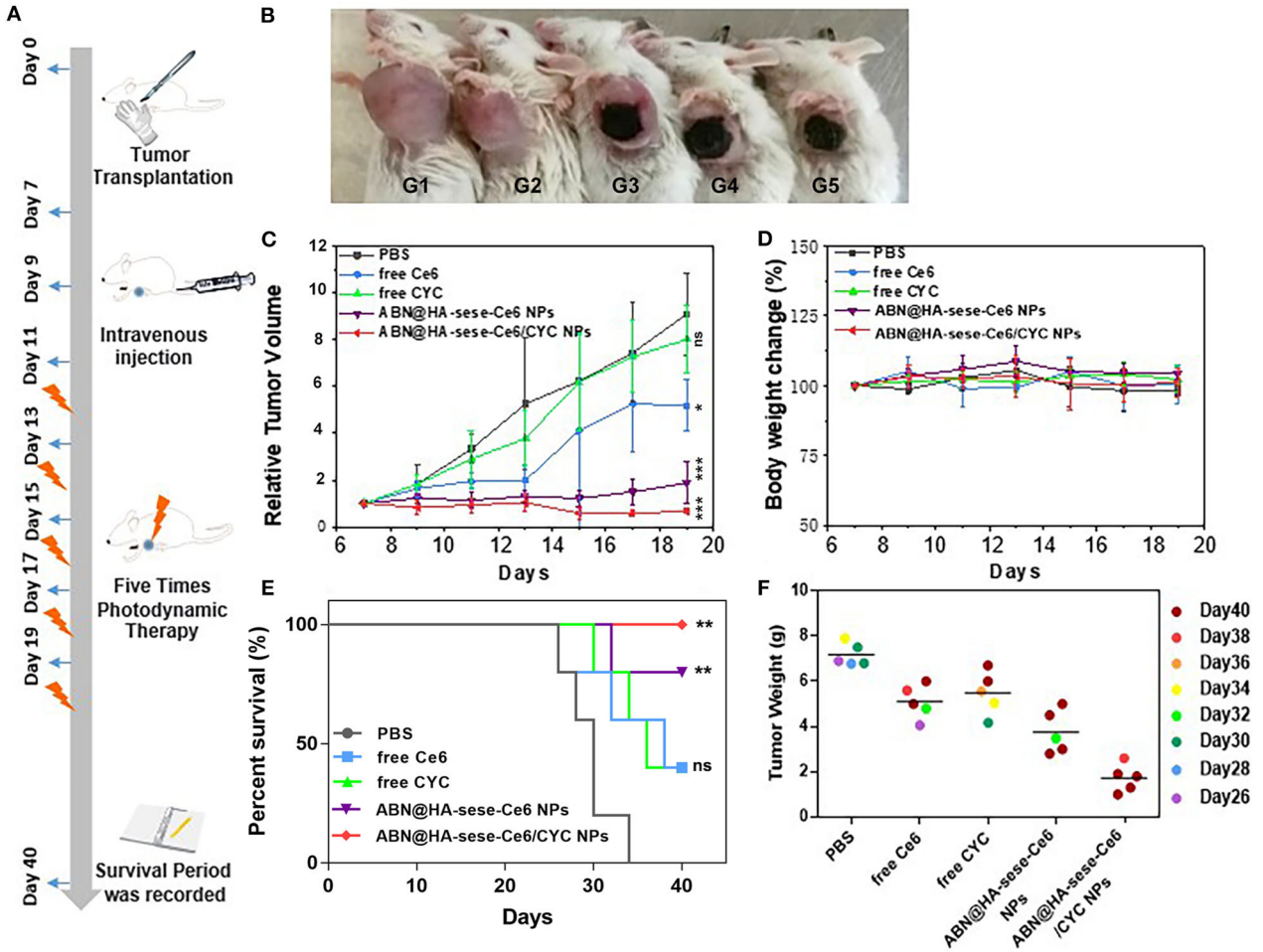

FIGURE 6 | Anti-tumor effects in breast cancer bearing mice model. **(A)** Schematic illustration of animal experiments. **(B)** Photos of tumor bearing mice in different treatment group (from left to right: PBS, free CYC, free Ce6, ABN@HA-sese-Ce6 NPs, ABN@HA-sese-Ce6/CYC NPs treatment group). **(C)** Tumor volume curve of mice treated with PBS, free Ce6, free CYC, ABN@HA-sese-Ce6 NPs, ABN@HA-sese-Ce6/CYC NPs ($n = 5$). The data are mean ± SD, $^{*}p < 0.05$, $^{**} < 0.01$, $^{***} < 0.001$ vs. PBS group. **(D)** Body weight change curve of mice in above groups. **(E)** The survival curve of mice in different groups. $^{*}p < 0.05$, $^{**} < 0.01$, $^{***} < 0.001$ vs. PBS group ($n = 5$). **(F)** Excised tumor weight of mice in above treatment groups when natural death or on Day 40 (endpoint).

frontiers in Chemistry

ORIGINAL RESEARCH
published: 11 February 2020
doi: 10.3389/fchem.2020.00052

Construction of Multicolor Upconversion Nanotheranostic Agent for *in-situ* Cooperative Photodynamic Therapy for Deep-Seated Malignant Tumors

Tongtong Hong[1,2†], *Yanxialei Jiang*[2†], *Zihong Yue*[1,2], *Xinyue Song*[2*], *Zonghua Wang*[1*] *and Shusheng Zhang*[2]

[1] *Shandong Sino-Japanese Center for Collaborative Research of Carbon Nanomaterials, College of Chemistry and Chemical Engineering, Qingdao University, Qingdao, China,* [2] *Collaborative Innovation Center of Tumor Marker Detection Technology, Equipment and Diagnosis-Therapy Integration in Universities of Shandong, Shandong Provincial Key Laboratory of Detection Technology for Tumor Markers, College of Chemistry and Chemical Engineering, Linyi University, Linyi, China*

OPEN ACCESS

Edited by:
Wansong Chen,
Central South University, China

Reviewed by:
Dalong Ni,
Shanghai Jiao Tong University, China
Xinxin Zhang,
Shanghai Institute of Materia Medica (CAS), China

***Correspondence:**
Xinyue Song
songxinyue428@163.com
Zonghua Wang
wangzonghua@qdu.edu.cn

[†] *These authors have contributed equally to this work*

Specialty section:
This article was submitted to Nanoscience, a section of the journal Frontiers in Chemistry

Received: *06 December 2019*
Accepted: *16 January 2020*
Published: *11 February 2020*

Citation:
Hong T, Jiang Y, Yue Z, Song X, Wang Z and Zhang S (2020) Construction of Multicolor Upconversion Nanotheranostic Agent for in-situ Cooperative Photodynamic Therapy for Deep-Seated Malignant Tumors. Front. Chem. 8:52. doi: 10.3389/fchem.2020.00052

Upconversion nanoparticles (UCNPs)-based photodynamic nanotheranostic agents could address the main drawbacks of photosensitizer molecules (PSs) including instability in aqueous solution and rapid clearance. Due to the relatively weak luminescence intensity of UCNPs and insufficient reactive oxygen species (ROSs), UCNPs-based photodynamic therapy (UCNPs-PDT) was discounted for deep-seated tumors. Thus, we proposed a PSs-modulated sensitizing switch strategy. Indocyanine green (ICG) as an NIR organic dye was proved to effectively enhance the luminescence intensity of UCNPs. Herein, four-color UCNPs were coated with a silica layer which loaded ICG and PSs while the thickness of silica layer was controlled to assist the sensitization function of ICG and activation of PSs. Under the drive of mitochondria-targeting ligand, the prepared nanotheranostic agent would accumulate in the mitochondria where ROSs were *in-situ* produced and then cell apoptosis was induced. Due to the cooperative PDT and high tissue-penetration depth of NIR laser, the prepared upconversion nanotheranostic agent could achieve significant inhibition on the deep-seated tumors.

Keywords: nanotheranostic agent, photodynamic therapy, reactive oxygen species, tumors, upconversion nanoparticles

INTRODUCTION

As an exogenous stimulus for activatable theranostics, light presents the advantages of high spatiotemporal selectivity and negligible side effects, and has been widely applied for photothermal, photodynamic, and/or photo-triggered chemo/gene therapy (Huang et al., 2014). Photodynamic therapy (PDT) use photosensitizers (PS) to produce reactive oxygen species (ROSs) which could selectively and irreversibly destroy cancer cells and tumor tissue without damaging adjacent healthy ones. However, its clinical applications are mainly limited by its short tissue penetration depth, easily aggregated PS molecules and insufficient generation of ROSs (Chatterjee et al., 2018). Under the excitation of near infrared (NIR) light, upconversion nanoparticles (UCNPs) could emit Uv-Vis

luminescence. Thus, UCNPs have the obvious merits of high tissue-penetration depth, negligible auto-fluorescence background, and low biotoxicity (Liu Y. et al., 2016). Under the excitation of NIR, UCNPs as the energy donor could effectively excite PS molecules (energy acceptor) to perform PDT via the luminescence resonance energy transfer (LRET) strategy (Fan et al., 2014; Liu et al., 2015; Chen et al., 2017). Nevertheless, the quantum yield and luminescence efficiency of UCNPs are relatively low due to the forbidden 4f-4f electronic transitions of lanthanide ions, weak absorption ability for NIR light and low doped concentration of the activators (below 2 mol%) (Ge et al., 2017). Thus, UCNPs-based PDT efficacy is discounted, especially for the deep-seated malignant tumors.

Recently, an interesting dye-sensitization strategy was proposed to improve the absorption ability of UCNPs for NIR and enhance their UCL intensity (Wei et al., 2006; Zou et al., 2012, 2016; Chen et al., 2015; Wu et al., 2016; Lee et al., 2017; Wang et al., 2017; Xu et al., 2017; Garfield et al., 2018). In this sensitization system, organic dyes with strong NIR absorption ability could harvest NIR energy, then transfer its excited-state energy to sensitizer ions of UCNPs via multistep non-radiative energy transfer process. Based on its sensitization ability, a specific NIR organic dye was used as both the recognition unit for targets and an effective sensitizer for UCL to develop a target-modulated sensitizing switch to break through the signal-to-background limit of upconversion nanoprobes. The reaction between the dye and targets would switch on the sensitization and afford a significantly increased LERT efficiency (Liang et al., 2018). Herein, we tried to design a photosensitizers-modulated sensitizing switch for UCNPs-based photodynamic nanotheranostic agent. Among NIR organic dyes, indocyanine green (ICG) could effectively sensitize Yb^{3+} and largely improve the luminescence intensity of UCNPs via the Förster-type energy transfer (Yan et al., 2016). Approved by the U.S. Food and Drug Administration (FDA), and ICG could serve as an NIR agent to achieve photothermal therapy (PTT)/PDT effect under the excitation of 800 nm. As reported, UCNPs-based drug delivery systems have been developed to solve the intrinsic problems of ICG, including instability in aqueous solution, rapid clearance, self-bleaching as well as absence of targeting (Yan et al., 2016), and mainly applicated for PTT (Zheng et al., 2013, Huang et al., 2014; Lv et al., 2017). Moreover, UCNPs with four colors have not been studied for phototherapy. Herein, we developed a feasible cooperative PDT nanotheranostic agent which used four-color UCNPs as the core, a thin silica layer for loading triple photosensitizer molecules [Hypocrellin A (HA), methylene blue (MB) and ICG] as the medium layer and mitochondria targeting ligand modified polyethylene glycol as the outer layer. Under the excitation of NIR, UCNPs would excite ICG molecules, which would further transfer their excited energy to emitters ions, thus the luminescence efficiency of UCNPs was enhanced, which was beneficial for the further excitation of PS molecules and the improvement of the photodynamic efficacy. The thin silica layer would assist the sensitization function of ICG and the activation of triple PS molecules (Yue et al., 2018; Song et al., 2019). Thus, ICG as PS molecules and NIR sensitizer could effectively enhance PDT efficacy. The short half-life (<40 ns) and restricted action distance (<20 nm) of the generated ROSs usually limit the therapeutic efficacy of PDT (Thomas et al., 2017; Purushothaman et al., 2019). In this study, under the drive of mitochondria-targeting ligands, the obtained nanotheranostic agent would selectively accumulate in the mitochondria where ROSs were produced under the excitation of NIR laser and then the mitochondria-mediated cell apoptosis was induced (**Scheme 1**). Due to the enhanced luminescence intensity and high tissue-penetration depth of NIR laser, the developed multicolor upconversion nanotheranostic agent could achieve a significant inhibition effect on the deep-seated tumor.

MATERIALS AND METHODS

Chemicals and Materials

Rare earth oxides, including Y_2O_3, Yb_2O_3, Tm_2O_3, and Ho_2O_3, were provided by the Sigma-Aldrich Corp while 1-octadecene (ODE), oleic acid (OA), and PS molecules were purchased from the Aladdin Reagent, Ltd. (Shanghai, China). The Sinopharm Chemical Reagent Co., Ltd. (Shanghai, China) offered other chemical reagents of analytical grade. An OKP purification system (Shanghai Laikie Instrument Corp., China) was used to prepare the aqueous solution. Mice were bought from Hubei Biossci Biotechnology Co., Ltd. (Wuhan, China) and the animal experiment was guided by the Animal Care and Use Committee of Linyi University.

Characterizations

The size and morphology of the prepared nanoparticles were observed under the transmission electron microscope (TEM, model: JEM-2010, JEOL) and their crystalline phase was determined by the X-ray powder diffractometer (D8 ADVANCE, CuKα radiation, $\lambda = 1.5405$Å). A fluorescence spectrophotometer (mode: F-4600, Hitachi) equipped with an external NIR laser was used to obtain the upconversion luminescence spectra. The UV-Vis absorption spectra of the prepared nanoparticles were characterized with an Agilent UV-Vis spectrophotometer (model: Cary 60) and their ζ potentials were acquired with the Zeta-size nano instrument (Zen 3600, Malvern Instruments Ltd.). The two-photon laser scanning confocal microscope (model: Leica TCS SP5) was used to trace the fluorescence information and get the fluorescence images. The *in vitro* cytotoxicity of the obtained nanotheranostics was evaluated by the CCK-8 test which was performed on a Microplate Reader (Thermo Scientific Multi-skan Mk3). Flow cytometry (cytoflex, beckmancoulter, America) was used to analyze the cellular fluorescence information and cell apoptosis.

Preparation of the Nanotheranostic Agent

Preparation of UCNPs

Based on the previously reported method, 0.05 mmol/L $Y(oleate)_3$ and $Ln(oleate)_3$ were prepared in OA/ODE mixing solution (v/v = 1:1) (Wei et al., 2006; Li et al., 2015). The molar ratio of lanthanide ions was Y:Yb:Tm:Ho = 54.5:40:0.5:5. Then, UCNPs with a $NaYF_4$@$NaYF_4$:Yb,Tm,Ho@$NaYF_4$ structure were prepared via the layer-by-layer seed-mediated shell growth strategy (Song et al., 2017, 2018). Firstly, to prepare the $NaYF_4$

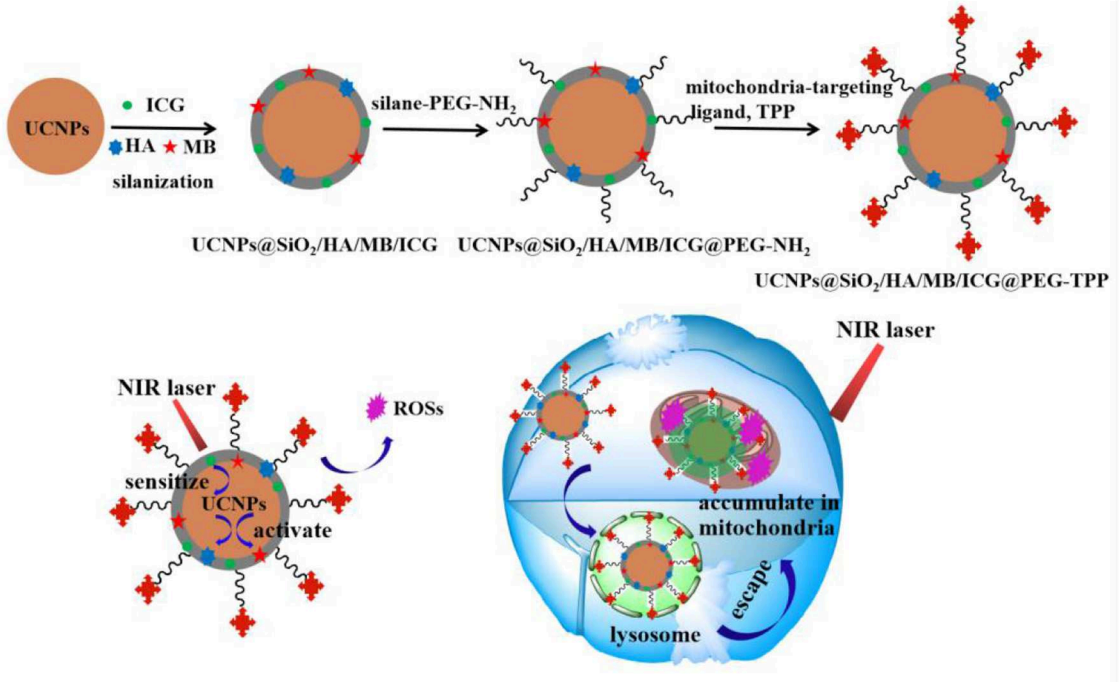

SCHEME 1 | Schematic image for the synthetic procedure of the UCNPs@SiO_2/HA/MB/ICG@PEG-TPP nanotheranostic agent and its theranostic functions for the photodynamic therapy.

core, 20.0 mL $Y(oleate)_3$ solution and 0.84 g NaF were mixed and reacted at 110°C under the protection of argon (Ar) for 1.0 h, and then further reacted at 340°C for another 2.0 h. Secondly, 8.0 mL $Ln(oleate)_3$ solution was slowly injected into the above solution and reacted at 340°C for 20 min to grow the luminescent shell on the surface of the $NaYF_4$ core. Lastly, 12.0 mL $Y(oleate)_3$ solution was added and reacted for another 20 min to prepare the outer shell $NaYF_4$. The prepared UCNPs were obtained by precipitation in 2-fold volume of ethanol, centrifugally collected, and washed with hexane/ethanol (v/v = 1:6) for several times. The obtained UCNPs were finally dispersed in cyclohexane.

Preparation of UCNPs@SiO_2/HA/MB/ICG

The silica layer grew on the surface of UCNPs via the water-in-oil reverse microemulsion method (Liu et al., 2014). The detailed preparation process was as follows: reverse micelles were first formed by homogeneously mixing Igepal CO-520 (0.660 mL) into cyclohexane (10.0 mL). Afterward, 0.450 mmol of the prepared oleic acid protected UCNPs was added into the above reverse micelles and strongly stirred for 1.0 h. Via the ligand exchange between oleate ligand and Igepal CO-520, UCNPs were entrapped in the water pool. Photosensitizer molecules including HA solution (90 μL, 5.0 mg/mL, ethanol), equal amount of ICG solution and MB aqueous solution were added in sequence. Then, 60 μL ammonia (30%) was added dropwise and stirred for 2.0 h to make the solution alkaline. Finally, 90 μL tetraethyl orthosilicate (TEOS) was slowly added into the solution and reacted for 24 h. Thus, the silica layer grew on the surface of UCNPs via the classic hydrolysis and condensation. Based on the proposed procedure, single PS molecules loaded nanoprobes and the control nanoprobe, UCNPs@SiO_2, were prepared.

Preparation of UCNPs@SiO_2/HA/MB/ICG@PEG-TPP

To enhance dispersibility, the obtained UCNPs@SiO_2/HA/MB/ICG nanoprobe was modified with amino-PEG. 10.0 mg of the prepared UCNPs@SiO_2/HA/MB/ICG nanoprobe was added into 5.0 mL of silane-PEG-NH_2 and shook slowly for 12 h to obtain the UCNPs@SiO_2/HA/MB/ICG@PEG. Then, the mitochondria-targeted ligand, 3-carboxypropyl triphenyl-phosphonium bromide (CTPB), was attached onto the surface of the prepared nanoprobe via the covalent reaction. 8.0 mg of the UCNPs@SiO_2/HA/MB/ICG@PEG nanoprobe was collected by centrifugation, then redispersed in 8.0 mL of CTPB solution (0.86 mg/mL, methanol) and reacted for 12 h via the catalysis of 1-(3-dimethylaminopropyl)-3-ethylcarbodiimide hydrochloride (EDC, 3.46 mg/mL). The obtained UCNPs@SiO_2/HA/MB/ICG@PEG-TPP nanotheranostic agent was washed with water several times and then stored in PBS buffer solution for further use.

Evaluation of the Prepared Nanotheranostic Agent

Detection of the Produced ROSs in Aqueous Solution

The commonly used fluorescence dye, 9,10-anthracenediyl-bis(methylene)dimalonic acid (ABDA), could irreversibly react with ROSs to induce the decrease in its fluorescence intensity at 407 nm (Chen et al., 2016; Dong et al., 2016). Thus,

the change of the fluorescence intensity of ABDA could be used to evaluate the generated ROSs in aqueous solution. ABDA (10 μM, DMSO) was added into 1.0 mg/mL of the prepared UCNPs@SiO_2/HA/MB/ICG@PEG-TPP solution and the mixture was irradiated with NIR laser (980 nm, 1.5 W/cm^2) for 21 min. Every irradiation lasted for 3 min with an interval of 1 min. After irradiation, ABDA was excited at 380 nm and its fluorescence was recorded at 407 nm. Each time point was operated five times ($n = 5$).

Cellular Uptake and Localization

To evaluate the cellular uptake and localization, MCF-7 cancer cells cultured in glass coverslips were incubated with 70 μg/mL of the UCNPs@SiO_2/HA/MB/ICG@PEG-TPP nanotheranostic agent for different times. MCF-7 cancer cells were washed with PBS buffer several times and then imaged immediately with a two-photon laser confocal scanning microscope. The fluorescence images of the prepared UCNPs@SiO_2/HA/MB/ICG@PEG-TPP nanotheranostic agent were recorded at the wavelength range of 515–575 nm and excited by the 980 nm laser while the mitochondria of MCF-7 cancer cells were stained with a commercial fluorescent dye, the MitoTracker® Deep Red. Fluorescence signal was recorded at the wavelength range of 650–720 nm under the excitation of 633 nm.

In vitro ROSs Detection

The *in vitro* ROSs was detected with the flow cytometry and laser confocal scanning microscope. For the flow cytometry, the prepared UCNPs@SiO_2/HA/MB/ICG@PEG-TPP nanotheranostic agent (70 μg/mL) was used to incubate MCF-7 cancer cells for 12.0 h. Afterwards, MCF-7 cancer cells were washed with PBS buffer and then divided into two parallel subgroups, the experimental group, which was treated with laser, and the control group without the excitation. After being excited under the NIR laser (980 nm, 1.5 W/cm^2) for 4 min, MCF-7 cancer cells were cultured for another 24 h. Then, the two parallel subgroups were collected and resuspended in 2′,7′-dichlorofluorescin diacetate staining solution (DCFH-DA, diluted with serum-free DMEM by 5,000-fold) for 30 min, washed with PBS and injected for flow cytometry. For *in-situ* observation of ROSs, MCF-7 cancer cells were stained with DCFH-DA solution (10 μM, serum-free DMEM) in a cell incubator for 30 min after incubation with the prepared nanotheranostic agent, and then excited under the laser. Then, MCF-7 cancer cells were washed with PBS buffer several times to remove excess dyes and then observed in 1.0 mL of PBS buffer under the scanning confocal microscope. Under an excitation of 488 nm, the green channel (500–540 nm) was used to obtain the fluorescence information of DCF which was the oxidization product of DCFH-DA by ROSs.

Observation of the Changes of the Mitochondrial Membrane Potential ($\Delta\Psi_m$)

The $\Delta\Psi_m$ changes were also detected with flow cytometry and laser confocal scanning microscope. MCF-7 cancer cells were treated with the procedure described for ROSs detection. After irradiation and incubation for further 24 h, the collected MCF-7 cancer cells were resuspended in 1.0 mL of serum-free DMEM containing 25 μL JC-1 staining solution for 20 min, washed with cold JC-1 buffer solution and used for flow cytometry. For

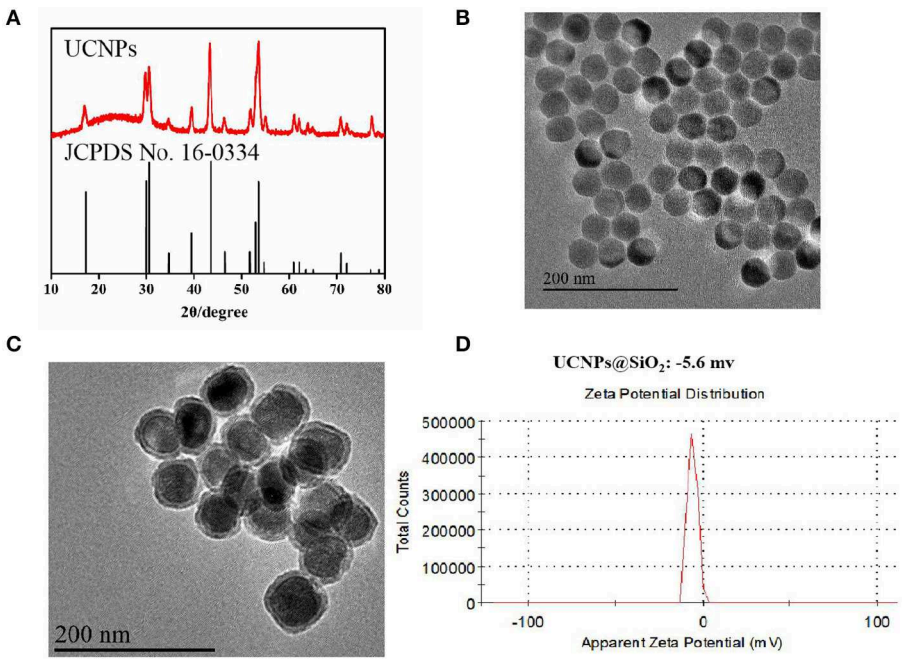

FIGURE 1 | (A) XRD images of the prepared UCNPs; **(B)** TEM images of the prepared UCNPs; **(C)** TEM images of the prepared UCNPs@SiO_2; **(D)** Zeta-potential of the prepared UCNPs@SiO_2.

in-situ observation of the $\Delta\Psi_m$ changes, MCF-7 cancer cells were incubated with 1.0 mL of JC-1 staining solution in the cell incubator for 20 min, washed with cold JC-1 buffer solution and then imaged under the laser scanning confocal microscope. The fluorescence information of JC-1 was obtained at green channel (λ_{ex} = 488 nm, λ_{em} = 500–550 nm) and red channel (λ_{ex} = 561 nm, λ_{em} = 580–640 nm), respectively.

PDT Efficacy Assay in Living Cells

In this experiment, the *in vitro* PDT efficacy of the obtained nanotheranostic agent was examined with the CCK-8 assay and flow cytometry. Four parallel experiments were chosen. MCF-7 cancer cells were treated with (a) PBS, (b) the prepared nanotheranostic agent only, (c) laser irradiation (980 nm, 1.5 W/cm^2, 4.0 min with an interval of 1.0 min), (d) the prepared nanotheranostic agent and laser irradiation. To process the CCK-8 assay, MCF-7 cancer cells cultured in the 96-well-microtiter plates were incubated with the obtained nanotheranostic agent (70 μg/mL). After 12 h, MCF-7 cancer cells were washed with PBS buffer, excited under the NIR laser and then incubated for another 24 h. Afterward, the CCK-8 agent (10 μL) was added into each pore and incubated cells for 2 h. Finally, the microplate reader was used to record the absorbance of MCF-7 cancer cells at 450 nm (Yue et al., 2018; Song et al., 2019).

The effects of the prepared nanotheranostic agent and NIR irradiation on the cytotoxicity were evaluated by the flow cytometry. MCF-7 cancer cells were treated with (a) PBS, (b) the prepared nanotheranostic agent (70 μg/mL, 12 h), (c) laser irradiation (980 nm, 1.5 W/cm^2, 4.0 min with an interval of 1.0 min), (d) the prepared nanotheranostic agent and laser irradiation. After treatment, MCF-7 cancer cells were collected, stained with apoptosis staining solution for 5.0 min (500 μL binding buffer, 6 μL Annexin V-FITC staining solution and 7 μL PE staining solution) and then injected for flow cytometry analysis. Based on the manufacturer's instruction, the necessary fluorescence compensation was adjusted (Song et al., 2019).

In vivo PDT Efficacy Assay

The *in vivo* PDT efficacy of the prepared UCNPs@SiO_2/HA/MB/ICG@PEG-TPP nanotheranostic agent was evaluated via animal experiment. The animal study was reviewed and approved by the Animal Care and Use Committee of Linyi University. First, cancer cells at the density of 1 × 10^6 were injected into the Bald/c nude mouse (6 weeks, around 20 g). Experiments were performed when the tumors grew to the tumor volume of 100–130 mm^3. To mimic the deep-seated tumor, a piece of mouse tissue with a thickness of 7 mm was covered on the tumor surface. The tumor-bearing mice were injected with the prepared nanotheranostic agent (0.6 mg/ml, 50 μL) and then their tumor section irradiated with the NIR laser after 12 h (980 nm, 1.5 W/cm^2, 4.0 min with an interval of 1.0 min). Afterward, the tumor volume (V = length × width^2/2) was recorded every 2 days. On the seventh day, the same amount of prepared nanotheranostic agent was injected into the mice again

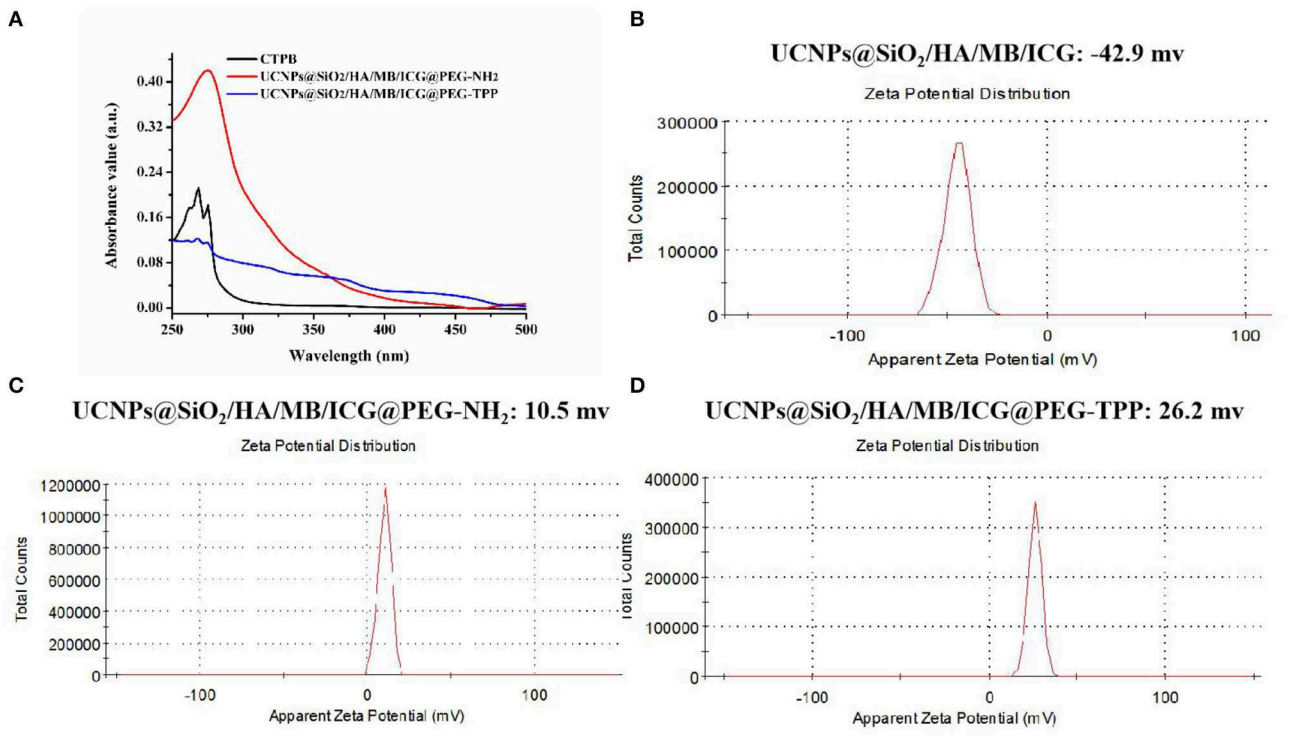

FIGURE 2 | (A) Uv-Vis spectra of CTPB, UCNPs@SiO_2/HA/MB/ICG@PEG-NH_2, UCNPs@SiO_2/HA/MB/ICG@PEG-TPP; Zeta-potential of **(B)** UCNPs@SiO_2/HA/MB/ICG; **(C)** UCNPs@SiO_2/HA/MB/ICG@PEG-NH_2; **(D)** UCNPs@SiO_2/HA/MB/ICG@PEG-TPP.

and then the tumor section was irradiated with the NIR laser. After 13 days, the mice were sacrificed to obtain the main organs for hematoxylin and eosin (H&E) staining and tumor section for H&E staining, TUNEL staining and Caspase-3 staining. To evaluate the PDT efficacy of the prepared nanotheranostic agent, three other parallel control groups were, respectively, (a) only injected with PBS, (b) laser irradiation alone, (c) only injected with the nanotheranostic agent.

RESULTS AND DISCUSSION

Characterization of the UCNPs@SiO_2/HA/MB/ICG@TPP Nanotheranostic Agent

Since the sensitization effects of the ICG dye could alleviate the luminescence concentration quenching effect of Yb^{3+} (Wei et al., 2006), the doping ratio of the luminescence layer (Y:Yb:Tm:Ho = 54.5:40:0.5:5) was chosen to obtain multi-color UCNPs (**Figure S1**). Based on the layer-by-layer seed mediated shell growth strategy, UCNPs were obtained with pure hexagonal phase (**Figure 1A**) and homogeneous particles sizes (**Figure 1B**). Based on the modified water-in-oil reverse microemulsion method (Purushothaman et al., 2019), dense silica was homogeneously grown on the surface of UCNPs with a thickness of 6.2–8.3 nm (**Figure 1C**) with the finial zeta-potential of −5.6 mv (**Figure 1D**). During the silanization, PS molecules could be easily incorporated into the silica layer without further modification with a concentration of 19.6–26.8 μg/mg, which was confirmed by the UV-Vis analysis (**Figure S2A**) and zeta-potential (**Figure S2B**). In addition, the introduction of ICG could enhance the luminescence intensity of UCNPs, which could further improve the photodynamic efficacy (**Figure S3**).

In this experiment, the prepared UCNPs@SiO_2/HA/MB/ICG nanoprobe was coated with PEG-NH_2 via the silanization reaction and then the mitochondria recognition ligand, TPP, was further attached through the carbodiimide reaction to obtain the final nanotheranostic agent, UCNPs@SiO_2/HA/MB/ICG@PEG-TPP (Liu et al., 2014). As displayed in **Figure 2A**, the obtained UCNPs@SiO_2/HA/MB/ICG@PEG-TPP showed the characteristic Uv-Vis peak of the TPP functional group, proving the satisfactory modification. The Zeta-potential of the UCNPs nanoprobe became positive when coated with PEG-NH_2 (**Figures 2B,C**), and the mitochondria-targeting ligand, TPP, could further increase the Zeta-potential of the nanoprobe, which could benefit their accumulation in the mitochondria (**Figure 2D**).

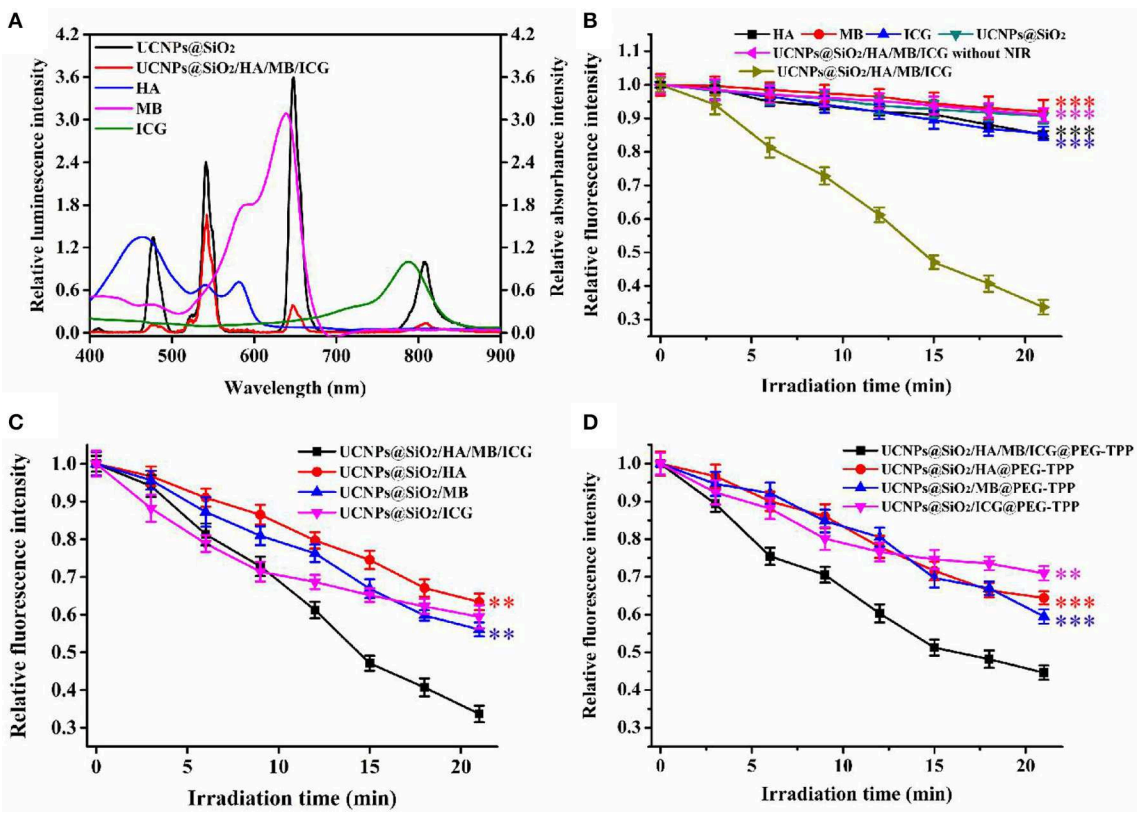

FIGURE 3 | (A) Relative luminescence intensity of UCNPs@SiO_2 and UCNPs@SiO_2/HA/MB/ICG, relative absorbance value of HA, MB and ICG; **(B)** ROSs production of HA, MB, ICG, UCNPs@SiO_2, UCNPs@SiO_2/HA/MB/ICG under the irradiation of NIR laser (1.5 W/cm^2), and UCNPs@SiO_2/HA/MB/ICG without the irradiation; **(C)** ROSs production of the prepared nanoprobe under the irradiation of NIR laser; **(D)** ROSs production of the TPP modified nanoprobes under the irradiation of NIR laser. Each time point was operated five times and error bars represent standard deviation ($n = 5$). The data was analyzed by the T-test. $^{**}p < 0.01$ and $^{***}p < 0.001$.

PDT Efficacy of the Prepared Nanotheranostic Agent in Aqueous Solution

The shortened energy transfer distance and the well-matched spectra guaranteed a high energy transfer efficiency. As shown in **Figure 3A** and **Figure S4**, with the concentration of PS molecules increasing, the quenching yields increased to 91.4, 89.2, and 85.9% for luminescence peaking at 478, 648, and 808 nm, respectively. The ROSs indicator, 9,10-anthracenediyl-bis(methylene)dimalonic acid (ABDA), was further used to evaluate the ROSs generated in aqueous solution. As shown in **Figure 3B**, only the prepared nanotheranostic agent under the excitation of NIR laser could produce ROSs. By contrast, only PS molecules and the prepared UCNPs@SiO_2 nanoparticles played a negligible effect on the fluorescence intensity of ABDA upon NIR irradiation. Similarly, the finial nanotheranostic agent in the absence of NIR irradiation did not have an obvious effect on the fluorescence intensity of ABDA. Thus, the final nanotheranostic agent and NIR were two indispensable parameters for the ROSs generation. Due to the cooperative photodynamic effects, ROSs produced by the prepared nanotheranostic agent could quench 66.3% of the fluorescence intensity of ABDA after 21.0 min of irradiation, which was much more than the corresponding single PS-involved nanoprobes and other reported UCNPs-based PDT nanoprobes (**Figure 3C**; Gnanasammandhan et al., 2016; He et al., 2016). After modification with TPP, the constructed nanotheranostic agent, UCNPs@SiO_2/HA/MB/ICG@PEG-TPP, also showed obvious advantages in the production of ROSs (**Figure 3D**).

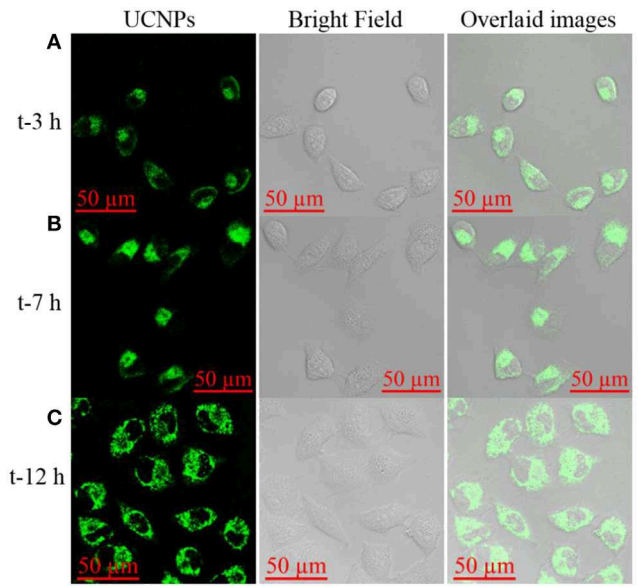

FIGURE 4 | Upconversion luminescence imaging of MCF-7 cells treated with 70 μg/mL of the prepared nanoprobe for **(A)** 3 h, **(B)** 7 h, and **(C)** 12 h. Green channel was collected the 515–575 nm under the excitation of NIR laser to obtain the UCNPs information; Bright field was used to obtain the cell information.

Cellular Uptake and Localization

To validate the application of the prepared nanotheranostic agent in the cell imaging and PDT, its cytotoxicity was first studied with the CCK-8 assay. As shown in **Figure S5**, MCF-7 cancer cells could keep above 95% of cell viability when treated with 0–0.125 mg/mL of the prepared nanotheranostic agent. The cell biocompatibility and distribution were observed

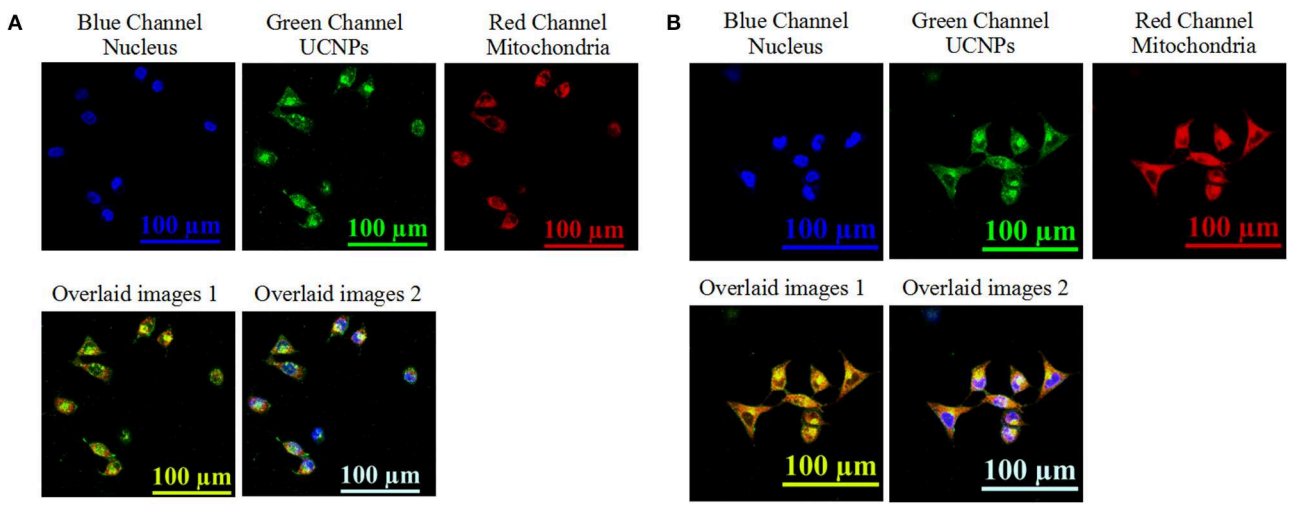

FIGURE 5 | Upconversion luminescence imaging of MCF-7 cells treated with 70 μg/mL of **(A)** the prepared UCNPs@SiO_2/HA/MB/ICG, **(B)** UCNPs@SiO_2/HA/MB/ICG@PEG-TPP. The nucleus information was collected at the blue channel from 420 nm to 480 nm under the excitation of 405 nm laser; the UCNPs information was collected at the green channel from 515 to 575 nm under the excitation of NIR laser; the mitochondria information was collected at the red channel form 650 to 720 nm under the excitation of 633 nm; overlaid image 1 consisted of the green channel and red channel; overlaid image 2 consisted of the blue channel, green channel, and red channel.

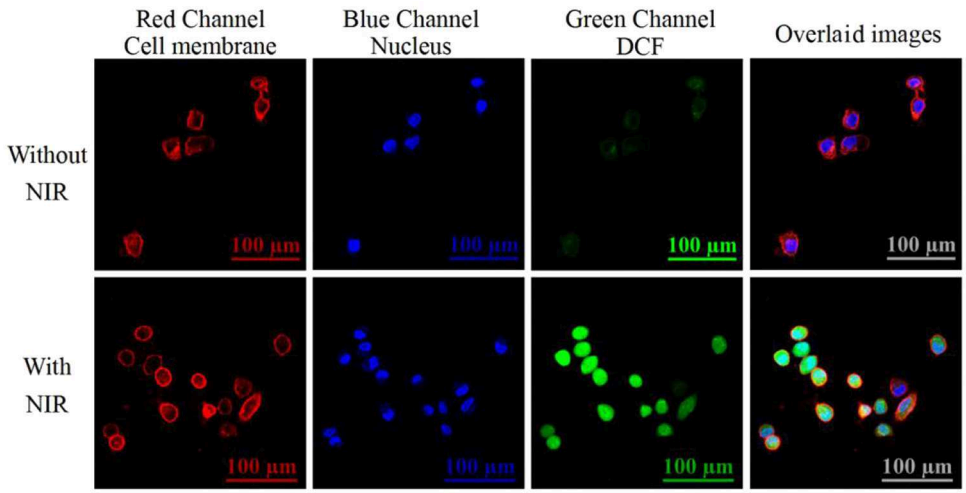

FIGURE 6 | Confocal lasers scanning microscope (CLSM) images of intracellular ROSs. MCF-7 cancer cells were incubated with 70 μg/mL of the prepared nanotheranostic agent for 12 h. The cell membrane information was collected at the red channel from 600 to 650 nm under the excitation of 561 nm laser. The nucleus information was collected at the blue channel from 420 to 480 nm under the excitation of 405 nm laser; The ROSs information was collected at the green channel from 500 to 540 nm under the excitation of 488 nm. Overlaid images consisted of the three channels.

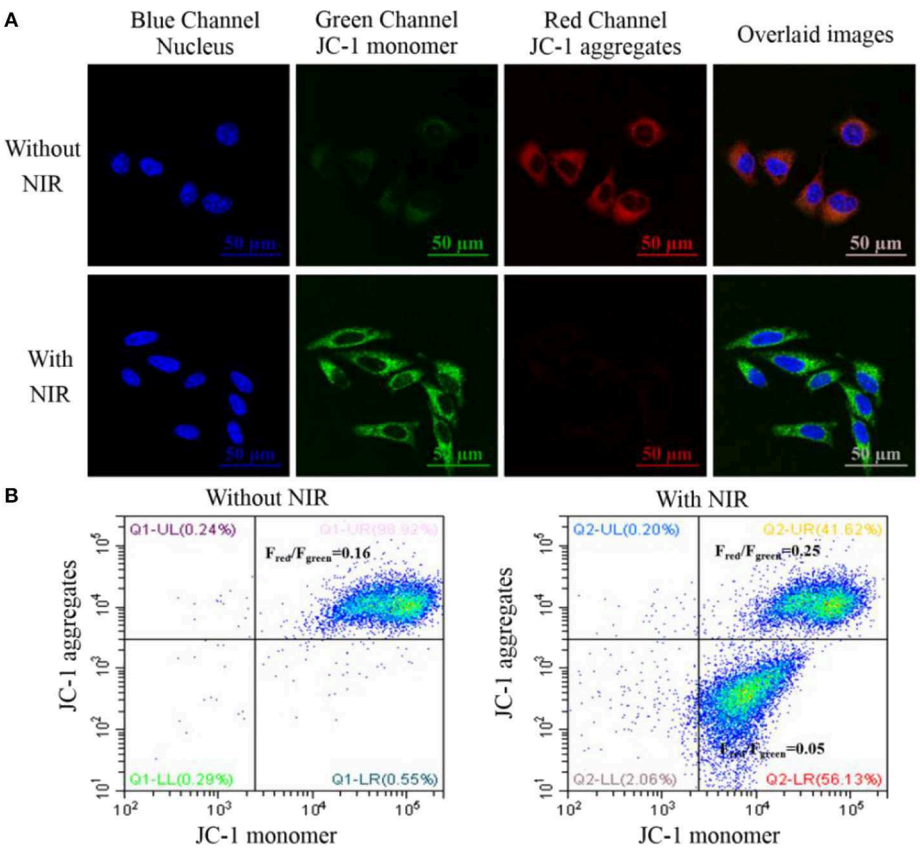

FIGURE 7 | (A) CLSM images of intracellular mitochondrial membrane potential stained with the JC-1 dye. MCF-7 cancer cells were incubated with 70 μg/mL of the prepared nanotheranostic agent for 12 h. The nucleus information was recorded at the blue channel from 420 to 480 nm under the excitation of 405 nm. The fluorescence signal of the monomeric JC-1 dye was recorded at the green channel from 500 to 550 nm under the excitation of 488 nm; the fluorescence signal of the aggregated JC-1 dye was recorded at the red channel from 580 to 640 nm under the excitation of 561 nm; overlaid images of the three channels; **(B)** flow cytometry to evaluate the $\Delta\Psi_m$ change of MCF-7 cancer cells using JC-1 staining.

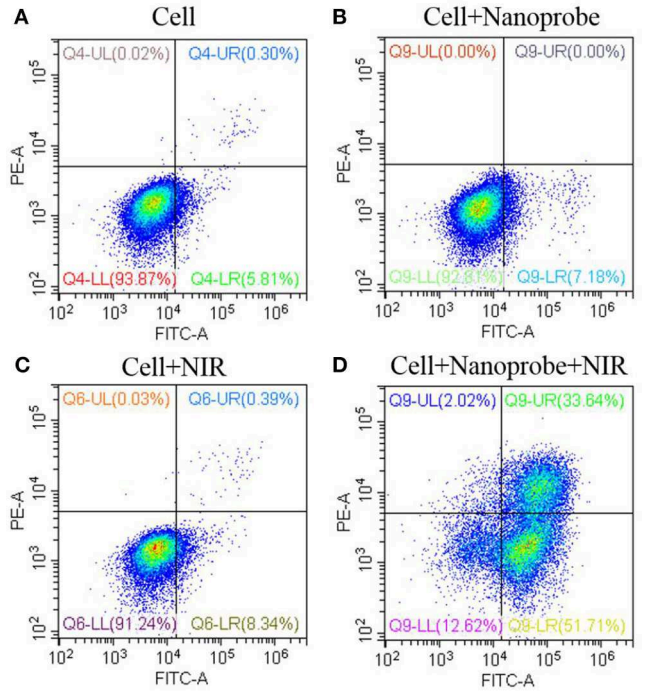

FIGURE 8 | Cell viability (%) of the UCNPs@SiO_2/HA/MB/ICG@PEG-TPP nanotheranostic agent treated with **(A)** PBS, **(B)** nanoprobe, **(C)** NIR irradiation, **(D)** nanoprobe and NIR irradiation.

under the two-photon confocal lasers scanning microscope. As demonstrated in **Figure 4**, the prepared nanotheranostic agent was firstly endocytosed into MCF-7 cancer cells and gradually captured in the lysosome/endosome in the first 7 h. With the incubation time prolonged to 12 h, the nanotheranostic agent was successfully escaped and released into the cytoplasm.

The localization of the prepared nanotheranostic agent within cells was further evaluated. As illustrated in **Figure 5**, the prepared UCNPs@SiO_2/HA/MB/ICG nanoprobe was mainly distributed in the cytoplasm (**Figure 5A**). When compared to the UCNPs@SiO_2/HA/MB/ICG@PEG-TPP nanoprobe treated groups (**Figure 5B**), the fluorescence signals of the UCNPs and MitoTracker dye were overlapped well, proving that the functional group, TPP, would drive the prepared UCNPs@SiO_2/HA/MB/ICG@PEG-TPP nanotheranostic agent to accumulate in the mitochondria where the *in-situ* PDT was achieved.

Intracellular ROSs Generation

We further investigated the ability of the internalized nanotheranostic agent to produce ROSs in living cells with the fluorescent dye, 2,7-dichlorofluorescin diacetate (DCFH-DA). Once diffused into the cells, DCFH-DA as a cell-permeable oxidant-sensing probe would be converted into DCFH by related esterase, and then oxidized to DCF by ROSs which would emit bright green fluorescence when excited (Kim et al., 2014; Hou et al., 2016). Thus, the generation of ROSs would be reflected by the fluorescence signal of DCF which was recorded and imaged with the flow cytometry and confocal microscope (**Figure 6** and **Figure S6**). As shown in **Figure S6**, MCF-7 cancer cells did not display obvious increased green fluorescence when only irradiated with the NIR laser or only incubated with the nanoprobe, proving the applicability of the used NIR laser (irradiation intensity: 1.5 W/cm^2, irradiation time: 4 min with an interval of 1.0 min) for PDT and negligible cytotoxicity of the prepared nanotheranostic agent. By contrast, the internalized nanotheranostic agent could produce intracellular ROSs under the irradiation of NIR laser. As shown in the confocal laser scanning microscope images (**Figure 6**), the irradiation of NIR laser could activate the UCNPs@SiO_2/HA/MB/ICG@PEG-TPP nanoprobe distributed in the mitochondria of MCF-7 cancer cells to produce ROSs which could oxidize DCFH into DCF with bright green fluorescence when excited.

Mitochondrial Membrane Potential Measurement

PDT was shown to induce mitochondrial-dependent cell apoptosis which was related to the release of the pro-apoptotic proteins and caspase activation. The mitochondrial membrane potential ($\Delta\Psi_m$) plays an important role in the biological activities in mitochondria and its decrease is an important indicator to assess the dysfunction of mitochondria (Crompton, 1999; Liu et al., 2014; Liu Y. Y. et al., 2016). In this experiment, the $\Delta\Psi_m$ change could be studied with JC-1 fluorescence dye which would tend to aggregate in red fluorescence with high $\Delta\Psi_m$ and become monomeric in green fluorescence with low $\Delta\Psi_m$. Thus, the change of its fluorescence intensity (F_{red}/F_{green}) would reflect the mitochondrial membrane status. As shown in **Figure 7A**, JC-1 dye in the group only treated with the nanotheranostic agent would display weak green and strong red fluorescence while JC-1 dye in the group treated with the nanotheranostic agent and NIR laser would display stronger green and weaker red fluorescence, which was attributed to the decreased $\Delta\Psi_m$ by the produced ROSs. The decrease in $\Delta\Psi_m$ was further evaluated with flow cytometry (**Figure 7B**). In absence of NIR laser irradiation, F_{red}/F_{green} was around 0.16 while about 56.13% of MCF-7 cells were moved into the below quadrant with a large decrease in F_{red}/F_{green} ratio (0.05) after excited with NIR laser.

Cancer Cell Apoptosis Induced by the Prepared Nanoprobe

Based on the generated ROSs and $\Delta\Psi_m$ impair, mitochondrial-dependent cell apoptosis was expected. The cell apoptosis was first evaluated with the CCK-8 assay. As demonstrated in **Figure S7**, the NIR irradiation or the nanoprobe alone would have no significant influence on the cell viability. However, when treated with the designed photodynamic nanotheranostic agent, MCF-7 cancer cells could only retain 17.3% of cell viability. Moreover, the introduced triple PS molecules and designed photosensitizers-modulated sensitizing switch would improve the generation of ROSs and bring higher PDT efficacy. Moreover, the cell apoptosis was further analyzed by the

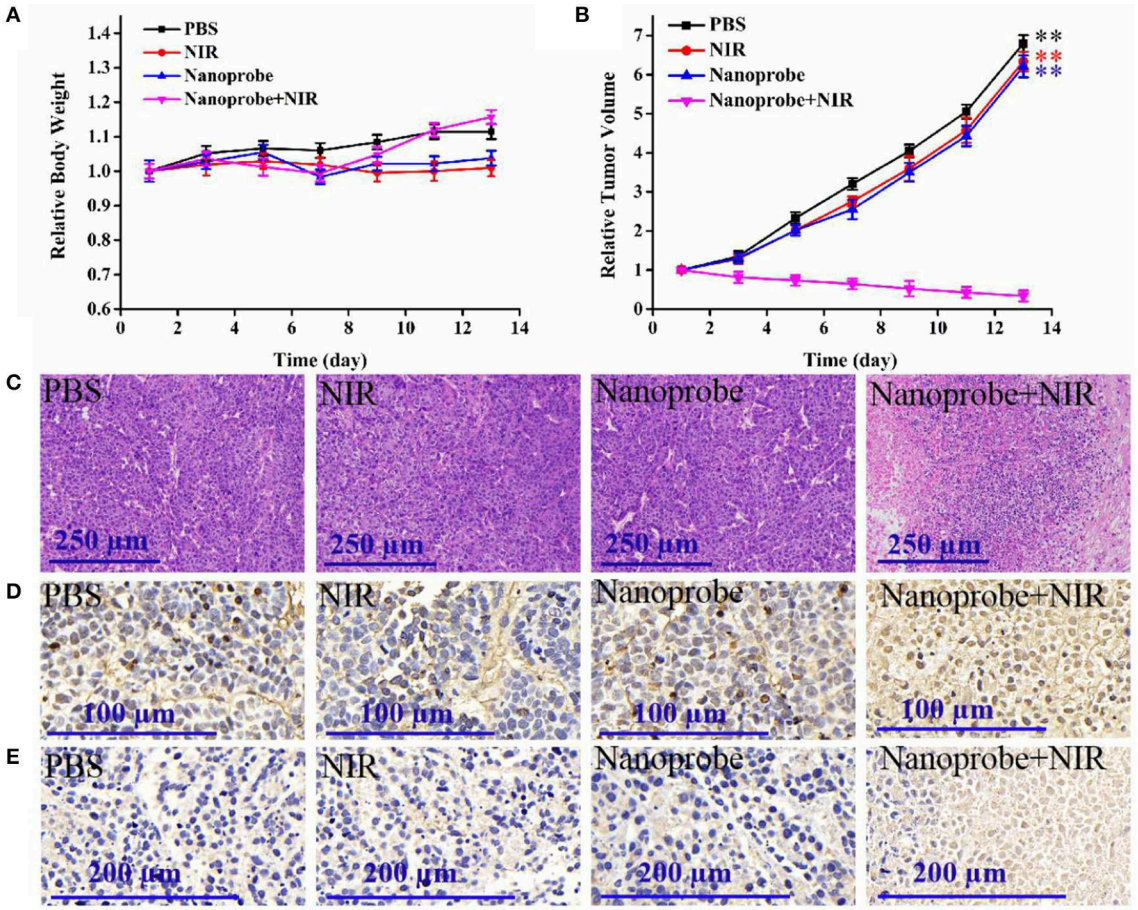

FIGURE 9 | (A) Time-dependent mice body weight curves and **(B)** tumor growth curves of different groups of mice with various treatments, **(C)** H&E staining, **(D)** TUNEL staining, and **(E)** caspase-3 staining of the dissected tumor section on the thirteenth day with different treatments. Four parallel experiments were operated, and error bars represent standard deviation ($n = 4$). The data was analyzed by the *T*-test. $^{**}p < 0.01$.

flow cytometry which could distinguish the cells with high viability, early apoptosis, late apoptosis, or necrosis. In the control groups, more than 91% of cancer cells kept high viability and were located in the lower left quadrant (**Figure 8**). After being incubated with the prepared nanotheranostic agent and excited by the NIR laser, around 51.71 and 33.64% of cancer cells shifted from the high viability to early apoptosis and late apoptosis, respectively. Thus, the apoptosis was a major cell death modality induced by the prepared nanotheranostic agent.

In vivo PDT Efficacy of the Prepared Nanotheranostic Agent

Furthermore, the *in vivo* therapeutic effect of the developed nanotheranostic agent was studied on xenograft mice. The experiment began when the tumor-bearing nude mice displayed tumor volumes of 100–130 mm^3. Four groups with different treatments were designed: (a) injected with PBS buffer solution, (b) injected with the prepared nanotheranostic agent, (c) irradiated with NIR laser, (d) injected with the prepared nanotheranostic agent and then irradiated with the NIR laser. Every 2 days, we measured and recorded the changes in animal weight and tumor volume. There were no significant weight loss (**Figure 9A**) nor obvious tissue abnormalities recorded in the H&E staining in all groups (**Figure S8**), proving the minimal systemic toxicity of the prepared nanotheranostic agent. As expected, tumors in group b and group c increased by 6.2- to 6.3-fold with a similar growth rate to those in group a (**Figure 9B** and **Figure S9**). Due to the *in-situ* synergistic PDT efficacy, the prepared nanotheranostic agent would remarkably inhibit the tumor growth without recurrence which would finally induce 66% decrease of the tumor volume. The PDT efficacy of the prepared nanotheranostic agent was further verified by the histological results. When compared, tumor sections in group 4 displayed obvious blank areas as well as nuclear shrinkage and fragmentation due to the PDT efficacy (**Figure 9C**). Furthermore, the cell death mechanism induced by the prepared nanotheranostic agent was further studied with the TUNEL staining and Caspase-3 staining. As shown in **Figure 9D**, most cancer cells in the tumor section of groups a-c kept their

spherical nuclei intact, thus the corresponding treatment did not affect the normal growth of the tumor. Contrarily, an increased amount of cancer cells displayed TUNEL positive nuclei in group d due to DNA fragmentation. The tumor section was further analyzed with the Caspase-3 staining. Consistent with TUNEL staining, cancer cells in the tumor section of group d also displayed positive Caspase-3 staining, implying that the produced ROSs could induce Caspase-mode cell apoptosis which involved the release of cytochrome c from the mitochondria to the cytosol, caspase activation, and other relative events leading to apoptosis (**Figure 9E**).

CONCLUSIONS

Herein, we have developed a multi-color UCNPs-based nanotheranostic agent. Attributed to the ICG sensitization, multi-color UCNPs with high doping ratio of activators were prepared and used for loading triple PS molecules. The controlled thin silica layer could shorten the energy transfer distance, assist the sensitization function of ICG and activation of photosensitizer molecules. Thus, ROSs generated by the prepared nanotheranostic agent could quench 66.3% of the fluorescence intensity of ABDA after 21.0 min of irradiation. The modification of mitochondria-targeting ligand, TPP, drove the prepared nanotheranostic agent to accumulate in the mitochondria where ROSs were generated *in-situ*, and a high mitochondria-mediated cancer cells apoptosis (cell apoptosis ratio, 85.3%) was induced. Since the designed photodynamic nanotheranostic agent could produce increased intracellular ROSs, make the mitochondria dysfunction and induce cell apoptosis, it showed an obvious suppression effect on the deep-seated malignant tumors which would finally induce a 66% decrease of the tumor volume without obvious normal tissue impair and biotoxicity. Therefore, the developed nanotheranostic agent would act as an effective UCNPs-PDT nanoplatform and has great potential for the treatment of the deep-seated malignant tumors.

DATA AVAILABILITY STATEMENT

The raw data supporting the conclusions of this article will be made available by the authors, without undue reservation, to any qualified researcher.

ETHICS STATEMENT

This animal study was reviewed and approved by the Animal Care and Use Committee of Linyi University.

AUTHOR CONTRIBUTIONS

TH and YJ operated this work. ZY performed the statistical analysis. XS and ZW contributed to the design of the study and wrote this manuscript. SZ contributed to the conception of this study.

FUNDING

This work was financially supported by the National Natural Science Foundation of China (Nos. 21605068 and 21605073), the Key Research Plan of Shandong Province (No. 2017GGX40110), and the Key Project of Research and Development Plan of Linyi City (No. 2016GG027).

ACKNOWLEDGMENTS

Thanks all the colleagues in Shandong Provincial Key Laboratory of Detection Technology for Tumor Markers, Linyi University.

SUPPLEMENTARY MATERIAL

The Supplementary Material for this article can be found online at: https://www.frontiersin.org/articles/10.3389/fchem.2020.00052/full#supplementary-material

REFERENCES

Chatterjee, D. K., Fong, L. S., and Zhang, Y. (2018). Nanoparticles in photodynamic therapy: an emerging paradigm. *Adv. Drug Deliv. Rev.* 60, 1627–1637. doi: 10.1016/j.addr.2008.08.003

Chen, C. W., Chan, Y. C., Hsiao, M., and Liu, R. S. (2016). Plasmon-enhanced photodynamic cancer therapy by upconversion nanoparticles conjugated with Au nanorods. *ACS Appl. Mater. Inter.* 8, 32108–32119. doi: 10.1021/acsami.6b07770

Chen, D. X., Tao, R., Tao, K., Chen, B. Q., Choi, S. K., Tian, Q., et al. (2017). Efficacy dependence of photodynamic therapy mediated by upconversion nanoparticles: subcellular positioning and irradiation productivity. *Small* 13:1602053. doi: 10.1002/smll.201602053

Chen, G., Damasco, J., Qiu, H., Shao, W., Ohulchanskyy, T. Y., Valiev, R. R., et al. (2015). Energy-cascaded upconversion in an organic dye-sensitized core/shell fluoride nanocrystal. *Nano Lett.* 15, 7400–7407. doi: 10.1021/acs.nanolett.5b02830

Crompton, M. (1999). The mitochondrial permeability transition pore and its role in cell death. *Biochem. J.* 341, 233–249. doi: 10.1042/0264-6021:3410233

Dong, C., Liu, Z., Wang, S., Zheng, B., Guo, W., Yang, W., et al. (2016). A protein-polymer bioconjugate-coated upconversion nanosystem for simultaneous tumor cell imaging, photodynamic therapy, and chemotherapy. *ACS Appl. Mater. Inter.* 8, 32688–32698. doi: 10.1021/acsami.6b11803

Fan, W., Shen, B., Bu, W., Chen, F., He, Q., Zhao, K., et al. (2014). A smart upconversion-based mesoporous silica nanotheranostic system for synergetic chemo-/radio-/photodynamic therapy and simultaneous MR/UCL imaging. *Biomaterials* 35, 8992–9002. doi: 10.1016/j.biomaterials.2014.07.024

Garfield, D. J., Borys, N. J., Hamed, S. M., Torquato, N. A., Tajon, C. A., Tian, B., et al. (2018). Enrichment of molecular antenna triplets amplifies upconverting nanoparticle emission. *Nat. Photonics* 12, 402–407. doi: 10.1038/s41566-018-0156-x

Ge, X. Q., Liu, J., and Sun, L. (2017). Controlled optical characteristics of lanthanide doped upconversion nanoparticles for emerging applications. *Dalton Trans.* 46, 16729–16737. doi: 10.1039/c7dt03049e

Gnanasammandhan, M. K., Idris, N. M., Bansal, A., Huang, K., and Zhang, Y. (2016). Near-IR photoactivation using mesoporous silica-coated $NaYF_4$:Yb,Er/Tm upconversion nanoparticles. *Nat. Protoc.* 11, 688–713. doi: 10.1038/nprot.2016.035

He, L. C., Dragavon, J., Cho, S. Y., Mao, C. C., Yildirim, A., Ma, K., et al. (2016). Self-assembled gold nanostar-$NaYF_4$:Yb/Er clusters for multimodal imaging, photothermal and photodynamic therapy. *J. Mater. Chem. B* 4, 4455–4461. doi: 10.1039/c6tb00914j

Hou, Z. Y., Deng, K. R., Li, C. X., Deng, X. R., Lian, H. Z., Cheng, Z. Y., et al. (2016). 808 nm Light-triggered and hyaluronic acid-targeted dual-photosensitizers nanoplatform by fully utilizing Nd^{3+}-sensitized upconversion emission with enhanced anti-tumor efficacy. *Biomaterials* 101, 32–46. doi: 10.1016/j.biomaterials.2016.05.024

Huang, P., Rong, P., Jin, A., Yan, X., Zhang, M. G., Lin, J., et al. (2014). Dye-loaded ferritin nanocages for multimodal imaging and photothermal therapy. *Adv. Mater.* 26, 6401–6408. doi: 10.1002/adma.201400914

Kim, J., Santos, Q. A., and Park, J. H. (2014). Selective photosensitizer delivery into plasma membrane for effective photodynamic therapy. *J. Control. Release* 191, 98–104. doi: 10.1016/j.jconrel.2014.05.049

Lee, J., Yoo, B., Lee, H., Cha, G. D., Lee, H. S., Cho, Y., et al. (2017). Ultra-wideband multi-dye-sensitized upconverting nanoparticles for information security application. *Adv. Mater.* 29:1603169. doi: 10.1002/adma.201603169

Li, Z., Lv, S., Wang, Y., Chen, Y., and Liu, Z. (2015). Construction of LRET-based nanoprobe using upconversion nanoparticles with confined emitters and bared surface as luminophore. *J. Am. Chem. Soc.* 137, 3421–3427. doi: 10.1021/jacs.5b01504

Liang, T., Li, Z., Wang, P., Zhao, F., Liu, J., and Liu, Z. (2018). Breaking through the signal-to-background limit of upconversion nanoprobes using a target-modulated sensitizing switch. *J. Am. Chem. Soc.* 140, 14696–14703. doi: 10.1021/jacs.8b07329

Liu, B., Li, C. X., Yang, D. M., Hou, Z. Y., Ma, P. A., Cheng, Z. Y., et al. (2014). Upconversion-luminescent core/mesoporous-silica-shell structured beta-$NaYF_4$:Yb^{3+},Er^{3+}@SiO_2@$mSiO_2$ composite nanospheres: fabrication and drug-storage/release properties. *Eur. J. Inorg. Chem.* 11, 1906–1913. doi: 10.1002/ejic.201301460

Liu, Y., Kang, N., Lv, J., Zhou, Z., Zhao, Q., Ma, L., et al. (2016). Deep photoacoustic/luminescence/magnetic resonance multimodal imaging in living subjects using high-efficiency upconversion nanocomposites. *Adv. Mater.* 28, 6411–6419. doi: 10.1002/adma.201506460

Liu, Y., Liu, Y., Bu, W., Cheng, C., Zuo, C., Xiao, Q., et al. (2015). Hypoxia induced by upconversion-based photodynamic therapy: towards highly effective synergistic bioreductive therapy in tumors. *Angew. Chem. Int. Ed.* 54, 8105–8109. doi: 10.1002/anie.201500478

Liu, Y. Y., Zhang, J. W., Zuo, C. J., Zhang, Z., Ni, D. L., Zhang, C., et al. (2016). Upconversion nano-photosensitizer targeting into mitochondria for cancer apoptosis induction and cyt c fluorescence monitoring. *Nano Res.* 9, 3257–3266. doi: 10.1007/s12274-016-1204-9

Lv, R., Wang, D., Xiao, L., Chen, G., Xia, J., and Prasad, P. N. (2017). Stable ICG-loaded upconversion nanoparticles: silica core/shell theranostic nanoplatform for dual-modal upconversion and photoacoustic imaging together with photothermal therapy. *Sci. Rep.* 7:15753. doi: 10.1038/s41598-017-16016-x

Purushothaman, B., Choi, J., Park, S., Lee, J. J., Samson, A. A. S., Hong, S., et al. (2019). Biotin-conjugated PEGylated porphyrin self-assembled nanoparticles co-targeting mitochondria and lysosomes for advanced chemo-photodynamic combination therapy. *J. Mater. Chem. B* 7, 65–79. doi: 10.1039/c8tb01923a

Song, X., Yue, Z., Hong, T., Wang, Z., and Zhang, S. (2019). Sandwich-structured upconversion nanoprobes coated with a thin silica layer for mitochondria-targeted cooperative photodynamic therapy for solid malignant tumors. *Anal. Chem.* 91, 8549–8557. doi: 10.1021/acs.analchem.9b01805

Song, X., Zhang, J., Yue, Z., Wang, Z., Liu, Z., and Zhang, S. (2017). Dual-activator codoped upconversion nanoprobe with core multishell structure for *in vitro* and *in vivo* detection of hydroxyl radical. *Anal. Chem.* 89, 11021–11026. doi: 10.1021/acs.analchem.7b02995

Song, X. Y., Yue, Z. H., Zhang, J. Y., Jiang, Y. X. L., Wang, Z. H., and Zhang, S. S. (2018). Multicolor upconversion nanoprobes based on a dual luminescence resonance energy transfer assay for simultaneous detection and bioimaging of $[Ca^{2+}]_i$ and pH_i in living cells. *Chem. Eur. J.* 24, 6458–6463. doi: 10.1002/chem.201800154

Thomas, A. P., Palanikumar, L., Jeena, M. T., Kim, K., and Ryu, J. H. (2017). Cancer-mitochondria-targeted photodynamic therapy with supramolecular assembly of HA and a water soluble NIR cyanine dye. *Chem. Sci.* 8, 8351–8356. doi: 10.1039/c7sc03169f

Wang, X., Valiev, R. R., Ohulchanskyy, T. Y., Ågren, H., and Yang, C., Chen, G. (2017). Dye-sensitized lanthanide-doped upconversion nanoparticles. *Chem. Soc. Rev.* 46, 4150–4167. doi: 10.1039/c7cs00053g

Wei, Y., Lu, F. Q., Zhang, X. R., and Chen, D. P. (2006). Synthesis of oil-dispersible hexagonal-phase and hexagonal-shaped $NaYF_4$:Yb,Er nanoplates. *Chem. Mater.* 18, 5733–5737. doi: 10.1021/cm0606171

Wu, X., Zhang, Y., Takle, K., Bilsel, O., Li, Z., Lee, H., et al. (2016). Dye-sensitized core/active shell upconversion nanoparticles for optogenetics and bioimaging applications. *ACS Nano* 10, 1060–1066. doi: 10.1021/acsnano.5b06383

Xu, J., Yang, P., Sun, M., Bi, H., Liu, B., Yang, D., et al. (2017). Highly emissive dye-sensitized upconversion nanostructure for dual-photosensitizer photodynamic therapy and bioimaging. *ACS Nano* 11, 4133–4144. doi: 10.1021/acsnano.7b00944

Yan, F., Wu, H., Liu, H., Deng, Z., Liu, H., Duan, W., et al. (2016). Molecular imaging-guided photothermal/photodynamic therapy against tumor by iRGD-modified indocyanine green nanoparticles. *J. Control. Release* 224, 217–228. doi: 10.1016/j.jconrel.2015.12.050

Yue, Z., Hong, T., Song, X., and Wang, Z. (2018). Construction of a targeted photodynamic nanotheranostic agent using upconversion nanoparticles coated with an ultrathin silica layer. *Chem. Commun.* 54, 10618–10621. doi: 10.1039/c8cc05121f

Zheng, M., Yue, C., Ma, Y., Gong, P., Zhao, P., Zheng, C., et al. (2013). Single-step assembly of DOX/ICG loaded lipid-polymer nanoparticles for highly effective chemo-photothermal combination therapy. *ACS Nano* 7, 2056–2067. doi: 10.1021/nn400334y

Zou, W., Visser, C., Maduro, J. A., Pshenichnikov, M. S., and Hummelen, J. C. (2012). Broadband dye-sensitized upconversion of near-infrared light. *Nat. Photonics* 6, 560–564. doi: 10.1038/nphoton.2012.158

Zou, X., Xu, M., Yuan, W., Wang, Q., Shi, Y., Feng, W., et al. (2016). A water-dispersible dye-sensitized upconversion nanocomposite modified with phosphatidylcholine for lymphatic imaging. *Chem. Commun.* 52, 13389–13392. doi: 10.1039/c6cc07180e

Conflict of Interest: The authors declare that the research was conducted in the absence of any commercial or financial relationships that could be construed as a potential conflict of interest.

frontiers in Chemistry

ORIGINAL RESEARCH
published: 15 April 2020
doi: 10.3389/fchem.2020.00212

Preparation of Poloxamer188-*b*-PCL and Study on *in vitro* Radioprotection Activity of Curcumin-Loaded Nanoparticles

Xiaona Lin[1], *Yongli Shi*[2]*, *ShaSha Yu*[2], *Siyi Li*[2], *Wenhui Li*[2], *Meishuang Li*[2], *Shengxi Chen*[2], *Yuanbo Wang*[2] *and Mei Cong*[2]

[1] Tianjin Key Laboratory of Radiation Medicine and Molecular Nuclear Medicine Institute of Radiation Medicine, Chinese Academy of Medical Sciences and Peking Union Medical College, Tianjin, China, [2] College of Pharmacy, Xinxiang Medical University, Xinxiang, China

A novel polymer of poloxamer188-*b*-PCL was synthesized via a ring-opening polymerization. Fourier transform infrared spectroscopy (FTIR), Raman, and ^{1}H nuclear magnetic resonance (^{1}H NMR) spectra were used to study the structures of obtained poloxamer188-*b*-PCL. The thermo-stability of poloxamer188 -*b*-PCL was carried out with a thermal gravimetric analyzer (TGA), and cytotoxicity was obtained using the CCK8 method. Cargo-free and curcumin (CUR)-loaded poloxamer188-*b*-PCL NPs were fabricated via the solvent evaporation method. The morphology, particle size distribution, and stability of cargo-free NPs were studied with a scanning electron microscope (SEM) and laser particle analyzer. The *in vitro* radioprotection activity of CUR-loaded NPs was performed. FTIR, Raman, and ^{1}H NMR spectra confirmed that poloxamer188-*b*-PCL was obtained. TGA curves suggested poloxamer188-*b*-PCL had better thermo-stability than original poloxamer188. Cell tests suggested that the cargo-free NPs had no cytotoxicity. SEM image showed that the cargo-free NPs were spherical with a diameter of 100 nm. Free radical scavenging experiments proved that CUR-loaded NPs had better antioxidant activity than CUR solutions. CUR-loaded NPs could be detected in all tissues, including liver, kidneys and lung. In summary, this work demonstrated a feasibility of developing an injective formulation of CUR and provided a protection agent in caner radiotherapy.

Keywords: poloxamer188-*b*-PCL, nanoparticles, antioxidant activity, curcumin, caner radiotherapy

OPEN ACCESS

Edited by:
Xiaoli Wei,
University of California, San Diego, United States

Reviewed by:
Runliang Feng,
University of Jinan, China
Weiwei Wang,
Chinese Academy of Medical Sciences and Peking Union Medical College, China
Hua Gong,
University of California, San Diego, United States

***Correspondence:**
Yongli Shi
shiyongli2005@163.com

Specialty section:
This article was submitted to Nanoscience, a section of the journal Frontiers in Chemistry

Received: *31 December 2019*
Accepted: *06 March 2020*
Published: *15 April 2020*

Citation:
Lin X, Shi Y, Yu S, Li S, Li W, Li M, Chen S, Wang Y and Cong M (2020) Preparation of Poloxamer188-b-PCL and Study on in vitro Radioprotection Activity of Curcumin-Loaded Nanoparticles. Front. Chem. 8:212. doi: 10.3389/fchem.2020.00212

INTRODUCTION

Curcumin (CUR), a natural chemical, is first extracted from the rhizomes of zingiberaceae or araceae plants (Zhao et al., 2015). CUR is an infrequent diketone pigment which is distributed in plants. Because of the low toxicity, CUR is applied as a colorant in the field of foods (Mishra and Daswal, 2007; Epstein et al., 2010; Lüer et al., 2014), which is approved by the World Health Organization (WHO), the Food and Drug Administration (FDA), and many countries. In recent years, CUR is been one of the top-selling natural edible pigments. Furthermore, CUR has broad clinical application, i.e., antioxidant activity (Esatbeyoglu et al., 2015; Llano et al., 2019; Wang et al., 2019), anti-tumor (Ohtsu et al., 2002; Kunnumakkara et al., 2007; Yan et al., 2017),

anti-inflammatory (Aggarwal and Harikumar, 2009; Fadus et al., 2017; Hussain et al., 2017), and anti-hyperlipidemia (Huang et al., 2018; Panahi et al., 2018; Wang et al., 2018), and so on. In particular, bioactivities of curcumin as an effective chemopreventive agent, chemo-/radio-sensitizer for tumor cells, and chemo-/radio-protector for normal organs, are of extraordinary research interests in the literature (Farhood et al., 2018).

However, in their clinical applications, CUR molecules show certain drawbacks, e.g., low solubility (Lim et al., 2018; Peng et al., 2018), poor stability (Kharat et al., 2017; Luo et al., 2017), low absorptivity (Gopi et al., 2017), and short half-life (Hussain et al., 2017). These weaknesses lead to the low bioavailability of CUR and limit its further applications. It is reported that CUR can be detected in the body when the oral dosage is up to 10–12 g. Administrating 10 mg/kg of CUR by intravenous injection, the peak plasma concentration of a rat is only 0.36 μg/ml. After 15 min of gavage (1.0 g/kg CUR), the concentration of CUR in rat plasma is only 0.13 μg/ml, and 1.0 h later, the peak plasma concentration is only 0.22 μg/ml (Akinyemi et al., 2017). Six hours later, CUR cannot be detected in rat blood. After gavage, 90% CUR is found in the stomach and small intestine, and few CUR molecules can be detected in the blood, liver, and kidneys. Therefore, improving the stability and bio-availability of CUR will be important for future directions.

It has been reported that polymeric nanoparticles (NPs) can be used to improve the water solubility and stability of hydrophobic drugs (Levard et al., 2012; Krull et al., 2017). Therefore, CUR-loaded polymer NPs can prevent these molecules from being oxidized and improve their stability as well as their bioavailability. For biological applications, the matrix of NPs should have good biodegradability, biocompatibility, and no cytotoxicity. Poloxamer188, a non-ionic surfactant, is the block copolymer of polyoxyethylene and polypropylene oxide (Armstrong et al., 1995). Due to its excellent biocompatibility and low bio-toxicity, poloxamer188 is widely used in pharmaceuticals to improve the solubility of hydrophobic molecules (Ofokansi et al., 2012), enhance the stability of model drugs (Huang et al., 2008), and accelerate the absorbance of bioactive components. Furthermore, Poloxamer188 has a terminal hydroxyl group, which can be modified for further application. Caprolactone (CL) is a non-toxic chemical intermediate, which is usually used as monomers to fabricate Polycaprolactone (PCL) which is a high performance polymer. Due to its excellent bio-compatibility, PCL can be used as the material support growth of cells (John and Qi, 2008). In addition, good bio-degradability allows PCL to be completely degraded within 12 months in the natural environment.

Poloxamer 188 (Pluronic F68, F68) employed as a surfactant, can cause sensitization of multiple drug resistance (MRD) tumors to various anticancer agents and enhance drug transport across blood brain and intestinal barriers. Poloxamer188 blended into PCL could affect the microspheres' morphology and control drug release (Ma and Song, 2007). In this study, a novel copolymer was prepared via a ring-opening polymerization with poloxamer188 and ε-CL as monomers. Hydrogen nuclear magnetic spectra (^{1}H NMR), Fourier transform infrared spectroscopy (FTIR), Raman spectra were used to confirm the obtained poloxamer188-*b*-PCL. CUR was selected as a model drug and loaded into the poloxamer188-*b*-PCL NPs to improve the stability of CUR. The morphology, size distribution, and stability of obtained NPs were studied. The *in vitro* free-radical-scavenging ability and antioxidant activity were also investigated to preliminarily evaluate its radioprotection ability.

EXPERIMENTAL

Materials and Methods

Poloxamer188 was the product of BASF (Germany). ε-CL, Tin(II) 2-ethylhexanoate, and CUR were bought from Energy chemical (Shanghai, China). Tetrahydrofuran (THF, CP) was obtained from Sinopharm Chemical Reagent Co., Ltd. 2, 2′-azino-bis(3-ethylbenzothiazoline-6-sulfonic acid) (ABTS) and 1,1-diphenyl-2- picrylhydrazyl (DPPH) were the products of Energy chemical (Shanghai, China). Trichloroacetic acid, potassium ferricyanide, and ferric trichloride were obtained from Aladdin Industrial Corporation (Shanghai, China). Other organic reagents were bought from Tianjin Beichen chemical reagent Co., Ltd (Tianjin, China), and used as received without any further purification.

Synthesis of Poloxamer188-*b*-PCL

Poloxamer188-*b*-PCL was prepared via a ring-opening polymerization with Poloxamer188 and ε-PCL as monomers (as shown in **Figure 1A**). 1.60 g of poloxamer188 and 200 μl of Tin(II) 2-ethylhexanoate were dissolved into 3.20 g of ε-CL. Next, air in the reaction tube was removed by a vacuum pump, and then the tube was sealed up in nitrogen atmosphere. After being reacted at 130°C for 10.0 h, the crude poloxamer188-*b*-PCL was synthesized. Then 1.0 ml methylene chloride was used to dissolve the crude products, and the refined polymers were obtained by dropwise adding the above mentioned solution into 50 ml ice-cooled methyl alcohol. After filtering, refined poloxamer188-*b*-PCL dried at 40°C for 24 h.

Characterization on Copolymers

The FTIR spectra of poloxamer188, ε-CL, and PCL were obtained from an FTS-135 (BIO-RAD, USA) spectrometer, scanning from 4,000 to 500 cm^{-1}. KBr pellets were prepared under a hydraulic pressure of 400.0 kg at the KBr and specimen ratio of 10:1 (m/m). Meanwhile, Raman spectra were also used to study the structure of final copolymers. All spectra were recorded on a Metage OPAL Portable Raman System (ProRoman L-785, EVWAVE Optronics. lnc), covering a range of 3,200–3250 cm^{-1} at a spectral resolution of 4 cm^{-1}, and each sample was scanned for 10 times.

^{1}H NMR spectrum was used to analyze the structure of the obtained copolymers. ^{1}HNMR spectra were recorded on a Bruker 400 MH_Z nuclear magnetic resonance instrument with $CDCl_3$.

Mettler-Toledo TGA/DSC-2 (Switzerland) was sued to study the thermo-stability of poloxamer188 and poloxamer188-*b*-PCL. About 5.0 mg of samples were loaded into ceramic pans (50 μl), and their TGA curves were recorded under the atmosphere of high purity nitrogen (flow rate of 20 ml/min) heating from 25 to 500°C at the rate of 10°C/min.

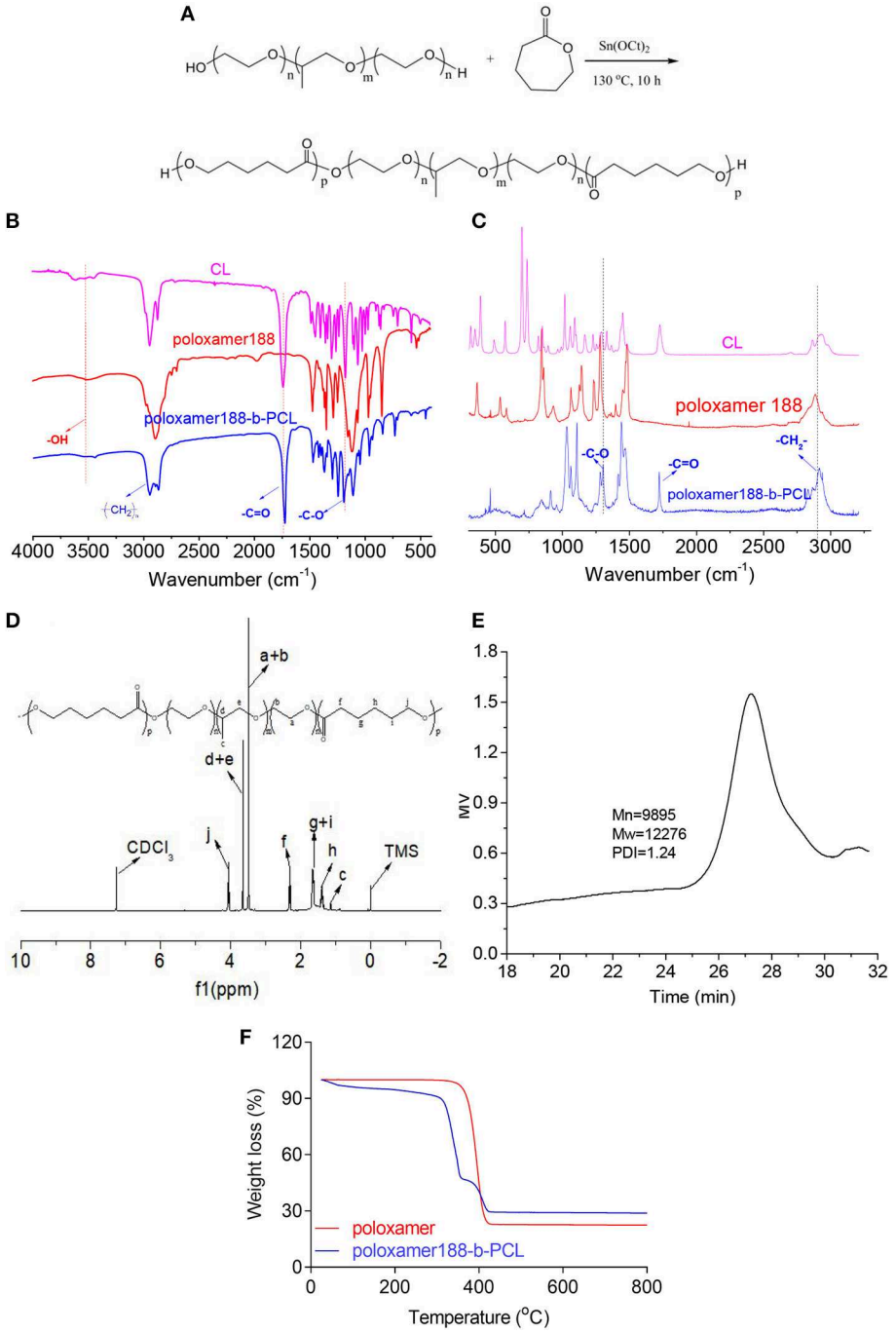

FIGURE 1 | Synthetic process of poloxamer188-*b*-PCL polymers **(A)**. The block polymers were synthesized via the ring-opening polymerization with poloxamer188 and ε-CL as starting materials; FTIR spectra of ε-CL, poloxamer188, and poloxamer188-*b*-PCL polymers **(B)**. The absorption peak of –C=O group was found in the spectrum of final polymer, which confirmed the obtaining of the poloxamer188-*b*-PCL polymers; Raman spectra of ε-CL, poloxamer188, and poloxamer188-*b*-PCL polymers **(C)**; ^{1}H NMR spectrum of poloxamer188-*b*-PCL polymers **(D)**. The ^{1}H NMR spectrum also confirmed the obtaining of poloxamer188-*b*-PCL polymers; GPC curve of poloxamer188-*b*-PCL polymers **(E)**. The Mw of obtained polymer was 12,276 D; TGA curves of poloxamer188 and poloxamer188-*b*-PCL polymers **(F)**. TGA curves indicated that the poloxamer188-*b*-PCL polymers improved the thermo-stability of poloxamer188.

The molecular weight of poloxamer188-*b*-PCL was measured with Waters 1515 GPC (Waters Company, USA). THF was selected as the mobile phase, and the flow rate was set as 1.0 ml/min. Polystyrene with the molecular weights of 100–500,000 were used as reference substances.

Fabrication of Poloxamer188-*b*-PCL NPs

Poloxamer188-*b*-PCL NPs were fabricated by a solvent evaporation method (Alshamsan, 2014). One hundred milligrams of poloxamer188-*b*-PCL was dissolved into 3.0 ml THF. Under magnetic stirring (350 rpm), the polymer/THF solution was slowly added into 100 ml deionized water. Then, the solution was stirred for another 12 h. After removing the residual THF, the poloxamer188-*b*-PCL NPs were fabricated. The CUR-loaded NPs were fabricated with the same method. 10.0 mg CUR and 100 mg poloxamer188-*b*-PCL were dissolved into 3.0 ml THF, and the other steps were the same as described above.

Stability of Cargo-Free NPs

Six test tubes each with 4.0 ml cargo-free NPs solutions were incubated in a 80°C water bath. At the time points of 0 min, 10 min, 20 min, 30 min, 40 min, and 60 min, one tube was fetched to measure the size distribution of the cargo-free NPs. 2.0 ml NPs solution was loaded into a cuvette, and the size distribution was measured with a Malvern Zatasizer (Nano-ZS90, UK) under room temperature. Each sample was measured for three times.

10% of Bovine Serum Albumin (BSA) was added into a cargo-free NPs solution to study their colloidal stability (Zuo et al., 2015). The NPs solution without BSA was used as a control. At the time points of 0, 2, 4, 6, 8, 10, 12, and 24 h, the hydrodynamic diameters and PDI of NPs solutions were measured with a Malvern Zatasizer (Nano-ZS90, UK).

Cytotoxicity

The cytotoxicity of cargo-free poloxamer188-*b*-PCL NPs was carried out with a CCK8 method. KYSE520 cells were seeded in 96-well plates at a density of 8.0×10^3 cells/ml. These cells were incubated at 37°C for 48 h with 10.0 μl of cargo-free NPs solutions with the concentrations of 30.0, 60.0, 250, and 1,000 μg/ml, respectively. Before harvest, 10.0 μl CCK8 solutions were added into the wells. After additional 4 h incubation at 37°C, the absorbance was measured at 450 nm using a microplate reader (Bio-Rad Model 680, UK).

Cells Uptake

KYSE520 cells were seeded in 6-well plates at the density of 10, 000 cells per well. The culture medium was kept at 37°C and maintained in a humidified atmosphere containing 95% air and 5% CO_2. Forty-eight hours later, 100 μg/ml CUR/DMSO solution and CUR-NPs suspension (containing 100 μg/ml CUR) were added into the culture medium. The cells were incubated for another 8 h, and then the cells were washed with 1.0 ml phosphate buffer solution (10 mM, pH 7.4) three times to remove the free CUR and CUR-NPs. The fluorescence intensities of cells were observed with a laser scanning confocal microscope (LSCM, Leica AF 6500, Germany).

In vitro Antioxidant Activity

ABTS Free Radical ($ABTS^{\cdot+}$) Scavenging Experiments (Li et al., 2017; Rashed et al., 2018)

38.4 mg of ABTS was dissolved into 10 ml deionized water to prepare the ABTS base solution (7 mM). K2S2O8/H2O solution (4.9 mM) was used as K2S2O8 base solution. Both solutions were mixed together and stayed for 12–16 h to be used as the $ABTS^{\cdot+}$ stock solution. Before usage, the absorbance of stock solution was diluted to A734 = 0.7± 0.02 with phosphate buffer (PBS, pH = 7.4), which was used as operating fluid.

The test fluids were CUR-loaded NPs solutions and CUR/alcohol solutions with the CUR concentrations of 0, 1, 5, 10, 20, 25, and 50 μg/L, respectively. One hundred and forty microliters of test fluids were added into 4.0 ml $ABTS^{\cdot+}$ operating fluid ($A_{734} = 0.7 \pm 0.02$). After a 6 h reaction in a 30°C water bath, the absorbance of the above mentioned solutions was measured with a UV-2700 ultraviolet spectrophotometer (734 nm). PBS (pH = 7.4) was selected as the blank control. The clearance rate of $ABTS^{\cdot+}$ was calculated following Equation (1):

$$C_{ABTS^{\cdot+}} = \frac{A_c - A_s}{A_c} \times 100 \quad (1)$$

Where: $C_{ABTS\cdot+}$ was the clearance of $ABTS^{\cdot+}$; A_s and A_c were absorbance of samples and blank controls, respectively. When the absorbance of $ABTS^{\cdot+}$ clearance was 50%, the sample concentrations were recorded as SC_{50}.

DPPH Free Radical Scavenging Experiments (Ju et al., 2011; Ullah et al., 2017)

1.9716 g of DPPH was dissolved into 50 ml alcohol to be used as a stock solution, which was kept in a dark place under room temperature. CUR-loaded NPs solutions and CUR/alcohol solutions with concentrations of 0, 1, 5, 10, 20, 25, and 50 μg/L were selected as test solutions. 2.0 ml of the test solution was added into the isopycnic DPPH solution, and the mixture was kept in a dark place for 30 min. The absorbance of the above mentioned solution was then measured with a UV-2700 ultraviolet spectrophotometer at 517 nm. The clearance rate of $ABTS^{\cdot+}$ was calculated following Equation (2):

$$C_{\mathrm{DPPH}} = \frac{A_c - A_s}{A_c} \times 100 \quad (2)$$

Where: C_{DPPH} was the clearance of $ABTS^{\cdot+}$; A_s and A_c were absorbance of samples and blank controls, respectively. When the absorbance of clearance of DPPH was 50%, the sample concentrations were recorded as SC_{50}.

Reducing Power (Shabbir et al., 2013)

The mixture of 2.0 ml test solution, 2.5 ml potassium ferricyanide solution and 2.5 ml PBS (pH 6.82) was incubated in a 50°C water-bath for 20 min. When the mixture was cooled in an ice-water bath, another 2.5 ml trichloroacetic acid solution (10 w/w%) was added into the above mentioned mixture. After centrifugation (3,000 r/min, 10 min), 2.5 ml supernate was added into the mixture of 2.5 ml deionized water and 0.5 ml ferric trichloride solution (0.1 w/w%). Ten minutes later, the absorbance of the mixture was measured with a UV-2700 ultraviolet spectrophotometer at 710 nm.

In vivo Distribution of Poloxamer188-*b*-PCL NPs

In the animal experiment, rhodamine B (RhB) was used as a fluorescence probe. RhB-loaded Poloxamer188-*b*-PCL NPs were prepared following the method which was described above (section Fabrication of Poloxamer188-*b*-PCL NPs). C57 rats were treated with 200 μl RhB-loaded Poloxamer188-*b*-PCL NPs (10 mg/ml) by intraperitoneal injection. At proper intervals, the rats were sacrificed and their viscera (i.e., heart, liver, spleen, lungs, and kidneys) removed. The fluorescence intensity of all the viscera was examined using the CRI Maestro *in vivo* imaging system (CRI Corporation, Woburn, MA, USA) at 523 nm.

All of rats were housed in individual cages in a controlled environment with free access to food and water. The experiment was carried out in accordance with the People's Republic of China national standards (GB/T16886.6-1997).

RESULTS AND DISCUSSION

Characterization on Poloxamer188-*b*-PCL

FTIR spectra of the obtained polymer were shown in **Figure 1B**. In the spectrum of ε-CL, the absorption peak observed at 1742.9 cm^{-1} was due to the stretching vibration of carbonyl groups (Yin et al., 2017). By contrast, this peak was not observed in the spectrum of poloxamer188. However, such peak was found in final polymers. Further, the peak at 3,515.5 cm^{-1} could be attributed to the stretching vibration of –OH (Barka et al., 2013), which was observed in the spectra of poloxamer188-*b*-PCL. These data indicated that the esterification reaction was performed between poloxamer188 and ε-CL. Raman spectra gave the similar results (as shown in **Figure 1C**). The diffraction maximum at 1,720 cm^{-1} (-C=O) was observed in the spectra of ε-CL and final polymers. Besides, another diffraction maximum at 1,250 cm^{-1} was assigned to the vibration of -C-O groups. Therefore, it could be speculated that new ester bonds generated in the final polymers.

The ^{1}H NMR spectrum of final polymers is shown in **Figure 1D.** It can be seen that bands assigning to the protons of PCL chains were observed at 2.3 ppm (-CO-**CH_2**-, f), 1.6 ppm (-**CH_2**-, g+i), 1.4 ppm (-**CH_2**-, h), and 4.0 ppm (-O-**CH_2**-, j), respectively (Ali et al., 2017). The bands of H atoms assigned to poloxamer188 were observed at 1.0 ppm (-**CH_3**, c), 3.7 ppm (-O-C**H_2**-C**H**-, d+e), and 3.5 ppm (-C**H_2**-C**H_2**-O-, a+b), respectively (Jacobsson, 2005). **Figure 1E** provides the GPC results of poloxamer188-*b*-PCL. It can be seen that the GPC curve was a single summit structure which was symmetrically distributed. The PDI (M_w/M_n) of poloxamer188-*b*-PCL was 1.24, which suggested that the molecular weight distribution was narrow. In conclusion, these studies confirmed that poloxamer188-*b*-PCL was obtained.

The thermo-stability of poloxamer188-*b*-PCL was studied and the TGA results are shown in **Figure 1F**. The initial decomposition temperature of poloxamer188 was observed at 340°C with a mass loss of 74%, which could be attributed to the breaking of ether bonds and –OH groups. By contrast, two decomposition events were found in the TGA curve of poloxamer188-*b*-PCL. The first event was observed at 300–350°C with a mass loss of 50%, which was assigned to the decomposition of poloxamer188 chains (Abdelrazek et al., 2016). The event at 370–410°C (mass loss of 15%) was due to the thermal rupture of PCL chains (Nadal et al., 2016). The differences between both curves indicated that poloxamer188-*b*-PCL had better thermo-stability than original poloxamer188.

Stability of Poloxamer188-*b*-PCL NPs

In ultrapure water, the amphipathic polymer poloxamer188-*b*-PCL could self-assemble into NPs with hydrophobic cores and hydrophilic shells. The obtained cargo-free NPs showed a diameter of 119.9 ± 0.5 nm with a PDI of 0.03 ± 0.02 (**Figure 2A**), which suggested that the particle size distribution of obtained NPs was narrow and well-proportioned. Furthermore, it can be seen from SEM image (**Figure 2A** insert, left) that the obtained NPs were spherical with a diameter of about 100 nm, which is consistent with the results obtained from the laser particle analyzer. Similarly, the concentrations of NaCl did not influence the size distribution of cargo-free NPs (as shown in **Figure 2B**).

Heating could increase the energy of NPs, and conglomeration would happen among NPs. The thermo-stability of cargo-free NPs was studied in a 80°C water-bath, and results were shown in **Figure 2C**. It could be seen that the cargo-free NPs showed excellent thermo-stability. During the water-bath (80°C), the NPs' diameters were fluctuated between 110 and 120 nm, and the PDIs were all in the range of 0.02–0.2. These data indicate that the obtained NPs had a good thermodynamic stability.

After adsorption by protein, it was difficult for the NPs to be delivered to the targets, and the drug-loaded NPs would not be effective. Therefore, the NPs should have protein resistance. As shown in **Figure 2D**, although the particle size distribution of the NPs solution with 10% BSA was slightly bigger than that of the original NPs solution, their diameters still fluctuated between 110 and 120 nm. This phenomenon illustrates that the poloxamer188-*b*-PCL NPs could not be adsorbed by BSA, and had good protein resistance.

Furthermore, the biomaterial should be non-toxic. The cytotoxicity of poloxamer188-*b*-PCL NPs was reflected by cell viability. In **Figure 2E**, in incubation with the NPs solutions (30.0, 60.0, 250, and 1,000 μg/ml, respectively), the viability of KYSE520 cells were over 90%. The high viability of all cells indicates that the cargo-free poloxamer188-*b*-PCL NPs had no cytotoxicity, and could be used as a biomaterial.

In vitro Antioxidant Activity

After 24 h, the $ABTS^{\cdot+}$ scavenging experiments were carried out, and their scavenging rates can be seen in **Figure 3A**. In different concentrations, CUR-loaded NPs gave higher $ABTS^{\cdot+}$ scavenging rates. After a *t*-test analysis, significant differences were found between CUR-loaded NPs and CUR/alcohol solutions (***$P < 0.001$). As shown in **Figure 3B**, the CS50 of CUR/alcohol solutions and CUR-loaded NPs were 62.3 ± 2.9 and 47.5 ± 2.6 mg/ml, respectively (**$P < 0.01$). Similarly, CUR-loaded NPs exhibited excellent DPPH scavenging effects (**Figure 2C**). Twenty-four hours later, most CUR-loaded NPs solutions had

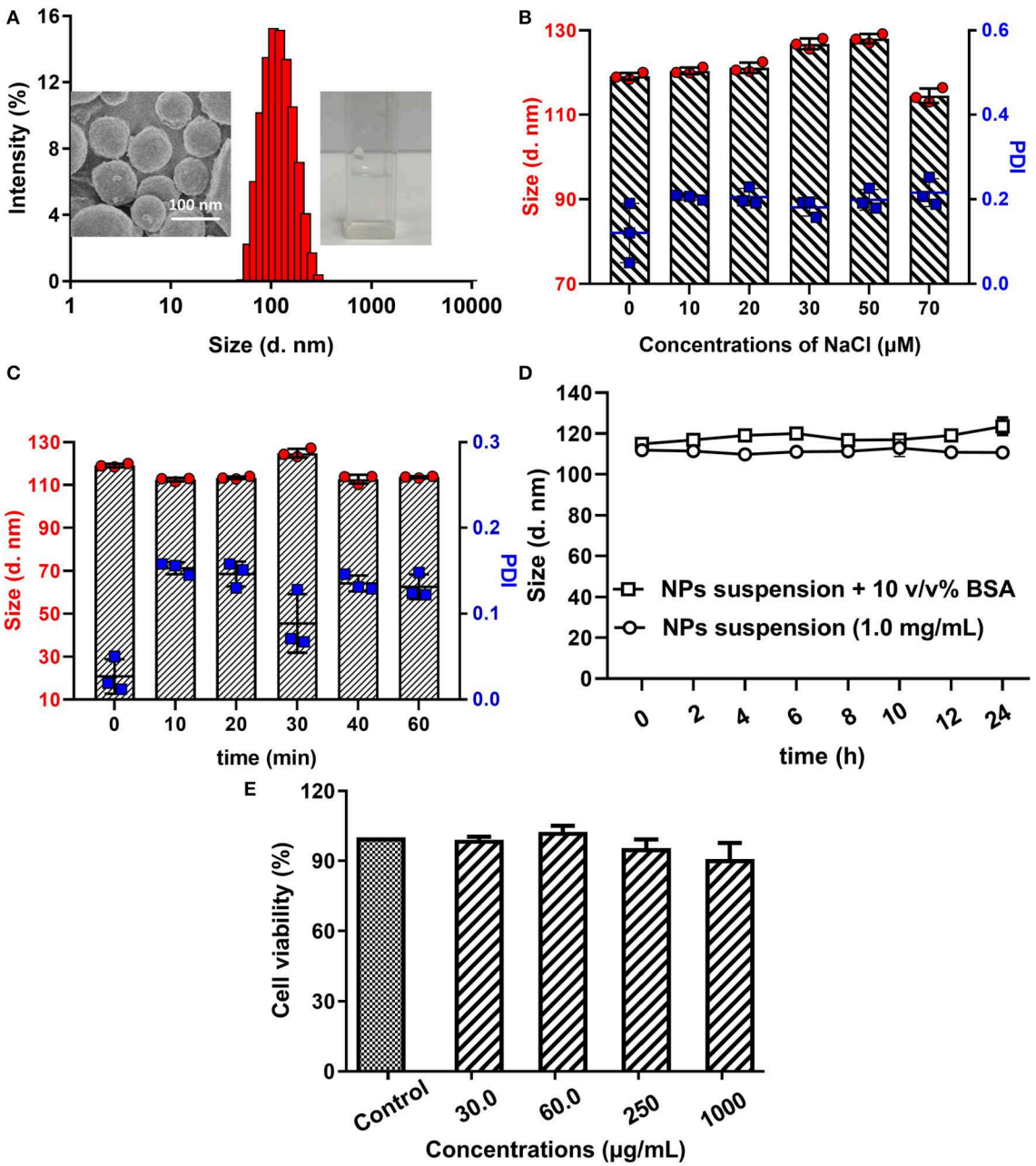

FIGURE 2 | Size distribution of poloxamer188-*b*-PCL NPs **(A)**, SEM image of cargo-free NPs (insert, left), and poloxamer188-*b*-PCL NPs solution (insert, right). The average diameter of the obtained NPs was 119.9 ± 0.5 nm with a PDI of 0.03 ± 0.02; the different stability of cargo-free NPs in various NaCl solution **(B)**. The cargo-free NPs showed an excellent stability in NaCl solutions; the thermo-stability of cargo-free NPs **(C)**. The size distribution of poloxamer188-*b*-PCL NPs in BSA solution **(D)**. After 60 min incubation under 80°C, the cargo-free NPs had good stability; the stability of cargo-free NPs in 10% BSA solution; Cytotoxicity of the cargo-free NPs **(E)**. Cell results indicated that the poloxamer188-*b*-PCL NPs did not show obvious cytotoxicity.

higher DPPH scavenging rates than those of CUR/alcohol solutions ($^{*}P < 0.05$) (as shown in **Figure 3C**). The CS50 of CUR-loaded NPs and CUR/alcohol solutions were 15.0 ± 0.8 and 10.3 ± 1.1 mg/ml, respectively ($^{***}P < 0.001$) (as shown in **Figure 3D**). These differences could be attributed to the various stabilities of CUR. In CUR/alcohol solutions, CUR molecules were easily oxidized by oxygen, while the CUR-loaded NPs were difficult to destroy. Therefore, the new prepared CUR/alcohol solutions had better antioxidant activities than those of CUR-loaded NPs (**Figure 1S**). However, 24 h later, with the oxidization of CUR/alcohol solutions, their antioxidant activities decreased.

It was reported that the antioxidant activities of substances were proportional to their reducing power. The reducing materials provided H atoms with the ability to break the free radial chains, which generated antioxidant activities. In this study, the H atoms from CUR reduced Fe^{3+} into

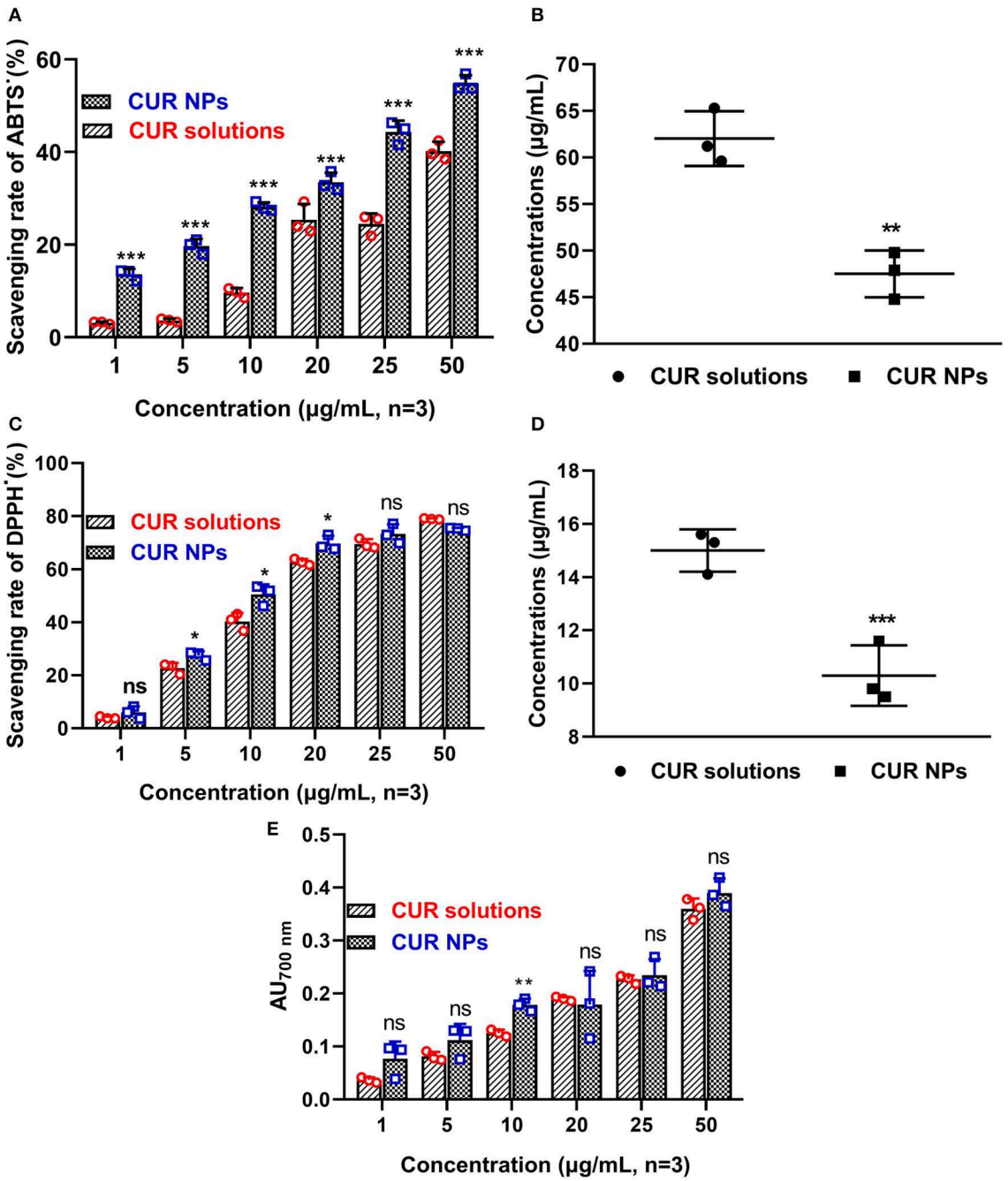

FIGURE 3 | ABTS·+ scavenging experiments of original CUR and CUR-loaded poloxamer188-*b*-PCL NPs **(A)**. The CUR-loaded NPs had better ABTS·+ scavenging rate than that of original CUR powder; The SC_{50} of original CUR and CUR-loaded poloxamer188-*b*-PCL NPs **(B)**; DPPH· scavenging experiments of original CUR and CUR-loaded poloxamer188-*b*-PCL NPs **(C)**. The CUR-loaded NPs had better DPPH• scavenging rate than that of original CUR powder; The SC_{50} of original CUR and CUR-loaded poloxamer188-*b*-PCL NPs **(D)**; the reducing power of original CUR and CUR-loaded poloxamer188-*b*-PCL NPs **(E)**. $^{*}p < 0.05$; $^{**}p < 0.01$; $^{***}p < 0.001$.

Fe^{2+}, which prevented the generation of peroxide. This process is a Prussian blue reaction, and the products had a maximum absorbency of 700 nm. The higher absorbency suggested the sample had better reducing power. The reducing powers of CUR-loaded NPs and CUR/alcohol solutions are shown in **Figure 3E**. Most CUR molecules were encapsulated in NPs, and newly prepared CUR/alcohol solutions had better reducing powers than CUR-loaded NPs (**Figure 2S**). However, 24 h later, both materials had similar reducing powers. In general, CUR-loaded NPs had better *in vitro* antioxidant activity than that of CUR/alcohol solutions.

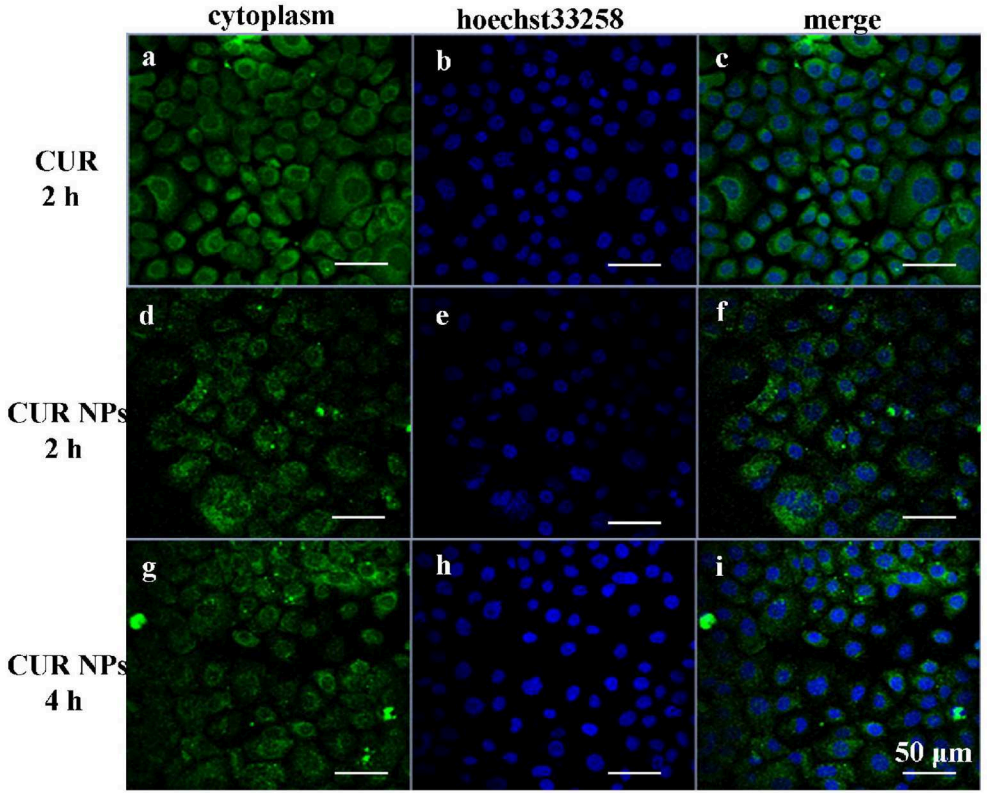

FIGURE 4 | Fluorescence microscopy of KYSE520 cells incubated with free CUR and CUR-loaded NPs at equivalent CUR concentrations. It could be seen that the CUR-loaded NPs could be ingested by KYSE520 cells. **(a)** The cytoplasm of KYSE520 cells after 2 h of treating with CUR; **(b)** The cell nucleus of KYSE520 cells after 2 h of treating with hoechst33258; **(c)** The merge image of **(a,b)**; **(d)** The cytoplasm of KYSE520 cells after 2 h of treating with CUR NPs; **(e)** The cell nucleus of KYSE520 cells after 2 h of treating with hoechst33258; **(f)** The merge image of **(d,e)**; **(g)** The cytoplasm of KYSE520 cells after 4 h of treating with CUR NPs; **(h)** The cell nucleus of KYSE520 cells after 4 h of treating with hoechst33258; **(i)** The merge image of **(g,h)**.

The information on curcumin suggests that the radioprotective effect might be mainly due to its ability to reduce oxidative stress after exposure ionizing radiation. Therefore, CUR-loaded NPs will have better clinical efficacy than a curcumin drug during radiotherapy of cancer.

Cell Uptake

Usually, cells uptake CUR molecules via free diffusion, while CUR-loaded NPs enter cells via endocytosis. Therefore, CUR-loaded NPs provided lower fluorescence intensity than that of CUR molecules. **Figure 4** shows the fluorescence photographs of KYSE520 cells incubated with CUR solutions and CUR-loaded NPs, respectively. At 2 h, more CUR molecules were up-taken by cells. Therefore, KYSE520 cells treated with CUR molecules showed stronger fluorescence intensity than those treated with CUR-loaded NPs. However, with time, more CUR-loaded NPs entered into cells and more CUR molecules were decomposed by cells, and both batches of cells had a similar fluorescence intensity. These phenomena illustrate that the CUR-loaded NPs could be endocytosed by Cells, and had better stability than CUR solutions.

Bio-Distribution of RhB-Loaded Poloxamer188-*b*-PCL NPs

The *in vivo* distribution of the Poloxamer188-*b*-PCL NPs was carried out with RhB as a fluorescence probe. **Figures 5a,b** displays the RhB levels in various viscera, i.e., heart, liver, spleen, lungs, and kidneys. After intraperitoneal injection, the RhB-loaded NPs could distribute fast in all tissues. The RhB-loaded NPs were mainly distributed in liver, lungs, and kidneys (**Figure 5a**). The highest fluorescence intensity was found in liver, which was over 2000 A.U., and the spleen showed the lowest intensity at 135 A.U. (as shown in **Figure 5c**). Similar results were observed after 2 h of injection (**Figure 5b**), but all fluorescence intensity decreased. The result revealed NPs selective distribution in different tissues. The presence of NPs in the kidney and lung is of special interest because protection of these tissues from radiation damage is key to recovery and host survival during caner radiotherapy.

CONCLUSIONS

A novel block polymer of poloxamer188-*b*-PCL was synthesized via the ring-opening polymerization. ^{1}H NMR, Raman, and FTIR spectra confirmed that poloxamer188-*b*-PCL

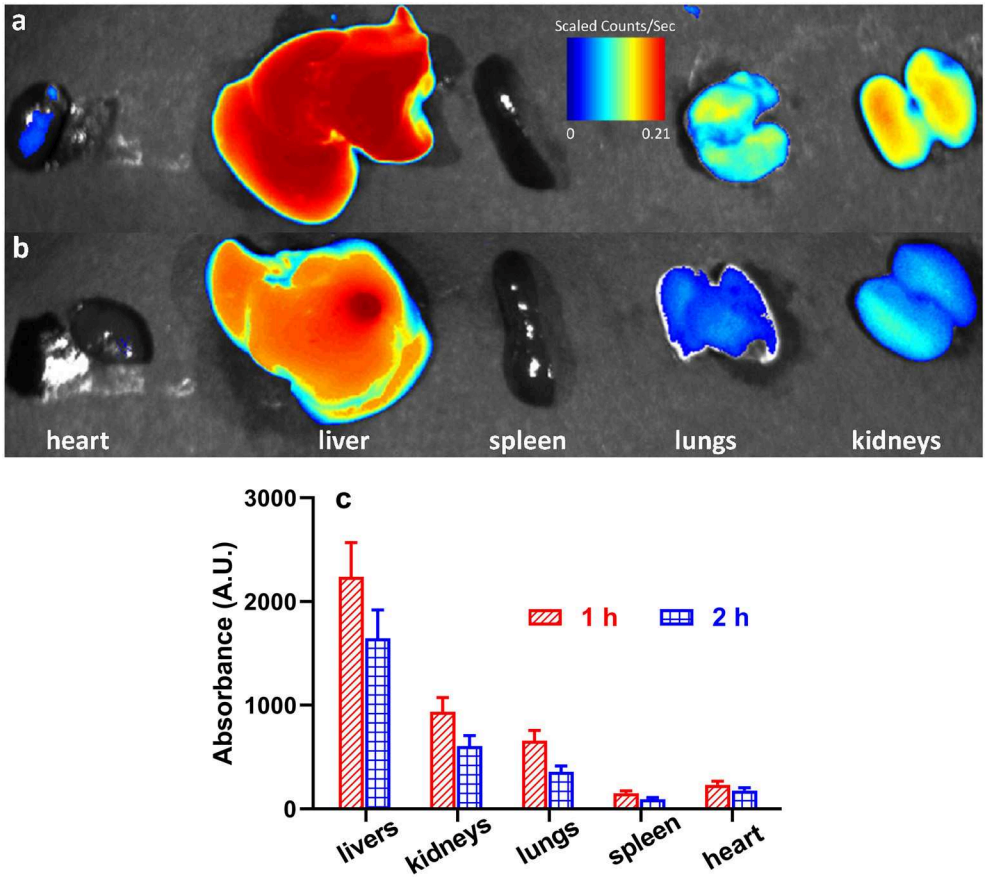

FIGURE 5 | Representative fluorescent images of rat's viscera (i.e., heart, liver, spleen, lungs, and kidneys) after 1 h **(a)** and 2 h **(b)** of intraperitoneal injection of RhB-loaded NPs; the fluorescent intensity of heart, liver, spleen, lungs, and kidneys **(c)**.

polymers were obtained. The GPC curve showed that the Mw of poloxamer188-*b*-PCL polymers was 12,000 D. The poloxamer188-*b*-PCL NPs were fabricated using a solvent-evaporation method. The obtained NPs showed an average diameter of about 100 nm. The cargo-free NPs showed a high stability in different NaCl solutions and temperature conditions. Cell tests indicated that the poloxamer188-*b*-PCL NPs did not have obvious cytotoxicity. As a potential radioprotection agent, CUR-loaded poloxamer188-*b*-PCL NPs improved the *in vitro* antioxidant activity of the crude CUR powder. Importantly, the CUR-loaded poloxamer188-*b*-PCL NPs could be ingested by KYSE520 cells. The animal experiment showed that RhB-loaded NPs could bio-distribute into the liver, kidney, and lung. Therefore, the poloxamer188-*b*-PCL NPs improved the stability and antioxidant activity of CUR. Furthermore, such CUR loaded NPs provided a potential protector against damage from radiotherapy cancer treatment.

DATA AVAILABILITY STATEMENT

All datasets generated for this study are included in the article/**Supplementary Material**.

ETHICS STATEMENT

The animal study was reviewed and approved by Institute of Radiation Medicine, Chinese Academy of Medical Science & Peking Union Medical College.

AUTHOR CONTRIBUTIONS

YS and XL designed experiments and analyzed experimental results and wrote the manuscript. SY, WL, SL, ML, SC, YW, and MC carried out *in vitro* experiments. XL carried out *in vivo* experiments.

FUNDING

This work was supported by the National Science Foundation for Young Scientists of China (Grant Nos. 81703458 and 81903567).

SUPPLEMENTARY MATERIAL

The Supplementary Material for this article can be found online at: https://www.frontiersin.org/articles/10.3389/fchem.2020.00212/full#supplementary-material

REFERENCES

Abdelrazek, E. M., Hezma, A. M., El-Khodary, A., and Elzayat, A. M. (2016). Spectroscopic studies and thermal properties of PCL/PMMA biopolymer blend. *Egypt. J. Basic Appl. Sci.* 3, 10–15. doi: 10.1016/j.ejbas.2015.06.001

Aggarwal, B. B., and Harikumar, K. B. (2009). Potential therapeutic effects of curcumin, the anti-inflammatory agent, against neurodegenerative, cardiovascular, pulmonary, metabolic, autoimmune and neoplastic diseases. *Int. J. Biochem. Cell Biol.* 41, 40–59. doi: 10.1016/j.biocel.2008.06.010

Akinyemi, A. J., Oboh, G., Fadaka, A. O., Olatunji, B. P., and Akomolafe, S. (2017). Curcumin administration suppress acetylcholinesterase gene expression in cadmium treated rats. *Neurotoxicology* 62, 75–79. doi: 10.1016/j.neuro.2017.05.004

Ali, R., Farah, A., and Binkhathlan, Z. (2017). Development and characterization of methoxy poly(ethylene oxide)-block-poly(ε-caprolactone) (PEO-b-PCL) micelles as vehicles for the solubilization and delivery of tacrolimus. *Saudi Pharm. J.* 25:258. doi: 10.1016/j.jsps.2016.06.009

Alshamsan, A. (2014). Nanoprecipitation is more efficient than emulsion solvent evaporation method to encapsulate cucurbitacin I in PLGA nanoparticles. *Saudi Pharm. J.* 22, 219–222. doi: 10.1016/j.jsps.2013.12.002

Armstrong, J. K., Meiselman, H. J., and Fisher, T. C. (1995). Inhibition of red blood cell-induced platelet aggregation in whole blood by a nonionic surfactant, poloxamer 188 (RheothRx injection). *Thrombosis Res.* 79, 437–450. doi: 10.1016/0049-3848(95)00134-D

Barka, N., Ouzaouit, K., Abdennouri, M., and Makhfouk, M. E. (2013). Dried prickly pear cactus (*Opuntia ficus* indica) cladodes as a low-cost and eco-friendly biosorbent for dyes removal from aqueous solutions. *J. Taiwan Inst. Chem. Eng.* 44, 52–60. doi: 10.1016/j.jtice.2012.09.007

Epstein, J., Sanderson, I. R., and Macdonald, T. T. (2010). Curcumin as a therapeutic agent: the evidence from *in vitro*, animal and human studies. *Br. J. Nutr.* 103, 1545–1557. doi: 10.1017/S0007114509993667

Esatbeyoglu, T., Ulbrich, K., Rehberg, C., Rohn, S., and Rimbach, G. (2015). Thermal stability, antioxidant, and anti-inflammatory activity of curcumin and its degradation product 4-vinyl guaiacol. *Food Funct.* 6:887. doi: 10.1039/C4FO00790E

Fadus, M. C., Lau, C., Bikhchandani, J., and Lynch, H. T. (2017). Curcumin: an age-old anti-inflammatory and anti-neoplastic agent. *J. Traditional Compl. Med.* 7, 339–346. doi: 10.1016/j.jtcme.2016.08.002

Farhood, M., Mortezaee, K., Goradel, N. H., Khanlarkhani, N., Salehi, E., Nashtaei, M. S., et al. (2018). Curcumin as an anti-inflammatory agent: implications to radiotherapy and chemotherapy. *J. Cell. Physiol.* 234, 5728–5740. doi: 10.1002/jcp.27442

Gopi, S., Jacob, J., Varma, K., Jude, S., Amalraj, A., Arundhathy, C. A., et al. (2017). Comparative oral absorption of curcumin in a natural turmeric matrix with two other curcumin formulations: an open-label parallel-arm study. *Phytotherapy Res. Ptr* 31:1883. doi: 10.1002/ptr.5931

Huang, Y., Qi, Y., Du, J. Q., and Zhang, D. F. (2018). Protosappanin A protects against atherosclerosis via anti- hyperlipidemia, anti-inflammation and NF-κB signaling pathway in hyperlipidemic rabbits. *Iran. J. Basic Med. Sci.* 21, 33–38. doi: 10.22038/IJBMS.2017.18840.5029

Huang, Z., Wang, Y., and Li, X. (2008). Effect of poloxamer-188, ELP and Tween-80 on stability of emulsification in vaccine. *J. Gansu Agric. Univ.* 43, 21–24.

Hussain, Z., Thu, H. E., Amjad, M. W., Hussain, F., Ahmed, T. A., and Khan, S. (2017). Exploring recent developments to improve antioxidant, anti-inflammatory and antimicrobial efficacy of curcumin: a review of new trends and future perspectives. *Mater. Sci. Eng. C Mater. Biol. Appl.* 77:1316. doi: 10.1016/j.msec.2017.03.226

Jacobsson, S. P. (2005). Quantification of aldehyde impurities in poloxamer by 1 H NMR spectrometry. *Anal. Chim. Acta* 552, 160–165. doi: 10.1016/j.aca.2005.07.050

John, P. C. L., and Qi, R. (2008). Cell division and endoreduplication: doubtful engines of vegetative growth. *Trends Plant Sci.* 13, 121–127. doi: 10.1016/j.tplants.2008.01.004

Ju, K. Y., Lee, Y., Lee, S., Park, S. B., and Lee, J. K. (2011). Bioinspired polymerization of dopamine to generate melanin-like nanoparticles having an excellent free-radical-scavenging property. *Biomacromolecules* 12, 625–632. doi: 10.1021/bm101281b

Kharat, M., Du, Z., Zhang, G., and Mcclements, D. J. (2017). Physical and chemical stability of curcumin in aqueous solutions and emulsions: impact of pH, temperature, and molecular environment. *J. Agric. Food Chem.* 65:1525. doi: 10.1021/acs.jafc.6b04815

Krull, S. M., Moreno, J., Li, M., Bilgili, E., and Dav,é, R. N. (2017). Critical material attributes (CMAs) of strip films loaded with poorly water-soluble drug nanoparticles: III. Impact of drug nanoparticle loading. *Int. J. Pharm.* 523, 33–41. doi: 10.1016/j.ijpharm.2017.03.023

Kunnumakkara, A. B., Guha, S., Krishnan, S., Diagaradjane, P., Gelovani, J., and Aggarwal, B. B. (2007). Curcumin potentiates antitumor activity of gemcitabine in an orthotopic model of pancreatic cancer through suppression of proliferation, angiogenesis, and inhibition of nuclear factor-kappaB-regulated gene products. *Cancer Res.* 67, 3853–3861. doi: 10.1158/0008-5472.CAN-06-4257

Levard, C., Hotze, E. M., Lowry, G. V., and Jr, G.E.B. (2012). Environmental Transformations of silver nanoparticles: impact on stability and toxicity. *Environ. Sci. Technol.* 46:6900. doi: 10.1021/es2037405

Li, X., Hong, X., Qian, J., Gang, W., Lin, L., Li, C., et al. (2017). The mechanism of (+) taxifolin's protective antioxidant effect for •OH-treated bone marrow-derived mesenchymal stem cells. *Cell. Mol. Biol. Lett.* 22:31. doi: 10.1186/s11658-017-0066-9

Lim, L. M., Tran, T. T., Long, W. J., Wang, D., Cheow, W. S., and Hadinoto, K. (2018). Amorphous ternary nanoparticle complex of curcumin-chitosan-hypromellose exhibiting built-in solubility enhancement and physical stability of curcumin. *Colloids Surfaces B Biointerfaces* 167:483. doi: 10.1016/j.colsurfb.2018.04.049

Llano, S., Gómez, S., Londoño, J., and Restrepo, A. (2019). Antioxidant activity of curcuminoids. *Phys. Chem. Chem. Phys.* 21, 3752–3760. doi: 10.1039/C8CP06708B

Lüer, S. C., Goette, J., Troller, R., and Aebi, C. (2014). Synthetic versus natural curcumin: bioequivalence in an *in vitro* oral mucositis model. *BMC Compl. Altern. Med.* 14:53. doi: 10.1186/1472-6882-14-53

Luo, C. Q., Xing, L., Cui, P. F., Qiao, J. B., He, Y. J., Chen, B. A., et al. (2017). Curcumin-coordinated nanoparticles with improved stability for reactive oxygen species-responsive drug delivery in lung cancer therapy. *Int. J. Nanomed.* 12, 855–869. doi: 10.2147/IJN.S122678

Ma, G., and Song, C. (2007). PCL/poloxamer 188 blend microsphere for paclitaxel delivery: influence of poloxamer 188 on morphology and drug release. *J. Appl. Polymer Sci.* 104, 1895–1899. doi: 10.1002/app.25866

Mishra, A., and Daswal, S. (2007). Curcumin, a natural colorant as initiator for photopolymerization of styrene: kinetics and mechanism. *Colloid Polymer Sci.* 285, 1109–1117. doi: 10.1007/s00396-007-1662-4

Nadal, J. M., Gomes, M. L., Borsato, D. M., Almeida, M. A., Barboza, F. M., Zawadzki, S. F., et al. (2016). Spray-dried solid dispersions containing ferulic acid: comparative analysis of three carriers, *in vitro* dissolution, antioxidant potential and *in vivo* anti-platelet effect. *Drug Dev. Industr. Pharmacy* 42, 1813–1824. doi: 10.3109/03639045.2016.1173055

Ofokansi, K. C., Kenechukwu, F. C., Toge, B. K., Ogwu, N. N., and Agbo, C. P. (2012). Preparation and characterization of poloxamer 188 solid dispersions of indomethacin. *J. Pharm. Allied Sci.* 9, 1553–1557.

Ohtsu, H., Xiao, Z., Ishida, J., Nagai, M., Wang, H., Itokawa, H., et al. (2002). Antitumor Agents. 217.† curcumin analogues as novel androgen receptor antagonists with potential as anti-prostate cancer agents. *J. Med. Chem.* 45, 5037–5042. doi: 10.1021/jm020200g

Panahi, Y., Ahmadi, Y., Teymouri, M., Johnston, T. P., and Sahebkar, A. (2018). Curcumin as a potential candidate for treating hyperlipidemia: a review of cellular and metabolic mechanisms. *J. Cell. Physiol.* 233, 141–152. doi: 10.1002/jcp.25756

Peng, S., Li, Z., Zou, L., Liu, W., Liu, C., and Mcclements, D. J. (2018). Improving curcumin solubility and bioavailability by encapsulation in saponin-coated curcumin nanoparticles prepared using a simple pH-driven loading method. *Food Funct.* 9, 1829–1839. doi: 10.1039/C7FO01814B

Rashed, M. M. A., Ghaleb, A. D. S., Li, J. P., Nagi, A., Yuan, H. W., Zhu, W. Y., et al. (2018). Enhancement of mass transfer intensification for essential oil release from lavandula pubescence using integrated ultrasonic-microwave technique and enzymatic pretreatment. *Acs Sustain. Chem. Eng.* 6:7b02860. doi: 10.1021/acssuschemeng.7b02860

Shabbir, M., Khan, M. R., and Saeed, N. (2013). Assessment of phytochemicals, antioxidant, anti-lipid peroxidation and anti-hemolytic activity of extract and various fractions of Maytenus royleanus leaves. *Chem. Commun.* 13:143. doi: 10.1186/1472-6882-13-143

Ullah, F., Iqbal, N., Ayaz, M., Sadiq, A., Ullah, I., Ahmad, S., et al. (2017). DPPH, ABTS free radical scavenging, antibacterial and phytochemical evaluation of crude methanolic extract and subsequent fractions of *Chenopodium botrys* aerial parts. *Pak. J. Pharm. Sci.* 30, 761–766.

Wang, H., Gong, X., Guo, X., Liu, C., Fan, Y. Y., Zhang, J., et al. (2019). Characterization, release, and antioxidant activity of curcumin-loaded sodium alginate/ZnO hydrogel beads. *Int. J. Biol. Macromol.* 121:1118. doi: 10.1016/j.ijbiomac.2018.10.121

Wang, W. Q., Yin, Y. P., Jun, L., and Xuan, L. J. (2018). Halimane-type diterpenoids from Vitex rotundifolia and their anti-hyperlipidemia activities. *Phytochemistry* 146, 56–62. doi: 10.1016/j.phytochem.2017.12.002

Yan, J., Wang, Y., Jia, Y., Liu, S., Tian, C., Pan, W., et al. (2017). Co-delivery of docetaxel and curcumin prodrug via dual-targeted nanoparticles with synergistic antitumor activity against prostate cancer. *Biomed. Pharmacother.* 88, 374–383. doi: 10.1016/j.biopha.2016.12.138

Yin, M., Huang, J., Yu, J., Chen, G., and Qu, S. (2017). Hydrophilic film polymerized on the inner surface of PMMA tube by an atmospheric pressure plasma jet. *Mater. Res. Exp.* 4:076405. doi: 10.1088/2053-1591/aa7acf

Zhao, Z., Xie, M., Li, Y., Chen, A., Li, G., Zhang, J., et al. (2015). Formation of curcumin nanoparticles via solution-enhanced dispersion by supercritical CO2. *Int. J. Nanomed.* 10:3171. doi: 10.2147/IJN.S80434

Zuo, H., Gu, Z., Cooper, H., and Xu, Z. P. (2015). Crosslinking to enhance colloidal stability and redispersity of layered double hydroxide nanoparticles. *J. Colloid Interface Sci.* 459, 10–16. doi: 10.1016/j.jcis.2015.07.063

Conflict of Interest: The authors declare that the research was conducted in the absence of any commercial or financial relationships that could be construed as a potential conflict of interest.

frontiers in Chemistry

ORIGINAL RESEARCH
published: 28 April 2020
doi: 10.3389/fchem.2020.00358

Oxygen-Sufficient Nanoplatform for Chemo-Sonodynamic Therapy of Hypoxic Tumors

Biying Huang[1], Sijie Chen[1], Wenjing Pei[1], Yan Xu[1], Zichao Jiang[2], Chengcheng Niu[1] and Long Wang[2]**

[1] Department of Ultrasound Diagnosis, The Second Xiangya Hospital, Central South University, Changsha, China,
[2] Department of Orthopedics, Xiangya Hospital, Central South University, Changsha, China

Modulation of hypoxia is an essential factor for enhancing the effects of antitumor therapies, especially sonodynamic therapy and chemotherapy. To improve the efficacy of combination therapy by reversing the hypoxic tumor microenvironment, we developed shell-core structured PPID-NPs, which were designed with a polymer shell onto the sonosensitizer and a chemotherapeutic drug were loaded and a perfluorocarbon core loaded with oxygen. The perfluorocarbon core provides sufficient oxygen not only for causing the sonosensitizer to produce more singlet oxygen to induce cell apoptosis but also for reducing drug resistance to enhance therapeutic efficacy. Furthermore, the release of chemotherapeutic drugs at the tumor site can be controlled. Thus, PPID-NPs can efficiently inhibit the growth of breast cancer by synergistic therapy under ultrasound exposure. We believe that our oxygen-sufficient nanoplatform could be an ideal therapeutic system for hypoxic tumors.

Keywords: chemo-sonodynamic therapy, perfluorocarbon, tumor hypoxia microenvironment, reactive oxygen species, oxygen sufficient nanoplatform

OPEN ACCESS

Edited by:
Jianhua Zhang,
Tianjin University, China

Reviewed by:
Piaoping Yang,
Harbin Engineering University, China
Xijian Liu,
Shanghai University of Engineering Sciences, China
Zhou Yang,
Southwest Jiaotong University, China

****Correspondence:***
Chengcheng Niu
niuchengcheng@csu.edu.cn
Long Wang
dr_wanglong@csu.edu.cn

Specialty section:
This article was submitted to Nanoscience, a section of the journal Frontiers in Chemistry

Received: *08 February 2020*
Accepted: *07 April 2020*
Published: *28 April 2020*

Citation:
Huang B, Chen S, Pei W, Xu Y, Jiang Z, Niu C and Wang L (2020) Oxygen-Sufficient Nanoplatform for Chemo-Sonodynamic Therapy of Hypoxic Tumors. Front. Chem. 8:358. doi: 10.3389/fchem.2020.00358

INTRODUCTION

Tumor hypoxia results from deteriorating diffusion geometry, structural abnormalities of tumor vessels, and disturbed microcirculation (Hockel and Vaupel, 2001). It is widely accepted that hypoxia can promote tumor propagation and malignant progression (Unruh et al., 2003; Vaupel and Mayer, 2007). Moreover, hypoxia can induce resistance to therapy, such as chemotherapy (Unruh et al., 2003; Cheng et al., 2015; Chen et al., 2017) and sonodynamic therapy. In sonodynamic therapy, which was developed from photodynamic therapy, a sonosensitizer can translate energy absorbed from ultrasound (US) into oxygen to produce reactive oxygen species (ROS). The insufficient oxygen supply in tumors greatly hinders the efficacy of sonodynamic therapy. Moreover, during the SDT process, a large amount of oxygen is consumed, which worsens the hypoxic tumor microenvironment. Therefore, it is essential to develop ways of overcoming this obstacle. Hyperbaric oxygen (HBO) therapy was first exploited to modulate tumor hypoxia (Al-Waili et al., 2005); however, HBO causes lung injury and neurotoxicity, significantly limiting its clinical application (Saugstad, 2012). To date, nanomaterials have been synthesized to deliver or produce oxygen, including calcium peroxide (CaO_2), manganese dioxide (MnO_2), hemoglobin, and hydrogen peroxide (H_2O_2)- or catalase-loaded nanoparticles (Chen et al., 2016; Liu et al., 2017; Gu et al., 2018; Jia et al., 2018; Xu et al., 2018; Yang et al., 2018; Zhu et al., 2018; Sun et al., 2019), which hold promise

for improving therapeutic outcomes. Among these methods, some studies have taken advantage of endogenous H_2O_2 in the tumor, which reacts with either catalase or MnO_2 nanoparticles to produce oxygen. However, these methods are restricted by the amount of H_2O_2 available in tumors (Song et al., 2016), the poor biocompatibility of Mn^{2+} itself and their insufficient oxygen delivery efficiency. There are some other alternatives proposed as "blood substitutes," such as hemoglobin-based oxygen carriers and perfluorocarbon-based oxygen carriers. Hemoglobin-based oxygen carriers are able to load oxygen under a high oxygen partial pressure (pO_2) in the lungs and release it under the lower pO_2 in the tissue (Luo et al., 2018). However, without undergoing a reduction, free Hb in circulation rapidly becomes the met form and releases toxic free heme, causing kidney tubule damage and even renal failure (Buehler et al., 2007, 2010), vasoconstriction and systemic hypertension (Bialas et al., 2019). Therefore, more efforts should be made to search for effective and highly biosafe oxygen carriers. Perfluorocarbon (PFC) compounds are chemically and biologically inert synthetic materials with high oxygen solubility. Compared to Hb, PFCs can dissolve large amounts of oxygen without saturation instead of reversibly binding oxygen. In particular, PFCs are stable under processing, storage, and usage conditions and are not prone to oxidation. Moreover, with the augmented fraction of inspired oxygen (FiO_2), PFC can load more oxygen in circulation and rapidly diffuse to tissues via an O_2 gradient (Cabrales et al., 2004; Bialas et al., 2019). Surprisingly, in addition to the characteristics mentioned above, perfluorotributylamine (PFTBA), one type of PFC, has a platelet inhibition effect that can enhance RBC infiltration at tumor sites to promote oxygen delivery (Zhou et al., 2018). Therefore, PFTBA holds great potential in delivering oxygen to tumors.

To date, many studies on tumor therapy have focused on designing combination therapies, especially SDT and chemotherapy (Qian et al., 2016; Lin et al., 2019). In the combination therapy between SDT and chemotherapy, ROS are generated under US irradiation, which can exert killing cell ability (Bai et al., 2012; Pan et al., 2018). With the help of US exposure, the release of a chemotherapeutic drug at the tumor would be promoted, and the chemo-drug resistance of cancer cells would be reversed (Wu et al., 2019). However, although *in vivo* results have shown a better therapeutic effect comparable to that of single therapy, hypoxia is still an obstacle that weakens the therapeutic efficacy (Shen et al., 2015; Wu et al., 2019). In this study, encouraged by the outstanding characteristic of PFTBA, we built an oxygen nanoplatform (PPID-NPs) to augment the efficacy of sonodynamic-chemotherapy against breast cancer. In this nanoplatform, we designed core-shell nanoparticles with a polymer shell and a PFTBA core, in which the sonosensitizer IR780, doxorubicin hydrochloride (DOX) and oxygen were loaded (**Figure 1**). The shell of these NPs was composed of an FDA-approved polymer, poly(lactic-co-glycolic) acid (PLGA), with high biodegradability and excellent biocompatibility. The core of these NPs was composed of PFTBA as the oxygen carrier. DOX, as a broad-spectrum antitumor drug, was encapsulated in these NPs to enhance the efficacy of sonodynamic-chemotherapy. The sonosensitizer IR780, as a prototypical near-infrared (NIR) heptamethine cyanine agent, has been greatly explored for anticancer therapy, including sonodynamic and photodynamic therapy (Thomas et al., 2017; Zhang et al., 2019). However, its poor solubility in biological fluids, fast clearance, and acute toxicity (at high doses) hinder the further use of IR780. To address these critical limitations, IR780 can be loaded into our nanoplatform to achieve high solubility, low toxicity, and long residence time (Alves et al., 2018). In this work, we successfully prepared the oxygen-sufficient nanoplatform PPID-NPs, and *in vitro* and *in vivo* experiments verified their wonderful oxygen-loading capacity and excellent anticancer performance. Thus, PPID-NPs can be applied as useful agents for enhancing the efficacy of chemo-sonodynamic therapy against hypoxic tumors.

MATERIALS AND METHODS

Materials

IR-780 iodide, PLGA, and polyvinyl alcohol (PVA) were purchased from Sigma-Aldrich (USA). Liquid PFTBA was obtained from BioRike (China). DOX was purchased from Solarbio Co. Ltd. (China). A reactive oxygen species assay kit DCFH-DA was purchased from Beyotime Biotechnology (China), and the singlet oxygen sensor green (SOSG) probe was provided by Thermo Fisher (USA). Other reagents were of analytical purity and were used without further purification.

Preparation of PPID-NPs

Nanoparticles were prepared using a single emulsion evaporation method based on our group's previous study (Wang et al., 2018). Briefly, 25 mg of PLGA was completely dissolved in chloroform, and then 1 mg of IR780, 1 mg DOX of (dissolved in 100 μL of deionized water) and 100 μL of PFTBA were added to the PLGA solution. Finally, 8 mL of 4% w/v PVA solution was added to the PLGA solution and emulsified for 2 min with an ultrasonic processor in an ice bath. The resulting emulsion was mixed in 10 mL of deionized water and stirred for 3 h. Next, the resulting NPs were washed with deionized water (10 000 rpm, 20 min) until the supernatant became colorless. When the precipitate was resuspended with PBS, PPID-NPs were pre-saturated with a medical oxygen cylinder for 15 min in an ice bath and stored at 4°C. We termed the NPs as PPID-NPs. All procedures were performed in the dark. The same procedure was used to prepare PPI-NPs without DOX, PI-NPs without DOX and PFTBA, and PLGA/PFTBA NPs without DOX and IR780. These NPs were used as controls.

Characterizations

The morphology of the PPID-NPs was observed by transmission electron microscopy (TEM, Jem-1400 plus). The size distribution, polydispersity, and zeta potential were analyzed by a Malvern size analyzer (ZEN3600, Malvern Instruments, US). Stability experiments of the NPs were performed in 1× PBS or in 10% fetal bovine serum (FBS) with a dynamic laser scattering (DLS) instrument over 7 days. The presence of IR780 in the NPs was verified on a UV–vis–NIR spectrophotometer (UV-2450, Shimadzu, Japan). The presence of DOX in the NPs

was identified using a fluorescence spectrophotometer (F-4600 FL, Hitachi, Japan).

Determination of IR780/DOX Entrapment Efficiency and Loading Efficiency

A 10 mg/mL nanoparticle solution was subjected to lyophilization. After 24 h, they were weighed, dissolved in DMSO, and diluted to a suitable concentration, and the absorbance values at the maximum absorption peak positions of IR780 and DOX were measured by ultraviolet-visible spectrophotometry. The concentration was calculated using the corresponding standard curve.

$$\text{Encapsulation efficiency}(\%) = W_E/W_O \times 100(\%)$$
$$\text{Drug loading efficiency}(\%) = W_E/W_N \times 100(\%)$$

W_E: weight of IR780 (DOX) in nanoparticles after lyophilization
W_O: original input of IR780 (DOX)
W_N: weight of the nanoparticles after lyophilization.

DOX Release From PPID-NPs With US Irradiation

The drug release experiment was divided into two groups: (1) PPID-NPs without US irradiation and (2) PPID-NPs with US irradiation. First, PPID-NPs (25 mg) were reconstituted in 1 ml of PBS (PH = 7.4) and loaded into a dialysis bag (M_w = 8,000 Da). Group 2 was subjected to US irradiation (2.0 W/cm^2) for 5 min. The two groups were placed on a shaker whose speed was 100 rpm. At the desired time points, 1 mL of dialysate was removed, and then fresh buffer was added back to the reservoir. Each DOX concentration in the dialysate was obtained by a fluorescence spectrometer, and the accumulative amount of DOX released was calculated according to the standard curve. Each group was tested in triplicate, and the data are given as the mean ± SD.

Measurement of ROS in the Cell-Free System

The production of $^1O_2$ was measured using SOSG as a fluorescent probe. This experiment was divided into three groups: (1) PPI-NPs, (2) PI-NPs (10 mg/mL), and (3) PBS. For each group, 100 μL of solution was added to 1 ml of PBS. Then, 1 μL of SOSG (2.5 mM) in methanol was mixed in a quartz cuvette. The US irradiation time (1 MHz, 1 W/cm^2, 40% duty cycle) using a US transducer (WED-100, WELLD Medical Electronics, China) was 0, 30, 60, 90, 120, or 150 s. The fluorescence spectra of SOSG were acquired on a fluorescence spectrometer with an excitation wavelength of 504 nm.

$$\text{Relative } {}^1O_2 \text{ production efficiency}: F/F_0$$

F: fluorescence intensity of the three groups under US irradiation
F_0: fluorescence intensity of the three groups before US irradiation.

Oxygen Storage and Release of PPID-NPs

The oxygen delivery experiment was divided into three groups: (1) PPID-NPs, (2) PID-NPs, (3) Water. First, 1 mL of each group were oxygenated by a medical oxygen cylinder for 5 min in a gas bottle. Second, 4 mL of degassed water was loaded into the glass bottle with a rubber topper, and a 50 ml syringe was used to exhaust the gas in the bottle to simulate a hypoxic environment. Then, the oxygenated solution was rapidly transferred into the bottle. The real-time oxygen concentration in the bottle was measured by a portable oxygen analyzer (AMT08 DO Meter). The oxygen concentration was recorded every 10 s.

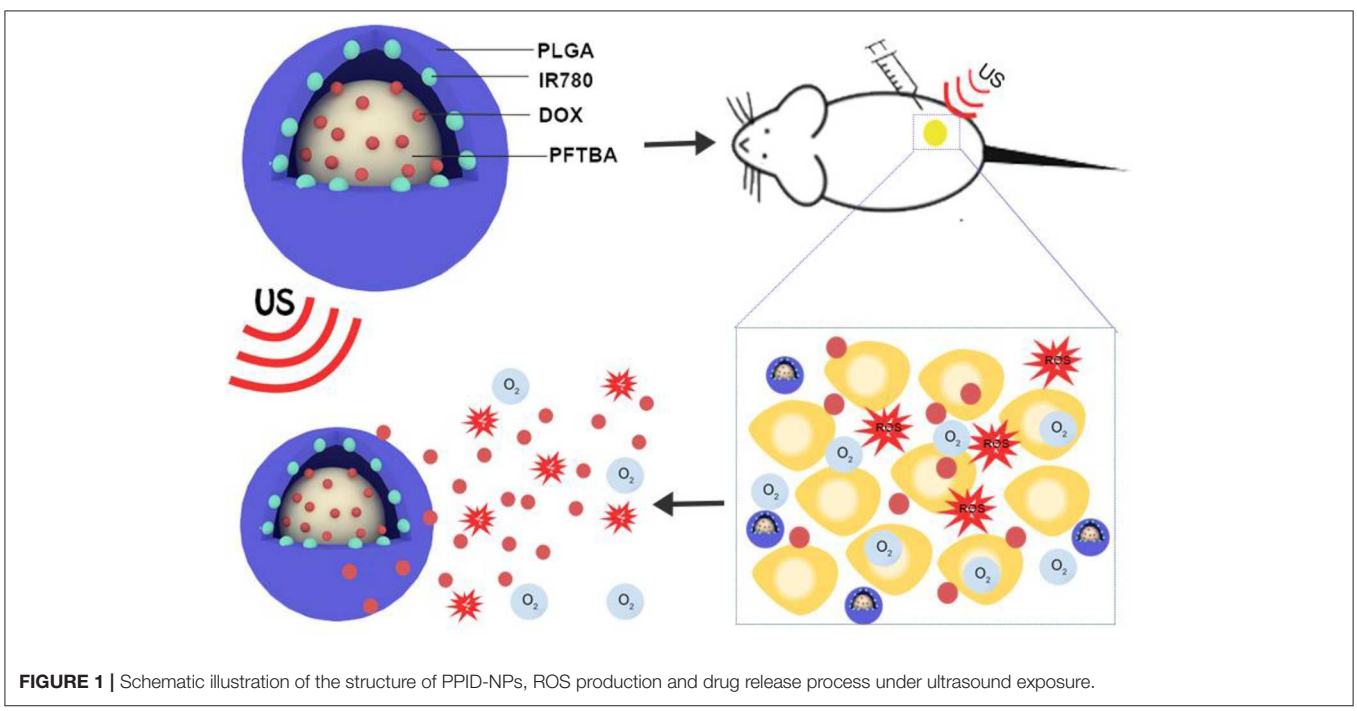

FIGURE 1 | Schematic illustration of the structure of PPID-NPs, ROS production and drug release process under ultrasound exposure.

Cell Culture

For cell culture under hypoxic and normoxic conditions, 4T1 breast cancer cells and MCF-7 cells were cultured in 1,640 medium in an atmosphere of 21% O_2 and 5% CO_2 at 37°C to mimic a normoxic environment. For comparison, an atmosphere of <5% O_2 at 37°C was used to mimic the hypoxic tumor microenvironment.

Cellular-Level ROS Generation

A cellular level ROS assay kit, DCFH-DA, was used to detect intracellular ROS production. 4T1 cells (1×10^5 cells per well) were seeded in six-well plates and randomly divided into five groups: (1) PBS, (2) US-only, (3) PPI-NPs, (4) PI-NPs + US, and (5) PPI-NPs + US. After 24 h of incubation, DCFH-DA (10 μM) was added to each well. Then, the corresponding treatments were administered to each group. Finally, ROS production was determined by fluorescence microscopy after three washes with PBS.

Cellular Apoptosis Experiment

4T1 cells (1×10^5 cells in each well) and MCF-7 cells were seeded in 6-well plates, cultured overnight, and then divided into five groups: (1) PBS, (2) US-only (1.0 W/cm^2, 2 min), (3) PPI-NPs, (4) DOX, (5) PPID-NPs + US (1.0 W/cm^2, 2 min). The volume of all NP solutions was 150 μL (10 mg/mL), and the content of free DOX was equal to that in the NPs (13.2 μg). Then, all 4T1 cells and MCF-7 cells were washed twice with PBS, stained with propidium iodide (PI) and DAPI, and imaged by fluorescence microscopy.

In vitro Biocompatibility of PPID-NPs

The vitro biocompatibility of PPID-NPs was tested on 4T1 and MCF-7 cells using a standard CCK-8 assay. Cells were seeded in two of 96-well plates with a density of 7×10^3 cells per milliliter and cultured in normoxic and hypoxic environments overnight. The hypoxic environment was created by an AnaeroPack (Mitsubishi Gas Chemical Co, Inc.) and a 2.5 L sealable culture tank; when the color of the oxygen indicator changed from purple to pink, a hypoxic environment was successfully formed, and PPID-NPs in cell culture medium at different concentrations (0, 75, 150, 300, 600, or 800 μg/mL) were added. After 24 h of incubation, the cell viability was measured by a cell counting kit-8 (CCK-8).

In vitro Antitumor Study

4T1 cells and MCF-7 cells were seeded into two 96-well plates (1×10^4 cells) and cultured overnight under normoxic or hypoxic conditions. The cells were randomly divided into six groups: (1) PBS, (2) US-only, (3) DOX, (4) PI-NPs +US, (5) PPI-NPs + US, and (6) PPID-NPs +US. Then, the cells were cultured with

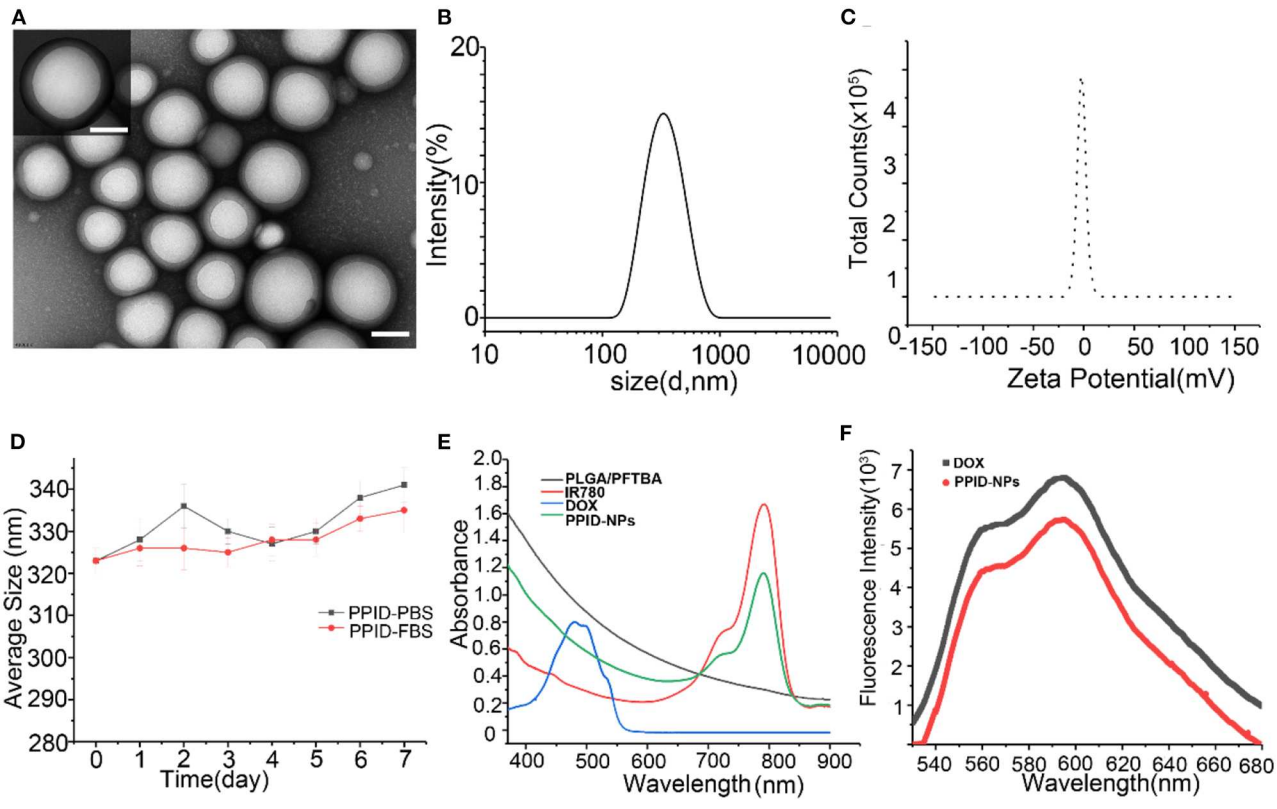

FIGURE 2 | (A) TEM images of PPID-NPs (scale bar, 100 nm). **(B,C)** Size and zeta intensity distributions of PPID-NPs. **(D)** Average size of PPID-NPs in 1× PBS or 10%FBS for 7 days. **(E)** UV-vis-NIR absorption spectra of free IR780, DOX, PLGA/PFTBA NPs, and PPID-NPs. **(F)** Fluorescence spectra of PPID-NPs and DOX.

NPs (300 μg/mL) in 1,640 medium for 4 h. After discarding the above culture medium, the cells were washed three times with PBS, and complete medium was added to each well. Then, groups (2), (4), (5), and (6) were exposed to US (1 MHz, 1 W/cm^2) for 2 min. To carry out US irradiation, the space between the probe and plate was full of an ultrasonic coupling agent. After 24 h of incubation, the cell viability was determined using a CCK-8 cytotoxicity assay kit.

In vivo Tumor Hypoxia Environment After Different Treatments

BALB/c mice (5 weeks, female) were obtained from the Laboratory Animal Center of Central South University (China) and maintained in accordance with the guidelines of the Department of Laboratory Animals, Central South University, China. Breast tumor-bearing mice were established by the subcutaneous injection of 4T1 cells (2×10^6) into the right flank, and the tumor volume was calculated according to formula $1/2\ a \times b \times c$ (a, tumor long diameter; b, tumor short diameter; c, tumor height). When the tumor volume reached 100 mm^3, the breast tumor-bearing mice ($n = 3$) were divided into three groups: (1) saline, (2) PI-NPs, and (3) PPI-NPs. After the NPs were intratumorally injected, all mice were sacrificed, and tumor tissues were immunohistochemically stained with an antibody against hypoxia-inducible factor-1α (HIF-1α) after 24 h.

Combination Therapy Between SDT and Chemotherapy *in vivo*

Breast tumor-bearing mice were randomly divided into 5 groups ($n = 5$) when the tumor volumes reached 60 mm^3: (1) saline, (2) US-only, (3) DOX, (4) PPI-NPs + US, (5) PPID-NPs + US; for each group, 75 μL of the corresponding treatment solution was intratumorally injected into the mice every 2 days. All NPs were at a concentration of 25 mg/mL, with a DOX concentration of 0.22 mg/mL. The tumors of the mice in groups (3), (4), and (5) were exposed to US (2 W/cm^2, 5 min) after injection. Body weight and tumor volume were recorded every other day for 14 days. One day later, the tumors of the mice were harvested, and hematoxylin and eosin (H&E) staining was performed. A terminal deoxynucleotidyl transferase-mediated dUTP nick-end labeling kit (TUNEL, Promega, Madison, WI) was used to observe cell apoptosis. Tumor cell proliferation was analyzed by tumor immunohistochemical staining with Ki-67 antibody.

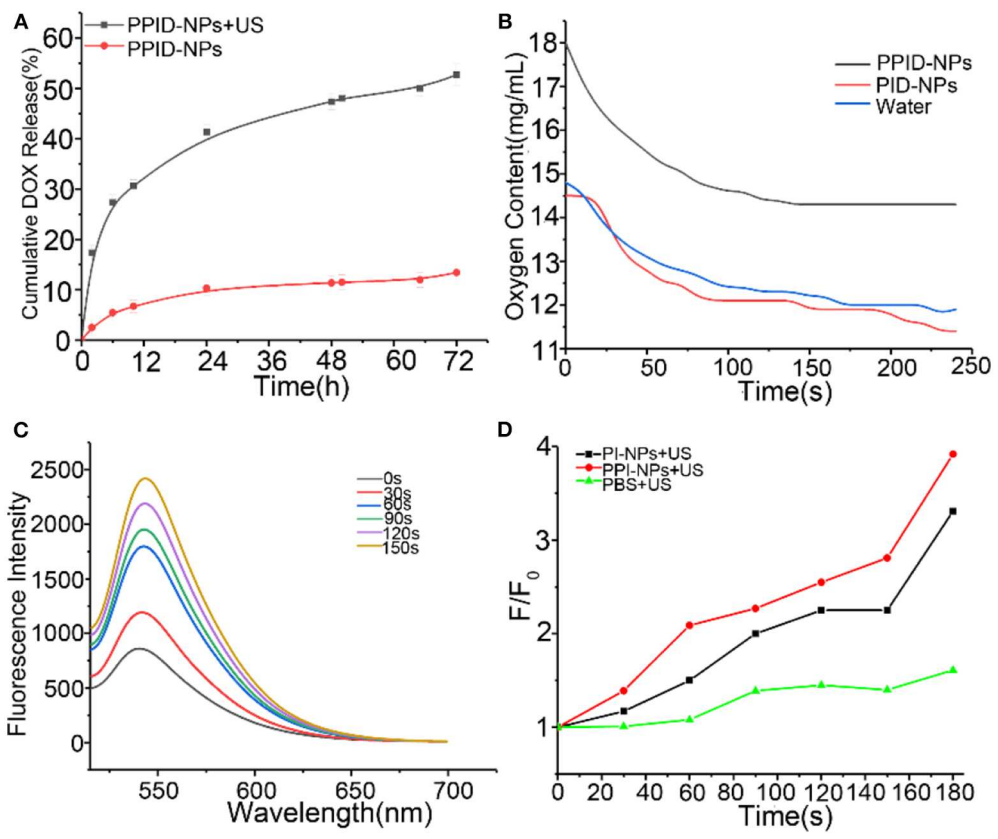

FIGURE 3 | (A) After 72 h, DOX release from PPID-NPs with or without US irradiation (1 MHz, 1.0 W/cm^2). **(B)** Oxygen content of water and PPID-NPs. **(C)** Time-dependent $^1O_2$ generation of PPI-NPs as irradiated by US (1 MHz, 1.0 W/cm^2). The concentration of IR780 was 21.6 μg/mL. **(D)** The time-dependent fluorescence increment of SOSG under ultrasound irradiation.

Pharmacokinetics and Biodistribution

Tumor-bearing BALB/c mice were injected with 200 μL of PPID-NPs and PI-NPs (the concentration of IR780 was 2.0 mg/kg) through the tail vein. For biodistribution study, submandibular vein blood of the mice was collected at different time points (0, 4, 12, 24, 48, and 72 h) for UV-Vis-NIR spectrophotometry analysis. After injection of NPs 24 h, a portion of the major organs and the tumors of the mice were collected, lysed in DMSO and homogenized to test the IR780 contents with a UV-Vis-NIR spectrophotometer. The NPs content was calculated from the IR780 content in the blood or organs from a standard curve.

RESULTS AND DISCUSSION

Characterization

PPID-NPs were prepared by a single emulsion evaporation method. The TEM image in **Figure 2A** showed that the NPs were spherical. The average size from DLS analysis was 320 nm, and the surface charge was −2.0 mV (**Figures 2B,C**). The stability of the NPs in PBS and FBS solution were monitored by dynamic light scattering (**Figure 2D**). The average hydrodynamic diameter of the NPs in PBS solution increased from 323 to 340 nm in a week, accompanied by a polydispersity index (PDI) increase from 0.033 to 0.23. By contrast, the NPs in the FBS solution showed a slight change in hydrodynamic diameter, which increased by approximately 10 nm, and the change in PDI was negligible. This result implied that the PPID-NPs were so stable that they could be studied *in vivo*. From the UV–vis–NIR absorption spectra of PPID-NPs, the PLGA/PFTBA nanoparticles show no absorption intensity in the range of 400–900 nm, free IR780 solution has an absorption peak at 780-795 nm, and DOX has an absorption peak at approximately 480 nm (**Figure 2E**). The spectrum of the PPID-NPs showed an absorption peak at 780-790 nm, indicating the successful loading of IR780. The fluorescence spectrum of the PPID-NPs showed the same peak of DOX (Ex: 480 nm), which confirmed that DOX was successfully loaded in the NPs (**Figure 2F**). At a concentration of 25 mg/mL, the IR780 encapsulation efficiency was 54.08%, the drug loading efficiency was 2.0%, the DOX encapsulation efficiency was 22.22%, and the drug loading efficiency was 1.0%.

DOX Release From PPID-NPs Under US Exposure

To investigate the DOX release profile from the PPID-NPs, we explored whether US irradiation promoted the release of DOX from the NPs. Compared with PPID-NPs alone (**Figure 3A**),

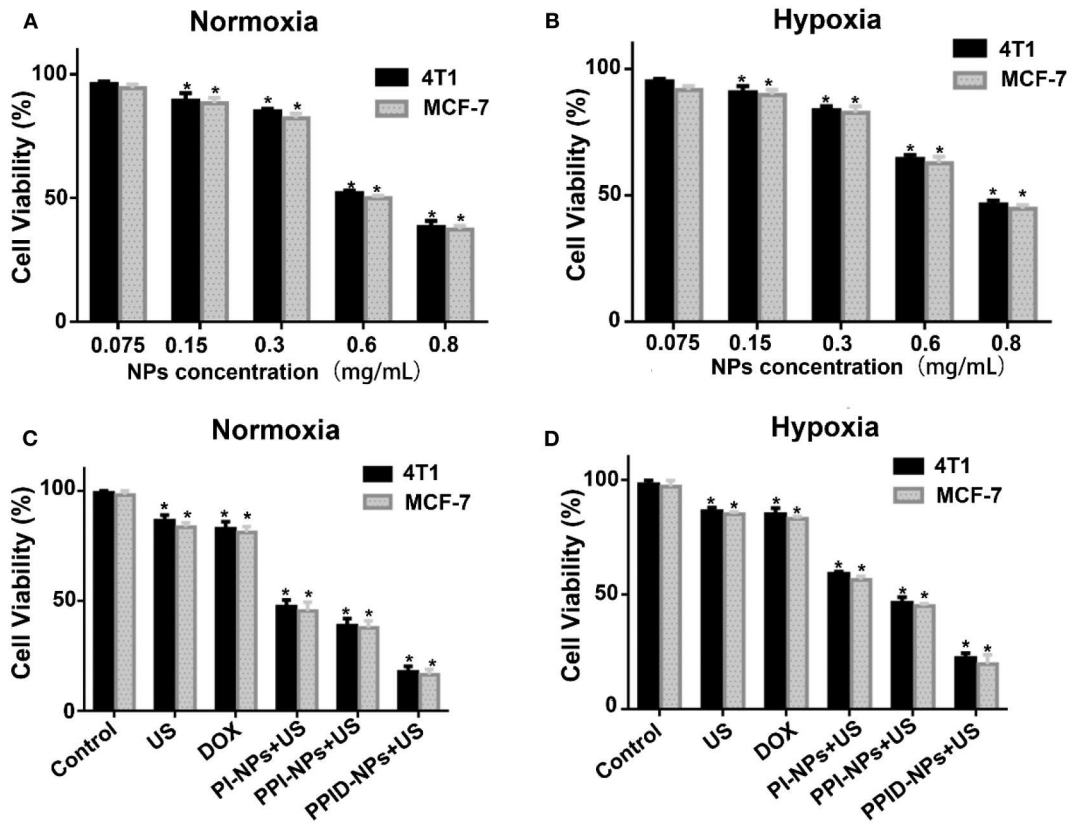

FIGURE 4 | (A,B) Cell viability of 4T1 and MCF-7 cells incubated with different concentrations of PPID-NPs under normoxia environment **(A)** and hypoxia environment **(B)** (*$p < 0.05$, compared with the 0.075 mg/mL nanoparticles concentration group). **(C,D)** Cell viability of 4T1 and MCF-7 cells under different treatments in normoxia environment **(C)** and hypoxia environment **(D)** (*$p < 0.05$, compared with the control group).

PPID-NPs with US irradiation exhibited considerably higher DOX release, and the release rate of DOX approached 53% within 72 h. However, for the NP-alone group, the drug release rate was only 12%, revealing that the DOX release rate was quite slow. Furthermore, when the NPs were combined with US irradiation, the DOX release from the NPs was sharply accelerated in 12 h. Hence, US irradiation could greatly enhance the DOX release rate from the NPs.

Oxygen Delivery Ability of PPID-NPs

The oxygen loading and release profiles of PPID-NPs were analyzed under hypoxic conditions. After oxygen loading, the oxygen concentration in the PPID-NPs group was 18.0 mg/mL, while the oxygen concentration in the degassed water group was only 14.8 mg/mL and PID-NPs only 14.5 mg/mL. In the following 240 s, the oxygen concentration in the PPID-NPs group was obviously higher than that in the degassed water group and PID-NPs group at every time point (**Figure 3B**). These results verified the good oxygen-loading capacity and sustained oxygen release property of PPID-NPs in a hypoxic environment. Thus, PPID-NPs hold high promise for alleviating hypoxic conditions in tumors and enhancing oxygen-dependent SDT efficacy.

Singlet Oxygen Production Experiments

The $^1O_2$ generation by PPI-NPs under US irradiation was measured using SOSG as a probe. At a final IR780 concentration of 21.6 μg/mL, the fluorescence intensity of SOSG at 540 nm increased drastically with prolonged irradiation duration (1.0 W/cm^2), indicating the excellent $^1O_2$ generation ability of PPI-NPs (**Figure 3C**) and further SDT potential against cancer. As shown in **Figure 3D**, for the PI-NP group (not containing PFTBA) under US irradiation, the fluorescence intensity of SOSG was increased by 320%. Surprisingly, for the PPI-NP group (containing PFTBA) under the same conditions, the fluorescence intensity of SOSG was increased as high as 400%. Therefore, more $^1O_2$ generation is produced, which can be attributed to the extra oxygen provided by PFTBA in

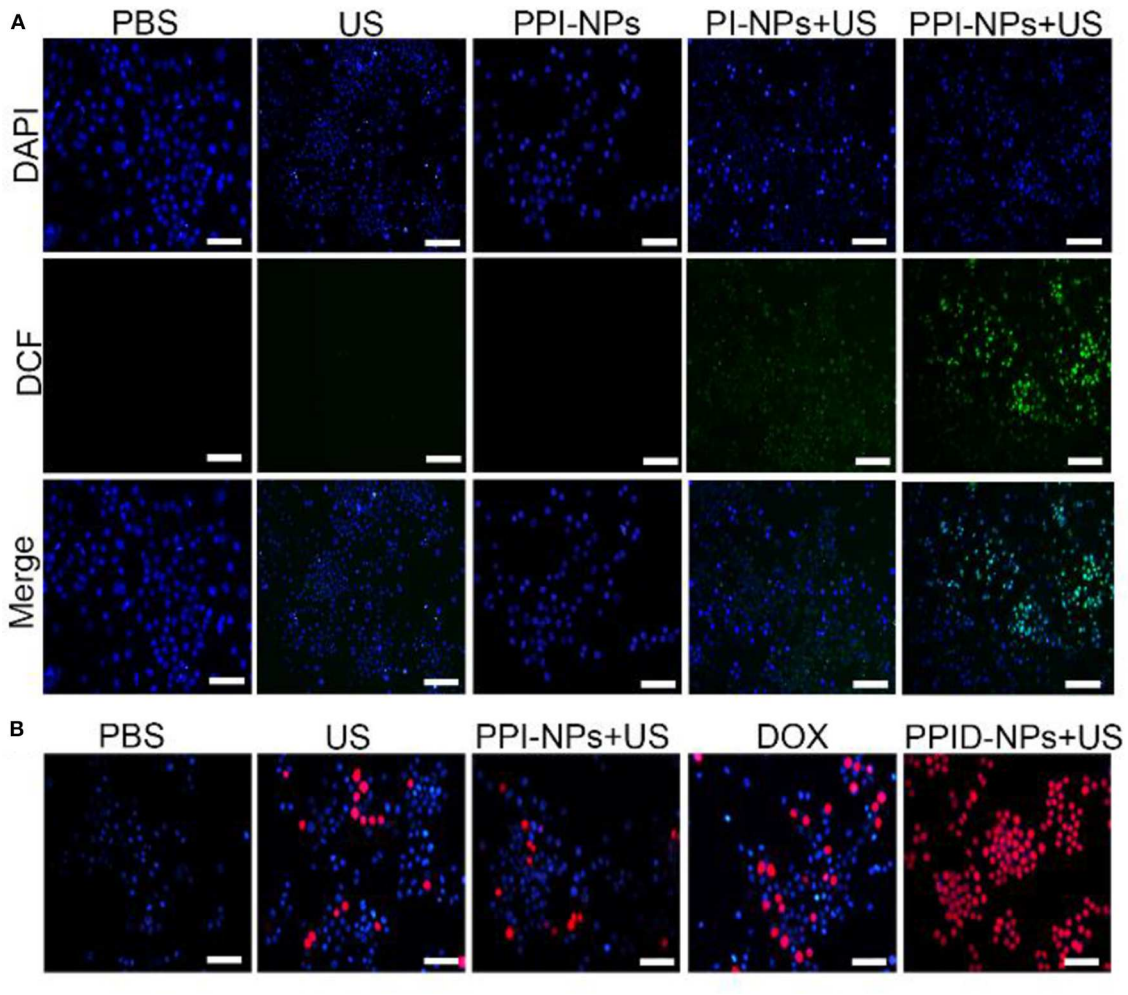

FIGURE 5 | (A) Fluorescence microscope images of DCFH-DA stained 4T1 cells subjected to various treatments (scale bar, 100 μm). **(B)** Fluorescence microscope images of DAPI and PI costained 4T1 cells after various treatments (scale bar, 100 μm).

the SDT process. The outstanding oxygen-loading capacity of PFTBA in the NPs conferred enhanced SDT efficiency in the following study.

In vitro Biocompatibility of PPID-NPs

The viabilities of 4T1 cells and MCF-7 cells in normoxic and hypoxic environments were measured via CCK-8 assay. As shown in **Figures 4A,B**, there was no obvious decrease in cell viability when the NPs concentration was 75 μg/mL under both normoxic and hypoxic conditions, PPID-NPs showed the little toxicity. As the NPs concentration increased, the 4T1 cell viabilities under normoxic conditions gradually decreased to 90.0, 74.2, 62.3, and 43.2%, and the cell viabilities under hypoxic conditions gradually decreased to 87.7, 77.7, 48.7, and 32.3% due to the increasing amount of DOX in the NPs, and MCF-7 cells showed the similar result. To explore the SDT efficiency, we used 300 μg/mL PPID-NPs as an optimum concentration for our subsequent cell experiments.

In vitro Antitumor Activity

The antitumor effect was assessed via a CCK-8 assay under normoxic and hypoxic conditions. As shown in **Figure 4C**, in the normoxic environment, the 4T1 cell viabilities of the DOX group and US-only group were 82.2 and 86.1%. For MCF-7cell, the cell viabilities of both groups were 83%, which means that both DOX and US exposure had slight toxicity to cells. In the PI-NP or PPI-NP group combined with US exposure, the cell viabilities further decreased to 47.5 and 38.2%, respectively. Due to the SDT effect of the sonosensitizer IR780 in both NPs, ROS are generated and directly kill cells. Compared with the PI-NP + US group, the PPI-NP + US group obviously induced more cell apoptosis, which verified that the PFTBA in the PPI-NPs could load more oxygen into the NPs and thus produce more $^1O_2$ under US exposure, resulting in much more cell apoptosis. Furthermore, with the help of DOX, the PPID-NP +US group induced apoptosis in a large majority of cells because of the high efficiency of the combinatorial therapy. As shown in **Figure 4D**, the cell viabilities of the DOX group and US-only group were 85.1 and 83.3%, respectively, in the hypoxic environment. Combined with US exposure, the cell viabilities of the PI-NP group, PPI-NP group and PPID-NP group were 59.5, 46.7, and 21.8%, respectively. These results showed that the cell viabilities determined with the CCK-8 assay in a hypoxic environment were almost consistent with those in a normoxic environment. And the similar result from MCF-7cell was further proved that. Therefore, the oxygen-rich nanoplatform PPID-NPs with US can achieve desirable cytotoxicity in *in vitro* experiments.

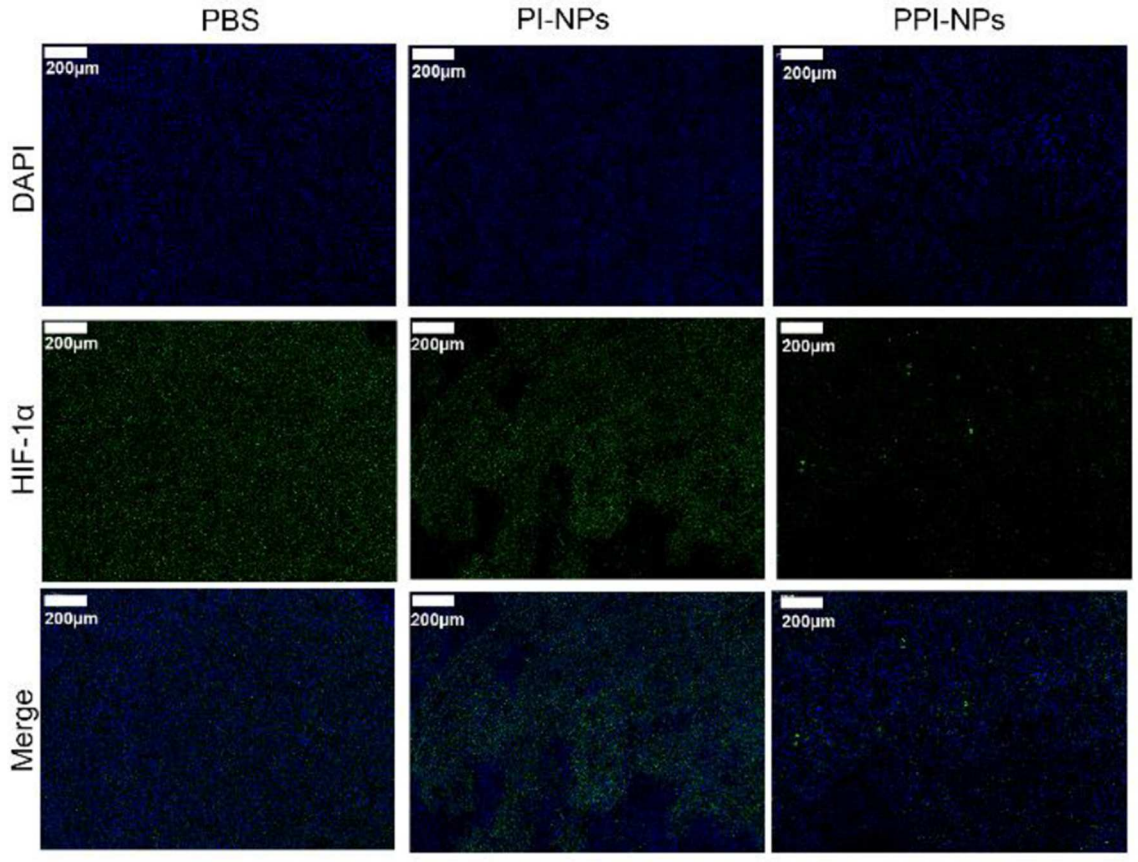

FIGURE 6 | Representative immunofluorescence images of tumor slices stained by the HIF-1α under different treatments (scale bar, 200 μm).

Intracellular ROS Generation

The intracellular sonodynamic activity of PPID-NPs was examined using DCFH-DA as a probe for intracellular oxidative stress. To illustrate the ability of the NPs to produce $^1O_2$(one type of ROS), we used PPI-NPs without DOX in the following experiments. Cells were randomly divided into five groups: (1) PBS, (2) US-only, (3) PPI-NPs, (4) PI-NPs + US, and (5) PPI-NPs + US. As shown in **Figure 5A**, 4T1 cells treated with PPI-NPs alone or US irradiation had intracellular green fluorescence as low as that of the blank control. In contrast, green fluorescence was observed in groups 4 and 5, which illustrated that both the sonosensitizer and US exposure were necessary for $^1O_2$ production. Compared with group 4, group 5 exhibited obviously stronger green fluorescence intensity, which suggested that the PPI-NPs containing PFTBA could carry more oxygen and produce more $^1O_2$ under US exposure than could PI-NPs without PFTBA loading. Therefore, with the addition of PFTBA, oxygen-loaded NPs had significantly enhanced sonodynamic activity due to the sufficient oxygen supply.

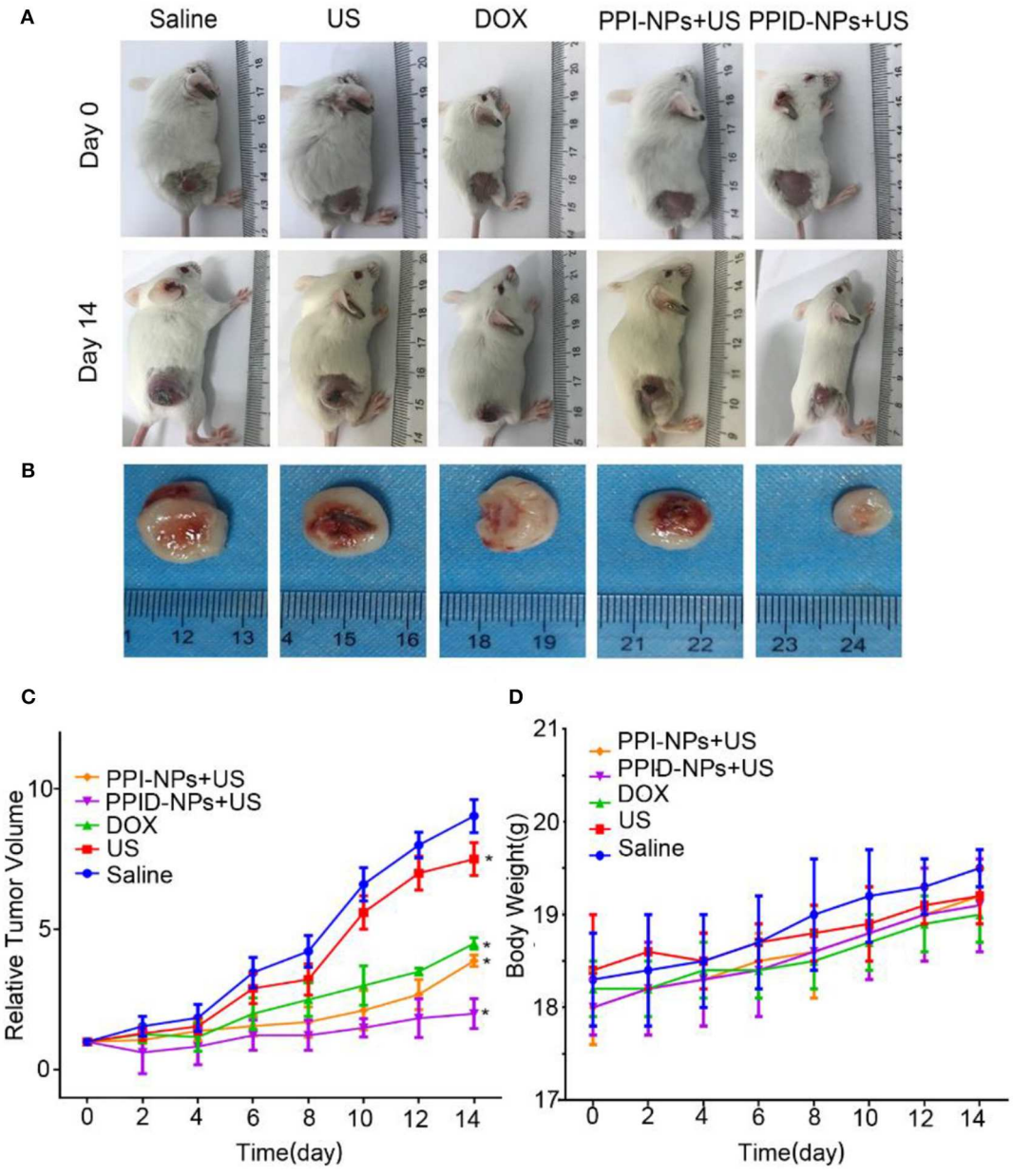

FIGURE 7 | (A) The digital photos of representative mice before and after different treatments. **(B)** The digital photos of tumor from mice after treatments at day 14. **(C)** Tumor growth curves of different groups of mice ($n = 5$) after various treatments (values are the mean ± SD, $n = 5$, $^*p < 0.05$, compared with saline, Dunnett's multiple comparisons test). **(D)** The weight growth curves of different groups of mice ($n = 5$) after various treatments.

Cellular Apoptosis Experiment

To explore the potent anticancer activity of the PPID-NPs, a live/dead staining assay was carried out. As shown in **Figure 5B**, all cells were stained with DAPI, and dead cells were stained with PI. There were a few dead cells (red fluorescence) in the US-only group, suggesting that US irradiation alone could not lead to cell death. When exposed to DOX, some dead cells were observed. Compared with the other groups, the PPID-NP +US group exhibited mainly cells that were destroyed by the combination effect of chemo-sonodynamic activity. This result further confirmed that sonodynamic-chemotherapy has better anticancer efficacy than each single therapy by itself.

In vivo Tumor Hypoxia Environment After Different Treatments

Hypoxia-inducible factors (HIFs) are transcription factors that are expressed in the hypoxic tumor microenvironment (Ajith, 2018). PFTBA was used to store and deliver oxygen to overcome hypoxia in the tumor site. To verify the anti-hypoxic efficacy of the NPs *in vivo*, a HIF-1α probe was applied to evaluate the hypoxia status in the tumor tissues after different treatments: (1) saline, (2) PI-NPs without PFTBA, and (3) PPI-NPs containing PFTBA. As shown in **Figure 6**, DAPI stained the cellular nuclei blue, and the HIF-1α probe stained the hypoxic cells green. The tumor tissue treated with PBS and PI-NPs displayed strong green fluorescence with high expression of HIF-1α, which indicated hypoxic tumor conditions. Comparatively, for the group treated with PPI-NPs, much weaker and less green immunofluorescence corresponding to HIF-1α expression was observed, demonstrating that tumor hypoxia was significantly ameliorated by PPI-NPs.

In vivo Antitumor Effect

Encouraged by the excellent *in vitro* performance of the PPID-NPs, then the *in vivo* performance on 4T1 tumor-bearing mice were investigated. The tumor-bearing mice were divided into 5 groups: (1) saline, (2) US irradiation, (3) DOX, (4) PPI-NPs + US, (5) PPID-NPs + US. Digital photographs of tumor-bearing mice at day 0 and day 14 are shown in **Figure 7A**. The *ex vivo* tumors at day 14 are shown in **Figure 7B**. After 14 days, compared to the original tumor volume, the tumor volumes increased 9.0-fold for the control group and 8.5-fold for

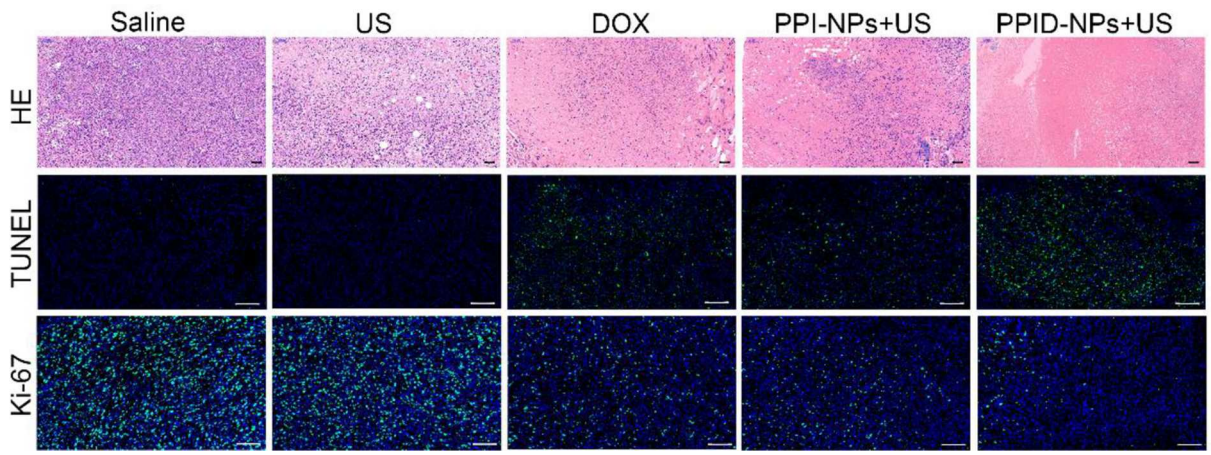

FIGURE 8 | H&E staining and TUNEL and Ki-67 assays of tumor tissue slices after various treatments (scale bar, 50 μm).

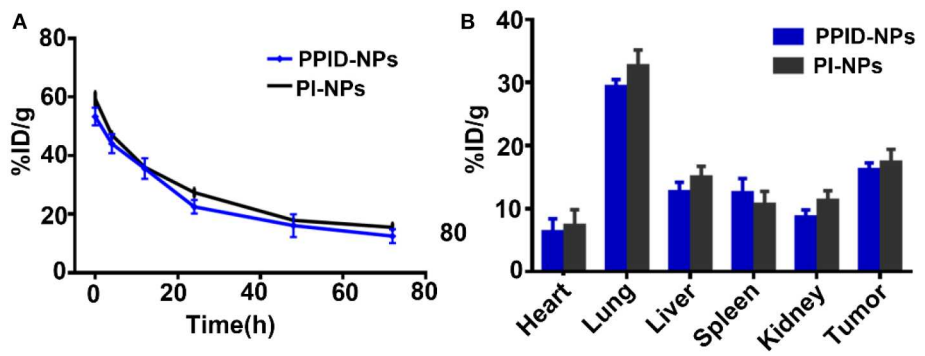

FIGURE 9 | (A) *in vivo* pharmacokinetic curves over a span of 72 h after intravenous injection of PPID-NPs or PI-NPs. **(B)** Biodistribution of PPID-NPs or PI-NPs at 24 h after the injection.

the US group, indicating that US irradiation had no significant antitumor effect (**Figure 7C**). Compared with the original tumor volume on day 0, the tumor volume on day 14 was increased 4.2-fold for the DOX-only group and 4.0-fold for the PI-NP + US group, which suggested that both DOX and PPI-NPs + US have an obvious antitumor effect *in vivo*. When the mice were treated with PPID-NPs and US irradiation, compared to the original tumor volume, the tumor volume slowly increased 2.0-fold. The *ex vivo* tumors also showed that the tumor size after combination therapy was much smaller than that after the other therapies (**Figure 7B**). This result indicated that combination therapy could effectively inhibit tumor growth and that the antitumor effect of combination therapy was better than that each therapy separately. The curves for the mouse body weight relative to time after different treatments are shown in **Figure 7D**. The body weights of the mice in the five groups were measured during the treatments, and no significant weight loss was discovered, implying the good biosafety of our treatments.

Tissue histological analysis, including H&E staining and the TUNEL and Ki-67 assays was carried out to confirm the therapeutic effect (**Figure 8**). According to the H&E staining and TUNEL assay results, almost none of the tumor cells were dead in the saline or US-only group, suggesting that US has no obvious antitumor activity. In contrast, the DOX and PPI-NP + US groups showed considerable cell death in the H&E staining and TUNEL assay result, indicating that either chemotherapy or SDT by itself has a significant antitumor effect. However, the PPID-NP combined with US irradiation group exhibited better antitumor efficacy than each of the single therapy groups. The H&E staining and TUNEL assay results confirmed that most of the tumor cells were destroyed. For the Ki-67 assay, the saline and US-only group showed many proliferative cells stained with green fluorescence. By contrast, fewer proliferative cells were observed in the other three groups. Compared with the DOX or PPI-NP + US group, the PPID-NP + US group had weaker green fluorescence intensity, indicating that most tumor cells had reduced proliferation and decreased malignancy. These pathology assays showed that PPID-NP with US treatment was more effective than treatment with PPI-NPs + US or DOX alone, suggesting that synergistic chemotherapy and sonodynamic therapy could provide greatly enhanced antitumor therapeutic efficacy.

Pharmacokinetics and Biodistribution

To investigate the *in vivo* metabolism of the NPs, tumor-bearing BALB/c mice were injected with 200 μL of PPID-NPs or PI-NPs (the concentration of IR780 was 2.0 mg/kg) through the tail vein. At different time points (0, 4, 12, 24, 48, and 72 h), submandibular vein blood of the mice was collected for UV-Vis-NIR spectrophotometry analysis. As shown in **Figure 9A**, after the first 24 h, the concentration of PPID-NPs in blood was decreased to 35.6% of the injected dose per gram of tissue (ID/g), and after the 3th 24 h, the concentration of PPID-NPs in blood was down to 12.5% ID/g. Similarly, the concentration of PI-NPs in blood was 36.0% ID/g in the first 24 h and 15.5% ID/g in the 3th 24 h, there was no significantly difference between two groups at each tested time point.

For the *in vivo* biodistribution analysis of the NPs, the major organs and tumors of the mice were collected, lysed in DMSO and homogenized to test the IR780 contents with a UV-Vis-NIR spectrophotometer. After injection of NPs for 24 h, three mice in each group were euthanized to measure the NPs distribution in the major organs. As shown in **Figure 9B**, the majority of the NPs accumulated in the lung due to the enriched RES uptake, the concentration of PPID-NPs and PI-NPs in lungs were 29.3 and 32.7%, respectively, which has no significant different between two groups. The concentration of PPID-NPs and PI-NPs in tumors were 16.2 and 17.3%, respectively, which was higher than other RES organs, such liver, spleen. That maybe contribute to the mitochondria-targeted ability of IR780, which were reported by other published articles (Zhang et al., 2018, 2019; Yang et al., 2020).

CONCLUSION

In summary, we successfully developed an oxygen-sufficient nanoplatform, PPID-NPs, to enhance the efficiency of synergistic sonodynamic-chemotherapy in hypoxic tumors. On the one hand, PPID-NPs can deliver oxygen to tumors and enhance the efficacy of oxygen-dependent SDT. On the other hand, PPID-NPs used as a drug delivery system could accelerate DOX release under US exposure. Importantly, the *in vitro* and *in vivo* results confirmed that chemo-sonodynamic therapy possesses high efficiency for anticancer therapy. Therefore, PPID-NPs, as an oxygen-sufficient nanoplatform, could be used as an ideal therapeutic system for hypoxic tumors.

DATA AVAILABILITY STATEMENT

All datasets generated for this study are included in the article/supplementary material.

ETHICS STATEMENT

The animal study was reviewed and approved by Ethics Committee of Central South University.

AUTHOR CONTRIBUTIONS

BH and CN: conceptualization and data curation. BH and LW: methodology. SC, WP, YX, and ZJ: analysis and investigation. BH: writing original draft preparation. CN: writing-review and editing. LW: supervision.

FUNDING

This project was funded by the National Natural Science Foundation of China (Grant Nos. 81974267 and 81601883), Hunan Provincial Natural Science Foundation of China (Grant No. 2018JJ3861), and Hunan Provincial Health Commission Research Foundation Project (B2019166).

REFERENCES

Ajith, T. A. (2018). Current insights and future perspectives of hypoxia-inducible factor-targeted therapy in cancer. *J. Basic. Clin. Physiol. Pharmacol*. 30, 11–18. doi: 10.1515/jbcpp-2017-0167

Alves, C. G., Lima-Sousa, R., de Melo-Diogo, D., Louro, R. O., and Correia, I. J. (2018). IR780 based nanomaterials for cancer imaging and photothermal, photodynamic and combinatorial therapies. *Int. J. Pharm.* 542, 164–75. doi: 10.1016/j.ijpharm.2018.03.020

Al-Waili, N. S., Butler, G. J., Beale, J., Hamilton, R. W., Lee, B. Y., and Lucas, P. (2005). Hyperbaric oxygen and malignancies: a potential role in radiotherapy, chemotherapy, tumor surgery and phototherapy. *Med. Sci. Monit*. 11, RA279–RA289. doi: 10.1097/01.mlg.0000167579.48279.00

Bai, W. K., Shen, E., and Hu, B. (2012). The induction of the apoptosis of cancer cell by sonodynamic therapy: a review. *Chin. J. Cancer Res.* 24, 368–73. doi: 10.3978/j.issn.1000-9604.2012.08.03

Bialas, C., Moser, C., and Sims, C. A. (2019). Artificial oxygen carriers and red blood cell substitutes. *J. Trauma Acute Care Surg.* 87, S48–S58. doi: 10.1097/ta.0000000000002250

Buehler, P. W., D'Agnillo, F., Hoffman, V., and Alayash, A. I. (2007). Effects of endogenous ascorbate on oxidation, oxygenation, and toxicokinetics of cell-free modified hemoglobin after exchange transfusion in rat and guinea pig. *J. Pharmacol. Exp. Ther.* 323, 49–60. doi: 10.1124/jpet.107.126409

Buehler, P. W., Zhou, Y., Cabrales, P., Jia, Y., Sun, G., Harris, D. R., et al. (2010). Synthesis, biophysical properties and pharmacokinetics of ultrahigh molecular weight tense and relaxed state polymerized bovine hemoglobins. *Biomaterials* 31, 3723–3735. doi: 10.1016/j.biomaterials.2010.01.072

Cabrales, P., Tsai, A. G., Frangos, J. A., Briceno, J. C., and Intaglietta, M. (2004). Oxygen delivery and consumption in the microcirculation after extreme hemodilution with perfluorocarbons. *Am. J. Physiol Heart Circ. Physiol*. 287, H320–H330. doi: 10.1152/ajpheart.01166.2003

Chen, J., Luo, H., Liu, Y., Zhang, W., Li, H., Luo, T., et al. (2017). Oxygen-self-produced nanoplatform for relieving hypoxia and breaking resistance to sonodynamic treatment of pancreatic cancer. *ACS Nano* 11, 12849–12862. doi: 10.1021/acsnano.7b08225

Chen, Q., Feng, L., Liu, J., Zhu, W., Dong, Z., Wu, Y., et al. (2016). Intelligent albumin-MnO_2 nanoparticles as pH-/H_2 O_2 -responsive dissociable nanocarriers to modulate tumor hypoxia for effective combination. *Therapy. Adv. Mater.* 28, 7129–7136. doi: 10.1002/adma.201601902

Cheng, Y., Cheng, H., Jiang, C., Qiu, X., Wang, K., Huan, W., et al. (2015). Perfluorocarbon nanoparticles enhance reactive oxygen levels and tumour growth inhibition in photodynamic therapy. *Nat. Commun.* 6:8785. doi: 10.1038/ncomms9785

Gu, T., Cheng, L., Gong, F., Xu, J., Li, X., Han, G., et al. (2018). Upconversion composite nanoparticles for tumor hypoxia modulation and enhanced near-infrared-triggered photodynamic therapy. *ACS Appl Mater. Interfaces* 10, 15494–15503. doi: 10.1021/acsami.8b03238

Hockel, M., and Vaupel, P. (2001). Tumor hypoxia: definitions and current clinical, biologic, and molecular aspects. *J. Natl. Cancer Inst*. 93, 266–276. doi: 10.1093/jnci/93.4.266

Jia, Q., Ge, J., Liu, W., Zheng, X., Chen, S., Wen, Y., et al. (2018). A magnetofluorescent carbon dot assembly as an acidic HO_2 -driven oxygenerator to regulate tumor hypoxia for simultaneous bimodal imaging and enhanced photodynamic. *Therapy. Adv. Mater*. 30:e1706090. doi: 10.1002/adma.201706090

Lin, X., Song, J., Chen, X., and Yang, H. (2019). Ultrasound activated sensitizers and applications. *Angew. Chem. Int. Ed. Engl.* doi: 10.1002/anie.201906823. [Epub ahead of print].

Liu, C. P., Wu, T. H., Liu, C. Y., Chen, K. C., Chen, Y. X., Chen, G. S., et al. (2017). Self-supplying O_2 through the catalase-like activity of gold nanoclusters for photodynamic therapy against hypoxic cancer cells. *Small* 13:1700278. doi: 10.1002/smll.201700278

Luo, Z., Tian, H., Liu, L., Chen, Z., Liang, R., Chen, Z., et al. (2018). Tumor-targeted hybrid protein oxygen carrier to simultaneously enhance hypoxia-dampened chemotherapy and photodynamic therapy at a single dose. *Theranostics* 8, 3584–3596. doi: 10.7150/thno.25409

Pan, X., Wang, H., Wang, S., Sun, X., Wang, L., Wang, W., et al. (2018). Sonodynamic therapy (SDT): a novel strategy for cancer nanotheranostics. *Sci China Life Sci.* 61, 415–426. doi: 10.1007/s11427-017-9262-x

Qian, X., Zheng, Y., and Chen, Y. (2016). Micro/nanoparticle-augmented sonodynamic therapy (SDT): breaking the depth shallow of photoactivation. *Adv. Mater.* 28, 8097–80129. doi: 10.1002/adma.201602012

Saugstad, O. D. (2012). Hyperoxia in the term newborn: more evidence is still needed for optimal oxygen therapy. *Acta Paediatr.* 101, 34–38. doi: 10.1111/j.1651-2227.2011.02546.x

Shen, S., Wu, L., Liu, J., Xie, M., Shen, H., Qi, X., et al. (2015). Core-shell structured Fe_3O_4@TiO_2-doxorubicin nanoparticles for targeted chemo-sonodynamic therapy of cancer. *Int. J. Pharm.* 486, 380–388. doi: 10.1016/j.ijpharm.2015.03.070

Song, X., Feng, L., Liang, C., Yang, K., and Liu, Z. (2016). Ultrasound triggered tumor oxygenation with oxygen-shuttle nanoperfluorocarbon to overcome hypoxia-associated resistance in cancer therapies. *Nano Lett.* 16, 6145–6153. doi: 10.1021/acs.nanolett.6b02365

Sun, Q., Bi, H., Wang, Z., Li, C., Wang, C., Xu, J., et al. (2019). O_2-generating metal-organic framework-based hydrophobic photosensitizer delivery system for enhanced photodynamic therapy. *ACS. Appl* Mater. Interfaces 11, 36347–36358. doi: 10.1021/acsami.9b11607

Thomas, A. P., Palanikumar, L., Jeena, M. T., Kim, K., and Ryu, J. H. (2017). Cancer-mitochondria-targeted photodynamic therapy with supramolecular assembly of HA and a water soluble NIR cyanine dye. *Chem. Sci.* 8, 8351–8356. doi: 10.1039/c7sc03169f

Unruh, A., Ressel, A., Mohamed, H. G., Johnson, R. S., Nadrowitz, R., Richter, E., et al. (2003). The hypoxia-inducible factor-1 alpha is a negative factor for tumor therapy. *Oncogene* 22, 3213–3220. doi: 10.1038/sj.onc.1206385

Vaupel, P., and Mayer, A. (2007). Hypoxia in cancer: significance and impact on clinical outcome. *Cancer Metastasis. Rev.* 26, 225–239. doi: 10.1007/s10555-007-9055-1

Wang, L., Chen, S., Zhu, Y., Zhang, M., Tang, S., Li, J., et al. (2018). Triple-modal imaging-guided chemo-photothermal synergistic therapy for breast cancer with magnetically targeted phase-shifted nanoparticles. *ACS. Appl. Mater. Interfaces* 10, 42102–42114. doi: 10.1021/acsami.8b16323

Wu, P., Dong, W., Guo, X., Qiao, X., Guo, S., Zhang, L., et al. (2019). Responsive blended nanoparticles: cascade-amplifying synergistic effects of sonochemotherapy with on-demand boosted drug release during SDT process. *Adv. Healthc. Mater*. 8:e1900720. doi: 10.1002/adhm.201900720

Xu, J., Han, W., Yang, P., Jia, T., Dong, S., Bi, H, et al. (2018). Tumor microenvironment-responsive mesoporous MnO_2-coated upconversion nanoplatform for self-enhanced tumor theranostics. *Adv. Funct. Mater*. 28:1803804. doi: 10.1002/adfm.201803804

Yang, Z., Wang, J., Liu, S., Li, X., Miao, L., Yang, B., et al. (2020). Defeating relapsed and refractory malignancies through a nano-enabled mitochondria-mediated respiratory inhibition and damage pathway. *Biomaterials* 229:119580. doi: 10.1016/j.biomaterials.2019.119580

Yang, Z. L., Tian, W., Wang, Q., Zhao, Y., Zhang, Y. L., Tian, Y., et al. (2018). Oxygen-evolving mesoporous organosilica coated prussian blue nanoplatform for highly efficient photodynamic therapy of tumors. *Adv. Sci.* 5:1700847. doi: 10.1002/advs.201700847

Zhang, L., Wang, D., Yang, K., Sheng, D., Tan, B., Wang, Z., et al. (2018). Mitochondria-targeted artificial "Nano-RBCs" for amplified synergistic cancer phototherapy by a single NIR irradiation. *Adv. Sci.* 5:1800049. doi: 10.1002/advs.201800049

Zhang, L., Yi, H., Song, J., Huang, J., Yang, K., Tan, B., et al. (2019). Mitochondria-targeted and ultrasound-activated nanodroplets for enhanced deep-penetration sonodynamic cancer therapy. *ACS. Appl Mater Interfaces* 11, 9355–9366. doi: 10.1021/acsami.8b21968

Zhou, Z., Zhang, B., Wang, H., Yuan, A., Hu, Y., and Wu, J. (2018). Two-stage oxygen delivery for enhanced radiotherapy by perfluorocarbon nanoparticles. *Theranostics* 8, 4898–4911. doi: 10.7150/thno.27598

Zhu, H., Li, J., Qi, X., Chen, P., and Pu, K. (2018). Oxygenic hybrid semiconducting nanoparticles for enhanced photodynamic. *Therapy Nano Lett.* 18, 586–594. doi: 10.1021/acs.nanolett.7b04759

Conflict of Interest: The authors declare that the research was conducted in the absence of any commercial or financial relationships that could be construed as a potential conflict of interest.

frontiers in Chemistry

ORIGINAL RESEARCH
published: 07 May 2020
doi: 10.3389/fchem.2020.00377

Platelet-Membrane-Camouflaged Zirconia Nanoparticles Inhibit the Invasion and Metastasis of Hela Cells

Yinghui Shang[1], Qinghai Wang[2], Jian Li[1], Qiangqiang Zhao[1], Xueyuan Huang[1], Hang Dong[1], Haiting Liu[1], Rong Gui[1] and Xinmin Nie[3]**

[1] Department of Blood Transfusion, the Third Xiangya Hospital, Central South University, Changsha, China, [2] Department of Cardiology, the Second Hospital of Shandong University, Jinan, China, [3] Clinical Laboratory of the Third Xiangya Hospital, Central South University, Changsha, China

OPEN ACCESS

Edited by:
Xiaoli Wei,
University of California, San Diego,
United States

Reviewed by:
Xiaoyi Wang,
University of Connecticut,
United States
Xiaoli Liu,
Technical University of
Denmark, Denmark

***Correspondence:**
Rong Gui
aguirong@163.com
Xinmin Nie
niexinmin7440@sina.com

Specialty section:
This article was submitted to
Nanoscience,
a section of the journal
Frontiers in Chemistry

Received: 31 January 2020
Accepted: 09 April 2020
Published: 07 May 2020

Citation:
Shang Y, Wang Q, Li J, Zhao Q,
Huang X, Dong H, Liu H, Gui R and
Nie X (2020)
Platelet-Membrane-Camouflaged
Zirconia Nanoparticles Inhibit the
Invasion and Metastasis of Hela Cells.
Front. Chem. 8:377.
doi: 10.3389/fchem.2020.00377

Zirconia nanoparticles (ZrO2 NPs) are widely applied in the field of biomedicine. In this study, we constructed a nanoplatform of ZrO2 NPs coated with a platelet membrane (PLTm), named PLT@ZrO2. PLTm nanovesicles camouflage ZrO2 NPs, prevent nanoparticles from being cleared by macrophage, and target tumor sites. Compared to ZrO2 alone, PLT@ZrO2 is better at inhibiting the invasion and metastasis of Hela cells *in vitro* and *in vivo*. *In vitro*, PLT@ZrO2 inhibited the growth and proliferation of Hela cells. Scratch-wound healing recovery assay demonstrated that PLT@ZrO2 inhibited Hela cells migration. Transwell migration and invasion assays showed that PLT@ZrO2 inhibited Hela cells migration and invasion. *In vivo*, PLT@ZrO2 inhibited the tumor growth of Xenograft mice and inhibited the lung and liver metastasis of Hela cells. Immunofluorescence and Western blotting results showed that anti-metastasis protein (E-cadherin) was upregulated and pro-metastasis proteins (N-cadherin, Smad4, Vimentin, E-cadherin,β-catenin, Fibronectin, Snail, Slug, MMP2, Smad2) were down-regulated. Our study indicated that PLT@ZrO2 significantly inhibits tumor growth, invasion, and metastasis.

Keywords: platelet membrane, zirconia, invasion, metastasis, anticancer

INTRODUCTION

Zirconium oxide nanoparticles (ZrO2 NPs) possess many good electrochemical properties, such as non-toxicity, thermal stability, wide band gap, and excellent electrical and surface performances (Yang et al., 2007). ZrO2-based biosensors for oral cancer drug detection (Kumar et al., 2016), and electrochemical sensors for anticancer drugs by ZrO2 NPs-decorated nanocomposite (Venu et al., 2018), have also been implemented. Sulphated zirconia nanoparticles have been studied in anticancer applications (Mftah et al., 2015) and sulfated zirconia nanoparticles doped by iron-manganese are cytotoxic to cancer cells (Al-Fahdawi et al., 2015). Moreover, ZrO2 NPs have exhibited cytotoxicity against human carcinoma cell lines (Balaji et al., 2017), but their antitumor activity and mechanism has not been explored thoroughly.

Current studies have indicated that tumor metastasis is facilitated by blood platelets (PLTs) (Karpatkin and Pearlstein, 1981; Gasic, 1984; Tanaka et al., 1986; Chen et al., 1992; Honn and Tang, 1992a,b; Nieswandt et al., 1999), and platelets and tumor cells are bound by P-selectin and the CD44 receptor (Borsig et al., 2001; Hu et al., 2015a) with capture based on structure (Sabrkhany et al., 2018). Previous studies have indicated that platelet-membrane-camouflaged black phosphorus quantum dots could target tumor sites (Shang et al., 2019), but it has not been studied whether platelet-membrane-camouflaged nanoparticles can target tumor metastasis.

Although surgical techniques and chemotherapy regimens have improved, metastasis remains a serious barrier to the effective treatment for patients with cervical cancer (Li et al., 2016), and the prognosis of patients suffered from metastatic cervical cancer is poor (Peng et al., 2016). To address these challenges, we constructed platelet-membrane-camouflaged ZrO2 NPs (PLT@ZrO2) to investigate targeting of metastatic tumors and anti-metastasis activity.

MATERIALS AND METHODS

Materials

Zirconia nanoparticles (XF101) were prepared by the XFNANO Materials Tech Co., Ltd. (China). Yeasen Biotechnology (China) provided Cy5, Rhodamine B (RhB), Hoechst 33342, and distearyl phosphatidyl ethanolamine-fluorescein isothiocyanate (DSPE-FITC). Solarbio (China) provided dialysis membranes (2 kD). Whatman (USA) provided polycarbonate porous membrane syringe filters (200 nm). Life Technologies (USA) provided RPMI-1640, Dulbecco's modified Eagle medium (DMEM) (high glucose), fetal bovine serum (FBS), and trypsin EDTA. Servicebio Technology Co., Ltd. (China) supplied One Step TUNEL Apoptosis Assay Kit, DAPI, Calcein-AM, crystal violet, hematoxylin and eosin (HE), anti-N-cadherin, anti-Vimentin, anti-E-cadherin, anti-β-catenin, anti-Fibronectin, anti-Snail, anti-Smad4, anti-Slug, anti-MMP2, anti-Smad2, anti-β-actin, anti-GAPDH antibodies, horseradish peroxidase (HRP) goat anti-rabbit IgG secondary antibodies, cy3 goat anti-IgG and FITC goat anti-IgG secondary antibodies, and a prestained protein ladder.

Cells and Animals

The Cancer Research Institute of Central South University gifted the Hela human cervical cancer cell line. The Hela cells were cultured in DMEM (high glucose) containing 10% FBS. RAW264.7 macrophages were cultured in RPMI-1640 medium containing 10% FBS. All cells were incubated at 37°C in a 5% CO_2 incubator. Hunan SJA Laboratory Animal Co., Ltd provided 6 week old female Balb/c nude mice.

PLTm Vesicles Preparation

PLTs were obtained by centrifugation (1,500 rpm, 5 min) and double washing with PBS of whole blood from female Balb/c nude mice. PLTm vesicles of ∼150 nm were prepared by repeated freezing (at −80°C, 2 h) and thawing (at 37°C, 10 min) PLTs, and ultrasonic treatment (2 min, 42 kHZ, 100 W) of PLTs (Hu et al., 2015b).

Construction of PLT@ZrO2

Ultrasonic treatment (5 min, 42 k Hz, 100 W) of ZrO2 NPs with an equal volume of PLTm vesicles promoted camouflage of the nanoparticles. After filtration with porous syringe filters (200 nm) and centrifugation (2,500 rpm, 10 min), PLTm vesicles which did not camouflage ZrO2 NPs were settled out and the PLT@ZrO2 were obtained. Generally, 300 μL ZrO2 NPs (50 μg/mL) were mixed with 300 μL PLTm vesicles to pr2Eepare 300 μL PLT@ZrO2.

Characterization of PLT@ZrO2

A transmission electron microscope (TEM) (Tecnai G2 Spirit, FEI, USA) was used to check the morphology and size of PLT@ZrO2. We could observe the size of the nanoparticles as well as identify whether the nanoparticles were encapsulated into PLTm vesicles. A silicon chip dipped in anhydrous ethanol containing PLT@ZrO2 was examined with atomic force microscopy (AFM) (MFP-3D-S, Asylum Research, USA) to detect the heights of nanoparticles. Zetasizer Nano ZS (Malvern Nano series, Malvern, U.K.) was used to measure the particle sizes and surface charges. UV/vis spectroscopy (ScanDrop, Analytik Jena, Germany) was applied to detect the absorbance of PLT@ZrO2.

Cell Viability of Hela Cells Assessed Through Crystal Violet Staining

Hela cells were inoculated into 35 mm dishes (2×10^5/dish). After 24 h, the cells were treated with new medium, ZrO2, PLTm vesicles or PLT@ZrO2. The concentration of ZrO2 NPs used in this study was 50 μg/mL. After 24 h, crystal violet 300 μl was added into each well and then washed with PBS to assess the viable cells.

Scratch-Wound Healing Recovery Assays

Hela cells were seeded in a 6-well plate (1×10^5/well). After 24 h, the culture medium was removed, straight incisions were made by a 10 μl pipette tip, and then cells were washed with PBS to remove detached and suspended cells. The remaining cells were given new medium, ZrO2, PLTm vesicles, or PLT@ZrO2, respectively. The concentration of ZrO2 NPs used in this study was 50 μg/mL. After 24 h, pictures of the scratches were taken under an inverted phase contrast microscope (Axio Observer, ZEISS, Germany), and the extent of wound healing recovery was assessed by the wound area in each group.

Migration and Invasion Assays

Transwell Permeable Supports (Corning Inc., USA) were used to assay cell migration and invasion. Hela cells (about 1×10^4/well) suspended in 200 μl serum-free medium with ZrO2, PLTm vesicles, or PLT@ZrO2, were plated onto Transwell filter inserts in 24-well plates for migration assays. The concentration of ZrO2 NPs used in this study was 50 μg/mL. The corresponding cell suspensions plated onto Transwell filter inserts coated with Matrigel were used for invasion assays. We used 500 μl DMEM containing 10% FBS plated in the lower chambers as a chemoattractant. After incubation for 24 h, a cotton swab was used to remove the cells in the upper chamber. Cells on the bottom side were stained with Calcein-AM (Jang et al., 2012)

and photographed under an inverted fluorescence microscope at excitation wavelength of 530 nm and emission wavelength of 590 nm. Pictures were quantified and analyzed using MetaXpress software (Molecular Devices).

Biocompatibility of PLT@ZrO2

Hemolytic rates and RAW 264.7 macrophages phagocytosis were conducted to estimate the biocompatibility of PLT@ZrO2. After incubating ZrO2 NPs or PLT@ZrO2 (from 0.1 to 0.8 mg/mL) with 5% red blood cell suspension at 37°C for 2 h, the mixture was centrifuged (3,500 rpm, 5 min), and the absorbance at 545 nm of the supernatant was measured by a microplate reader. Ultra-pure water and PBS incubated with 5% red blood cell suspension was used as a positive and negative control, respectively. We calculated the hemolytic ratio as follows: hemolytic rate% = (experimental sample absorbance—negative control absorbance)/(positive control absorbance—negative control absorbance) × 100%. RAW 264.7 macrophages (1×10^5/well) were seeded into a 6-well plate and treated with 2 mL PLT@ZrO2-RhB or ZrO2-RhB for 24 h to assess the ability of PLT@ZrO2 to evade the immune response. In the nanocomposite, the concentration of ZrO2 NPs was 50 μg/mL. After staining the cell nuclei with Hoechst 33342 (Crowley et al., 2016), pictures taken from a laser confocal fluorescence microscope (LCFM) (TCS SP8 CARS, Leica, Germany) were used to assess the phagocytosis of PLT@ZrO2 by macrophages and the fluorescence intensity.

PLT@ZrO2 Distribution Assay *In vivo*

Hela tumor-bearing mice were injected through the tail vein with the Cy5-labeled PLT@ZrO2 or Cy5-labeled ZrO2 to evaluate the targeting capability of PLT@ZrO2 *in vivo*. The dosage of Cy5 in the nanocomposite was 3 μg/kg. After administration, a Xenogen IVIS Lumina XR imaging system (Caliper Life Sciences, USA) was applied to detect the fluorescence intensity of the mice at 6, 24, and 48 h, respectively. The mice were then euthanized, and tumor tissues and visceral tissues were harvested for further imaging. Then the tumor tissues were made into frozen sections and observed under an inverted fluorescence microscope.

PLT@ZrO2 Treatment in Cervical Cancer-Bearing Mice

To explore *in vivo* anticancer effect, we injected Hela cells (1×10^6) in 100 μL PBS through the hypodermic and tail vein, to establish subcutaneous tumors and metastasis tumors, respectively. Tumor volume was calculated as follow: V = 1/2 ×

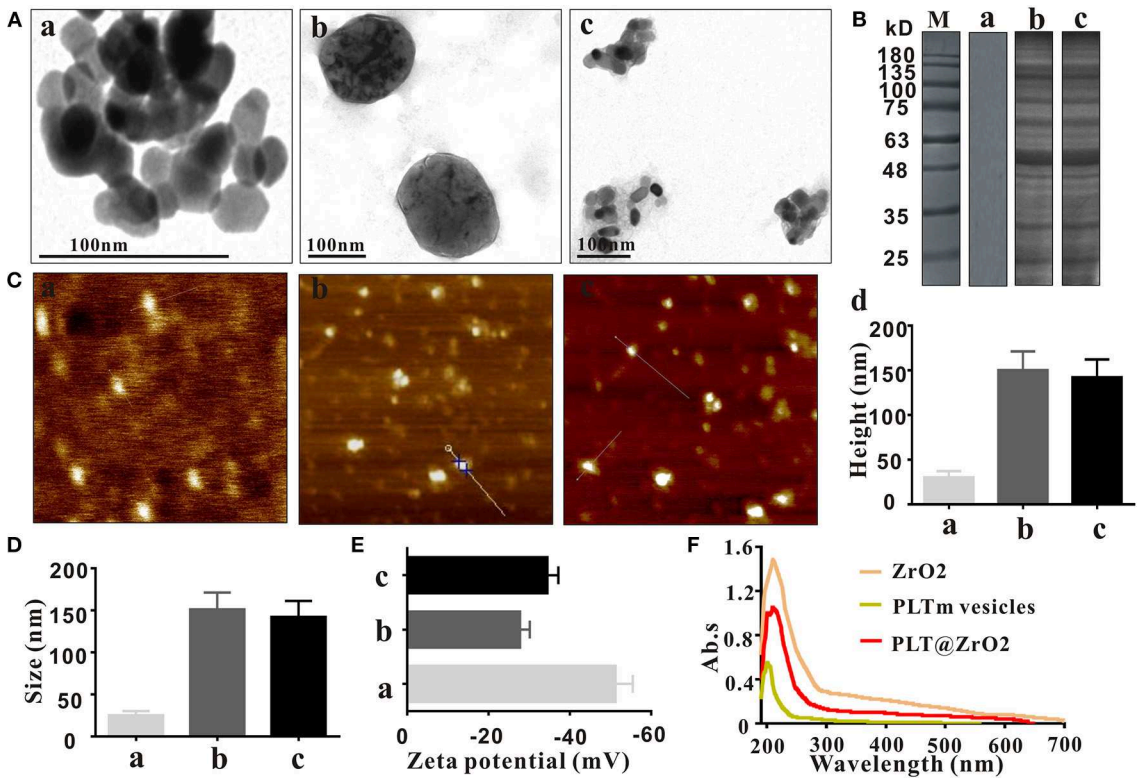

FIGURE 1 | Characterization of PLT@ZrO2. **(A)** TEM images of ZrO2, PLTm vesicles, and PLT@ZrO2. Scale bar: 100 nm. a, ZrO2; b, PLTm vesicles; c, PLT@ZrO2. **(B)** SDS-PAGE protein assessment. M, Marker; a, ZrO2; b, PLTm vesicles; c, PLT@ZrO2. **(C)** The heights of ZrO2, PLTm vesicles, and PLT@ZrO2 observed under AFM. a, ZrO2; b, PLTm vesicles; c, PLT@ZrO2; d, Quantitative assay of heights of ZrO2, PLTm vesicles, and PLT@ZrO2. **(D)** The particle size of ZrO2, PLTm vesicles, and PLT@ZrO2. a, ZrO2; b, PLTm vesicles; c, PLT@ZrO2. **(E)** Zeta potential of ZrO2, PLTm vesicles, and PLT@ZrO2. a, ZrO2; b, PLTm vesicles; c, PLT@ZrO2. **(F)** UV-Vis spectra of ZrO2, PLTm vesicles, and PLT@ZrO2.

$D \times L^2$, where V refers to volume, D refers to the longitudinal diameter and L refers to the latitudinal diameter. Day 0 (D0) represents the first day when subcutaneous tumor volumes exceed 100 mm^3. Fifteen mice were randomly assigned to 3 groups ($n = 5$) and injected with 100 μL of PBS, PLTm, or PLT@ZrO2 through tail vein once a day for 3 consecutive days. The dosage of ZrO2 was 50 mg/kg/d. The tumor sizes and body weights of the mice were measured, and tumor volumes were calculated once every 4 days. All mice were euthanized on day 14 (D14). Whole blood, tumors, and internal organs (hearts, livers, spleens, lung, and kidney) were collected. Whole blood was collected and measured by a five-part differential hematology analyzer (BC-5390, Mindray, China). After centrifugation (3,000 rpm, 10 min), an automatic biochemical analyzer (7100, HITACHI, Japan) and an immunology analyzer (Cobas 6000 e601, ROCHE, USA) were applied to detect the serum enzyme levels. All collected organs and tumors were fixed in 4% paraformaldehyde and frozen at −80°C. The frozen tumor tissues were used for Western blotting analysis. The fixed tissues were embedded in paraffin, sliced into sections, and then stained for HE and immunofluorescence.

Immunofluorescence Analysis

Immunofluorescence analysis was performed by immunofluorescence staining of TUNEL, N-cadherin, Vimentin, E-cadherin, β-catenin, and Fibronectin according to standard protocols (Hseu et al., 2019). The sections were then counterstained with DAPI (Chazotte, 2011), observed under an inverted fluorescence microscope, and photographed.

Western Blotting Analysis

Proteins were extracted from tumor tissue lysates using RIPA buffer. The concentrations of total proteins were quantified with a BCA protein assay kit. Protein expressions were assessed by

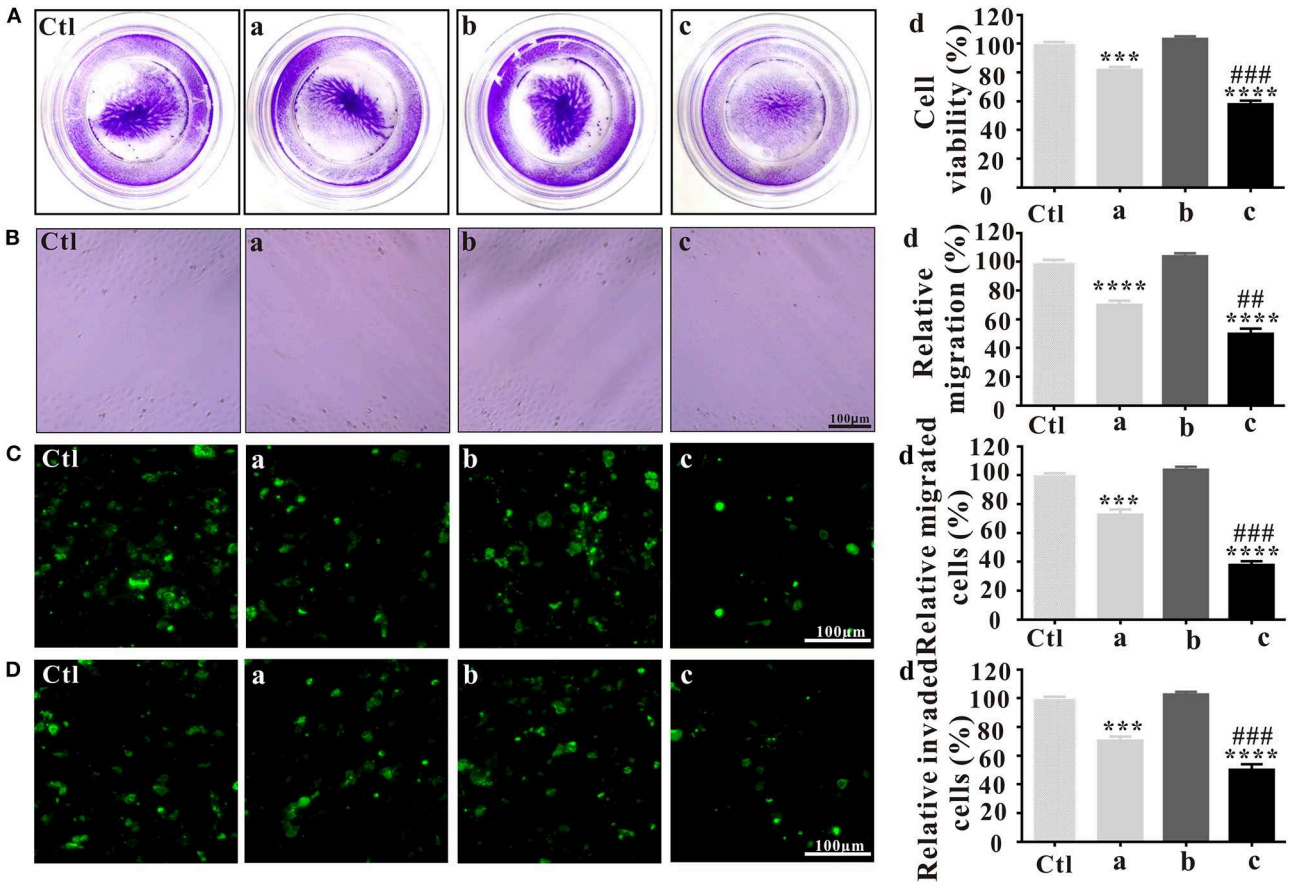

FIGURE 2 | *In vitro* antitumor effects of PLT@ZrO2. **(A)** Cell viability assay after treated with ZrO2, PLTm vesicles, or PLT@ZrO2. Ctl, control; a, ZrO2; b, PLTm vesicles; c, PLT@ZrO2; d, Semi-quantitative assay of cell viability after treated with ZrO2, PLTm vesicles, or PLT@ZrO2. **(B)** Scratch-wound healing recovery assays after treated with ZrO2, PLTm vesicles, or PLT@ZrO2, respectively. Ctl, control; a, ZrO2; b, PLTm vesicles; c, PLT@ZrO2; d, Semi-quantitative assay of migration rate after treated with ZrO2, PLTm vesicles, or PLT@ZrO2. **(C)** Transwell migration assay after treated with ZrO2, PLTm vesicles, or PLT@ZrO2, respectively. Ctl, control; a, ZrO2; b, PLTm vesicles; c, PLT@ZrO2; d, Semi-quantitative assay of migration rate after treated with ZrO2, PLTm vesicles, or PLT@ZrO2. **(D)** Transwell invasion assays after treated with ZrO2, PLTm vesicles, or PLT@ZrO2, respectively. Ctl, control; a, ZrO2; b, PLTm vesicles; c, PLT@ZrO2; d, Semi-quantitative assay of invasion rate after treated with ZrO2, PLTm vesicles, or PLT@ZrO2. Data are mean ± SD ($n = 3$). Compared to the control group: $^{***}p < 0.001$ and $^{****}p < 0.0001$; compared to the ZrO2 group: $^{\#\#}p < 0.01$ and $^{\#\#\#}p < 0.001$.

immunoblot analysis of tumor tissue lysates (40 μg) in the presence of rabbit antibodies against Snail, Smad4, Vimentin, Slug, N-cadherin, MMP2, Smad2, GAPDH (1:1,000, Servicebio Technology, China), and mouse antibodies against E-cadherin and β-actin (1:1,000, Servicebio Technology, China), according to standard protocols (Hseu et al., 2019).

Statistical Analysis

SPSS Software 20.0 was used for statistical analysis. Data are expressed as the mean ± SD. One-way ANOVA was used to assess the differences between groups, and Tukey's posttest was performed (* indicates $p < 0.05$, ** indicates $p < 0.01$, *** indicates $p < 0.001$, and **** indicates $p < 0.0001$).

RESULTS AND DISCUSSION

Characterization of the PLT@ZrO2 Nanocomposite

ZrO2 NPs were monodispersed with diameters averaging 25 nm (**Figure 1Aa**), larger than the spherical shaped ZrO2 NPs (of ∼9–11 nm) extracted from E. globulus leaf (Balaji et al., 2017). The diameter of PLTm vesicles was about 150 nm (**Figure 1Ab**), consistent with the previous report (Shang et al., 2019). Ultrasonic treatment facilitated encapsulation of ZrO2 NPs by PLTm vesicles to form PLT@ZrO2 nanocomposites. As shown in **Figure 1Ac**, several ZrO2 NPs were camouflaged by one PLTm vesicle. The SDS-PAGE results (**Figure 1B**) indicated that the proteins of PLT@ZrO2 nanocomposites were almost the same as PLTm nanovesicles. The heights of ZrO2 NPs, PLTm nanovesicles and PLT@ZrO2 nanocomposites observed under an AFM were 30.0 ± 7.2, 150 ± 21.1, and 142 ± 20.2 nm (**Figure 1C**). Dynamic light scattering (DLS) data (**Figure 1D**) showed that the average size of PLT@ ZrO2 nanocomposites were 140 nm, slightly smaller than PLTm nanovesicles and consistent with the data from AFM. Zeta potential of ZrO2 NPs was −51.5 ± 3.1 mV. After encapsulation, Zeta potential of PLT@ZrO2 was −34.5 ± 2.7 mV, similar to that of PLTm nanovesicles (−27.8 ± 2.4 mV) (**Figure 1E**), indicating successful camouflage. Results from UV-vis spectrometry (**Figure 1F**) showed that PLT@ZrO2 possesses absorption peaks at 210 and 200 nm, consistent with those of ZrO2 NPs and PLTm nanovesicles detected alone. These findings demonstrated the successful preparation of PLT@ZrO2.

In vitro Antitumor Effects of PLT@ ZrO2

In vitro Effects of PLT@ZrO2 Nanocomposite on Hela Cells Viability

Before investigating the anti-metastatic potential of PLT@ZrO2, we used crystal violet staining to assess the viability of Hela cells

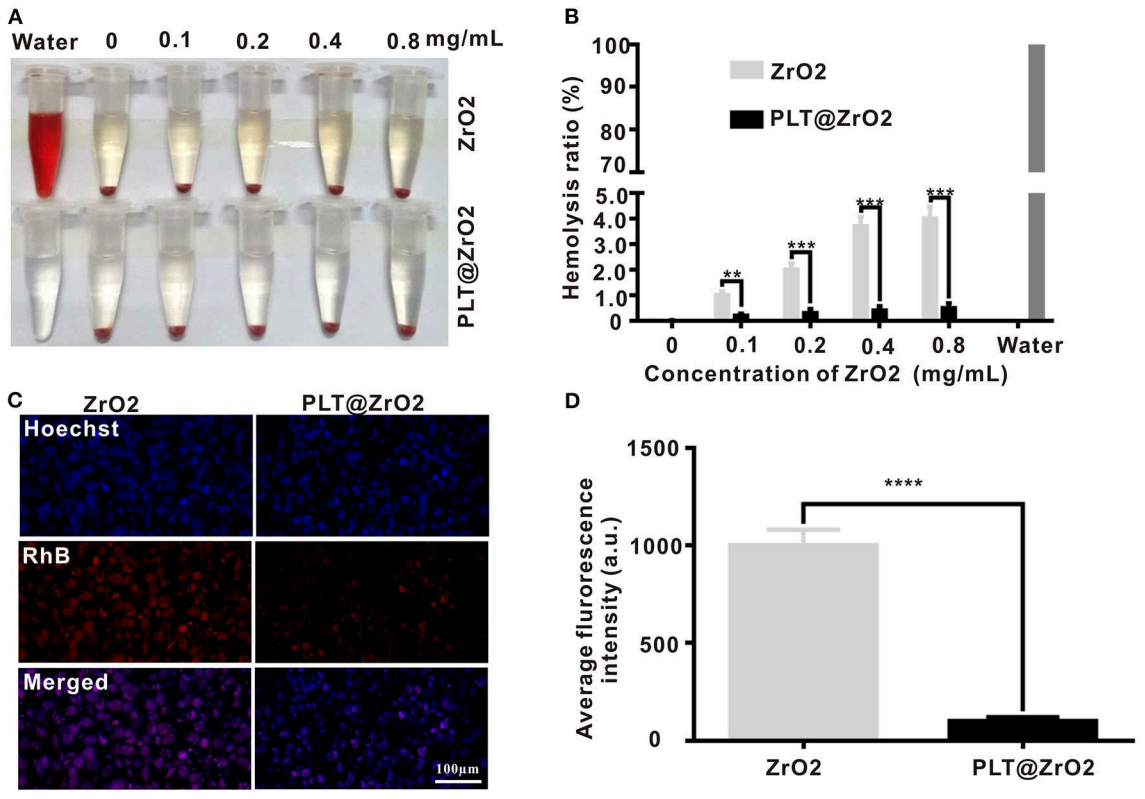

FIGURE 3 | Biocompatibility of PLT@ZrO2. **(A)** Pictures of RBC suspensions after treatment with various concentrations of ZrO2 or PLT@ZrO2. **(B)** Hemolytic rate after treatment with various concentrations of ZrO2 or PLT@ZrO2. **(C)** Images of RAW264.7 cells upon culture with ZrO2-RhB or PLT@ZrO2-RhB for 24 h taken by a LCFM. Scale bar: 100 μm. **(D)** Average fluorescence intensity of RAW264.7 cells after cultured with ZrO2-RhB or PLT@ZrO2-RhB for 24 h. Data are presented as mean ± SD ($n = 3$). Compared to the ZrO2 group: **$p < 0.01$, ***$p < 0.001$, and ****$p < 0.0001$.

after treatment with ZrO2, PLTm vesicles and PLT@ZrO2. Our results showed that compared with ZrO2, PLT@ZrO2 greatly inhibited viability, indicating that PLT camouflaging enhanced the inhibitory effect of ZrO2 NPs (**Figure 2A**). This may be due to increased local concentration of ZrO2 when PLTm vesicles bind to tumor cells (Shang et al., 2019).

PLT@ZrO2 Potently Inhibits Hela Cells Migration and Invasion

In the scratch-wound healing recovery assay (**Figure 2B**), ZrO2 NPs partly inhibited wound healing of Hela cells. PLT@ZrO2 greatly inhibited Hela cell migration, while PLTm did not inhibit Hela cells migration.

As shown in **Figure 2C**, treatment with ZrO2 NPs alone inhibited the migration of Hela cells by ∼30%, and PLT@ZrO2 exerted significant additional anti-migration effect. The Transwell invasion assay (**Figure 2D**) revealed that PLT@ZrO2 dramatically inhibited cells invading through Matrigel-coated filters, thus significantly decreasing the metastasis of Hela cells. The above results demonstrated that PLTm vesicle camouflaging improved the inhibitory effect of ZrO2 NPs on the migration and invasion of Hela cells.

Biocompatibility of the PLT@ZrO2 Nanocomposite

We evaluated the toxicities of ZrO2 NPs and PLT@ZrO2 by observing their hemolytic effects on RBCs. As shown in **Figure 3A**, the hemolytic rate after treatment with ZrO2 NPs, even in the concentration of 0.8 mg/mL, was <4.5%. PLT@ZrO2 had a value (0.5 ± 0.29%) significantly lower than that of ZrO2 NPs (**Figure 3B**), indicating that PLTm vesicle camouflaging improved the biosafety and hemocompatibility of ZrO2 NPs.

ZrO2 NPs and PLT@ZrO2 labeled with RhB (red fluorescent signals) were applied to detect the anti-phagocytosis effect. After incubation with ZrO2-RhB for 24 h, RAW264.7 macrophages showed strong red fluorescent signals (**Figure 3C**), demonstrating phagocytosis. However, weak fluorescent signals were observed after treatment with PLT@ZrO2-RhB, indicating that phagocytic activity was significantly weakened. Macrophages treated with PLT@ZrO2-RhB showed lower average fluorescence than that of cells treated with ZrO2-RhB (**Figure 3D**). The above results suggested that PLTm nanovesicle camouflaging prevents phagocytosis of ZrO2 NPs by macrophages, thus reducing their clearance and extending the circulation time.

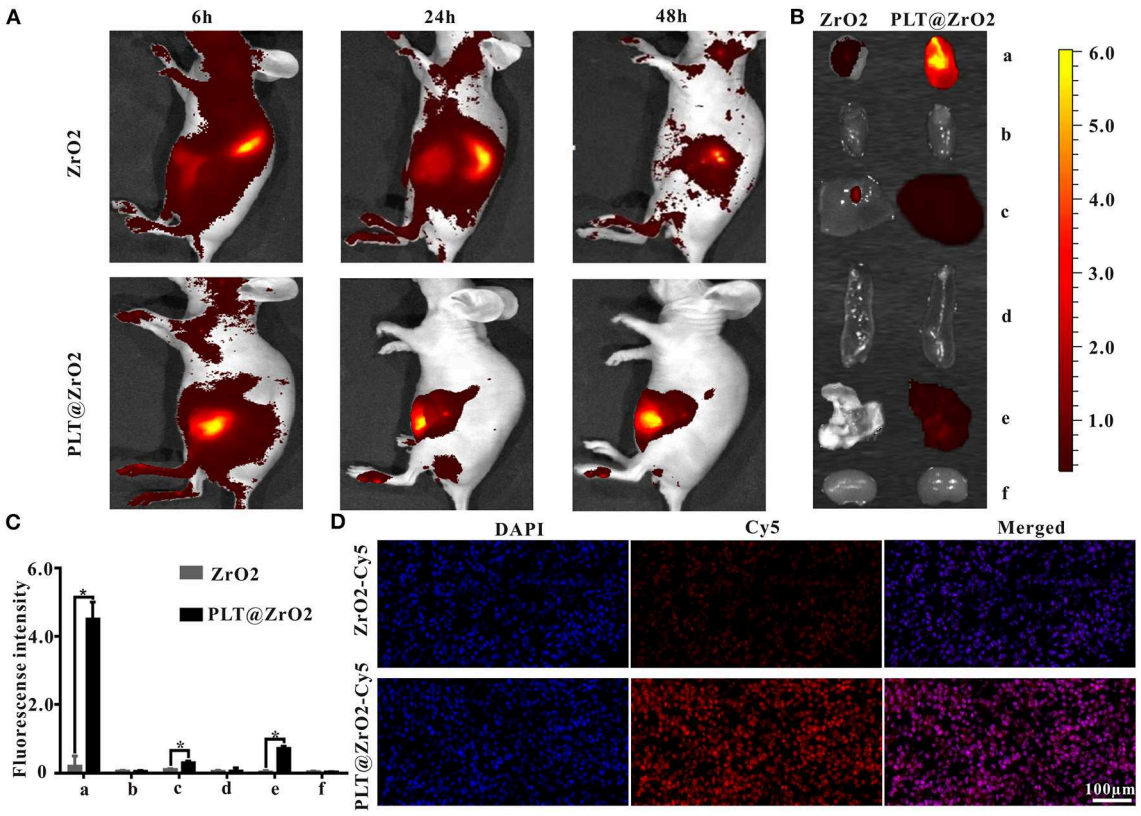

FIGURE 4 | *In vivo* distribution of PLT@ZrO2 through intravenous injection. **(A)** *In vivo* fluorescent images of nude mice at 6, 24, and 48 h upon intravenous treatment with ZrO2-Cy5 or PLT@ZrO2-Cy5. **(B)** Bioluminescent images of tumors and visceral tissues at 48 h post-treatment with ZrO2-Cy5 or PLT@ZrO2-Cy5. **(C)** Semi-quantitative assay of fluorescent intensities of tumor and other tissue samples. a, Tumor; b, heart; c, liver; d, spleen; e, lung; f, kidney. **(D)** Fluorescent images of tumors from nude mice 48 h upon administration of ZrO2-Cy5 or PLT@ZrO2-Cy5. Scale bar: 100 μm. Data are presented as the mean ± SD ($n = 3$). Compared to the ZrO2 group: $^*p < 0.05$.

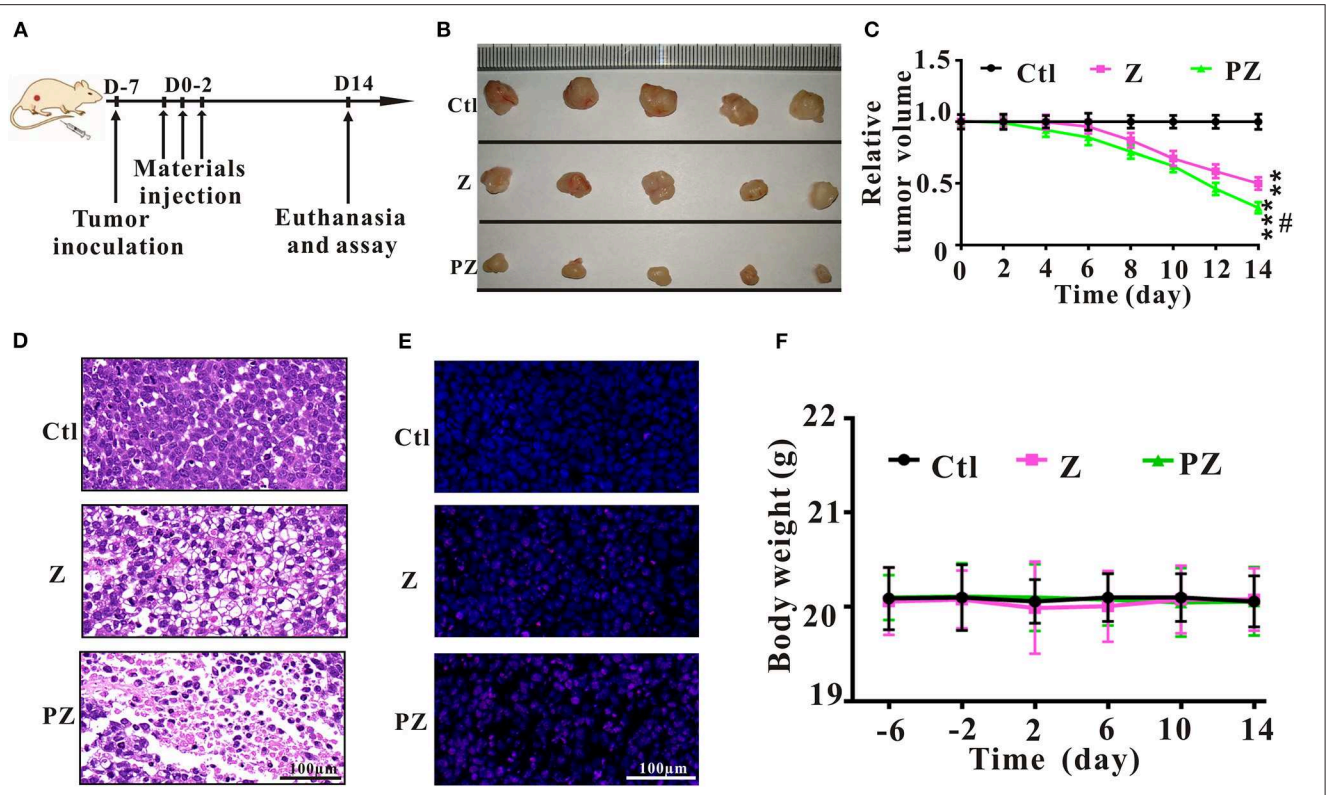

FIGURE 5 | Anticancer effects of ZrO2 and PLT@ZrO2 on Hela cells bearing BALB/c nude mice. **(A)** The scheme of experiment process. **(B)** The representative picture of tumors after treated with ZrO2 or PLT@ZrO2. **(C)** The changes of tumor volume after treated with ZrO2 or PLT@ZrO2. **(D)** The representative cell morphology of tumor tissues after treated with ZrO2 or PLT@ZrO2, and HE staining. **(E)** TUNEL assay after treated with ZrO2 or PLT@ZrO2. **(F)** Changes of body weight after treated with ZrO2 or PLT@ZrO2. Ctl, Control; Z, ZrO2; PZ, PLT@ZrO2. Scale bar: 100 μm. Data are presented as the mean ± SD ($n = 3$). Compared to the control group: $^{**}p < 0.01$ and $^{***}p < 0.001$; compared to the ZrO2 group: $^{\#}p < 0.05$.

The above results suggested that PLT@ZrO2 nanocomposite outperformed ZrO2 NPs in biocompatibility.

In vivo Distribution of PLT@ZrO2 Through Intravenous Injection

Due to the ability of PLTm vesicles to escape phagocytosis by immune cells and bind to tumor cells (Shang et al., 2019), PLT@ZrO2 has the potential to accumulate in tumors that have metastasized. To verify this hypothesis, we assessed biodistribution of PLT@ZrO2 using PLT@ZrO2 conjugated by Cy5. We used ZrO2 NPs conjugated by Cy5 as a control. As shown in **Figure 4A**, after administration of PLT@ZrO2-Cy5, we observed increased fluorescent intensity at tumor sites compared to ZrO2-Cy5, demonstrating increased retention of PLT@ZrO2. At 48 h after intravenous injection, PLT@ZrO2-Cy5 retentions in tumor, liver and lungs were greater than those of ZrO2-Cy5 ($P < 0.05$) (**Figures 4B,C**), and more intense red fluorescence in tumor tissue in the PLT@ZrO2 group was observed (**Figure 4D**), suggesting that retention of PLT@ZrO2-Cy5 in tumor sites exceeded that of ZrO2-Cy5 and PLT@ZrO2 nanocomposites have excellent tumor targeting efficiency.

Antitumor Effects of PLT@ZrO2 *In vivo*

To further explore the anticancer effect of PLT@ZrO2, we conducted *in vivo* assays in tumor-bearing mice that underwent Hela cells injection (**Figure 5A**). Compared to the ZrO2 group, tumor volumes in the PLT@ZrO2 group were smaller (**Figures 5B,C**), indicating that PLT@ZrO2 significantly inhibited tumor growth. As shown by HE (**Figure 5D**) and TUNEL staining (**Figure 5E**), we observed more necrotic and apoptotic cells in tumor tissues with PLT@ZrO2 compared to ZrO2. The above findings demonstrate that PLT@ZrO2 induced stronger anticancer effects than ZrO2 alone. The body weights of mice in PLT@ZrO2 group did not decline, indicating no obvious systemic toxicity (**Figure 5F**).

Tumor metastasis, an important feature of malignant tumors, is a complex and multistep process, regulated by genetic, and epigenetic changes (Gupta and Massagué, 2006; Tiwari et al., 2013). It is recognized that epithelial-mesenchymal transition (EMT) plays an important role in invasion and metastasis (van Zijl et al., 2009). EMT initiates the early steps of tumor metastasis and spread of tumor cells by endowing them greater motility and invasiveness (Thiery et al., 2009).

Wnt/β-catenin signaling plays a vital role in accelerating the process of EMT and metastasis (Zhou et al., 2016; Liu et al., 2017).

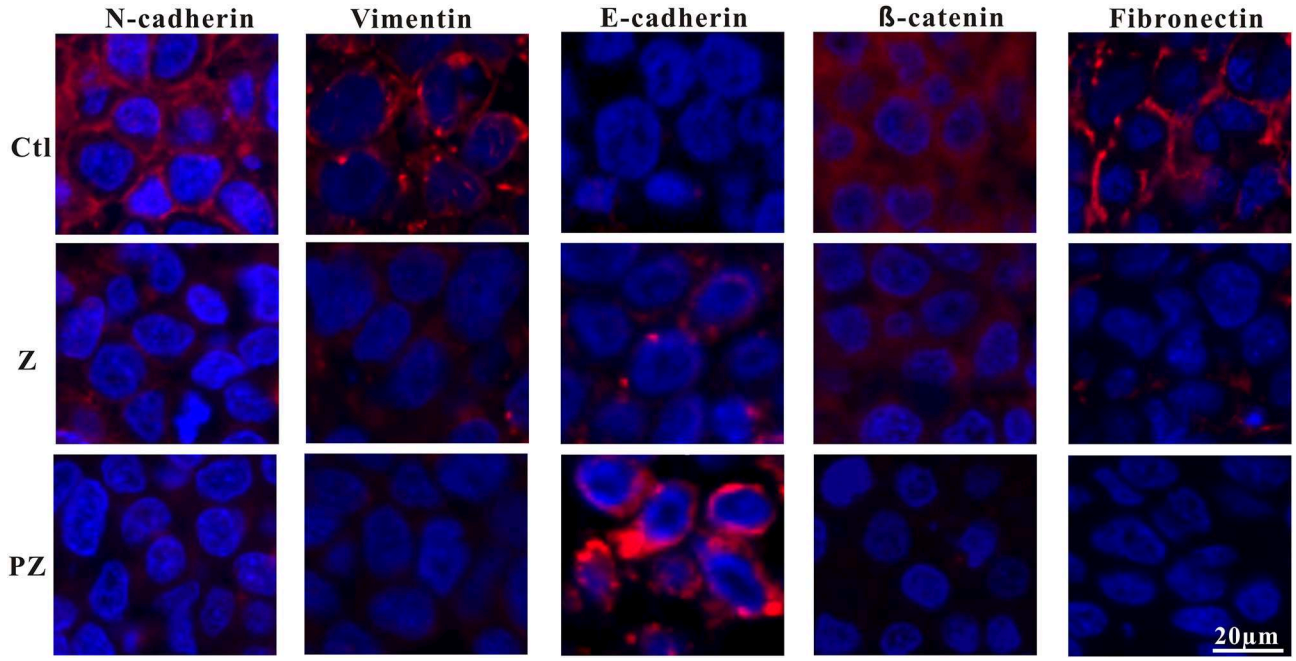

FIGURE 6 | Immunofluorescence pictures of tumor sections after treated with ZrO2 or PLT@ZrO2 and stained with N-cadherin, Vimentin, E-cadherin, β-catenin, and Fibronectin. Ctl, Control; Z, ZrO2; PZ, PLT@ZrO2. Scale bar: 20 μm.

Constitutive activation of the Wnt/β-catenin pathway results in the reduction of E-cadherin and induction of EMT (Goto et al., 2017), thereby enabling metastasis and invasion by reducing cell-to-cell contact (Onder et al., 2008). Moreover, downregulation of E-cadherin followed by EMT plays an important role in metastasis initiation (Shu et al., 2019). Previous studies have demonstrated that upregulation of N-cadherin is associated with tumor invasion and metastasis (Watson-Hurst and Becker, 2006; Hao et al., 2012; Mrozik et al., 2018). As shown in **Figure 6**, compared to ZrO2 NPs alone, treatment with PLT@ZrO2 downregulated N-cadherin and β-catenin (red fluorescence), and upregulated E-cadherin (red fluorescence), indicating that PLT@ZrO2 potentially inhibits tumor invasion and metastasis.

Reduction of epithelial proteins, such as E-cadherin (Onder et al., 2008), and increase of mesenchymal proteins, such as vimentin (Huber et al., 2005), are hallmarks of EMT. Vimentin, a 57 kDa type III intermediate filament protein, is critical for cell adhesion, migration, and signaling (Ivaska et al., 2007), and is essential to the progression and prognosis of cancer through EMT (Gugnoni et al., 2016; Sun and Fang, 2016). Fibronectin, a tumor-associated extracellular matrix protein, facilitates polymerization of fibrillar components on adherent and suspended tumor cell surfaces and maintains structure and motility in cell migration (Cheng et al., 1998; Huang et al., 2008; Shi et al., 2010; Knowles et al., 2015). As shown in **Figure 6**, compared with ZrO2 NPs, treatment with PLT@ZrO2, reduced Fibronectin and Vimentin (red fluorescence), indicating that PLT@ZrO2 could significantly inhibit tumor invasion and metastasis.

The EMT program is regulated by 3 EMT-inducing transcription factors families: Snail, Twist and Zeb (Ansieau et al., 2014; Puisieux et al., 2014). Slug (termed Snail2), can inhibit E-cadherin expression and promote EMT (Wang et al., 2009). Previous study has demonstrated that Slug regulates malignant transformation and metastasis of various cancers (Alves et al., 2009). WNT, TGF-β, NOTCH, and SHH signaling pathways play crucial roles in activation of EMT-related transcription factors, including Snail, Slug, Zeb1/2, and Twist (Nieszporek et al., 2019).

The adhesion molecule, N-cadherin, is related to invasive ability in cancers, and its overexpression facilitates motility and invasion (Nakajima et al., 2004). Slug and Snail inhibit E-cadherin expression; thus their overexpression promotes EMT (Hotz et al., 2007; Grzegrzolka et al., 2015). As shown in **Figure 7**, compared with ZrO2 NPs, treatment with PLT@ZrO2 downregulated N-cadherin, Slug, and Snail and upregulated E-cadherin, indicating that PLT@ZrO2 strongly inhibited EMT.

Matrix metallopeptidases (MMPs) degrade the extracellular matrix and basement membrane (Lengyel et al., 2001), enhancing the spread of cancer cells to distant sites (Shen et al., 2017). MMP2 and MMP9 degrade collagen IV in the extracellular basement membrane (Roomi et al., 2010) and rearrange the extracellular matrix during invasion and migration of cancer cells (Nabeshima et al., 2002; Alaseem et al., 2019). Moreover, active level of MMP2 in cancer cells is related to invasion and metastasis (Celentano et al., 2020). As shown in **Figure 7**, compared with ZrO2 NPs, treatment with PLT@ZrO2, significantly downregulated MMP2.

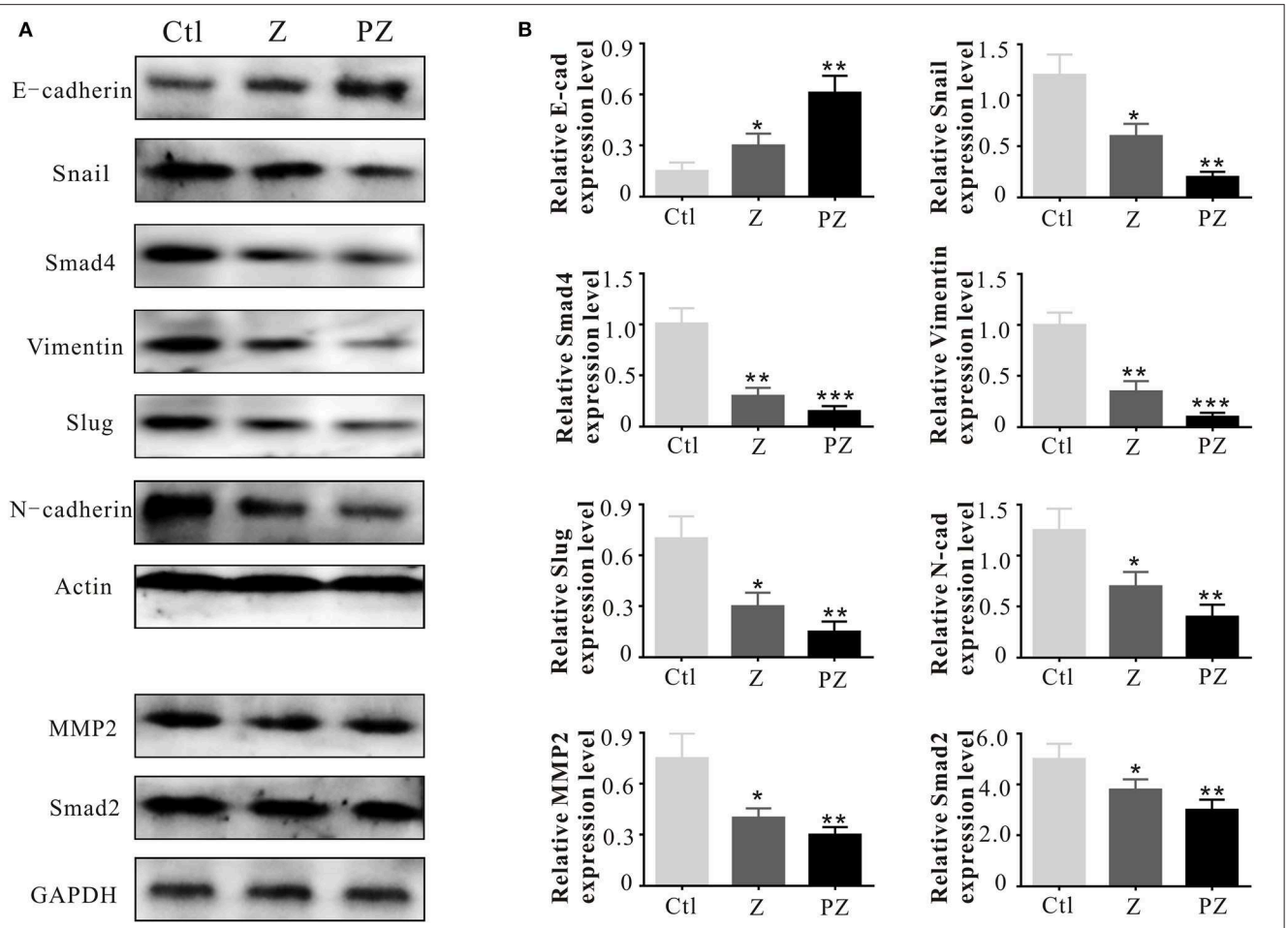

FIGURE 7 | Invasion and metastasis associated protein expressions. **(A)** Invasion and metastasis associated protein expressions in tumor tissues at 14th day after intravenous injection of ZrO2 or PLT@ZrO2. **(B)** Semi-quantitative assay of invasion and metastasis associated protein expressions in tumor tissues at 14th day after intravenous injection of ZrO2 or PLT@ZrO2. Ctl, Control; Z, ZrO2; PZ, PLT@ZrO2. Data are mean ± SD ($n = 3$). Compared to the control group: $^{*}p < 0.05$, $^{**}p < 0.01$, and $^{***}p < 0.001$.

Vimentin promotes the stemness of cancer cells by phosphorylation of Slug to initiate EMT (Virtakoivu et al., 2015). Additionally, Vimentin is essential for membrane localization and appropriate activation of MT1-MMP, which is essential for endothelial sprouting (Kwak et al., 2012). As shown in **Figure 7**, Vimentin was down-regulated after treatment with PLT@ZrO2, indicating inhibition of EMT initiation.

The TGF-β1 receptor, Smad, forms a heteromeric complex with Smad2 and Smad4. The activated Smad factor enters the nucleus and regulates the transcription of target genes to promote cell biological behaviors, such as proliferation, invasion, and EMT (Liu et al., 2016; Li et al., 2018). As shown in **Figure 7**, compared with ZrO2 NPs, after treated with PLT@ZrO2, Smad2, and Smad4 were downregulated, indicating that PLT@ZrO2 strongly inhibited tumor proliferation, invasion, and EMT.

We observed lung and liver metastasis in the control and ZrO2 groups, while metastasis in the PLT@ZrO2 group was absent (**Figure 8A**). The maximum cross sections of lungs and livers stained by HE showed that the size of lungs and livers metastasis foci were larger in the control group compared to the ZrO2 group, while no metastasis foci were found in the sections of lungs and livers in the PLT@ZrO2 group (**Figure 8B**), indicating that PLT@ZrO2 could inhibit metastasis to the lungs and liver.

Toxic and Side Effects of Vital Tissues and Organs

After treatment with PLT@ZrO2, white blood cell (WBC), RBC and PLT counts did not decrease (**Table 1**), indicating that PLT@ZrO2 did not induce hematological toxicity. To assess the effects of PLT@ZrO2 on visceral organs, serum enzyme level detection and histological assessment were performed.

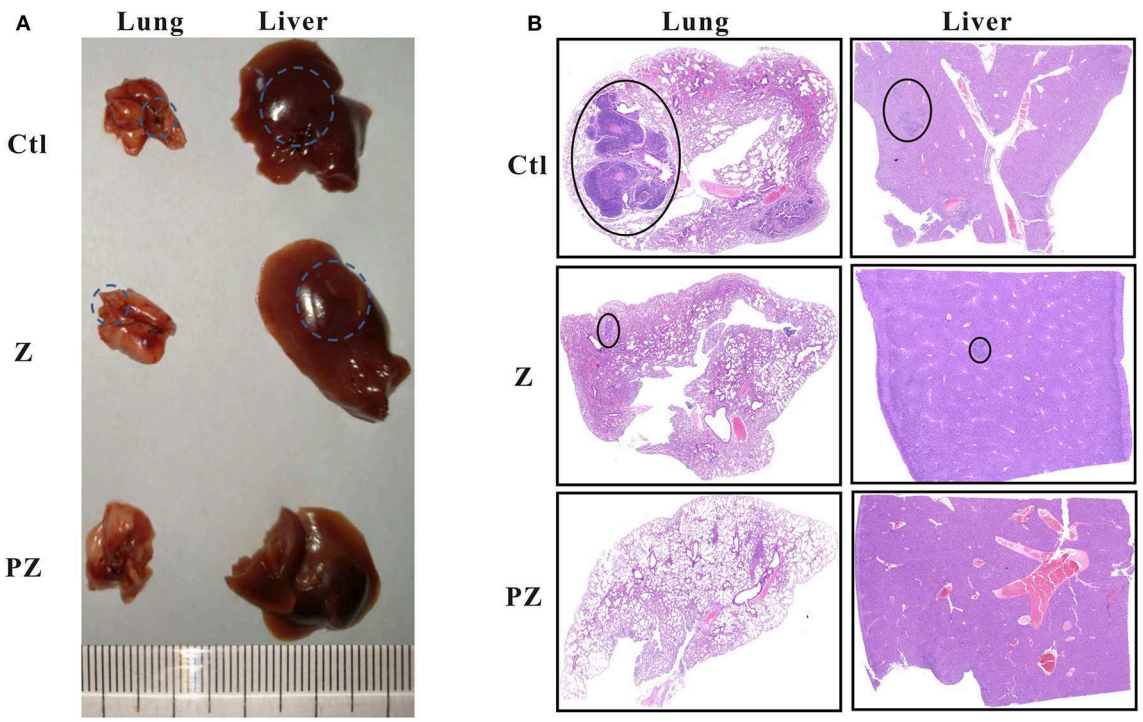

FIGURE 8 | Effects of PLT@ZrO2 on lung and liver metastasis of tumor. **(A)** The representative picture of lungs and livers after treated with ZrO2 or PLT@ZrO2. **(B)** The maximum cross sections of lung and liver sections stained by HE. The circles indicate the metastatic focuses in lungs and livers. Ctl, Control; Z, ZrO2; PZ, PLT@ZrO2.

TABLE 1 | The blood cell counts, the enzyme level and myocardial enzyme spectrum analysis of tumor bearing mice after treated with ZrO2, and PLT@ZrO2.

	Control	ZrO2	PLT@ ZrO2
Blood cell count			
WBC (10^9/L)	7.4 ± 0.3	7.3 ± 0.5	7.4 ± 0.5
RBC (10^{12}/L)	11.3 ± 1.2	11.3 ± 1.2	11.3 ± 1.0
HGB (g/dL)	14.6 ± 0.5	14.5 ± 0.4	14.5 ± 0.6
HCT (%)	49.2 ± 1.4	49.2 ± 1.3	49.0 ± 1.5
PLT (10^{11}/L)	8.6 ± 0.4	8.5 ± 0.5	8.4 ± 0.6
Serum enzyme level			
ALT (U/L)	25.5 ± 2.4↑	19.8 ± 1.8↑	9.5 ± 0.6
AST (U/L)	108.8 ± 2.3↑	97.9 ± 2.2↑	48.2 ± 2.4
Urea (mmol/L)	2.1 ± 0.2	2.1 ± 0.2	2.2 ± 0.3
CRE (μmol/L)	6.7 ± 0.3	6.7 ± 0.4	6.8 ± 0.4
Myocardial enzyme spectrum			
TNT-HS (pg/ml)	48.7 ± 3.6	48.4 ± 3.7	48.8 ± 4.1
CK (U/L)	3780.0 ± 121.5	3785.3 ± 127.1	3791.4 ± 125.8
LDH-L (U/L)	7690.5 ± 120.2	7692.5 ± 122.3	7700.4 ± 131.8
CK-MB (U/L)	3770.9 ± 86.3	3782.7 ± 103.4	3792.9 ± 115.1
Myo (ng/mL)	72.9 ± 2.9	73.6 ± 2.5	73.9 ± 3.5

Data are mean ± SD (n = 3).

As shown in **Table 1**, there were no alterations in blood urea nitrogen (BUN) and creatinine (Cr), indicating that PLT@ZrO2 did not result in kidney dysfunction. Due to tumor invasion and metastasis, alanine transaminase (ALT), and aspartate amino-transferase (AST) in the control group and ZrO2 group were significantly elevated, but levels in the PLT@ZrO2 group were normal, indirectly indicating that PLT@ZrO2 inhibited the liver invasion and metastasis of Hela cells. Indicators of cardiac function, such as Lactate dehydrogenase (LDH), hypersensitive troponin T (TNT-HS), creatinine kinase (CK), creatinine kinase-MB (CK-MB), and myoglobin (Myo), were not elevated in the PLT@ ZrO2 group (**Table 1**). Histological images of heart, spleen, and kidney did not show abnormalities in both ZrO2 and PLT@ZrO2 groups (**Figure 9**). These results indicated that PLT@ZrO2 could inhibit the elevation of ALT and AST and exhibit fewer side effects.

CONCLUSION

In this study, we have shown PLT@ZrO2, a PLTm vesicle-encapsulated ZrO2 nanocomposite, targeted subcutaneous and metastatic tumor sites, enhanced the anticancer effects of ZrO2, and inhibited tumor invasion and metastasis. ZrO2 NPs coated with PLTm vesicles escaped phagocytosis by immune cells, extended their retention, and targeted tumor sites. Additionally, we did not observe systemic toxicity after treatment with PLT@ZrO2. The PLT@ZrO2 nanocomposite has potential as a non-toxic and efficient targeted anticancer platform capable of inhibiting tumor growth, invasion and metastasis.

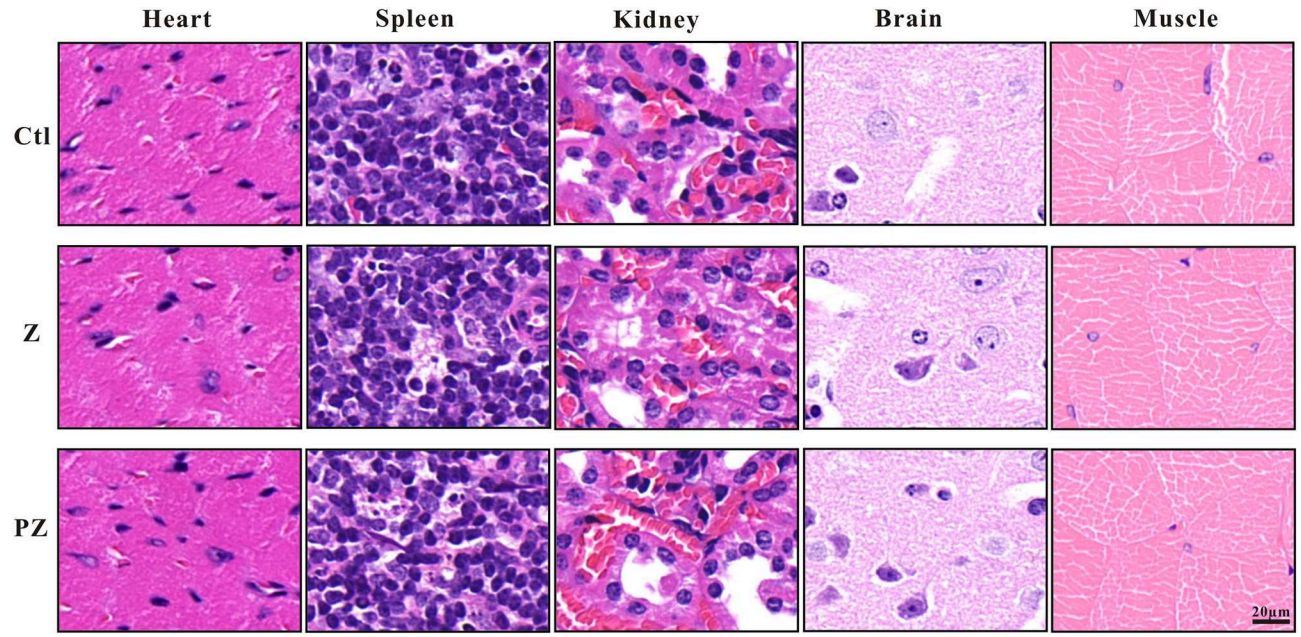

FIGURE 9 | Histological images of heart, spleen, kidney, brain and skeletal muscle after ZrO2 or PLT@ZrO2 treatment and HE staining. Ctl, Control; Z, ZrO2; PZ, PLT@ZrO2. Scale bar: 20 μm.

DATA AVAILABILITY STATEMENT

The original data supporting this article conclusions will be made available to any qualified researcher by the authors without reservation.

ETHICS STATEMENT

The ethics committee of Third Xiangya Hospital of Central South University (No. 2017-s75) approved the animal experiment, and the guidelines released by the Ministry of Science and Technology of the People's Republic of China in September 30th, 2006 guided the animal care.

AUTHOR CONTRIBUTIONS

The manuscript was written through contributions of all authors. All authors have given approval to the final version of the manuscript.

FUNDING

This work was supported by the National Natural Science Foundations of China (Nos. 81971748, 81600461, 81602801), and the Graduate Self-Exploration and Innovation Project of Central South University of China under Grant (No. 2019zzts363).

REFERENCES

Alaseem, A., Alhazzani, K., Dondapati, P., Alobid, S., Bishayee, A., and Rathinavelu, A. (2019). Matrix metalloproteinases: a challenging paradigm of cancer management. *Semin. Cancer Biol.* 56, 100–115. doi: 10.1016/j.semcancer.2017.11.008

Al-Fahdawi, M. Q., Rasedee, A., Al-Qubaisi, M. S., Alhassan, F. H., Rosli, R., El Zowalaty, M. E., et al. (2015). Cytotoxicity and physicochemical characterization of iron-manganese-doped sulfated zirconia nanoparticles. *Int. J. Nanomed.* 10, 5739–5750. doi: 10.2147/IJN.S82586

Alves, C. C., Carneiro, F., Hoefler, H., and Becker, K. F. (2009). Role of the epithelial-mesenchymal transition regulator Slug in primary human cancers. *Front. Biosci.* 14, 3035–3050. doi: 10.2741/3433

Ansieau, S., Collin, G., and Hill, U. (2014). EMT or EMT-promoting transcription factors, where to focus the light? *Front. Oncol.* 4:353. doi: 10.3389/fonc.2014.00353

Balaji, S., Mandal, B. K., Ranjan, S., Dasgupta, N., and Chidambaram, R. (2017). Nano-zirconia - evaluation of its antioxidant and anticancer activity. *J. Photochem. Photobiol. B*170, 125–133. doi: 10.1016/j.jphotobiol.2017.04.004

Borsig, L., Wong, R., Feramisco, J., Nadeau, D. R., Varki, N. M., and Varki, A. (2001). Heparin and cancer revisited: mechanistic connections involving platelets, P-selectin, carcinoma mucins, and tumor metastasis. *Proc. Natl. Acad. Sci. U.S.A.* 98, 3352–3357. doi: 10.1073/pnas.061615598

Celentano, A., Yap, T., Paolini, R., Yiannis, C., Mirams, M., Koo, K., et al. (2020). Inhibition of matrix metalloproteinase-2 modulates malignant behaviour of oral squamous cell carcinoma cells. *J. Oral. Pathol. Med.* doi: 10.1111/jop.12992. [Epub ahead of print].

Chazotte, B. (2011). Labeling nuclear DNA using DAPI. *Cold Spring Harb. Protoc.* 2011:pdb prot5556. doi: 10.1101/pdb.prot5556

Chen, Y. Q., Liu, B., Tang, D. G., and Honn, K. V. (1992). Fatty acid modulation of tumor cell-platelet-vessel wall interaction. *Cancer Metastasis Rev.* 11, 389–409. doi: 10.1007/BF01307189

Cheng, H. C., Abdel-Ghany, M., Elble, R. C., and Pauli, B. U. (1998). Lung endothelial dipeptidyl peptidase IV promotes adhesion and metastasis of rat

breast cancer cells via tumor cell surface-associated fibronectin. *J. Biol. Chem.* 273, 24207–24215. doi: 10.1074/jbc.273.37.24207

Crowley, L. C., Marfell, B. J., and Waterhouse, N. J. (2016). Analyzing cell death by nuclear staining with hoechst 33342. *Cold Spring Harb Protoc.* 2016:pdb.prot087205. doi: 10.1101/pdb.prot087205

Gasic, G. J. (1984). Role of plasma, platelets, and endothelial cells in tumor metastasis. *Cancer Metastasis Rev.* 3, 99–114. doi: 10.1007/BF00047657

Goto, H., Kimmey, S. C., Row, R. H., Matus, D. Q., and Martin, B. L. (2017). FGF and canonical Wnt signaling cooperate to induce paraxial mesoderm from tailbud neuromesodermal progenitors through regulation of a two-step epithelial to mesenchymal transition. *Development* 144, 1412–1424. doi: 10.1242/dev.143578

Grzegrzolka, J., Biala, M., Wojtyra, P., Kobierzycki, C., Olbromski, M., Gomulkiewicz, A., et al. (2015). Expression of EMT markers SLUG and TWIST in breast cancer. *Anticancer Res.* 35, 3961–3968.

Gugnoni, M., Sancisi, V., Manzotti, G., Gandolfi, G., and Ciarrocchi, A. (2016). Autophagy and epithelial-mesenchymal transition: an intricate interplay in cancer. *Cell Death Dis.* 7:e2520. doi: 10.1038/cddis.2016.415

Gupta, G. P., and Massagué, J. (2006). Cancer metastasis: building a framework. *Cell* 127, 679–695. doi: 10.1016/j.cell.2006.11.001

Hao, L., Ha, J. R., Kuzel, P., Garcia, E., and Persad, S. (2012). Cadherin switch from E- to N-cadherin in melanoma progression is regulated by the PI3K/PTEN pathway through Twist and Snail. *Br. J. Dermatol.* 166, 1184–1197. doi: 10.1111/j.1365-2133.2012.10824.x

Honn, K. V., and Tang, D. (1992b). Hemostasis and malignancy: an overview. *Cancer Metastasis Rev.* 11, 223–226. doi: 10.1007/BF01307178

Honn, K. V., and Tang, D. G. (1992a). Adhesion molecules and tumor cell interaction with endothelium and subendothelial matrix. *Cancer Metastasis Rev.* 11, 353–375. doi: 10.1007/BF01307187

Hotz, B., Arndt, M., Dullat, S., Bhargava, S., Buhr, H. J., and Hotz, H. G. (2007). Epithelial to mesenchymal transition: expression of the regulators snail, slug, and twist in pancreatic cancer. *Clin. Cancer Res.* 13, 4769–4776. doi: 10.1158/1078-0432.CCR-06-2926

Hseu, Y. C., Lin, Y. C., Rajendran, P., Thigarajan, V., Mathew, D. C., Lin, K. Y., et al. (2019). Antrodia salmonea suppresses invasion and metastasis in triple-negative breast cancer cells by reversing EMT through the NF-kappaB and Wnt/beta-catenin signaling pathway. *Food Chem. Toxicol.* 124, 219–230. doi: 10.1016/j.fct.2018.12.009

Hu, C. M., Fang, R. H., Wang, K. C., Luk, B. T., Thamphiwatana, S., Dehaini, D., et al. (2015b). Nanoparticle biointerfacing by platelet membrane cloaking. *Nature* 526, 118–121. doi: 10.1038/nature15373

Hu, Q., Sun, W., Qian, C., Wang, C., Bomba, H. N., and Gu, Z. (2015a). Anticancer platelet-mimicking nanovehicles. *Adv Mater.* 27, 7043–7050. doi: 10.1002/adma.201503323

Huang, L., Cheng, H. C., Isom, R., Chen, C. S., Levine, R. A., and Pauli, B. U. (2008). Protein kinase cepsilon mediates polymeric fibronectin assembly on the surface of blood-borne rat breast cancer cells to promote pulmonary metastasis. *J. Biol. Chem.* 283, 7616–7627. doi: 10.1074/jbc.M705839200

Huber, M. A., Kraut, N., and Beug, H. (2005). Molecular requirements for epithelial-mesenchymal transition during tumor progression. *Curr. Opin. Cell Biol.* 17, 548–558. doi: 10.1016/j.ceb.2005.08.001

Ivaska, J., Pallari, H. M., Nevo, J., and Eriksson, J. E. (2007). Novel functions of vimentin in cell adhesion, migration, and signaling. *Exp Cell Res.* 313, 2050–2062. doi: 10.1016/j.yexcr.2007.03.040

Jang, Y. Y., Cho, D., Kim, S. K., Shin, D. J., Park, M. H., Lee, J. J., et al. (2012). An improved flow cytometry-based natural killer cytotoxicity assay involving calcein AM staining of effector cells. *Ann. Clin. Lab. Sci.* 42, 42–49.

Karpatkin, S., and Pearlstein, E. (1981). Role of platelets in tumor cell metastases. *Ann. Intern. Med.* 95, 636–641. doi: 10.7326/0003-4819-95-5-636

Knowles, L. M., Gurski, L. A., Maranchie, J. K., and Pilch, J. (2015). Fibronectin matrix formation is a prerequisite for colonization of kidney tumor cells in fibrin. *J. Cancer* 6, 98–104. doi: 10.7150/jca.10496

Kumar, S., Sharma, J. G., Maji, S., and Malhotra, B. D. (2016). Nanostructured zirconia decorated reduced graphene oxide based efficient biosensing platform for non-invasive oral cancer detection. *Biosens. Bioelectron.* 78, 497–504. doi: 10.1016/j.bios.2015.11.084

Kwak, H. I., Kang, H., Dave, J. M., Mendoza, E. A., Su, S. C., Maxwell, S. A., et al. (2012). Calpain-mediated vimentin cleavage occurs upstream of MT1-MMP membrane translocation to facilitate endothelial sprout initiation. *Angiogenesis* 15, 287–303. doi: 10.1007/s10456-012-9262-4

Lengyel, E., Schmalfeldt, B., Konik, E., Späthe, K., Härting, K., Fenn, A., et al. (2001). Expression of latent matrix metalloproteinase 9 (MMP-9) predicts survival in advanced ovarian cancer. *Gynecol. Oncol.* 82, 291–298. doi: 10.1006/gyno.2001.6243

Li, H., Wu, X., and Cheng, X. (2016). Advances in diagnosis and treatment of metastatic cervical cancer. *J. Gynecol. Oncol.* 27:e43. doi: 10.3802/jgo.2016.27.e43

Li, X. Y., Ban, G. F., Al-Shameri, B., He, X., Liang, D. Z., and Chen, W. X. (2018). High-temperature requirement protein A1 regulates odontoblastic differentiation of dental pulp cells via the transforming growth factor beta 1/smad signaling pathway. *J. Endod.* 44, 765–772. doi: 10.1016/j.joen.2018.02.003

Liu, C. C., Cai, D. L., Sun, F., Wu, Z. H., Yue, B., Zhao, S. L., et al. (2017). FERMT1 mediates epithelial-mesenchymal transition to promote colon cancer metastasis via modulation of beta-catenin transcriptional activity. *Oncogene* 36, 1779–1792. doi: 10.1038/onc.2016.339

Liu, Y., Qian, J., Li, X., Chen, W., Xu, A., Zhao, K., et al. (2016). Long noncoding RNA BX357664 regulates cell proliferation and epithelial-to-mesenchymal transition via inhibition of TGF-beta1/p38/HSP27 signaling in renal cell carcinoma. *Oncotarget* 7, 81410–81422. doi: 10.18632/oncotarget.12937

Mftah, A., Alhassan, F. H., Al-Qubaisi, M. S., El Zowalaty, M. E., Webster, T. J., Sh-Eldin, M., et al. (2015). Physicochemical properties, cytotoxicity, and antimicrobial activity of sulphated zirconia nanoparticles. *Int. J. Nanomed.* 10, 765–774. doi: 10.2147/IJN.S66058

Mrozik, K. M., Blaschuk, O. W., Cheong, C. M., Zannettino, A. C. W., and Vandyke, K. (2018). N-cadherin in cancer metastasis, its emerging role in haematological malignancies and potential as a therapeutic target in cancer. *BMC Cancer* 18:939. doi: 10.1186/s12885-018-4845-0

Nabeshima, K., Inoue, T., Shimao, Y., and Sameshima, T. (2002). Matrix metalloproteinases in tumor invasion: role for cell migration. *Pathol. Int.* 52, 255–264. doi: 10.1046/j.1440-1827.2002.01343.x

Nakajima, S., Doi, R., Toyoda, E., Tsuji, S., Wada, M., Koizumi, M., et al. (2004). N-cadherin expression and epithelial-mesenchymal transition in pancreatic carcinoma. *Clin. Cancer Res.* 10(12 Pt 1), 4125–4133. doi: 10.1158/1078-0432.CCR-0578-03

Nieswandt, B., Hafner, M., Echtenacher, B., and Männel, D. N. (1999). Lysis of tumor cells by natural killer cells in mice is impeded by platelets. *Cancer Res.* 59, 1295–1300.

Nieszporek, A., Skrzypek, K., Adamek, G., and Majka, M. (2019). Molecular mechanisms of epithelial to mesenchymal transition in tumor metastasis. *Acta Biochim. Pol.* 66, 509–520. doi: 10.18388/abp.2019_2899

Onder, T. T., Gupta, P. B., Mani, S. A., Yang, J., Lander, E. S., and Weinberg, R. A. (2008). Loss of E-cadherin promotes metastasis via multiple downstream transcriptional pathways. *Cancer Res.* 68, 3645–3654. doi: 10.1158/0008-5472.CAN-07-2938

Peng, L., Yuan, X., Jiang, B., Tang, Z., and Li, G. C. (2016). LncRNAs: key players and novel insights into cervical cancer. *Tumour Biol.* 37, 2779–2788. doi: 10.1007/s13277-015-4663-9

Puisieux, A., Brabletz, T., and Caramel, J. (2014). Oncogenic roles of EMT-inducing transcription factors. *Nat. Cell Biol.* 16, 488–494. doi: 10.1038/ncb2976

Roomi, M. W., Monterrey, J. C., Kalinovsky, T., Rath, M., and Niedzwiecki, A. (2010). *In vitro* modulation of MMP-2 and MMP-9 in human cervical and ovarian cancer cell lines by cytokines, inducers and inhibitors. *Oncol Rep.* 23, 605–614. doi: 10.3892/or_00000675

Sabrkhany, S., Kuijpers, M. J. E., Knol, J. C., Olde Damink, S. W. M., Dingemans, A. C., Verheul, H. M., et al. (2018). Exploration of the platelet proteome in patients with early-stage cancer. *J. Proteom.* 177, 65–74. doi: 10.1016/j.jprot.2018.02.011

Shang, Y., Wang, Q., Wu, B., Zhao, Q., Li, J., Huang, X., et al. (2019). Platelet-membrane-camouflaged black phosphorus quantum dots enhance anticancer effect mediated by apoptosis and autophagy. *ACS Appl. Mater. Interf.* 11, 28254–28266. doi: 10.1021/acsami.9b04735

Shen, C. J., Chan, S. H., Lee, C. T., Huang, W. C., Tsai, J. P., and Chen, B. K. (2017). Oleic acid-induced ANGPTL4 enhances head and neck squamous cell carcinoma anoikis resistance and metastasis via up-regulation of fibronectin. *Cancer Lett.* 386, 110–122. doi: 10.1016/j.canlet.2016.11.012

Shi, F., Harman, J., Fujiwara, K., and Sottile, J. (2010). Collagen I matrix turnover is regulated by fibronectin polymerization. *Am. J. Physiol. Cell Physiol.* 298, C1265–1275. doi: 10.1152/ajpcell.00341.2009

Shu, J., Wang, L., Han, F., Chen, Y., Wang, S., and Luo, F. (2019). BTBD7 downregulates E-cadherin and promotes epithelial-mesenchymal transition in lung cancer. *Biomed. Res. Int.* 2019:5937635. doi: 10.1155/2019/5937635

Sun, L., and Fang, S. (2016). Epigenetic regulation of epithelial-mesenchymal transition. *Cell Mol. Life Sci.* 73, 4493–4515. doi: 10.1007/s00018-016-2303-1

Tanaka, N. G., Tohgo, A., and Ogawa, H. (1986). Platelet-aggregating activities of metastasizing tumor cells. V. In situ roles of platelets in hematogenous metastases. *Invasion Metastasis* 6, 209–224.

Thiery, J. P., Acloque, H., Huang, R. Y., and Nieto, M. A. (2009). Epithelial-mesenchymal transitions in development and disease. *Cell* 139, 871–890. doi: 10.1016/j.cell.2009.11.007

Tiwari, N., Tiwari, V. K., Waldmeier, L., Balwierz, P. J., Arnold, P., Pachkov, M., et al. (2013). Sox4 is a master regulator of epithelial-mesenchymal transition by controlling Ezh2 expression and epigenetic reprogramming. *Cancer Cell* 23, 768–783. doi: 10.1016/j.ccr.2013.04.020

van Zijl, F., Zulehner, G., Petz, M., Schneller, D., Kornauth, C., Hau, M., et al. (2009). Epithelial-mesenchymal transition in hepatocellular carcinoma. *Future Oncol.* 5, 1169–1179. doi: 10.2217/fon.09.91

Venu, M., Venkateswarlu, S., Reddy, Y. V. M., Seshadri Reddy, A., Gupta, V. K., Yoon, M., et al. (2018). Highly sensitive electrochemical sensor for anticancer drug by a zirconia nanoparticle-decorated reduced graphene oxide nanocomposite. *ACS Omega* 3, 14597–14605. doi: 10.1021/acsomega.8b02129

Virtakoivu, R., Mai, A., Mattila, E., De Franceschi, N., Imanishi, S. Y., Corthals, G., et al. (2015). Vimentin-ERK signaling uncouples slug gene regulatory function. *Cancer Res.* 75, 2349–2362. doi: 10.1158/0008-5472.CAN-14-2842

Wang, S. P., Wang, W. L., Chang, Y. L., Wu, C. T., Chao, Y. C., Kao, S. H., et al. (2009). p53 controls cancer cell invasion by inducing the MDM2-mediated degradation of Slug. *Nat. Cell Biol.* 11, 694–704. doi: 10.1038/ncb1875

Watson-Hurst, K., and Becker, D. (2006). The role of N-cadherin, MCAM and beta3 integrin in melanoma progression, proliferation, migration and invasion. *Cancer Biol. Ther.* 5, 1375–1382. doi: 10.4161/cbt.5.10.3241

Yang, Y., Wang, Z., Yang, M., Li, J., Zheng, F., Shen, G., et al. (2007). Electrical detection of deoxyribonucleic acid hybridization based on carbon-nanotubes/nano zirconium dioxide/chitosan-modified electrodes. *Analyt. Chim. Acta* 584, 268–274. doi: 10.1016/j.aca.2006.11.055

Zhou, Q., Abraham, A. D., Li, L., Babalmorad, A., Bagby, S., Arcaroli, J. J., et al. (2016). Topoisomerase IIalpha mediates TCF-dependent epithelial-mesenchymal transition in colon cancer. *Oncogene* 35, 4990–4999. doi: 10.1038/onc.2016.29

Conflict of Interest: The authors declare that the research was conducted in the absence of any commercial or financial relationships that could be construed as a potential conflict of interest.

frontiers in Chemistry

REVIEW
published: 17 June 2020
doi: 10.3389/fchem.2020.00496

Recent Advances in Rare-Earth-Doped Nanoparticles for NIR-II Imaging and Cancer Theranostics

*Zhenfeng Yu, Christina Eich and Luis J. Cruz**

Translational Nanobiomaterials and Imaging Group, Department of Radiology, Leiden University Medical Center, Leiden, Netherlands

Fluorescence imaging in the second near infrared window (NIR-II, 1,000–1,700 nm) has been widely used in cancer diagnosis and treatment due to its high spatial resolution and deep tissue penetration depths. In this work, recent advances in rare-earth-doped nanoparticles (RENPs)—a novel kind of NIR-II nanoprobes—are presented. The main focus of this study is on the modification of RENPs and their applications in NIR-II *in vitro* and *in vivo* imaging and cancer theranostics. Finally, the perspectives and challenges of NIR-II RENPs are discussed.

Keywords: NIR-II, rare-earth-doped nanoparticles, modification, *in vitro* and *in vivo* imaging, cancer theranostics

OPEN ACCESS

Edited by:
Jianhua Zhang,
Tianjin University, China

Reviewed by:
Fan Zhang,
Fudan University, China
Hong-Min Meng,
Zhengzhou University, China

****Correspondence:***
Luis J. Cruz
l.j.cruz_ricondo@lumc.nl

Specialty section:
This article was submitted to Nanoscience, a section of the journal Frontiers in Chemistry

Received: *24 March 2020*
Accepted: *14 May 2020*
Published: *17 June 2020*

Citation:
Yu Z, Eich C and Cruz LJ (2020) Recent Advances in Rare-Earth-Doped Nanoparticles for NIR-II Imaging and Cancer Theranostics. Front. Chem. 8:496. doi: 10.3389/fchem.2020.00496

INTRODUCTION

Cancer is one of the world's most lethal diseases, and there are no particularly effective treatments to date. Cancer patients must endure chemotherapy and radiotherapy, followed by long-term medications, which are a great burden on their body and mind. For people not to be afflicted by cancer, it is necessary to diagnose the disease in an early stage and personalize treatments based on each patient's individual variability and medical profile (Rubin et al., 2014). Molecular imaging modalities can be useful for the comprehensive evaluation of essential biomolecules and can facilitate the non-invasive visualization of cell function and biochemical processes in biological systems (Kuimova et al., 2009; Weissleder et al., 2016; Yang et al., 2017a). They are well-recognized as powerful techniques that provide more comprehensive anatomical, physiological and functional information in early cancer detection, drug delivery, as well as monitoring treatment effectiveness (Quon and Gambhir, 2005; Weissleder and Pittet, 2008; Willmann et al., 2008). Currently, varieties of molecular imaging techniques are widely used in the medical field, including magnetic resonance imaging (MRI), X-ray computed tomography (CT), positron emission tomography (PET), single-photon emission tomography (SPECT), and optical fluorescent light imaging (FLI) (**Figure 1**). However, these methods have some disadvantages. For example, CT and MRI often require high doses of contrast agents; PET and SPECT require radioactive tracers that can put both patients and operators in danger (O'Leary et al., 1999; Mariani et al., 2001, 2002; Tsien, 2003). Also, they need to be optimized to obtain more accurate information due to their long scanning time and low sensitivity/spatial resolution (Toussaint et al., 1996; Paulus et al., 2000).

In recent years, optical imaging has attracted much attention in various fields, predominantly preclinical research because it provides excellent real-time visualization, high sensitivity and spatial resolution, especially in early detection and diagnosis of cancer. Generally, most of the conventional imaging agents operate in the short-wavelength region (e.g., the ultraviolet (UV) and visible

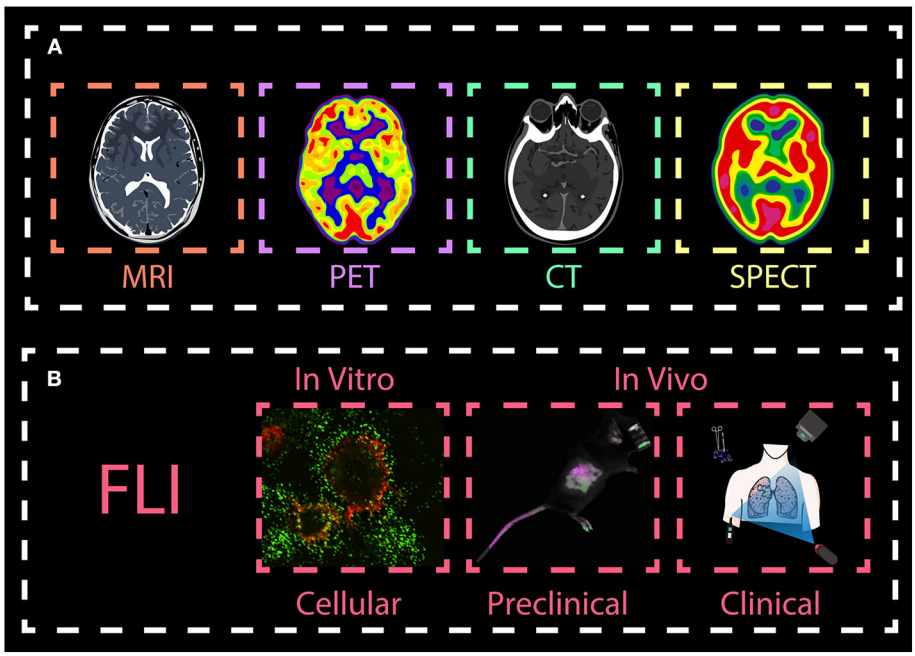

FIGURE 1 | Overview molecular imaging techniques. The main imaging methods are **(A)** magnetic resonance imaging (MRI), X-ray computed tomography (CT), positron emission tomography (PET), single-photon emission tomography (SPECT), and **(B)** optical fluorescent light imaging (FLI). While MRI, PET, CT, and SPECT are widely used in the clinics, FLI techniques are mainly used in biomedical preclinical research *in vitro* and *in vivo*, with the exception of fluorescence image-guided surgery, a medical imaging technique used to detect fluorescently labeled structures during surgery. This review, we will focus on introducing FLI from both *in vitro* and *in vivo* imaging.

regions). In these regions, light signals are easily absorbed and scattered by certain biological tissues (such as muscle, skin and body fluids). This leads to high autofluorescence, low signal-to-background ratio and low tissue penetration (Yang et al., 2017b,c). Besides, high-energy light can lead to photo-toxicity damage in biological tissues. To circumvent these problems, optical imaging in the near-infrared (NIR) region, which is located in the so-called "biological window," has gained much attention (**Figure 2**). Imaging agents in the first near-infrared window (NIR-I, 700–900 nm) are gradually being known by researchers, and can provide deep and sensitive bioimaging. However, their limited tissue penetration depth (less to 1 cm) and large photon scattering losses in biological samples still restrict their use further in biomedical diagnosis and therapy. To address these challenges, novel materials that enable fluorescent imaging in the NIR-II window (10,00–1,700 nm) for biomedical applications have been developed. They show better resolution because they have deeper penetration (∼1.8 cm) and lower autofluorescence. Therefore, there is need to synthesize the novel NIR-II agents with high efficiency and resolution for biological imaging application (Fan and Zhang, 2019).

So far, many types of fluorescent agents with emission in the NIR-II region have been extensively applied for effective bio-sensing and real-time *in vitro* and *in vivo* imaging of living species (**Figure 2**). They include single-walled carbon nanotubes (SWNTs) (Gong et al., 2013; Liang et al., 2014), organic dyes (Lei et al., 2019; Wang et al., 2019a), conjugated polymers (Hong et al., 2014), quantum dots (QDs) (Li C. et al., 2014), and rare-earth-doped nanoparticles (RENPs) (Fan et al., 2019; Wang et al., 2019b). However, most of them have some disadvantages, such as the broad emission bandwidths of SWNTs, short accumulation time of organic dyes, high toxicity, low quantum yield and low solubility of QDs. These disadvantages will vastly inhibit their further applications in NIR-II imaging. RENPs are good candidates for NIR-II optical imaging, because they show minimal photo-bleaching, superior luminescent lifetimes, excellent tunable emission wavelengths and low biotoxicity (Rocha et al., 2014; Wang et al., 2014; Dong et al., 2015; Hemmer et al., 2016; Jiang et al., 2016; Kamimura et al., 2017).

Rare earth elements constitute a class of lanthanide ions found in the 6th row of the periodic table (La, Ce, Pr, Nd, Pm, Sm, Eu, Gd, Tb, Dy, Ho, Er, Tm, Yb, Lu), as well as two other elements closely related to the lanthanides—yttrium (Y) and scandium (Sc). Due to the incompletely filled 4f shell and the spin-orbital coupling of 4f free ions, they possess extremely complex optical properties. One of the most interesting features of these ions is their photoluminescence. The luminescence of the trivalent lanthanide ions arises from f-f transitions of the 4f shell and f-d transitions in the 4f-5d shell. The f-f transitions also provide the lanthanide elements with rich energy level structures in the UV, VIS and NIR ranges. As they can be tuned from the UV to the NIR region, most nanomaterials made of rare-earth elements can be classified into two major categories: Upconversion nanoparticles (UCNPs) and downconversion

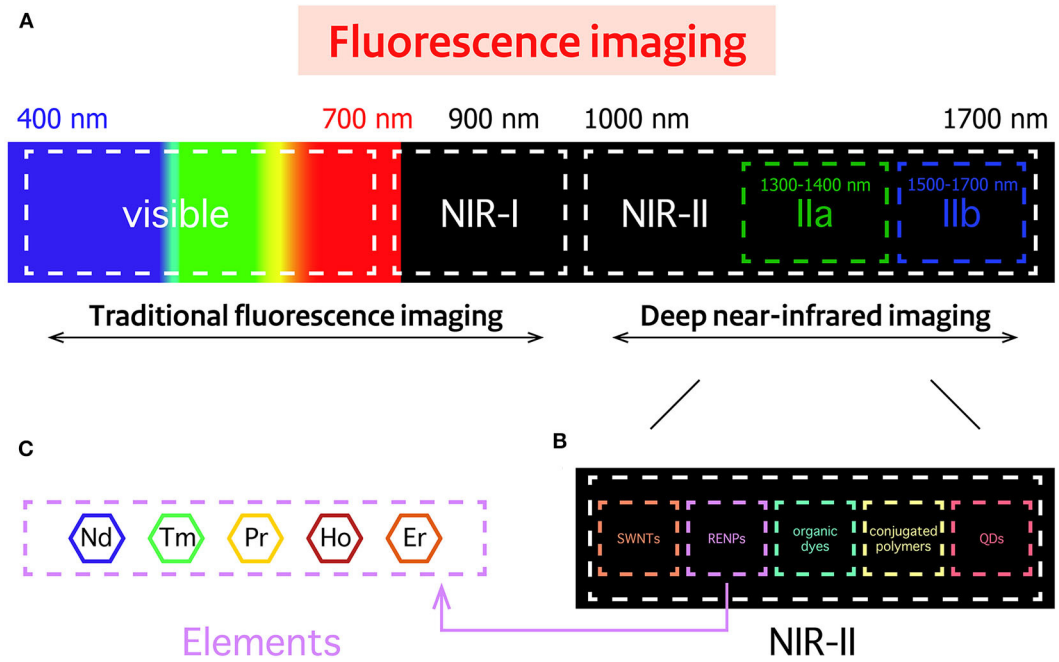

FIGURE 2 | Spectral overview fluorescence imaging techniques. **(A)** Spectral ranges of traditional fluorescence imaging techniques, including the near-infrared (NIR)-I region, and the deep NIR-II region. **(B)** Imaging probes commonly used in the NIR-II region: Single walled nanotubes (SWNTs), rare-earth-doped nanoparticles (RENPs), organic dyes, conjugated polymers, and quantum dots (QDs). **(C)** Neodymium (Nd)-, thulium (Tm)-, praseodymium (Pr)-, holmium (Ho)-, and erbium (Er)-containing RENPs have attracted wide attention.

nanoparticles (DCNPs). DCNPs can downconvert a high energy photon into two or more low-energy photons. In contrast, UCNPs can convert long-wavelength light (low energy) to short wavelength (high energy). Unfortunately, due to the unique anti-Stokes optical properties of UCNPs, most of the NIR-II nanoprobes belong to the category of DCNPs. Until now, a large number of studies have shown that by using suitable sensitizers, UCNPs can obtain longer excitation wavelength for NIR-II imaging (Zhang et al., 2020). For example, emissions in the NIR-II region of Ho^{3+} and Nd^{3+} could be obtained from Er^{3+} sensitized UCNPs (Liu et al., 2018).

Based on the excellent characteristics of rare-earth ions, such as their low photobleaching, various absorption and emission wavelengths, and low energy losses, NIR light-mediated RENPs have been widely used in *in vitro* and *in vivo* imaging of biomolecules. Commonly, this kind of downconverting nanoparticle combines rare-earth ions and an inorganic crystalline host lattice (e.g., $NaYF_4$, $NaLuF_4$, and CaF_2). The host can also provide an environment for energy transfer from a sensitizer to a rare-earth dopant resulting in NIR-II fluorescence.

This review mainly introduces the recent advances in RENPs fluorescent imaging in the NIR-II region. In particular, we focus on the modification of these nanoparticles by lipids or dyes, and their use in cancer diagnosis and therapy. Then, the challenges and prospects of RENPs are discussed.

MAIN KINDS OF RENPs

Based on the energy level of the rare earth elements, most RENPs possess upconversion and downconversion properties. Up to date, thanks to the effort of many researchers, five of them are reported and extensively explored as activators emitting in NIR-II regions, having excellent downconversion emission (1,060/1,300 nm for Nd^{3+}, 1,470 nm for Tm^{3+}, 1,310 nm for Pr^{3+}, 1,185 nm for Ho^{3+}, and 1,525 nm for Er^{3+}) (Liu et al., 2016) (**Figure 2**).

Nd-Doped Nanoparticles

According to recent studies, Nd^{3+} has gained attention for bioimaging applications due to its special illumination at 808 nm and deep tissue penetration (Wang et al., 2013). With strong absorption at 730 nm, 808 nm or 860 nm, Nd^{3+} can transfer photons with the generation of electrons from the $^4I_{9/2}$ ground state to the $^4F_{7/2}$, $^4F_{5/2}$, or $^4F_{3/2}$; then the electrons move back to the $^4F_{3/2}$ state, which can reduce the overheating effect of tissues usually caused by 980 nm light. As a result of the two transitions, the emission corresponds to 1,060 nm ($^4F_{3/2} \rightarrow {}^4I_{11/2}$) and 1,330 nm ($^4F_{3/2} \rightarrow {}^4I_{13/2}$) in the NIR-II region. Thus, it provides a good way to avoid autofluorescence of tissue.

Earlier attempts of using Nd-doped nanomaterials as NIR-II biomedical imaging agents have been described (Villa et al., 2015; Yu et al., 2018). In 2002, Stouwdam et al. first realized that Nd^{3+} doped LaF_3 nanoparticles can be utilized as a

polymer-based optical component under 514 nm laser excitation (Stouwdam and van Veggel, 2002). Then, Wang et al. developed the synthesized method of LaF_3: Nd^{3+}. It was carried out in aqueous solution at low temperature, and showed great NIR-II emission under 802 nm laser excitation (Wang et al., 2006). In 2014, LaF_3: Nd^{3+} nanoparticles were used to obtain both *in vitro* and *in vivo* images in cancer cells and mice by Rocha et al. The results showed that LaF_3: Nd^{3+} nanoparticles are a very promising fluorescent nanoprobe for bioimaging in the second NIR window (Rocha et al., 2014). One year later, Villa and his group did an exciting work on high-contrast *in vivo* imaging in the second biological window (Villa et al., 2015). This work showed how to produce autofluorescence free, high contrast *in vivo* fluorescence imaging with 1340 nm emission band of SrF_2: Nd^{3+} nanoparticles. They found that autofluorescence of animal diet can extend up to about 1,100 nm, which demonstrated that food-related infrared autofluorescence has an impact on the study of reliable biodistribution. In the past 3 years, some new host matrices have been reported, such as $LiYF_4$ (Jiang et al., 2016), $GdPO_4$ (Yang et al., 2018), $CaTiO_3$ (Li et al., 2015), and $NaDyF_4$ (Liu et al., 2017). As we know, higher Nd^{3+} doping will result in severe quenching of concentration, so to induce great fluorescence signals, the concentration of Nd^{3+} should be controlled between 1 and 5%. Thanks to intensive research, most of these new Nd^{3+} doped systems are nowadays not only used *in vivo* NIR-II imaging but also in X-ray CT bioimaging or MRI. Owing to the large X-ray absorption coefficient of Gd^{3+}, Dy^{3+}, dual-mode molecular imaging has become a new trend in bioimaging, such as NIR-II imaging/CT, NIR-II imaging/MRI, NIR-II imaging/PET.

Despite the efforts made so far as seen above, low optical effects are still a major drawback. However, sensitizers and core-shell structures that can be used to increase the signal-to-noise ratio are gradually becoming more known in the field of NIR-II bioimaging, disease detection and treatment. For example, $NaGdF_4$: Nd^{3+}, Yb^{3+}, Tm^{3+} is a novel nanomaterial which uses Gd^{3+} as bridge ions and finally traps energy by the initial activator ions (Nd^{3+}) (Zhang et al., 2015). Other previous studies also showed that co-doping with Y^{3+} effectively reduced the aggregation of Nd^{3+} in CaF_2, resulting in a greater luminescence enhancement of Nd^{3+} (Yu et al., 2018). Chen et al. synthesized high quantum yield core/shell $NaGdF_4$: 3%Nd^{3+}@$NaGdF_4$ nanoparticles with an average size of 15 nm. An *in vitro* and *in vivo* NIR-II bioimaging was obtained by loading HeLa cells with $NaGdF_4$: 3%Nd^{3+}@$NaGdF_4$ nanoparticles and transferring $NaGdF_4$: 3%Nd^{3+}@$NaGdF_4$ nanoparticles in a nude mouse model (Chen et al., 2012). CaF_2 was also used as the shell material to make NaYF4: Yb, Nd@CaF_2 core/shell nanoparticles, which resulted in high contrast multiplexed *in vivo* imaging in the NIR-II region (Ortgies et al., 2018). In 2018, inspired by Chen's work, Wang et al. fabricated $NaGdF_4$: 5%Nd^{3+}@$NaGdF_4$ by the successive layer-by-layer (SILAR) method. To obtain DCNPs-L1-FSHβ nanoprobes via an EDC/NHS reaction, image-guided surgery for metastatic ovarian cancer could be improved. Utilizing these novel nanoprobes, metastases with $\leq$1 mm can be completely resected under the guidance of NIR-II imaging (Wang P. et al., 2018). A recent report showed that the ultra-small $NaGdF_4$: 5 %Nd@$NaGdF_4$ (4.38 $\pm$ 0.57 nm) nanoparticles can be applied in the precise inflammation bioimaging by ROS (reactive oxygen species)-responsive cross-linking after modification with GSH (Glu-Cys-Gly) (Wang et al., 2014; Zhao et al., 2019). An interesting work based on supramolecular self-assembly strategy is developed for NIR-II imaging assembly and disassembly through $NaGdF_4$: 10%Y, 25%Yb, 0.5%Tm@$NaGdF_4$ UCNP@azobenzene and $NaGdF_4$: 5%Nd@$NaGdF_4$ DCNP@β-cyclodextrin. The new strategy allows flexible assembly and disassembly of nanoparticles by controlling different NIR-lasers, which can reduce the background of biological imaging and long-term cytotoxicity, while providing technical support for further accurate image-guided tumor surgery (Zhao M. et al., 2018). As only a few NIR-II fluorophores can be used directly for bone imaging without linking to targeted ligands, He et al. demonstrated DSPE-mPEG encapsulated with β-phase $NaYF_4$: 7%Nd@$NaYF_4$ can be used for bone and vascular imaging, even real-time image-guided lymph node mapping and resection (He et al., 2019) (**Table 1**).

Er-Doped Nanoparticles

With the rapid development of the RENPs, Er^{3+} doped nanoprobes are mainly synthesized as upconversion nanomaterials and applied in the VIS and NIR-I regions. In 2011, Y_2O_3: Yb, Er nanoparticles modified by PEG-b-PVBP and PEG-PO_3H_2 showed NIR emission at 1,550 nm in organs of live mice (Kamimura et al., 2011). Then people considered Er^{3+} as a better dopant since it can exhibit strong downconversion luminescence in NIR-IIb region. Nanoprobes employed in the NIR-IIb region are better for bioimaging, owing to their deeper tissue penetration, higher spatial and temporal resolution and lower autofluorescence than those in the NIR-IIa region; but rare-earth based nanoprobes with high spatial and temporal resolution imaged in NIR-IIb region are still very scarce. There is no doubt that the special characteristic of Er^{3+} solves the main problem that has plagued researchers for a long time. Two years later, Naczynski et al. first used $NaYF_4$: Yb, Ln (Ln: Er, Ho, Tm or Pr) for *in vivo* imaging of tumors. They demonstrated that Er^{3+} doped nanoprobes were the brightest one. Especially, by encapsulating RENPs with albumin, they provided a good method to improve tumor accumulation (Naczynski et al., 2013). Then, Er^{3+} codoped Yb^{3+} nanoprobes have attracted increasing attention due to their special application potential. Polyacrylic acid (PAA) modified $NaYF_4$: Gd/Yb/Er nanoprobes have been synthesized and have opened the opportunities for NIR-IIb *in vivo* imaging, non-invasive brain vessel imaging and tiny tumor detection guided by optical imaging (Xue et al., 2018). In 2016, Dang et al. used the well-established technology, Layer-by-Layer (LbL) to design a NIR-II based theranostic platform by $NaYF_4$: Yb, Er-PLA/DXS/PLA/HA nanoprobes, which can accumulate in diseased sites and demonstrate diagnostic capabilities within an ovarian tumor mouse model. This study demonstrated that these nanoprobes can serve as a promising theranostic platform to monitor the progression and treatment of serous ovarian cancer (Dang et al., 2016). Indeed, core-shell is well known for its unique ability to enhance the Er^{3+} emission at NIR-II region.

TABLE 1 | Typical of Nd-RENPs NIR-II nano-composites.

NIR-II compositions	Excitation wavelength (nm)	Emission wavelength (nm)	Ligands	Applications
SrF_2: Nd^{3+}	808	900–1,500	–	*In vitro* and *in vivo* NIR-II imaging
CaF_2: Y^{3+}, Nd^{3+}	808	1,058	–	*In vivo* NIR-II imaging
LaF_3: Nd^{3+}	808	910, 1,050, 1,330	–	*In vitro* and *in vivo* NIR-II imaging
$LiYF_4$: 5%Nd^{3+}	808	900, 1,050, 1,330	EDTMP	Bio-imaging and biodetection
$GdPO_4$: Nd^{3+}	808	1,050, 1,330	DOX	Dual-modal *in vivo* NIR-II/X-ray bioimaging and pH-responsive drug delivery
$NaDyF_4$: 10%Nd	808	1,050, 1,330	Gallic acid-Fe(III)	NIR-II imaging, MRI imaging, PTT
$NaGdF_4$: Nd^{3+}, Yb^{3+}, Tm^{3+}	800	980, 1,060	–	NIR-II imaging, MRI imaging
$NaGdF_4$: Nd^{3+}@$NaGdF_4$	740/900	1,050, 1,300	–	*In vitro* and *in vivo* NIR-II imaging
$NaYF_4$: Yb,Nd@CaF_2	808	980, 1,350	Poly(acrylic acid)	Lifetime-gated *in vivo* multiplexed imaging
$NaGdF_4$: 5%Nd@$NaGdF_4$	808	1060	DSPE-PEG-NH2-DNA-FSHβ	Image-guided surgery for metastatic ovarian cancer
$NaGdF_4$: 5%Nd@$NaGdF_4$	808	–	GSH (Glu–Cys–Gly)	*In vivo* inflammation Imaging
β- $NaYF_4$: 7%Nd@ NaYF4	808	1064, 1345	DSPE-mPEG	NIR-II imaging of bone, vascular tissue and thrombi

This special structure does not only delay the degradation of dopant but also decreases the quenching effects and strengthens fluorescence. Simple $NaYF_4$: Yb/Er@$NaYF_4$ nanoprobes have been prepared to realize real-time surveillance of metastatic lesions (Kantamneni et al., 2017). Deng et al. proposed Sc-based probes (KSc_2F_7: Yb^{3+}/Er^{3+}), which are significantly different from the traditional $NaYF_4$ host. After modification with PAA, they showed a ∼1.70-fold stronger fluorescence than the PAA-$NaYF_4$ nanocrystals under 980 nm excitation. On this basis, they performed the first case of through-skull fluorescence imaging of brain vessels with KSc_2F_7: Yb^{3+}/Er^{3+} probes (Deng et al., 2018). Normally, Yb^{3+} can transfer energy to Er $^4I_{11/2}$ level to release non-radiative photons to the $^4I_{13/2}$ level, and then radiate to the $^4I_{15/2}$ level to produce the 1,550 nm downconversion emission. During this process, upconversion and quenching effects will decrease the intensity of Er^{3+} downconversion emission. As an alternative, Ce^{3+} is developed as a doping element in Er-doped nanoparticles to improve the NIR-II downconversion emission by efficiently accelerating non-radiative relaxation of Er $^4I_{11/2} \rightarrow {}^4I_{13/2}$. $NaYbF_4$: 2%Er, 2%Ce@$NaYF_4$ nanoparticles have been made to prove Ce^{3+} can highly suppress the upconversion with the downconversion pathway boosted by about 9-fold. This can lead to fast NIR-II cerebral-vasculatures imaging by modified PMF-PEG (Zhong et al., 2017). The synthesis of $NaCeF_4$: Er/Yb@$NaCeF_4$ has further verified the efficient energy transfer of Yb^{3+}-Er^{3+}-Ce^{3+}. Surface modification with DSPE-PEG2000-COOH proved to be a useful method to detect uric acid and can be a key approach in a physiological survey and clinical diagnosis (Lei et al., 2018). Interesting research has been done to design and implant QR codes into a mouse by incorporating $NaYF_4$: Tm^{3+}/Er^{3+}@$NaYF_4$ into polydimethylsiloxane (PDMS) matrices. The QR code consists of black squares arranged in a square grid on a white background according to certain rules, and the imaging device can read the data from the horizontal and vertical components of the image. It provides a possibility for NIR-II *in vivo* information storage and decoding (Zhang et al., 2019). A core/multishell structure ($NaGdF_4$@$NaGdF_4$: Yb/Er@$NaYF_4$: Yb@$NaNdF_4$: Yb) has also been used for breast cancer diagnostics *in vivo* (Fan et al., 2018). Recent progress has focused on the diversification of Er-doped rare-earth nanoparticles. $NaYF_4$: Er nanoparticles conjugated with the indocyanine green dye (ICG) have been applied to bioimaging in the NIR-II window because of their high spatial resolution. Due to high absorption cross-section of ICG, excitation efficiency of Er^{3+} is increased by the energy transfer mechanism and has proved the potential of ICG-$NaYF_4$: Er nanoconjugates for multimodal theranostics (Wang D. et al., 2018) (**Figure 3**). Since NIR-II imaging-guided photothermal therapy (PTT) is rarely explored, Liu et al. have successfully developed a core-shell structured $NaLuF_4$: Gd/Yb/Er NRs@PDA as a nanoplatform that can simultaneously be used to diagnose and treat tumors. It can not only be used to realize NIR-II imaging but also to enable image-guided PTT (Li X. et al., 2019).

SYNTHESIS AND MODIFICATION

At present, RENPs are synthesized by a solvothermal method, which is technically mature. Solvothermal synthesis is a solution chemistry method that crystallizes nanomaterials of different sizes and morphologies directly from solution under a certain temperature and pressure. To synthesize RENPs with uniform size and morphology, good dispensability and high luminous efficiency, the size and morphology have to be controlled by adjusting the ratio of raw materials, temperature and solvents (Mai et al., 2007; Zhang et al., 2007; Tan et al., 2009, 2013; Wang et al., 2010; Yuan et al., 2013). On the other hand, because this process cannot precisely control the distribution

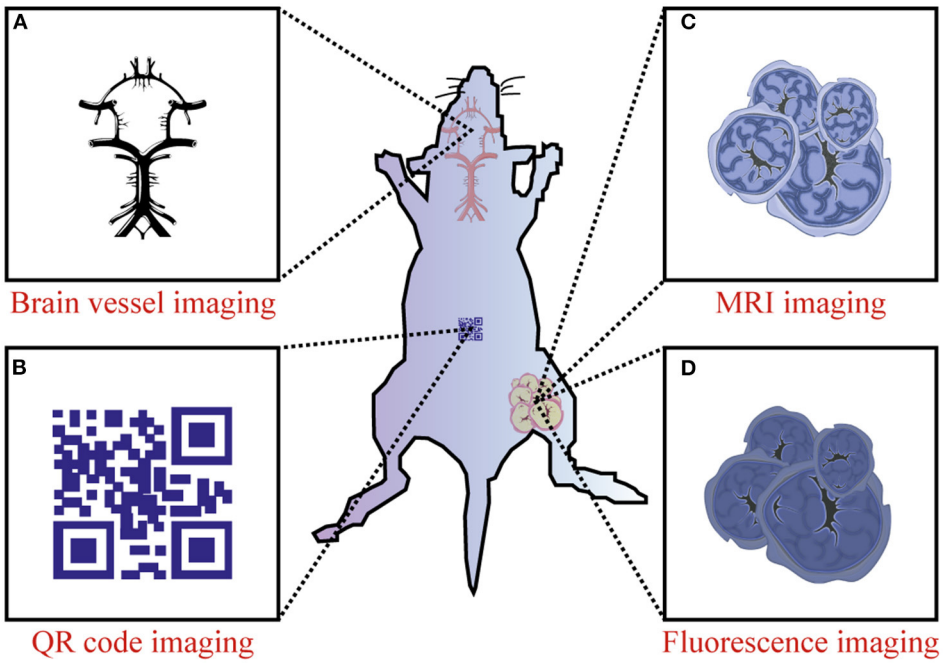

FIGURE 3 | Preclinical application of Er-RENPs in the NIR-II region. **(A)** NIR-II brain vessel imaging, **(B)** NIR-II QR code imaging and **(C,D)** dual mode MRI imaging/ NIR-II fluorescence imaging.

of dopants, the local relative enrichment of the dopants usually occurs, resulting in the reduction of luminescent efficiency. In order to avoid the deficiency, one pot successive layer-by-layer (SLBL) strategy is used to synthesize homogeneous doping core (HOC) nanoparticles by growing uniform shells (Li X. et al., 2014, 2019). However, RENPs prepared with oleic acid as reagent are hardly soluble in water and difficult to attach to biomolecules. This limits their application in cell labeling and fluorescent imaging. It is therefore necessary to convert a hydrophobic group into a hydrophilic group by surface modification (for example, -COOH, $-NH_2$, or -SH). Alternatively, Dong et al. have reported the oleate ligands attached to the UCNPs surface can be replaced by nitrosonium tetrafluoroborate ($NOBF_4$) (Dong et al., 2011). Currently, the main surface modification methods used are ligand oxidation, ligand exchange and layer-by-layer self-assembly (Wang and Liu, 2009; Li and Lin, 2010). The nanoparticle size does not increase after the water-soluble modification using the ligand exchange method, and it is not easy to control the exchange efficiency and effect of water solubility. After using ligand oxidation for modification, due to the shortening of the ligand carbon chain, polar solvent water cannot be effectively suppressed not to quench the fluorescence, and also the fluorescence intensity is much weaker. This method is only suitable for the oxidation of ligands containing carbon-carbon double bonds (C=C). Therefore, it is still a hot Research Topic to select effective water-soluble modification methods to obtain RENPs with small particle size, good water solubility and high fluorescence intensity. The following is a brief summary to the currently used surface modification methods (**Figure 4**).

Ligand Oxidation

The ligand oxidation method requires a strong oxidizing agent (Lemieux-von Rudloff reagent, etc.) to oxidize the carbon-carbon double bond to a carboxyl group, which is on the surface-coated oleic acid ligand. This reaction can obtain hydrophilic, carboxylic acid-functional RENPs. Thus, the RENPs not only have good water solubility, but also can be directly coupled with diverse biomolecules.

Ligand Exchange

The ligand exchange method is used to replace an organic ligand having weak coordination and hydrophobicity with a strong hydrophilic organic ligand on the surface of the material. This process makes the RENPs hydrophilic and water-soluble.

Layer-by-Layer Self-Assembly Method

The principle of the layer-by-layer self-assembly method (Wang et al., 2002) is to first wrap a layer of polymer compound with a certain charge on the surface of hydrophobic RENPs. When it is added to a solution of an opposite charged polymer compound, another opposite charged polymer compound can be attracted to the first layer. In this way, the layers are adsorbed, and the upper fluorescent group can be converted, which is possible by alternating self-assembled layers into a polymer layer on the surface of the RENPs. The thickness of the polymer layer can be regulated by changing the number of self-assembled layers so that the RENPs can be stably dispersed in water and have good biocompatibility.

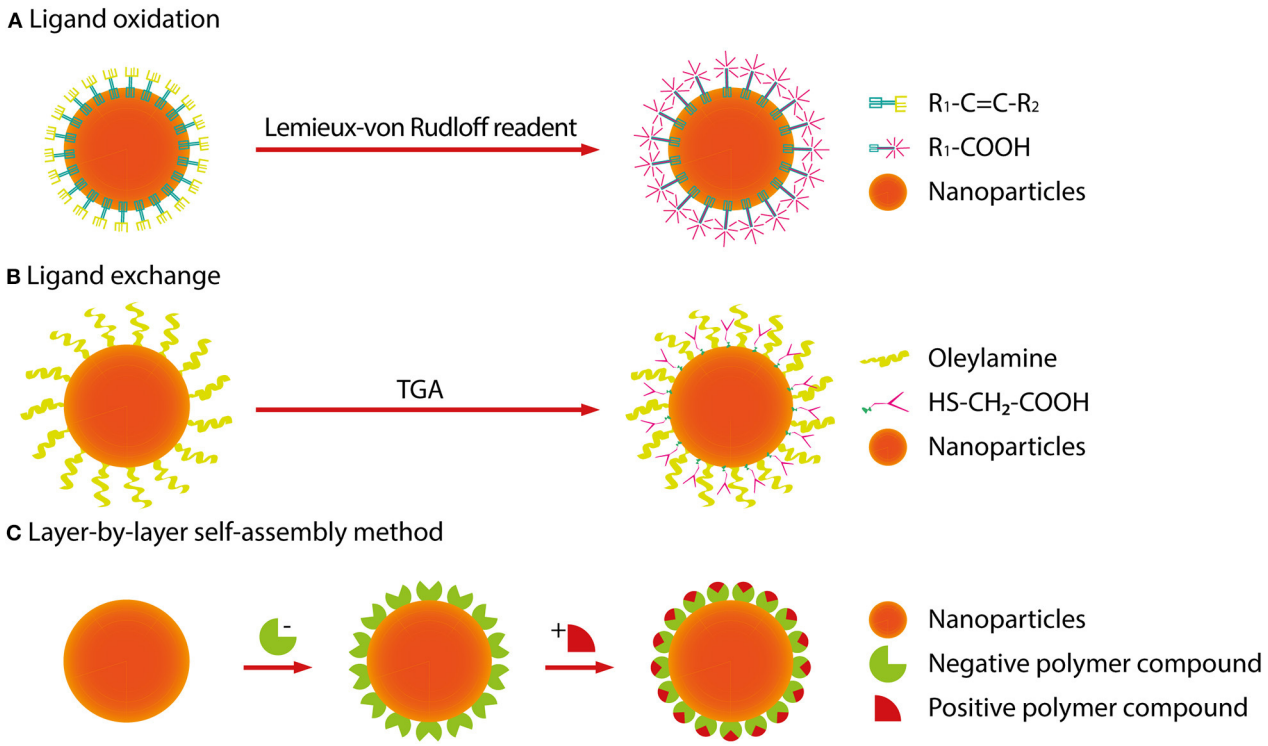

FIGURE 4 | Surface modification methods of RENPs. **(A)** The ligand oxidation method requires a strong oxidizing agent (Lemieux-von Rudloff reagent, etc.) to oxidize the carbon-carbon double bond to a carboxyl group. **(B)** The ligand exchange method is used to replace an organic ligand having weak coordination and hydrophobicity with a strong hydrophilic organic ligand. **(C)** The layer-by-layer self-assembly method relies mainly on the attractive force between oppositely charged molecules, alternately deposits dense monolayers of charged molecules onto oppositely charged surfaces.

CANCER THERANOSTICS WITH NIR-II RENPs

Currently, clinically approved indocyanine green (ICG) and methylene blue (MB) have been used as contrast agents to depict tumor margins in preclinical cancer models and human patients (Winer et al., 2010; Vahrmeijer et al., 2013; Wang et al., 2015). However, these rapidly excreted probes possess short tumor retention times and affect the process of cancer treatment. Due to the renal filtration threshold of ~40 kD, most fluorescent probes accumulate largely in the organs of reticuloendothelial system, such as the liver and spleen, leading to long-term safety concerns. Therefore, NIR-II RENPs probes with long tumor retention times, high signal-to-background ratio and deep tissue penetration have aroused great interest in investigating their applications for cancer theranostics. To reduce the retention time of nanoparticles in the reticuloendothelial system, excretable NIR-II nanoparticles, RENPs@Lips, have been developed for medical imaging and surgical navigation. Under the guidance of NIR-II imaging, RENPs@Lips showed excellent performance in intraoperative identification of orthotopic tumor vessels and embolization surgery, and could be used in sentinel lymph node biopsies in tumor-bearing mice (Li D. et al., 2019). CXCR-4-targeted functional nanoprobes (fReANC) have been demonstrated to detect up to 10.5 mm of deep-seeded subtissue microlesions in lung metastatic models of breast cancer, providing a reliable platform for the detection of targeted subtissue cancerous lesions (Zevon et al., 2015). At the same time, Dang et al. compared several available LbL NIR-II probes, found that rare-earth-based down-conversion nanoparticles can define vascular and skeletal structures, and were evaluated as diagnostic probes for high-grade serous ovarian cancer with the highest resolution out of all tested probes (Dang et al., 2016). NIR-II RENPs, with the least interference from scattering and autofluorescence, seemed to represent a promising tool for photothermal therapy (PTT) and photodynamic therapy (PDT). He et al. have designed a unique $NaGdF_4$: Nd@$NaGdF_4$@$NaGdF_4$: Yb, Er@$NaGdF_4$: Yb@$NaNdF_4$: Yb (LDNPs-5) structure by attaching Au25 clusters and poly(ethylene glycol) (PEG) molecules on nanostructure. Under 808 nm light irradiation, the special LDNPs can efficiently kill tumor cells *in vitro* and *in vivo* due to a synergistic effect arising from the combination of PTT effect generated from Nd^{3+} with PDT (He et al., 2016). In addition, a three-layer core-shell-shell nanocomposite ($NaYF_4$: Nd^{3+}@$NaLuF_4$@PDA_{18}) showed an excellent PTT effect in ablation tumors (Dai et al., 2017). Recently, dual-mode SWIR imaging and MRI guided PTT was performed in a nude mouse model by using $NaErF_4$@$NaGdF_4$ (Er@Gd), which can effectively be used to ablate tumors and provide a new way for cancer theranostics (Ma et al., 2018).

$NaErF_4$@$NaYF_4$@$NaNdF_4$@Prussian blue (PB) encapsulated in a phospholipid PEG micelle (PEG-CSS@PB) served as an efficient theranostic agent for NIR-II-image guided PTT. In this study, tumors treated with PTT shrank ∼12-fold compared with untreated tumors (Wang et al., 2019c). To achieve accurate tumor localization and a high cancer therapeutic efficacy, Liu et al. developed an ultrasmall pH-responsive photothermal gallic acid-iron complex-modified $NaDyF_4$: Nd nanoprobe to enhance cancer theranostic by *in situ* aggregation (Liu et al., 2017). In addition, a theranostic nanoparticle based on RENPs has been developed for gene therapy. Polyethylenimine (PEI) coated β-$NaY_{0.78}F_4$:$Yb_{0.20}$,$Er_{0.02}$@$NaYF_4$ was designed to deliver genetic cargo in an *in vitro* cancer model and detected tumor lesions in a lung metastases model of breast cancer. This strategy will make it possible to develop a nanotheranostic platform based on NIR-II RENPs for gene therapy (Zhao Z. et al., 2018). In summary, NIR-II RENPs have great potential in cancer theranostics.

DISCUSSION

Overall, RENPs are promising candidates for NIR-II biomedical imaging due to their low toxicity, high photostability, deep tissue penetration, and tunable pharmacokinetic behavior. Despite these successful gains, challenges still remain in the bioimaging applications of NIR-II RENPs. One of them is the limitation of the emission center, which is the fluorescence core of the RENPs. As we know, five rare earth elements (Nd^{3+}, Tm^{3+}, Pr^{3+}, Ho^{3+}, Er^{3+}) can be the emission centers in NIR-II RENPs, which are excited by 808 nm or 980 nm lasers. However, the RENPs that have been developed are still mainly based on Nd^{3+} and Er^{3+} as the emission centers, which greatly limits the development and application of near-infrared probe types. Although other rare earth elements have also been presented, such efforts should be devoted to design novel NIR-II RENPs probes. For example, Liu et al. used Er^{3+} as a sensitizer and Ho^{3+} as an emitter to make a core-shell structured $NaErF_4$: Ho@$NaYF_4$ nanoparticle, which emitted at 1,180 nm (Liu et al., 2018). Besides that, the size of the RENPs has always been a concern in bioimaging. Smaller size nanoparticles can effectively enter biological tissues, even cells, but the luminescence intensity of nanomaterials will decrease. Although the commonly used core-shell structure can enhance the luminescence intensity, it will increase the size, making it difficult for the nanoparticles to gain entry into biological tissues and the digestion time will become longer. Designing suitable size nanoparticles is still an essential task to promote the NIR-II bioimaging applications of RENPs. All of these studies in the past decades have pointed out that RENPs will play an important role in drug delivery tracking and multispectral molecular imaging in the near future.

AUTHOR CONTRIBUTIONS

ZY, CE, and LC structured the review. ZY wrote the review. CE and LC revised the text. All authors contributed to the article and approved the submitted version.

FUNDING

ZY was supported by the CSC scholarship. CE was supported by the research program VENI with project number 916.181.54, which is (partly) financed by the Dutch Research Council (NWO). LC was supported by project grants from the European Commission H2020-MSCA-RISE (644373—PRISAR), H2020-MSCA-RISE (777682—CANCER), H2020-WIDESPREAD-05-2017-Twinning (807281—ACORN), H2020-WIDESPREAD-2018-03 (852985—SIMICA), H2020-SCA-RISE-2016 (734684—CHARMED), and MSCA-ITN-2015-ETN (675743-ISPIC), 861190 (PAVE), 857894 (CAST), 859908 (NOVA-MRI); 860173 (RISE-WELL); 872860 (PRISAR2) and research program VIDI (project number 723.012.110) of Dutch Research Council (NWO).

ACKNOWLEDGMENTS

We would like to thank E. L. Kaijzel for proof-reading of the manuscript.

REFERENCES

Chen, G., Ohulchanskyy, T. Y., Liu, S., Law, W. C., Wu, F., Swihart, M. T., et al. (2012). Core/shell $NaGdF_4$: Nd^{3+}/$NaGdF_4$ nanocrystals with efficient near-infrared to near-infrared downconversion photoluminescence for bioimaging applications. *ACS Nano*. 6, 2969–2977. doi: 10.1021/nn2042362

Dai, Y., Yang, D., Yu, D., Cao, C., Wang, Q., Xie, S., et al. (2017). Mussel-inspired polydopamine-coated lanthanide nanoparticles for NIR-II/CT dual imaging and photothermal therapy. *ACS Appl. Mater. Interf.* 9, 26674–26683. doi: 10.1021/acsami.7b06109

Dang, X., Gu, L., Qi, J., Correa, S., Zhang, G., Belcher, A. M., et al. (2016). Layer-by-layer assembled fluorescent probes in the second near-infrared window for systemic delivery and detection of ovarian cancer. *Proc. Natl. Acad. Sci U.S.A.* 113, 5179–5184. doi: 10.1073/pnas.1521175113

Deng, Z., Li, X., Xue, Z., Jiang, M., Li, Y., Zeng, S., et al. (2018). A high performance sc-based nanoprobe for through-skull fluorescence imaging of brain vessels beyond 1500 nm. *Nanoscale* 10, 9393–9400. doi: 10.1039/C8NR00305J

Dong, A., Ye, X., Chen, J., Kang, Y., Gordon, T., Kikkawa, J. M., et al. (2011). A generalized ligand-exchange strategy enabling sequential surface functionalization of colloidal nanocrystals. *J. Am. Chem. Soc.* 133, 998–1006. doi: 10.1021/ja108948z

Dong, H., Du, S. R., Zheng, X. Y., Lyu, G. M., Sun, L. D., Li, L. D., et al. (2015). Lanthanide Nanoparticles: from Design toward Bioimaging and Therapy. *Chem. Rev*. 115, 10725–10815. doi: 10.1021/acs.chemrev.5b00091

Fan, Y., Wang, P., Lu, Y., Wang, R., Zhou, L., Zheng, X., et al. (2018). Lifetime-engineered NIR-II nanoparticles unlock multiplexed *in vivo* imaging. *Nat. Nanotechnol*. 13, 941–946. doi: 10.1038/s41565-018-0221-0

Fan, Y., Wang, S., and Zhang, F. (2019). Optical multiplexed bioassays for improved biomedical diagnostics. *Angew. Chem. Int. Ed*. 58, 13208–13219. doi: 10.1002/anie.201901964

Fan, Y., and Zhang, F. (2019). A new generation of NIR-II probes: lanthanide-based nanocrystals for bioimaging and biosensing. *Adv. Opt. Mater*. 7:1801417.doi: 10.1002/adom.201801417

Gong, H., Peng, R., and Liu, Z. (2013). Carbon nanotubes for biomedical imaging: the recent advances. *Adv. Drug Deliv. Rev*. 65, 1951–1963. doi: 10.1016/j.addr.2013.10.002

He, F., Feng, L., Yang, P., Liu, B., Gai, S., Yang, G., et al. (2016). Enhanced up/down-conversion luminescence and heat: simultaneously achieving in one single

core-shell structure for multimodal imaging guided therapy. *Biomaterials*.105, 77–88. doi: 10.1016/j.biomaterials.2016.07.031

He, S., Chen, S., Li, D., Wu, Y., Zhang, X., Liu, J., et al. (2019). High affinity to skeleton rare earth doped nanoparticles for near-infrared II imaging. *Nano Lett*.19, 2985–2992. doi: 10.1021/acs.nanolett.9b00140

Hemmer, E., Benayas, A., Légar, É, F., and Vetrone, F. (2016). Exploiting the biological windows: current perspectives on fluorescent bioprobes emitting above 1000 nm. *Nanoscale Horiz*. 1, 168–184. doi: 10.1039/C5NH00073D

Hong, G., Zou, Y., Antaris, A. L., Diao, S., Wu, D., Cheng, K., et al. (2014). Ultrafast fluorescence imaging *in vivo* with conjugated polymer fluorophores in the second near-infrared window. *Nat. Commun*. 5, 1–9. doi: 10.1038/ncomms5206

Jiang, X., Cao, C., Feng, W., and Li, F. (2016). Nd^{3+}-doped $LiYF_4$ nanocrystals for bio-imaging in the second near-infrared window. *J. Mater. Chem. B* 4, 87–95. doi: 10.1039/C5TB02023A

Kamimura, M., Kanayama, N., Tokuzen, K., Soga, K., and Nagasaki, Y. (2011). Near-infrared (1550 nm) *in vivo* bioimaging based on rare-earth doped ceramic nanophosphors modified with PEG-b-poly (4-vinylbenzylphosphonate). *Nanoscale* 3, 3705–3713. doi: 10.1039/c1nr10466g

Kamimura, M., Matsumoto, T., Suyari, S., Umezawa, M., and Soga, K. K. (2017). Ratiometric near-infrared fluorescence nanothermometry in the OTN-NIR (NIR II/III) biological window based on rare-earth doped β-$NaYF_4$ nanoparticles, *J. Mater. Chem. B* 5, 1917–1925. doi: 10.1039/C7TB00070G

Kantamneni, H., Zevon, M., Donzanti, M. J., Zhao, X., Sheng, Y., Barkund, S. R., et al. (2017). Surveillance nanotechnology for multi-organ cancer metastases. *Na. Biomed Eng*. 1, 993–1003. doi: 10.1038/s41551-017-0167-9

Kuimova, M. K., Botchway, S. W., Parker, A. W., Balaz, M., Collins, H. A., Anderson, H. L., et al. (2009). Imaging intracellular viscosity of a single cell during photoinduced cell death. *Nat. Chem*. 1, 69–73. doi: 10.1038/nchem.120

Lei, X., Li, R., Tu, D., Shang, X., Liu, Y., You, W., et al. (2018). Intense near-infrared-II luminescence from $NaCeF_4$: Er/Yb nanoprobes for *in vitro* bioassay and *in vivo* bioimaging. *Chem. Sci*. 9, 4682–4688. doi: 10.1039/C8SC00927A

Lei, Z., Sun, C., Pei, P., Wang, S., Li, D., Zhang, X., et al. (2019). Stable, wavelength-tunable fluorescent dyes in the NIR-II region for *in vivo* high-contrast bioimaging and multiplexed biosensing. *Angew. Chem*. 131, 8250–8255. doi: 10.1002/ange.201904182

Li, C., and Lin, J. (2010). Rare earth fluoride nano-/microcrystals: synthesis, surface modification and application. *J. Mater. Chem*. 20, 6831–6847. doi: 10.1039/c0jm00031k

Li, C., Zhang, Y., Wang, M., Zhang, Y., Chen, G., Li, L., et al. (2014). *In vivo* real-time visualization of tissue blood flow and angiogenesis using Ag_2S quantum dots in the NIR-II window. *Biomaterials* 35, 393–400. doi: 10.1016/j.biomaterials.2013.10.010

Li, D., He, S., Wu, Y., Liu, J., Liu, Q., Chang, B., et al. (2019). Excretable lanthanide nanoparticle for biomedical imaging and surgical navigation in the second near-infrared window. *Adv. Sci*. 6:1902042.doi: 10.1002/advs.201902042

Li, X., Jiang, M., Zeng, S., and Liu, H. (2019). Polydopamine coated multifunctional lanthanide theranostic agent for vascular malformation and tumor vessel imaging beyond 1500 nm and imaging-guided photothermal therapy. *Theranostics*. 9:3866. doi: 10.7150/thno.31864

Li, X., Shen, D., Yang, J., Yao, C., Che, R., Zhang, F., et al. (2013). Successive layer-by-layer strategy for multi-shell epitaxial growth: shell thickness and doping position dependence in upconverting optical properties. *Chem. Mater*. 25, 106–112.doi: 10.1021/cm3033498

Li, X., Wang, R., Zhang, F., and Zhao, D. (2014). Engineering homogeneous doping in single nanoparticle to enhance upconversion efficiency. *Nano Lett*. 14, 3634–3639.doi: 10.1021/nl501366x

Li, X., Zhang, Q., Ahmad, Z., Huang, J., Ren, Z., Weng, W., et al. (2015). Near-infrared luminescent $CaTiO_3$: Nd^{3+} nanofibers with tunable and trackable drug release kinetics. *J. Mater. Chem. B* 3, 7449–7456. doi: 10.1039/C5TB01158B

Liang, C., Diao, S., Wang, C., Gong, H., Liu, T., Hong, G., et al. (2014). Tumor metastasis inhibition by imaging-guided photothermal therapy with single-walled carbon nanotubes. *Adv. Mater*. 26, 5646–5652. doi: 10.1002/adma.201401825

Liu, L., Wang, S., Zhao, B., Pei, P., Fan, Y., Li, X., et al. (2018). Er^{3+} sensitized 1530 nm to 1180 nm second near-infrared window upconversion nanocrystals for *in vivo* biosensing. *Angew. Chem. Int. Ed*. 57, 7518–7522. doi: 10.1002/anie.201802889

Liu, T. M., Conde, J., Lipinski, T., Bednarkiewicz, A., and Huang, C. C. (2016). Revisiting the classification of NIR-absorbing/emitting nanomaterials for *in vivo* bioapplications. *NPG Asia Mater*. 8, e295–e295. doi: 10.1038/am.2016.106

Liu, Y., Fan, H., Guo, Q., Jiang, A., Du, X., and Zhou, J. (2017). Ultra-small pH-responsive Nd-doped $NaDyF_4$ nanoagents for enhanced cancer theranostic by in situ aggregation. *Theranostics* 7:4217. doi: 10.7150/thno.21557

Ma, L., Liu, Y., Liu, L., Jiang, A., Mao, F., Liu, D., et al. (2018). Simultaneous activation of short-wave infrared (SWIR) light and paramagnetism by a functionalized shell for high penetration and spatial resolution theranostics. *Adv. Func. Mater*. 28:1705057. doi: 10.1002/adfm.201705057

Mai, H. X., Zhang, Y. W., Sun, L. D., and Yan, C. H. (2007). Size-and phase-controlled synthesis of monodisperse $NaYF_4$: yb, Er nanocrystals from a unique delayed nucleation pathway monitored with upconversion spectroscopy. *J. Phys. Chem. C* 111, 13730–13739. doi: 10.1021/jp073919e

Mariani, G., Gipponi, M., Moresco, L., Villa, G., Bartolomei, M., Mazzarol, G., et al. (2002). Radioguided sentinel lymph node biopsy in malignant cutaneous melanoma. *J. Nucl. Med*. 43, 811–827.

Mariani, G., Moresco, L., Viale, G., Villa, G., Bagnasco, M., Canavese, G., et al. (2001). Radioguided sentinel lymph node biopsy in breast cancer surgery. *J Nucl. Med*. 42, 1198–1215.

Naczynski, D. J., Tan, M. C., Zevon, M., Wall, B., Kohl, J., Kulesa, A., et al. (2013). Rare-earth-doped biological composites as *in vivo* shortwave infrared reporters. *Nat. Commun*. 4:2199. doi: 10.1038/ncomms3199

O'Leary, D. H., Polak, J. F., Kronmal, R. A., Manolio, T. A., Burke, G. L., Wolfson, S. K., et al. (1999). Carotid-artery intima and media thickness as a risk factor for myocardial infarction and stroke in older adults. *N. Engl. J. Med*. 340, 14–22. doi: 10.1056/NEJM199901073400103

Ortgies, D. H., Tan, M., Ximendes, E. C., Del Rosal, B., Hu, J., Xu, L., et al. (2018). Lifetime-encoded infrared-emitting nanoparticles for *in vivo* multiplexed imaging. *ACS Nano*.12, 4362–4368. doi: 10.1021/acsnano.7b09189

Paulus, M. J., Gleason, S. S., Kennel, S. J., Hunsicker, P. R., and Johnson, D. K. (2000). High resolution X-ray computed tomography: an emerging tool for small animal cancer research. *Neoplasia* 2, 62–70. doi: 10.1038/sj.neo.7900069

Quon, A., and Gambhir, S. S. (2005). FDG-PET and beyond: molecular breast cancer imaging. *J. Clin. Oncol*. 23, 1664–1673. doi: 10.1200/JCO.2005.11.024

Rocha, U., Kumar, K. U., Jacinto, C., Villa, I., Sanz-Rodríguez, F., de la Cruz, M. D. C. I., et al. (2014). Neodymium-doped LaF_3 nanoparticles for fluorescence bioimaging in the second biological window. *Small* 10, 1141–1154. doi: 10.1002/smll.201301716

Rubin, E. H., Allen, J. D., Nowak, J. A., and Bates, S. E. (2014).Developing precision medicine in a global world. *Clin. Cancer Res*. 20, 1419–1427. doi: 10.1158/1078-0432.CCR-14-0091

Stouwdam, J. W., and van Veggel, F. C. (2002). Near-infrared emission of redispersible Er^{3+}, Nd^{3+}, and Ho^{3+} doped LaF3 nanoparticles. *Nano Lett*. 2, 733–737. doi: 10.1021/nl025562q

Tan, M. C., Kumar, G. A., Riman, R. E., Brik, M. G., Brown, E., and Hommerich, U. (2009). Synthesis and optical properties of infrared-emitting YF_3: Nd nanoparticles. *J. Appl. Phys*. 106:063118. doi: 10.1063/1.3168442

Tan, M. C., Naczynski, D. J., Moghe, P. V., and Riman, R. E. E. (2013). Engineering the design of brightly-emitting luminescent nanostructured photonic composite systems. *Aust. J. Chem*. 66, 1008–1020.doi: 10.1071/CH13221

Toussaint, J. F., Lamuraglia, G. M., Southern, J. F., Fuster, V., and Kantor, H. L. (1996). Magnetic resonance images lipid, fibrous, calcified, hemorrhagic, and thrombotic components of human atherosclerosis *in vivo*. *Circulation* 94, 932–938. doi: 10.1161/01.CIR.94.5.932

Tsien, R. Y. (2003). Imagining imaging's future. *Nat. Rev. Mol. Cell Biol.* (Suppl.). 4:SS16-SS21. doi: 10.1038/nrm1196

Vahrmeijer, A. L., Hutteman, M., Van Der Vorst, J. R., Van De Velde, C. J., and Frangioni, J. V. (2013). Image-guided cancer surgery using near-infrared fluorescence. *Nat. Rev. Clin. Oncol*. 10, 507–518. doi: 10.1038/nrclinonc.2013.123

Villa, I., Vedda, A., Cantarelli, I. X., Pedroni, M., Piccinelli, F., Bettinelli, M., et al. (2015). 1.3 μm emitting SrF_2: Nd^{3+} nanoparticles for high contrast *in vivo* imaging in the second biological window. *Nano Res*. 8, 649–665. doi: 10.1007/s12274-014-0549-1

Wang, D., Rogach, A.L., and Caruso, F. (2002). Nanocrystal-labeled biofunctional colloids. *Nano Lett*. 2:857. doi: 10.1021/nl025624c

Wang, D., Wang, D., Kuzmin, A., Pliss, A., Shao, W., Xia, J., et al. (2018). ICG-sensitized $NaYF_4$: er nanostructure for theranostics. *Adv. Opt. Mater.* 6:1701142. doi: 10.1002/adom.201701142

Wang, F., and Liu, X. (2009). Recent advances in the chemistry of lanthanide-doped upconversion nanocrystals. *Chem. Soc. Rev.* 38, 976–989. doi: 10.1039/b809132n

Wang, F., Zhang, Y., Fan, X., and Wang, M. (2006). Facile synthesis of water-soluble LaF_3: Ln 3+ nanocrystals. *J. Mater. Chem.*16, 1031–1034. doi: 10.1039/b518262j

Wang, H., Agarwal, P., Zhao, S., Yu, J., Lu, X., and He, X. (2015). A biomimetic hybrid nanoplatform for encapsulation and precisely controlled delivery of theranostic agents. *Nat. Commun.* 6, 1–13.doi: 10.1038/ncomms10081

Wang, P., Fan, Y., Lu, L., Liu, L., Fan, L., Zhao, M., et al. (2018). NIR-II nanoprobes in-vivo assembly to improve image-guided surgery for metastatic ovarian cancer. *Nat. Commun.* 9:2898. doi: 10.1038/s41467-018-05113-8

Wang, Q., Tan, M. C., Zhuo, R., Kumar, G. A., and Riman, R. E. (2010). A solvothermal route to size-and phase-controlled highly luminescent $NaYF_4$: Yb, Er up-conversion nanocrystals. *J. Nanosci. Nanotechnol.* 10, 1685–1692. doi: 10.1166/jnn.2010.2120

Wang, R., Li, X., Zhou, L., and Zhang, F. (2014). Epitaxial seeded growth of rare-earth nanocrystals with efficient 800 nm near-infrared to 1525 nm short-wavelength infrared downconversion photoluminescence for *in vivo* bioimaging. *Angew. Chem. Int. Ed.* 53, 12086–12090. doi: 10.1002/anie.201407420

Wang, S., Fan, Y., Li, D., Sun, C., Lei, Z., Lu, L., et al. (2019a). Anti-quenching NIR-II molecular fluorophores for *in vivo* high-contrast imaging and pH sensing. *Nat. Commun.*10, 1–11. doi: 10.1038/s41467-019-09043-x

Wang, S., Liu, L., Fan, Y., El-Toni, A. M., Alhoshan, M. S., Li, D., et al. (2019b). *In vivo* high-resolution ratiometric fluorescence imaging of inflammation using NIR-II nanoprobes with 1550 nm emission. *Nano Lett.* 19, 2418–2427.doi: 10.1021/acs.nanolett.8b05148

Wang, X., Li, H., Li, F., Han, X., and Chen, G. (2019c). Prussian blue-coated lanthanide-doped core/shell/shell nanocrystals for NIR-II image-guided photothermal therapy. *Nanoscale* 11, 22079–22088. doi: 10.1039/C9NR07973D

Wang, Y. F., Liu, G. Y., Sun, L. D., Xiao, J. W., Zhou, J. C., and Yan, C. H. (2013). Nd^{3+}-sensitized upconversion nanophosphors: efficient *in vivo* bioimaging probes with minimized heating effect. *ACS Nano.* 7, 7200–7206. doi: 10.1021/nn402601d

Weissleder, R., and Pittet, M. J. (2008). Imaging in the era of molecular oncology. *Nature* 452, 580–589. doi: 10.1038/nature06917

Weissleder, R., Schwaiger, M. C., Gambhir, S. S., and Hricak, H. (2016). Imaging approaches to optimize molecular therapies. *Sci. Transl. Med.* 8:355ps16. doi: 10.1126/scitranslmed.aaf3936

Willmann, J. K., Van Bruggen, N., Dinkelborg, L. M., and Gambhir, S. S. (2008). Molecular imaging in drug development. *Nat. Rev. Drug Discov.* 7, 591–607. doi: 10.1038/nrd2290

Winer, J. H., Choi, H. S., Gibbs-Strauss, S. L., Ashitate, Y., Colson, Y. L., and Frangioni, J. V. (2010). Intraoperative localization of insulinoma and normal pancreas using invisible near-infrared fluorescent light. *Ann. Surg. Oncol.* 17, 1094–1100. doi: 10.1245/s10434-009-0868-8

Xue, Z., Zeng, S., and Hao, J. (2018). Non-invasive through-skull brain vascular imaging and small tumor diagnosis based on NIR-II emissive lanthanide nanoprobes beyond 1500 nm. *Biomaterials* 171, 153–163. doi: 10.1016/j.biomaterials.2018.04.037

Yang, Q., Li, X., Xue, Z., Li, Y., Jiang, M., and Zeng, S. (2018). Short-wave near-infrared emissive $GdPO_4$: Nd $^{3+}$ theranostic probe for *in vivo* bioimaging beyond 1300 nm. *RSC Adv.* 8, 12832–12840. doi: 10.1039/C7RA12864A

Yang, Y., Aw, J., and Xing, B. (2017c).Nanostructures for NIR light-controlled therapies. *Nanoscale* 9, 3698–3718. doi: 10.1039/C6NR09177F

Yang, Y., Chao, Y., Liu, J., Dong, Z., He, W., Zhang, R., et al. et al. (2017a). Core-shell and co-doped nanoscale metal-organic particles (NMOPs) post-synthesis cation exchange for multimodal imaging and synergistic thermo-radiotherapy. *NPG Asia Mater.* 9:e344. doi: 10.1038/am.2016.205

Yang, Y., Mu, J., and Xing, B. (2017b).Photoactivated drug delivery and bioimaging. *Wiley Interdiscip. Rev. Nanomed. Nanobiotechnol.* 9:e1408. doi: 10.1002/wnan.1408

Yu, Z. F., Shi, J. P., Li, J. L., Li, P. H., and Zhang, H. W. (2018). Luminescence enhancement of CaF_2: Nd^{3+} nanoparticles in the second near-infrared window for *in vivo* imaging through Y^{3+} doping. *J. Mater. Chem. B* 6, 1238–1243. doi: 10.1039/C7TB03052E

Yuan, D., Tan, M. C., Riman, R. E., and Chow, G. M. (2013). Comprehensive study on the size effects of the optical properties of $NaYF_4$: Yb, Er nanocrystals. *J. Phys. Chem. C* 117, 13297–13304. doi: 10.1021/jp403061h

Zevon, M., Ganapathy, V., Kantamneni, H., Mingozzi, M., Kim, P., Adler, D., et al. (2015). CXCR-4 targeted, short wave infrared (SWIR) emitting nanoprobes for enhanced deep tissue imaging and micrometastatic cancer lesion detection. *Small* 11, 6347–6357. doi: 10.1002/smll.201502202

Zhang, F., Wan, Y., Yu, T., Zhang, F., Shi, Y., Xie, S., et al. (2007). Uniform nanostructured arrays of sodium rare-earth fluorides for highly efficient multicolor upconversion luminescence. *Angew. Chem., Int. Ed.* 46, 7976–7979. doi: 10.1002/anie.200702519

Zhang, H., Chen, Z. H., Liu, X., and Zhang, F. (2020). A mini-review on recent progress of new sensitizers for luminescence of lanthanide doped nanomaterials. *Nano Res.* 1-15. doi: 10.1007/s12274-020-2661-8

Zhang, H., Fan, Y., Pei, P., Sun, C., Lu, L., and Zhang, F. (2019). Tm^{3+}-Sensitized NIR-II Fluorescent Nanocrystals for *in vivo* Information Storage and Decoding. *Angew. Chem.*131, 10259–10263. doi: 10.1002/ange.201903536

Zhang, X., Zhao, Z., Zhang, X., Cordes, D. B., Weeks, B., Qiu, B., et al. (2015). Magnetic and optical properties of $NaGdF_4$: Nd^{3+}, Yb^{3+}, Tm^{3+} nanocrystals with upconversion/downconversion luminescence from visible to the near-infrared second window. *Nano Res.* 8, 636–648. doi: 10.1007/s12274-014-0548-2

Zhao, M., Li, B., Wang, P., Lu, L., Zhang, Z., Liu, L., et al. (2018). Supramolecularly engineered NIR-II and upconversion nanoparticles in vivo assembly and disassembly to improve bioimaging. *Adv. Mater.* 30:1804982. doi: 10.1002/adma.201804982

Zhao, M., Wang, R., Li, B., Fan, Y., Wu, Y., Zhu, X., et al. (2019). Precise *in vivo* inflammation imaging using in situ responsive cross-linking of glutathione-modified ultra-small NIR-II lanthanide nanoparticles. *Angew. Chem.* 131, 2072–2076. doi: 10.1002/ange.201812878

Zhao, Z., Kantamneni, H., He, S., Pelka, S., Venkataraman, A. S., Kwon, M., et al. (2018). Surface-modified shortwave-infrared-emitting nanophotonic reporters for gene-therapy applications. *ACS Biomater. Sci. Eng.* 4, 2350–2363. doi: 10.1021/acsbiomaterials.8b00378

Zhong, Y., Ma, Z., Zhu, S., Yue, J., Zhang, M., Antaris, A. L., et al. (2017). Boosting the down-shifting luminescence of rare-earth nanocrystals for biological imaging beyond 1500 nm. *Nat. Commun.* 8:737. doi: 10.1038/s41467-017-00917-6</A>

Conflict of Interest: The authors declare that the research was conducted in the absence of any commercial or financial relationships that could be construed as a potential conflict of interest.

frontiers in Chemistry

ORIGINAL RESEARCH
published: 26 June 2020
doi: 10.3389/fchem.2020.00488

pH and Redox Dual-Sensitive Covalent Organic Framework Nanocarriers to Resolve the Dilemma Between Extracellular Drug Loading and Intracellular Drug Release

Chaoyu Wang[1], *Huiming Liu*[2,3], *Shuai Liu*[2,3], *Zhijun Wang*[4] *and Jianhua Zhang*[2,3]*

[1] School of Chemistry and Chemical Engineering, Mudanjiang Normal University, Mudanjiang, China, [2] Key Laboratory of Systems Bioengineering of the Ministry of Education, Department of Polymer Science and Engineering, School of Chemical Engineering and Technology, Tianjin University, Tianjin, China, [3] Tianjin Key Laboratory of Membrane Science and Desalination Technology, Tianjin University, Tianjin, China, [4] People's Hospital of Yujiang District, Yingtan, China

Cancer poses a serious threat to human health. To enhance the efficacy of tumor chemotherapy, it is urgent to develop novel and effective nanocarriers with the ability to efficiently load and deliver anticancer drugs. Covalent organic frameworks (COF)-based nanocarriers (CONs) have exhibited great potential for drug loading due to their porous structure and high surface area. However, the function of tumor intracellular-triggered drug release has barely been integrated. Herein we first synthesized a kind of hydrazide and disulfide bonds containing building block (4,4'-Dihydrazide diphenyl disulfide, **DHDS**), which was used to develop a PEGylated pH and redox dual-sensitive CONs (denoted HY/SS-CONs) for efficiently loading and delivering doxorubicin (DOX). The obtained HY/SS-CONs can achieve a very high loading content of DOX and very low premature leakage at physiological condition. However, under tumor intracellular microenvironment, HY/SS-CONs with acid-cleavable hydrazone bonds, and GSH-exchangeable disulfide bonds will undergo rapid disintegration, and efficiently release DOX to kill tumor cells. The COFs-based dual-sensitive nanocarriers provide a promising solution to the dilemma of extracellular drug loading and tumor intracellular drug release.

Keywords: covalent organic frameworks, nanocarriers, dual-sensitive, drug delivery, doxorubicin

OPEN ACCESS

Edited by:
Tianyi Ma,
The University of Newcastle, Australia

Reviewed by:
Yin Wang,
Virginia Tech, United States
Xin Du,
University of Science and Technology Beijing, China

***Correspondence:**
Jianhua Zhang
jhuazhang@tju.edu.cn

Specialty section:
This article was submitted to Nanoscience, a section of the journal Frontiers in Chemistry

Received: *16 April 2020*
Accepted: *11 May 2020*
Published: *26 June 2020*

Citation:
Wang C, Liu H, Liu S, Wang Z and Zhang J (2020) pH and Redox Dual-Sensitive Covalent Organic Framework Nanocarriers to Resolve the Dilemma Between Extracellular Drug Loading and Intracellular Drug Release. Front. Chem. 8:488. doi: 10.3389/fchem.2020.00488

INTRODUCTION

Cancer has posed a lethal threat to humans around the world. As a major treatment modality, chemotherapy by use of anticancer drugs has achieved obvious success in prolonging patient survival. Nevertheless, the clinical efficacy of chemotherapy is still far from satisfactory and severely limited by the intrinsic limitations of anticancer drugs, including poor stability, low water solubility, nonspecific drug distribution, and terrible side effects to healthy tissues (Chabner and Roberts, 2005). Over the past several decades, a great number of nanoparticulate drug delivery systems, such as liposomes (Bozzuto and Molinari, 2015), polymer-based micelles (Kamaly et al., 2016), inorganic and metal nanocarriers (Huang et al., 2011; Zhang H. et al., 2018; Vines et al., 2019; Xu et al., 2019), and nanogels (Zhang et al., 2015; Yu et al., 2018; Zhao X. et al., 2018), as well as

hybrid nanoplatforms (Raemdonck et al., 2014), have been designed and applied to overcome the drawbacks associated with conventional drug formulations. Apparently, these nanocarriers have demonstrated their ability to protect the drugs from premature degradation, increase the drug solubility, improve the drug accumulation within tumors, and enhance the tumor's intracellular distribution of drug, thus leading to a higher efficiency and lower toxicity. However, the potential of these nanocarriers is far from being fully exploited and there are still some issues and improvements that need to be addressed (Mura et al., 2013; Dawidczyk et al., 2014; Blanco et al., 2015; Shi et al., 2017).

One of major limitations for most traditional nanocarriers is their low capacity for loading drugs (Blanco et al., 2015; Shi et al., 2017). For example, the drug loading of conventional liposomes and polymeric micelles is often below 1 and 5%, respectively. The low drug loading content always results in insufficient efficacy. Therefore, to achieve an ideal therapeutic outcome, it demands an increase in dosage and/or frequency of administration, often leading to a higher risk of adverse effects caused by the drugs and pharmaceutical excipients. In addition, some nanocarriers, especially those derived from assembly process, often suffer from premature drug leakage, thus causing poor therapeutic efficacy and severe systemic toxicity (Blanco et al., 2015; Shi et al., 2017). Apparently, it is imperative to develop more sophisticated nanocarriers with the ability to effectively load drugs and stably retain the payloads in the bloodstream.

During the last decade, covalent organic frameworks (COFs), as a class of newly emerged crystalline porous polymers, have attracted enormous attention. COFs were linked by dynamic covalent bonds such as imine, imide, azine, hydrazone, and boronate ester, and made from building blocks that were mainly consisted of lightweight elements (H, B, C, N, and O) (Diercks and Yaghi, 2017). COFs possess some desirable and unique features, including tunable pore geometry, large surface area, outstanding crystallinity, intrinsic adaptability, and excellent flexibility in molecular architecture, and functional design, thus exhibiting great potential for various applications (Sakaushi and Antonietti, 2015; Waller et al., 2015; Kandambeth et al., 2018; Song et al., 2019; Zhao et al., 2019). Recently, these porous frameworks opened up a new avenue for exciting opportunities in biomedical and pharmaceutical fields, especially for drug delivery (Fang et al., 2015; Bai et al., 2016; Vyas et al., 2016; Mitra et al., 2017; Wu and Yang, 2017; Hashemzadeh and Raissi, 2018; Zhao F. et al., 2018; Liu et al., 2020). The COFs as drug carriers have demonstrated some unique advantages. Some COFs-based drug delivery systems were proven to possess high loading capacity and minimized drug leakage due to the porous structure, high surface area, and π-π stacking interactions between COFs and drugs (Liu H. et al., 2019; Wang et al., 2019). However, the high and stable drug loading usually signifies slow drug release, leading to insufficient drug accumulation at the target site. These intrinsic limitations often cause treatment failure and even multidrug resistance, which severely impeded the practical applications of COFs-based carriers in anticancer drug delivery (Blanco et al., 2015; Fang et al., 2015; Shi et al., 2017; Zhao F. et al., 2018).

The physiological pH of blood and normal tissues is about 7.4, but the tumor intracellular endo/lysosomal pH ranges from 4.0 to 6.5. In addition, the glutathione concentration (GSH, 2–10 mM) within tumor cells is substantially higher than extracellular levels (1–2 μM) in plasma. The difference in pH value and GSH level between tumor intracellular and extracellular microenvironment is advantageous for the specifically targeted and controlled drug release (Cheng et al., 2011; Lee et al., 2013; Mura et al., 2013; Blanco et al., 2015; Du et al., 2018). Moreover, pH- and/or GSH-stimulus-sensitive nanocarriers have been widely reported for the controllable drug release in tumor cells (Zhang et al., 2013; Deng et al., 2015; Ma et al., 2018; Liu F. et al., 2019), which are based on the tumor cell microenvironment-sensitive bonds, such as acid-cleavable hydrazone, or acetal bonds and GSH-exchangeable disulfide bonds. Nevertheless, the function of intracellular-triggered drug release has barely been integrated into the COFs-based drug delivery systems.

In this study, we designed and prepared a kind of pH and redox dual-sensitive covalent organic framework nanocarriers (CONs) for efficiently loading and delivering doxorubicin (DOX). As shown in **Scheme 1**, we first synthesized a kind of new building block (4,4'-Dihydrazide diphenyl disulfide, **DHDS**), which has both two hydrazide bonds and a disulfide bond. Then, the hydrazone and disulfide-containing COFs (**HY/SS-COFs**) were prepared by use of a versatile Schiff-base reaction between DHDS and benzene-1,3,5-tricarbaldehyde (**BTA**). After ultrasound exfoliation and co-assembly with Poloxamer 188 (PEG-PPG-PEG, an FDA-approved pharmaceutic adjuvant), the pH and redox dual-sensitive nanocarriers (denoted as **HY/SS-CONs**) were prepared. HY/SS-CONs can efficiently load DOX due to their porous structure and high surface area, as well as the hydrophobic and π-π stacking interactions between HY/SS-CONs and DOX. Moreover, HY/SS-CONs can undergo structural disintegration under tumor cell microenvironment and rapidly release the payload in response to low pH and high GSH level in tumor cells. The PEG chains of Poloxamer 188 anchored on the outer surface of HY/SS-CONs can improve the dispersion stability in water and long-circulation capacity. The designed HY/SS-CONs have the ability to balance extracellular drug loading and intracellular drug release, thus holding great promise for anticancer drug delivery.

MATERIALS AND METHODS

Materials

1,3,5-benzenetricarboxaldehyde (BTA), 4-sulfhydryl benzoic acid methyl ester (SBME), and glutathione (GSH) were purchased from Aladdin Reagent Limited Company (Shanghai, China). Poloxamer 188 with an average molecular weight of about 8,400 daltons was purchased from Jiaxing Sicheng Chemical Co., Ltd. (Zhejiang, China). Doxorubicin (DOX) was purchased from Meilunbio Company (Dalian, China). All other reagents were commercially available without further purification.

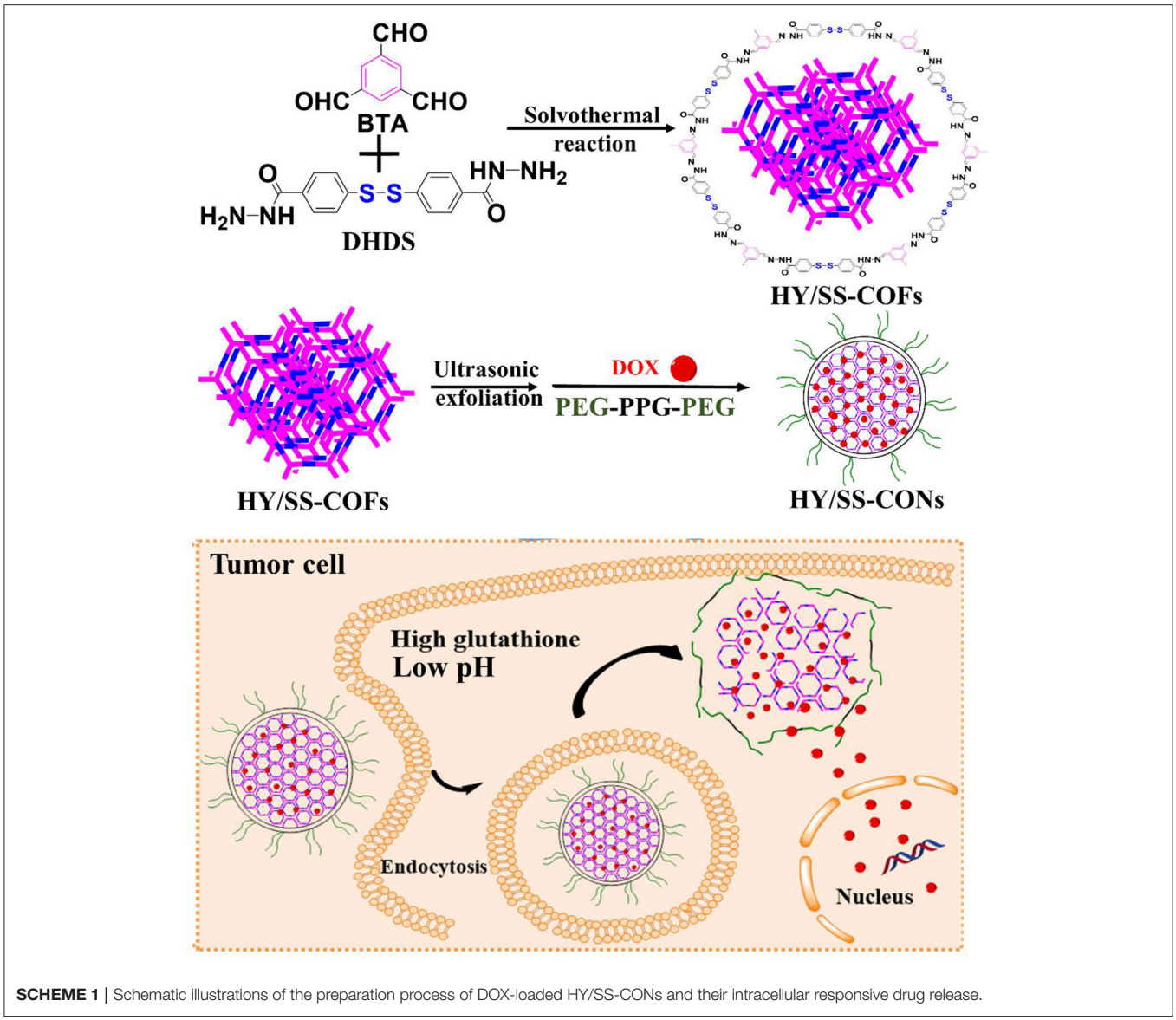

SCHEME 1 | Schematic illustrations of the preparation process of DOX-loaded HY/SS-CONs and their intracellular responsive drug release.

Synthesis and Characterizations of 4,4'-Dihydrazide Diphenyl Disulfide (DHDS)

The hydrazide groups were firstly introduced to prepare 4-sulfhydryl benzoic acid hydrazide (SBH). Briefly, 4-sulfhydryl benzoic acid methyl ester (SBME) (1 g, 5.6 mmol) was dissolved in anhydrous methanol, and then the hydrazine hydrate solution (7 ml, 80%) was dropwise added. After completely mixing, the reaction was performed for 24 h at 60°C under string. After rotary evaporation to remove the solution and recrystallization, the faint yellow solid SBH was obtained. Subsequently, the SBH (0.57 g, 3.4 mmol) and iodine (0.44 g, 1.7 mmol) were dissolved in anhydrous ethanol. After dropwise addition of triethylamine (1.5 mL, 10.2 mmol), the reaction was performed for 24 h at room temperature. Sodium thiosulfate solution (10%) was added into above mixture to remove the excessive unreacted iodine. After adjusting the pH value to about 5.0 using 0.01 M HCl, the yellow solid DHDS was obtained after filtration, washing by water, and drying in vacuum. The molecular structure of DHDS was confirmed by ^{1}H-NMR and electrospray ionization mass spectrometry (ESI-MS). ^{1}H-NMR spectra were recorded in *d*-DMSO using Varian Inova-500M spectrometer instrument (Varian Inc. Palo Alto, USA). The ESI-MS was a single-quadrupole VG-platform spectrometer with MassLynx version 3.1. The ESI-MS data were obtained in positive-ion mode. Sodium formate was added to the solvent to enhance the electrospray ion current. The skimmer voltage was 40 V.

Synthesis and Characterizations of HY/SS-COFs and HY/SS-CONs

The HY/SS-COFs described in **Scheme 1** were synthesized by solvothermal synthesis methods. Briefly, BTA (32.4 mg, 0.2 mmol) and DDS (100.2 mg, 0.3 mmol) were completely dissolved

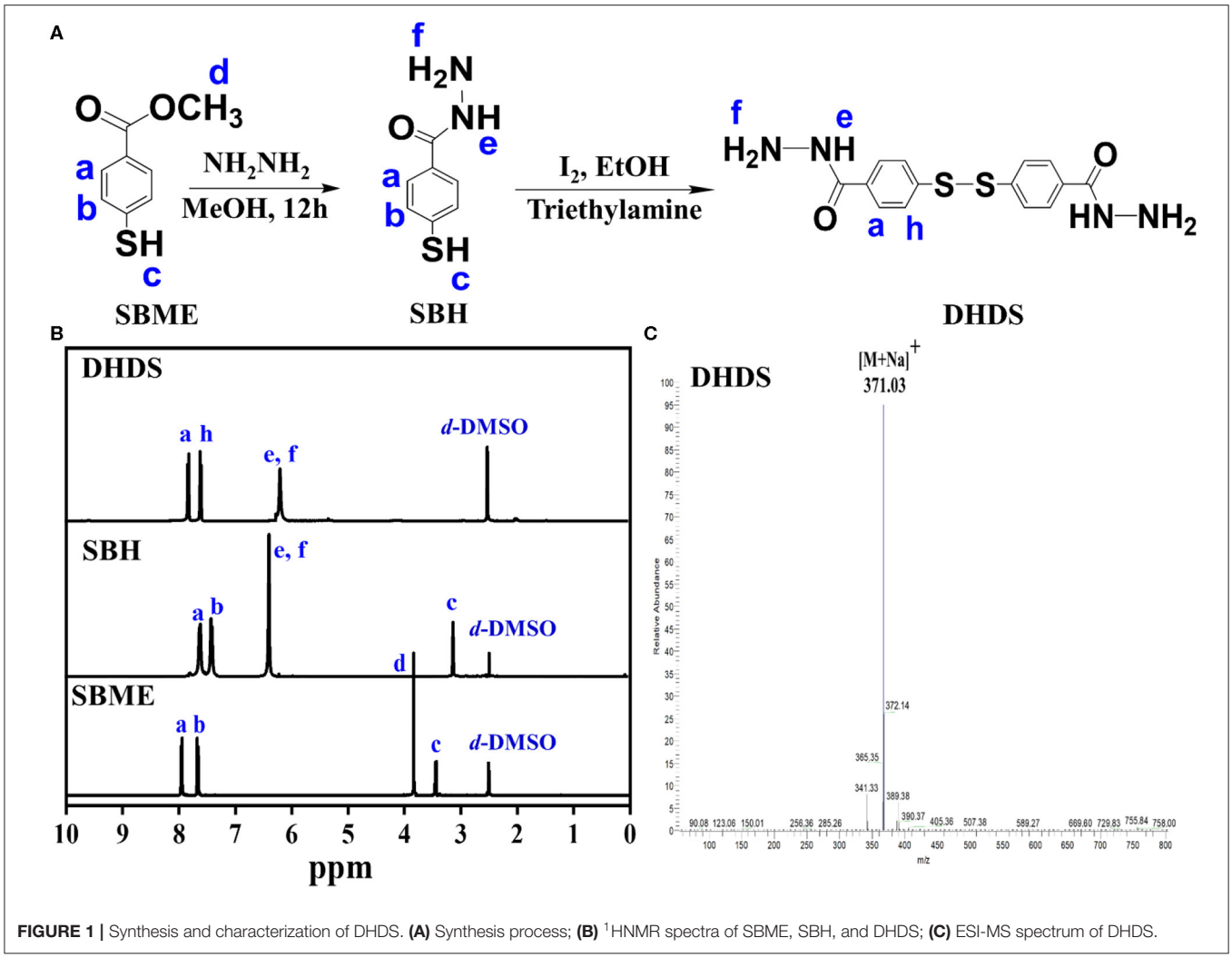

FIGURE 1 | Synthesis and characterization of DHDS. **(A)** Synthesis process; **(B)** ^{1}HNMR spectra of SBME, SBH, and DHDS; **(C)** ESI-MS spectrum of DHDS.

in the mixture of 1,4-dioxane and mesitylene (10 mL, 1:3 in voL) in a Schlenk tube. The mixture was degassed by three freeze-evacuate-thaw cycles and then heated at 120°C in a thermostatic oil bath for 72 h. After centrifugation, repeated washing by tetrahydrofuran, and vacuum drying, the yellow solid product (HY/SS-COFs) were obtained. After sonication exfoliation for about 10 min, HY/SS-COFs were broken into CONs with size of 100 nm. Sonication was carried out with a Skymen JM-03D-28 ultrasonic cleaner with a power of 120 W (Skymen Cleaning Equipment Co., Ltd, Shenzhen, China). The DOX was encapsulated into CONs by the equilibrium adsorption and diffusion. Briefly, CONs (100 mg) were dispersed into n-hexane solution (10 mL) of DOX (30 mg/mL) and then slowly stirred for 24 h at room temperature under dark conditions. The DOX-loaded CONs were obtained by centrifugation, repeated washing by n-hexane, and vacuum drying. To prepare drug-free and drug-loaded PEGylation HY/SS-COFs, the drug-free and drug-loaded CONs (100 mg) were dispersed into DMSO solution (10 mL) containing Poloxamer 188 (2 g). After sonication for about 5 min, the mixture was dropwise added into deionized water (50 mL) under stirring. After full dispersion for about 24 h, DMSO and free Poloxamer 188 was removed by dialysis for 24 h in water at room temperature with a dialysis bag (MWCO = 50000 g/mol). Finally, the drug-free and drug-loaded HY/SS-COFs were obtained after lyophilization.

The size and morphology of above HY/SS-COFs and HY/SS-CONs under different conditions were measured by dynamic light scattering (DLS, Zetasizer Nano ZS90), scan electron microscopy (SEM, Hitachi S-4800), and/or transmission electron microscope (TEM, JEOL JEM-2100F). The powder X-ray diffraction (PXRD) detections were carried out using a Bruker D8 Focus diffractometer (Bruker AXS, Germany). The pore size distribution and surface area were determined by nitrogen adsorption/desorption experiment with a Micrometric ASAP 2010 instrument. The specific area was calculated using Brunauer-Emmett-Teller (BET) model and the pore size was obtained from Barrett-Joyner-Halenda (BJH) method. Thermogravimetry (TGA) was measured on a NETZSCH STA 449 C thermogravimetric analyzer from 0 to 800°C at a heating rate of 10°C/min in nitrogen flow. Fourier transform infrared

spectroscopy (FTIR) was carried out with a Perkin-Elmer FTIR spectrometer (Perkin Elmer, Waltham, USA).

The DOX loading content as well as *in vitro* release behavior under different conditions (pH 7.4 and pH 5.0 with or without 10 mM GSH) at 37°C were investigated. The amount of DOX in DOX-loaded HY/SS-CONs was determined by a WFZ-26A UV/Vis spectrophotometer at 480 nm. Typically, DOX-loaded HY/SS-CONs (1 mg) were dispersed in distilled water (10 mL) and incubated at room temperature for 24 h after adding 1.0 mol/L HCl (1 mL) with 10 mM GSH. After the complete disintegration of HY/SS-CONs, the concentration of DOX was analyzed by UV/Vis spectrophotometer and calculated using a calibration curve of different DOX concentrations in an identical solvent mixture. To test the drug release behaviors, DOX-loaded HY/SS-CONs solution (1.0 mg/mL) was sealed in a dialysis bag with a MWCO of 3500. The dialysis bag was immersed in a screw capped bottle containing appropriate buffer medium (20 mL) in a shaking bath at 37°C. At regular time intervals, 5.0 mL of the release solution was removed and the same volume of fresh buffer solution was added to maintain a constant volume of the released medium. The amount of the released drug was determined by UV/Vis spectrophotometer at 480 nm. All experiments were carried out in triplicate.

The dispersion stability and GSH and/or pH-triggered size and morphological transitions of HY/SS-CONs were investigated as below. Drug-loaded HY/SS-CONs (0.5 mg) were dispersed in PBS (5.0 mL) at pH 7.4. The size changes were determined after predesignated incubation time by DLS measurement and Tyndall phenomenon. To investigate the hemodynamic stability, the particle size of HY/SS-CONs (0.1 mg/mL) in pH 7.4 PBS containing 5% bovine serum albumin (BSA) at 37°C was measured at fixed time points. The GSH and/or pH-sensitivity of HY/SS-CONs was evaluated by DLS measurement of size change with time of drug-loaded HY/SS-CONs in PBS pH 5.0 with 10 mM GSH.

In vitro Cytotoxicity Test and Cellular Uptake Evaluation

The MTT assay was utilized to evaluate the cellular toxicity of free DOX, drug-free, and drug-loaded HY/SS-CONs. HepG2 cells were seeded into a 96-well plate with a density of 1×10^5 cells per well and incubated for 24 h at 37°C with 5% CO_2. Then the Dulbecco's Modified Eagle's medium (DMEM) was discarded and the cells were washed twice with pH 7.4 PBS solution. Various concentrations of drug-free HY/SS-CONs in PBS at pH 7.4 were added into the wells for co-culture with the cells for 24 h. After incubation, the MTT assay was carried out to determine the cell viability. According to similar protocols, the cellular toxicity toward HepG2 cells of free DOX and DOX-loaded HY/SS-CONs with an equivalent DOX concentration was investigated. HepG2 cells were incubated for 24 h with free DOX and DOX-loaded HY/SS-CONs in PBS at pH 7.4, respectively. All experiments were carried out in quintuplicate to determine mean values and standard deviations. To investigate the cellular uptake of HY/SS-CONs, HepG2 cells were seeded into a confocal microscopic dish at a density of 1×10^5 per dish and incubated in DMEM medium at 37°C for 24 h. And then the culture medium was replaced by PBS solution containing pure DOX or DOX-loaded HY/SS-CONs at a concentration of 10 μg/mL. After incubation for 4 h, the cells were washed with PBS solution three times and then stained with DAPI for 5 min. After repeated wash with PBS solution, cellular endocytosis was evaluated using a confocal laser scanning microscope (TCS SP8, Leica).

RESULTS AND DISCUSSION

Synthesis and Characterizations of DHDS

DHDS has both two hydrazide bonds and a disulfide bond, which can act as building blocks for construction of pH and redox sensitive COFs with acid-cleavable hydrazone and GSH-exchangeable disulfide bonds. The synthesis process of DHDS was shown in **Figure 1A**. First, the precursor SBME was hydrazide-functionalized, then the obtained SBH was oxidized to produce DHDS. ^{1}HNMR was used to monitor the chemical transformations of SBME and SBH in the reaction process and determine the composition and structure of DHDS. As shown in **Figure 1B**, the ^{1}HNMR spectrum of DHDS exhibited the characteristic peaks of phenyl ring at 7.7–8.0 ppm (**a**, **h**) and the characteristic peaks corresponding to hydrazide at about 6.2 ppm (**e**, **f**). In addition, the disappeared peaks of the methyl protons (**d**) at about 3.8 ppm of SBME and the disappeared peak of sulfhydryl protons (**c**) of SBH can be used to further confirm the formation of DHDS. Moreover, after the integration of the respective peak or peak groups from left to right in the ^{1}HNMR spectrum of DHDS, it can be found that the area of the peak at 6.2 ppm (**e**, **f**) is 1.5 times greater than the area of the peak at 7.9 ppm (**a**) or 7.7 ppm (**h**). This result is very close to its theoretical value, thus indicating the molecular structure of DHDS. The ESI-MS was used to further confirm the molecular structure of DHDS, as shown in **Figure 1C**. The mass spectrum of DHDS was dominated by the protonated ions $[M+Na]^+$ at m/z 371.03 and exhibited negligible fragmentation. The observed molecular mass is in excellent agreement with the theoretical value of DHDS, demonstrating the successful synthesis of DHDS.

Synthesis and Characterization of HY/SS-COFs

A series of COFs has demonstrated great potential as a promising platform for effective loading and delivery of various drugs, because of their unique and attractive features (Fang et al., 2015; Bai et al., 2016; Vyas et al., 2016; Mitra et al., 2017; Wu and Yang, 2017; Hashemzadeh and Raissi, 2018; Zhao F. et al., 2018; Liu et al., 2020). In particular, the hydrazone-linked COFs based on Schiff-base chemistry exhibited a high stability under physiological conditions but acid-cleavable property within tumoral acid microenvironment, providing some unique advantages for biomedical, and pharmaceutical applications (Segura et al., 2016; Zhao F. et al., 2018). The hydrazone and disulfide bonds-bearing HY/SS-COFs were prepared by use of a solvothermal Schiff-base reaction between commercially available BTA and DHDS as building blocks. The obtained HY/SS-COFs were characterized in detail, as shown in **Figure 2**.

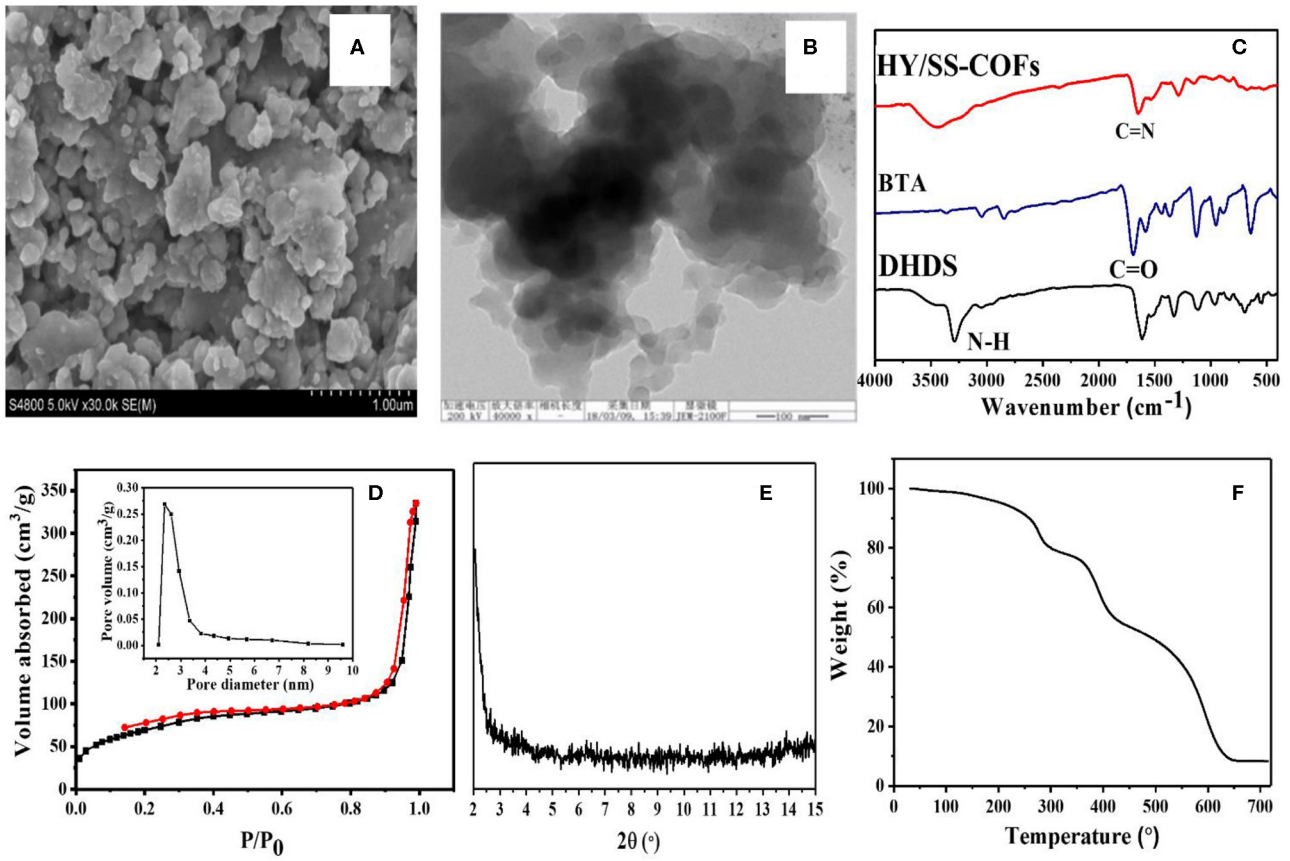

FIGURE 2 | Characterizations of HY/SS-COFs. **(A)** SEM image and **(B)** TEM image; **(C)** FTIR spectra of HY/SS-COFs, BTA, and DHDS; **(D)** Nitrogen adsorption and desorption isotherms. The inset shows pore size of HY/SS-COFs; **(E)** PXRD pattern; **(F)** TGA curve.

SEM image of HY/SS-COFs indicates the shapes of HY/SS-COFs are irregular slices consisted of small flake-like structures (**Figure 2A**). A further inspection of the structures by TEM in **Figure 2B** indicated that the HY/SS-COFs have a spherical nanoparticle-like morphology. The FTIR spectra of HY/SS-COFs, BTA, and DHDS were shown in **Figure 2C**. It can be seen that DHDS showed the characteristic peaks, such as amines (-NH-) at about 3,320 cm^{-1} and disulfide (-S-S-) at about 510 cm^{-1}. On inspection of the FTIR spectrum, DHDS presented a characteristic peak of -C-N- bonds at about 1,420 cm^{-1}, which further indicated the successful preparation of DHDS. Compared with the FTIR spectrum of DHDS, the presence of a weak imine C=N stretch at about 1,620 cm^{-1} was observed in the FTIR spectrum of HY/SS-COFs. Furthermore, the absence of the aldehydic C-H and C=O stretching vibrations of BTA further confirmed the formation of HY/SS-COFs. Nitrogen adsorption/desorption analysis of HY/SS-COFs was shown in in **Figure 2D**. The results indicated that HY/SS-COFs possess a very high surface area of 328 m^2/g and narrow pore size distribution with pore size of about 2.5 nm. PXRD indicates the formation of HY/SS-COFs had a poor crystalline structure (**Figure 2E**). The thermal stability of HY/SS-COFs was monitored using TGA, as shown in **Figure 2F**. The result indicates HY/SS-COFs have excellent thermal stability and their decomposition behavior occurs at nearly over 300°C. About 10% of the weight loss was observed at the temperature lower than 300°C. This weight loss below 300°C may be due to the loss of the absorbed solvent or monomers in the pores of cores, as well as the unreacted hydrazone or aldehyde groups at the termini of COFs (Ma et al., 2016; Xiong et al., 2020). Subsequently, HY/SS-COFs showed a sharp weight loss profile at the temperature higher than 400°C and ∼60% weight loss was observed between 400 and 700°C. This significant weight loss can be attributed to the structural destruction and decomposition of COFs.

Preparation and Characterization of HY/SS-CONs

COFs had great potential for drug loading and delivery. However, before entering into the blood circulation system, the COFs have to be exfoliated into nanoscale platelets and be surface-modified (such as PEGylation) in order to overcome the physicochemical and physiological stability limitations (Zhao F. et al., 2018). The ultrasonic exfoliation was widely used to exfoliate COFs. Moreover, the co-assembly of nanoscale COFs with PEG-containing amphiphilic polymers has been proven to act as an efficient approach to anchor PEG chains

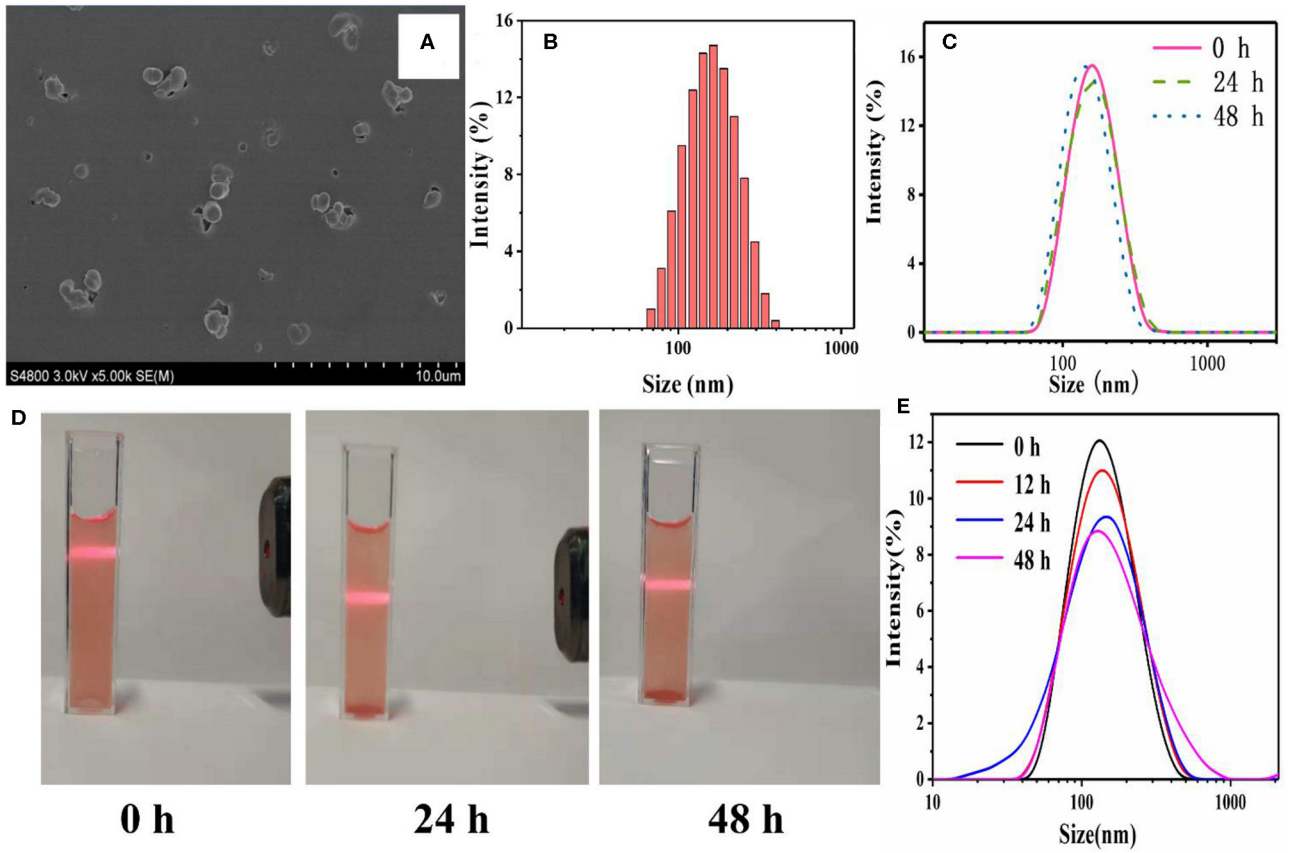

FIGURE 3 | Characterizations of HY/SS-CONs. **(A)** SEM image and **(B)** DLS pattern; **(C)** Storage stability of DOX-loaded HY/SS-CONs at pH 7.4; **(D)** Tyndall phenomena of DOX-loaded HY/SS-CONs at pH 7.4; **(E)** Hemodynamic stability of HY/SS-CONs in PBS pH 7.4 containing 5% BSA at 37°C.

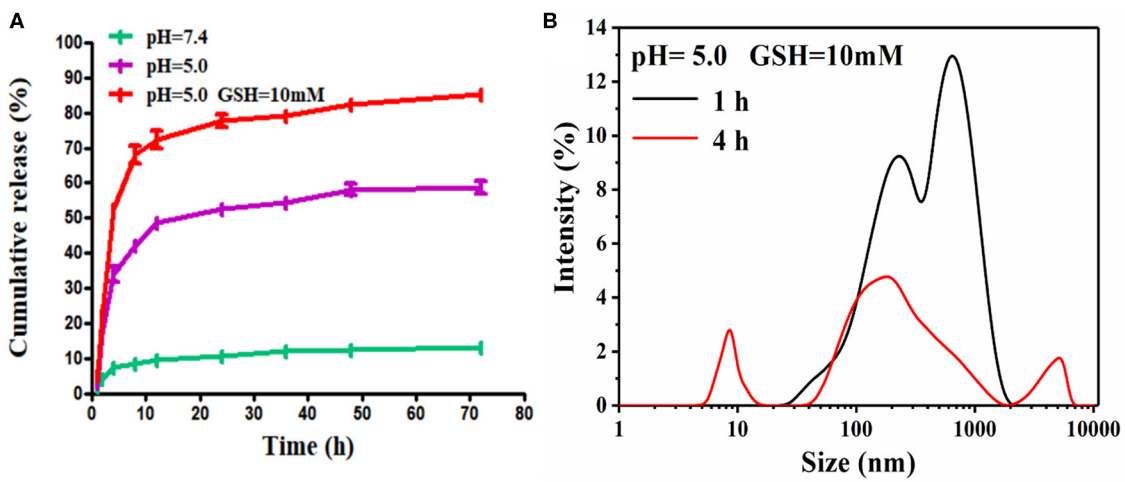

FIGURE 4 | pH and redox dual sensitiveness of HY/SS-CONs. **(A)** Drug release profiles of DOX-loaded HY/SS-CONs under PBS 7.4, PBS pH 5.0, and PBS pH 5.0 with 10 mM GSH; **(B)** Size changes of HY/SS-CONs incubated at pH 5.0 with 10 mM GSH for different time.

onto the outer surface of COFs (Zhang G. et al., 2018; Liu F. et al., 2019; Wang et al., 2020). The PEGylated nanoscale COFs, [i.e., HY/SS-CONs, were readily prepared by through the co-assembly of FDA-approved Poloxamer 188 (a kind of PEG-containing amphiphilic polymer, PEG-PPG-PEG), with the nanoscale HY/SS-COFs formed by ultrasonic exfoliation].

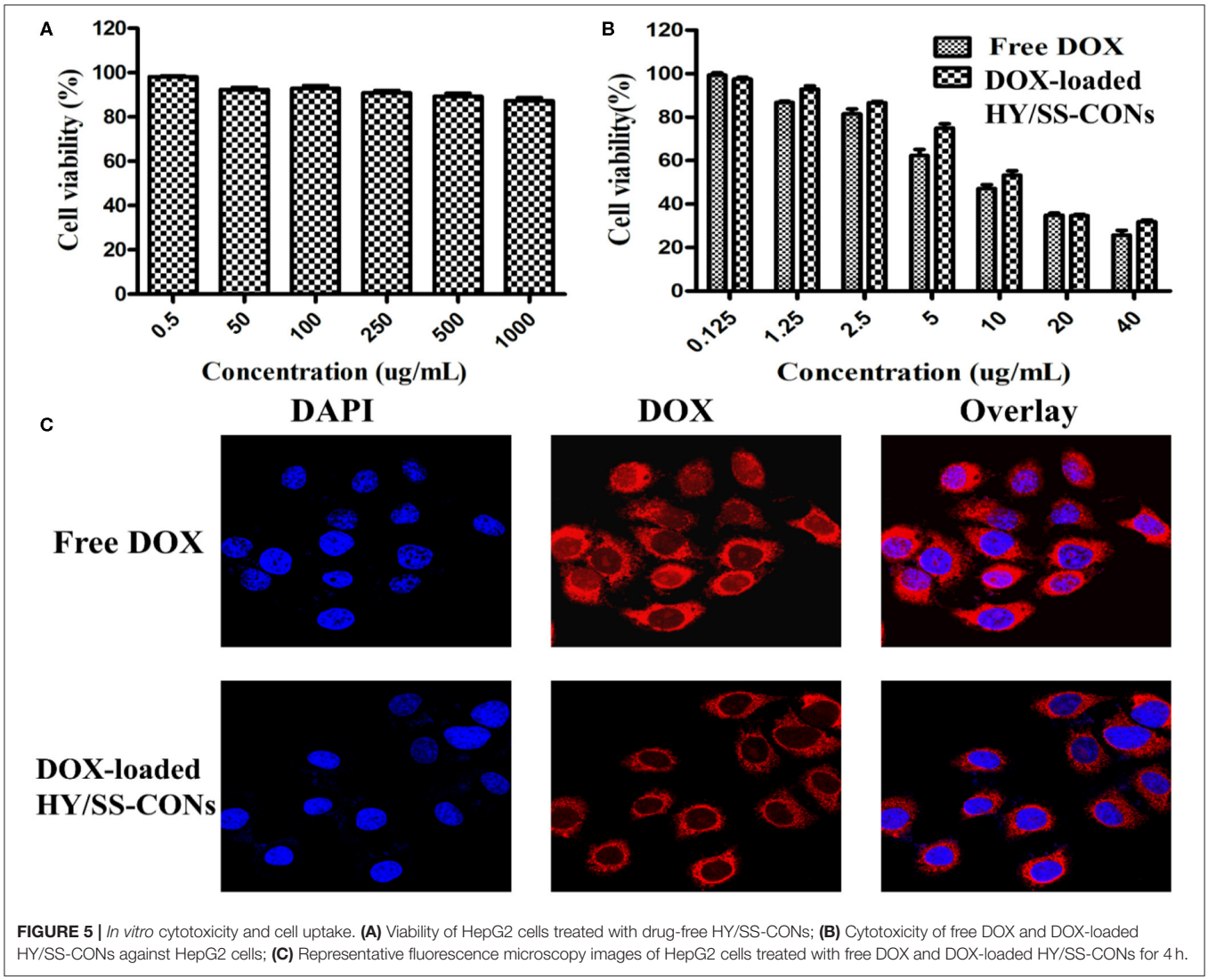

FIGURE 5 | *In vitro* cytotoxicity and cell uptake. **(A)** Viability of HepG2 cells treated with drug-free HY/SS-CONs; **(B)** Cytotoxicity of free DOX and DOX-loaded HY/SS-CONs against HepG2 cells; **(C)** Representative fluorescence microscopy images of HepG2 cells treated with free DOX and DOX-loaded HY/SS-CONs for 4 h.

Due to the hydrogen bond and hydrophobic interactions, the hydrophobic PPG chain of Poloxamer 188 chains can adsorbed onto the surface of nanoscale HY/SS-COFs to generate HY/SS-CONs. After effective removal of excess Poloxamer 188 by dialysis, the HY/SS-CONs were obtained and characterized. As shown in **Figure 3A**, the SEM image of HY/SS-CONs clearly indicates its nearly spherical morphology. The particle sizes of HY/SS-CONs in SEM image is about 120 ± 20 nm. The hydrodynamic size of HY/SS-CONs was tested by DLS and shown in **Figure 3B**, indicating a size of about 140 nm with relatively high monodispersity. The dispersion stability is an important factor for the application of nanocarriers. As shown in **Figure 3C**, a significant size fluctuation was not observed for about 48 h, indicating a high long-term stability. The dispersion stability of HY/SS-CONs in PBS pH 7.4 was further confirmed by the stable Tyndall phenomena in **Figure 3D** indicated that F68@SS-COFs can be stably dispersed. The excellent stability of HY/SS-CONs can be ascribed to the combined effect of the steric stabilization of PEGylated shell preventing flocculation and the steady CONs core ensuring integrity of nanostructure. The size change as a function of incubation time for HY/SS-CONs in PBS pH 7.4 containing 5% BSA at 37°C is shown in **Figure 3E**. No significant change in size can indicate the absence of aggregation or sedimentation, mainly due to the steric stabilization of PEGylated shell to minimize interactions with proteins and maintain the hemodynamic stability.

Drug Loading and Dual-Sensitive Release

The hydrophobic DOX can be efficiently encapsulated into HY/SS-CONs. The drug loading content of HY/SS-CONs was found to be about 18%. The high loading capacity of DOX was due to the fact that HY/SS-CONs had a large pore surface area. Moreover, the other factor can be ascribed to the strong hydrophobic interactions and the π-π stacking interactions between aromatic rings of CONs and DOX. Apparently, this kind of high drug loading content of HY/SS-CONs should be desirable for effective chemotherapy. The drug release from the DOX-loaded HY/SS-CONs were comparatively investigated under PBS

7.4, PBS pH 5.0, and PBS pH 5.0 with 10 mM GSH. The presence of PBS pH 5.0 and 10 mM GSH was used to mimic the tumor intracellular microenvironment. As shown in **Figure 4A**, the DOX release from the HY/SS-CONs in PBS pH 7.4 was very low. Only about 10% of the total encapsulated DOX was released at 72 h. This may be due to the strong interactions between CONs and DOX as well as the extremely low solubility of DOX at pH 7.4. However, the DOX-loaded HY/SS-CONs exhibited an evidently acid- and GSH-dependent release profile. The DOX release rate in PBS pH 5.0 was much higher than that in PBS pH 7.4, indicating the acid-induced disintegration of HY/SS-CONs, increasing the release rate of DOX. Moreover, the DOX release from HY/SS-CONs in the PBS pH 5.0 with 10 mM GSH was significantly higher than that without GSH. In the presence of PBS pH 5.0 and 10 mM GSH, the cumulative release of DOX can fast achieve about 50% in 4 h and about 90% in 72 h, indicating the acid and GSH dual-triggered disintegration of HY/SS-CONs. To confirm the acid and GSH triggered disintegration, DLS was used to measure the size change of HY/SS-CONs after incubation in PBS pH 5.0 with 10 mm GSH for different time. Compared with the size change of HY/SS-CONs in **Figure 3C**, it can be found in **Figure 4B** that a significantly different size distribution of HY/SS-CONs after incubation in PBS pH 5.0 with 10 mm GSH for 1 h was observed. Moreover, after incubation for 4 h, HY/SS-CONs presented a more dramatic fluctuation of size, which can be ascribed to the acid and GSH dual-triggered disassembly and thus the aggregation of HY/SS-CONs fragments due to hydrophobic and π-π stacking interactions. Collectively, the HY/SS-CONs had a very high loading capacity of DOX, but meanwhile possessed a controlled drug release behavior under tumor intracellular microenvironment, which should be very beneficial for cancer treatment.

In vitro Cytotoxicity and Cell Uptake

The viability of HepG2 cells treated with HY/SS-CONs for 24 h was investigated and shown in **Figure 5A**. HY/SS-CONs had no significant cytotoxicity to the cells. The PEGylated shell coated on the surface of CONs core should contribute the improved biocompatibility. The antitumor activity of free DOX and DOX-loaded HY/SS-CONs was investigated and presented in **Figure 5B**. The antitumor activity of DOX-loaded HY/SS-CONs exhibited a similar activity with the free DOX. The half inhibitory concentration (IC_{50}) values of the DOX-loaded HY/SS-CONs was slightly higher than that of free DOX. Their cell killing activity was in accordance with the cell uptake as demonstrated in **Figure 5C**. Images of the HepG2 cells incubated with free DOX and DOX-loaded HY/SS-CONs at equivalent DOX concentrations for 4 h. After incubation with free DOX, the strong fluorescence signal in the cell cytoplasm can be observed. The free DOX molecules can rapidly enter cells by a passive diffusion mechanism. The DOX fluorescence intensity for the tumor cells treated with HY/SS-CONs was slightly lower than those treated with free DOX. The nanoscale HY/SS-CONs were internalized through an endocytosis mechanism following an acid- and GSH-triggered fast drug release, thus leading to a similar DOX fluorescence compared with free DOX. Compared with free DOX, the acid and redox dual-sensitive HY/SS-CONs can achieve a very high DOX distribution within tumor cells, which are expected to realize an improved anticancer activity.

CONCLUSIONS

In this work, we designed and prepared a kind of novel PEGylated pH and redox dual-sensitive HY/SS-CONs for effective loading and delivery of DOX. HY/SS-CONs with a PEG shell and a multifunctional core derived from the acid-cleavable hydrazone and redox-responsive disulfide bonds linked COFs. The results indicated that the HY/SS-CONs with well-controlled morphology and good biocompatibility were obtained, which can achieve a high DOX loading content and maintain stability under extracellular condition, but realize intracellular fast drug delivery in response to the low pH and high GSH concentration within tumor cells, leading to an effective antitumor activity to tumor cells. Considering the simple preparation process, high drug loading capacity, and desirable pH and redox dual-responsiveness, the HY/SS-CONs designed herein are expected to serve as a promising nanoplatform for anticancer drug delivery.

DATA AVAILABILITY STATEMENT

The raw data supporting the conclusions of this article will be made available by the authors, without undue reservation.

AUTHOR CONTRIBUTIONS

HL and SL carried out the experiments and drafted the manuscript. ZW participated in the design of the study. CW wrote and revised this paper. JZ supervised the whole study. All authors reviewed the final version of the manuscript and approved it for publication.

ACKNOWLEDGMENTS

We gratefully acknowledge the financial support provided by Natural Science Foundation of Tianjin City (19JCYBJC17200) and Ph.D. Early Development Foundation of Mudanjiang Normal University (MNUB201713).

REFERENCES

Bai, L. S. Z., Phua, W. Q., Lim, A., Jana, Z., Luo, H. P., Tham, L., et al. (2016). Nanoscale covalent organic frameworks as smart carriers for drug delivery. *Chem. Commun*. 52, 4128–4131. doi: 10.1039/C6CC00853D

Blanco, E., Shen H., and Ferrari, M. (2015). Principles of nanoparticle design for overcoming biological barriers to drug delivery. *Nat. Biotechnol*. 33, 941–951. doi: 10.1038/nbt.3330

Bozzuto, G., and Molinari, A. (2015). Liposomes as nanomedical devices. *Int. J. Nanomed*. 10, 975–999. doi: 10.2147/IJN.S68861

Chabner, B. A., and Roberts, T. G. Jr. (2005). Chemotherapy and the war on cancer. *Nat. Rev. Cancer* 5, 85–98. doi: 10.1038/nrc1529

Cheng, R., Feng, F., Meng, F., Deng, C., Feijen, J., and Zhong, Z. (2011). Glutathione-responsive nano-vehicles as a promising platform for targeted intracellular drug and gene delivery. *J. Control Release* 152, 2–12. doi: 10.1016/j.jconrel.2011.01.030

Dawidczyk, C. M., Russell L. M., and Searson, P. C. (2014). Nanomedicines for cancer therapy: state-of-the-art and limitations to pre-clinical studies that hinder future developments. *Front. Chem*. 2:69. doi: 10.3389/fchem.2014.00069

Deng, L., Dong H., Dong A., and Zhang, J. (2015). A strategy for oral chemotherapy via dual pH-sensitive polyelectrolyte complex nanoparticles to achieve gastric survivability, intestinal permeability, hemodynamic stability and intracellular activity. *Eur. J. Pharm. Biopharm*. 97, 107–117. doi: 10.1016/j.ejpb.2015.10.010

Diercks, C. S., and Yaghi, O. M. (2017). The atom, the molecule, and the covalent organic framework. *Science* 355:eaal1585. doi: 10.1126/science.aal1585

Du, X., Kleitz, F., Li, X., Huang, H., Zhang, X., and Qiao, S. Z. (2018). Disulfide-bridged organosilica frameworks: designed, synthesis, redox-triggered biodegradation, and nanobiomedical applications. *Adv. Func. Mater.* 28:1707325. doi: 10.1002/adfm.201707325

Fang, Q., Wang, J., Gu, S., Kaspar, R. B., Zhuang, Z., Zheng, J., et al. (2015). 3D porous crystalline polyimide covalent organic frameworks for drug delivery. *J. Am. Chem. Soc*. 137, 8352–8355. doi: 10.1021/jacs.5b04147

Hashemzadeh, H., and Raissi, H. (2018). Covalent organic framework as smart and high efficient carrier for anticancer drug delivery: a DFT calculations and molecular dynamics simulation study. *J. Phys. D Appl. Phys*. 51:345401. doi: 10.1088/1361-6463/aad3e8

Huang, H. C., Barua, S., Sharma, G., Dey, S. K., and Rege, K. (2011). Inorganic nanoparticles for cancer imaging and therapy. *J. Control. Release* 155, 344–357. doi: 10.1016/j.jconrel.2011.06.004

Kamaly, N., Yameen, B., Wu, J., and Farokhzad, O. C. (2016). Degradable controlled-release polymers and polymeric nanoparticles: mechanisms of controlling drug release. *Chem. Rev*. 116, 2602–2663. doi: 10.1021/acs.chemrev.5b00346

Kandambeth, S., Dey, K., and Banerjee, R. (2018). Covalent organic frameworks: chemistry beyond the structure. *J. Am. Chem. Soc*. 141, 1807–1822. doi: 10.1021/jacs.8b10334

Lee, M. H., Yang, Z., Lim, C. W., Lee, Y. H., Dongbang, S., Kang, C., et al. (2013). Disulfide-cleavage-triggered chemosensors and their biological applications. *Chem. Rev*. 113, 5071–5109. doi: 10.1021/cr300358b

Liu, F., Lin, L., Zhang, Y., Sheng, S., Wang, Y., Xu, C., et al. (2019). Two-dimensional nanosheets with high curcumin loading content for multimodal imaging-guided combined chemo-photothermal therapy. *Biomaterials* 223:119470. doi: 10.1016/j.biomaterials.2019.119470

Liu, H., Shi, X., Wu, D., Khshen, F. K., Deng, L., Dong, A., et al. (2019). Injectable, biodegradable, thermosensitive nanoparticles-aggregated hydrogel with tumor-specific targeting, penetration, and release for efficient postsurgical prevention of tumor recurrence. *ACS Appl. Mater. Interfaces* 11, 19700–19711. doi: 10.1021/acsami.9b01987

Liu, S., Yang, J., Guo, R., Deng, L., Dong, A., and Zhang, J. (2020). Facile fabrication of redox-responsive covalent organic framework nanocarriers for efficiently loading and delivering doxorubicin. *Macromol. Rapid Commun*. 41:1900570. doi: 10.1002/marc.201900570

Ma, H., Liu, B., Li, B., Zhang, L., Li, Y. G., Tan, H. Q., et al. (2016). Cationic covalent organic frameworks: a simple platform of anionic exchange for porosity tuning and proton conduction. *J. Am. Chem. Soc*. 138, 5897–5903. doi: 10.1021/jacs.5b13490

Ma, J., Deng, H., Zhao, F., Deng, L., Wang, W., Dong, A., et al. (2018). Liposomes-camouflaged redox-responsive nanogels to resolve the dilemma between extracellular stability and intracellular drug release. *Macromol. Biosci*. 18:201800049. doi: 10.1002/mabi.201800049

Mitra, S., Sasmal, H. S., Kundu, T., Kandambeth, S., Illath, K., Diaz Diaz, D., et al. (2017). Targeted drug delivery in covalent organic nanosheets (CONs) via sequential postsynthetic modification. *J. Am. Chem. Soc*. 139, 4513–4520. doi: 10.1021/jacs.7b00925

Mura, S., Nicolas, J., and Couvreur, P. (2013). Stimuli-responsive nanocarriers for drug delivery. *Nat. Mater*. 12, 991–1003. doi: 10.1038/nmat3776

Raemdonck, K., Braeckmans, K., Demeester, J., and De Smedt, S. C. (2014). Merging the best of both worlds: hybrid lipid-enveloped matrix nanocomposites in drug delivery. *Chem. Soc. Rev*. 43, 444–472. doi: 10.1039/C3CS60299K

Sakaushi, K., and Antonietti, M. (2015). Carbon- and nitrogen-based organic frameworks. *Acc. Chem. Res*. 48, 1591–1600. doi: 10.1021/acs.accounts.5b00010

Segura, J. L., Mancheno, M. J., and Zamora, F. (2016). Covalent organic frameworks based on schiff-base chemistry: synthesis, properties and potential applications. *Chem. Soc. Rev*. 45, 5635–5671. doi: 10.1039/C5CS00878F

Shi, J., Kantoff, P. W., Wooster, R., and Farokhzad, O. C. (2017). Cancer nanomedicine: progress, challenges and opportunities. *Nat. Rev. Cancer* 17, 20–37. doi: 10.1038/nrc.2016.108

Song, Y., Sun, Q., Aguila, B., and Ma, S. (2019). Opportunities of covalent organic frameworks for advanced applications. *Adv. Sci*. 6:1801410. doi: 10.1002/advs.201801410

Vines, J. B., Yvon, J. H., Ryu, N. E., Lim, D. J., and Park, H. (2019). Gold nanoparticles for photothermal cancer therapy. *Front. Chem*. 7:167. doi: 10.3389/fchem.2019.00167

Vyas, V. S., Vishwakarma, M., Moudrakovski, I., Haase, F., Savasci, G., Ochsenfeld, C., et al. (2016). Exploiting noncovalent interactions in an imine-based covalent organic framework for quercetin delivery. *Adv. Mater*. 28, 8749–8754. doi: 10.1002/adma.201603006

Waller, P. J., Gandara, F., and Yaghi, O. M. (2015). Chemistry of covalent organic frameworks. *Acc. Chem. Res*. 48, 3053–3063. doi: 10.1021/acs.accounts.5b00369

Wang, K., Zhang, Z., Lin, L., Chen, J., Hao, K., Tian, H., et al. (2019). Covalent organic nanosheets integrated heterojunction with two strategies to overcome hypoxic-tumor photodynamic therapy. *Chem. Mater*. 31, 3313–3323. doi: 10.1021/acs.chemmater.9b00265

Wang, S. B., Chen, Z. X., Gao, F., Zhang, C., Zou, M. Z., Ye, J. J., et al. (2020). Remodeling extracellular matrix based on functional covalent organic framework to enhance tumor photodynamic therapy. *Biomaterials* 234:119772. doi: 10.1016/j.biomaterials.2020.119772

Wu, M. X., and Yang, Y. W. (2017). Applications of covalent organic frameworks (COFs): from gas storage and separation to drug delivery. *Chinese Chem. Lett*. 28, 1135–1143. doi: 10.1016/j.cclet.2017.03.026

Xiong, S., Wang, Y., Wang, X., Chu, J., Zhang, R., Gong, M., et al. (2020). Schiff base type conjugated organic framework nanofibers: solvothermal synthesis and electrochromic properties. *Sol. Energ. Mat. Sol. C* 209:110438. doi: 10.1016/j.solmat.2020.110438

Xu, C., Lei, C., and Yu, C. Z. (2019). Mesoporous silica nanoparticles for protein protection and delivery. *Front. Chem*. 7:290. doi: 10.3389/fchem.2019.00290

Yu, L., Dong, A., Guo, R., Yang, M., Deng, L., and Zhang, J. (2018). DOX/ICG coencapsulated liposome-coated thermosensitive nanogels for NIR-triggered simultaneous drug release and photothermal effect. *ACS Biomater. Sci. Eng*. 4, 2424–2434. doi: 10.1021/acsbiomaterials.8b00379

Zhang, G., Li, X., Liao, Q., Liu, Y., Xi, K., Huang, W., et al. (2018). Water-dispersible PEG-curcumin/amine-functionalized covalent organic framework nanocomposites as smart carriers for *in vivo* drug delivery. *Nat. Commun*. 9:2785. doi: 10.1038/s41467-018-04910-5

Zhang, H., Li, Q., Liu, R., Zhang, X., Li, Z., and Luan, Y. (2018). A versatile prodrug strategy to *in situ* encapsulate drugs in MOF nanocarriers: a case of cytarabine-IR820 prodrug encapsulated ZIF-8 toward chemo-photothermal therapy. *Adv. Funct. Mater*. 28:1802830. doi: 10.1002/adfm.201802830

Zhang, J., Gao, W., Fang, R. H., Dong, A., and Zhang, L. (2015). Synthesis of nanogels via cell membrane-templated polymerization. *Small* 11, 4309–4313. doi: 10.1002/smll.201500987

Zhang, J., Lin, X., Liu, J., Zhao, J., Dong, H., Deng, L., et al. (2013). Sequential thermo-induced self-gelation and acid-triggered self-release process of drug-conjugated nanoparticles: a strategy for the sustained and controlled drug delivery to tumors. *J. Mater. Chem. B* 1, 4667–4677. doi: 10.1039/c3tb20597e

Zhao, F., Dong, A., Deng, L., Guo, R., and Zhang, J. (2019). Morphology control and property design of boronate dynamic nanostructures. *Polym. Chem*. 10, 2436–2446. doi: 10.1039/C9PY00217K

Zhao, F., Liu, H., Mathe, S. D. R., Dong, A., and Zhang, J. (2018). Covalent organic frameworks: from materials design to biomedical application. *Nanomaterials* 8:15. doi: 10.3390/nano8010015

Zhao, X., Deng, L., Deng, H., Dong, A., Wang, W., and Zhang, J. (2018). *In situ* template polymerization to prepare liposome-coated PDMAEMA nanogels

with controlled size, high stability, low cytotoxicity, and responsive drug release for intracellular dox release. *Macromol. Chem. Physi.* 219:201800071. doi: 10.1002/macp.201800071

Conflict of Interest: The authors declare that the research was conducted in the absence of any commercial or financial relationships that could be construed as a potential conflict of interest.

frontiers in Chemistry

ORIGINAL RESEARCH
published: 14 July 2020
doi: 10.3389/fchem.2020.00565

A Nano-Traditional Chinese Medicine Against Lymphoma That Regulates the Level of Reactive Oxygen Species

Qiangqiang Zhao[1,2], Jian Li[1], Bin Wu[3], Yinghui Shang[1], Xueyuan Huang[1], Hang Dong[1], Haiting Liu[1], Rong Gui[1] and Xinmin Nie[1]**

[1] Department of Blood Transfusion, The Third Xiangya Hospital, Central South University, Changsha, China, [2] Department of Hematology, The Qinghai Provincial People's Hospital, Xining, China, [3] Department of Transfusion Medicine, Wuhan Hospital of Traditional Chinese and Western Medicine, Tongji Medical College, Huazhong University of Science and Technology, Wuhan, China

Jolkinolide B (JB) is a bioactive compound isolated from a Chinese herbal medicine that exerts antitumor activity. However, the anti-lymphoma effect of JB and its mechanism are yet to be revealed. Because free JB has poor pharmacokinetics and weak antitumor efficacy, we opted to use black phosphorus quantum dot (BPQD) nanomaterials as a drug loading platform to synthesize a nano-traditional Chinese medicine (nano-TCM) called BPQDs@JB. Compared with free JB, Raji cells administrated with BPQDs@JB exhibited the cell viability of 19.85 ± 1.02%, and the production of intracellular reactive oxygen species (ROS) was promoted. Likewise, BPQDs@JB was capable of rising the apoptosis rate of Raji cells to 34.98 ± 1.76%. In nude mice transplanted tumor model administrated with BPQDs@JB, the tumor tissue sections administrated with BPQDS@JB achieved a conspicuous red fluorescence, demonstrating the presence of most ROS production in the BPQDS@JB. TUNEL achieved a number of positive (brown) nuclei *in vivo*, revealing that BPQDS@JB could significantly induce tumor tissue apoptosis. As revealed from the mentioned results, BPQDs@JB can generate considerable ROS and interfere with the redox state to inhibit tumor. In brief, BPQDs@JB may be adopted as a treatment option for lymphoma.

Keywords: black phosphorus quantum dots, Jolkinolide B, apoptosis, reactive oxygen species, lymphoma

OPEN ACCESS

Edited by:
Xiaoli Wei,
University of California, San Diego, United States

Reviewed by:
Dongsheng He,
China Pharmaceutical University, China
Huang Yong,
Guangxi Medical University, China

***Correspondence:**
Rong Gui
aguirong@163.com
Xinmin Nie
niexinmin7440@sina.com

Specialty section:
This article was submitted to Nanoscience, a section of the journal Frontiers in Chemistry

Received: *15 January 2020*
Accepted: *02 June 2020*
Published: *14 July 2020*

Citation:
Zhao Q, Li J, Wu B, Shang Y, Huang X, Dong H, Liu H, Gui R and Nie X (2020) A Nano-Traditional Chinese Medicine Against Lymphoma That Regulates the Level of Reactive Oxygen Species. Front. Chem. 8:565. doi: 10.3389/fchem.2020.00565

INTRODUCTION

Jolkinolide B (JB) is a bioactive compound extracted from *Euphorbia fischeriana*, which grows at high altitude and is a traditional Chinese medicine (TCM) with high medicinal value (Yan et al., 2019). In recent years, research on the antitumor and antiviral effects of JB has gained increased attention (Gao et al., 2016; Xu et al., 2016). In fact, previous studies have shown that JB exhibits antitumor effect on numerous tumor cells. For instance, Yan et al. (Gao and Han, 2018) revealed that JB inhibits the proliferation of non-small cell lung cancer cells by downregulating the expression of hexokinase 2. JB can induce apoptosis and anti-metastasis of the breast cancer cell line, MDA-MB-231 (Xu et al., 2013; Sun et al., 2015; Shen et al., 2017). Previously, JB was also found to induce the apoptosis of the human leukemic cells, HL-60 and THP-1 cells, through the JAK2/STAT3 pathway (Wang et al., 2013). The above studies suggest that JB can be used to treat malignant tumors; however, its anti-lymphoma effect has not yet been reported. To provide an experimental basis for its use in the clinic, we aimed to explore the effect of JB on lymphoma and its possible mechanism.

There are some defects in the active ingredient of TCM (e.g., poor water solubility, low bioavailability and rapid clearance *in vivo*), which limits its clinical application to a certain extent (Yang et al., 2011). With the emergence of nanotechnology, however, these problems have been improved. The loading of TCM into nanocarriers can increase their stability and improve their water solubility, bioavailability, and distribution in tumor tissues through the enhanced permeability and retention (EPR) effect on tumors (Khan et al., 2019). Because of its good biocompatibility, high specific surface area, and drug loading rate (Shao et al., 2016), black phosphorus nanoparticle quantum dot (BPQD) serves as an ideal candidate carrier for drug delivery and antitumor therapy (Li et al., 2017).

BPQD, an ultra-small derivative of BP nanosheet, was discovered in 2015 (Zhang et al., 2015). Because P is a key element in the human body, BPQP can be degraded into non-toxic and biocompatible phosphorus oxide (phosphate or phosphonate), which is well tolerated in the human body (Wang et al., 2015). Guo et al. (2018) confirmed that BPQDs do not exhibit evident cytotoxicity and can be cleared by the kidney. Furthermore, Huang et al. (2019) used erythrocyte membrane camouflage BPQDs combined with doxorubicin and Kirenol as an antitumor therapy. Shang et al. (2019) used BPQDs to load Hederagenin to mediate apoptosis and autophagy against breast cancer. Based on the above results, BPQD is a non-toxic, safe, and efficient nano-drug delivery platform.

To provide a reference for the clinical treatment of lymphoma with nano-TCM according to the above findings, we aimed to construct and synthesize BPQDs@JB nano-TCM and perform a preliminary assessment to derive the strategy and mechanism of this anti-lymphoma TCM nanodrug delivery system (**Figure 1**).

MATERIALS AND METHODS

Materials

The BPQD dispersions were purchased from Yuanduo Biotechnology (China). JB was purchased from Desite Biology (China). DMSO and the dialysis membranes (2 kD) were obtained from Solarbio Science & Technology (China). The Annexin V-FITC/PI apoptosis detection kit was purchased from BD Biosciences (China). The ROS test kit was obtained from Beyotime Biotechnology (China). The CCK-8 cell counting kit was purchased from Dojindo Chemical Technology (Japan). Fetal bovine serum (FBS) and RPMI-1,640 were purchased from Biological Industries (Israel). TdT *in situ* apoptosis detection kit was purchased from R&D Systems (China). DAPI was produced by Servicebio Technology (China). The polycarbonate porous membrane syringe filter (200 nm) was purchased from Whatman (USA).

Cell Culture

Human lymphoma Raji cells were purchased from the Advanced Research Center of Central South University and cultured in RPMI-1,640 medium containing 10% fetal bovine serum. The cells were cultured in a cell incubator at 37°C and 5% CO_2.

Preparation of BPQDs@JB

PBS we used was sterilized at high temperature to reduce the solubility of oxygen in water, i.e., oxygen could be released. BPQDs (1 mg) was dissolved in PBS. JB (1 mg) was dissolved in DMSO. Afterwards, BPQDs@JB was built in a nitrogen-filled environment. After being stirred at 25°C for 24 h, free JB was removed by 2 kD dialysis membrane at ambient temperature. The samples after dialysis were employed to determine the concentration of JB, and the samples after being dialysed were filtered 30 times with a filter under a pore diameter of 200 nm. After the solution was collected and centrifugated at (10,000 rpm × 2 min), the precipitates were washed with ddH_2O 3 times to synthesize BPQDs@JB. The encapsulation efficiency (EE) and load efficiency (LE) of JB were calculated (Zhao et al., 2020) using EE% = Total mass of JB- mass of JB in supernatant/Total mass of JB × 100%; LE% = Total mass of JB-total mass of JB in supernatant/(Total mass of JB-total mass of JB in supernatant) + mass of BPQDs × 100%.

Characterization of BPQDs@JB

The morphology of BPQD was detected with a transmission electron microscope (TEM, Tecnai G2 F20, USA). The particle size and zeta potential values of BPQD were respectively determined with a Zetasizer Nano ZS (Malvern Nano series, Malvern, UK). The absorbance of BPQDs, JB, and BPQDs@JB was measured by UV/Vis spectroscopy (ScanDrop, Analytik Jena, Germany).

BPQDs@JB Release Properties for JB *in vitro*

The *in vitro* drug release experiments were carried out under pH 7.4 and pH 5.0 conditions to determine the ability of BPQDs@JB to release JB in a pH-dependent manner. Thereafter, 1 mL of BPQDs@JB was added to 20 mL of PBS solutions with pH values of 7.4 and 5.0, respectively, and dialyzed at 37°C. The absorbance of JB in the dialysate was measured by a microplate reader (PerkinElmer EnSpire, USA) (Shang et al., 2019). The concentration and cumulative release of JB were calculated complying with the standard curve. The cumulative release percentage (%) of JB in BPQDs@JB at each time point under different conditions was calculated, and the cumulative release curve of time drug was plotted (Zhou et al., 2017).

Cell Viability of BPQDs@JB Assessed by CCK-8

After Raji cells were inoculated into 96-well plates with 5×10^3 cells per well for 24 h, they were treated with 0, 5, 10, 20, 40, and 80 μmol/L of the free JB drug. After 24 h of incubation, 10 μL of CCK-8 was added to each well for an additional 4 h of incubation. Absorbance was then detected at 450 nm. Raji cells were also treated with PBS, BPQDs, JB, and BPQDs@JB, according to the above steps, and the cell survival rates were respectively detected.

Apoptosis Assay of BPQDs@JB by Flow Cytometry *in vitro*

To evaluate the antitumor effect of BPQDs@JB *in vitro*, we employed an Annexin V-FITC/PI apoptosis kit and detected the

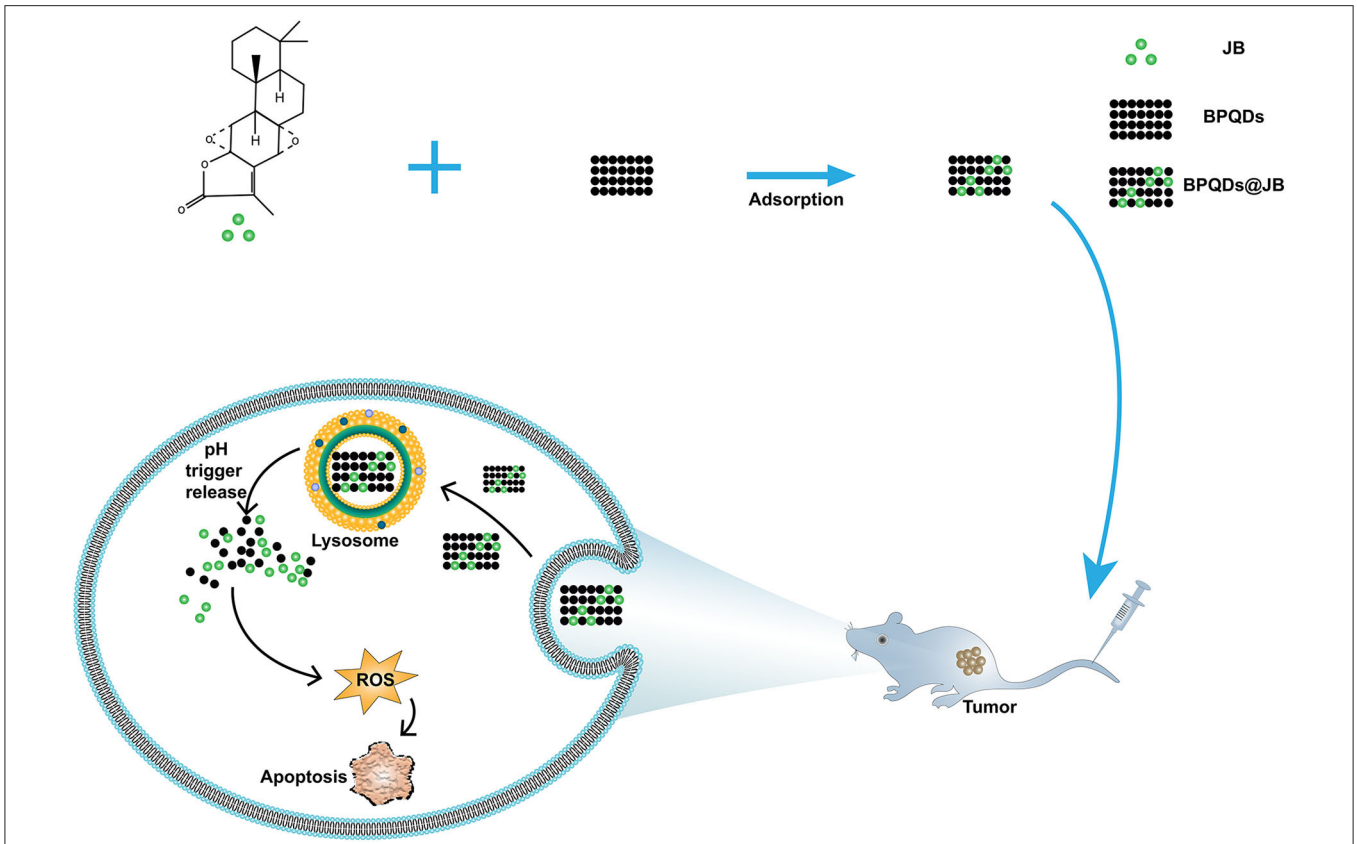

FIGURE 1 | Construction of BPQDs@JB and the schematic diagram of its anti-lymphoma mechanism.

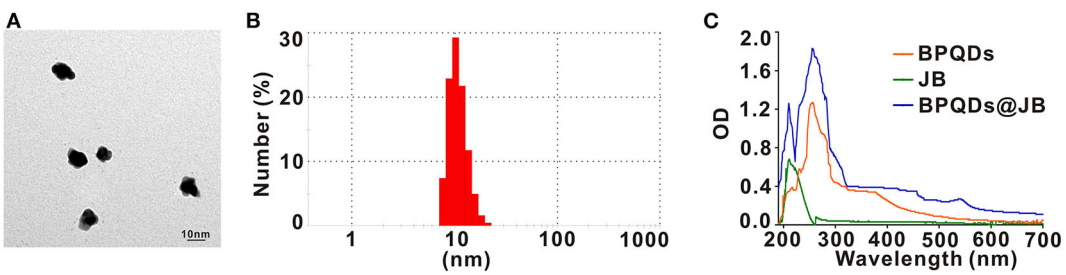

FIGURE 2 | Characterization of BPQDs@JB. **(A)** TEM images of BPQDs. Scale bar: 10 nm. **(B)** Hydraulic radius of BPQDs. **(C)** UV/Vis spectra of BPQDs, JB, and BPQDs@JB.

apoptosis of Raji cells. Briefly, Raji cells were inoculated into a 6-well plate with 1×10^5 cells/well. Thereafter, the cells were treated with PBS, BPQDs, JB, and BPQDs@JB for 24 h. The level of apoptosis was detected by flow cytometry (FACS CantoTM II, BD, USA).

ROS Assay of BPQDs@JB by Flow Cytometry *in vitro*

Raji cells in logarithmic growth phase were inoculated in 6-well plates at the density of 1×10^5 cells/mL. After being cultured for 12 h, the cells were administrated with PBS, BPQDs, JB and BPQDs@JB, respectively. After being cultured for 24 h, the cells were collected. DCFH-DA was diluted to 10 μmol/L in final concentration with serum-free RPMI-1,640 medium. Each well was incubated with 100 μL diluted DCFH-DA, at 37°C, 5% CO_2 incubator for 20 min. The cells were washed gently with serum-free RPMI-1,640 medium 3 times to remove the DCFH-DA that did not enter the cells (the cells should not be sucked out). Photographs were taken under an inverted fluorescence microscope. Flow cytometry was adopted to detect the fluorescence intensity before and after the action of the drug. The excitation wavelength was 488 nm, and the emission wavelength was 525 nm (Li et al., 2019).

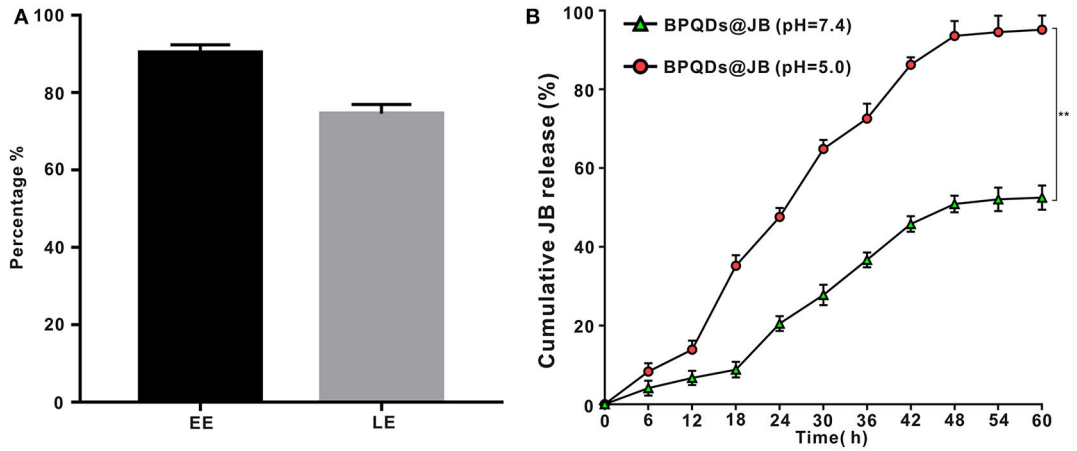

FIGURE 3 | Drug LE of BPQDs and the release rate of BPQDs@JB. **(A)** EE and LE of BPQDs. **(B)** Cumulative release rates of JB from BPQDs@JB at different pH-values (7.4 and 5.0). Compared with the BPQDs@JB (pH = 7.4) group, $^{**}p < 0.01$.

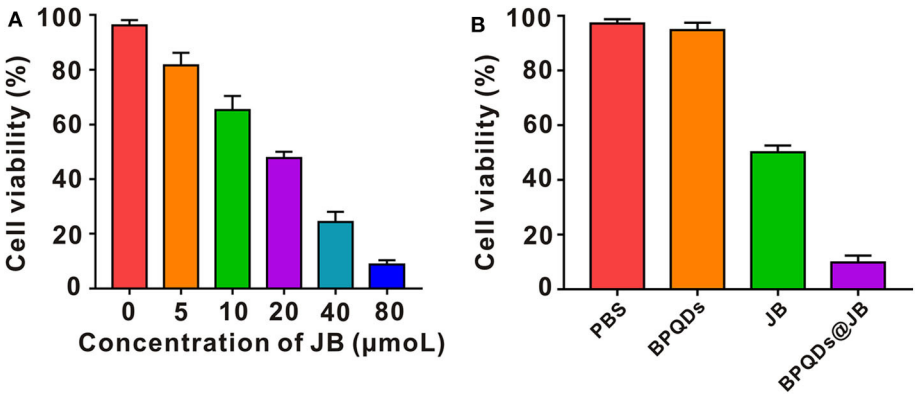

FIGURE 4 | Effect of BPQDs@JB on Raji cell viability *in vitro*. **(A)** Viability of Raji cells following treatment with different concentrations of JB (IC50). **(B)** Raji cell viability following the administration of PBS, BPQDs, JB, and BPQDs@JB for 24 h. Data are presented as mean ± SD ($n = 3$).

Establishment of the Tumor-Bearing Mouse Model of Lymphoma

Six-week-old Balb/c nude mice were purchased from Hunan SJA Experimental Animal Co., Ltd (China). Each mouse was subcutaneously injected 6×10^7 Raji cells/100 μL. When a tumor volume of 100 mm^3 was achieved, this indicated the successful establishment of the tumor model.

BPQDs@JB Treatment in Lymphoma-Bearing Mice

After animals were randomly divided into four groups ($n = 3$), 100 μL of PBS, BPQDs, JB, and BPQDs-JB was injected into the tail vein of mice every 3 days for a total of four times. Thereafter, the tumor size of animals were measured every 3 days. On day 21, the animals were killed and their tumors and visceral tissues (heart, liver, spleen, lung, and kidney) were collected. Tumor tissues and organs were fixed with 4% formalin and frozen at −80°C. The fixed tissues were embedded in paraffin and sliced into sections for H&E staining, immunofluorescent staining, and immunohistochemical staining.

TABLE 1 | A table to summarize all data in **Figure 4B** by putting the respective numbers.

	PBS	BPQDs	JB	BPQDs@JB
Cell viability (%)	97.17 ± 1.68	94.83 ± 2.56	50.08 ± 2.37***	19.85 ± 1.02****

*Compared with the PBS group, ***$p < 0.001$, ****$p < 0.0001$.*

ROS and TUNEL Assays *in vivo*

Briefly, paraffin-embedded tissue samples were dewaxed for antigen recovery. Thereafter, the nuclei of apoptotic cells were identified with a TDT *in situ* apoptosis kit. The morphology of cells was observed and images were captured with a light microscope. ROS was observed via DCFH-DA immunofluorescence staining. The nucleus was stained with DAPI. The images were analyzed and captured with a laser confocal microscope (LCFM, LSM700, Germany).

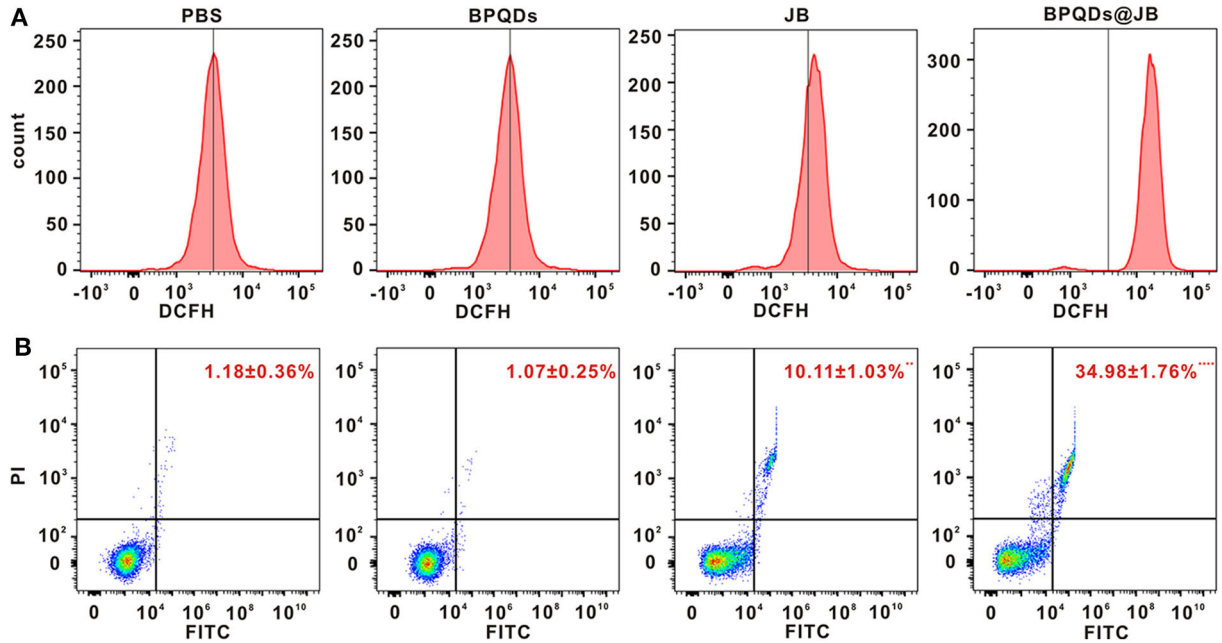

FIGURE 5 | ROS and Apoptosis assessment by flow cytometry *in vitro*. **(A)** Flow cytometric detection of ROS level in Raji cells treated with PBS, BPQDs, JB, and BPQDS@JB for 24 h. **(B)** Flow cytometric assessment of the level of apoptosis in Raji cells administered PBS, BPQDs, JB, and BPQDS@JB for 24 h. Data are presented as mean ± SD ($n = 3$). Compared with the PBS group, $^{**}p < 0.01$, $^{****}p < 0.0001$.

Statistical Analysis

Data were assessed by SPSS 18.0 and expressed as mean ± SD. Intergroup differences were assessed by One-Way ANOVA, followed by Tukey's *post-hoc* test ($^{*}p < 0.05$, $^{**}p < 0.01$, $^{***}p < 0.001$, and $^{****}p < 0.0001$).

RESULTS AND DISCUSSION

Preparation and Characterization of BPQDs@JB Nano-TCM

To prepare the BPQDs@JB nano-TCM, JB was first loaded into BPQDs to derive BPQDs@JB (**Figure 1**). Through TEM imaging, BPQDs and BPQDs@JB were recognized to be monodispersed (**Figure 2A** and **Figure S1A**), the obtained BPQDs and BPQDs@JB were 12 nm in size on average by dynamic light scattering (**Figure 2B** and **Figure S1B**). Since BPQDs is negatively charged in water (Tayari et al., 2015). Small molecule drugs with positive charge are likely to be adsorbed by BPQDs by electrostatic interaction (Chen et al., 2017). Thus, the interaction mechanism between BPQDs and JB may be the electrostatic interaction of charge adsorption. As shown in **Figure S1C**, the Zeta potentials of BPQDs and BPQDs@JB were −37.26 ± 1.7 mV, −28.07 ± 1.6 mV, respectively. UV/Vis spectra (**Figure 2C**) of BPQDs@JB revealed absorption peaks at 256 and 211 nm, which align with the absorption peaks of BPQDs and JB, respectively. Therefore, BPQDs@JB was successfully assembled.

EE and LE of the Drug, and the Release Rate of BPQDs@JB

As new two-dimensional material, black phosphorus, which has good biodegradability, could be utilized in drug delivery (Chen et al., 2017). Compared to BP nanosheets, BPQD is more attractive for drug delivery systems owing to its smaller size (Geng et al., 2018). By using BPQD-loaded drugs, we found that the EE and LE of JB in the BPQDs@JB nano-TCM were 90.3 ± 2.1% and 74.6 ± 2.4%, respectively (**Figure 3A**). Thereafter, we proceeded to evaluate the drug release characteristics of BPQDs@JB. As shown in **Figure 3B**, when BPQDs@JB exhibited a pH of 5.0, the cumulative release rates of JB at 6, 12, 18, 24, 30, 36, 42, 48, 54, and 60 h were 8.3 ± 2.1%, 13.9 ± 2.3%, 35.2 ± 2.7%, 47.6 ± 2.3%, 64.9 ± 2.3%, 72.6 ± 3.8%, 86.3 ± 1.9%, 93.6 ± 3.8%, 94.5 ± 4.2%, 95.2 ± 3.6%, respectively, and at pH 7.4, the cumulative release rate of JB at 6, 12, 18, 24, 30, 36, 42, 48, 54, and 60 h were 3.9 ± 1.3%, 5.9 ± 1.8%, 8.8 ± 2.0%, 20.5 ± 1.9%, 27.8 ± 2.6%, 36.5 ± 1.9%, 45.3 ± 2.0%, 50.9 ± 2.1%, 52.1 ± 3.0%, 52.5 ± 3.1%, respectively. Therefore, the release rate of JB at pH 5.0 was higher than that at pH 7.4. Moreover, an increase in cumulative drug release was identified, thereby indicating the accelerated degradation of BPQDs under acidic conditions (Zhou et al., 2018). Because the tumor environment is weakly acidic (Matsumoto et al., 2017), BPQDs@JB is a type of nano-TCM released in response to pH, which is beneficial for the treatment of tumor. Generally, the above findings demonstrate that BPQD is an efficient drug carrier, and an acidic environment enables the release of JB from BPQDs@JB.

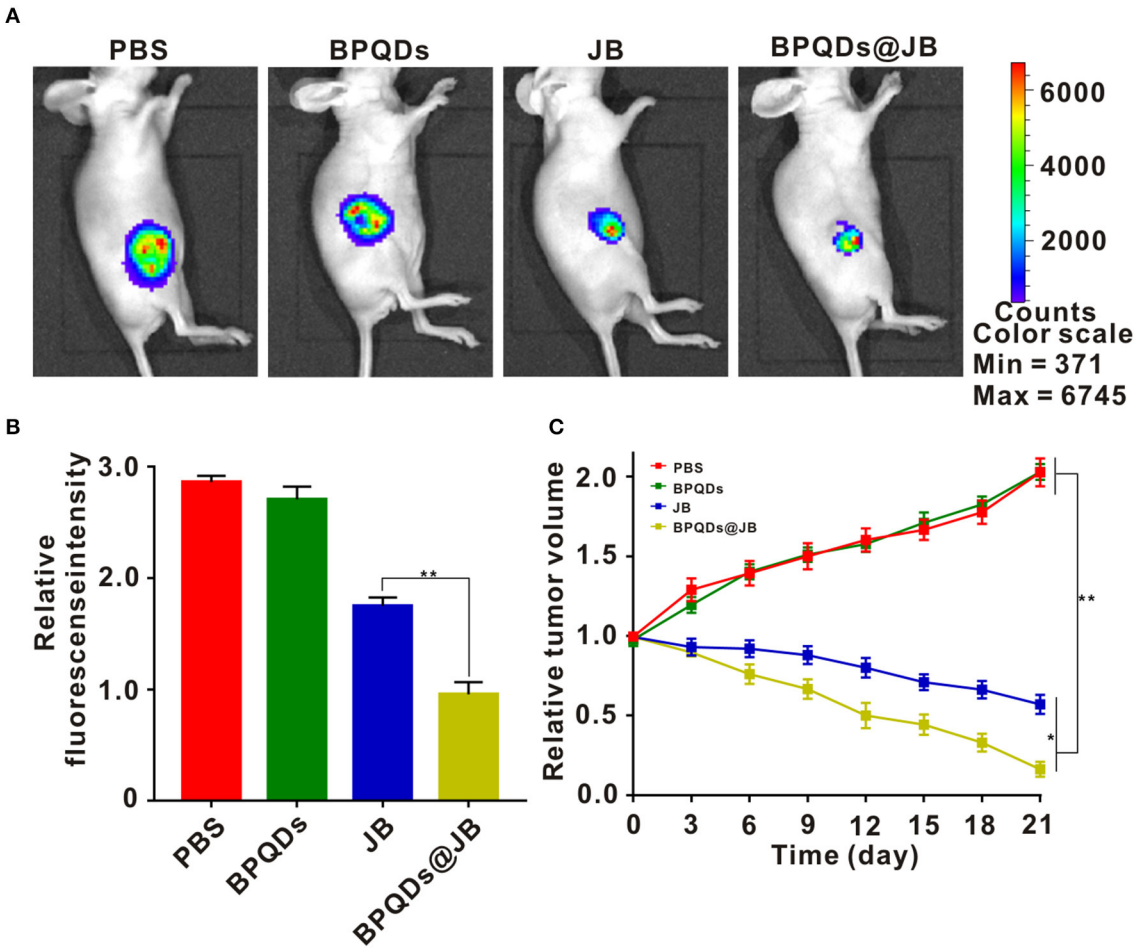

FIGURE 6 | Antitumor effects of BPQDs@JB *in vivo*. **(A)** After intravenous injection of PBS, BPQDS, JB, and BPQDs@JB into the tail vein of nude mice, the fluorescence signal images of tumor tissues were detected on day 21. **(B)** Semi-quantitative evaluation of the fluorescence signal of tumor tissue samples in each group. **(C)** Changes in tumor volume in the Raji tumor-bearing mouse model during treatment. Data are expressed as mean ± SD ($n = 3$; $^{*}p < 0.05$, $^{**}p < 0.01$).

Effect of BPQDs@JB on Raji Cell Viability *in vitro*

Raji cells were isolated and established from Burkitt's lymphoma of the left upper jaw in an 11-year-old black boy, i.e., the origin of B cells (Theofilopoulos et al., 1974). Since Burkitt's Lymphoma is considered a highly invasive and malignant non-Hodgkin's Lymphoma (Ribrag et al., 2016), Raji cells were taken to conduct the experimental study. Raji cells were administrated with BPDs at concentrations of 0, 0.25, 0.5, 1.0, and 2.0 mg/mL for 24 h, respectively, and the cell viability rate was determined by CCK-8. As shown in supporting Information **Figure S2**, the cell viability rate of Raji cells incubated with a series of concentrations of BPDs for 24 h, of which the viability rate of Raji cells administrated with 2.0 mg/mL CCM@MSNs was as high as 90%. Therefore, BPQDs (concentration of 0.25 mg/ml) were taken as the follow-up experiment. Then, Raji cells were treated with different concentrations of JB. According to the cell survival rate, the IC50 value of JB was ∼20 μmol/L (**Figure 4A**). Thus, JB (concentration of 20 μmol/L) for the follow-up experiment. To compare the survival rate of Raji cells between BPQDs@JB and free JB, the JB in BPQDs@JB was diluted to 20 μmol/L in concentration for the follow-up experiment. Thereafter, Raji cells were respectively treated with PBS, BPQDs, JB, and BPQDs@JB. As shown in **Figure 4B** and **Table 1,** the CCK-8 results revealed that PBS and BPQDs had no evident toxic effects on Raji cells. The cell viability of Raji cells administrated with free JB was 50.08 ± 2.37%. However, the cell viability of Raji cells administrated with BPQDs@JB was (19.85 ± 1.02%). Compared with JB group, the cell viability of BPQDs@JB group decreased significantly. Therefore, BPQDs@JB nano-TCM has a stronger anti-lymphoma effect than using JB alone.

ROS and Apoptosis Assessment by Flow Cytometry *in vitro*

Oxidative stress caused by reactive oxygen species (ROS) might serve as an important factor in tumor occurrence and development. Recent studies have shown that excessive ROS can lead to the apoptosis and necrosis of tumor cells (Wu

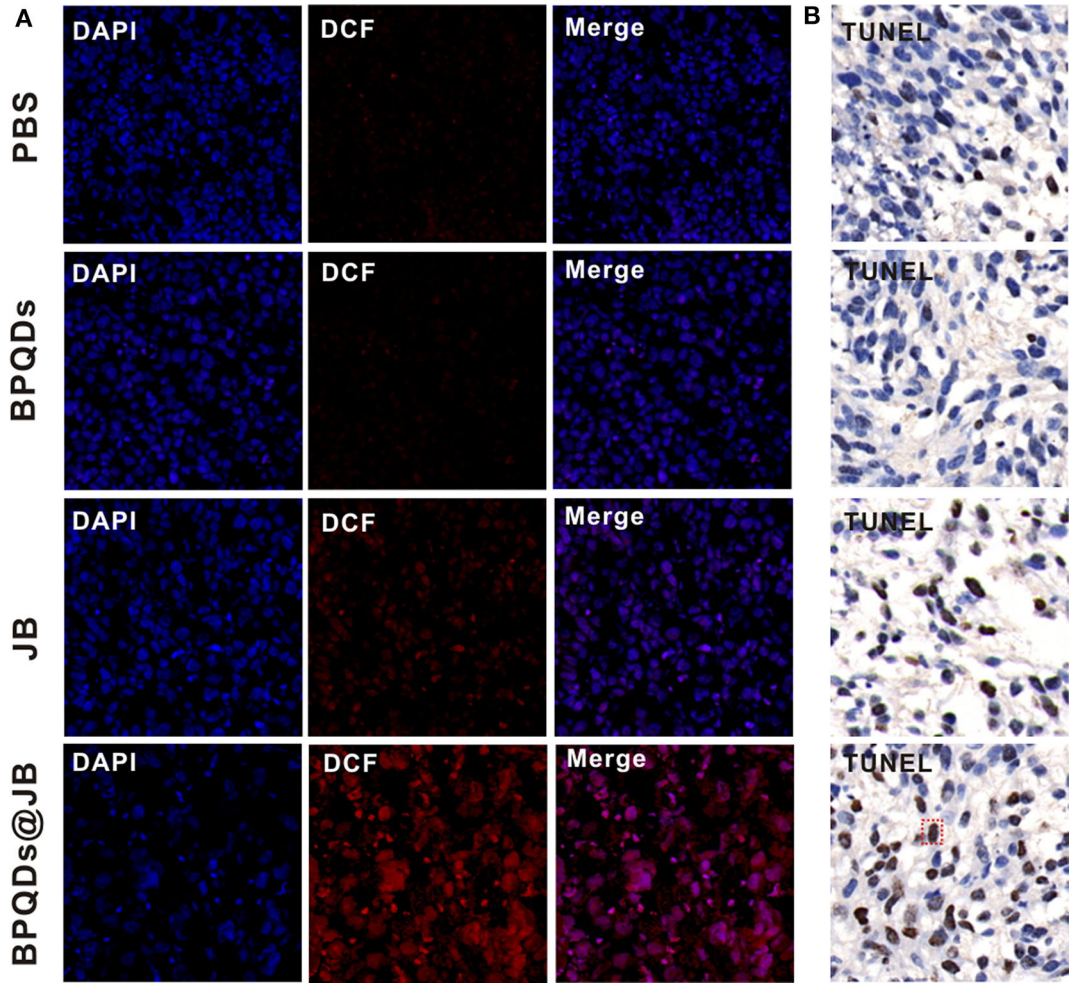

FIGURE 7 | Changes in the level of ROS and the results of the TUNEL assay. **(A)** After 21 days of administering PBS, BPQDs, JB, and BPQDs@JB into the tail vein of mice, the level of ROS in the tumor tissue was detected by immunofluorescence. **(B)** Tumor tissues were assessed at 21 days after intravenous injection of PBS, BPQDs, JB, and BPQDs@JB via TUNEL assays.

et al., 2019). Ren et al. (2016) revealed that psoralen induces DNA damage and apoptosis in breast cancer cells by inducing ROS production. To verify whether JB can kill Raji cells via ROS production, we sought to determine the effect of PBS, BPQDs, JB, and BPQDs@JB on Raji cells by flow cytometry. As shown in **Figure 5A** and **Figure S3A**, compared to treatment with PBS and BPQDs, treatment with the BPQDs@JB nano-TCM or JB could cause a shift to the right in the histogram, suggesting that the latter two groups can produce a large amount of ROS, with BPQDS@JB producing more ROS than JB. The same result is shown in **Figure S3B**, the red fluorescence intensity of BPQDs@JB was significantly stronger than that of other groups, revealing that BPQDs@JB can significantly increase ROS in Raji cells. Flow cytometry was subsequently employed to further detect the apoptotic effect of PBS, BPQDs, JB, and BPQDs@JB on Raji cells. As shown in **Figure 5B**, compared to the PBS group, the BPQD group did not cause significant apoptosis of Raji cells. However, after treatment with BPQDs@JB nano-TCM, the apoptotic rate of Raji cells was 34.98 ± 1.76%, a value higher than that achieved following treatment with JB (10.11 ± 1.03%). This finding indicates that BPQDs@JB nano-TCM could better induce Raji cell apoptosis than free JB. Therefore, BPQDs@JB nano-TCM can induce apoptosis of Raji cells via ROS production.

Antitumor Effects of BPQDs@JB *in vivo*

Herein, we employed the Raji tumor-bearing mouse model to elucidate the anti-lymphoma effects of BPQDs@JB *in vivo*. PBS, BPQDs, JB, and BPQDs@JB were injected into the tail vein of Raji tumor-bearing mice. On day 21, these nude mice were observed with a live imager. As shown in **Figures 6A,B**, the tumor fluorescence signal intensity of the JB group and BPQDs@JB group was significantly weaker than that of the PBS group and BPQDs group. Further, the tumor fluorescence signal intensity of the BPQDs@JB group was weaker than that of the other groups. Similarly, as illustrated in **Figure 6C**, after 21 days of monitoring the changes in tumor volume, BPQDs@JB

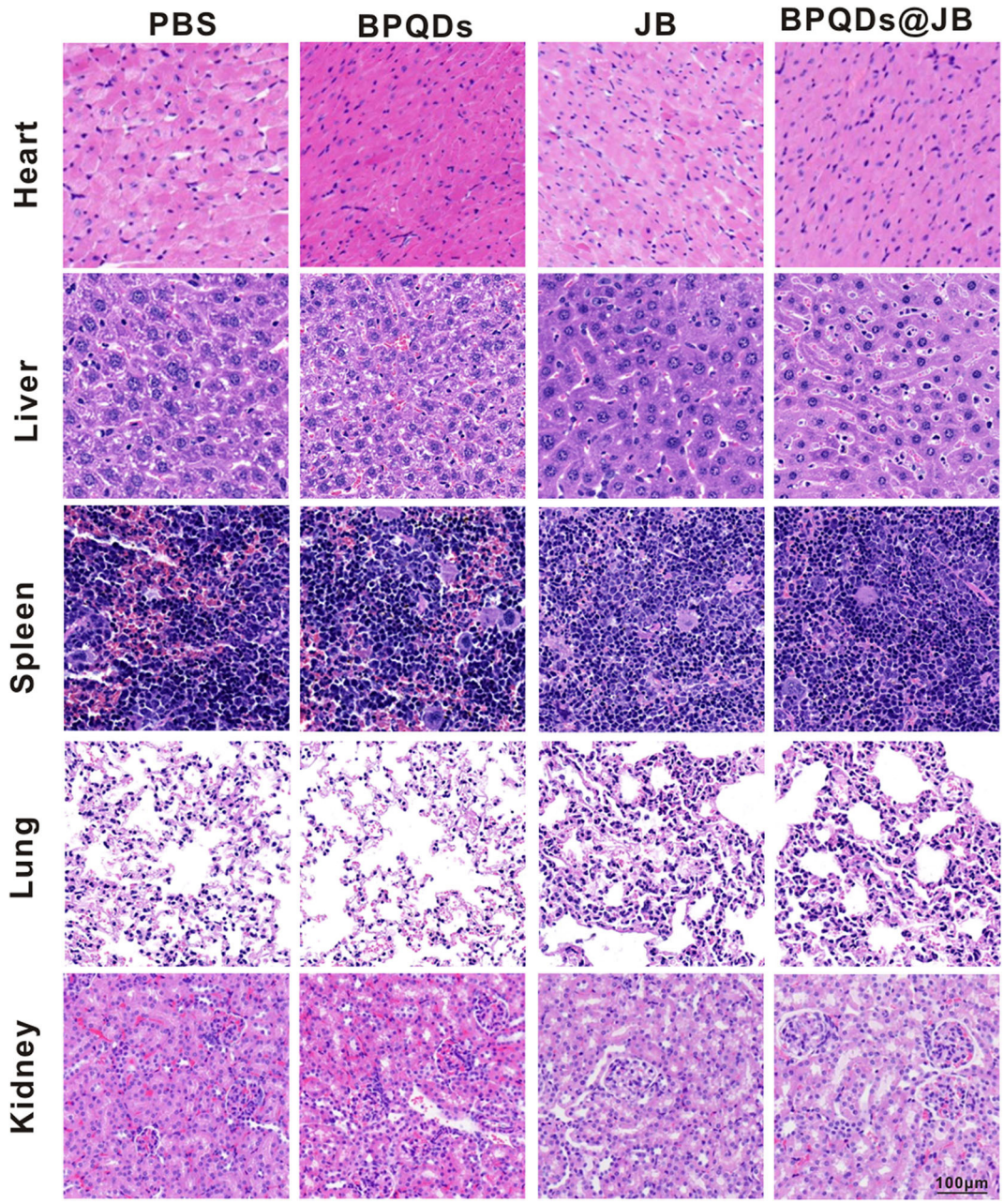

FIGURE 8 | PBS, BPQDs, JB, and BPQDS@JB were injected into the tail vein of nude mice for 21 days. The heart, liver, spleen, lung, and kidney of nude mice were retrieved for histological imaging. Scale bar: 100 μm.

exerted a better anti-lymphoma effect than JB alone. These findings suggest that BPQDs@JB exhibits an enhanced antitumor effect *in vivo*.

Change in ROS Level and the Results of the TUNEL Assay

imbalance in ROS level in tumor cells can activate the apoptotic pathway and induce apoptosis (Uthaman et al., 2019). Therefore, breaking the redox state in tumor cells is an effective strategy for the treatment of tumors. Presently, this strategy has been employed to synthesize numerous drugs, which are either being developed or have entered clinical trials, and exhibit good anticancer effects (Martin-Cordero et al., 2012; Raza et al., 2017). As BPQDs@JB nano-TCM produced a large amount of ROS against lymphoma *in vitro*, we opted to further detect the level of ROS produced by BPQDs@JB *in vivo*. As shown in **Figure 7A**, the tumor tissue sections treated with BPQDS@JB exhibited a Conspicuous red fluorescence. However, the fluorescence exhibited by sections treated with

JB was significantly weaker than that exhibited by sections treated with BPQDS@JB. A slight red fluorescence was also observed in the PBS group and BPQD group, suggesting that most ROS production occurred in the BPQDS@JB group. We proceeded to use the TUNEL method to detect the level of apoptosis in tumor tissue. As shown in **Figure 7B**, the number of positive (brown) nuclei in the BPQDs@JB group was significantly greater than that in other groups. Such finding indicates that the results of TUNEL detection in tumor tissue sections *in vivo* were consistent with those of the apoptosis induced by BPQDs@JB *in vitro*. These results suggest that BPQDs@JB can produce excessive ROS to inhibit tumor and interfere with the new strategy of the redox state against lymphoma.

Safety Evaluation of Important Organs by BPQDs@JB

BPQD nano-TCM exerted a significant anti-lymphoma effect *in vitro* and *in vivo*. To verify the safety of BPQD nano-TCM *in vivo*, we used H&E staining to determine its toxic effect on the heart, liver, spleen, lung, and kidney. The histological data of the heart, liver, spleen, lung, and kidney revealed no abnormalities in the PBS group, BPQD group, JB group, and BPQDs@JB group (**Figure 8**). There were no abnormal changes in WBC, HGB, PLT, ALT, AST, BUN, CRE, CK, and Myo in nude mice treated with PBS, BPQDs, JB, and BPQDs@JB (**Supporting Table 1**). Such findings demonstrate that BPQDs@JB did not cause any side effects and may serve as a safe and effective nano-TCM.

CONCLUSIONS

In the present study, we revealed that the newly derived two-dimensional material, BPQD, exhibit many properties with a high drug-loading rate, which is similar to an aircraft carrier, thereby enabling its transport of numerous drug molecules. The release of JB from BPQDs@JB can be accelerated in the acidic microenvironment of the tumor. As a result, BPQDs@JB nano-TCM kills lymphoma cells by regulating ROS. Because of these characteristics, BPQD is a non-toxic and efficient drug delivery platform. To summarize, herein, we revealed the role and potential mechanism of BPQDs@JB nano-TCM in the treatment of lymphoma. Hopefully, it can provide a novel idea for the treatment of lymphoma.

DATA AVAILABILITY STATEMENT

All datasets generated for this study are included in the article/**Supplementary Material**.

ETHICS STATEMENT

The animal study was reviewed and approved by the experimental protocols involving all mouse in the present study were approved by the Institutional Animal Care and Use Committee of Xiangya Medical College of Central South University, and the mouse were kept according to the institutional ethical guidelines of Central South University.

AUTHOR CONTRIBUTIONS

RG and XN designed the experiment. QZ carried out the experiment. JL, BW, YS, XH, HD, and HL contributed to analyze the experimental results. QZ wrote the manuscript. All authors contributed to the article and approved the submitted version.

FUNDING

This work was supported by the National Natural Science Foundation of China (Nos. 8157120841, 81971748, and 81301507); the Fundamental Research Funds for the Central Universities of Central South University under Grant (No. 2019zzts366); the guiding project of Qinghai Provincial Health and Family Planning Commission (2018-wjzdx-17).

ACKNOWLEDGMENTS

First of all, I would like to thank my mentor, RG, for her careful guidance on the development of the project, the details of the experiment, and the writing of the thesis. I would like to acknowledge JL and BW for their concern and help, which enabled me to tide over the difficulties in my life and study. Finally, I would like to thank my parents and thank them for their support as always.

SUPPLEMENTARY MATERIAL

The Supplementary Material for this article can be found online at: https://www.frontiersin.org/articles/10.3389/fchem.2020.00565/full#supplementary-material

REFERENCES

Chen, W., Ouyang, J., Liu, H., Chen, M., Zeng, K., Sheng, J., et al. (2017). Black phosphorus nanosheet-based drug delivery system for synergistic photodynamic/photothermal/chemotherapy of cancer. *Adv. Mater.* 29:3864. doi: 10.1002/adma.201603864

Gao, C., Yan, X., Wang, B., Yu, L., Han, J., Li, D., et al. (2016). Jolkinolide b induces apoptosis and inhibits tumor growth in mouse melanoma b16f10 cells by altering glycolysis. *Sci. Rep.* 6:36114. doi: 10.1038/srep36114

Gao, X., and Han, H. (2018). Jolkinolide b inhibits glycolysis by downregulating hexokinase 2 expression through inactivating the akt/mtor pathway in non-small cell lung cancer cells. *J. Cell Biochem.* 119, 4967–4974. doi: 10.1002/jcb.26742

Geng, S., Wu, L., Cui, H., Tan, W., Chen, T., Chu, P. K., et al. (2018). Synthesis of lipid-black phosphorus quantum dot bilayer vesicles for near-infrared-controlled drug release. *Chem. Commun. (Camb)* 54, 6060–6063. doi: 10.1039/C8CC03423K

Guo, T., Wu, Y., Lin, Y., Xu, X., Lian, H., Huang, G., et al. (2018). Black phosphorus quantum dots with renal clearance property for efficient photodynamic therapy. *Small* 14:2815. doi: 10.1002/smll.201702815

Huang, X., Wu, B., Li, J., Shang, Y., Chen, W., Nie, X., et al. (2019). Anti-tumour effects of red blood cell membrane-camouflaged black phosphorous quantum dots combined with chemotherapy and anti-inflammatory therapy. *Artif. Cells Nanomed. Biotechnol.* 47, 968–979. doi: 10.1080/21691401.2019.1584110

Khan, S., Setua, S., Kumari, S., Dan, N., Massey, A., Hafeez, B. B., et al. (2019). Superparamagnetic iron oxide nanoparticles of curcumin enhance gemcitabine therapeutic response in pancreatic cancer. *Biomaterials* 208, 83–97. doi: 10.1016/j.biomaterials.2019.04.005

Li, W. D., Yu, S., Luo, S. M., Shen, W., Yin, S., and Sun, Q. Y. (2019). Melatonin defends mouse oocyte quality from benzo[ghi]perylene-induced deterioration. *J. Cell. Physiol.* 234, 6220–6229. doi: 10.1002/jcp.27351

Li, Y., Liu, Z., Hou, Y., Yang, G., Fei, X., Zhao, H., et al. (2017). Multifunctional nanoplatform based on black phosphorus quantum dots for bioimaging and photodynamic/photothermal synergistic cancer therapy. *ACS Appl. Mater. Interfaces* 9, 25098–25106. doi: 10.1021/acsami.7b05824

Martin-Cordero, C., Leon-Gonzalez, A. J., Calderon-Montano, J. M., Burgos-Moron, E., and Lopez-Lazaro, M. (2012). Pro-oxidant natural products as anticancer agents. *Curr. Drug Targets* 13, 1006–1028. doi: 10.2174/138945012802009044

Matsumoto, A., Stephenson-Brown, A. J., Khan, T., Miyazawa, T., Cabral, H., Kataoka, K., et al. (2017). Heterocyclic boronic acids display sialic acid selective binding in a hypoxic tumor relevant acidic environment. *Chem. Sci.* 8, 6165–6170. doi: 10.1039/C7SC01905J

Raza, M. H., Siraj, S., Arshad, A., Waheed, U., Aldakheel, F., Alduraywish, S., et al. (2017). Ros-modulated therapeutic approaches in cancer treatment. *J. Cancer Res. Clin. Oncol.* 143, 1789–1809. doi: 10.1007/s00432-017-2464-9

Ren, G., Luo, W., Sun, W., Niu, Y., Ma, D. L., Leung, C. H., et al. (2016). Psoralidin induced reactive oxygen species (ros)-dependent DNA damage and protective autophagy mediated by nox4 in breast cancer cells. *Phytomedicine* 23, 939–947. doi: 10.1016/j.phymed.2016.05.008

Ribrag, V., Koscielny, S., Bosq, J., Leguay, T., Casasnovas, O., Fornecker, L. M., et al. (2016). Rituximab and dose-dense chemotherapy for adults with burkitt's lymphoma: a randomised, controlled, open-label, phase 3 trial. *Lancet* 387, 2402–2411. doi: 10.1016/S0140-6736(15)01317-3

Shang, Y., Wang, Q., Wu, B., Zhao, Q., Li, J., Huang, X., et al. (2019). Platelet-membrane-camouflaged black phosphorus quantum dots enhance anticancer effect mediated by apoptosis and autophagy. *ACS Appl. Mater. Interfaces* 11, 28254–28266. doi: 10.1021/acsami.9b04735

Shao, J., Xie, H., Huang, H., Li, Z., Sun, Z., Xu, Y., et al. (2016). Biodegradable black phosphorus-based nanospheres for *in vivo* photothermal cancer therapy. *Nat. Commun.* 7:12967. doi: 10.1038/ncomms12967

Shen, L., Zhang, S. Q., Liu, L., Sun, Y., Wu, Y. X., Xie, L. P., et al. (2017). Jolkinolide a and jolkinolide b inhibit proliferation of a549 cells and activity of human umbilical vein endothelial cells. *Med. Sci. Monit.* 23, 223–237. doi: 10.12659/MSM.902704

Sun, C., Cui, H., Yang, H., Du, X., Yue, L., Liu, J., et al. (2015). Anti-metastatic effect of jolkinolide b and the mechanism of activity in breast cancer mda-mb-231 cells. *Oncol. Lett.* 10, 1117–1122. doi: 10.3892/ol.2015.3310

Tayari, V., Hemsworth, N., Fakih, I., Favron, A., Gaufres, E., Gervais, G., et al. (2015). Two-dimensional magnetotransport in a black phosphorus naked quantum well. *Nat. Commun.* 6:7702. doi: 10.1038/ncomms8702

Theofilopoulos, A. N., Bokisch, V. A., and Dixon, F. J. (1974). Receptor for soluble c3 and c3b on human lymphoblastoid (raji) cells. Properties and biologocal significance. *J. Exp. Med.* 139, 696–711. doi: 10.1084/jem.139.3.696

Uthaman, S., Pillarisetti, S., Mathew, A. P., Kim, Y., Bae, W. K., Huh, K. M., et al. (2019). Long circulating photoactivable nanomicelles with tumor localized activation and ros triggered self-accelerating drug release for enhanced locoregional chemo-photodynamic therapy. *Biomaterials* 232:119702. doi: 10.1016/j.biomaterials.2019.119702

Wang, H., Yang, X., Shao, W., Chen, S., Xie, J., Zhang, X., et al. (2015). Ultrathin black phosphorus nanosheets for efficient singlet oxygen generation. *J. Am. Chem. Soc.* 137, 11376–11382. doi: 10.1021/jacs.5b06025

Wang, J. H., Zhang, K., Niu, H. Y., Shu, L. H., Yue, D. M., Li, D., et al. (2013). Jolkinolide b from euphorbia fischeriana steud induces in human leukemic cells apoptosis via jak2/stat3 pathways. *Int. J. Clin. Pharmacol. Ther.* 51, 170–178. doi: 10.5414/CP201807

Wu, B., Huang, X. Y., Li, L., Fan, X. H., Li, P. C., Huang, C. Q., et al. (2019). Attenuation of diabetic cardiomyopathy by relying on kirenol to suppress inflammation in a diabetic rat model. *J. Cell. Mol. Med.* 23, 7651–7663. doi: 10.1111/jcmm.14638

Xu, H. Y., Chen, Z. W., Hou, J. C., Du, F. X., and Liu, J. C. (2013). Jolkinolide b induces apoptosis in mcf-7 cells through inhibition of the pi3k/akt/mtor signaling pathway. *Oncol. Rep.* 29, 212–218. doi: 10.3892/or.2012.2113

Xu, X., Liu, N., Zhang, Y. X., Cao, J., Wu, D., Peng, Q., et al. (2016). The protective effects of hjb-1, a derivative of 17-hydroxy-jolkinolide b, on lps-induced acute distress respiratory syndrome mice. *Molecules* 21:77. doi: 10.3390/molecules21010077

Yan, Y., Wang, Y., Wang, X., Liu, D., Wu, X., Xu, C., et al. (2019). The effects of jolkinolide b on hepg2 cells as revealed by (1)h-nmr-based metabolic profiling. *Eur. J. Pharmacol.* 842, 10–19. doi: 10.1016/j.ejphar.2018.10.025

Yang, J., Ni, B., Liu, J., Zhu, L., and Zhou, W. (2011). Application of liposome-encapsulated hydroxycamptothecin in the prevention of epidural scar formation in new zealand white rabbits. *Spine J.* 11, 218–223. doi: 10.1016/j.spinee.2011.01.028

Zhang, X., Xie, H., Liu, Z., Tan, C., Luo, Z., Li, H., et al. (2015). Black phosphorus quantum dots. *Angew. Chem. Int. Ed. Engl.* 54, 3653–3657. doi: 10.1002/anie.201409400

Zhao, Q., Li, J., Wu, B., Shang, Y., Huang, X., Dong, H., et al. (2020). Smart biomimetic nanocomposites mediate mitochondrial outcome through aerobic glycolysis reprogramming: a promising treatment for lymphoma. *ACS Appl. Mater. Interfaces* 12, 22687–22701. doi: 10.1021/acsami.0c05763

Zhou, S., Wu, D., Yin, X., Jin, X., Zhang, X., Zheng, S., et al. (2017). Intracellular ph-responsive and rituximab-conjugated mesoporous silica nanoparticles for targeted drug delivery to lymphoma b cells. *J. Exp. Clin. Cancer Res.* 36:24. doi: 10.1186/s13046-017-0492-6

Zhou, W., Cui, H., Ying, L., and Yu, X. F. (2018). Enhanced cytosolic delivery and release of crispr/cas9 by black phosphorus nanosheets for genome editing. *Angew. Chem. Int. Ed. Engl.* 57, 10268–10272. doi: 10.1002/anie.201806941

Conflict of Interest: The authors declare that the research was conducted in the absence of any commercial or financial relationships that could be construed as a potential conflict of interest.

frontiers in Chemistry

MINI REVIEW
published: 16 July 2020
doi: 10.3389/fchem.2020.00535

Indocyanine Green Nanoparticles: Are They Compelling for Cancer Treatment?

Marta Sevieri[1], Filippo Silva[1], Arianna Bonizzi[1], Leopoldo Sitia[1], Marta Truffi[2], Serena Mazzucchelli[1] and Fabio Corsi[1,2]**

[1] Laboratorio di Nanomedicina, Dipartimento di Scienze Biomediche e Cliniche "L. Sacco", Università di Milano, Milan, Italy, [2] Laboratorio di Nanomedicina e Imaging Molecolare, Istituti Clinici Scientifici Spa-Società Benefit IRCCS, Pavia, Italy

Indocyanine green (ICG) is a Food and Drug Administration–approved near-infrared fluorescent dye, employed as an imaging agent for different clinical applications due to its attractive physicochemical properties, high sensitivity, and safety. However, free ICG suffers from some drawbacks, such as relatively short circulation half-life, concentration-dependent aggregation, and rapid clearance from the body, which would confine its feasible application in oncology. Here, we aim to discuss encapsulation of ICG within a nanoparticle formulation as a strategy to overcome some of its current limitations and to enlarge its possible applications in cancer diagnosis and treatment. Our purpose is to provide a short but exhaustive overview of clinical outcomes that these nanocomposites would provide, discussing opportunities, limitations, and possible impacts with regard to the main clinical needs in oncology.

Keywords: nanoparticles, cancer, indocyanine green (ICG), diagnosis, treatment

OPEN ACCESS

Edited by:
Xiaoli Wei,
University of California, San Diego, United States

Reviewed by:
Yuanyuan Su,
Soochow University, China
Feihu Wang,
Johns Hopkins University, United States

***Correspondence:**
Serena Mazzucchelli
serena.mazzucchelli@unimi.it
Fabio Corsi
fabio.corsi@unimi.it

Specialty section:
This article was submitted to Nanoscience, a section of the journal Frontiers in Chemistry

Received: *08 April 2020*
Accepted: *25 May 2020*
Published: *16 July 2020*

Citation:
Sevieri M, Silva F, Bonizzi A, Sitia L, Truffi M, Mazzucchelli S and Corsi F (2020) Indocyanine Green Nanoparticles: Are They Compelling for Cancer Treatment? Front. Chem. 8:535. doi: 10.3389/fchem.2020.00535

INTRODUCTION

Recently, growing attention has been addressed to nanocarriers for Indocyanine green (ICG) delivery with the purpose of overcoming some of its current limitations and to expand its possible applications in cancer diagnosis and treatment (Wang et al., 2018). ICG is a widely investigated near infrared (NIR) fluorescent agent, approved for clinical use by the Food and Drug Administration (FDA) in the 1950s (Landsman et al., 1976; Alius et al., 2018). Over the past decade, NIR optical imaging using ICG has become determining for a variety of applications, including lymphangiography, intra-operative lymph node (LN) identification, tissue perfusion, detection of vital structures, and tumor imaging (Fox and Wood, 1960; Starosolski et al., 2017). ICG displays several advantages thoroughly verified during its long clinical use: it is easy to use, cost-effective, radiation-free, and safe. Although ICG fluorescent imaging represents a promising medical tool, its application remains limited due to the intrinsic issues related to ICG degradation and rapid blood clearance (Muckle, 1976; Saxena et al., 2003; Zheng et al., 2012). Therefore, many studies suggest that the exploitation of ICG-based nano-formulations (micelles, polymeric nanoparticles, silica nanoparticles, and liposomes) could boost the efficacy, specificity, and biosafety of this imaging agent for potential oncological applications (Yan et al., 2016; Egloff-Juras et al., 2019).

PROPERTIES OF ICG

ICG is an amphiphilic tricarbocyanine dye used in the biomedical field for almost six decades for different purposes (Schaafsma et al., 2011; Hill et al., 2015). ICG is an anionic, water-soluble, and fluorescent molecule with a molecular weight of 751 Da and that displays absorption and fluorescence emission in the NIR wavelength region (Zhao et al., 2014). These properties allow deep penetration of the signal and minimize interference of tissues' autofluorescence, making it suitable for bio-imaging uses (Wang et al., 2004; Yuan et al., 2004). Moreover, since it is an FDA-approved dye, well studied in its already known clinical applications, its introduction to new clinical applications is greatly simplified (Alander et al., 2012; Valente et al., 2019). Additionally, due to its photosensitizing properties, ICG can be used to generate oxygen species (ROS) or heat, aiming to destroy cancer cells in photodynamic therapy (PDT) and photothermal therapy (PTT) (Dolmans et al., 2003; Kuo et al., 2012). Despite these compelling properties, the application of ICG is restricted due to its concentration-dependent aggregation, quick degradation, and poor photostability. Furthermore, its non-specific binding to plasma proteins determines a relatively short circulation half-life, and its non-specific targeting remains a limitation (Kirchherr et al., 2009; Yaseen et al., 2009).

ICG AS AN NIR FLUORESCENT CONTRAST AGENT: CLINICAL APPLICATIONS

As previously mentioned, ICG has an excellent safety profile and, following injection of a clinical standard dose (0.1–0.5 mg/kg), immediately interacts with plasma proteins, acting as an excellent vascular agent for evaluating both the blood perfusion and lymphatic drainage (Alford et al., 2009; Marshall et al., 2010; Boni et al., 2015). Once excited at the wavelength of about 820 nm, ICG emits a fluorescent signal detectable by specific scopes and cameras to allow identification of anatomical structures where the dye localizes (Luo et al., 2011; Daskalaki et al., 2014). Indeed, ICG is used in intraoperative angiography for assessment of superficial eye vessels and in the evaluation of coronary artery bypass grafts, peripheral vascular disease, and solid organ transplantation (Reuthebuch et al., 2004; Sekijima et al., 2004; Desai et al., 2006; Kang et al., 2010a,b; Baillif et al., 2011). Moreover, since, once injected intravenously, ICG is excreted exclusively via the liver, it is used to assess hepatic function (Daskalaki et al., 2014). In addition to these applications, ICG is employed in NIR fluorescence image-guided oncologic surgery with the purpose of identifying structures that need to be resected (e.g., tumor tissue, lymph nodes) and spared, contributing to support the surgeon's decision-making process (Boni et al., 2015; Baiocchi et al., 2018).

Of note, NIR fluorescence imaging via ICG can provide real-time identification of tumor margins and affected lymph nodes (LN) in breast and skin cancers, improving local control of the disease and allowing a more conservative surgery (Sevick-Muraca et al., 2008; Fujiwara et al., 2009; Murawa et al., 2009). Sentinel LN (SLN) mapping is important to detect involved LN and is required for cancer staging, prognosis prediction, and therapy selection (Schaafsma et al., 2011; Wang et al., 2018). Here, ICG is injected near the tumor and flows via lymph circulation to LN, displaying them when lit with excitation light (Tanaka et al., 2006; Alander et al., 2012; Wishart et al., 2012; Verbeek et al., 2014). ICG-NIR fluorescence imaging has been applied also to intraoperative tumor detection in order to ensure a total tumor resection (Gotoh et al., 2009; Onda et al., 2016; Rossi et al., 2018). Indeed, exploiting ICG hepatic clearance and the enhanced permeability and retention (EPR) effect, liver tumors could be identified (Ishizawa et al., 2009; Huang et al., 2018).

To date, the application of ICG as an NIR fluorescence imaging agent in oncology is an active and promising area, but it also has limitations. Aside from the problems inherent with some of its physicochemical properties, ICG is a non-targeted or extremely low targeted tracer, which greatly precludes its application for specific cancer imaging (Landsman et al., 1976; Marshall et al., 2010; Wang et al., 2018; Egloff-Juras et al., 2019).

ICG-NPs AND CANCER: PRECLINICAL STUDIES

Recently, the development of multifunctional ICG-NPs, offering both diagnostic and therapeutic solutions in cancer, has captured the attention of researchers (Han et al., 2018). To overcome the limitations previously discussed, several ICG-NPs have been proposed and tested, both *in vitro* and *in vivo* (Liu et al., 2019b; ZhuGe et al., 2019), displaying increased circulation time and improved ICG optical properties and achieving tumor-specific accumulation. Many advantages derive from their use: combining or encapsulating it to/into NPs results in the extension of ICG half-life. Additionally, functionalization with specific cancer-related antibodies may result in preferential accumulation of ICG at the tumor site. Furthermore, ICG-NPs may be useful to limit ICG aggregation and photodegradation as well as to improve its stability in aqueous solutions (Ishizawa et al., 2009; Liu et al., 2019c; ZhuGe et al., 2019). ICG has been loaded or conjugated to a variety of nanostructures, such as polymer-based NPs, lipid-based NPs, and silica NPs with different surface modifications and functionalization strategies (**Figure 1A**). Among the plethora of ICG-NPs for different targets and applications, we focused on the following main applications for cancer treatment: PDT and PTT (i), *in vivo* imaging and image-guided surgery (ii), and multimodal therapy (iii) (**Figure 1B**). A summary of all significant examples of ICG-NPs developed for these applications has been inserted in **Table 1**.

PDT is an emerging, minimally invasive cancer treatment based on the production of ROS in response to a source of light, the presence of oxygen and a photosensitizer (i.e., ICG) (ZhuGe et al., 2019). Although this option seems promising for many cancers (Gross et al., 2003; Ritch and Punnen, 2017), selective delivery of the photosensitizers at target tissues/cells remains insufficient for successful clinical use (Zhen et al., 2013). Since PDT could generate an antitumor immune response, ICG-loaded liposomes were studied in combination with NIR

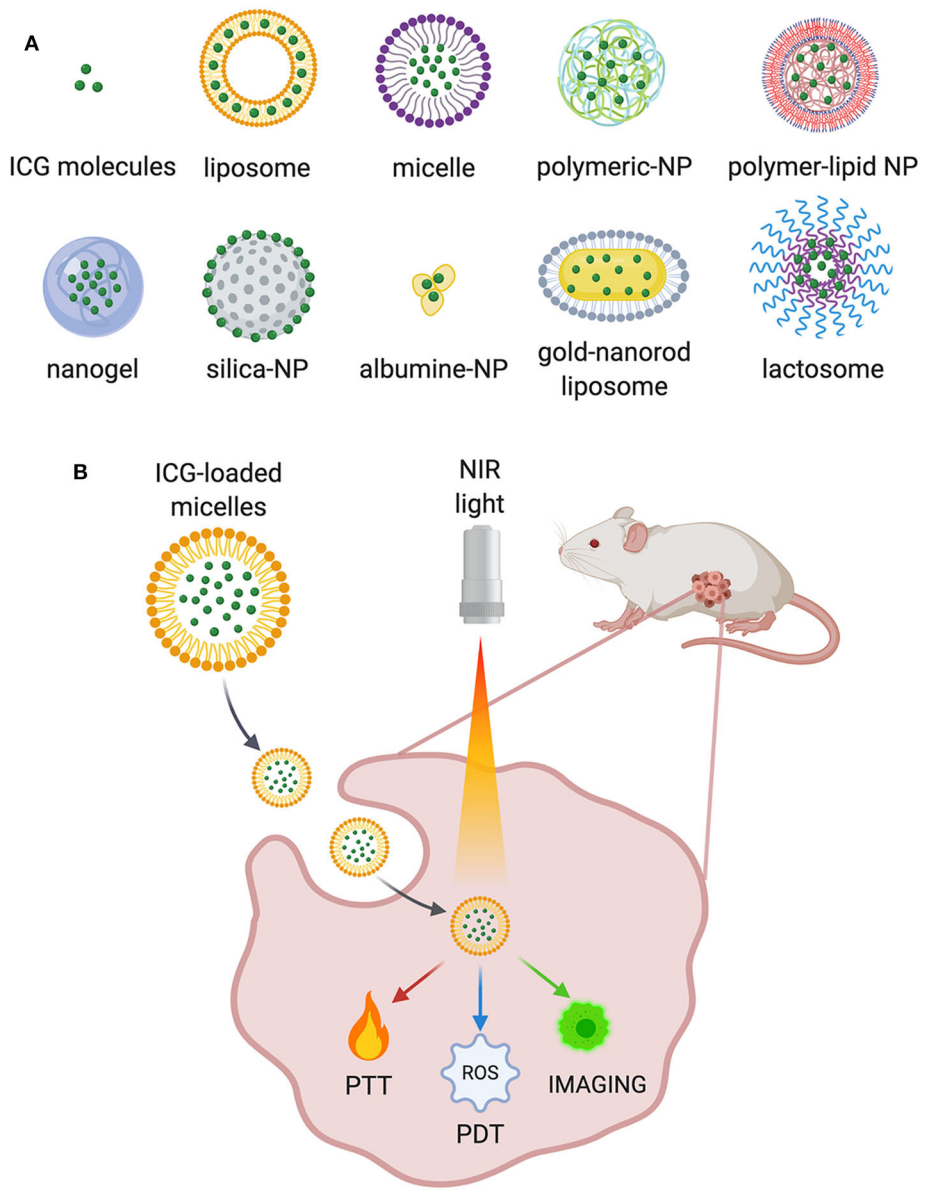

FIGURE 1 | (A) Some examples of the ICG-NPs obtained with different materials and conjugation techniques. **(B)** Main applications of ICG-NPs in cancer treatment.

irradiation, demonstrating suppression of brain tumor growth and suggesting the potential application for the treatment of tumors near the brain surface (Shibata et al., 2019). Super carbonate apatite-ICG NPs improved ICG uptake in tumor cells and its antitumor effect in a colorectal xenograft model, serving as a useful vehicle for ICG-based PDT (Tamai et al., 2018). Also, hydroxyethyl starch-oleic acid ICG-NPs exhibited excellent stability and efficient ROS generation and increased cellular uptake and tumor accumulation compared to free ICG (Hu et al., 2019).

In addition to PDT, PTT also arose as a promising approach for cancer treatment by using NIR-light to generate heat and achieve tumor ablation (Li et al., 2019a). The main challenge with PTT is that heat could also damage the healthy surrounding tissue and fail to eradicate metastatic cells. Several NPs with excellent NIR light absorption have been developed as PTT agents, including gold, copper, carbon NPs, and NIR dyes (Lv et al., 2017). Also, ICG has been exploited in a multitude of NPs as a PTT agent (Doughty et al., 2019). ICG-conjugated micelles have been investigated for breast and lung cancer treatment displaying increased circulation time, accurate tumor targeting, and efficient PTT effect compared with free ICG (Li et al., 2019b; Zhu et al., 2019). Another work proposed the functionalization with folic acid to achieve accumulation on MCF-7 breast cancer cells, obtaining a significant tumor growth inhibition (Zheng et al., 2014). A formulation of pH-responsive

TABLE 1 | Summary of all significant examples of ICG nanoparticles studied *in vivo*.

ICG-NPs: preclinical research					
Nanoparticle type	**Conjugation technique**	**Target**	**Aim/use**	**Achievements/findings**	**References**
Calcium phosphate nanoparticles	ICG encapsulation	Breast cancer	Fluoroprobing	Improved half life Improved photostability Biocompatibility	Altinoglu et al., 2008
Water-responsive phospholipid-calcium-carbonate hybrid nanoparticle	ICG loading doxorubicin loading	Breast cancer	PTT	Good tissue penetration Decreased metastatic areas	Liu et al., 2019b
Super carbonate apatite nanoparticles	ICG loading	Colorectal adenocarcinoma	PDT	Fluorescence enhancement Significant tumor growth retardation	Tamai et al., 2018
Hydrophobic superparamagnetic iron oxide nanoparticles	ICG loading doxorubicin coating	Glioblastoma	MRI imaging Chemotherapy	BBB crossing Accumulation at the tumor site	Shen et al., 2018
Graphene oxide hybrid nano-composites	Electrostatic interaction with ICG	Colorectal adenocarcinoma	PTT	Citotoxicity in cancer cells only	Sharker et al., 2015
Polyamidoamine (PAMAM)-coated silica nanoparticles	ICG coating	Sentinel lymph nodes	Sentinel lymph node imaging	Facilitatation of sentinel lymph node biopsy procedures	Tsuchimochi et al., 2013
PL-PEG-mAb nanoparticles	ICG-PEG conjugation	Glioblastoma Breast cancer	PTT Imaging	Good targeting Tumor reduction	Zheng et al., 2012
PLGA-PEG-R837 nanoparticles	ICG encapsulation	Breast cancer	PTT Immunotherapy	Great antitumor effect Strong immune-memory effect	Chen et al., 2016
PEG-PCL-C3 hybrid nanoparticles	ICG-PEG conjugation	Oral squamous cell carcinoma	PTT PDT	*In vivo* safety Active role in reducing tumor volume	Ren et al., 2017
Levan nanoparticles	ICG encapsulation	Breast cancer	Imaging	Selective targeting of cancer cells	Kim et al., 2015
Silk fibroin nanoparticles cross-linked by proanthocyanidins	ICG encapsulation	Glioblastoma	PTT	Stable photothermal properties Decrease of tumor volume	ZhuGe et al., 2019
Silk fibroin nanoparticles	ICG encapsulation	Glioblastoma	PTT	Inhibition of tumor growth	Xu et al., 2018
Hyaluronic acid nanoformulation	ICG entrapment	Pancreatic cancer	Tumor detection	Safe contrast agent	Qi et al., 2018
Hyaluronic acid nanoformulation	ICG entrapment	Breast cancer	Image-guided surgery	Good contrast enhancement	Hill et al., 2015
Hyaluronic acid nanogels	ICG entrapment	Breast cancer	Imaging	Improved imaging of metastatic lymph nodes	Mok et al., 2012
Polymer-lipid nanoparticles	ICG encapsulation	Pancreatic cancer	PTT	Suppression of tumor growth	Zhao et al., 2014
Mannosylated liposomes	ICG encapsulation	Sentinel lymph nodes	Sentinel lymph node imaging	Increased liposomal stability Good optical properties	Jeong et al., 2013
Liposomes	Lipid-bound ICG	Healthy organism	Imaging	Fluorescence enhancement	Kraft and Ho, 2014
Liposomes	ICG-iDOPE incorporation	Glioblastoma	PDT	Suppression of tumor growth	Shibata et al., 2019
Gold nanorod@liposome core–shell nanoparticles	ICG loading	Liver cancer	Photoacoustic tomography Surgery Guidance	Prolonged half-life Preoperative detection of liver cancer	Guan et al., 2017
Micelles	ICG-PEG conjugation	Lung carcinoma	PTT	Tumor detection Inhibition of tumor growth	Li et al., 2019b
Micelles	ICG/retinal loading	Murine breast cancer	PTT	Suppression of tumor growth	Zhu et al., 2019
Lactosomes (micelles assembled from block copolymers)	ICG loading	Metastatic lymph nodes in gastric cancer	PDT Imaging	Selective accumulation in metastatic lymph nodes	Tsujimoto et al., 2015
*Phospholipid nanoprobes Folic acid-phospholipid nanoparticles	ICG-PEG conjugation	Glioblastoma Breast cancer	PTT Imaging	Selective imaging of cancer cells Selective killing of cancer cells	Zheng et al., 2011
Folate-targeted lipid nanoparticles	ICG/oxygen loading	Ovarian cancer	PTT PDT Imaging	Good targeting Increased PDT efficacy	Liu et al., 2019c

(Continued)

TABLE 1 | Continued

ICG-NPs: preclinical research					
Nanoparticle type	**Conjugation technique**	**Target**	**Aim/use**	**Achievements/findings**	**References**
Folic acid-targeted nanoparticles	ICG loading	Breast cancer	PTT	Significant targeting to MCF-7 tumors Tumor growth inhibition	Zheng et al., 2014
HDL nanoparticles	ICG encapsulation	Murine breast cancer	PTT PDT	Deep tumor penetration Enhanced tumor necrosis	Sheng et al., 2019
Human ferritin	Photosensitizer encapsulation	Glioblastoma	PDT	High phototoxicity in tumors Normal tissue left unaffected	Zhen et al., 2013
BSA nanoparticles	ICG coating artemisin encapsulation	Epidermal carcinoma	PTT PDT	Synergistic photo-chemotherapy	Ma et al., 2018
Human serum albumin	ICG adsorption	Murine breast cancer	PTT PDT	Tumor margin detenction Tumor eradication without regrowth	Sheng et al., 2014
§Human serum albumin	ICG adsorption	Breast cancer	Sentinel lymph node mapping	Clinical trial	Hutteman et al., 2011

**in vitro research only.*
§clinical trial.

polymeric nano-complexes of graphene oxide and ICG (Sharker et al., 2015) was effective in providing selective sensitivity to tumor environment and tumor regression, confirming its clinical usefulness. Also, in studies with ICG-loaded polymer-lipid NPs against pancreatic cancer (Zhao et al., 2014) and silk fibroin NPs addressing glioblastoma (Xu et al., 2018), the main advantages observed, compared to free ICG, were an extended circulation time and *in vivo* stability, together with the ability to specifically target cancer cells (Sheng et al., 2019).

An assortment of ICG-NPs also has been developed for bioimaging applications as agents for tumor identification. Since early detection is crucial for the prompt diagnosis and successful treatment of cancer, the benefits of using NPs as vector for ICG to the tumor site would be significant. ICG-incorporating liposomes provide enhanced visualization of the popliteal LN and downstream LN, detected across 1.5 cm of muscle tissue, and free ICG only enables 0.5 cm detection (Kraft and Ho, 2014). Hyaluronic acid (HA) NPs allow contrast enhancement (Hill et al., 2015), and levan NPs display good targeted imaging of breast tumors and the suitability to encapsulate hydrophobic drugs (Kim et al., 2015). ICG-HA–derived NPs improve the NIR signal for intraoperative detection of pancreas and splenic metastasis compared to ICG (Qi et al., 2018), and also nanogels display good performance in targeted imaging of cancers and LN metastases in addition to the feasible drug-encapsulation in their hydrophobic core (Mok et al., 2012). ICG-doped calcium phosphate NPs display increased deep-tissue penetration (Altinoglu et al., 2008). Another promising strategy involves its effectiveness as a photoacoustic-fluorescence imaging probe in liver cancer detection (Guan et al., 2017). Overall, all the considered formulations display a non-toxic safety profile, a longer circulation time, and a higher tumor accumulation than free ICG. This would provide the potential to increase the completeness of surgery and the chances of a better outcome. Furthermore, different ICG-NPs were suggested as contrast agents for SLN mapping. Mannosilated ICG-liposomes show improved stability and fluorescence signal by exploiting their specific recognition by macrophages, making it a good agent for SLN and LN imaging (Jeong et al., 2013). Silica NPs loaded with technetium and ICG improve LN detection in real time although further studies are necessary to assess the appropriate dose (Tsuchimochi et al., 2013), and ICG-loaded lactosomes provide an improved LN detection and a inhibited growth upon PDT treatment (Tsujimoto et al., 2015). The only example tested in the clinic concerns the use of ICG adsorbed to human serum albumin (ICG:HSA) aiming to improve detection and better retention in the SLN after intradermal injection. However, this trial performed on breast cancer patients showed no advantage of ICG:HSA for SLN mapping (Hutteman et al., 2011).

Very often, the applications described above have been used in combination to obtain better therapeutic results. Indeed, many authors consider the use of ICG for imaging-guided PTT, allowing simultaneously tumor detection and eradication. ICG-PL-PEG NPs were investigated *in vitro* for cell imaging and selective PTT, proving to be an interesting multifunctional system (Zheng et al., 2011), and Liu and coworkers provide a synergistic strategy for both offering contrast enhancement and tumor growth reduction against ovarian cancer (Liu et al., 2019c). Furthermore, the successful application of HSA-ICG NPs for *in vivo* imaging and tumor margin detection following PDT/PTT synergic phototherapy has been reported (Sheng et al., 2014). Many authors also insist on the strength of the synergistic combination of PTT and PDT to obtain better therapeutic results (Ren et al., 2017; Sheng et al., 2019; Zhu et al., 2019).

Moreover, since monotherapy, either PTT or PDT usually suffers from incomplete tumor killing, leading potentially to tumor relapse (Ma et al., 2018); a combination with chemotherapy could optimize the cancer treatment. In this context, chemotherapy drugs combined with phototherapy have been studied. Doxorubicin has been exploited in superparamagnetic iron oxide NPs with ICG displaying good imaging ability, showing accumulation in the tumor site and high

antitumor efficacy with few side effects in glioma-bearing rats (Shen et al., 2018). Phospholipid-calcium-carbonate NPs loaded with doxorubicin and ICG demonstrate strong tumor-homing properties and a synergistic effect in terms of tumor growth reduction (Liu et al., 2019b). Regarding cancer immunotherapy, the photothermal ablation of tumors with immune-adjuvant ICG-NPs, seems promising in activating immune responses potentially applicable for metastasis treatment (Chen et al., 2016). Overall, multimodal therapies appear to enhance the therapeutic effects and prevent possible recurrences.

ICG-NPs: OPPORTUNITIES, LIMITATIONS AND POSSIBLE IMPACTS IN ONCOLOGY

Implementing a plethora of different ICG-NPs makes the comparison between them especially difficult. Overall, the most promising strategies are related to actively targeted ICG-NPs, but there is a significant gap in outcomes between preclinical cancer models and their translation into clinical practice. As previously discussed, several recent studies are focusing on the development of ICG-NPs, aiming to exploit the advantages of ICG in order to further increase cancer therapies.

First, ICG-NPs could be effective in improving the already existing imaging techniques, either by prolonging ICG half-life or by selectively addressing the molecule to cancer cells only; that could be particularly relevant when trying to identify metastases as well as being useful to early detection of cancer cells in case of relapse. The chance to use NPs-ICG as drugs to directly treat tumors represents an additional advantage. By exploiting the ability of ICG to both generate heat and ROS in response to NIR, ICG-NPs could be used for PTT, PDT, or both in order to elicit antitumor response (Han et al., 2018; Liu et al., 2019c). Indeed, the accumulation of ICG in tumor cells and their exposure to light, determines a localized increase in temperature that causes cell damage by apoptosis and necrosis, resulting in tumor ablation (Melamed et al., 2015; Pérez-Hernández et al., 2015). In the meantime, in the presence of oxygen, light-activated ICG also generates ROS, leading to cell death and tissue destruction (Allison and Moghissi, 2013). Nevertheless, recent studies are quite misleading about the application of PTT and PDT, which rely on different therapeutic mechanisms. However, when ICG is used, both effects could be achieved although with a distinct tumor cell–killing contribution by each (Liu et al., 2019a). More clarity about which strategy is being referred to is necessary since, through ICG, one thing does not exclude the other, and the related side effects should be considered as well. Both PTT and PDT are promising for the treatment of several malignancies; however, it is important to understand which aspect to target to design the appropriate NPs (Pinto and Pocard, 2018).

The first concern is about immunogenicity. Although it is common opinion that ICG itself is not toxic and that ICG-NPs can be selectively targeted to the tumor, it is still uncertain if other tissues could be affected by the treatment. NPs must not elicit an immune response and demonstrate not to be toxic for the organism.

A second issue is obvious: cancer is not a single disease. Tumors may be solid or not, have clear or irregular borders, spread in easily reachable districts or in hard-to-treat areas. Additionally, similar tumors may have different density, vasculature, and tumor microenvironment. Here, the ability of ICG-NPs to penetrate into the tumor is unclear, thus making it hard to decide if ICG-NPs should be addressed to primary tumors and metastases or used as adjuvants after surgery (Tsujimoto et al., 2015; Sheng et al., 2019). Research on ICG-NPs should develop the optimal strategy for real clinical applications on each disease instead of just developing NPs that prove to be effective at a preclinical stage but are difficult to translate into clinical trials.

Regarding the multitude of developed ICG-NPs, one fact is evident: every group focuses on the NP type they are used to working with as well as on the tumor model they know better (**Table 1**). Such an approach is both useful and harmful. On the one hand, long-term expertise in developing a specific NP could be addressed to the production of highly effective ICG-NPs; on the other hand, several cancer models should be tested to evaluate the efficacy of the proposed treatment in different contexts. Focusing on a single model could be limiting if the purpose is to design a consistent model for the development of new therapies. Options to design ICG-NPs are unlimited, and many could be adjusted to target different tumors (Han et al., 2018). NPs can be further enriched by conjugation with other molecules: monoclonal antibodies, fluorescence probes and drugs in order to maximize the antitumor effect of the ICG-NPs (Zheng et al., 2011; Sheng et al., 2014; Ma et al., 2018). Here, given that the enhancement of targeting is crucial to prevent damage of healthy tissues, NPs should be selectively directed to the tumor, either inserting targeting molecules or by exploiting the intrinsic ability of some carriers to bind cancer.

Despite all the advantages deriving from ICG-NPs and the huge amount of solutions proposed so far, a pool of clinical applications have not been outlined yet, thus making it impossible to determine which ones have the potential to become actual drugs. The answer is not one and only: different nanoparticles could be used to treat different tumors, and different molecules could be attached to improve their selectivity. Therefore, developing dozens of different ICG-NPs is not of help in finding the best alternatives that could be eventually tested in clinical trials.

On top of everything, when discussing the potentiality of ICG-NPs in therapy, an uncomfortable yet necessary question should be raised about the costs of clinical trials involving NPs: developing such molecules, especially when they are combined with chemotherapeutic drugs and/or patented monoclonal antibodies, has been proved to be extremely expensive, thus limiting the possibility to produce high amounts of molecules to be used in clinical trials.

DISCUSSION

In conclusion, the potential of ICG-conjugated NPs is undeniable, mostly because they could possibly be directed toward several cancer types with incredibly high specificity

(Bozkulak et al., 2009; Montazerabadi et al., 2012). Indeed, they could overcome some of the limitations of current treatments, especially regarding tumors that are poorly accessible by drugs or hard to treat, and they could also limit the side effects usually associated to conventional therapies (Montazerabadi et al., 2012). However, obtaining specific cell targeting as well as maintaining high drug concentration at the tumor site remain the main challenges as they are both necessary conditions for the implementation of ICG-NPs–based imaging, PTT, and PDT. This is the reason why the currently known ICG-NPs have not successfully reached the translation into clinics so far. Therefore, an improved active targeting is required for a major impact on human health. Moreover, since the penetration depth of light in tissues could be limited, even with NIR lasers, endoscope-based clinical devices equipped with a laser may be demanded in order to reach successful outcomes in clinical practice (Chen et al., 2016). Some sort of consensus should also be achieved about the most promising formulations and the real aims of the proposed interventions: PTT, PDT, and imaging are not interchangeable terms, and more precision is required when deciding which therapies would be worth testing. In addition, before trying to develop new ICG-NPs, the economic impact of a potential trial involving such NPs must be carefully considered. Expertise and deep knowledge in the field are mandatory, but feasibility will eventually determine if a promising molecule will ever be translated into an actual therapy.

AUTHOR CONTRIBUTIONS

MS, FS, AB, and LS contributed in manuscript writing and figure preparation. SM, MT, and FC contributed in manuscript writing, editing, and critical review. All authors contributed to the article and approved the submitted version.

ACKNOWLEDGMENTS

SM acknowledges Pediatric Clinical Research Center Romeo and Enrica Invernizzi that supports her position. LS and AB postdoctoral and doctoral fellowships are supported by University of Milan. The authors acknowledge University of Milan for support in open access publication.

REFERENCES

Alander, J. T., Kaartinen, I., Laakso, A., Pätilä, T., Spillmann, T., Tuchin, V. V., et al. (2012). A review of indocyanine green fluorescent imaging in surgery. *Int. J. Biomed. Imaging* 2012, 1–26. doi: 10.1155/2012/940585

Alford, R., Simpson, H. M., Duberman, J., Hill, G. C., Ogawa, M., Regino, C., et al. (2009). Toxicity of organic fluorophores used in molecular imaging: literature review. *Mol. Imaging* 8, 341–354. doi: 10.2310/7290.2009.00031

Alius, C., Oprescu, S., Balalau, C., and Elena Nica, A. (2018). Indocyanine green enhanced surgery; principle, clinical applications and future research directions. *J. Clin. Invest. Surg.* 3, 1–8. doi: 10.25083/2559.5555/31.18

Allison, R. R., and Moghissi, K. (2013). Photodynamic therapy (PDT): PDT mechanisms. *Clin. Endosc.* 46, 24–29. doi: 10.5946/ce.2013.46.1.24

Altinoglu, E. I., Russin, T. J., Kaiser, J. M., Barth, B. M., Eklund, P. C., Kester, M., et al. (2008). Near-infrared emitting fluorophore-doped calcium phosphate nanoparticles for *in vivo* imaging of human breast cancer. *ACS Nano* 2, 2075–2084. doi: 10.1021/nn800448r

Baillif, S., Wolff, B., Paoli, V., Gastaud, P., and Mauget-Faÿsse, M. (2011). Retinal fluorescein and indocyanine green angiography and spectral-domain optical coherence tomography findings in acute retinal pigment epitheliitis. *Retina* 31, 1156–1163. doi: 10.1097/IAE.0b013e3181fbcea5

Baiocchi, G. L., Diana, M., and Boni, L. (2018). Indocyanine green-based fluorescence imaging in visceral and hepatobiliary and pancreatic surgery: state of the art and future directions. *World J. Gastroenterol.* 24, 2921–2930. doi: 10.3748/wjg.v24.i27.2921

Boni, L., David, G., Mangano, A., Dionigi, G., Rausei, S., Spampatti, S., et al. (2015). Clinical applications of indocyanine green (ICG) enhanced fluorescence in laparoscopic surgery. *Surg. Endosc.* 29, 2046–2055. doi: 10.1007/s00464-014-3895-x

Bozkulak, O., Yamaci, R. F., Tabakoglu, O., and Gulsoy, M. (2009). Phototoxic effects of 809-nm diode laser and indocyanine green on MDA-MB231 breast cancer cells. *Photodiagnosis. Photodyn. Ther.* 6, 117–121. doi: 10.1016/j.pdpdt.2009.07.001

Chen, Q., Xu, L., Liang, C., Wang, C., Peng, R., and Liu, Z. (2016). Photothermal therapy with immune-adjuvant nanoparticles together with checkpoint blockade for effective cancer immunotherapy. *Nat. Commun.* 7:13193. doi: 10.1038/ncomms13193

Daskalaki, D., Fernandes, E., Wang, X., Bianco, F. M., Elli, E. F., Ayloo, S., et al. (2014). Indocyanine green (ICG) fluorescent cholangiography during robotic cholecystectomy: results of 184 consecutive cases in a single institution. *Surg. Innov.* 21, 615–621. doi: 10.1177/1553350614524839

Desai, N. D., Miwa, S., Kodama, D., Koyama, T., Cohen, G., Pelletier, M. P., et al. (2006). A randomized comparison of intraoperative indocyanine green angiography and transit-time flow measurement to detect technical errors in coronary bypass grafts. *J. Thorac. Cardiovasc. Surg* 132, 585–594. doi: 10.1016/j.jtcvs.2005.09.061

Dolmans, D. E. J. G. J., Fukumura, D., and Jain, R. K. (2003). Photodynamic therapy for cancer. *Nat. Rev. Cancer* 3, 380–387. doi: 10.1038/nrc1071

Doughty, A., Hoover, A., Layton, E., Murray, C., Howard, E., and Chen, W. (2019). Nanomaterial applications in photothermal therapy for cancer. *Materials* 12:779. doi: 10.3390/ma12050779

Egloff-Juras, C., Bezdetnaya, L., Dolivet, G., and Lassalle, H.-P. (2019). NIR fluorescence-guided tumor surgery: new strategies for the use of indocyanine green. *Int. J. Nanomed.* 14, 7823–7838. doi: 10.2147/IJN.S207486

Fox, I. J., and Wood, E. H. (1960). Indocyanine green: physical and physiologic properties. *Proc. Staff Meet. Mayo Clin* 35, 732–744.

Fujiwara, M., Mizukami, T., Suzuki, A., and Fukamizu, H. (2009). Sentinel lymph node detection in skin cancer patients using real-time fluorescence navigation with indocyanine green: preliminary experience. *J. Plast. Reconstr. Aesthet. Surg.* 62, e373–e378. doi: 10.1016/j.bjps.2007.12.074

Gotoh, K., Yamada, T., Ishikawa, O., Takahashi, H., Eguchi, H., Yano, M., et al. (2009). A novel image-guided surgery of hepatocellular carcinoma by indocyanine green fluorescence imaging navigation. *J. Surg. Oncol.* 100, 75–79. doi: 10.1002/jso.21272

Gross, S., Gilead, A., Scherz, A., Neeman, M., and Salomon, Y. (2003). Monitoring photodynamic therapy of solid tumors online by BOLD-contrast MRI. *Nat. Med.* 9, 1327–1331. doi: 10.1038/nm940

Guan, T., Shang, W., Li, H., Yang, X., Fang, C., Tian, J., et al. (2017). From detection to resection: photoacoustic tomography and surgery guidance with indocyanine green loaded gold nanorod@liposome core–shell nanoparticles in liver cancer. *Bioconjugate Chem.* 28, 1221–1228. doi: 10.1021/acs.bioconjchem.7b00065

Han, Y.-H., Kankala, R. K., Wang, S.-B., and Chen, A.-Z. (2018). Leveraging engineering of indocyanine green-encapsulated polymeric nanocomposites for biomedical applications. *Nanomaterials* 8:360. doi: 10.3390/nano8060360

Hill, T. K., Abdulahad, A., Kelkar, S. S., Marini, F. C., Long, T. E., Provenzale, J. M., et al. (2015). Indocyanine green-loaded nanoparticles for image-guided tumor surgery. *Bioconjugate Chem.* 26, 294–303. doi: 10.1021/bc5005679

Hu, H., Chen, J., Yang, H., Huang, X., Wu, H., Wu, Y., et al. (2019). Potentiating photodynamic therapy of ICG-loaded nanoparticles by depleting GSH with PEITC. *Nanoscale* 11, 6384–6393. doi: 10.1039/C9NR01306G

Huang, S.-W., Ou, J.-J., and Wong, H. P. (2018). The use of indocyanine green imaging technique in patient with hepatocellular carcinoma. *Transl. Gastroenterol. Hepatol.* 3, 95–95. doi: 10.21037/tgh.2018.10.15

Hutteman, M., Mieog, J. S. D., van der Vorst, J. R., Liefers, G. J., Putter, H., Löwik, C. W. G. M., et al. (2011). Randomized, double-blind comparison of indocyanine green with or without albumin premixing for near-infrared fluorescence imaging of sentinel lymph nodes in breast cancer patients. *Breast Cancer Res. Treat.* 127, 163–170. doi: 10.1007/s10549-011-1419-0

Ishizawa, T., Fukushima, N., Shibahara, J., Masuda, K., Tamura, S., Aoki, T., et al. (2009). Real-time identification of liver cancers by using indocyanine green fluorescent imaging. *Cancer* 115, 2491–2504. doi: 10.1002/cncr.24291

Jeong, H.-S., Lee, C.-M., Cheong, S.-J., Kim, E.-M., Hwang, H., Na, K. S., et al. (2013). The effect of mannosylation of liposome-encapsulated indocyanine green on imaging of sentinel lymph node. *J. Liposome Res.* 23, 291–297. doi: 10.3109/08982104.2013.801488

Kang, Y., Lee, J., Kwon, K., and Choi, C. (2010a). Application of novel dynamic optical imaging for evaluation of peripheral tissue perfusion. *Int. J. Cardiol.* 145, e99–101. doi: 10.1016/j.ijcard.2008.12.166

Kang, Y., Lee, J., Kwon, K., and Choi, C. (2010b). Dynamic fluorescence imaging of indocyanine green for reliable and sensitive diagnosis of peripheral vascular insufficiency. *Microvasc. Res.* 80, 552–555. doi: 10.1016/j.mvr.2010.07.004

Kim, S.-J., Bae, P. K., and Chung, B. H. (2015). Self-assembled levan nanoparticles for targeted breast cancer imaging. *Chem. Commun.* 51, 107–110. doi: 10.1039/C4CC07679F

Kirchherr, A.-K., Briel, A., and Mäder, K. (2009). Stabilization of indocyanine green by encapsulation within micellar systems. *Mol. Pharmaceutics* 6, 480–491. doi: 10.1021/mp8001649

Kraft, J. C., and Ho, R. J. Y. (2014). Interactions of indocyanine green and lipid in enhancing near-infrared fluorescence properties: the basis for near-infrared imaging *in vivo*. *Biochemistry* 53, 1275–1283. doi: 10.1021/bi500021j

Kuo, W.-S., Chang, Y.-T., Cho, K.-C., Chiu, K.-C., Lien, C.-H., Yeh, C.-S., et al. (2012). Gold nanomaterials conjugated with indocyanine green for dual-modality photodynamic and photothermal therapy. *Biomaterials* 33, 3270–3278. doi: 10.1016/j.biomaterials.2012.01.035

Landsman, M. L., Kwant, G., Mook, G. A., and Zijlstra, W. G. (1976). Light-absorbing properties, stability, and spectral stabilization of indocyanine green. *J. Appl. Physiol.* 40, 575–583. doi: 10.1152/jappl.1976.40.4.575

Li, Z., Chen, Y., Yang, Y., Yu, Y., Zhang, Y., Zhu, D., et al. (2019a). Recent advances in nanomaterials-based chemo-photothermal combination therapy for improving cancer treatment. *Front. Bioeng. Biotechnol.* 7:293. doi: 10.3389/fbioe.2019.00293

Li, Z., Yin, Q., Chen, B., Wang, Z., Yan, Y., Qi, T., et al. (2019b). Ultra-pH-sensitive indocyanine green-conjugated nanoprobes for fluorescence imaging-guided photothermal cancer therapy. *Nanomedicine* 17, 287–296. doi: 10.1016/j.nano.2019.02.001

Liu, P., Yang, W., Shi, L., Zhang, H., Xu, Y., Wang, P., et al. (2019a). Concurrent photothermal therapy and photodynamic therapy for cutaneous squamous cell carcinoma by gold nanoclusters under a single NIR laser irradiation. *J. Mater. Chem. B* 7, 6924–6933. doi: 10.1039/C9TB01573F

Liu, X., Wang, C., Ma, H., Yu, F., Hu, F., and Yuan, H. (2019b). Water-responsive hybrid nanoparticles codelivering ICG and DOX effectively treat breast cancer via hyperthermia-aided DOX functionality and drug penetration. *Adv. Healthcare Mater.* 8:1801486. doi: 10.1002/adhm.201801486

Liu, Y., Chen, S., Sun, J., Zhu, S., Chen, C., Xie, W., et al. (2019c). Folate-targeted and oxygen/indocyanine green-loaded lipid nanoparticles for dual-mode imaging and photo-sonodynamic/photothermal therapy of ovarian cancer *in vitro* and *in vivo*. *Mol. Pharmaceutics* 16, 4104–4120. doi: 10.1021/acs.molpharmaceut.9b00339

Luo, S., Zhang, E., Su, Y., Cheng, T., and Shi, C. (2011). A review of NIR dyes in cancer targeting and imaging. *Biomaterials* 32, 7127–7138. doi: 10.1016/j.biomaterials.2011.06.024

Lv, R., Wang, D., Xiao, L., Chen, G., Xia, J., and Prasad, P. N. (2017). Stable ICG-loaded upconversion nanoparticles: silica core/shell theranostic nanoplatform for dual-modal upconversion and photoacoustic imaging together with photothermal therapy. *Sci. Rep.* 7:15753. doi: 10.1038/s41598-017-16016-x

Ma, Y., Liu, X., Ma, Q., and Liu, Y. (2018). Near-infrared nanoparticles based on indocyanine green-conjugated albumin: a versatile platform for imaging-guided synergistic tumor chemo-phototherapy with temperature-responsive drug release. *Onco. Targets Ther.* 11, 8517–8528. doi: 10.2147/OTT.S183887

Marshall, M. V., Rasmussen, J. C., Tan, I.-C., Aldrich, M. B., Adams, K. E., Wang, X., et al. (2010). Near-infrared fluorescence imaging in humans with indocyanine green: a review and update. *Open Surg. Oncol. J.* 2, 12–25. doi: 10.2174/1876504101002010012

Melamed, J. R., Edelstein, R. S., and Day, E. S. (2015). Elucidating the fundamental mechanisms of cell death triggered by photothermal therapy. *ACS Nano* 9, 6–11. doi: 10.1021/acsnano.5b00021

Mok, H., Jeong, H., Kim, S.-J., and Chung, B. H. (2012). Indocyanine green encapsulated nanogels for hyaluronidase activatable and selective near infrared imaging of tumors and lymph nodes. *Chem. Commun.* 48:8628. doi: 10.1039/c2cc33555g

Montazerabadi, A. R., Sazgarnia, A., Bahreyni-Toosi, M. H., Ahmadi, A., and Aledavood, A. (2012). The effects of combined treatment with ionizing radiation and indocyanine green-mediated photodynamic therapy on breast cancer cells. *J. Photochem. Photobiol. B* 109, 42–49. doi: 10.1016/j.jphotobiol.2012.01.004

Muckle, T. J. (1976). Plasma proteins binding of indocyanine green. *Biochem. Med.* 15, 17–21. doi: 10.1016/0006-2944(76)90069-7

Murawa, D., Hirche, C., Dresel, S., and Hünerbein, M. (2009). Sentinel lymph node biopsy in breast cancer guided by indocyanine green fluorescence. *Br. J. Surg.* 96, 1289–1294. doi: 10.1002/bjs.6721

Onda, N., Kimura, M., Yoshida, T., and Shibutani, M. (2016). Preferential tumor cellular uptake and retention of indocyanine green for *in vivo* tumor imaging: *In vivo* tumor imaging using indocyanine green. *Int. J. Cancer* 139, 673–682. doi: 10.1002/ijc.30102

Pérez-Hernández, M., del Pino, P., Mitchell, S. G., Moros, M., Stepien, G., Pelaz, B., et al. (2015). Dissecting the molecular mechanism of apoptosis during photothermal therapy using gold nanoprisms. *ACS Nano* 9, 52–61. doi: 10.1021/nn505468v

Pinto, A., and Pocard, M. (2018). Photodynamic therapy and photothermal therapy for the treatment of peritoneal metastasis: a systematic review. *Pleura and Peritoneum* 3:20180124. doi: 10.1515/pp-2018-0124

Qi, B., Crawford, A. J., Wojtynek, N. E., Holmes, M. B., Souchek, J. J., Almeida-Porada, G., et al. (2018). Indocyanine green loaded hyaluronan-derived nanoparticles for fluorescence-enhanced surgical imaging of pancreatic cancer. *Nanomedicine* 14, 769–780. doi: 10.1016/j.nano.2017.12.015

Ren, S., Cheng, X., Chen, M., Liu, C., Zhao, P., Huang, W., et al. (2017). Hypotoxic and rapidly metabolic PEG-PCL-C3-ICG nanoparticles for fluorescence-guided photothermal/photodynamic therapy against OSCC. *ACS Appl. Mater. Interfaces* 9, 31509–31518. doi: 10.1021/acsami.7b09522

Reuthebuch, O., Häussler, A., Genoni, M., Tavakoli, R., Odavic, D., Kadner, A., et al. (2004). Novadaq SPY: intraoperative quality assessment in off-pump coronary artery bypass grafting. *Chest* 125, 418–424. doi: 10.1378/chest.125.2.418

Ritch, C. R., and Punnen, S. (2017). Photodynamic therapy for low risk prostate cancer. *BMJ,* 356:575. doi: 10.1136/bmj.j575

Rossi, G., Tarasconi, A., Baiocchi, G., De' Angelis, G. L., Gaiani, F., Di Mario, F., et al. (2018). Fluorescence guided surgery in liver tumors: applications and advantages. *Acta Biomed.* 89, 135–140. doi: 10.23750/abm.v89i9-S.7974

Saxena, V., Sadoqi, M., and Shao, J. (2003). Degradation kinetics of indocyanine green in aqueous solution. *J. Pharm. Sci.* 92, 2090–2097. doi: 10.1002/jps.10470

Schaafsma, B. E., Mieog, J. S. D., Hutteman, M., van der Vorst, J. R., Kuppen, P. J. K., Löwik, C. W. G. M., et al. (2011). The clinical use of indocyanine green as a near-infrared fluorescent contrast agent for image-guided oncologic surgery. *J. Surg. Oncol.* 104, 323–332. doi: 10.1002/jso.21943

Sekijima, M., Tojimbara, T., Sato, S., Nakamura, M., Kawase, T., Kai, K., et al. (2004). An intraoperative fluorescent imaging system in organ transplantation. *Transplant. Proc.* 36, 2188–2190. doi: 10.1016/j.transproceed.2004.09.001

Sevick-Muraca, E. M., Sharma, R., Rasmussen, J. C., Marshall, M. V., Wendt, J. A., Pham, H. Q., et al. (2008). Imaging of lymph flow in breast cancer patients after microdose administration of a near-infrared fluorophore: feasibility study. *Radiology* 246, 734–741. doi: 10.1148/radiol.2463070962

Sharker, S., M, Lee, J. E., Kim, S. H., Jeong, J. H., In, I., et al. (2015). pH triggered *in vivo* photothermal therapy and fluorescence nanoplatform of cancer based on responsive polymer-indocyanine green integrated reduced graphene oxide. *Biomaterials* 61, 229–238. doi: 10.1016/j.biomaterials.2015.05.040

Shen, C., Wang, X., Zheng, Z., Gao, C., Chen, X., Zhao, S., et al. (2018). Doxorubicin and indocyanine green loaded superparamagnetic iron oxide nanoparticles with PEGylated phospholipid coating for magnetic resonance with fluorescence imaging and chemotherapy of glioma. *Int. J. Nanomedicine* 14, 101–117. doi: 10.2147/IJN.S173954

Sheng, Y., Wang, Z., Ngandeu Neubi, G. M., Cheng, H., Zhang, C., Zhang, H., et al. (2019). Lipoprotein-inspired penetrating nanoparticles for deep tumor-targeted shuttling of indocyanine green and enhanced photo-theranostics. *Biomater. Sci.* 7, 3425–3437. doi: 10.1039/C9BM00588A

Sheng, Z., Hu, D., Zheng, M., Zhao, P., Liu, H., Gao, D., et al. (2014). Smart human serum albumin-indocyanine green nanoparticles generated by programmed assembly for dual-modal imaging-guided cancer synergistic phototherapy. *ACS Nano* 8, 12310–12322. doi: 10.1021/nn5062386

Shibata, S., Shinozaki, N., Suganami, A., Ikegami, S., Kinoshita, Y., Hasegawa, R., et al. (2019). Photo-immune therapy with liposomally formulated phospholipid-conjugated indocyanine green induces specific antitumor responses with heat shock protein-70 expression in a glioblastoma model. *Oncotarget* 10, 175–183. doi: 10.18632/oncotarget.26544

Starosolski, Z., Bhavane, R., Ghaghada, K. B., Vasudevan, S. A., Kaay, A., and Annapragada, A. (2017). Indocyanine green fluorescence in second near-infrared (NIR-II) window. *PLoS ONE* 12:e0187563. doi: 10.1371/journal.pone.0187563

Tamai, K., Mizushima, T., Wu, X., Inoue, A., Ota, M., Yokoyama, Y., et al. (2018). Photodynamic therapy using indocyanine green loaded on super carbonate apatite as minimally invasive cancer treatment. *Mol. Cancer Ther.* 17, 1613–1622. doi: 10.1158/1535-7163.MCT-17-0788

Tanaka, E., Choi, H. S., Fujii, H., Bawendi, M. G., and Frangioni, J. V. (2006). Image-guided oncologic surgery using invisible light: completed pre-clinical development for sentinel lymph node mapping. *Ann. Surg. Oncol.* 13, 1671–1681. doi: 10.1245/s10434-006-9194-6

Tsuchimochi, M., Hayama, K., Toyama, M., Sasagawa, I., and Tsubokawa, N. (2013). Dual-modality imaging with 99mTc and fluorescent indocyanine green using surface-modified *silica* nanoparticles for biopsy of the sentinel lymph node: an animal study. *EJNMMI Res.* 3:33. doi: 10.1186/2191-219X-3-33

Tsujimoto, H., Morimoto, Y., Takahata, R., Nomura, S., Yoshida, K., Hiraki, S., et al. (2015). Theranostic photosensitive nanoparticles for lymph node metastasis of gastric cancer. *Ann. Surg. Oncol.* 22, 923–928. doi: 10.1245/s10434-015-4594-0

Valente, S. A., Al-Hilli, Z., Radford, D. M., Yanda, C., Tu, C., and Grobmyer, S. R. (2019). Near infrared fluorescent lymph node mapping with indocyanine green in breast cancer patients: a prospective trial. *J. Am. Coll. Surg.* 228, 672–678. doi: 10.1016/j.jamcollsurg.2018.12.001

Verbeek, F. P. R., Troyan, S. L., Mieog, J. S. D., Liefers, G.-J., Moffitt, L. A., Rosenberg, M., et al. (2014). Near-infrared fluorescence sentinel lymph node mapping in breast cancer: a multicenter experience. *Breast Cancer Res. Treat.* 143, 333–342. doi: 10.1007/s10549-013-2802-9

Wang, H., Li, X., Tse, B. W.-C., Yang, H., Thorling, C. A., Liu, Y., et al. (2018). Indocyanine green-incorporating nanoparticles for cancer theranostics. *Theranostics* 8, 1227–1242. doi: 10.7150/thno.22872

Wang, X., Ku, G., Wegiel, M. A., Bornhop, D. J., Stoica, G., and Wang, L. V. (2004). Noninvasive photoacoustic angiography of animal brains *in vivo* with near-infrared light and an optical contrast agent. *Opt. Lett.* 29:730. doi: 10.1364/OL.29.000730

Wishart, G. C., Loh, S.-W., Jones, L., and Benson, J. R. (2012). A feasibility study (ICG-10) of indocyanine green (ICG) fluorescence mapping for sentinel lymph node detection in early breast cancer. *Eur. J. Surg. Oncol.* 38, 651–656. doi: 10.1016/j.ejso.2012.05.007

Xu, H.-L., ZhuGe, D.-L., Chen, P.-P., Tong, M.-Q., Lin, M.-T., Jiang, X., et al. (2018). Silk fibroin nanoparticles dyeing indocyanine green for imaging-guided photo-thermal therapy of glioblastoma. *Drug Deliv.* 25, 364–375. doi: 10.1080/10717544.2018.1428244

Yan, F., Wu, H., Liu, H., Deng, Z., Liu, H., Duan, W., et al. (2016). Molecular imaging-guided photothermal/photodynamic therapy against tumor by iRGD-modified indocyanine green nanoparticles. *J. Control. Release* 224, 217–228. doi: 10.1016/j.jconrel.2015.12.050

Yaseen, M. A., Yu, J., Jung, B., Wong, M. S., and Anvari, B. (2009). Biodistribution of encapsulated indocyanine green in healthy mice. *Mol. Pharmaceutics* 6, 1321–1332. doi: 10.1021/mp800270t

Yuan, B., Chen, N., and Zhu, Q. (2004). Emission and absorption properties of indocyanine green in Intralipid solution. *J. Biomed. Opt.* 9, 497–503. doi: 10.1117/1.1695411

Zhao, P., Zheng, M., Yue, C., Luo, Z., Gong, P., Gao, G., et al. (2014). Improving drug accumulation and photothermal efficacy in tumor depending on size of ICG loaded lipid-polymer nanoparticles. *Biomaterials* 35, 6037–6046. doi: 10.1016/j.biomaterials.2014.04.019

Zhen, Z., Tang, W., Guo, C., Chen, H., Lin, X., Liu, G., et al. (2013). Ferritin nanocages to encapsulate and deliver photosensitizers for efficient photodynamic therapy against cancer. *ACS Nano* 7, 6988–6996. doi: 10.1021/nn402199g

Zheng, M., Zhao, P., Luo, Z., Gong, P., Zheng, C., Zhang, P., et al. (2014). Robust ICG theranostic nanoparticles for folate targeted cancer imaging and highly effective photothermal therapy. *ACS Appl. Mater. Interfaces* 6, 6709–6716. doi: 10.1021/am5004393

Zheng, X., Xing, D., Zhou, F., Wu, B., and Chen, W. R. (2011). Indocyanine green-containing nanostructure as near infrared dual-functional targeting probes for optical imaging and photothermal therapy. *Mol. Pharmaceutics* 8, 447–456. doi: 10.1021/mp100301t

Zheng, X., Zhou, F., Wu, B., Chen, W. R., and Xing, D. (2012). Enhanced tumor treatment using biofunctional indocyanine green-containing nanostructure by intratumoral or intravenous injection. *Mol. Pharm.* 9, 514–522. doi: 10.1021/mp200526m

Zhu, L., Li, P., Gao, D., Liu, J., Liu, Y., Sun, C., et al. (2019). pH-sensitive loaded retinal/indocyanine green micelles as an "all-in-one" theranostic agent for multi-modal imaging *in vivo* guided cellular senescence-photothermal synergistic therapy. *Chem. Commun.* 55, 6209–6212. doi: 10.1039/C9CC02567G

ZhuGe, D.-L., Wang, L.-F., Chen, R., Li, X.-Z., Huang, Z.-W., Yao, Q., et al. (2019). Cross-linked nanoparticles of silk fibroin with proanthocyanidins as a promising vehicle of indocyanine green for photo-thermal therapy of glioma. *Artif. Cells Nanomed. Biotechnol.* 47, 4293–4304. doi: 10.1080/21691401.2019.1699819

Conflict of Interest: The authors declare that the research was conducted in the absence of any commercial or financial relationships that could be construed as a potential conflict of interest.

frontiers in Chemistry

MINI REVIEW
published: 04 September 2020
doi: 10.3389/fchem.2020.00770

Photodynamic Therapy of Cancers With Internal Light Sources: Chemiluminescence, Bioluminescence, and Cerenkov Radiation

Yintang Zhang[1], *Yuanqiang Hao*[1]*, *Shu Chen*[2] and *Maotian Xu*[1]

[1] Henan Key Laboratory of Biomolecular Recognition and Sensing, College of Chemistry and Chemical Engineering, Henan Joint International Research Laboratory of Chemo/Biosensing and Early Diagnosis of Major Diseases, Shangqiu Normal University, Shangqiu, China, [2] Key Laboratory of Theoretical Organic Chemistry and Function Molecule of Ministry of Education, School of Chemistry and Chemical Engineering, Hunan University of Science and Technology, Xiangtan, China

Photodynamic therapy (PDT) is a promising and minimally invasive modality for the treatment of cancers. The use of a self-illuminating system as a light source provides an intriguing solution to the light penetration issues of conventional PDT, which have gained considerable research interest in the past few years. This mini review aimed to present an overview of self-illuminating PDT systems by using internal light sources (chemiluminescence, bioluminescence, and Cerenkov radiation) and to give a brief discussion on the current challenges and future perspectives.

Keywords: photodynamic therapy, cancers, internal light sources, chemiluminescence, bioluminescence, Cerenkov radiation

OPEN ACCESS

Edited by:
Wansong Chen,
Central South University, China

Reviewed by:
Huangxian Ju,
Nanjing University, China
Saji Uthaman,
Chungnam National University, South Korea

***Correspondence:**
Yuanqiang Hao
hao0736@163.com

Specialty section:
This article was submitted to Nanoscience, a section of the journal Frontiers in Chemistry

Received: *14 May 2020*
Accepted: *23 July 2020*
Published: *04 September 2020*

Citation:
Zhang Y, Hao Y, Chen S and Xu M (2020) Photodynamic Therapy of Cancers With Internal Light Sources: Chemiluminescence, Bioluminescence, and Cerenkov Radiation. Front. Chem. 8:770. doi: 10.3389/fchem.2020.00770

INTRODUCTION

Photodynamic therapy (PDT) is a promising non-invasive medical technique and has been clinically approved for treating various diseases, including bacterial and fungal infections, skin diseases, as well as several types of cancer (van Straten et al., 2017). In the past decades, advances in nanotechnology and materials science as well as the improvements of photosensitizers (PS) have promoted the rapid development of PDT (Chen et al., 2017; Glass et al., 2018; Ouyang et al., 2018a,b; Fan et al., 2019; Yue et al., 2019; Zeng et al., 2019). However, the conventional external light irradiations in PDT often suffer from rapid attenuation through the tissue, which limited the clinical use of PDT to some superficial or endoscope-accessible lesions. To overcome this barrier, different excitation sources, such as near-infrared (NIR) light and X-ray radiation, have been applied in combination with a number of judiciously designed photosensitizers, such as two-photon (Shen et al., 2016) or NIR light (Lan et al., 2019) excitation photosensitizers and upconversion photosensitizers (Liu et al., 2019). Nevertheless, it is still challenging to develop NIR photosensitizers with high absorption efficiency, and NIR light also has penetration limitation (i.e., 980-nm light is restricted to 1.5 cm). X-ray radiation, photon energy in the range of 0.1–100 keV, can overcome the limitation of the light penetration depth in the human body. But X-rays can ionize atoms and disrupt chemical bonds of normal biomolecules. Implanting fiber-optic light sources could be a viable approach to treat deep tissue, but it requires invasive procedures and cannot deal with tumor metastasis.

Internal light sources have emerged as an attractive alternative to outer light sources in a conventional PDT system for addressing the issue of light penetration (Magalhães et al., 2016; Ferreira et al., 2019). Some self-illuminating systems, including chemiluminescence (CL), bioluminescence (BL), and Cerenkov radiation (CR), are promising candidates as internal light sources for PDT as these self-illuminators are small in size (ranging from atomic/molecular to nanometer scale) and thus can be delivered to any pathological tissues. The use of self-illuminating systems as light sources in PDT has attracted increasing research interest in the past few years (Fan et al., 2016; Magalhães et al., 2016; Jiang et al., 2020). In this mini review, we summarize recent progress in the development of self-illuminating PDT systems, including chemiluminescence-, bioluminescence-, and Cerenkov radiation-mediated photodynamic therapy (**Figure 1**). The design strategies and chemical structures of these reported PDT systems will be emphasized. Current limitations and future directions will also be discussed.

CHEMILUMINESCENCE-MEDIATED PHOTODYNAMIC THERAPY

CL is a kind of self-luminescence phenomenon that results from some special types of chemical reactions. Up to now, chemiluminescence reactions have found a wide variety of applications (Iranifam, 2014; Shah et al., 2020) such as chemosensing, bioimaging, and therapy. The most commonly used chemiluminescence systems are luminol–H_2O_2 and oxalate ester–H_2O_2.

The first report of using luminol chemiluminescence as an excitation light source for PDT application was demonstrated by Laptev et al. (2006). A transferrin–hematoporphyrin (Tf–Hp) conjugate was used as the cancer cell targetable photosensitizer. The absorption spectra of Tf–Hp (one absorption peak at 412 nm) overlapped well with the CL emission band of luminol (350–550 nm). The addition of luminol can induce a noticeable intracellular CL over a 50-min period. The combination of luminol (10 μM) and the Tf–Hp conjugate (3 μM) resulted in 95% cytotoxicity against the erythroleukemic cell lines.

Yuan et al. (2012) developed a new chemiluminescence-mediated PDT by using a cationic oligo(*p*-phenylene vinylene) (OPV) as the photosensitizer. The cationic OPV could not only interact with the dianionic intermediates of luminol CL reaction to facilitate the occurrence of chemiluminescence resonance energy transfer (CRET) to excite OPV but could also bind to the negatively charged pathogen (cancer cells and fungi). The luminol chemiluminescence system with OPV displayed prominent cytotoxicity toward HeLa cells with a viability of <10%. Studies in tumor-bearing nude mice indicated that this self-illuminated PDT system could significantly inhibit the tumor growth *in vivo* without exerting apparent toxicity to the normal tissues. Based on the cationic OPV photosensitizer, the same research group proposed a novel electrochemiluminescence-mediated PDT system (Liu et al., 2018). Recently, Jiang's group reported a conjugated polymer nanoparticle-based multifunctional nanoplatform for oxygen-supplying and self-illuminating phototherapy (Jiang et al., 2019). The nanoplatform Hb–NPs was obtained by covalently coupling hemoglobin (Hb) to the polymer nanoparticle consisting of poly(styrene-*co*-maleic anhydride) (PSMA) and poly[2-methoxy-5-(2-ethylhexyloxy)-1,4-phenylenevinylene] (MEH–PPV). The polymer-conjugated Hb can simultaneously function as the oxygen carrier, the catalyst for the CL reaction of luminol with H_2O_2, as well as the PDT photosensitizer for generating reactive oxygen species (ROS). Thus, the presented system does not require an external light source and can overcome the problem of insufficient oxygen under hypoxia. In addition, the system can also be used to control the release of an anticancer prodrug, thus providing simultaneous phototherapy and chemotherapy.

The combination of different forms of photosensitizers with luminol CL has afforded a variety of other internal self-illuminating PDT systems, including tetra(hydroxyphenyl)chlorin (THPC)-encapsulated FH-Pdots [folic acid and horseradish peroxidase (HRP)-bifunctionalized polymer dots] (Zhang et al., 2014), 5-aminolevulinic acid (Chen et al., 2012), porphyrinic metal–organic frameworks (C_OTCPP MOFs) (Fang et al., 2019), chlorin e6-conjugated yellow-emissive carbon dots (y-CDs-Ce6) (Yang et al., 2020), and poly(lactic-*co*-glycolic acid) (PLGA)/luminol/HRP/DSPE-mPEG2000 co-precipitated nanoparticles (Lu et al., 2020). Covalent attachment of luminol to the photosensitizer into a single molecule is an additional strategy for constructing a CL-PDT system through the direct energy transfer from luminol to the photosensitizer. Yesilgul et al. (2017) designed a modular unimolecular erythrosine–luminol which can produce singlet oxygen in the presence of Cu^{2+} and hydrogen peroxide. Xu et al. (2019) synthesized a Ce6–luminol–PEG (CLP) conjugate which can self-assemble into core–shell nanoparticles. The nanoparticle can be exploited for inflammation imaging as well as for specifically killing cancer cells. In addition to the commonly used chemiluminophore of luminol, peroxyoxalate chemiluminescent (PO-CL) reaction also has the potential to supply internal light source for PDT. Romanyuk et al. (2017) developed a self-luminescing PDT strategy by using polymeric oxalate (POX) as the substrate of the PO-CL reaction and tetramethyl hematoporhyrin (TMHP) as both a photosensitizer and an activator for the PO-CL reaction. POX and TMHP were dispersed in dimethyl phthalate (DMP) droplets and stabilized with a surfactant of Pluronic L64. The L64/DMP/POX/TMHP dispersions can effectively produce O_2^1 and exert significant cytotoxicity under oxidative stress condition. Mao et al. (2017) designed a novel nanoplatform [C-TBD nanoparticles (NPs)] for image-guided PDT by co-encapsulating bis[2,4,5-trichloro-6-(pentyloxycarbonyl)phenyl]oxalate (CPPO) and the photosensitizer TBD into an amphiphilic copolymer Pluronic F-127. The astutely designed photosensitizer TBD displayed a bright aggregation-induced NIR emission and an efficient singlet oxygen generation. C-TBD NPs could precisely monitor the tumor site via chemiluminescence imaging and efficiently inhibit tumor growth through PO-CL exciting TBD to produce O_2^1 in the presence of H_2O_2, thus realizing simultaneous tumor diagnosis and treatment. Coelenterazine and its analogs can

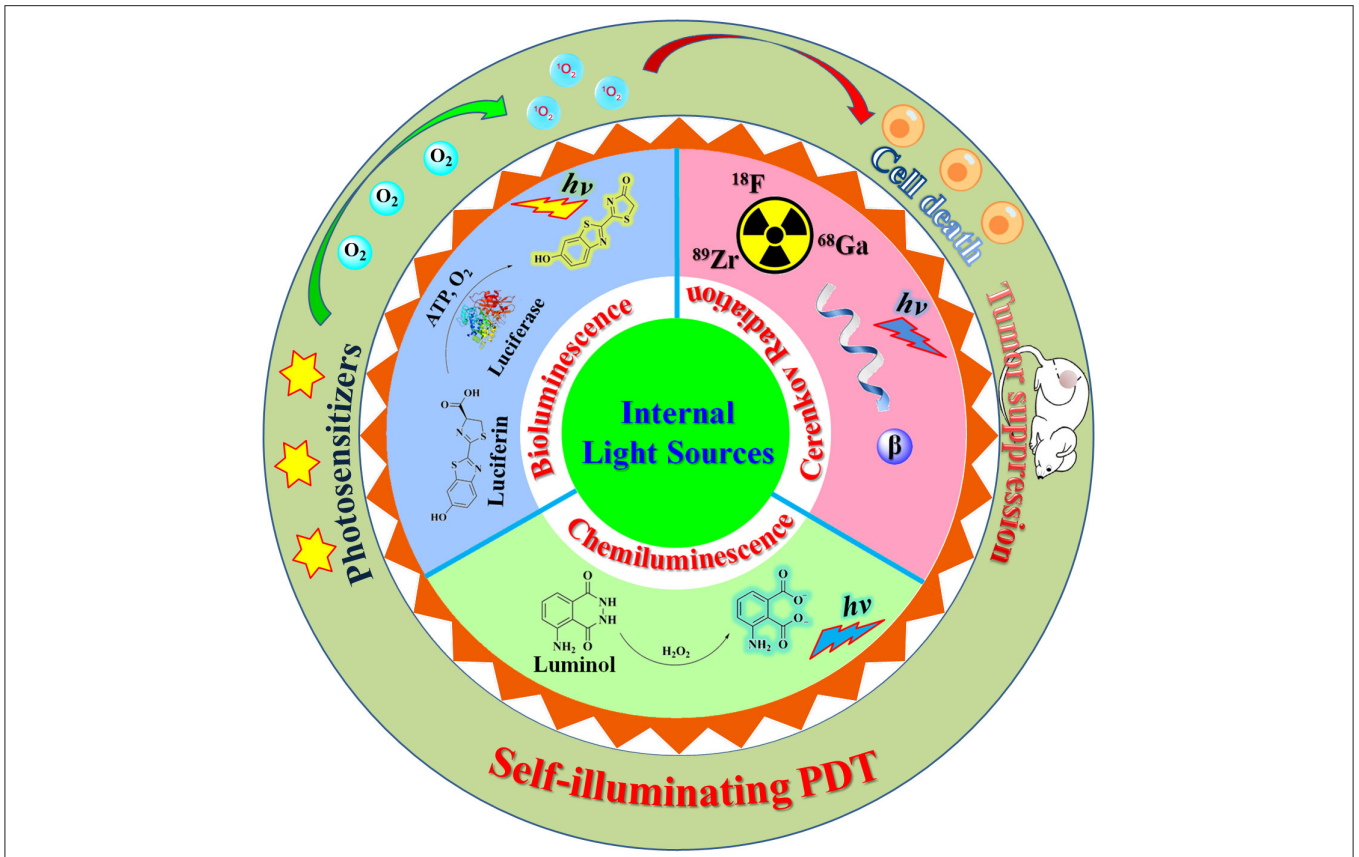

FIGURE 1 | Illustration of a self-illuminating photodynamic therapy (PDT) system based on internal light sources, including chemiluminescence, bioluminescence, and Cerenkov radiation.

also act as a self-activating agent for PDT (Pinto da Silva et al., 2019; Sun et al., 2019). In the presence of a superoxide anion (overexpressed in tumor cells), coelenterazine can be oxidized into a dioxetanone intermediate, which then decomposing into CO_2 and the excited coelenteramide. The product will further undergo intersystem crossing to the triplet state, thus inducing the generation of O_2^1. This process can be enhanced by the introduction of a bromine heteroatom due to the heavy atom effect (Pinto da Silva et al., 2019).

BIOLUMINESCENCE-MEDIATED PHOTODYNAMIC THERAPY

Bioluminescence can be considered as a special type of CL which involves the enzymatic oxidation of a small molecule substrate, such as the firefly luciferase–luciferin, and Renilla luciferase–coelenterazine systems (Magalhães et al., 2016; Hananya and Shabat, 2017). Theodossiou et al. firstly evaluated the potential of intracellular bioluminescence as a light source for PDT (Theodossiou et al., 2003). The classical firefly luciferin–luciferase system was used to excite the photosensitizer, Rose Bengal (RB), which has a high singlet oxygen quantum yield and a compatible absorption profile with the emission of oxyluciferin. Treating the luciferase-transfected NIH 3T3 cells with RB and D-luciferin led to a high rate of apoptosis (89%). This preliminary *in vitro* study demonstrated the possibility of a bioluminescence-mediated PDT to be a plausible treatment modality. However, the following work by Schipper et al. (2006) revealed that luciferase-expressing cells incubated with photosensitizer and D-luciferin did not show a significant difference in survival compared with the control groups. The authors demonstrated that this intracellular bioluminescence system cannot emit enough photons ($<1.03 \times 10^{-4}$ mJ cm^{-2} for 24 h treatment) to mediate photosensitizers to generate efficacious photodynamic toxicity.

In the above cases, the bioluminescent enzyme appeared in cells through gene expression, a technology that has not been applied in actual clinical treatment, so this bioluminescent system has difficulty in becoming an alternative excitation for PDT in the near future. Hsu et al. (2013) developed a new coelenterazine bioluminescence-mediated PDT system based on the bioluminescent QD-Rluc8 conjugate which was obtained by immobilizing Renilla luciferase onto quantum dot 655. In the presence of coelenterazine, QD-Rluc8 can display the distinct fluorescence emission of quantum dots (QDs) via bioluminescent resonance energy transfer (BRET) from the bioluminescent substrate to the QDs. Both *in vitro* and *in vivo* assays demonstrated that the bioluminescent QD-Rluc8 can stimulate the micelle-loaded photosensitizer meta-tetra(hydroxyphenyl)chlorin (m-THPC, Foscan) to produce ROS

and thus result in cell death and inhibition of tumor growth. As a potential alternative excitation source for PDT, QD-Rluc8 displayed several advantages, including a tunable emission wavelength and a relatively high irradiation dose (0.6–0.8 J cm^{-2}). Subsequently, Kim et al. (2015) evaluated whether BL can induce efficient PDT for tumors, especially in deep tissue. A similar BRET Luc-QD luminophore was employed as the BL source, and Ce6 was used as the photosensitizer. Confocal imaging showed that Luc-QD conjugates were mainly distributed on the cell surface instead of in the cytoplasm. Calculating from the emission spectra, the BRET efficiency of the Luc-QD system reached 60–65%. Luc-QD can excite the nearby photosensitizer, leading to an appreciable amount of activated Ce6 (3×10^8/min), which is higher than that (4×10^7/min) resulting from laser illumination (2.2 mW/cm^2). Cell imaging and cytotoxicity tests revealed that this BL-PDT system can generate significant intracellular ROS, thus resulting in membrane damage and cell death. Intravenous injection of Ce6, Luc-QD, and CTZ to tumor-implant mice can almost completely inhibit tumor growth. Furthermore, this BL-PDT can also suppress distant organ metastasis. Recently, Yang et al. (2018) reported a new BL-PDT system based on the polymer nanoparticle which was assembled from poly(lactic acid) and poly(lactic-*co*-glycolic acid) and was loaded with Rose Bengal and luciferase. *In vitro* photodynamic studies showed that this BL-PDT treatment can lead to significant toxicity toward cancer cells. *In vivo*, BL-PDT displayed that the growth of subcutaneous tumors can be remarkably inhibited, while normal organs, including the heart, liver, spleen, lung, and kidney, remained undamaged.

CERENKOV RADIATION-INDUCED PHOTODYNAMIC THERAPY

Cerenkov radiation (CR) is a luminescence phenomenon occurring from the interaction between high-speed charged particles (faster than the phase velocity of light) with the surrounding medium, which was theoretically predicted by Heaviside in 1888 and experimentally verified by Cerenkov in 1933 (Shaffer et al., 2017). In biomedical applications, the commonly used sources for producing Cerenkov radiation are radionuclides which can emit β particles (positrons or electrons) (Gill et al., 2015), such as ^{18}F, ^{64}Cu, ^{68}Ga, ^{89}Zr, ^{90}Y, ^{124}I, and ^{198}Au. The number of Cerenkov photons within a certain wavelength range is positively correlated to the kinetic energy (or velocity) of the β particle. Radionuclides emitting β particles with relatively higher energy, such as ^{68}Ga and ^{90}Y, would produce CR with higher intensity (Klein et al., 2019). In recent years, the Cerenkov phenomenon for biomedical applications (i.e., imaging and therapy) has gradually garnered significant attention, especially combining the rapid advancements in nanosciences and nanotechnologies (Shaffer et al., 2017; Cline et al., 2019; Ferreira et al., 2019).

In 2015, Kotagiri and coworkers reported a proof-of-concept study using CR from a common diagnostic clinical radiotracer, 2′-deoxy-2′-[^{18}F]fluoro-D-glucose ([^{18}F]-FDG), as the light source for PDT, denoted as CR-induced therapy (CRIT) (Kotagiri et al., 2015). By incorporating both apotransferrin (Tf) and titanocene (Tc) into TiO_2 nanoparticles, the authors designed and prepared an effective nanophotosensitizer (TiO_2-Tf–Tc) which can function with low-intense radiation. TiO_2 nanoparticles have the capability to effectively utilize CR, which locates predominantly within the ultraviolet to the blue spectral region (characteristic $1/\lambda^2$ spectrum), to generate hydroxyl and superoxide radicals. Tf can not only act as a stabilizer and dispersant for TiO_2 but also as a tumor-targeting agent. Tc can serve as a complementary photosensitizer for generating cyclopentadienyl and titanium-centered radicals. *In vitro* cellular experiments have shown that TiO_2-Tf can be endocytosed by tumor cells and, together with [^{18}F]-FDG, can lead to an appreciable decrease in cell viability. *In vivo* studies have demonstrated that the administrated TiO_2-Tf–Tc prefer to accumulate in the tumor tissue and that the co-administration of TiO_2-Tf–Tc and radionuclides efficiently inhibited the tumor growth and increased the median survival. These results demonstrated the possibility of utilizing CR as the internal exciting light for PDT photosensitizers, and this pioneering work opened a new avenue for the application of the Cerenkov effect in PDT, especially in a depth- and oxygen-independent manner. Following this study, Duan et al. (2018) reported another CRIT system by using ^{68}Ga-labeled bovine serum albumin (^{68}Ga-BSA) as a more efficient Cherenkov radiation emitter and dextran-modified TiO_2 nanoparticles (D-TiO_2 NPs) as the nanophotosensitizer. For comparison, [^{18}F]-FDG was also used throughout this study. Positron emission tomography (PET) images of tumor-bearing mice intratumorally injected with radionuclides revealed that both ^{68}Ga-BSA and [^{18}F]-FDG can predominantly stay in the tumor in similar amounts, whereas much more CR photon accumulation appeared in mouse loaded with ^{68}Ga-BSA. As a result, ^{68}Ga-BSA with D-TiO_2 exhibited a significantly enhanced PDT efficacy. Injection of ^{68}Ga-BSA and D-TiO_2 NPs into the tumor mass caused complete suppression of the tumor growth and a significant increase in median survival, while no obvious efficacy was observed for the other group, even with the combination of [^{18}F]-FDG and D-TiO_2 NPs.

In the above two studies, the Cerenkov source (radiotracer) and the PDT photosensitizer were used individually, as two detached elements. After administration, the radiotracer and photosensitizer would randomly distribute in the target location and within a relatively large distance. Thus, a large portion of the Cerenkov photons from the radiotracer may have probably been absorbed or scattered by the media instead of exciting the photosensitizer. To circumvent this problem, Kamkaew et al. (2016) designed an integrated CRIT system, [^{89}Zr]HMSN-Ce6, by loading the Cerenkov source (^{89}Zr) and photosensitizer (Ce6) into hollow mesoporous silica nanoparticles (HMSNs). *In vitro* imaging displayed that [^{89}Zr]HMSN-Ce6 can emit intense fluorescence (690–710 nm) in solution without external excitation light, which clearly confirmed the occurrence of energy transfer between ^{89}Zr and Ce6. *In vivo* CR-induced PDT studies further confirmed the efficacy of [^{89}Zr]HMSN-Ce6 to completely inhibit tumor growth. Subsequently, the same research group proposed a magnetic targetable CRIT system (Ni et al., 2018), ^{89}Zr-MNP/TCPP, which was prepared by

labeling PEGylated magnetic nanoparticles (MNP) with ^{89}Zr via Lewis acid–base interaction and then conjugating with the photosensitizer, meso-tetrakis(4-carboxyphenyl)porphyrin (TCPP), via amide coupling. Various imaging analyses (including PET, fluorescence, CL, and CRET) confirmed that the magnetic nanoparticles can be accumulated in tumor regions under an external magnetic field. The ^{89}Zr-MNP/TCPP ternary composite has shown efficient $^1O_2$ generation efficiency as well as a high magnetic-guided therapeutic efficacy. Recently, Yu's group proposed a novel "missile detonation" strategy for efficient CR-induced theranostics by the successive administration of a high dose of porphyrin–PEG nanocomplex (PPN) and a low dose of ^{89}Zr-labeled PPN (^{89}Zr-Df-PPN) (Yu et al., 2019). The PPN and ^{89}Zr-Df-PPN acted as the CR energy receiver/missile and ^{89}Zr-Df-PPN the CR energy donor/detonator, respectively. These therapeutic agents can be monitored via multimodal imaging, including fluorescence imaging, CRET imaging, and PET. This CRIT system could significantly inhibit tumor growth *in vivo* and cause substantial fragmentation of vascular in the tumor.

CONCLUSIONS AND PERSPECTIVES

In this review, we have summarized recent advances in the development of self-illuminating PDT systems. Internal light sources, including chemiluminescence, bioluminescence, and Cerenkov radiation, have been proven capable of exciting certain photosensitizers to produce ROS and generate efficacious photodynamic toxicity. The use of these internal light sources has great potential for depth-independent PDT, which would expand the scope of PDT in cancer treatment.

Despite the impressive progress outlined above, the current self-illuminating PDT systems still face several challenges, including a relatively low photon flux, the requirement of multicomponent reactions for CL and BL, limited wavelength range of the excitation light, etc. To overcome these shortcomings, several future directions for the design of self-illuminating PDT systems are proposed as follows:

(1) Nanocarrier technologies can be employed for increasing the amount of administrated self-illuminators. If the reactants for producing internal light, such as luminol, luciferase–luciferin pairs, and CR radiotracer, were loaded and delivered to the tumor tissues by proper nanocarriers, they would provide a higher local photon flux and, thus, more efficient PDT. The use of multifunctional nanoplatforms for a targeted delivery and controlled release of these illuminators is also recommended.

(2) Nanophotosensitizers are more suitable for self-illuminating PDT systems as they (metal oxide nanocrystals, QDs, polymer dots, etc.) have higher cross-sections for absorbing light compared with single small-molecule photosensitizers. Moreover, nanophotosensitizers, such as QDs, can be tuned to absorb light with wavelengths ranging from near-UV through visible to near-IR.

(3) The currently used internal light sources can be further expanded. Compared with the conventional CL systems of luminol–H_2O_2 and oxalate ester–H_2O_2, the newly developed triggerable dioxetanes are more attractive chemiluminescent probes (Hananya and Shabat, 2017) as they have tunable structures and emission features, high CL quantum yields, without the requirement of an enzyme/catalase and H_2O_2. Thus, triggerable dioxetanes hold great potential as internal light sources for PDT. The use of a structure-modified luciferin as the substrate is a desirable approach for tuning the emission wavelength of BL, which would expand the application of BL in PDT.

(4) The combined theranostic strategy is also an exciting trend for improving the efficacy of self-illuminating PDT as the integration of two or more treatments can generate synergistic effects for antitumor therapy. Thus, a promising future direction is to combine self-illuminating PDT with various other treatments, such as immunotherapy, chemotherapy, and photothermal therapy.

AUTHOR CONTRIBUTIONS

YH and YZ organized and wrote the manuscript. SC and MX discussed the results. All authors approved this manuscript.

FUNDING

This work was financially supported by the National Natural Science Foundation of China (Grant No. 21804085).

ACKNOWLEDGMENTS

This is a short text to acknowledge the contributions of specific colleagues, institutions, or agencies that aided the efforts of the authors.

REFERENCES

Chen, T.-C., Huang, L., Liu, C.-C., Chao, P.-J., and Lin, F.-H. (2012). Luminol as the light source for *in situ* photodynamic therapy. *Process Biochem.* 47, 1903–1908. doi: 10.1016/j.procbio.2012.06.025

Chen, W., Ouyang, J., Liu, H., Chen, M., Zeng, K., Sheng, J., et al. (2017). Black phosphorus nanosheet-based drug delivery system for synergistic photodynamic/photothermal/chemotherapy of cancer. *Adv. Mater.* 29:1603864. doi: 10.1002/adma.201603864

Cline, B., Delahunty, I., and Xie, J. (2019). Nanoparticles to mediate X-ray-induced photodynamic therapy and Cherenkov radiation photodynamic therapy. *WIREs Nanomed. Nanobiotechnol.* 11:e1541. doi: 10.1002/wnan.1541

Duan, D. B., Liu, H., Xu, Y., Han, Y. X., Xu, M. X., Zhang, Z. C., et al. (2018). Activating TiO_2 nanoparticles: gallium-68 serves as a high-yield photon emitter for cerenkov-induced photodynamic therapy. *ACS Appl. Mater. Interfaces* 10, 5278–5286. doi: 10.1021/acsami.7b17902

Fan, J. H., Fan, G. L., Yuan, P., Deng, F. A., Liu, L. S., Zhou, X., et al. (2019). A theranostic nanoprobe for hypoxia imaging and photodynamic tumor therapy. *Front. Chem.* 7:868. doi: 10.3389/fchem.2019.00868

Fan, W., Huang, P., and Chen, X. (2016). Overcoming the achilles' heel of photodynamic therapy. *Chem. Soc. Rev.* 45, 6488–6519. doi: 10.1039/C6CS00616G

Fang, L., Hu, Q., Jiang, K., Zhang, X., Li, B., Cui, Y., et al. (2019). An inner light integrated metal-organic framework photodynamic therapy system for effective

elimination of deep-seated tumor cells. *J. Solid State Chem*. 276, 205–209. doi: 10.1016/j.jssc.2019.05.015

Ferreira, C. A., Ni, D., Rosenkrans, Z. T., and Cai, W. (2019). Radionuclide-activated nanomaterials and their biomedical applications. *Angew. Chem. Int. Ed.* 58, 13232–13252. doi: 10.1002/anie.201900594

Gill, R. K., Mitchell, G. S., and Cherry, S. R. (2015). Computed cerenkov luminescence yields for radionuclides used in biology and medicine. *Phys. Med. Biol*. 60, 4263–4280. doi: 10.1088/0031-9155/60/11/4263

Glass, S., Trinklein, B., Abel, B., and Schulze, A. (2018). TiO2 as photosensitizer and photoinitiator for synthesis of photoactive TiO2-PEGDA hydrogel without organic photoinitiator. *Front. Chem*. 6:340. doi: 10.3389/fchem.2018.00340

Hananya, N., and Shabat, D. (2017). A glowing trajectory between bio- and chemiluminescence: from luciferin-based probes to triggerable dioxetanes. *Angew. Chem. Int. Ed*. 56, 16454–16463. doi: 10.1002/anie.201706969

Hsu, C.-Y., Chen, C.-W., Yu, H.-P., Lin, Y.-F., and Lai, P.-S. (2013). Bioluminescence resonance energy transfer using luciferase-immobilized quantum dots for self-illuminated photodynamic therapy. *Biomaterials* 34, 1204–1212. doi: 10.1016/j.biomaterials.2012.08.044

Iranifam, M. (2014). Analytical applications of chemiluminescence methods for cancer detection and therapy. *TrAC Trends Anal. Chem*. 59, 156–183. doi: 10.1016/j.trac.2014.03.010

Jiang, L., Bai, H., Liu, L., Lv, F., Ren, X., and Wang, S. (2019). Luminescent, oxygen-supplying, hemoglobin-linked conjugated polymer nanoparticles for photodynamic therapy. *Angew. Chem. Int. Ed*. 58, 10660–10665. doi: 10.1002/anie.201905884

Jiang, L., Liu, L., Lv, F., Wang, S., and Ren, X. (2020). Integration of self-luminescence and oxygen self-supply: a potential photodynamic therapy strategy for deep tumor treatment. *Chempluschem* 85, 510–518. doi: 10.1002/cplu.202000083

Kamkaew, A., Cheng, L., Goel, S., Valdovinos, H. F., Barnhart, T. E., Liu, Z., et al. (2016). Cerenkov radiation induced photodynamic therapy using chlorin e6-loaded hollow mesoporous silica nanoparticles. *ACS Appl. Mater. Interfaces* 8, 26630–26637. doi: 10.1021/acsami.6b10255

Kim, Y. R., Kim, S., Choi, J. W., Choi, S. Y., Lee, S.-H., Kim, H., et al. (2015). Bioluminescence-activated deep-tissue photodynamic therapy of cancer. *Theranostics* 5, 805–817. doi: 10.7150/thno.11520

Klein, J. S., Sun, C., and Pratx, G. (2019). Radioluminescence in biomedicine: physics, applications, and models. *Phys. Med. Biol*. 64:04TR01. doi: 10.1088/1361-6560/aaf4de

Kotagiri, N., Sudlow, G. P., Akers, W. J., and Achilefu, S. (2015). Breaking the depth dependency of phototherapy with cerenkov radiation and low-radiance-responsive nanophotosensitizers. *Nat. Nanotechnol*. 10, 370–379. doi: 10.1038/nnano.2015.17

Lan, M., Zhao, S., Liu, W., Lee, C.-S., Zhang, W., and Wang, P. (2019). Photosensitizers for photodynamic therapy. *Adv. Healthcare Mater*. 8:1900132. doi: 10.1002/adhm.201900132

Laptev, R., Nisnevitch, M., Siboni, G., Malik, Z., and Firer, M. A. (2006). Intracellular chemiluminescence activates targeted photodynamic destruction of leukaemic cells. *Br. J. Cancer* 95, 189–196. doi: 10.1038/sj.bjc.6603241

Liu, S., Yuan, H., Bai, H., Zhang, P., Lv, F., Liu, L., et al. (2018). Electrochemiluminescence for electric-driven antibacterial therapeutics. *J. Am. Chem. Soc*. 140, 2284–2291. doi: 10.1021/jacs.7b12140

Liu, Y., Meng, X., and Bu, W. (2019). Upconversion-based photodynamic cancer therapy. *Coord. Chem. Rev*. 379, 82–98. doi: 10.1016/j.ccr.2017.09.006

Lu, X., Song, X., Wang, Q., Hu, W., Shi, W., Tang, Y., et al. (2020). Chemiluminescent organic nanophotosensitizer for a penetration depth independent photodynamic therapy. *RSC Adv*. 10, 11861–11864. doi: 10.1039/D0RA01477J

Magalhães, C. M., Esteves da Silva, J. C. G., and Pinto da Silva, L. (2016). Chemiluminescence and bioluminescence as an excitation source in the photodynamic therapy of cancer: a critical review. *Chemphyschem* 17, 2286–2294. doi: 10.1002/cphc.201600270

Mao, D., Wu, W., Ji, S., Chen, C., Hu, F., Kong, D., et al. (2017). Chemiluminescence-guided cancer therapy using a chemiexcited photosensitizer. *Chem* 3, 991–1007. doi: 10.1016/j.chempr.2017.10.002

Ni, D. L., Ferreira, C. A., Barnhart, T. E., Quach, V., Yu, B., Jiang, D. W., et al. (2018). Magnetic targeting of nanotheranostics enhances cerenkov radiation-induced photodynamic therapy. *J. Am. Chem. Soc*. 140, 14971–14979. doi: 10.1021/jacs.8b09374

Ouyang, J., Deng, Y., Chen, W., Xu, Q., Wang, L., Liu, Z., et al. (2018a). Marriage of artificial catalase and black phosphorus nanosheets for reinforced photodynamic antitumor therapy. *J. Mater. Chem. B* 6, 2057–2064. doi: 10.1039/C8TB00371H

Ouyang, J., Wang, L., Chen, W., Zeng, K., Han, Y., Xu, Y., et al. (2018b). Biomimetic nanothylakoids for efficient imaging-guided photodynamic therapy for cancer. *Chem. Commun*. 54, 3468–3471. doi: 10.1039/C8CC00674A

Pinto da Silva, L., Núnez-Montenegro, A., Magalhães, C. M., Ferreira, P. J. O., Duarte, D., González-Berdullas, P., et al. (2019). Single-molecule chemiluminescent photosensitizer for a self-activating and tumor-selective photodynamic therapy of cancer. *Eur. J. Med. Chem*. 183:111683. doi: 10.1016/j.ejmech.2019.111683

Romanyuk, A. V., Grozdova, I. D., Ezhov, A. A., and Melik-Nubarov, N. S. (2017). Peroxyoxalate chemiluminescent reaction as a tool for elimination of tumour cells under oxidative stress. *Sci. Rep*. 7:3410. doi: 10.1038/s41598-017-03527-w

Schipper, M. L., Patel, M. R., and Gambhir, S. S. (2006). Evaluation of firefly luciferase bioluminescence mediated photodynamic toxicity in cancer cells. *Mol. Imaging Biol*. 8, 218–225. doi: 10.1007/s11307-006-0048-1

Shaffer, T. M., Pratt, E. C., and Grimm, J. (2017). Utilizing the power of cerenkov light with nanotechnology. *Nat. Nanotechnol*. 12, 106–117. doi: 10.1038/nnano.2016.301

Shah, S. N. A., Khan, M., and Rehman, Z. U. (2020). A prolegomena of periodate and peroxide chemiluminescence. *TrAC Trends Anal. Chem*. 122:115722. doi: 10.1016/j.trac.2019.115722

Shen, Y., Shuhendler, A. J., Ye, D., Xu, J.-J., and Chen, H.-Y. (2016). Two-photon excitation nanoparticles for photodynamic therapy. *Chem. Soc. Rev*. 45, 6725–6741. doi: 10.1039/C6CS00442C

Sun, S.-K., Wu, J.-C., Wang, H., Zhou, L., Zhang, C., Cheng, R., et al. (2019). Turning solid into gel for high-efficient persistent luminescence-sensitized photodynamic therapy. *Biomaterials* 218:119328. doi: 10.1016/j.biomaterials.2019.119328

Theodossiou, T., Hothersall, J. S., Woods, E. A., Okkenhaug, K., Jacobson, J., and MacRobert, A. J. (2003). Firefly luciferin-activated rose bengal. *Cancer Res*. 63:1818.

van Straten, D., Mashayekhi, V., de Bruijn, H. S., Oliveira, S., and Robinson, D. J. (2017). Oncologic photodynamic therapy: basic principles, current clinical status and future directions. *Cancers* 9:19. doi: 10.3390/cancers9020019

Xu, X., An, H., Zhang, D., Tao, H., Dou, Y., Li, X., et al. (2019). A self-illuminating nanoparticle for inflammation imaging and cancer therapy. *Sci. Adv*. 5:eaat2953. doi: 10.1126/sciadv.aat2953

Yang, K., Wang, C., Wei, X., Ding, S., Liu, C., Tian, F., et al. (2020). Self-illuminating photodynamic therapy with enhanced therapeutic effect by optimization of the chemiluminescence resonance energy transfer step to the photosensitizer. *Bioconjugate Chem*. 31, 595–604. doi: 10.1021/acs.bioconjchem.9b00740

Yang, Y., Hou, W., Liu, S., Sun, K., Li, M., and Wu, C. (2018). Biodegradable polymer nanoparticles for photodynamic therapy by bioluminescence resonance energy transfer. *Biomacromolecules* 19, 201–208. doi: 10.1021/acs.biomac.7b01469

Yesilgul, N., Uyar, T. B., Seven, O., and Akkaya, E. U. (2017). Singlet oxygen generation with chemical excitation of an erythrosine–luminol conjugate. *ACS Omega* 2, 1367–1371. doi: 10.1021/acsomega.7b00228

Yu, B., Ni, D., Rosenkrans, Z. T., Barnhart, T. E., Wei, H., Ferreira, C. A., et al. (2019). A "missile-detonation" strategy to precisely supply and efficiently amplify cerenkov radiation energy for cancer theranostics. *Adv. Mater*. 31:1904894. doi: 10.1002/adma.201904894

Yuan, H., Chong, H., Wang, B., Zhu, C., Liu, L., Yang, Q., et al. (2012). Chemical molecule-induced light-activated system for anticancer and

antifungal activities. *J. Am. Chem. Soc*. 134, 13184–13187. doi: 10.1021/ja304986t

Yue, J., Liang, L., Shen, Y., Guan, X., Zhang, J., Li, Z., et al. (2019). Investigating dynamic molecular events in melanoma cell nucleus during photodynamic therapy by SERS. *Front. Chem*. 6:665. doi: 10.3389/fchem.2018.00665

Zeng, K., Xu, Q., Ouyang, J., Han, Y., Sheng, J., Wen, M., et al. (2019). Coordination nanosheets of phthalocyanine as multifunctional platform for imaging-guided synergistic therapy of cancer. *ACS Appl. Mater. Interfaces* 11, 6840–6849. doi: 10.1021/acsami.8b22008

Zhang, Y., Pang, L., Ma, C., Tu, Q., Zhang, R., Saeed, E., et al. (2014). Small molecule-initiated light-activated semiconducting polymer dots: an integrated nanoplatform for targeted photodynamic therapy and imaging of cancer cells. *Anal. Chem*. 86, 3092–3099. doi: 10.1021/ac404201s

Conflict of Interest: The authors declare that the research was conducted in the absence of any commercial or financial relationships that could be construed as a potential conflict of interest.

The handling editor declared a past co-authorship with the authors YZ, YH, SC, MX.

frontiers in Bioengineering and Biotechnology

REVIEW
published: 08 October 2020
doi: 10.3389/fbioe.2020.01019

Ultrasmall Au and Ag Nanoclusters for Biomedical Applications: A Review

Jia Tang[1], Haihong Shi[1], Guanyu Ma[2], Liangping Luo[3] and Zhenghua Tang[2,4]**

[1] Medical Genetics Center, Jiangmen Maternity and Child Health Care Hospital, Jiangmen, China, [2] Guangzhou Key Laboratory for Surface Chemistry of Energy Materials, Guangzhou Higher Education Mega Centre, School of Environment and Energy, New Energy Research Institute, South China University of Technology, Guangzhou, China, [3] Department of Medical Imaging Center, The First Affiliated Hospital of Jinan University, Jinan University, Guangzhou, China, [4] Guangdong Engineering and Technology Research Center for Surface Chemistry of Energy Materials, Guangzhou Higher Education Mega Centre, School of Environment and Energy, South China University of Technology, Guangzhou, China

OPEN ACCESS

Edited by:
Jianhua Zhang, Tianjin University, China

Reviewed by:
Shivendu Ranjan, University of Johannesburg, South Africa
Xun Yuan, Qingdao University of Science and Technology, China
Nandita Dasgupta, VIT University, India

***Correspondence:**
Liangping Luo
tluolp@jnu.edu.cn
Zhenghua Tang
zhht@scut.edu.cn; 156073036@qq.com

Specialty section:
This article was submitted to Nanobiotechnology, a section of the journal Frontiers in Bioengineering and Biotechnology

Received: *11 June 2020*
Accepted: *04 August 2020*
Published: *08 October 2020*

Citation:
Tang J, Shi H, Ma G, Luo L and Tang Z (2020) Ultrasmall Au and Ag Nanoclusters for Biomedical Applications: A Review. Front. Bioeng. Biotechnol. 8:1019. doi: 10.3389/fbioe.2020.01019

Noble metal (e.g., Au, Ag, Pt, Pd, and their alloys) nanoclusters (NCs) have emerged as a new type of functional nanomaterial in nanoscience and nanotechnology. Owing to their unique properties, such as their ultrasmall dimension, enhanced photoluminescence, low toxicity, and excellent biocompatibility, noble metal NCs—especially Au and Ag NCs—have found various applications in biomedical regimes. This review summarizes the recent advances made in employing ultrasmall Au and Ag NCs for biomedical applications, with particular emphasis on bioimaging and biosensing, anti-microbial applications, and tumor targeting and cancer treatment. Challenges, including the shared and specific challenges for Au and Ag NC toward biomedical applications, and future directions are briefly discussed at the end.

Keywords: ultrasmall Au and Ag nanoclusters, biomedical applications, bioimaging and biosensing, anti-microbial applications, tumor targeting and cancer treatment

INTRODUCTION

The last decade has witnessed the great achievement of employing noble metal nanoparticles, with sizes typically between 2 and 100 nm, in biomedical applications (Li et al., 2017; Mohanta et al., 2020; Yang et al., 2020). Such applications are largely relied on for their optical properties, such as absorption, luminescence, surface scattering, and surface-enhancing capabilities. For instance, spherical Au nanoparticles (NPs) of ∼5–100 nm often display a strong absorption peak at ∼520 nm, otherwise called the surface plasmon resonance (SPR) peak, which can be fine-tuned by manipulating the size and morphology of the Au NPs. The SPR peak originates from the collective excitation of free electrons upon excitation by light (Murray, 2008; Chakraborty and Pradeep, 2017).

However, when the size of metal NPs shrink below 2 nm, the SPR peak disappears and discrete step-like absorption bands can be observed in the optical spectrum. Such ultrasmall NPs are called nanoclusters (NCs), and NCs exhibit significantly different physiochemical properties from relatively larger counterparts, such as having larger Stokes shift, enhanced fluorescence, excellent photostability, and so on (Tan and Jin, 2013; Chakraborty and Pradeep, 2017). In addition, by controlling the reaction kinetics, it is possible to prepare ultrasmall NCs with atomic precision, where the definitive composition and molecule-like properties can provide an ideal bridge to

establish the structure/function relationship for nanoscience and nanotechnology research, which are not achievable for NPs because of their polydisperse nature in terms of size, morphology, and structure (Tang et al., 2018; Du et al., 2020).

For biomedical applications, metal NCs have demonstrated some superior performances over their NP counterparts. For instance, when utilized in an *in vivo* setup, metal NPs couldn't escape from the kidney barrier, which might cause some severe side effects in the liver and spleen, but in stark contrast, the ultrafine size of metal NCs allow them to be efficiently cleared from the body without causing serious damage (Song et al., 2016). In biomedical research, it is highly desirable to have a reliable, sensitive, and biocompatible platform, and the materials employed are expected to be stable and to maintain their intrinsic properties. The target matrix, *in vivo* environment are also complex, therefore the capability to fine-tune the physiochemical properties of the materials without sacrificing the integrity of nanomaterials is critical, where the surface chemistry of NCs are beneficial to achieve this goal (Song et al., 2016).

The controllable synthesis, catalytic applications, and surface chemistry engineering of noble metal clusters, especially Au and Ag NCs, have been discussed in some recent reviews (Li and Jin, 2013; Chakraborty and Pradeep, 2017; Higaki et al., 2018; Tang et al., 2018; Yan et al., 2018; Kang and Zhu, 2019; Du et al., 2020). However, the recent advances of employing ultrasmall Au and Ag NCs for biomedical applications have not before been summarized. This review summarizes the recent progresses made in engineering Au and Ag NCs for biomedical applications, with particular emphasis placed on bioimaging and biosensing, anti-microbial applications, and tumor targeting and cancer treatment. In the conclusion, the challenges, including the shared and specific challenges for Au and Ag NC toward biomedical applications, and future research directions in this emerging and promising field are discussed.

ULTRASMALL Au AND Ag NCs FOR BIOMEDICAL APPLICATIONS

For Bioimaging and Biosensing

NCs are ultrasmall NPs; as the size approaches the Fermi-wavelength of the electrons, metal NCs exhibit molecule-like characteristics (Murray, 2008). For example, metal NCs always have discrete absorption energy states, excellent photostability, and strong luminescence, which is an intriguing property which makes them immediately suitable for biomedical research (Zheng et al., 2017b). Such luminescence produces a large Stokes shift and a long lifetime, and the photoluminescence wavelengths of NCs can be tuned from near infrared to ultraviolet by manipulating their size and composition. Three important features of NCs mainly contribute to the photoluminescence, namely the quantum size effects, the nature of the ligand, and the aggregation of the gold species and the aurophilic interactions (Li et al., 2020).

Early work that utilized the photoluminescence of Au NCs in the biomedical field mainly focused on bio-imaging. For instance, Conroy discovered that, through thermal treatment, the near infrared luminescence of mercaptosuccinic acid and tiopronin-protected Au NCs were drastically enhanced, probably due to the unstable non-luminescent molecules being transformed into stable luminescent clusters with narrow size distributions (Conroy et al., 2014). Meanwhile, PEGylation of the Au NCs was able to improve the permeation into the cytoplasm, and these PEGylated Au NCs can penetrate inside the cell nucleus in single cell imaging (Zhang et al., 2012; Conroy et al., 2014). Wang and Shao's groups fabricated l-carnosine protected fluorescent Au NCs, which exhibited bright blue photoluminescence and low toxicity for HeLa cell imaging (Li et al., 2016). In a recent report, Liu et al. prepared an atomic-precision Au cluster with 25 gold atoms and 18 peptide ligands, and such a cluster could serve as an NIR-II fluorophore with emission at 1,100–1,350 nm (Liu et al., 2019). The Au NCs based NIR-II imaging was able to monitor many small vessels thanks to the enhanced permeability of brain vessels after a stroke. It is conceivable that Au NCs can serve as NIR-II dye for biological imaging, especially brain imaging.

Recently, Yu et al. (2020) reported on the fabrication of water-soluble Au NCs which are protected by co-ligands, including a short dithiol pegylated chain (**AuMHA/TDT**). Intriguingly, the AuMHA/TDT sample exhibited a high brightness in the shortwave infrared (SWIR) spectrum with a detection above 1,250 nm. **Figure 1A** shows that the Au NCs were synthesized by using mercaptohexanoic acid (MHA) and tetra(ethylene glycol) dithiol (TDT) as co-ligands, while **Figure 1B** illustrates that they are monodispersed with an average diameter of 2.1 ± 0.6 nm. The dithiol ligand of TDT led to the presence of NIR absorbance features at 800, 910, and 1,140 nm (**Figure 1C**), while the anisotropic surface of Au NCs produced a 9-fold increase of photoluminescence in a longer wavelength range (**Figure 1D**). When using long-pass filters above 1,250 nm, AuMHA/TDT exhibited a 12-fold more intense signal, as manifested by the images in **Figure 1E**. Remarkably, the AuMHA/TDT had a quantum yield of ∼6%, higher than the other reported molecular Au NCs such as **Au25(SG)18** (Liu et al., 2019). It can be noted that there is a dramatic improvement of the spatial resolution in the SWIR, as compared to the NIR I (**Figure 1F**). The authors also conducted the Monte Carlo constrained restoration (MCR) method to further improve the spatial resolution and overcome the scattering from the skin and the tissues. Such imaging processing greatly enhanced the spatial resolution, as observed in **Figure 1G**. This study highlights the Au-NCs-based SWIR-emitting contrast agent for bio-imaging and other advanced bio-medical applications (Yu et al., 2020). However, such SWIR properties can only be achieved through rational ligand design, and the quantum yields still need to be improved.

Besides bio-imaging, Au NCs can also be utilized for biosensing. For example, Biswas et al. (2017) developed a new type of bovine serum albumin-capped Au nanoclusters (BSA-AuNCs) containing polymeric microcapsules as a H_2O_2 sensor, where the change in H_2O_2 within living cells can be visualized and intracellular H_2O_2 fluctuations in response to external stimuli were monitored. Such BSA-AuNCs possessed near infrared emitting behaviors, and when conjugated with chemically modified cellulose strips, they showed a nanomolar detection limit of mercuric ions (Bothra et al., 2017). Other

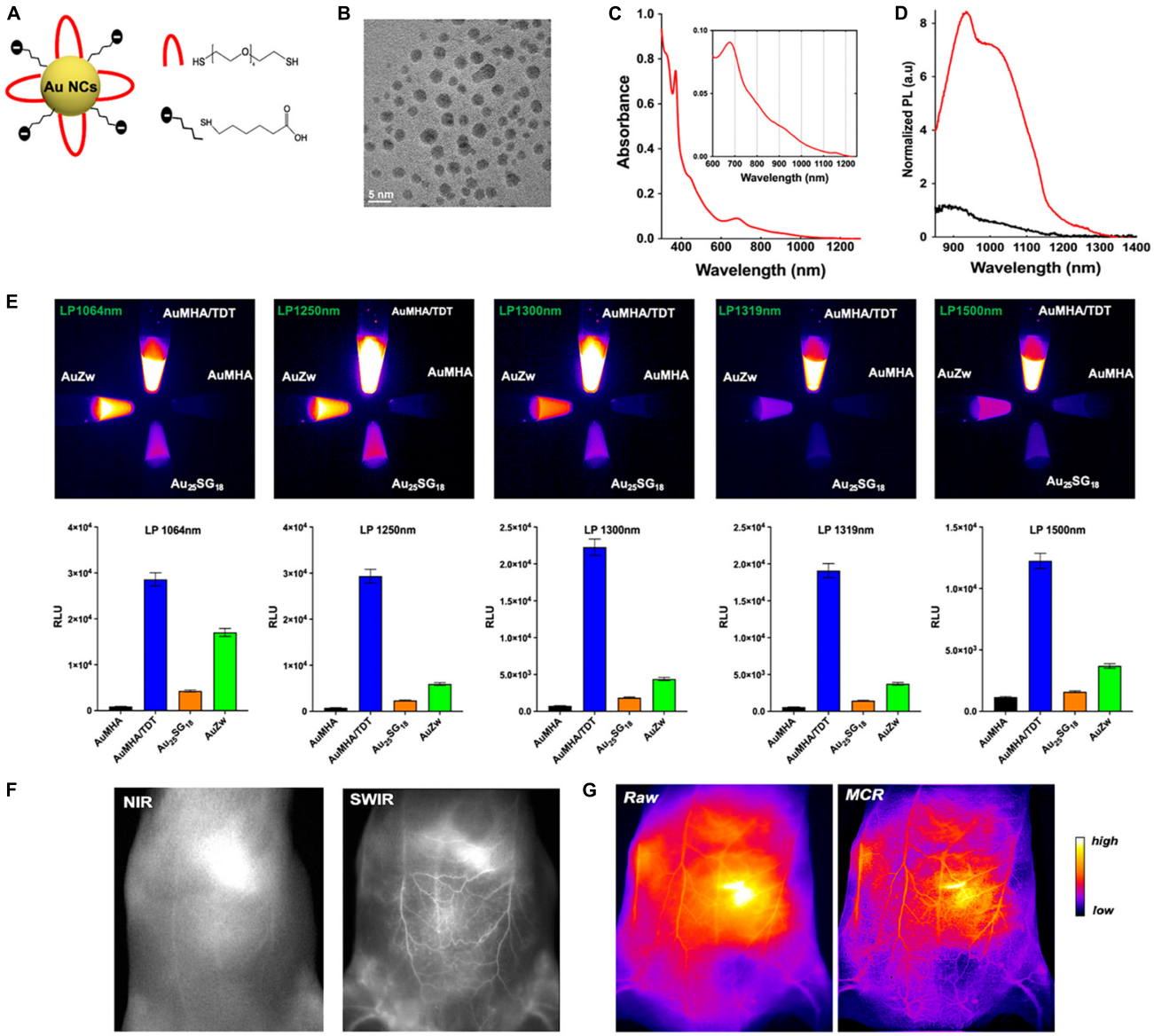

FIGURE 1 | (A) Scheme of the Au NCs AuMHA/TDT (MHA: black; TDT: red). **(B)** HR-TEM image of AuMHA/TDT. **(C)** Absorbance spectrum of AuMHA/TDT. **(D)** PL spectra of AuMHA (black line) and AuMHA/TDT (red line). **(E)** SWIR PL of AuMHA, AuMHA/TDT, $Au_{25}SG_{18}$, and AuZW under NIR excitation. **(F)** NIR I and SWIR imaging of mice 15 min after injection of AuMHA/TDT. **(G)** Non-invasive imaging of the mouse ventral area before (raw) and after MCR processing. Reproduced with permission. Copyright 2020, American Chemical Society.

biomolecules, such as peptide and protein, can also be used as capping agents to prepare fluorescent Au NCs toward sensing applications. Hossein-Nejad-Ariani et al. (2018) developed a peptide-capped Au-NCs-based biosensor for the detection of Listeria monocytogenes, which is portable, simple, fast, and can be operated by non-experts. Akyüz et al. (2019) fabricated chicken egg white protein capped Au NCs as a biosensor, which was able to determine the pro-oxidant activity of natural antioxidant compounds. Electrochemiluminescence (ECL) is another type of chemiluminescence, and the Au NCs hold the ECL properties that are not available from **Au NPs** (Wang et al., 2016; Chen et al., 2019). The ECL behaviors can also be designed for biosensing; for example, Zhang et al. reported that the ultrasensitive signal for detecting acetylthiocholine can be recorded on an Au-NCs-based ECL biosensors (Zhang et al., 2019).

Despite the relatively lower photostability toward oxidation of Ag, previous reports have shown that Ag NCs with the same ligand could have very intense fluorescence signals as well (Tao et al., 2015; Song et al., 2016). In an early study done by Le Guével et al. (2012), glutathione (GSH)-protected Ag NCs possessed sizes smaller than 2 nm and the yellow-emitting Ag NCs had a

quantum yield over 65%, and these Ag NCs were employed as fluorescent labels to visualize A549 cells. Interestingly, human hemoglobin (Hb) can be a stabilizer, reducer, and linker to synthesize Hb-AgNCs with single excitation and dual maximum emissions by a facile one-pot green approach without using toxic reductants such as **NaBH4 (**Shamsipur et al., 2018). The aggregation of oligomeric Ag(I)-Hb intermediates caused aggregation-induced emission (AIE), and such emissions were used as selective probes for HeLa cell imaging with high bio-compatibility and specificity (Shamsipur et al., 2018).

Fluorescent Ag NCs have also demonstrated great promise as substitutes for conventional probes and sensors. Yeh group reported the activatable and color-switchable properties of DNA-templated Ag NCs for DNA sensing (Obliosca et al., 2013). Yuan et al. developed a simple approach to detect cysteine with high sensitivity and selectivity by using highly luminescent Ag NCs, which showed superior selectivity for cysteine over the other 19 natural non-thiol-containing amino acids (Yuan et al., 2013b). Pan et al. (2018) fabricated a new paradigm for label-free amplified nucleic acid detection by combining the highly efficient signal-amplification capability of catalytic hairpin assembly (CHA) reaction with the spatially sensitive fluorescent Ag NCs, which can be integrated as an intact and smart apparatus.

Recently, Shamsipur et al. (2019) reported a new AIE-active luminescent sensor based on DNA-AgNCs/GO (graphene oxide) nanohybrids for the detection of triphosphate (ATP) and cytochrome (Cyt) c in cell lysates. The working principle is shown in **Figure 2**. In the absence of a target, the DNA-AgNCs are adsorbed onto the GO surface, while the fluorescence is enhanced because of the AIE enhancement characteristic of DNA-AgNCs when they are adsorbed onto the GO surface. Upon target binding, the conformation of specific aptamers is significantly altered and AgNCs are desorbed on the GO surface, leading to the restoration of the fluorescence signal (Shamsipur et al., 2019). This study opens a new avenue for designing noble metal NCs-based AIE sensors, where the performance stability of such Ag NCs-based AIE sensors must be further examined in future studies.

Anti-microbial Applications

Metallic Ag has been used to combat infection since ancient times (Rai et al., 2009). With the great advancements made in nanomaterial and nanotechnology, Ag's efficacy to fight wide-spectrum infections has been significantly improved in the form of Ag NPs (Wijnhoven et al., 2009; Marambio-Jones and Hoek, 2010). Thanks to the unique chemistry of Ag interacting with microorganisms, Ag can exert a broad-spectrum of antimicrobial properties through several killing mechanisms, including membrane damage, DNA destruction, and, particularly, generating reaction oxygen species (ROS) to perturb cell metabolism (Xiu et al., 2012; Chernousova and Epple, 2013; Rizzello and Pompa, 2014).

It is conceivable that when Ag NPs downsize the diameter to a sub-nanometer regime, the antibacterial efficacies of Ag can be significantly increased due to the much higher surface-to-volume ratio. Additionally, these Ag NCs with well-defined structures can produce other advantages, such as facile post-functionalization, good stability, and excellent and tunable photoluminescence, not to mention that the definitive composition and structure can provide an ideal platform to establish the correlation between the anti-microbial activities of the Ag NCs and their structures. Yuan et al. (2013a) synthesized a series of water-soluble thiolate Ag NCs with strong luminescence and tunable emissions, and these NCs possessed superior antimicrobial properties against the multidrug-resistant bacteria Pseudomonas aeruginosa by generating a high concentration of intracellular ROS. In another study, they discovered that different charge states can significantly affect the anti-microbial properties. The antimicrobial tests showed that Ag^{+}-enriched NCs had much higher antimicrobial activity than metallic Ag NCs for both gram negative (i.e., *P. aeruginosa* and *E. coli*) and gram positive (i.e., *B. subtilis* and *S. aureus*) bacteria (Yuan et al., 2014). Wang et al. (2020) showcased that the ultrasmall Ag NCs can be embedded in Luria-Bertani extract via light irradiation, and enhanced antibacterial activity with good bio-compatibility were achieved. Recently, Liu et al. (2020) reported on an Ag-NC-based hydrogel that exhibited a superior, broad spectrum antimicrobial performance against both gram-negative and gram-positive bacteria. It also demonstrated long-acting bactericidal efficacy compared with pristine Ag NCs, mainly thanks to its controllable release capability for Ag species.

More intriguingly, Ag NCs can be integrated with other bactericide to form an entity, which can act as a promising platform to improve the efficiency of antimicrobial agents. For instance, Zheng et al. (2016) designed an antimicrobial hybrid by conjugating molecular $Ag_{16}(SG)_9$ clusters with daptomycin (D-AgNCs), and such a hybrid showed improved bacterial killing efficiency over the physically mixed Ag NCs and daptomycin (D + AgNCs), mainly because the D-Ag NCs were able to effectively damage the bacterial membrane. The ROS was involved in destroying the bacteria wall, while N-acetyl-Lcysteine (NAC) could decrease the efficiency of Ag NCs by mitigating the ROS generated by Ag NCs. As illustrated in **Figure 3A**, NAC significantly inhibited the membrane damage. **Figure 3B** further provides supportive evidence that ROS was involved in the membrane damage induced by D-AgNCs. **Figure 3C** shows that the bacterial cells treated by D-AgNCs exhibited a right shift of propidium iodide intensity compared with D + AgNCs, indicating more PI were present inside the bacteria treated by D-AgNCs. Finally, **Figure 3D** demonstrates that D-AgNCs had a higher degree of lipidc peroxidation than D + AgNCs, implying that more ROS was generated by D-AgNCs (Zheng et al., 2016). Such an integrating strategy with other bactericide might be applicable for other antimicrobial applications, but the exact working mechanism of such an entity still needs to be further elucidated.

Bulk gold is known to be chemically inactive, however, when the size of Au decreases to nanoscale dimensions or even close to 1 nm or the sub-nanometer regime to form Au NPs and NCs, interesting physiochemical properties appear in Au NPs, and especially in Au NCs. These intriguing properties could spawn a wide spectrum of applications in various fields, including in biomedical research. For instance, by grafting known

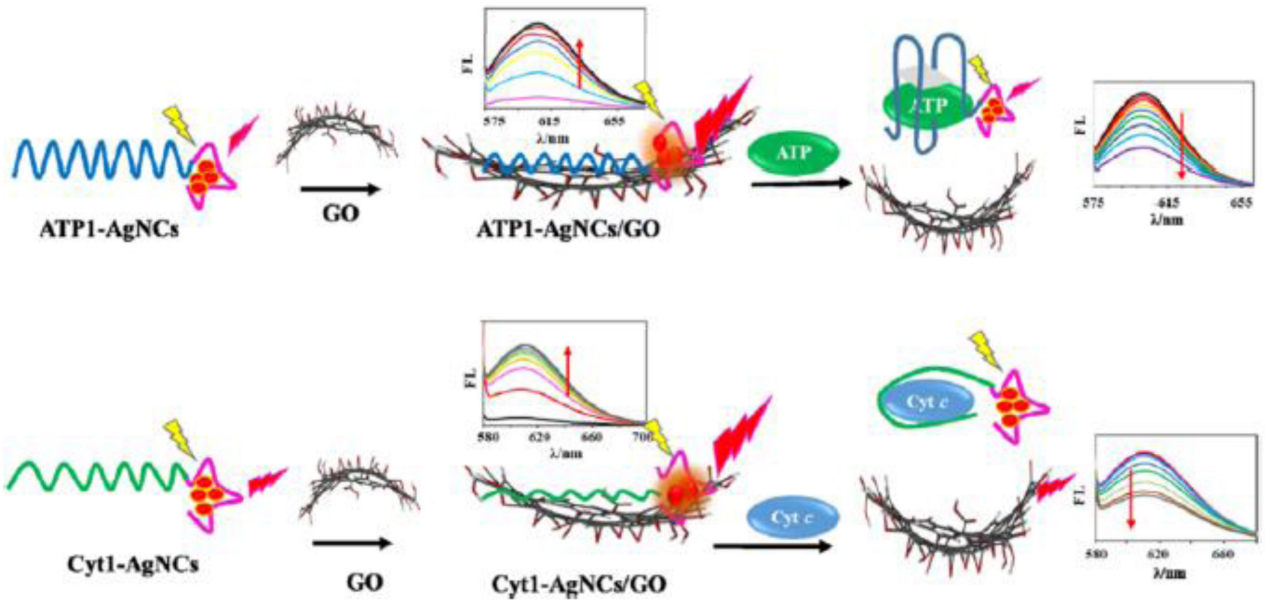

FIGURE 2 | Working principle of the label-free ATP and Cyt c sensing based on DNA-stabilized AgNCs/GO nanohybrids. Reproduced with permission, Copyright 2019, American Chemical Society.

antimicrobial compounds, such as ampicillin, antimicrobial peptides, and cationic or zwitterionic ligands, on the surface of Au NPs, Au NPs can act as passive drug carriers and exhibit some outstanding antimicrobial behaviors (Li et al., 2014; Huo et al., 2016; Kuo et al., 2016; Rai et al., 2016). Since enhanced anti-microbial activities can be obtained when the size of Ag NPs was reduced to the NC range, it is conceivable that the Au NCs also exhibit some bacteria killing properties. Indeed, Zheng et al. (2017a) found that ultrasmall Au NCs showed high broad-spectrum antimicrobial activities, which is actually absent in the Au NPs counterparts protected by the same ligand. Interestingly, Yang's group discovered that the translocation of Au NCs into non-photosynthetic bacteria could enable the photosynthesis of acetic acid from CO_2, and such photogenerated CO_2 fixation was able to operate continuously for several days (Zhang et al., 2018).

Another intriguing advantage for employing ultrasmall Au NCs for anti-microbial applications is that the surface of the Au NCs can be manipulated, which provides a paradigm to modulate the efficacy of Au NCs. By leveraging the molecular properties of ultrasmall Au NCs, the surface properties of the thiolate Au NCs were able to be precisely controlled at an atomic level. Zheng et al. (2018) fabricated a family of Au NCs with identical Au atoms in the core but different properties. Five different Au_{25} NCs with different ligands were synthesized, and the bacteria killing data are presented in **Figure 4** (Zheng et al., 2018). As illustrated in **Figure 4A** and left columns in **Figure 4D**, the $Au_{25}(MHA)_{18}$ NCs (MHA = 6-mercaptohexanoic acid) effectively killed ∼95% of *S. aureus*, and $Au_{25}(MBA)_{18}$ (MBA = 3-mercaptobenzoic acid) which carries the similar monotypic functional group of $-CO_2H$, exhibited a similar killing effect, where ∼93% of *S. aureus* population was effectively terminated. In stark contrast, $Au_{25}(Cys)_{18}$ (Cys = cysteamine hydrochloride) NCs drastically lost the effective antimicrobial properties, and only ∼15% of the *S. aureus* population was dead. An inverse relationship can be observed between the number of $-NH_2$ group on the Au_{25} NCs surface and the anti-microbial efficacy. As shown in **Figure 4B** and middle columns of **Figure 4D**, the more Cystm (Cystm = cysteamine hydrochloride) being capped on the NC surface, the lower the antimicrobial ability the NCs had. It suggests that, for $Au_{25}(Cys)_{18}$, more $-NH_2$ and less $-CO_2H$ could nullify the bacterial killing efficacy of the NCs. By incorporating MetH (MetH = 2-mercaptoethanol) on the NC surface, the resultant $Au_{25}(MetH)_x(MHA)_{18-x}$ could carry both $-CO_2H$ and –OH groups on the NCs surface. Interestingly, the impact of the –OH group toward the killing efficiency of Au_{25} NCs was not as remarkably decreased as those with the $-NH_2$ group, as illustrated in **Figure 4C** and the right columns of **Figure 4D**. Overall, more negatively charged Au NCs would generate more ROS, leading to a better bacterial killing efficiency (Zheng et al., 2018). This study showed the results are different from the common belief that positively charged Au NCs have better antimicrobial properties, but whether it is a special case still need to be explored. However, one can notice that the surface ligands are playing critically different roles in determining the antimicrobial behaviors, which opens an avenue for further development.

Tumor Targeting and Cancer Treatment

Thanks to the easy surface functionalities and their excellent optical properties, especially their intriguing luminescent behaviors, ultrasmall Au and Ag NCs have shown great potential for therapeutic applications toward tumor cell targeting and cancer treatment (Song et al., 2016; Zhang et al., 2020). To

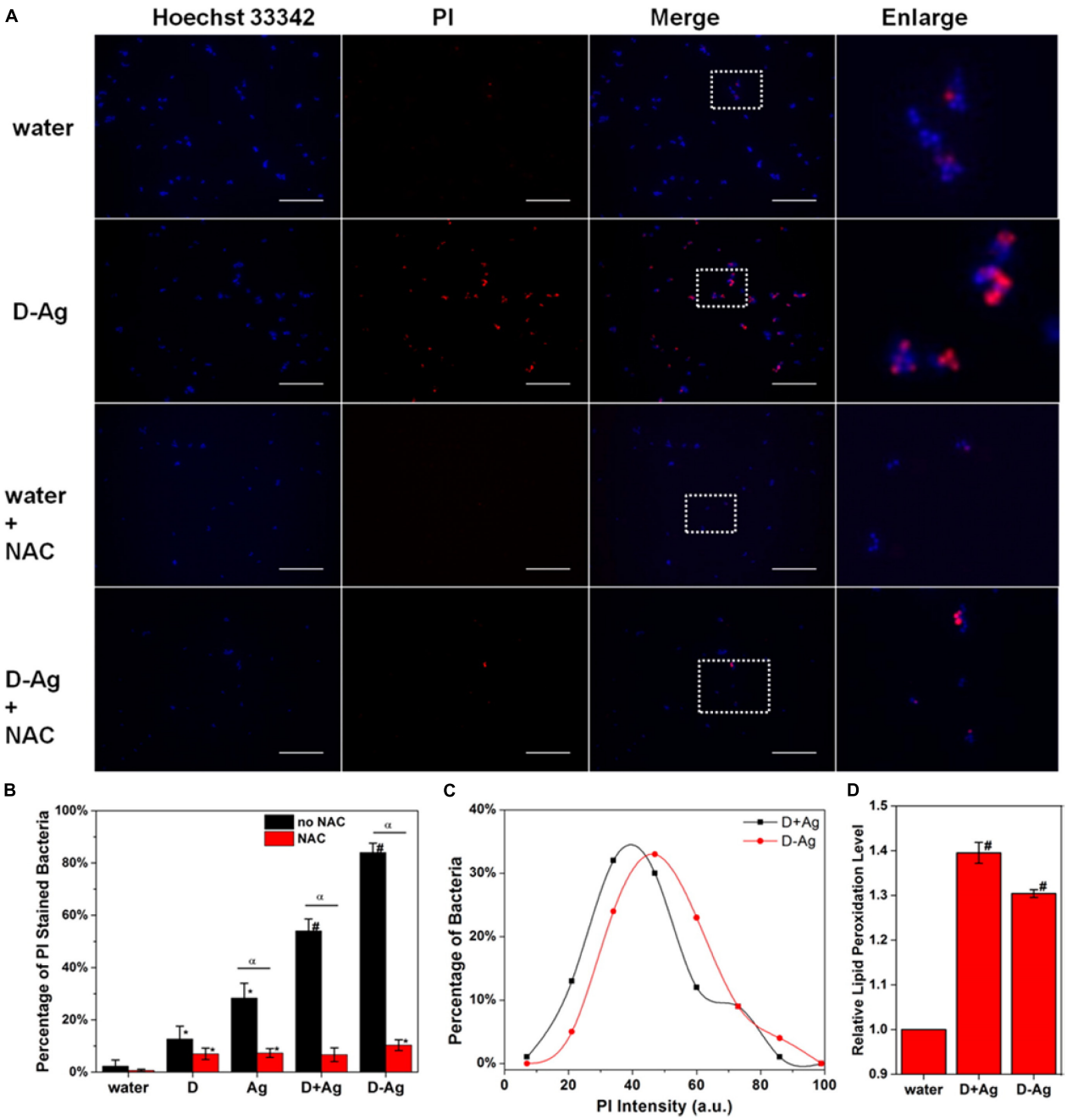

FIGURE 3 | (A) Representative fluorescence images of the bacterial cells after 2 h treatment. **(B)** Percentage of PI-stained bacteria to show damaged bacterial membrane. * is significant against the water treated group, $p < 0.05$; # is significant against the water-treated group, $p < 0.001$. α is significant difference against non-NAC-treated group, $p < 0.05$. **(C)** Histogram of the PI intensity in each individual bacterial cell treated with D + AgNCs (black line) and D-AgNCs (red line). **(D)** Relative lipid peroxidation level after incubation for 2 h, where the lipid peroxidation of the water-treated group was set as 1. # is significant against the water treated group, $p < 0.001$. Reproduced with permission, copyright 2016, American Chemical Society.

target cancer cells, biocompatible ligands, such as GSH, are normally employed. In 2014, Zhang et al. (2014a) groups reported the construction of a new type of radiosensitizer by integrating Au_{25} NCs with GSH and bovine serum albumin (BSA). Thanks to the strong radiotherapy enhancement from the Au core, the ultrasmall Au_{25} NCs capped by both GSH and BSA demonstrated superior tumor accumulation via the improved enhanced permeability and retention (EPR) effect, resulting in a stronger enhancement for cancer therapy than the much larger Au NPs. Such an enhancement can be probably attributed to the photoelectric effect and Compton scattering of Au_{25} NCs, where GSH-capped Au_{25} NCs exhibited a remarkable decrease

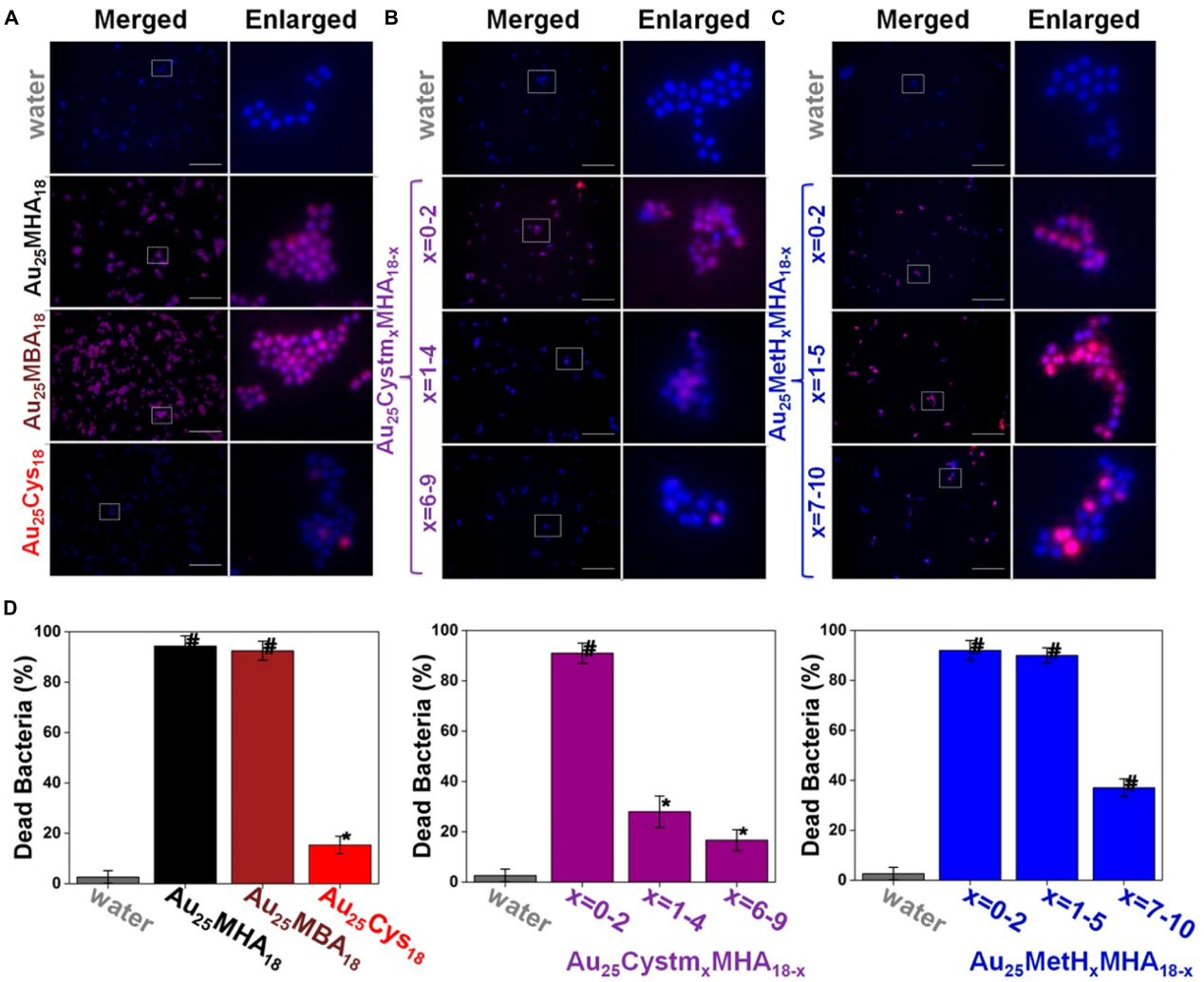

FIGURE 4 | Au_{25} NCs protected by thiolate ligands bearing a higher ratio of $–CO_2H$ groups showed better bacterial killing efficiency. **(A–C)** Merged and enlarged representative fluorescence images of the *S. aureus* after 2 h treatment of Au_{25} NCs. **(D)** Percentage of the dead *S. aureus* after being treated with different ligand-protected Au_{25} NCs for 2 h. *Significant against the water-treated group, $p < 0.05$; #Significant against the water-treated group, $p < 0.001$. Reproduced with permission, copyright 2018, American Chemical Society.

in tumor volume and weight as the radio sensitizer. Moreover, these clusters also exhibited very efficient renal clearance and had no obvious toxicity in the body, while in sharp contrast, BSA capped Au_{25} NCs were not able to be completely removed by the kidney and caused liver damage (Zhang et al., 2014a). Smaller Au NCs showed even better therapeutic effects. Zhang et al. (2014b) discovered that the ultrasmall sized clusters of $Au_{10-12}(SG)_{10-12}$ could increase the tumor uptake and the targeting specificity through the EPR effect, while the biocompatible GSH ligand with high exposure could further promote the tumor uptake by allowing the nano-molecules to escape the reticulo-endothelial system (RES) and activating the transporter on the cell surface.

The above strong size-dependent tumor targeting and renal clearance effects were further verified by Zheng's group with a series of few-atom AuNCs (Du et al., 2017). In this study, a series of atomically precise glutathione-coated AuNCs were prepared (Du et al., 2017). At 40 min upon injection into mice, much more Au_{10-11} and Au_{18} NCs were retained in the kidneys than Au_{25} NCs. In addition, the ratios of bladder to kidney intensity derived from the X-ray imaging followed an order of Au_{25} NCs > Au_{18} NCs > Au_{10-11} NCs. As the Au NCs are highly physiologically stable and resistant to serum protein adsorption in both short and long periods, such differences in bladder/kidney ratios strongly suggest that the kidney filtration is highly sensitive to the cluster size. Au_{25} NCs had the best clearance efficiency, comparable to the ~1.7 nm GSH-protected Au NPs (GS-AuNPs, average composition: ~Au201) (Zhou et al., 2011), while the Au_{10-11}, Au_{15}, and Au_{18} NCs had efficiencies between the 2.5 nm GS-AuNPs (Average composition: ~Au640) (Zhou et al., 2012) and 6 nm GS-AuNPs (Average composition: ~Au_{8856}), in which only about 4% could be cleared out of the body in 24 h (Zhou et al., 2011). In fact, it implies that the glomerulus,

composed of glycocalyx, endothelial cells, glomerular basement membrane (GBM), and podocyte, is actually no longer a one-directional "size-cutoff" slit, but has become an atomically precise "bandpass" barrier that can significantly slow down the renal clearance of ultrasmall Au NCs with sizes in the sub-nanometer regime (Du et al., 2017).

The above cases clearly demonstrate that, compared with larger Au NPs, the ultrasmall Au NCs hold great advantages for kidney filtration and hence can improve renal clearance. Another merit to employ NCs for cancer treatment is that the ligand of the Au NCs can be engineered and the endowed functions of the Au NCs can be correlated with the surface ligand and the metal core. Recently, Jia et al. (2019) reported that an alkynyl-terminated ligand protected Au_8 nanoclusters (Au_8NCs) and their radio sensitization for tumor targeting. As presented in **Figure 5A**, the $Au_8(C_{21}H_{27}O_2)_8$ NCs were synthesized through a one-pot method by reacting $C_{21}H_{28}O_2$ (levonorgestrel) with Me_2SAuCl. Au_8NCs exhibited satisfactory biocompatibility and high luminescent properties with a quantum yield of ~59%. It is generally believed that the production of ROS upon X-ray irradiation is crucial during radiotherapy, and the ROS burst attacks the covalent bond of DNA, resulting in cell apoptosis and/or cell death. The authors examined the underlying mechanism of Au_8NCs-mediated radio sensitization by measuring the intracellular ROS levels through confocal imaging. As illustrated in **Figure 5B**, the average intensity in the experimental group (Au_8NCs + 4 Gy) was 3.7 times greater than the group without the radiosensitizer, and the control group showed barely red fluorescence. The results solidly verified that the Au_8NCs were able to catalyze the ROS formation.

The radio sensitization effect of the Au_8NCs were then assessed *in vivo* by a tumor assay (Jia et al., 2019). The tests with a control group and phosphate-buffered saline (PBS)-treated group were also conducted as comparison. After the cells were injected into the mice and treated with different doses, the tumor size and body weight were monitored every day (**Figures 6A–E**). The tumor volumes in the control group increased about 5 times, however, the tumor volumes in the Au_8NCs + 4 Gy group drastically reduced. In addition, the relative body weights of the mice under different conditions remained almost unchanged over 14 days, suggesting low toxicity *in vivo*. Furthermore, hematoxylin and eosin staining of the tumors and organs was conducted to evaluate the treatment. Widespread damage was observed in the tumor tissue from the Au_8NCs + 4 Gy group compared to the other two

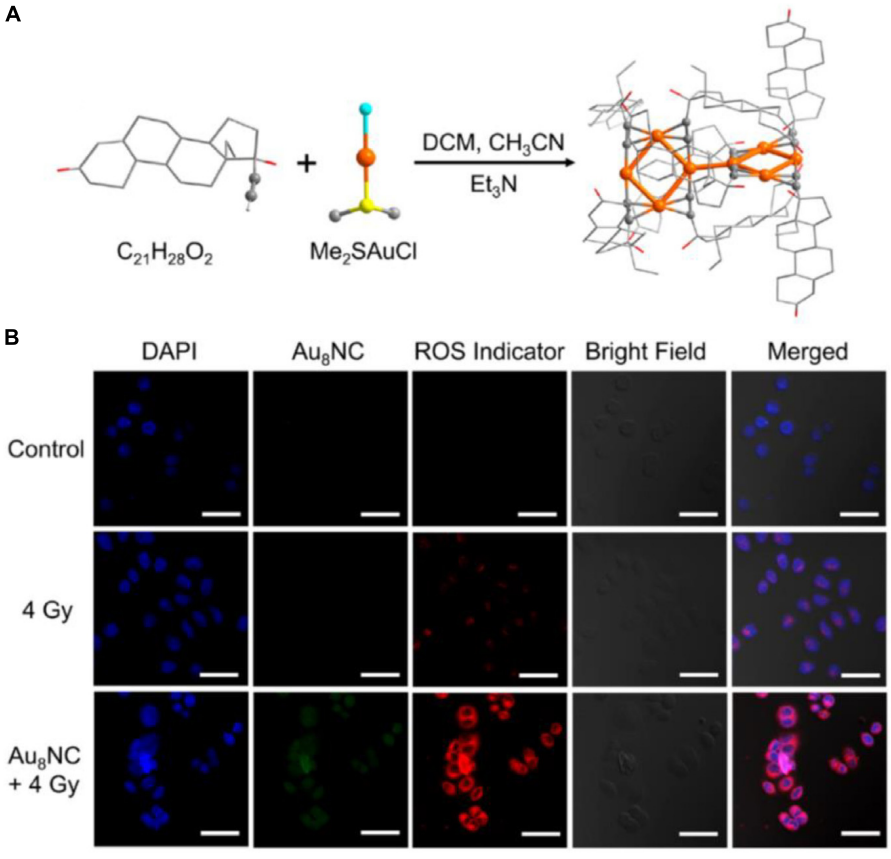

FIGURE 5 | (A) Schematic of the synthesis of Au_8NCs; color codes: orange indicates Au, red indicates O, yellow indicates S, turquoise indicates Cl, and gray indicates C. Hydrogen atoms are omitted. **(B)** Intracellular ROS imaging of EC1 cells at 6 h with different treatments. Reproduced with permission. Copyright 2019, American Chemical Society.

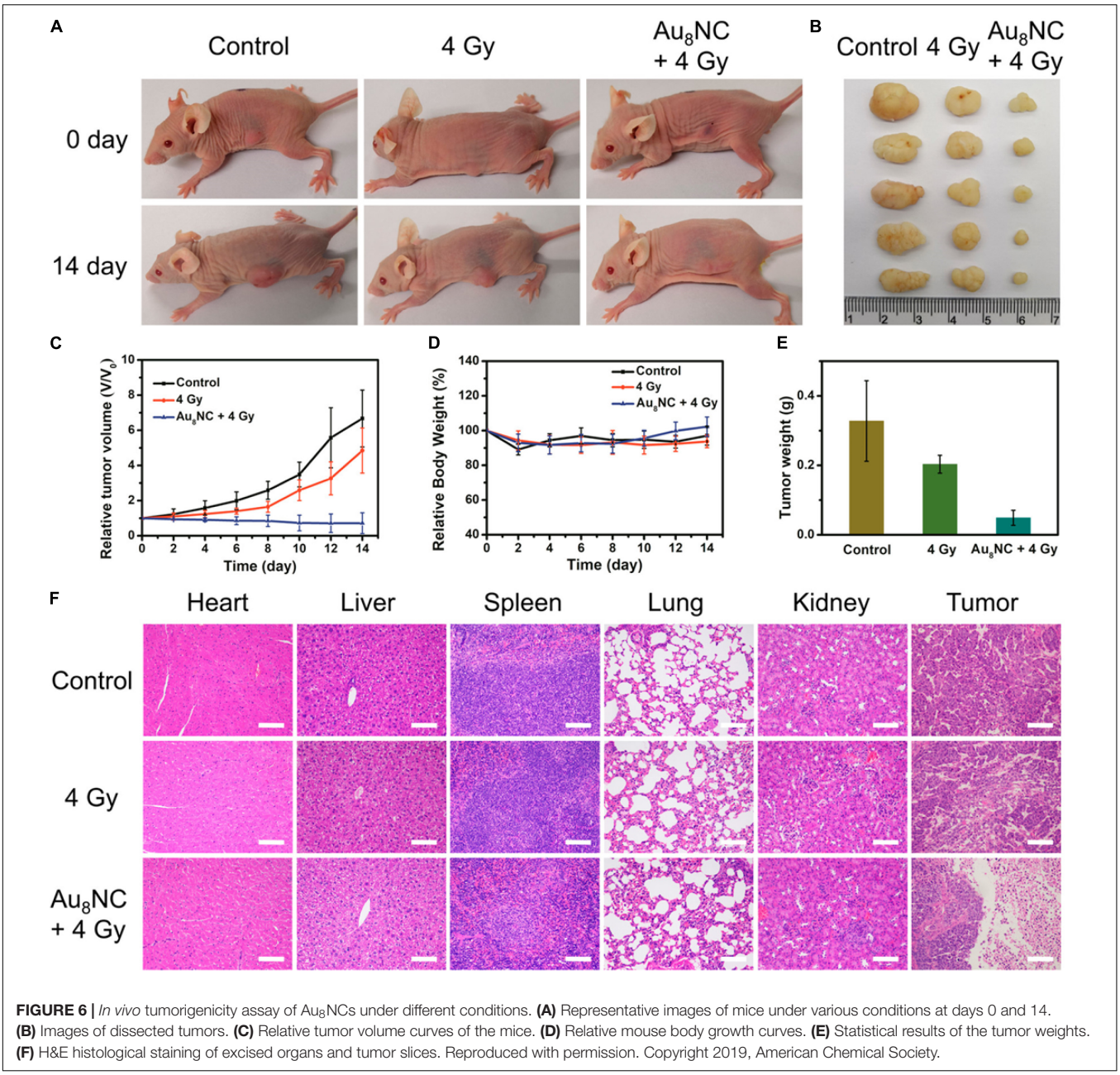

FIGURE 6 | *In vivo* tumorigenicity assay of Au_8NCs under different conditions. **(A)** Representative images of mice under various conditions at days 0 and 14. **(B)** Images of dissected tumors. **(C)** Relative tumor volume curves of the mice. **(D)** Relative mouse body growth curves. **(E)** Statistical results of the tumor weights. **(F)** H&E histological staining of excised organs and tumor slices. Reproduced with permission. Copyright 2019, American Chemical Society.

groups, and no histopathological abnormalities in the organs were observed (**Figure 6F**). These findings demonstrated the significantly enhanced tumor-suppressing efficacy of the Au-NCs-based sensitizer. Note that, in the Au_8NC, Au exhibited (I) valence without the presence of Au(0) species, that is, Au_8NC is a complex rather than a cluster, so if the size becomes larger, can the Au(0) species in the NCs affect the radio-sensitizing properties? To answer this question, further study might be necessary. Another interesting point for this investigation is that the ligand of levonorgestrel itself is a drug, hence Au_8NCs worked very well and can be highly stable. Introducing drug-based ligands might represent a future path for the development of atomically precise Au NCs as efficient radiosensitizers.

CHALLENGES AND OUTLOOKS

In summary, we have given a brief review of ultrasmall Au and Ag NCs for biomedical applications, with particular emphasis on bioimaging and biosensing, anti-microbial applications, and tumor targeting and cancer treatment. The unique properties of the Au and Ag NCs, including their ultrasmall size, excellent photoluminescence, post-functionalized surface chemistry, and outstanding bio-compatibility, mean they hold great potential for use in biomedical applications.

Although significant progress has been made, some critical challenges still remain to be resolved in future. These challenges can be listed as follows:

1. The targeting specificity issue. When using Au/Ag NCs for *in vivo* study, especially for therapeutics or diagnostics such as cancer treatment, the specificity must be enhanced. Although the surface capping ligand of NCs can be modified, low-cost and facile methods to tailor the ligands are still quite limited.
2. The comprehensive fundamental study of Au and Ag NCs in a biological environment is lacking. For *in vivo* study, the biological environment is very complex, and it still lacks the fundamental deep understanding on the interactions between Au/Ag NCs and the biological units. For instance, the effects of Au/Ag NCs on cell growth and living microorganisms over prolonged periods of time must be extensively and intensively studied. The systematic study also needs to be carried out to clarify the effects of the functionalities of Au/Ag NCs on their targeting, biodistributions, and toxicity in the complicated biological set-up.
3. The toxicity issue is still a big concern. Even if some previous reports have shown that most ultrasmall Au NCs can be cleared out of the body through the urinary system, the toxicity of the residual Au NCs still can be a problem when they are engineered by therapeutics and diagnostics *in vivo*. Ag NCs would be more complicated, as it may decompose to form Ag(0) substance, which imposed additional challenges for further study. The bio-nanotoxicity investigations are currently flourishing globally, but more attention is needed for biofunctionalized Au and Ag NCs.

As Au and Ag NCs possess different physiochemical properties, when engineering them for biomedical applications, they have some different specific challenges. For instance, Ag NCs have excellent anti-microbial capabilities but their stability is an issue, as Ag NCs can't be preserved for a prolonged time, such as a few months, without decomposition. However, for Au NCs, they are robust and some of them can be stable for over several months, but their anti-microbial properties are not as impressive as Ag NCs. Therefore, improving the stability of Ag NCs or synthesizing more stable Ag NCs should be a further direction, while enhancing the anti-microbial capabilities of Au NCs is also promising in the regime of using metal NCs for anti-microbial applications.

These shared and specific challenges of Au and Au NCs indicate great opportunities; future research efforts are encouraged to resolve the above-mentioned challenges. Resolving these challenges forms part of the outlook in this rapidly booming field. Besides that, some other research directions also deserve more focus. Specifically, the additional outlooks include:

1. The catalytic properties for Au and Ag NCs can be potentially exerted. It is well known that Au/Ag NCs possess extraordinary catalytic properties in various chemical reactions (Li and Jin, 2013; Tang et al., 2018; Du et al., 2020), but how to engineer their catalytic properties for biomedical processes still needs to be explored.
2. It holds great potential to integrate ultrasmall Au and Ag NCs with other biomolecules/biomaterials to function synergistically. Au and Ag NCs have some unique advantages, but they also possess some drawbacks that might be difficult to overcome. With the development of biological science and modern medicine, precise therapeutic or diagnostic studies are highly demanding. Although some advances have been made to couple Au and Ag NCs with other biomolecules/biomaterials, they is still much left to be developed to realize the "precise medicine."

Overall, ultrasmall Au/Ag NCs have some attractive features which are not available from the larger NP counterparts. With the rapid developments of medical techniques and nanotechnology, we anticipate more opportunities will be open up for Au/Ag NCs in biomedical applications.

AUTHOR CONTRIBUTIONS

JT, HS, and GM did the literature search and wrote the original manuscript. JT, LL, and ZT conceived the idea and provided financial support. LL and ZT polished the final manuscript. All authors contributed to the article and approved the submitted version.

FUNDING

This work was supported by the National Natural Science Foundation of China grants 81600404, 81771973, and 81971672, China Postdoctoral Science Foundation 2017M622916, Jiangmen City Returned Overseas Students Innovation and Entrepreneurship Project, the first batch of innovative and entrepreneurial talents in Jiangmen City, the fourth batch of medical and health science and technology projects in Jiangmen City 2017A3019 and 2019D008. We are grateful for the support from Guangzhou Key Laboratory of Molecular and Functional Imaging for Clinical Translation (201905010003), The Engineering Research Center of Medical Imaging Artificial Intelligence for Precision Diagnosis and Treatment, Guangdong Province, the Key Program of the Natural Science Foundation of Guangdong Province (2018B0303110011), Wu Jieping Medical Foundation (320.6750.19089-73), Guangdong genetic disease gene testing engineering technology research center, and Guangdong Province Special Project on Emergency Response to 2019-nCov Infection Technology (2020A111129034).

REFERENCES

Akyüz, E., Şen, F. B., Bener, M., Başkan, K. S., Tütem, E., and Apak, R. (2019). Protein-Protected gold nanocluster-based biosensor for determining the prooxidant activity of natural antioxidant compounds. *ACS Omega* 4, 2455–2462. doi: 10.1021/acsomega.8b03286

Biswas, A., Banerjee, S., Gart, E. V., Nagaraja, A. T., and McShane, M. J. (2017). Gold nanocluster containing polymeric microcapsules for intracellular

ratiometric fluorescence biosensing. *ACS Omega* 2, 2499–2506. doi: 10.1021/acsomega.7b00199

Bothra, S., Upadhyay, Y., Kumar, R., Ashok Kumar, S. K., and Sahoo, S. K. (2017). Chemically modified cellulose strips with pyridoxal conjugated red fluorescent gold nanoclusters for nanomolar detection of mercuric ions. *Biosens. Bioelectron.* 90, 329–335. doi: 10.1016/j.bios.2016.11.066

Chakraborty, I., and Pradeep, T. (2017). Atomically precise clusters of noble metals: emerging link between atoms and nanoparticles. *Chem. Rev.* 117, 8208–8271. doi: 10.1021/acs.chemrev.6b00769

Chen, S., Ma, H., Padelford, J. W., Qinchen, W., Yu, W., Wang, S., et al. (2019). Near infrared electrochemiluminescence of rod-shape 25-Atom AuAg nanoclusters that is hundreds-fold stronger than that of Ru(bpy)3 standard. *J. Am. Chem. Soc.* 141, 9603–9609. doi: 10.1021/jacs.9b02547

Chernousova, S., and Epple, M. (2013). Silver as antibacterial agent: ion. nanoparticle, and metal. *Angew. Chem., Int. Ed.* 52, 1636–1653. doi: 10.1002/anie.201205923

Conroy, C. V., Jiang, J., Zhang, C., Ahuja, T., Tang, Z., Prickett, C. A., et al. (2014). Enhancing near IR luminescence of thiolate Au nanoclusters by thermo treatments and heterogeneous subcellular distributions. *Nanoscale* 6, 7416–7423. doi: 10.1039/C4NR00827H

Du, B., Jiang, X., Das, A., Zhou, Q., Yu, M., Jin, R., et al. (2017). Glomerular barrier behaves as an atomically precise bandpass filter in a sub-nanometre regime. *Nat. Nanotechnol.* 12, 1096–1102. doi: 10.1038/nnano.2017.170

Du, Y., Sheng, H., Astruc, D., and Zhu, M. (2020). Atomically precise noble metal nanoclusters as efficient catalysts: a bridge between structure and properties. *Chem. Rev.* 120, 526–622. doi: 10.1021/acs.chemrev.8b00726

Higaki, T., Li, Q., Zhou, M., Zhao, S., Li, Y., Li, S., et al. (2018). Toward the tailoring chemistry of metal nanoclusters for enhancing functionalities. *Acc. Chem. Res.* 51, 2764–2773. doi: 10.1021/acs.accounts.8b00383

Hossein-Nejad-Ariani, H., Kim, T., and Kaur, K. (2018). Peptide-Based biosensor utilizing fluorescent gold nanoclusters for detection of listeria monocytogenes. *ACS Appl. Nano Mater.* 1, 3389–3397. doi: 10.1021/acsanm.8b00600

Huo, S., Jiang, Y., Gupta, A., Jiang, Z., Landis, R. F., Hou, S., et al. (2016). Fully zwitterionic nanoparticle antimicrobial agents through tuning of core size and ligand structure. *ACS Nano* 10, 8732–8737. doi: 10.1021/acsnano.6b04207

Jia, T.-T., Yang, G., Mo, S.-J., Wang, Z.-Y., Li, B.-J., Ma, W., et al. (2019). Atomically precise gold–levonorgestrel nanocluster as a radiosensitizer for enhanced cancer therapy. *ACS Nano* 13, 8320–8328. doi: 10.1021/acsnano.9b03767

Kang, X., and Zhu, M. (2019). Transformation of atomically precise nanoclusters by ligand-exchange. *Chem. Mater.* 31, 9939–9969. doi: 10.1021/acs.chemmater.9b03674

Kuo, Y.-L., Wang, S.-G., Wu, C.-Y., Lee, K.-C., Jao, C.-J., Chou, S.-H., et al. (2016). Functional gold nanoparticle-based antibacterial agents for nosocomial and antibiotic-resistant bacteria. *Nanomedicine* 11, 2497–2510. doi: 10.2217/nnm-2016-2232

Le Guével, X., Spies, C., Daum, N., Jung, G., and Schneider, M. (2012). Highly fluorescent silver nanoclusters stabilized by glutathione: a promising fluorescent label for bioimaging. *Nano Res.* 5, 379–387. doi: 10.1007/s12274-012-0218-211

Li, F., Lu, J., Kong, X., Hyeon, T., and Ling, D. (2017). Dynamic nanoparticle assemblies for biomedical applications. *Adv. Mater.* 29:1605897. doi: 10.1002/adma.201605897

Li, G., and Jin, R. (2013). Atomically precise gold nanoclusters as new model catalysts. *Acc. Chem. Res.* 46, 1749–1758. doi: 10.1021/ar300213z

Li, H., Chen, J., Huang, H., Feng, J.-J., Wang, A.-J., and Shao, L.-X. (2016). Green and facile synthesis of l-carnosine protected fluorescent gold nanoclusters for cellular imaging. *Sens. Actuators B: Chem.* 223, 40–44. doi: 10.1016/j.snb.2015.09.052

Li, H., Li, H., and Wan, A. (2020). Luminescent gold nanoclusters for in vivo tumor imaging. *Analyst* 145, 348–363. doi: 10.1039/C9AN01598A

Li, X., Robinson, S. M., Gupta, A., Saha, K., Jiang, Z., Moyano, D. F., et al. (2014). Functional gold nanoparticles as potent antimicrobial agents against multi-drug-resistant bacteria. *ACS Nano* 8, 10682–10686. doi: 10.1021/nn5042625

Liu, H., Hong, G., Luo, Z., Chen, J., Chang, J., Gong, M., et al. (2019). Atomic-Precision gold clusters for NIR-II imaging. *Adv. Mater.* 31:1901015. doi: 10.1002/adma.201901015

Liu, Y., Wang, S., Wang, Z., Yao, Q., Fang, S., Zhou, X., et al. (2020). The in situ synthesis of silver nanoclusters inside a bacterial cellulose hydrogel for antibacterial applications. *J. Mater. Chem. B* 8, 4846–4850. doi: 10.1039/D0TB00073F

Marambio-Jones, C., and Hoek, E. M. V. (2010). A review of the antibacterial effects of silver nanomaterials and potential implications for human health and the environment. *J. Nanopart. Res.* 12, 1531–1551. doi: 10.1007/s11051-010-9900-y

Mohanta, Y. K., Hashem, A., Abd_Allah, E. F., Jena, S. K., and Mohanta, T. K. (2020). Bacterial synthesized metal and metal salt nanoparticles in biomedical applications: an up and coming approach. *Appl. Organomet. Chem.* 34:e5810. doi: 10.1002/aoc.5810

Murray, R. W. (2008). Nanoelectrochemistry: metal nanoparticles. *Nanoelectrodes Nanopores. Chem. Rev.* 108, 2688–2720. doi: 10.1021/cr068077e

Obliosca, J. M., Liu, C., and Yeh, H.-C. (2013). Fluorescent silver nanoclusters as DNA probes. *Nanoscale* 5, 8443–8461. doi: 10.1039/C3NR01601C

Pan, M., Liang, M., Sun, J., Liu, X., and Wang, F. (2018). Lighting up fluorescent silver clusters via target-catalyzed hairpin assembly for amplified biosensing. *Langmuir* 34, 14851–14857. doi: 10.1021/acs.langmuir.8b01576

Rai, A., Pinto, S., Velho, T. R., Ferreira, A. F., Moita, C., Trivedi, U., et al. (2016). One-step synthesis of high-density peptide-conjugated gold nanoparticles with antimicrobial efficacy in a systemic infection model. *Biomaterials* 85, 99–110. doi: 10.1016/j.biomaterials.2016.01.051

Rai, M., Yadav, A., and Gade, A. (2009). Silver nanoparticles as a new generation of antimicrobials. *Biotechnol. Adv.* 27, 76–83. doi: 10.1016/j.biotechadv.2008.09.002

Rizzello, L., and Pompa, P. P. (2014). Nanosilver-based antibacterial drugs and devices: mechanisms, methodological drawbacks, and guidelines. *Chem. Soc. Rev.* 43, 1501–1518. doi: 10.1039/C3CS60218D

Shamsipur, M., Molaabasi, F., Sarparast, M., Roshani, E., Vaezi, Z., Alipour, M., et al. (2018). Photoluminescence mechanisms of dual-emission fluorescent silver nanoclusters fabricated by human hemoglobin template: from oxidation- and aggregation-induced emission enhancement to targeted drug delivery and cell imaging. *ACS Sustainable Chem. Eng.* 6, 11123–11137. doi: 10.1021/acssuschemeng.8b02674

Shamsipur, M., Molaei, K., Molaabasi, F., Hosseinkhani, S., Taherpour, A., Sarparast, M., et al. (2019). Aptamer-Based fluorescent biosensing of adenosine triphosphate and cytochrome c via aggregation-induced emission enhancement on novel label-free DNA-capped silver nanoclusters/graphene oxide nanohybrids. *ACS Appl. Mater. Interfaces* 11, 46077–46089. doi: 10.1021/acsami.9b14487

Song, X.-R., Goswami, N., Yang, H.-H., and Xie, J. (2016). Functionalization of metal nanoclusters for biomedical applications. *Analyst* 141, 3126–3140. doi: 10.1039/C6AN00773B

Tan, X., and Jin, R. (2013). Ultrasmall metal nanoclusters for bio-related applications. WIREs nanomed. *Nanobiotechnology* 5, 569–581. doi: 10.1002/wnan.1237

Tang, Z., Wu, W., and Wang, K. (2018). Oxygen reduction reaction catalyzed by noble metal clusters. *Catalysts* 8:65. doi: 10.3390/catal8020065

Tao, Y., Li, M., Ren, J., and Qu, X. (2015). Metal nanoclusters: novel probes for diagnostic and therapeutic applications. *Chem. Soc. Rev.* 44, 8636–8663. doi: 10.1039/C5CS00607D

Wang, T., Wang, D., Padelford, J. W., Jiang, J., and Wang, G. (2016). Near-Infrared electrogenerated chemiluminescence from aqueous soluble lipoic acid au nanoclusters. *J. Am. Chem. Soc.* 138, 6380–6383. doi: 10.1021/jacs.6b03037

Wang, Z., Fang, Y., Zhou, X., Li, Z., Zhu, H., Du, F., et al. (2020). Embedding ultrasmall Ag nanoclusters in Luria-Bertani extract via light irradiation for enhanced antibacterial activity. *Nano Res.* 13, 203–208. doi: 10.1007/s12274-019-2598-y

Wijnhoven, S. W. P., Peijnenburg, W. J. G. M., Herberts, C. A., Hagens, W. I., Oomen, A. G., Heugens, E. H. W., et al. (2009). Nano-silver – a review of available data and knowledge gaps in human and environmental risk assessment. *Nanotoxicology* 3, 109–138. doi: 10.1080/17435390902725914

Xiu, Z.-M., Zhang, Q.-B., Puppala, H. L., Colvin, V. L., and Alvarez, P. J. J. (2012). Negligible particle-specific antibacterial activity of silver nanoparticles. *Nano Lett.* 12, 4271–4275. doi: 10.1021/nl301934w

Yan, J., Teo, B. K., and Zheng, N. (2018). Surface chemistry of atomically precise coinage–metal nanoclusters: from structural control to surface reactivity and catalysis. *Acc. Chem. Res.* 51, 3084–3093. doi: 10.1021/acs.accounts.8b00371

Yang, W., Veroniaina, H., Qi, X., Chen, P., Li, F., and Ke, P. C. (2020). Soft and condensed nanoparticles and nanoformulations for cancer drug delivery and repurpose. *Adv. Therap.* 3:1900102. doi: 10.1002/adtp.201900102

Yu, Z., Musnier, B., Wegner, K. D., Henry, M., Chovelon, B., Desroches-Castan, A., et al. (2020). High-Resolution shortwave infrared imaging of vascular disorders using gold nanoclusters. *ACS Nano* 14, 4973–4981. doi: 10.1021/acsnano.0c01174

Yuan, X., Setyawati, M. I., Leong, D. T., and Xie, J. (2014). Ultrasmall Ag+-rich nanoclusters as highly efficient nanoreservoirs for bacterial killing. *Nano Res.* 7, 301–307. doi: 10.1007/s12274-013-0395-396

Yuan, X., Setyawati, M. I., Tan, A. S., Ong, C. N., Leong, D. T., and Xie, J. (2013a). Highly luminescent silver nanoclusters with tunable emissions: cyclic reduction–decomposition synthesis and antimicrobial properties. *NPG Asia Mater.* 5, e39. doi: 10.1038/am.2013.3

Yuan, X., Tay, Y., Dou, X., Luo, Z., Leong, D. T., and Xie, J. (2013b). Glutathione-Protected silver nanoclusters as cysteine-selective fluorometric and colorimetric probe. *Anal. Chem.* 85, 1913–1919. doi: 10.1021/ac3033678

Zhang, C., Fan, Y., Zhang, H., Chen, S., and Yuan, R. (2019). An ultrasensitive signal-on electrochemiluminescence biosensor based on Au nanoclusters for detecting acetylthiocholine. *Anal. Bioanal. Chem.* 411, 905–913. doi: 10.1007/s00216-018-1513-1519

Zhang, H., Liu, H., Tian, Z., Lu, D., Yu, Y., Cestellos-Blanco, S., et al. (2018). Bacteria photosensitized by intracellular gold nanoclusters for solar fuel production. *Nat. Nanotechnol.* 13, 900–905. doi: 10.1038/s41565-018-0267-z

Zhang, J., Fu, Y., Conroy, C. V., Tang, Z., Li, G., Zhao, R. Y., et al. (2012). Fluorescence intensity and lifetime cell imaging with luminescent gold nanoclusters. *J. Phys. Chem. C* 116, 26561–26569. doi: 10.1021/jp306036y

Zhang, S., Zhang, X., and Su, Z. (2020). Biomolecule conjugated metal nanoclusters: bio-inspiration strategies, targeted therapeutics, and diagnostics. *J. Mater. Chem. B* 8, 4176–4194. doi: 10.1039/C9TB02936B

Zhang, X.-D., Chen, J., Luo, Z., Wu, D., Shen, X., Song, S.-S., et al. (2014a). Enhanced tumor accumulation of Sub-2 nm gold nanoclusters for cancer radiation therapy. *Adv. Healthcare Mater.* 3, 133–141. doi: 10.1002/adhm.201300189

Zhang, X.-D., Luo, Z., Chen, J., Shen, X., Song, S., Sun, Y., et al. (2014b). Ultrasmall Au10–12(SG)10–12 nanomolecules for high tumor specificity and cancer radiotherapy. *Adv. Mater.* 26, 4565–4568. doi: 10.1002/adma.201400866

Zheng, K., Setyawati, M. I., Leong, D. T., and Xie, J. (2017a). Antimicrobial gold nanoclusters. *ACS Nano* 11, 6904–6910. doi: 10.1021/acsnano.7b02035

Zheng, Y., Lai, L., Liu, W., Jiang, H., and Wang, X. (2017b). Recent advances in biomedical applications of fluorescent gold nanoclusters. *Adv. Colloid Interface Sci.* 242, 1–16. doi: 10.1016/j.cis.2017.02.005

Zheng, K., Setyawati, M. I., Leong, D. T., and Xie, J. (2018). Surface ligand chemistry of gold nanoclusters determines their antimicrobial ability. *Chem. Mater.* 30, 2800–2808. doi: 10.1021/acs.chemmater.8b00667

Zheng, K., Setyawati, M. I., Lim, T.-P., Leong, D. T., and Xie, J. (2016). Antimicrobial cluster bombs: silver nanoclusters packed with daptomycin. *ACS Nano* 10, 7934–7942. doi: 10.1021/acsnano.6b03862

Zhou, C., Hao, G., Thomas, P., Liu, J., Yu, M., Sun, S., et al. (2012). Near-Infrared emitting radioactive gold nanoparticles with molecular pharmacokinetics. *Angew. Chem. Int. Ed.* 51, 10118–10122. doi: 10.1002/anie.201203031

Zhou, C., Long, M., Qin, Y., Sun, X., and Zheng, J. (2011). Luminescent gold nanoparticles with efficient renal clearance. *Angew. Chem. Int. Ed.* 50, 3168–3172. doi: 10.1002/anie.201007321

Conflict of Interest: The authors declare that the research was conducted in the absence of any commercial or financial relationships that could be construed as a potential conflict of interest.

frontiers in Bioengineering and Biotechnology

ORIGINAL RESEARCH
published: 15 October 2020
doi: 10.3389/fbioe.2020.00879

Enhancing Bioavailability and Stability of Curcumin Using Solid Lipid Nanoparticles (CLEN): A Covenant for Its Effectiveness

*Tanvi Gupta†, Joga Singh†, Sandeep Kaur, Simarjot Sandhu, Gurpal Singh and Indu Pal Kaur**

University Institute of Pharmaceutical Sciences, Panjab University, Chandigarh, India

Curcumin, very rightly referred to as "a wonder drug" is proven to be efficacious in a variety of inflammatory disorders including cancers. Antiaging, anti-inflammatory, antioxidant, antitumor, chemosensitizing, P-gp efflux inhibiting, and antiproliferative activity are some of the striking features of curcumin, highlighting its importance in chemotherapy. Curcumin inhibits Bcl-2, Bcl-XL, VEGF, c-Myc, ICAM-1, EGFR, STAT3 phosphorylation, and cyclin D1 genes involved in the various stages of breast, prostate, and gastric cancer proliferation, angiogenesis, invasion, and metastasis. The full therapeutic potential of curcumin however remains under explored mainly due to poor absorption, rapid metabolism and systemic elimination culminating in its poor bioavailability. Furthermore, curcumin is insoluble, unstable at various pH and is also prone to undergo photodegradation. Nanotechnology can help improve the therapeutic potential of drug molecules with compromised biopharmaceutical profiles. Solid lipid nanoparticles (SLNs) are the latest offshoot of nanomedicine with proven advantages of high drug payload, longer shelf life, biocompatibility and biodegradability, and industrial amenability of the production process. We successfully developed CLEN (Curcumin encapsulated lipidic nanoconstructs) containing 15 mg curcumin per ml of the SLN dispersion with highest (till date, to our knowledge) increase in solubility of curcumin in an aqueous system by 1.4×10^6 times as compared to its intrinsic solubility of 11 ng/ml and high drug loading (15% w/v with respect to lipid matrix). Zero-order release kinetics observed for CLEN versus first order release for free curcumin establish controlled release nature of the developed CLEN. It showed 69.78 times higher oral bioavailability with respect to free curcumin; 9.00 times higher than a bioavailable marketed formulation (CurcuWIN®). The formulation showed 104, 13.3, and 10-times enhanced stability at pH 6.8, 1.2, and 7.4, respectively. All these factors ensure the efficacy of CLEN in treating cancer and other inflammatory diseases.

Keywords: oral bioavailability, enhanced solubility, improved stability, pharmacokinetics, photodegradation

OPEN ACCESS

Edited by:
João Conde,
NOVA University Lisbon, Portugal

Reviewed by:
Stefano Leporatti,
Institute of Nanotechnology, Italian National Research Council, Italy
Rosalia Bertorelli,
Italian Institute of Technology (IIT), Italy

***Correspondence:**
Indu Pal Kaur
indupalkaur@yahoo.com

†These authors have contributed equally to this work

Specialty section:
This article was submitted to Nanobiotechnology, a section of the journal Frontiers in Bioengineering and Biotechnology

Received: *19 May 2020*
Accepted: *09 July 2020*
Published: *15 October 2020*

Citation:
Gupta T, Singh J, Kaur S, Sandhu S, Singh G and Kaur IP (2020) Enhancing Bioavailability and Stability of Curcumin Using Solid Lipid Nanoparticles (CLEN): A Covenant for Its Effectiveness. Front. Bioeng. Biotechnol. 8:879. doi: 10.3389/fbioe.2020.00879

INTRODUCTION

Phytochemicals are biologically active compounds that are synthesized within the flora to produce a characteristic taste, color, and aroma and are beneficial to humans when taken in appropriate amounts. Around 20,000 plants recorded in Ayurveda are used for their medicinal value in treating a variety of ailments. Modern medicine is starting to recognize the beneficial effects of herbs for

therapy, including curcumin, which is extensively studied, as evidenced by the publication of more than 6000 research publications appearing on curcumin in less than 20 years (Prasad et al., 2014).

Curcumin is the principal active ingredient of *Curcuma longa* (*Linn.*), popularly known as turmeric [Zingiberaceae family] (Gupta et al., 2012; Rahmani et al., 2018). It is native to the Indian subcontinent and Southeast Asia and is very popular as a condiment in the cuisines of this continent. Researchers across the globe have explored its antimicrobial, antioxidant, antidiabetic, anti-inflammatory, and anti-tumor capabilities (Aggarwal and Harikumar, 2009). Curcumin is documented for use in gastrointestinal problems (through downregulation of NF-kB, IL-6, TRPV-1, and STAT3) (Rajasekaran, 2011; Lopresti, 2018), liver diseases (inhibition of TGF-β) (Espinoza and Muriel, 2009), inflammatory conditions (suppression of TNF-α, IL-6, 8, and 12, COX-2, and iNOS) (Fadus et al., 2017; Hewlings and Kalman, 2017), and as an anticancer drug (repressing IL-10 and 18, AP-1, Pgp {Akt/IKKα- β/NF-kB axis} and activation of MAPK) (Liu and Ho, 2018; Tomeh et al., 2019). Curcumin shows potential in cancer management by significantly decreasing the elevated levels of Cyclin D1 and CDK4 (proteins involved in cell cycle progression) and thus arresting cell cycle at the G1 phase, causing cell growth inhibition/apoptosis (Vutakuri, 2018; Tan and Norhaizan, 2019). Curcumin improves reduced glutathione (GSH) levels coupled with the downregulation of NF-kB, both of which are useful for cancer control.

Adjuvant therapy involving the use of curcumin with conventional anticancer drugs, including doxorubicin, paclitaxel, cisplatin, etoposide, 5-fluorouracil, docetaxel, mitomycin C, tamoxifen, and cyclophosphamide is reported to enhance the chemotherapeutic effect of the latter. Curcumin acts by reducing transcriptional activation of the Pgp promoter (p65/p50) and inhibition of the CYP enzymes (CYP3A4, CYP2D6) (Saghatelyana et al., 2020) that are involved in drug metabolism. Curcumin also reduced cancer metastasis and suppressed expression of MMP-9, NF-kB, and COX-2 when administered in combination with other chemotherapeutic agents (Wilken et al., 2011; Wang et al., 2016).

Curcumin is often referred to as a 'wonder drug' because of the multiplicity of effects displayed by it, which are especially useful for management of multitarget diseases like cancers. However, the wide spectrum of curcumin remains under-exploited due to its insolubility (aqueous solubility of about 11 ng/ml), rapid metabolism, poor bioavailability, and physiological instability (undergoes degradation in water and at various physiological pH conditions), limiting its clinical application (Liu et al., 2016). Therefore, there is a need to develop a robust technology that can overcome the biopharmaceutical flaws inherent in the curcumin molecule (Flora et al., 2013).

Recent reports have proved that nanotechnology can be used to manage various issues with curcumin bioavailability (Gera et al., 2017; Karthikeyan et al., 2020). Basniwal et al. (2014) prepared nanoparticles of curcumin (2–40 nm) using a wet milling technique and carried out *in-vitro* testing against A549, HepG2, and A431 cancer cell lines (representing lung, liver, and skin cancer), which proved to have a significant antiproliferative effect in comparison to free curcumin. A nanogel containing curcumin exhibited almost three times potency in comparison with plain curcumin (Khosropanaha et al., 2016) in MDA-MB231 cells (breast cancer). Furthermore, curcumin nanoparticles exhibited significantly more uptake in both PC3 and HEK cell lines (prostate cancer cell lines and human embryonic kidney cell line). Specifically, the nanoparticles of curcumin have shown more toxic behavior in PC3. A study documented that the viability with nanocurcumin was lower at all the concentrations in comparison to curcumin in both the cell lines (Adahouna et al., 2017). In another investigation, curcumin nanoparticles showed 19 fold more growth inhibition on Colon-26 (colorectal cancer cell line) cells in contrast to free curcumin. This phenomenon was seen mainly due to greater binding and enhanced cellular uptake of nanoparticles (Chaurasia et al., 2016). Sustained release of curcumin from silk fibroin nanoparticles improved its cellular uptake into the cancer cells (HCT116; colon cancer cell) and reduced its cytotoxic effect on normal healthy cells (Xie et al., 2017).

Solid lipid nanoparticles (SLNs) are the latest development in the field of nanotechnology, offering the desirable properties of a high drug pay load, such as biocompatibility, small size, protection against chemical degradation, physical stability, enhanced cellular uptake, and controlled release in comparison to other nano delivery vehicles, including liposomes, nanoemulsions, micelles, and polymeric nanoparticles (Sun et al., 2012; Flora et al., 2013).

MATERIALS AND METHODS

Chemicals and Materials

The curcumin was donated by Sunpure Extracts Pvt. Ltd., New Delhi, India. Compritol® 888 ATO, Glyceryl Monostearate (GMS) was gifted by Gattefosse India Pvt. Ltd., and phospholipon 90G was also gifted by Lipoid, GmbH Germany. β-glucuronidase was purchased from Megazyme Ltd., Ireland. Tween 80 and polyethylene glycol 600 (CDH, New Delhi, India) were purchased from local vendors. CurcuWIN® was purchased as an online product from OmniActive Health Technologies. Acetonitrile (ACN), chloroform, and methanol (HPLC grade) manufactured by Merck Schuchardt OHG, Hohenbrunn, Germany, were also purchased locally. HPLC grade water was produced by a Milli-DI system by Millipore (Billerica, MA, United States). Syringe filters were purchased from Waters India Pvt. Ltd. All other reagents used in the study were of analytical grade.

Preparation of Curcumin Loaded Solid Lipid Nanoparticles (CLEN)

CLEN were prepared using a high pressure hot homogenization technique. The aqueous phase was prepared by adding tween 80, phospholipon 90G, and water in a beaker and heated to around 80°C. Lipid [Compritol®888 ATO and GMS (4:1)] was melted at 70–75°C and curcumin, dissolved in polyethylene glycol 600 was added to it. The obtained lipid mix was added to the aqueous phase under high-speed homogenization (8000 rpm for 8 min) to obtain a coarse emulsion. The latter was passed through a

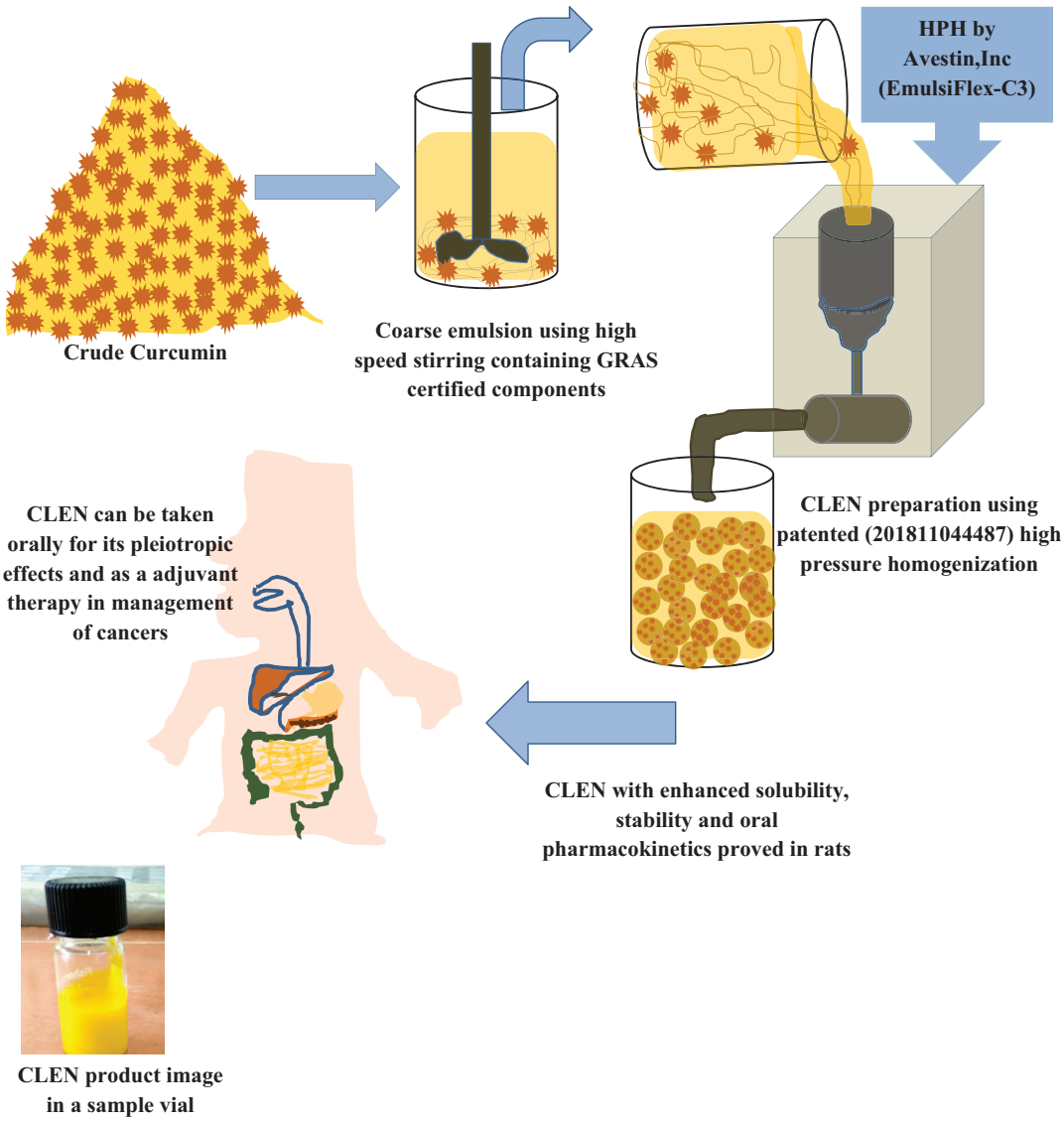

FIGURE 1 | Diagrammatic representation of CLEN preparation.

high pressure homogenizer (3 cycles; 500 psi) and the SLNs were formed by cooling the obtained dispersion to room temperature (**Figure 1**). A graphical representation of the process and its proposed applications is depicted in **Figure 1**.

Various formulations were prepared by varying types and concentrations of the lipid and by the concentration of phospholipon 90G to achieve a 1.5% w/v curcumin in the SLN dispersion.

Characterization of CLEN

Assay [Total Drug Content (TDC)] of Curcumin in CLEN Dispersion

Depending upon the solubility of Compritol®888 ATO, and GMS, methanol: chloroform (1:1) was chosen as a solvent for disrupting the SLNs. 1 ml of CLEN was suitably diluted to 5000 times with chloroform: methanol solvent system. The obtained solution was analyzed spectrophotometrically at λmax 425 nm using the corresponding blank. TDC was determined using the following equation:

$$\text{Total drug content (\%)} = \frac{\text{observed drug content}}{\text{Theoretical drug content}} \times 100$$

Determination of Entrapment Efficiency (EE)

The EE of CLEN was determined using the dialysis membrane method. Membrane (cut off 7 kDa MW) was soaked in double distilled water overnight before use. 1 mL of CLEN dispersion was placed in the pre-soaked dialysis bag tied at both ends and dialyzed against methanol (100 mL) at room temperature for 45 min. The amount of the drug remaining in the dialysis bag was analyzed spectrophotometrically following appropriate dilution

(5000 times) with methanol: chloroform (1:1) to calculate the amount of drug entrapped within the SLNs. EE was determined using the following equation:

$$\text{Entrapment Efficiency (\%)} = \frac{\text{Entrapped drug}}{\text{Total drug content}} \times 100$$

Particle Size Analysis, Polydispersity Index (PDI) and Zeta Potential

The mean diameter, PDI, and zeta potential of CLEN (n = 6) were determined after appropriate dilution (20 times) with double distilled water using Delsa^{TM} Nano C Particle Analyzer (Beckman Coulter, United States).

Field Emission Scanning Electron Microscopy (FESEM)

CLEN were observed microscopically using FESEM (H-7500, Hitachi Ltd., Japan) for uniformity of size, shape, and physical stability characteristic, i.e., aggregation or irregularity. FESEM has narrow probing beams at low and high electron energy which provides improved spatial resolution while minimizing sample damage. It provides topographical information at magnifications of 250-1,000,000X with ion-free images. A drop of the sample was placed on the carbon-coated copper grid to form a thin film on the grid. The grid was air dried and samples were viewed under FESEM.

Powder X-Ray Diffraction (PXRD)

The crystalline or amorphous nature of SLNs was confirmed by X-ray diffraction measurements carried out by an X-ray diffractometer. PXRD studies were performed by exposing the samples to Cu K_α radiation (45 kV, 40 mA) and scanning from 5° to 50°, 2θ at a step size of 0.017° and scan step time of 25 s. The instrument measures interlayer spacing d which is calculated from the scattering angle θ, using Bragg's equation $n\lambda = 2d \sin\theta$ where λ is the wavelength of the incident X-ray beam and n is the order of the interference. Obtained XRD patterns were compared for characteristic drug peak intensity.

Differential Scanning Calorimeter (DSC)

Differential scanning calorimeter thermograms of curcumin, CLEN, blank SLNs, and lipid mixture [Compritol®888 ATO and GMS (4:1)] were recorded on a Q20 differential scanning calorimeter. Samples were placed in aluminum hermetic pans and heated at a predefined rate of 10°C/min over the temperature range from 30 to 300°C in the nitrogen atmosphere.

Fourier Transform Infra-Red (FTIR)

Fourier transform infra-red spectra of curcumin, CLEN, blank SLNs, and lipid mixture [Compritol®888 ATO and GMS (4:1)] were recorded using the KBr pellet technique using 60 MHz Varian EM 360 (PerkinElmer, United States). The peaks obtained were compared for any significant changes.

In vitro Release of CLEN

The drug release studies were performed using a mixture of double distilled water and methanol (1:1, v/v) as the dissolution medium and using the dialysis bag method. The dialysis bags were soaked in double distilled water for 12 h prior to use. 0.5 ml each of CLEN and free curcumin dissolved in methanol was poured into the dialysis bag which was then tied at both the ends and placed in a beaker containing 100 ml of dissolution medium maintained at 37 ± 0.5°C and stirred at a rate of 100 rpm. Aliquots of the dissolution medium were withdrawn at different times and replaced with the same volume of fresh medium to maintain the sink conditions. The samples were analyzed spectrophotometrically at 425 nm.

Since curcumin is not stable at pH 1.2 (SGF) and 6.8 (SIF), SGF or SIF were not used for the release study.

Stability Studies

Long Term Stability

CLEN were placed at 5 ± 3°C for evaluating long term stability. Samples were withdrawn at 0, 1, and 3 months interval and evaluated for total drug content, entrapment efficiency, particle size, zeta potential, and PDI.

Hydrolytic Degradation Studies

The hydrolytic stability of CLEN and free curcumin was investigated at pH 1.2, phosphate buffer pH 6.8, phosphate buffer pH 7.4, and alkaline borate buffer pH 9 (Indian Pharmacopoeia and Commission, 2014). The stock solution of free curcumin (100 μg/ml) was prepared in methanol by dissolving 5 mg of curcumin in 50 ml of methanol. It was further diluted to 5 μg/ml with respective buffers (pH 1.2, pH 6.8, pH 7.4, and pH 9). In the case of CLEN, 1 ml dispersion was placed in a dialysis bag and dialyzed against methanol (100 ml) at room temperature for 45 min to remove the unentrapped drug. The total drug content (drug assay) of the dialyzed CLEN was determined and diluted suitably with water to prepare a 100 μg/ml stock, which was diluted further to 5 μg/ml with respective buffers. The stock solution and sample solution were prepared in amber colored volumetric flasks to avoid photodegradation. The solutions were prepared and incubated at 37°C. The samples were withdrawn at varying times, viz. 0, 0.5, 1, 2, 4, 6, 8, 10, 12, and 24 h. The samples were then analyzed using the UV/Visible spectrophotometer at λmax 425 nm. The absorbance read at zero time was considered as 100% and change in concentration and percentage degradation was determined accordingly.

The graph between concentration versus time, log concentration versus time, and percent drug remaining versus time were plotted. The degradation constant (k) for the first order was calculated by multiplying the slope of log concentration versus time plot with 2.303.

Particle Size Variation With pH and Time

CLEN were diluted (20 times) with buffers of pH 1.2, 6.8, and 7.4 and were incubated at 37°C. Samples were withdrawn at different time intervals and their particle size was determined to establish the stability of CLEN on oral administration.

Photostability Studies

The photostability studies on free curcumin (curcumin dispersion in 1% CMC) and CLEN were conducted according to ICH guidelines. Free curcumin and CLEN were stored in

both clear glass and amber colored containers. The samples were placed in the photostability chamber and exposed to light providing illumination of not less than 1.2 million lux hours for 10 days. After 10 days, free curcumin was evaluated for total drug content (assay) and CLEN were evaluated for total drug content, entrapment efficiency, particle size, zeta potential, and PDI.

BIOANALYTICAL METHOD VALIDATION

Method development and validation of analysis of curcumin in plasma were carried out following U.S. Food and Drug Administration guidelines. The method was validated for system suitability, specificity, sensitivity, recovery, precision, accuracy, and linearity.

A five point calibration curve of curcumin was prepared by spiking 40 μl of blank plasma with 10 μl each of the appropriate working dilution of curcumin to result in 25–500 ng/ml of curcumin.

High quality control (HQC: 500 ng/ml), medium quality control (MQC: 200 ng/ml), and low quality control (LQC: 25 ng/ml) samples were prepared similarly for validation.

Chromatographic Conditions

The determination of curcumin was carried out using a UPLC system (waters, Acquity UPLC H class). A reversed phase Accucore C18 column (100 mm × 4.6 mm, 2.6 μm; Thermo Scientific, Mumbai) was used. Acetonitrile: Water (1:1, isocratic) was run as the mobile phase and pH was adjusted to 3 with 0.1% acetic acid. The elution was performed at a flow rate of 0.10 mL/min and the analytical column was kept in a thermostatic oven at 35°C. The detection of curcumin was performed with a Waters Photodiode Array Detector at a set wavelength of 425 nm. The injection volume was 10 μL for all standards and samples. Curcumin was eluted approximately 15 min after injection. A series of standard solutions of curcumin (25–500 ng/mL) were prepared in acetonitrile: water.

PHARMACOKINETIC STUDIES

Study Design

For *in vivo* pharmacokinetic studies, post weaned (4-weeks old) female Wistar Rats weighing 250 g were fasted for 12 h prior to the study. The animals were divided into three groups (n = 3). Groups 1 and 2 were administered 100 mg/kg BW of CLEN and CurcuWIN® (a marketed product of curcumin claimed to show enhanced bioavailability), respectively, whereas group 3 was administered 100 mg/kg BW of free curcumin dispersed in 0.5% w/v carboxymethyl cellulose. There are variable reports on the suitable dose of curcumin in animals and several investigators have reported the use of 100 mg/kg dose of curcumin in bioavailability studies and for therapeutic effects (Takahashi et al., 2009; Ravichandran, 2013; Vatsavai and Kilari, 2016). Hence 100 mg/kg dose was used. The blood samples (0.5 ml) were withdrawn from retro-orbital plexus at different time intervals and collected into microcentrifuge tubes containing EDTA. Plasma was separated by centrifuging the blood samples at 10000 rpm for 6 min at 5°C. After centrifugation, the obtained plasma was stored at −20°C until analysis. All animal protocols were approved by the institutional animal ethics committee vide letter number 107/IAEC/18 and approval number PU/45/99/CPCSEA/IAEC/2017/89.

Sample Preparation (Extraction Procedure)

To 40 μl of plasma samples in an eppendorf tube, 150 μl of methanol and 300 μl of acetonitrile:water (1:1; pH 3) was added. 10 μl of the β-glucuronidase enzyme was added and incubated for 30 min at 37°C. The sample was vortexed for 5 min and centrifuged at 15,000 rpm to separate precipitated proteins. The supernatant was transferred to suitably labeled tubes.

The sample was filtered through a 0.2 μm syringe filter and was used for analysis using the developed UPLC method. All the conditions of UPLC were maintained as indicated under section "Chromatographic Conditions."

Data Analysis

The pharmacokinetic parameters were calculated using a non-compartmental model. The area under the concentration-time curve from time zero to time t (AUC_{0-t}) was calculated using the trapezoidal method. Peak concentration (C_{max}) and the time at which the peak concentration is achieved (T_{max}), were obtained directly from the individual concentration-time profiles. The area under the concentration-time curve from time zero to infinity was calculated by $AUC_{0-\infty} = AUC_{0-t} + C_t/K_e$, where C_t is the drug concentration observed at the last time and K_e is the apparent elimination rate constant obtained from the terminal slope of the individual concentration-time curves after logarithmic transformation of the concentration values and application of linear regression. AUMC was determined by plotting concentration × time (ct) versus time (t) using the trapezoidal method. Mean residence time (MRT) was calculated as = AUMC/AUC.

RESULTS AND DISCUSSION

Curcumin Loaded Solid Lipid Nanoparticles (CLEN)

Various formulations incorporating 10–15 mg (1–1.5%) of curcumin per ml of CLEN dispersion were prepared, as described in **Supplementary Table S1**. Most of these SLN systems, however, showed settling of curcumin crystals at the bottom of the SLN CLEN formulation within 24 h of preparation, upon keeping.

All the batches prepared with Compritol® 888 ATO with concentration varying from 4 to 10% w/w showed settling of the drug. However, no settling was observed when Precirol ATO 5® was used as the lipid component (F4 and F5). Howsoever, F5 formulation showed a particle size of ≥1 μ (1000 nm), hence, three batches of F4 were prepared and

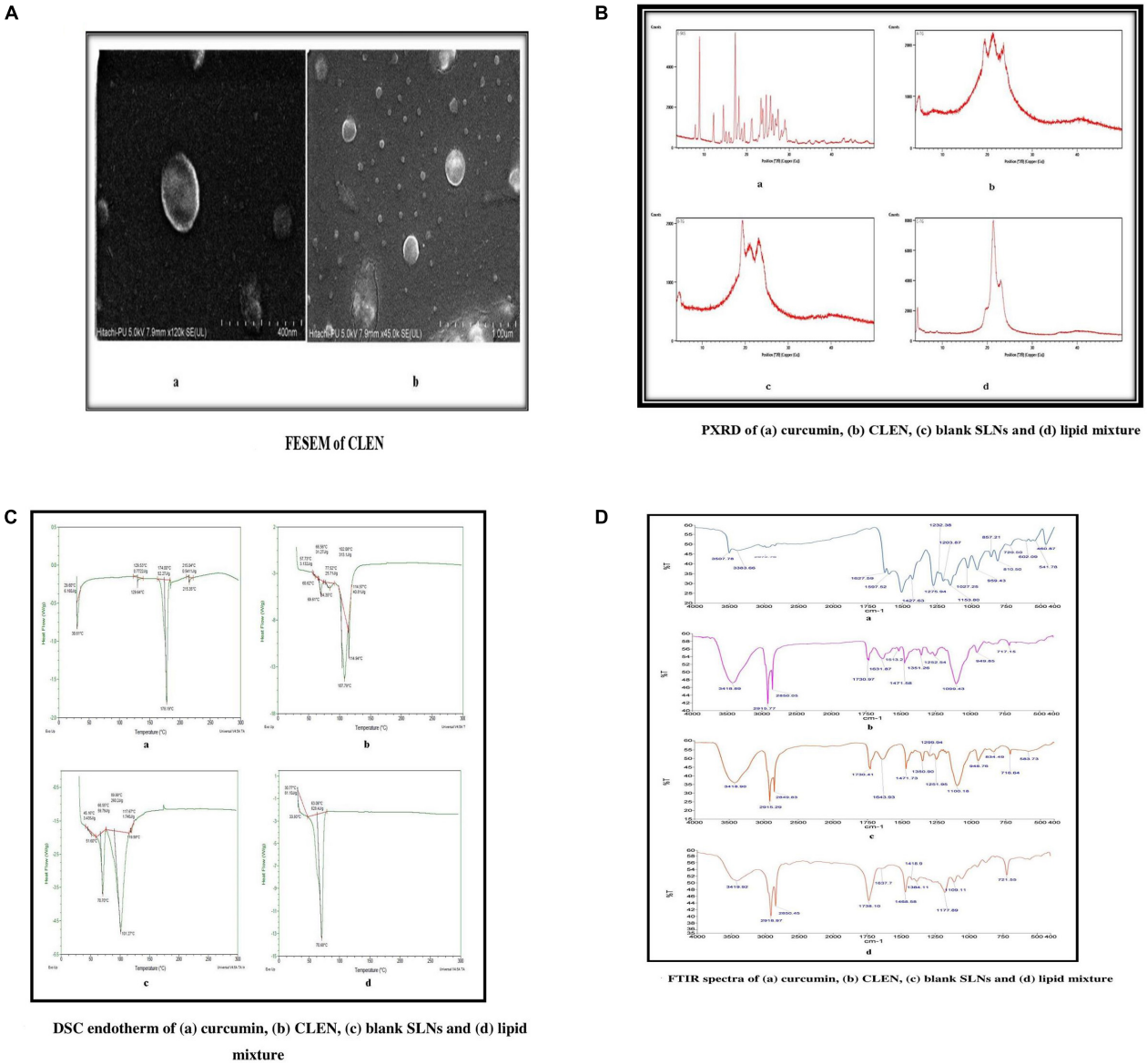

FIGURE 2 | (A) FESEM, **(B)** PXRD, **(C)** DSC, and **(D)** FTIR of CLEN and other components.

evaluated for TDC, entrapment efficiency, and particle size (**Supplementary Table S2**).

The particle size of the selected formulation F4 was also >700 nm. In the next part of the study, an attempt was made to decrease the particle size of the formulations F4 and F5 by varying stirring speeds and HPH cycles as shown in **Supplementary Table S3**.

It was observed that an increase in stirring speed and number of HPH cycles was not successful in achieving a particle size of <700 nm. Furthermore, F4 and F5 also showed settling of curcumin upon longer keeping (>2 weeks) and were thus rejected.

As the next option, we decided to combine Compritol 888 ATO® with GMS (lipid mixture) in different ratios to prepare CLEN formulation and the prepared formulations were observed for the settling of curcumin (**Supplementary Table S4**). It has been reported that curcumin showed maximum solubility in GMS when a panel of lipids was evaluated (Shrotriya et al., 2018). Our earlier studies indicated that lipid mixtures show greater imperfections and reduced crystallinity, allowing for better encapsulation of drug molecules (Bhandari and Kaur, 2013). Compritol 888 ATO® is a safe pharmaceutical excipient which results in nanosized and stable SLN formulations, in addition to the fact that curcumin shows some solubility in it (Shrotriya et al., 2018). Hence, we decided to combine GMS with Compritol 888 ATO® in the next set of curcumin SLN formulations (**Supplementary Table S4**).

Since no settling of the drug was observed, the prepared formulations (F8-F13) were evaluated for drug assay/TDC, entrapment efficiency, particle size, and PDI, as described in **Supplementary Table S5**.

Formulations (F8-F10) showed the presence of curcumin crystals when observed under a light microscope, indicating that the drug is present in undissolved/undispersed form, and was hence rejected. Out of the remaining three formulations (F11, F12, and F13), F13 was selected based on the fact that it achieved the highest drug concentration (15 mg/ml).

In the present investigation, we developed CLEN (curcumin encapsulated lipidic nanoconstructs; SLNs) dispersion (**Figure 1**), with a high drug loading (15% with respect to lipid matrix), and containing 15 mg curcumin per ml. It is the highest increase in solubility of curcumin in an aqueous system (1.4×10^6 times increase as compared to 11 ng/ml in water for free curcumin) coupled with high drug loading, reported till date, to the best of our knowledge.

Supplementary Table S6A summarizes features of curcumin SLNs reported previously in the literature and the technical advantage of the presently disclosed CLEN technology (Indian patent application no. 201811044487; PCT/IB2019/060162) and **Supplementary Table S6B** summarizes curcumin loaded nanoparticles (other than SLNs) investigated over a period of 5 years.

Characterization of CLEN

The TDC/ assay of CLEN was found to be 14.62 ± 0.14 mg/ml (97.46 ± 0.01%) (n = 6). The entrapment efficiency was 79.74 ± 0.88% (n = 6), and the average particle size was 540.2 ± 45.1 nm (n = 6). The average particle size of blank SLNs was 339.6 nm. A much larger particle size upon loading of curcumin indicates that curcumin is probably surface loaded in addition to being incorporated in the core of SLNs. The latter could be due to the high solubility of curcumin in the surfactant layer surrounding the SLNs. Tween 80 is presently used as the surfactant and PEG, though used as a solvent, is also known for its surfactant supporting properties and curcumin shows high solubility in both these components.

The PDI of CLEN and blank SLNs was 0.291 ± 0.062 (n = 6), and 0.332, respectively. While PDI of ≤0.3 is considered to be highly monodisperse, values of 0.3–0.4 are considered to be moderately polydisperse (Bhattacharjee, 2016).

The zeta potential of CLEN and blank SLNs was −10.88 ± 3.67 mV (n = 6) and −0.61 mV, respectively. When curcumin was loaded, the potential value of the particles decreased, which may be due to the free curcumin distributed in the water phase or potential diffusion layer (Xu et al., 2016) and can be attributed to the phenolic (OH^-) and diketonic functionalities of the curcumin (Pathak et al., 2015).

Field Emission Scanning Microscopy (FESEM)

The FESEM of CLEN showed that the particles were nearly spherical in shape and that they were present as individual entities rather than agglomerates, confirming their stability. An outer coating of the surfactant is observed in **Figure 2A**. The surfactant layer assigns stability to the particles preventing their aggregation.

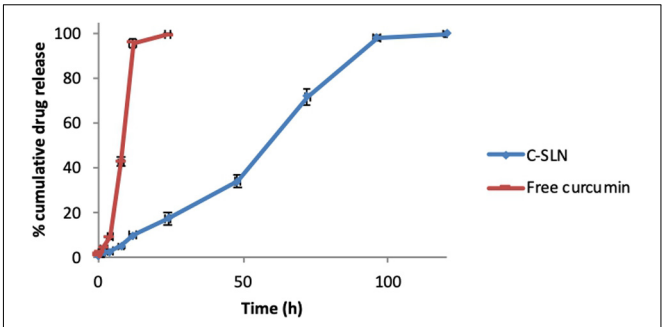

FIGURE 3 | *In vitro* release profile of curcumin from CLEN and free curcumin.

Powder X-Ray Diffraction

Powder X-ray diffraction patterns of curcumin, CLEN, blank SLNs, and lipid mixture are shown in **Figure 2B**. The PXRD pattern of curcumin exhibited peaks at 2θ scattered angles of 17.27°, 8.89°, 25.57°, and 24.54°, indicating its crystalline nature. The PXRD pattern of lipid mixture exhibited sharp peaks at 2θ scattered angles 21.31°, 22.96°, 4.46°, and 19.63°, again, establishing its crystalline state (**Figure 2B**). CLEN and blank SLNs, however, showed spectra differences from curcumin and the lipid mixture. Some characteristic peaks observed at 2θ scattered angles of 21.2°, 19.3°, and 23.5° in case of CLEN and 19.33°, 21.12°, and 22.95° in case of blank SLNs do correspond to the lipid mix. However, the typical pattern of peaks corresponding to free curcumin was missing, indicating loss of crystallinity and a shift toward the amorphous (Wang et al., 2012) and thus a more soluble state.

Differential Scanning Calorimetry (DSC)

Differential scanning calorimetry is a thermoanalytical technique in which the differences in the amount of heat required to maintain the sample and reference at the same temperature is measured as a function of temperature and time. In the case of pure curcumin, a melting endotherm appeared at 178.19°C corresponding to its reported melting point at 180–183°C. The CLEN, however, showed a broad endotherm starting from 60°C and extending to 115°C, with a sharp peak at 107.79°C (**Figure 2C**). The broadening of peaks indicates the amorphous nature of CLEN while the shift to a lower temperature indicates a nano size. The lipid mixture exhibited a sharp peak at 70.68°C,

TABLE 1 | Linear correlation coefficients obtained for *in vitro* release data from various models.

Model		Formulation	
		Free curcumin	CLEN
Zero order	r^2	0.856	0.978
First order	r^2	0.964	0.855
Higuchi	r^2	0.879	0.917
Hixson-Crowell	r^2	0.906	0.933
Korsmeyer-peppas	r^2	0.957	0.969
	n	1.149	0.841

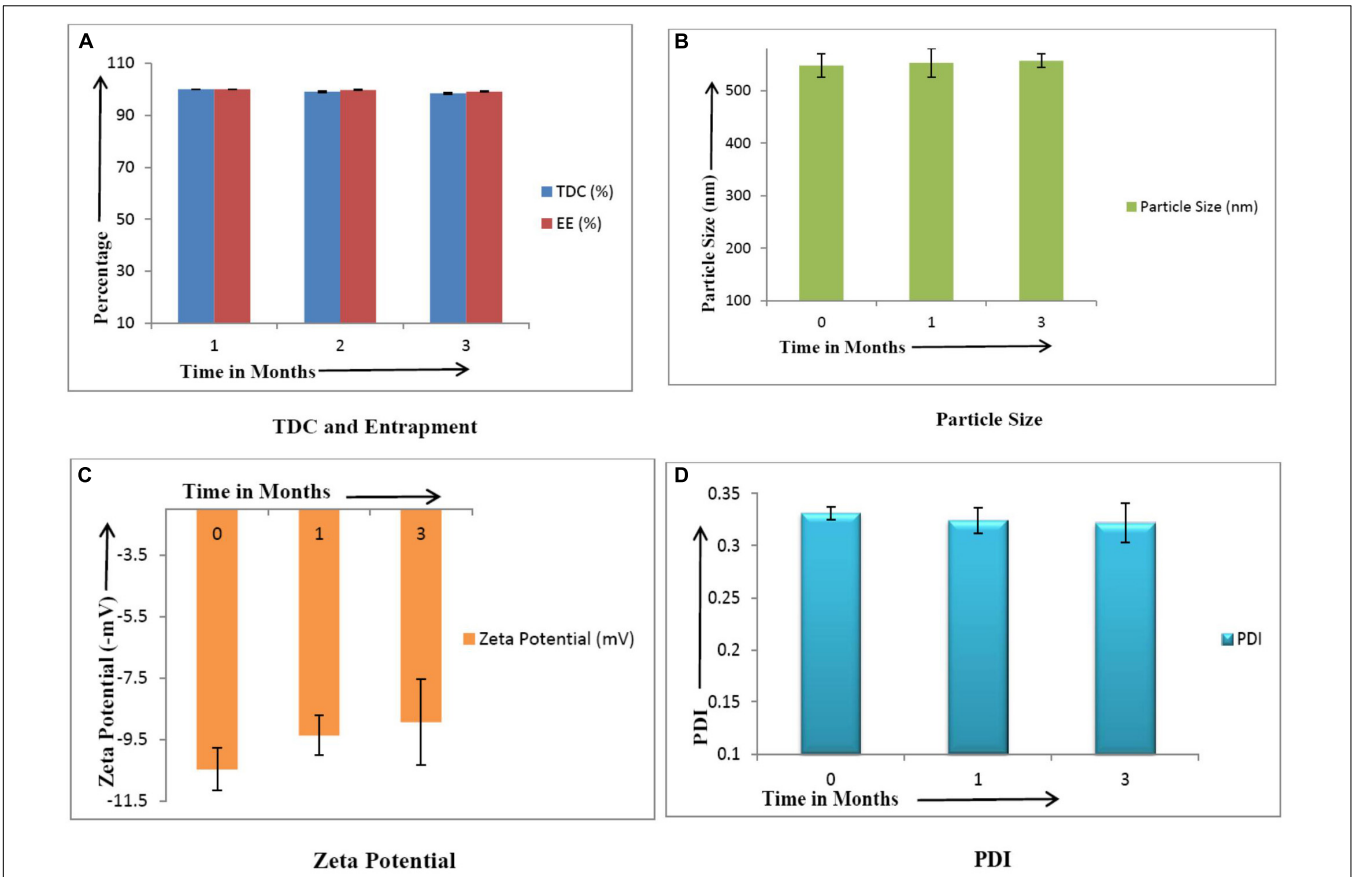

FIGURE 4 | Stability studies of CLEN (n = 3). There was no significant change ($p \leq 0.05$) in the values of various parameters upon storage. **(A)** TDC and Entrapment, **(B)** Particle Size, **(C)**, Zeta Potential, and **(D)** PDI.

TABLE 2 | Percentage remaining of free curcumin (F.Cur) and CLEN with time at various pH (n = 3).

Time	pH 1.2		pH 6.8		pH 7.4		pH 9	
(h)	F.Cur	CLEN	F.Cur	CLEN	F.Cur	CLEN	F.Cur	CLEN
0	100.00 ± 0.06	100.00 ± 0.03	100.00 ± 0.04	100.00 ± 0.06	100.0 ± 0.060	100.00 ± 0.06	100.00 ± 0.004	100.00 ± 0.03
0.08	89.23 ± 0.02	99.49 ± 0.04	94.93 ± 0.06	99.80 ± 0.01	96.33 ± 0.02	99.49 ± 0.05	82.59 ± 0.009	90.45 ± 0.004
0.25	88.29 ± 0.01	98.87 ± 0.03	87.63 ± 0.04	99.49 ± 0.02	93.81 ± 0.04	98.87 ± 0.04	61.43 ± 0.004	72.87 ± 0.006
0.5	85.60 ± 0.01	98.25 ± 0.03	81.95 ± 0.08	98.08 ± 0.02	84.17 ± 0.04	98.25 ± 0.07	32.76 ± 0.006	58.39 ± 0.006
1	87.24 ± 0.001	97.12 ± 0.03	79.72 ± 0.06	97.06 ± 0.01	75.92 ± 0.04	95.07 ± 0.07	20.48 ± 0.001	40.13 ± 0.003
2	72.37 ± 0.02	96.20 ± 0.03	66.73 ± 0.05	93.22 ± 0.03	67.20 ± 0.03	92.60 ± 0.06	15.70 ± 0.002	21.66 ± 0.005
3	68.74 ± 0.03	95.79 ± 0.03	62.68 ± 0.07	92.21 ± 0.03	61.01 ± 0.03	92.29 ± 0.05	9.90 ± 0.003	19.53 ± 0.005
4	62.76 ± 0.01	94.35 ± 0.03	57.81 ± 0.05	90.79 ± 0.02	49.08 ± 0.04	85.51 ± 0.07	2.39 ± 0.004	17.41 ± 0.006
5	61.01 ± 0.01	93.11 ± 0.03	43.61 ± 0.08	89.37 ± 0.03	40.60 ± 0.03	82.32 ± 0.06	–	11.46 ± 0.003
6	53.40 ± 0.02	92.39 ± 0.04	23.12 ± 0.04	89.07 ± 0.02	24.31 ± 0.01	81.50 ± 0.05	–	2.76 ± 0.006
24	15.76 ± 0.01	79.86 ± 0.08	11.36 ± 0.04	71.56 ± 0.02	13.99 ± 0.01	66.08 ± 0.05	–	–

which was, however, absent in CLEN. This may be due to the change of lipid to a completely amorphous form in SLN formulation (Chen et al., 2013).

Fourier Transform Infra-Red (FTIR)

Pure curcumin samples showed a sharp peak at 3507 cm^{-1} indicating the presence of –OH group (**Figure 2D**). The IR peaks obtained with CLEN, however, revealed an intermolecular stretching of the –OH groups (3400–3200 cm^{-1}) due to hydrogen bonding (Shelat et al., 2015). This may be regarded as a direct indication of the formation of SLNs, as the 3400–3200 cm^{-1} stretching was not observed in the case of curcumin or lipid mixture.

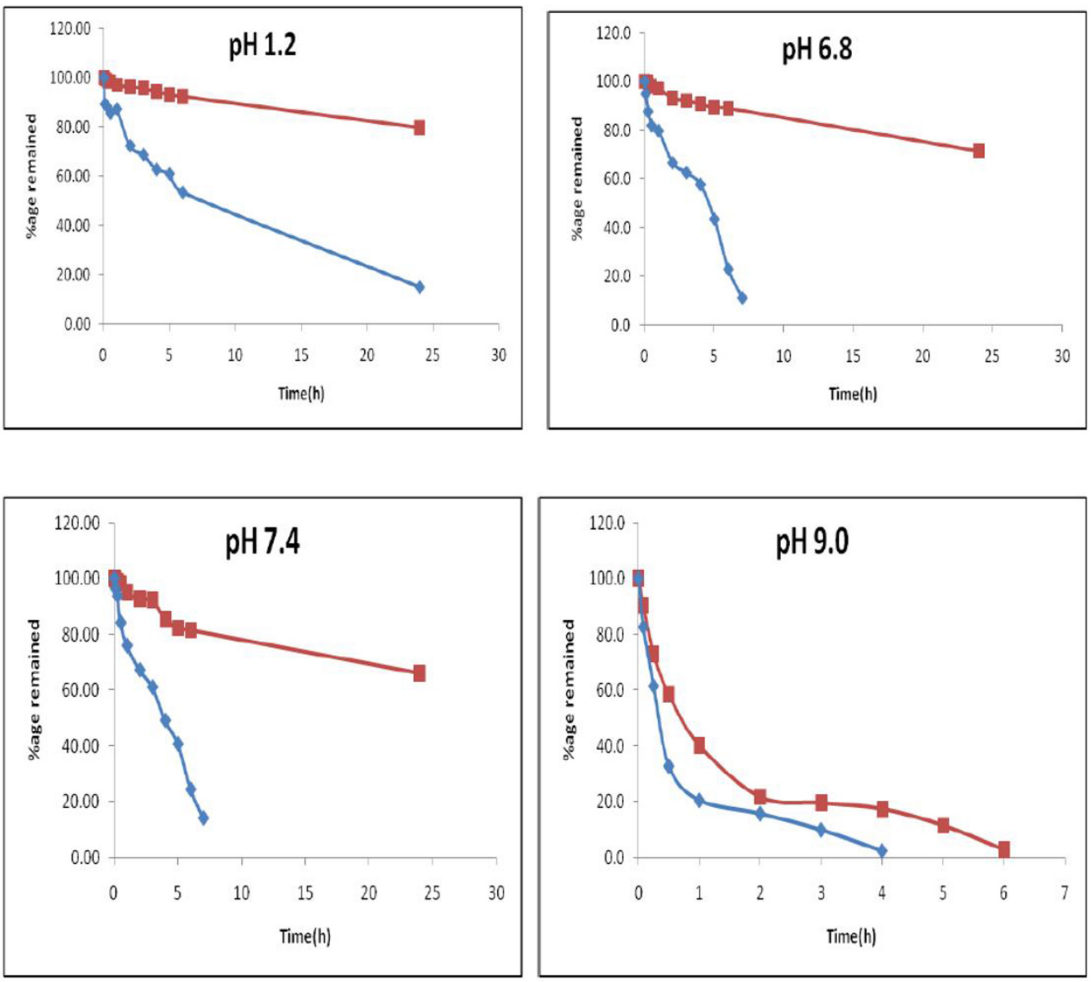

FIGURE 5 | Percentage remaining of curcumin versus time plot at various pH.

In vitro Release

The selection of a suitable release media was of significance with curcumin considering its insoluble nature and proneness to degradation in various buffer solutions. Curcumin shows significant solubility in methanol, so varying proportions of methanol were mixed with solutions buffered to pH 1.2 (stomach), 6.8 (proximal intestine), and 7.4 (distal part of small intestine/plasma). However, the addition of methanol led to precipitation of electrolytes from buffers.

TABLE 3 | Various degradation kinetics parameters for free curcumin and CLEN (n = 6).

Order	pH	Free cur			C-SLNs		
		k value	$^{t}1/2$	r^2	*k* value	$^{t}1/2$	r^2
zero order	pH 1.2	0.039	17.34	0.934	–	–	–
	pH 6.8	0.52	1.32	0.967	–	–	–
	pH 7.4	0.073	9.4	0.984	–	–	–
	pH 9	0.95	0.669	0.994	0.195	3.55	0.891
First order	pH 1.2	–	–	–	0.003	231	0.98
	pH 6.8	–	–	–	0.005	138	0.962
	pH 7.4	–	–	–	0.007	99	0.89

TABLE 4 | Change in particle size and PDI of CLEN with pH.

Dilution medium	Time (h)	Particle size# (nm)	PDI#
pH 1.2	0	458.9 ± 8.8	0.361 ± 0.012
	2	447.9 ± 7.4	0.352 ± 0.030
	4	489.3 ± 7.3	0.363 ± 0.013
pH 6.8	0	453.0 ± 20.5	0.320 ± 0.011
	2	434.3 ± 3.7	0.369 ± 0.012
	4	453.0 ± 17.0	0.363 ± 0.003
	6	475.1 ± 8.7	0.398 ± 0.006
pH 7.4	0	465.9 ± 12.5	0.332 ± 0.012
	24	596.7 ± 39.0*	0.341 ± 0.017

*#Particle size and PDI for the CLEN aqueous dispersion used in the experiment were 450.1 nm and 0.331, respectively. No significant change in particle size was observed at any pH or time except for those marked with * ($p \leq 0.05$).*

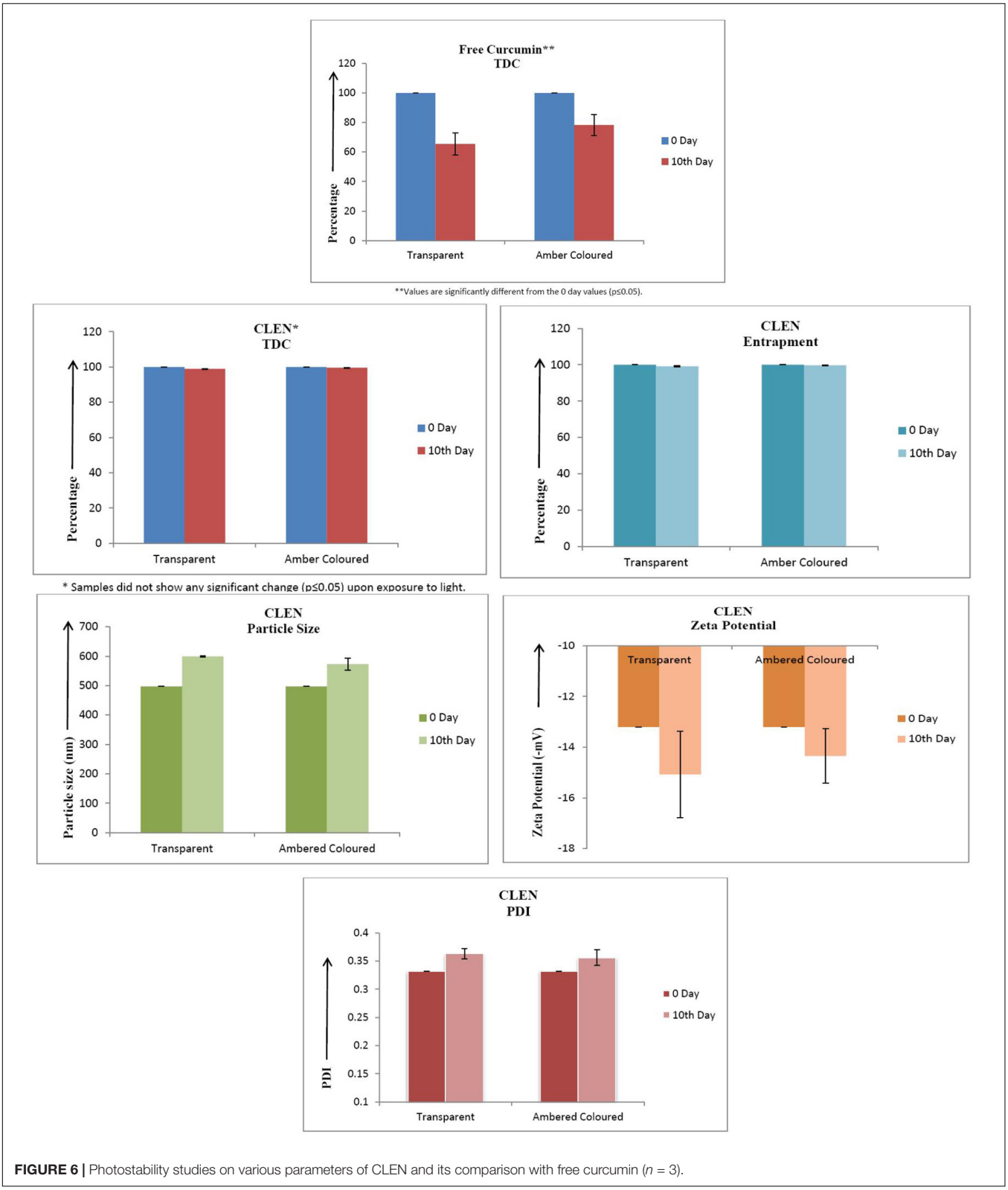

FIGURE 6 | Photostability studies on various parameters of CLEN and its comparison with free curcumin (n = 3).

The mixing of ethanol with the buffer solutions overcame this problem, but curcumin was found to degrade in these buffer solutions. Hence, methanol:water (1:1) was selected as a suitable release medium. Varying concentrations of methanol (10–50%) were tried, however, only 50% methanol in water could dissolve a sufficient quantity of

curcumin (present in 0.5 ml of CLEN dispersion), to ensure sink conditions.

The drug release from CLEN and free curcumin is shown above in **Figure 3**. The release from CLEN extended up to 120 h with 99.73 ± 1.12% release (**Figure 3**) and followed zero order release kinetics, i.e., controlled release (**Table 1**). A first order release was observed as expected with free curcumin and the drug was completely released within 24 h (**Table 1**).

Stability Studies

Long Term Stability

After 3 months of storage under refrigerated conditions, CLEN was found to be stable with no significant change ($p \leq 0.05$) in any of the parameters (**Figure 4**).

Hydrolytic Degradation

The study aimed to investigate if the encapsulation of curcumin within CLEN protects against hydrolytic degradation. Data from free curcumin was compared with those for CLEN (**Table 2** and **Figure 5**).

From the data generated in this study, it is observed that at acidic pH 1.2, CLEN did not show any significant degradation (approximately 8%) up to 6 h ($p < 0.05$). However, nearly 20% of curcumin entrapped within the SLNs degraded at 24 h ($P < 0.001$). In contrast, degradation of up to 50% and 85% is observed in 6 and 24 h, respectively for free curcumin. At pH 6.8, 77% free curcumin degraded within 6 h and 89% degraded within 24 h, whereas in the case of the entrapped drug (CLEN), we observed only a 10% degradation up to 6 h and 30% degradation up to 24 h. Similarly, at physiological pH 7.4, a significant amount (75%) of free curcumin was degraded within 6 h and 77% degraded in 24 h and at extreme pH 9, free curcumin showed approximately 98% degradation at 4 h while the same amount of curcumin degraded at 6 h. The data demonstrate that SLNs (red line for CLEN and blue line for curcumin) significantly protect the encapsulated curcumin against hydrolytic degradation (**Figure 5**).

The degradation kinetics of curcumin under various pH conditions and the stability of curcumin in physiological matrices reported earlier indicates that when curcumin was added to a 0.1 M phosphate buffer (pH 7.2), more than 90% of curcumin was degraded (Wang et al., 1997). The absorbance at 426 nm decreased to approximately 50% after 5 min, and after 10 min the remaining absorbance was only about 10%. However, we presently observed an almost 40% degradation at 4 h in pH 1.2 medium.

The order of kinetics of free curcumin was zero order at all investigated pH conditions, while in the case of CLEN, the order was first order except at pH 9 (zero order). However, even at pH 9, $t_{1/2}$ increased five times, and the rate constant of CLEN was 80% less than that for free curcumin. Very interestingly, at a physiological pH of 7.4, an almost 90% decrease in k value and a 10 times increase in $t_{1/2}$ was observed (**Table 3**). Similarly, protection provided at the other two pH buffers was also substantial and a similar increase in $t_{1/2}$ (13.3 times at pH 1.2 and 104 times at pH 6.8), and a decrease in k was observed in comparison to free curcumin.

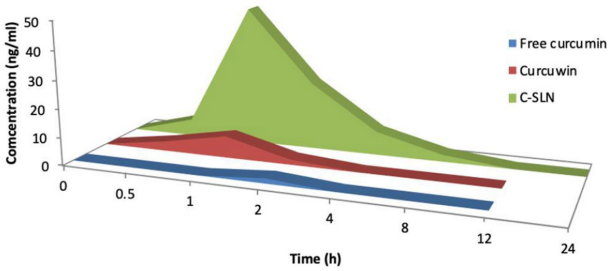

FIGURE 7 | Mean concentration-time area curve of curcumin rat after single oral does of free curcumin, curcumin® and CLEN.

Particle Size Variation With pH and Time

Variation in particle size at the above mentioned physiological pH was determined at times corresponding to their residence times in these parts of the gastrointestinal tract (g.i.t.). No significant ($p \leq 0.05$) change in size and PDI (**Table 4**) was observed at pH 1.2 and 6.8 indicating the stability of CLEN upon incubation at these pH values. This ensures that CLEN will be absorbed in the nano form from the g.i.t. Furthermore, at pH 7.4, even after incubation for 24 h, only a 6.7% increase in size was observed. It may thus be concluded that CLEN remain stable and maintain their integrity under these physiological conditions.

Photostability Studies

The study was undertaken to establish the photoprotection offered to curcumin by the lipid matrix of CLEN. It protected the encapsulated curcumin completely against photodegradation. On the other hand, 21.7% of degradation was observed upon storage of free curcumin in amber colored containers while it increased to 35% in transparent containers (**Figure 6**). No degradation (TDC/assay remained unchanged) occurred in the case of CLEN even upon storage in transparent containers. However, an increase in particle size was observed upon exposure to light. This may be attributed to increased collisions between particles due to imparted kinetic energy by light.

TABLE 5 | Various pharmacokinetic parameters obtained after a single oral dose of free curcumin, CurcuWIN® and CLEN administered to rats (n = 3).

Formulation	Dose (mg/kg)	$^{AUC}0–\infty$ (h×ng/ml)	Cmax (ng/ml)	Tmax (h)	$^{AUMC}0–\infty$ (h^2×ng/ml)	MRT (h)	Clearance (l/h/kg)	Relative bioavailability with respect to Free curcumin
Free curcumin	100	1.78	1.18	2	3.55	2	56287.29	1
CLEN	100	124.2	55.75	1	401.28	3.20	857.62	69.78
CurcuWIN®	100	16.02	8.52	1	20.43	1.27	6240.56	9.00

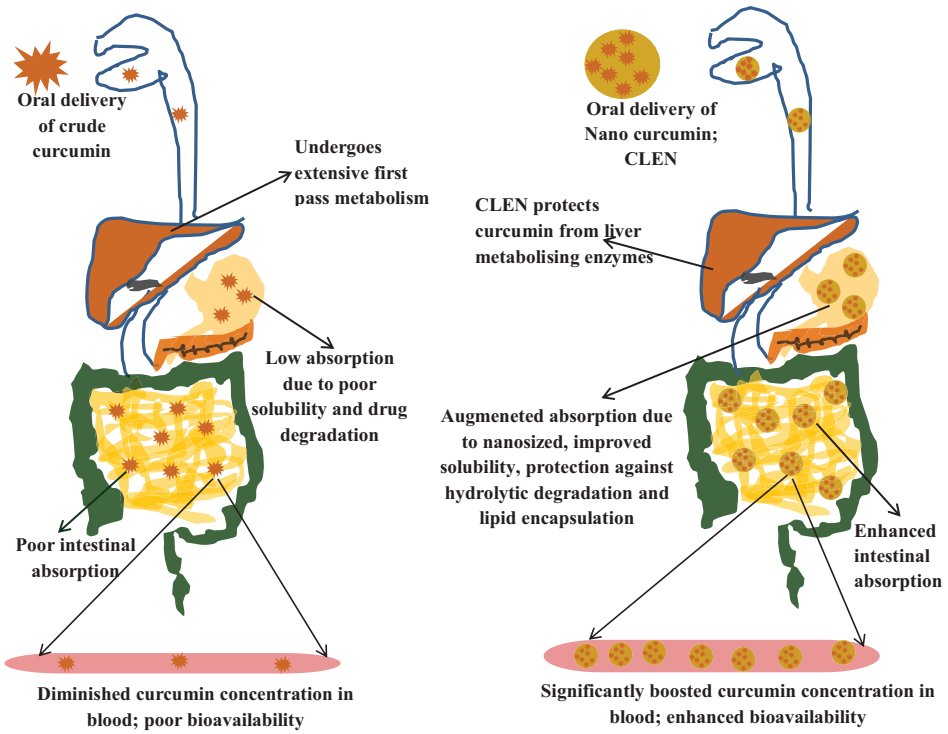

FIGURE 8 | Diagrammatic representation for benefits of encapsulation of curcumin as CLEN.

Bioanalytical Method Validation

A calibration curve of curcumin was found to be linear from 12 to 500 ng/ml in plasma samples. The system was confirmed to be suitable, selective, and specific for the determination of curcumin under the optimized chromatographic conditions, as no peak was observed in the chromatograms of blank plasma samples.

Limit of detection (LOD) and LLOQ were found to be 2 ng/ml and 25 ng/ml, respectively. The overall recovery was >80%. The individual recoveries at LQC, MQC, and HQC were 82.18, 86.18, and 83.42%, respectively.

The intra-day accuracy was 98.43–112.21% for QC samples with precision <2% and the inter-day accuracy was 99.17–107.83% for QC samples with precision <2.6%.

Pharmacokinetic Studies

Plasma concentration after oral administration of 100 mg/kg dose of CLEN and CurcuWIN® were compared with 100 mg/kg dose of free curcumin and plotted against time (**Figure 7**). The area under the curve was calculated using the trapezoidal method. The relevant parameters including C_{max}, T_{max}, $AUC_{0-\infty}$, and clearance are listed in **Table 5** above.

The studies revealed that relative bioavailability of free curcumin was increased by 69.78 times in the case of CLEN, whereas it was increased by only 9.00 times in CurcuWIN®. In a pharmacokinetic study performed on human volunteers, CurcuWIN® showed 136 times higher bioavailability than free curcumin (Jäger et al., 2014). From this, we can imply that CLEN may also show a bioavailability of 1047 times (136 × 7.7) when determined in humans.

Figure 8 shows the advantage of encapsulating curcumin as CLEN and its benefits at various sites in the physiological system when taken orally. Wei et al. (2014) formed a nanogel of curcumin using cholesteryl-hyaluronic acid which showed an improved circulation, slower clearance as observed by authors in a pharmacokinetic study in mice. We also observed a significantly slower clearance in the CLEN group (**Table 5**). The nanogel formulation showed excellent tumor growth inhibition in human pancreatic MiaPaCa-2 xenograft (5 fold) and murine mammary 4T1 orthotopic cancer models (2.5 fold) when analyzed for mean tumor volume with respect to the free curcumin group (Wei et al., 2014).

CONCLUSION

This study was successful in formulating CLEN containing 15 mg curcumin per ml of the SLN dispersion. The characterization of the prepared formulation helped us to conclude that the SLNs were formed successfully and were amorphous, confirming the presence of curcumin in a solubilized form.

Furthermore, CLEN exhibited a-zero order release in comparison to first order release by free curcumin, indicating the controlled release nature of the developed CLEN. Stability studies including photostability and hydrolytic degradation studies confirm the stability of CLEN and curcumin encapsulated within the lipid matrix.

Previous reports by numerous scientists have proved the regulatory effect of curcumin on NF-kB and its cytotoxic effect on cancer cell lines. The only limiting factor was the availability of curcumin in the physiological system to elicit a therapeutic response. This is suitably addressed by the presented CLEN formulation. With enhanced solubility, stability, permeability, and bioavailability, curcumin prepared CLEN could be explored for various therapies including cancers and other inflammation and oxidative stress related pathologies in the future.

DATA AVAILABILITY STATEMENT

The raw data supporting the conclusions of this article will be made available by the authors, without undue reservation.

ETHICS STATEMENT

The animal study was reviewed and approved by the Institutional Animal Ethical Committee Panjab University, Chandigarh.

AUTHOR CONTRIBUTIONS

IPK conceived the idea and developed the theory. TG, JS, and SK carried out the experiments. SS helped in the synthesis of CLEN and performed the analytic calculations under the supervision of IPK and GS. JS wrote the manuscript with support from SS. All authors contributed to the article and approved the submitted version.

FUNDING

JS was supported by the ICMR Senior Research Fellowship, New Delhi (45/78/2018-NAN/BMS). The publication grant was provided by the Panjab University.

ACKNOWLEDGMENTS

The UGC-CAS and DST-FIST laboratory facilities of the UIPS and DST-SAIF facility of Panjab University are duly acknowledged. The publication grant from Panjab University is acknowledged. They had however, no role in the study design, collection, analysis, interpretation of data, the writing of this article, or the decision to submit this research for publication.

SUPPLEMENTARY MATERIAL

The Supplementary Material for this article can be found online at: https://www.frontiersin.org/articles/10.3389/fbioe.2020.00879/full#supplementary-material

REFERENCES

Adahouna, M. A., Al-Akhrasb, M. A. H., Jaafara, M. S., and Bououdinac, M. (2017). Enhanced anti- cancer and antimicrobial activities of curcumin nanoparticles. *Artif. Cells Nanomed. Biotechnol.* 45, 98–107. doi: 10.3109/21691401.2015.1129628

Aggarwal, B. B., and Harikumar, K. B. (2009). Potential therapeutic effects of curcumin, the anti- inflammatory agent, against neurodegenerative, cardiovascular, pulmonary,metabolic, autoimmune and neoplastic diseases. *Int. J. Biochem. Cell Biol.* 41, 40–59. doi: 10.1016/j.biocel.2008.06.010

Basniwal, R. K., Khosla, R., and Jain, N. (2014). Improving the anticancer activity of curcumin using nanocurcumin dispersion in water. *Nutr. Cancer* 6, 1015–1022. doi: 10.1080/01635581.2014.936948

Bhandari, R., and Kaur, I. P. (2013). A method to prepare solid lipid nanoparticles with improved entrapment efficiency of hydrophilic drugs. *Curr. Nanosci.* 9, 211–220. doi: 10.2174/1573413711309020008

Bhattacharjee, S. (2016). DLS and zeta potential–what they are and what they are not? *J. Controll. Release* 235, 337–351. doi: 10.1016/j.jconrel.2016.06.017

Chaurasia, S., Chaubey, P., Patel, R. R., Kumar, N., and Mishra, B. (2016). Curcumin-polymeric nanoparticles against colon-26 tumor-bearing mice: cytotoxicity, pharmacokinetic and anticancer efficacy studies. *Drug Dev. Ind. Pharm.* 42, 694–700. doi: 10.3109/03639045.2015.1064941

Chen, J., Dai, W. T., He, Z. M., Gao, L., Huang, X., Gong, J. M., et al. (2013). Fabrication and evaluation of curcumin-loaded nanoparticles based on solid lipid as a new type of colloidal drug delivery system. *Indian J. Pharmac. Sci.* 75, 178–184.

Espinoza, Y. R., and Muriel, P. (2009). Pharmacological actions of curcumin in liver diseases or damage. *Liver. Int.* 6, 1457–1466. doi: 10.1111/j.1478-3231.2009.02086.x

Fadus, M. C., Lau, C., Bikhchandani, J., and Lynch, H. T. (2017). Curcumin: an age-old anti- inflammatory and anti-neoplastic agent. *J. Trad. Compl. Med.* 7, 339–346. doi: 10.1016/j.jtcme.2016.08.002

Flora, G., Gupta, D., and Tiwari, A. (2013). Nanocurcumin: a promising therapeutic advancement over native curcumin. *Crit. Rev. Ther. Drug Carr. Sys.* 30, 331–368. doi: 10.1615/critrevtherdrugcarriersyst.2013007236

Gera, M., Sharma, N., Ghosh, M., Huynh, D. L., Lee, S. J., Min, T., et al. (2017). Nanoformulations of curcumin: an emerging paradigm for improved remedial application. *Oncotarget* 8, 66680–66698. doi: 10.18632/oncotarget.19164

Gupta, S. C., Patchva, S., Koh, W., and Aggarwal, B. B. (2012). Discovery of curcumin, a component of the golden spice, and Its miraculous biological activities. *Clin. Exp. Pharmacol. Physiol* 39, 283–299. doi: 10.1111/j.1440-1681.2011.05648.x

Hewlings, S. J., and Kalman, D. S. (2017). Curcumin: a review of its' effects on human health. *Foods* 6, 1–11.

Indian Pharmacopoeia and Commission (2014). *Indian Pharmacopoeia, Government of India, Ministry of Health and Welfare*. New Delhi: Indian Pharmacopoeia Commission.

Jäger, R., Lowery, R. P., Calvanese, A. V., Joy, J. M., and Purpura, M. (2014). Comparative absorption of curcumin formulations. *Nutr. J.* 13:11.

Karthikeyan, A., Senthil, N., and Min, T. (2020). Nanocurcumin: a promising candidate for therapeutic applications. *Front. Pharmacol.* 11:1–24. doi: 10.3389/fphar.2020.00487

Khosropanaha, M. H., Dinarvanda, A., Nezhadhosseinia, A., Haghighia, A., Hashemia, S., Nirouzada, F., et al. (2016). Analysis of the antiproliferative effects of curcumin and nanocurcumin in MDA-MB231 as a breast cancer cell line. *Iran. J. Pharmaceut. Res.* 15, 231–239.

Liu, H. T., and Ho, Y. S. (2018). Anticancer effect of curcumin on breast cancer and stem cells. *Food Sci. Hum. Well.* 7, 134–137. doi: 10.1016/j.fshw.2018.06.001

Liu, W., Zhai, Y., Heng, X., Che, F. Y., Chen, W., Sun, D., et al. (2016). Oral bioavailability of curcumin: problems and advancements. *J. Drug Target.* 24, 694–702. doi: 10.3109/1061186x.2016.1157883

Lopresti, A. L. (2018). The problem of curcumin and its bioavailability: could its gastrointestinal influence contribute to Its overall health-enhancing effects? *Am. Soc. Nutr.* 9, 41–50. doi: 10.1093/advances/nmx011

Pathak, L., Kanwal, A., and Agrawal, Y. (2015). Curcumin loaded self assembled lipid-biopolymer nanoparticles for functional food applications. *J. Food Sci. Technol.* 52, 6143–6156. doi: 10.1007/s13197-015-1742-2

Prasad, S., Tyagi, A. K., and Aggarwal, B. B. (2014). Recent developments in delivery, bioavailability, absorption and metabolism of curcumin: the golden pigment from golden spice. *Cancer Res. Treat.* 46, 2–18. doi: 10.4143/crt.2014.46.1.2

Rahmani, A. H., Alsahli, M. A., Aly, S. M., Khan, M. A., and Aldebasi, Y. H. (2018). Role of curcumin in disease prevention and treatment. *Adv. Biomed. Res.* 7, 1–14.

Rajasekaran, S. A. (2011). Therapeutic potential of curcumin in gastrointestinal diseases. *World J. Gasteroinstestinal Pathophysiol.* 2, 1–14. doi: 10.4291/wjgp.v2.i1.1

Ravichandran, R. (2013). Pharmacokinetic study of nanoparticulate curcumin: oral formulation for enhanced bioavailability. *J. Biomater. Nanobiotechnol.* 4, 291–299. doi: 10.4236/jbnb.2013.43037

Saghatelyana, T., Tananyana, A., Janoyana, N., Tadevosyana, A., Petrosyana, H., Hovhannisyana, A., et al. (2020). Efficacy and safety of curcumin in combination with paclitaxel in patients with advanced, metastatic breast cancer: A comparative, randomized, double-blind, placebo-controlled clinical trial. *Phytomedicine* 70, 1–19.

Shelat, P., Mandowara, V. K., Gupta, D. G., and Patel, S. (2015). Formulation of curcuminoid loaded solid lipid nanoparticles in order to improve oral bioavailability. *Int. J. Pharm. Pharmaceutical Sci.* 7, 278–282.

Shrotriya, S., Ranpise, N., Satpute, P., and Vidhate, B. (2018). Skin targeting of curcumin solid lipid nanoparticles-engrossed topical gel for the treatment of pigmentation and irritant contact dermatitis. *Artif. Cell. Nanomed. Biotechnol.* 46, 1471–1482. doi: 10.1080/21691401.2017.1373659

Sun, M., Su, X., Ding, B., He, X., Liu, X., Yu, A., et al. (2012). Advances in nanotechnology-based delivery systems for curcumin. *Nanomedicine* 7, 1085–1100. doi: 10.2217/nnm.12.80

Tan, B. L., and Norhaizan, M. E. (2019). Curcumin combination chemotherapy:the implication and efficacy in cancer. *Molecules* 24, 1–21.

Takahashi, M., Uechi, S., Takara, K., Asikin, Y., and Wada, K. (2009). Evaluation of an oral carrier system in rats: bioavailability and antioxidant properties of liposome-encapsulated curcumin. *J. Agric. Food Chem.* 57, 9141–9146. doi: 10.1021/jf9013923

Tomeh, M. A., Hadianamrei, R., and Zhao, X. (2019). A review of curcumin and its derivatives as anticancer agents. *Mole. Sci.* 20, 1–26.

Vatsavai, L. K., and Kilari, E. K. (2016). Influence of curcumin on the pharmacodynamics and pharmacokinetics of gliclazide in animal models. *J. Exp. Pharmacol.* 8, 69–76. doi: 10.2147/JEP.S117042

Vutakuri, N. (2018). Curcumin - breast cancer therapeutic agent to replace allopathic treatments with extensive side effects. *J. Young Investig.* 35, 38–44.

Wang, K., Zhang, C., Bao, J., Jia, X., Liang, Y., Wang, X., et al. (2016). Synergistic chemopreventive effects of curcumin and berberine on human breast cancer cells through induction of apoptosis and autophagic cell death. *Sci. Rep.* 6, 1–14. doi: 10.1186/1475-2867-9-1

Wang, W., Zhu, R., Xie, Q., Li, A., Xiao, Y., Li, K., et al. (2012). Enhanced bioavailability and efficiency of curcumin for the treatment of asthma by its formulation in solid lipid nanoparticles. *Int. J. Nanomed.* 7, 3667–3677. doi: 10.2147/ijn.s30428

Wang, Y.-J., Pan, M.-H., Cheng, A.-L., Lin, L.-I., Ho, Y.-S., Hsieh, C.-Y., et al. (1997). Stability of curcumin in buffer solutions and characterization of its degradation products. *J. Pharm. Biomed. Anal.* 15, 1867–1876. doi: 10.1016/s0731-7085(96)02024-9

Wei, X., Senanayake, T. H., Anna Bohling, A., and Vinogradov, S. V. (2014). Targeted nanogel conjugate for improved stability and cellular permeability of curcumin: synthesis, pharmacokinetics, and tumor growth inhibition. *Mole. Pharmaceutics* 11, 3112–3122. doi: 10.1021/mp500290f

Wilken, R., Veena, M. S., Wang, M. B., and Srivatsan, E. S. (2011). Curcumin: A review of anti-cancer properties and therapeutic activity in head and neck squamous cell carcinoma. *Mole. Cancer* 10, 1–19.

Xie, M., Fan, D., Li, Y., He, X., Chen, X., Chen, Y., et al. (2017). Supercritical carbon dioxide-developed silk fibroin nanoplatform for smart colon cancer therapy. *Int. J. Nanomed.* 12, 7751–7761. doi: 10.2147/ijn.s145012

Xu, Y. Q., Chen, W. R., Tsosie, J. K., Xie, X., Li, P., Wan, J. B., et al. (2016). Niosome encapsulation of curcumin. *J. Nanomater.* 2016, 1–9. doi: 10.1155/2016/6365295

Conflict of Interest: The authors declare that the research was conducted in the absence of any commercial or financial relationships that could be construed as a potential conflict of interest.

frontiers in Chemistry

ORIGINAL RESEARCH
published: 22 October 2020
doi: 10.3389/fchem.2020.567652

Magnetic Silica Nanosystems With NIR-Responsive and Redox Reaction Capacity for Drug Delivery and Tumor Therapy

Chengzheng Jia[1†], *Hang Wu*[2†], *Keyi Luo*[1], *Weiju Hao*[1], *Shige Wang*[1*] and *Mingxian Huang*[1*]

[1] College of Science, University of Shanghai for Science and Technology, Shanghai, China, [2] Department of General Surgery, Xinhua Hospital, Shanghai Jiaotong University School of Medicine, Shanghai, China

In recent years, more and more researches have focused on tumor photothermal therapy and chemodynamic therapy. In this study, we prepared a multifunctional nanomaterial with potential applications in the above area. The Fe_3O_4 nanoparticles were synthesized with suitable size and uniformity and then coated with mesoporous silica and polydopamine. The unique core-shell structure not only improves the drug loading of the magnetic nanomaterials, but also produces high photothermal conversion efficiency. Furthermore, the reducibility of polydopamine was found to be able to reduce Fe^{3+} to Fe^{2+} and thus promote the production of hydroxyl radicals that can kill the tumor cells based on the Fenton reaction. The magnetic nanomaterials are capable of simultaneously combining photothermal and chemodynamic therapy and permit the efficient treatment for tumors in the future.

Keywords: photothermal therapy, Fenton reaction, chemodynamic therapy, magnetic nanoparticles, drug delivery

OPEN ACCESS

Edited by:
Jianhua Zhang,
Tianjin University, China

Reviewed by:
Ilídio Correia,
University of Beira Interior, Portugal
Piaoping Yang,
Harbin Engineering University, China

***Correspondence:**
Shige Wang
sgwang@usst.edu.cn
Mingxian Huang
hmx@usst.edu.cn

[†] *These authors have contributed equally to this work*

Specialty section:
This article was submitted to Nanoscience, a section of the journal Frontiers in Chemistry

Received: *30 May 2020*
Accepted: *01 September 2020*
Published: *22 October 2020*

Citation:
Jia C, Wu H, Luo K, Hao W, Wang S and Huang M (2020) Magnetic Silica Nanosystems With NIR-Responsive and Redox Reaction Capacity for Drug Delivery and Tumor Therapy. Front. Chem. 8:567652. doi: 10.3389/fchem.2020.567652

INTRODUCTION

Cancer is one of the leading causes of death in the world, especially malignant tumors, which poses a great threat to the safety of human life (Siegel et al., 2016). As a delivery system for therapeutic drugs, nanocarriers show a huge potential in cancer treatment. With the continuous development of nanotechnology, the genetic and drug loading capabilities of nanomaterials have received widespread attention (Jia et al., 2015). It has been a continuous effort to explore the novel preparation methods of nanomaterials for the effective therapy of tumors in the future (Qin et al., 2017). However, up to now, only a limited number of nanocarriers have been successfully used in the clinical treatment of cancer (Bulbake et al., 2017), because many nanocarriers either have a low drug-carrying capacity or have difficulty to efficiently reach the tumor site (Jia et al., 2015). The ideal nanocarrier should have a high drug loading efficiency and a suitable size, which can accurately transport the drug to the target area in the body for controlled release (Liu et al., 2014; Bose et al., 2016; Li et al., 2018).

In recent years, more and more functional materials have been introduced into the nanotechnology, and many new treatment methods have emerged, such as photothermal therapy (PTT), magnetocaloric therapy, and chemodynamic therapy (CDT) (Du et al., 2017; Chen et al., 2019; Wu et al., 2019; Zhou et al., 2020). These new treatments have greatly expanded the application of nanocarriers in the treatment of tumors. PTT is a new type of therapy with

low toxicity, high efficiency, and safety (Huang et al., 2017; Gulzar et al., 2018). Tumor tissue has enhanced permeability and retention than the normal one. Many nanomaterials with an appropriate size and photothermal conversion ability are used for tumor treatment (Huo et al., 2017; Wang et al., 2019, 2020). During PTT, tumor cells are killed by the heat of photothermal nanoparticles after being irradiated with near-infrared (NIR) laser (Li et al., 2018; Lin et al., 2018; Tiwari et al., 2019). PTT involves the use of photothermal materials that can effectively convert light radiation into heat to cure cancer via hyperthermia (Feng et al., 2018a). In the past few years, many documents have reported various materials with photothermal effects, such as metal sulfide, MnO_2, carbon-based graphene, precious metal Au, and the organic polypyrrole, polyaniline, polydopamine (PDA), etc (Jahanban-Esfahlan et al., 2015; Wang et al., 2015; Song et al., 2017; Feng et al., 2018b; Xu et al., 2018, 2020). However, many of them have drawbacks, and satisfactory therapeutic effects cannot be obtained (Feng et al., 2018b; Xue et al., 2019).

In the tumor microenvironment (TME), special metabolic pathways compared to normal cells cause it to become a place rich in large amounts of hydrogen ions and high reduction (Wu et al., 2019). Unlike normal cells, in the mitochondria of tumor cells, high concentrations of superoxide dismutase cause excessive H_2O_2 in the cells (Huo et al., 2017; Dong et al., 2019). Designing nanomaterials with CDT specificity in the TME has become a new way for tumor-targeting therapy. In CDT, nanomaterials precisely catalyze the reaction of H_2O_2 with Fe^{2+} (Fenton reaction), which in turn produce cytotoxic hydroxyl radicals (·OH) to kill tumor cells. Magnetic nanoparticles with tumor cell targeting, such as Fe_3O_4, are considered to be promising nanocatalytic enzymes that can generate ·OH for CDT (Feng et al., 2018b). In the Fenton reaction, magnetic Fe_3O_4 nanoparticles provide the Fe^{2+} needed for the reaction (Feng et al., 2018b). The continuous progress of the Fenton reaction depends on the conversion of Fe^{3+} to Fe^{2+} by materials with nanocatalytic capabilities. Because of its drug delivery ability and magnetocaloric effect, the superparamagnetic Fe_3O_4 nanomaterials have received extensive attention (Zhu et al., 2013). Moreover, Fe_3O_4 can provide a large number of Fe^{2+} to support the Fenton reaction for CDT of tumors (Zhao et al., 2018). Among many photothermal conversion materials, PDA has received special attention because of its good biocompatibility (Zhu et al., 2013). With the PDA coating, the nanoparticles have excellent PTT capability and good biocompatibility (Dai et al., 2017). Furthermore, the heat generated by PTT can further accelerate the release of the loaded drug in the nanoparticles. Moreover, PDA has a mild reducibility, which provides an inexhaustible motive force for the reduction of Fe^{3+} to Fe^{2+}, promotes the production of ·OH in tumor cells, and achieves the goal of killing tumor cells (**Schemes 1B,C**).

To combine the above functions in a single nanoplatform, we designed a novel nanosystem having multiple therapeutic efficacies. As shown in **Scheme 1A**, superparamagnetic Fe_3O_4 nanospheres with uniform size and good dispersibility were first prepared by the hydrothermal synthesis method (Gao et al., 2013; Jin et al., 2019). On the surface of the prepared Fe_3O_4 nanospheres, a thin layer of SiO_2 was coated (Tang and Cheng, 2013; Huang et al., 2017). Then, a thick layer of mesoporous silica nanospheres (MSNs) was evenly coated on SiO_2 (Tran et al., 2018). Finally, PDA and bovine serum albumin (BSA) were coated on the outer layer of the material, to form the biocompatible (Hu et al., 2010; Wang et al., 2011) magnetic Fe_3O_4@MSN@PDA@BSA nanoparticles (defined as FMPBs).

MATERIALS AND METHODS

Materials

Sodium acetate (anhydrous), 3,3′5,5,5′-tetramethyldiphenylamine (TMB), ferric chloride hexahydrate ($FeCl_3·6H_2O$), dopamine hydrochloride, poly(4-benzene) ethylene sulfonic acid–cobalt maleate sodium salt (PSSMA), sodium dihydrogen phosphate, triethanolamine (TEA), doxorubicin hydrochloride (DOX), Dulbecco modified eagle medium (DMEM), calcium fluoride (CaF_2), hexadecyl trimethyl ammonium bromide (CTAB), tetraethoxysilane (TEOS), acetone, ethanol, citric acid, disodium hydrogen phosphate, BSA, and sodium fluoride (NaF) were bought from Aladdin Reagents (China). Acetic acid, trisodium citrate, and citric acid were purchased from Sinopharm Chemical Reagent Co., Ltd. (China). Capstone FS-66 reagent was purchased from Sigma–Aldrich (USA). Human colon cancer cells (HT29) were purchased from the Institute of Biochemistry and Cell Biology, Chinese Academy of Sciences (Shanghai, China).

Preparation of the FMPBs Nanoparticles

For the synthesis of Fe_3O_4, 1.50 g of $FeCl_3·6H_2O$ and 1.0 g of PSSMA were added to 120 mL of ethylene glycol, heated to 70°C, and fully dissolved for 0.5 h. Then, 4.50 g sodium acetate and 0.75 g of CaF_2 were added to the mixed solution and continuously stirred for 2 h until fully dissolved. Using the hydrothermal synthesis method, the above-40-mL hot solution was transferred to a polytetrafluoroethylene autoclave with a capacity of 100 mL and reacted at 210°C for 10 h. The Fe_3O_4 nanospheres were separated using the magnet and washed three times with ethanol and water (5 min of sonication in each time). Finally, the obtained Fe_3O_4 nanospheres were dispersed in water. For the synthesis of Fe_3O_4@SiO_2, Fe_3O_4 was dispersed in water (0.1 g/mL) and sonicated for 5 min; 50 mL of the above solution was then mixed with 2.5 mL of 1% NaF solution. Then, a mixture solution of TEOS and ethanol with a mixing ratio of 1:10 was added to the above solution. The resultant solution was stirred quickly for 15 min and blended gently for 8 h using the Votex (MX-F). After the reaction, the solution was sonicated and washed three times with ethanol. For the synthesis of Fe_3O_4@MSN, 32 g CTAB and 6 mL TEA were dissolved in 500 mL deionized water. Fifty milliliters of capstone FS-66 (0.2 g/mL) dissolved in acetone was slowly added to the above solution. The mixed solution was stirred at a constant speed for 1 h. 25 mL of TEOS was quickly added to the mixed solution and shaken for 100 s. The obtained mixed solution was added to the Fe_3O_4@SiO_2 solution and slowly stirred for 6 h. The Fe_3O_4@MSN nanospheres were separated using the magnet and washed three times with ethanol. To coat PDA, 100 mg of dopamine hydrochloride was dissolved in 50 mL phosphate-buffered saline (PBS) (pH 8.5), which was

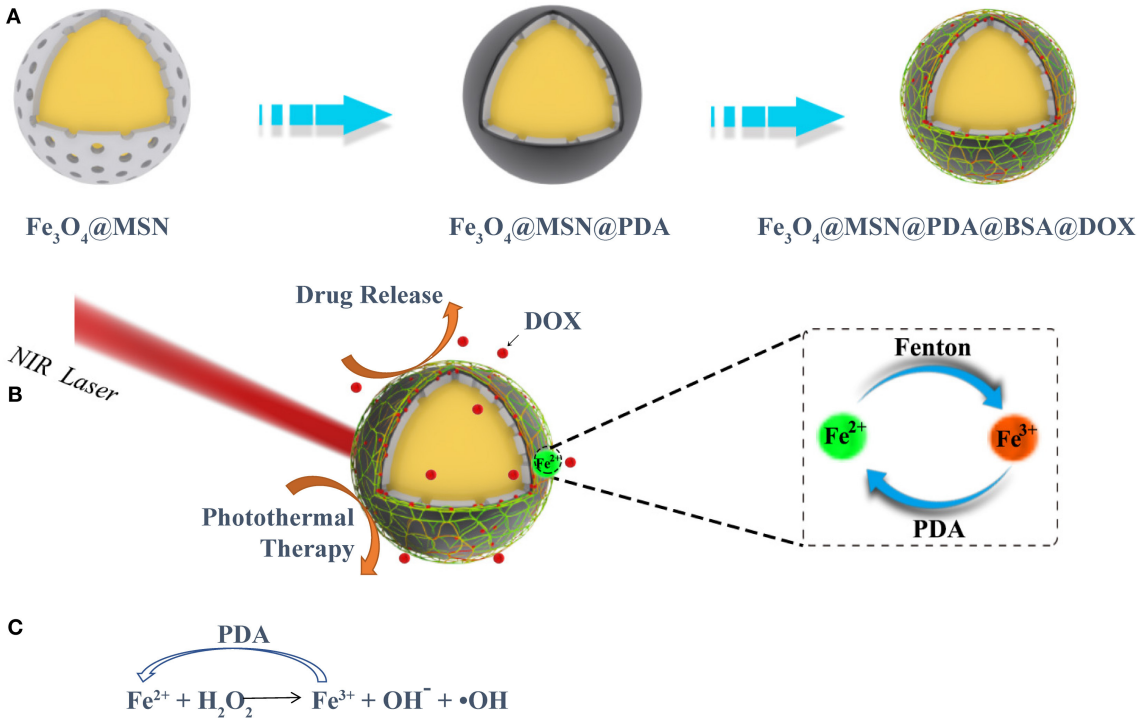

SCHEME 1 | (A) The preparation procedures of the FMPBs, **(B)** the ability of FMPBs photothermal treatment and CDT, **(C)** the repeated redox reaction between FMPBs and PDA.

then added with 100 mg of Fe_3O_4@MSN, and sonicated for 5 min and stir slowly for 6 h. To link with BSA, 100 mg BSA was added to the above solution, and then stirring was continued for 6 h. After magnetic separation of the above solution, the product was washed three times with water, lyophilized, and stored at 4°C.

Characterizations

Scanning electron microscope (SEM, Zeiss Merlin Compact) was used to observe the morphology and size of the prepared nanoparticles. X-ray energy-dispersive spectroscopy (EDS, X-MAX-20mm2) was used to determine the elemental composition of the nanoparticles. A transmission electron microscope (TEM) image was taken using a Talos F200X microscope. Thermal gravimetric analysis (TGA, Shimadzu TGA-50) was used to detect the mass percentage of different substances of FMPBs. Quantum Design PPMS-9 (USA) was used to measure the magnetic property of nanoparticles. The X-ray diffraction (XRD) pattern of FMPB nanoparticles was measured by Bruker/D8ADVANCE (DE). Using TriStar II 3020 (USA), the Bernauer–Emmett–Teller (BET) pore size distribution and diameter of FMPB nanoparticles were tested. The dynamic light scattering (DLS) diameter and zeta potential of FMPBs at 25°C were measured by NanoZSZEN3600 (Malvern Instruments). The photothermal conversion performance of FMPB nanoparticles was tested using a laser-producing setup (Shanghai Connor Fiber Co., Ltd). The Fourier transform infrared (FTIR) spectrum of FMPBs was measured by Nicolet Nexus 670. The FTIR data were collected in the range of 500 to 4,000 cm^{-1}. The Hitachi spectrometer was used to monitor the Fenton response of FMPBs.

Catalytic Activities of FMPBs

Using TMB as a substrate, the effect of different substances on the Fenton reaction was studied. TMB (0.8 mM), H_2O_2 (5 mM), Fe_3O_4@MSN, Fe_3O_4@MSN@PDA, and FMPBs (1 mg/mL) were mixed and reacted for 1 min. The absorbance of different coated nanoparticles at the same concentration was measured to determine whether ·OH was produced. To study the effect of PDA on Fenton reaction, 1 mg/mL of Fe_3O_4, Fe_3O_4@MSN, Fe_3O_4@MSN@PDA, or FMPBs was added to TMB/H_2O_2, and the solution absorbance at 651 nm was immediately recorded using the ultraviolet, visible, and NIR (UV-vis-NIR spectrometer, HITACHI U-3900). The measurement lasted for 300 s. To study the effect of H_2O_2 concentration on the production of ·OH, different concentrations of H_2O_2 (concentrations of 2.5, 5.0, 10, 25, and 50 μg/mL) were reacted with FMPBs, and the absorbance of the mixed solution at 651 nm was measured using the UV-vis-NIR spectrometer. To study the effect of temperature on ·OH, the spectrometer was used to measure the absorbance of the mixed solution at 651 nm at different temperatures. To study the effect of pH on the generation of ·OH, the spectrometer was used to measure the absorbance of the mixed solution at 651 nm at different pHs. The measurement must last for 300 s.

Photothermal Conversion Performance of FMPBs

The absorption of FMPBs in the NIR range was detected by UV-vis-NIR. The NIR laser (wavelength = 808 nm, 1 W/cm^2) was used to continuously irradiate the FMPBs solutions with different concentrations (0.1, 0.2, 0.5, and 1 mg/mL, 200 μL) for 500 s. To study the power density–dependent temperature profiles of FMPBs, an NIR laser (808 nm) with different power densities (0.2, 0.5, 0.8, and 1.0 W/cm^2) was used to continuously irradiate the FMPBs aqueous solution (200 μL of 1 mg/mL) for 500 s. To prove the long-term photothermal durability, the FMPBs were stored at room temperature in water (1 mg/mL) for 15 days and continuously irradiated with NIR laser (wavelength = 808 nm, 0.8 W/cm^2) for 600 s. Using a laser with a power density of 0.8 W/cm^2 and continuous irradiation for 15 min, the photothermal conversion efficiency of FMPBs was measured. The selected concentration of FMPBs is 0.5 mg/mL, and the volume is 200 μL. The photothermal conversion efficiency (η) of FMPB is calculated according to the formula (1). The photothermal stability of FMPBs was studied by continuously irradiating for five consecutive cycles and recording temperature changes during temperature rise and fall (power density: 0.8 W/cm^2). In the above experiments, the FLIR E60 thermal imaging camera was used to record the temperature change value and thermal image of the irradiated solution.

$$\eta = \frac{\mathbf{hS}\,(\mathbf{T_{max}} - \mathbf{T_{surr}}) - \mathbf{Q_{dis}}}{\mathbf{I}\left(\mathbf{1} - \mathbf{10^{A\lambda}}\right)} \tag{1}$$

In vitro Cytocompatibility Examination and Hemocompatibility

FMPBs and HT29 cells were incubated together to study the biocompatibility. The DMEM was supplemented with 10% fetal bovine serum and 100 units/mL of penicillin and 0.1 mg/mL of streptomycin. Cells cultured in the above solution were placed in a humidified 37°C incubator. The cells prepared above were cultured in 96-well-plates (8,000 cells per well) for 24 h. FMPBs with different concentrations were added to the wells, and the number of treated cells was quantitatively studied using the CCK-8 kit after 48 h of continuous cultivation. The above experiment also requires the use of live/dead kits to stain the cells and use phase-contrast microscopy (Leica DM IL LED) to qualitatively study the morphology of HT29 cells.

Kunming mouse red blood cells (mRBCs) were kindly provided by Xinhua Hospital, Shanghai Jiaotong University School of Medicine. For *in vitro* hemocompatibility assay, 0.4 mL mRBCs were mixed with 1.2 mL FMPBs and incubated at 37°C for 2 h (final FMPB concentration: 0.5, 1.0, 1.5, and 2.0 mg/mL). The mRBCs mixed with water or PBS were set as the positive or negative control. After that, the supernatant of the above solution was collected by centrifugation, and the absorbance at 570 nm was detected using UV-vis-NIR spectrophotometer. The hemolytic percentage (HP%) was calculated according to the calculation formula (2). All animal experiments are in compliance with the policies of the Ministry of Health under the guidance of Changhai Hospital of the Second Military Region various animal experiments.

$$\mathbf{HP}\,(\%) = \frac{(\mathbf{D_t} - \mathbf{D_{nc}})}{(\mathbf{D_{pc}} - \mathbf{D_{nc}})} \times \mathbf{100}\% \tag{2}$$

Determination of Drug Loading Efficiency

The *in vitro* drug loading study was performed as follows: FMPBs with different concentrations are added to the solution of DOX and stirred for 24 h in the dark. The FMPB nanoparticles were washed twice with PBS and centrifuged at 10,000 rpm for 5 min. The supernatant is unadsorbed DOX, and its absorbance at 480 nm was measured using the UV-vis-NIR spectrophotometer to calculate the concentration of DOX (Zhao et al., 2018; Wu et al., 2019). Formula (3) and formula (4) were used to calculate the loading percentage and loading efficiency of DOX, respectively. W_t is the mass of used DOX. W_s is the mass of the unadsorbed DOX. W is the total mass of the carrier and the drug.

$$\textbf{Loading percentage}\ (\%) = \frac{\mathbf{W_t} - \mathbf{W_s}}{\mathbf{W}} \times \mathbf{100}\% \tag{3}$$

$$\textbf{Loading efficiency}\ (\%) = \frac{\mathbf{W_t} - \mathbf{W_s}}{\mathbf{W_t}} \times \mathbf{100}\% \tag{4}$$

In vitro Drug Release Studies

In vitro drug release studies were performed using the dialysis bag method at two different temperatures of 37° and 47°C or different pH of 6.4 and 7.4. DOX-loaded FMPBs of the same concentration were added to PBS (pH 7.4) and citrate buffer (pH 6.4). The same volume (1 mL) of the above solution was transferred into a dialysis bag (MWCO: 14KD, width 44 mm) and placed in a plastic tube, which was then incubated in a different release buffer at 37° or 47°C with shaking. At different time intervals, the released solution (1 mL) was removed, and 1 mL of the corresponding buffer was added to the solution. The absorbance at 480 nm of the released solution was monitored to calculate the *in vitro* release data and determine the kinetics and mechanism of DOX using equation (5).

$$\textbf{cumulative release}\ (\%) = \frac{\mathbf{v_e}\sum_0^{\mathbf{n}}\mathbf{c_i}}{\mathbf{v_0 c_a}} \times \mathbf{100}\% \tag{5}$$

In vitro Tumor Therapy

In this work, 0.2 mol/L of H_2O_2 was added in DMEM, and the pH of solutions was adjusted to 6.4 with HCl. After that, 8,000 cells/well of HT29 cells were cultured with 0.1mL DMEM in 96-well-plate for 12 h. Then, FMPBs in fresh DMEM (0, 0.25, 0.5, and 1 mg/mL) were added in 96-well-plates ($n = 3$). The solution was then irradiated with 808-nm laser (1 W/cm^2) for 5 min. Finally, the treated cells were incubated for 24 h. CCK-8 kit and dead/live kit were used to study the cell viability according to the instructions. Leica DM IL LED inverted phase-contrast microscope was used to capture the stained cells (live cells showed green fluorescence and dead cells with red).

Statistical Analysis

The one-way analysis of variance statistical analysis method was used to assess the significance of the assay data, $^{*}p < 0.05$, $^{**}p < 0.01$, $^{***}p < 0.001$.

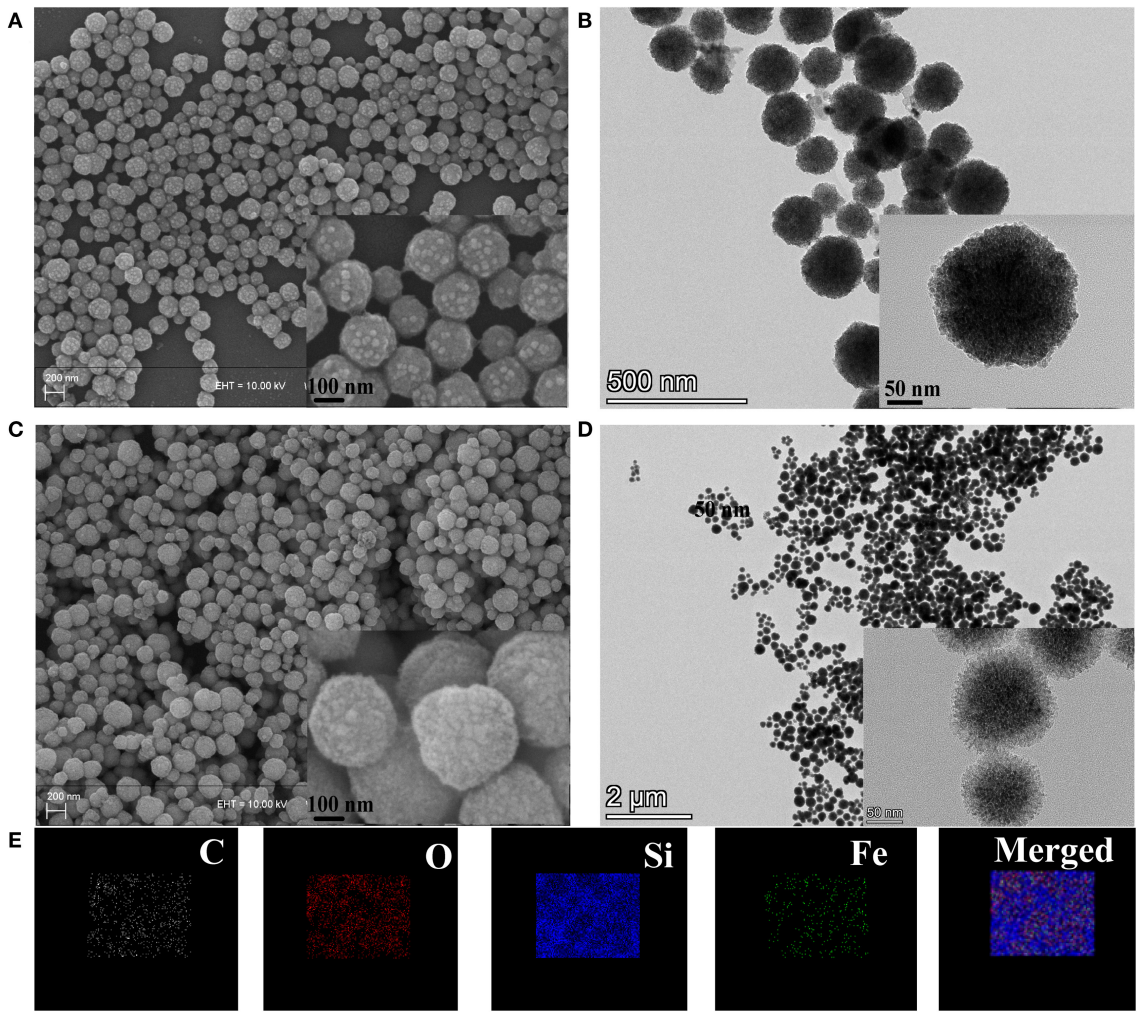

FIGURE 1 | (A) SEM images of Fe_3O_4, **(B)** TEM images of Fe_3O_4, **(C)** SEM images of FMPBs, **(D)** TEM images of FMPBs, inserted images in panels **(A–D)** are the enlarged view, **(E)** elemental distribution mapping of FMPBs.

RESULTS AND DISCUSSION

Synthesis and Characterizations of FMPBs

As shown in **Scheme 1A**, we prepared nanocarriers with Fe_3O_4 as the core and with mesoporous silica, PDA, and BSA as the coating layers. The as-prepared Fe_3O_4 nanoparticles were spherical with a diameter of about 150 to 180 nm (**Figures 1A,B**). Moreover, it was reported that a thin layer of SiO_2 coated on the Fe_3O_4 nanoparticles is necessary for the formation of a mesoporous silica layer (Jin et al., 2019). Thus, before coating mesoporous silica, we coated a thin SiO_2 shell on the surface of Fe_3O_4 in advance. It was found that the FMPB nanospheres have good dispersion and uniform particle size, and the diameter is 250 ± 15 nm (**Figure 1C**). The TEM images show that the synthesized monodisperse FMPBs exhibit a porous structure, and a layer of PDA and BSA was coated on the surface of the nanospheres (**Figures S1, S2**). Mesoporous silica was evenly coated on Fe_3O_4, and its mesoporous structure is visible. The core-shell structure can be observed more clearly by the high-resolution TEM (**Figure 1D**). The dispersibility and mesoporous pore structure of nanoparticles are well preserved in FMPBs. Moreover, the hydrodynamic dimensions of Fe_3O_4, Fe_3O_4@MSN, Fe_3O_4@MSN@PDA, and FMPBs were determined as 167 ± 10.4, 203 ± 7.6, 446 ± 50.9, and 380 ± 34.3 nm, respectively (**Figure S3**). After the PDA coating, the particle size is twice that of the original. This is because the presence of amino groups in the PDA makes it easy to adhere to each other. Notably, the DLS diameter is larger than the real size determined by TEM. This is because the surface of FMPBs is coated with a layer of water molecules in an aqueous solution. There are relevant literature reports that the pore size in the leaky tumor vasculatures is 380–780 nm (Barua and Mitragotri, 2014). Therefore, we have reason to believe that FMPBs with a size of 250 to 380 nm can enter tumor cells. When the outer layer of Fe_3O_4@MSN@PDA is grafted with BSA, the amino group is combined with the BSA carboxyl group, and the adhesion

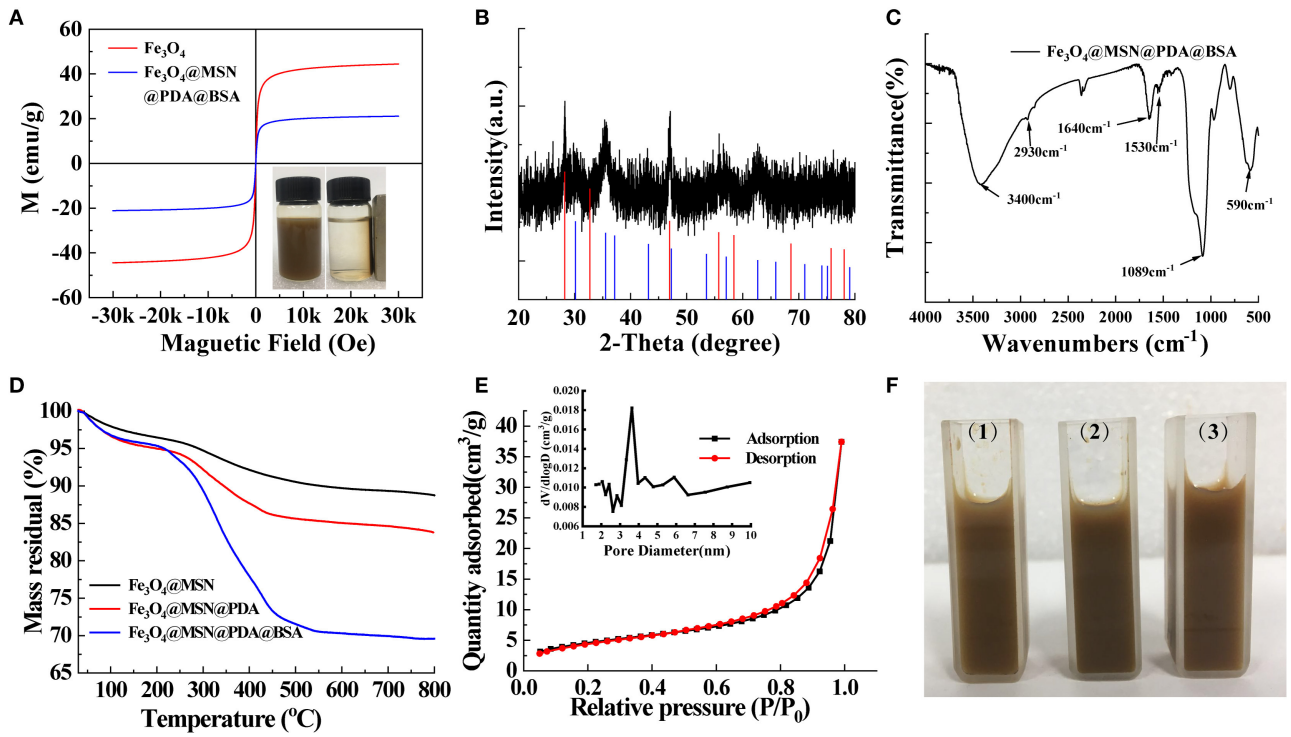

FIGURE 2 | (A) VSM of Fe_3O_4 and FMPBs, the inserted picture is digital photograph of FMPBs in water that were separated by a magnet; **(B)** powder XRD pattern of FMPBs containing CaF_2 and Fe_3O_4; **(C)** FTIR spectra of FMPBs; **(D)** TGA curves of different nanoparticles; **(E)** BET and BJH measurement results for FMPBs; **(F)** photographic image of FMPBs that were dissolved in water (1), PBS (2), and DMEM (3).

is greatly reduced. The zeta potentials of Fe_3O_4, Fe_3O_4@MSN, Fe_3O_4@MSN@PDA, and FMPBs are -58.94 ± 5.64, -87.55 ± 9.11, 6.23 ± 0.172, and -49.92 ± 2.19 mV, respectively (**Figure S4**). Through the element mapping (**Figure 1E**) and the EDS analysis (**Figures S5, S6**), it can be seen that C, O, Si, and Fe in FMPBs are evenly distributed. The above characterizations confirmed that FMPB nanospheres with high dispersibility were successfully prepared.

The magnetism, pore size, and coating effect of the material were then analyzed. The magnetic properties of Fe_3O_4 and FMPBs were analyzed with a vibrating sample magnetometer (VSM) at room temperature (**Figure 2A**). It can be seen from the magnetization curve that the saturation magnetizations of Fe_3O_4 and FMPBs are 44.43 and 21.1 emu/g, respectively. The saturation magnetization of the FMPBs is smaller than Fe_3O_4 NPs. This can be attributed to that the non-magnetic MSN/PDA/BSA layer on the surface of the Fe_3O_4 NPs reduced the magnetization. Besides, the S shape of the hysteresis loop indicates that the FMPBs are superparamagnetic. The digital photograph of FMPBs in the water separated by the magnet also confirms its good magnetic properties.

The structure of the as-prepared FMPBs was studied by XRD. As shown in **Figure 2B**, the diffraction peaks of FMPBs in the figure are consistent with the standard Fe_3O_4 (JCPDS No. 19-0629) that was marked by the blue line in the scale. Besides, the peak positions of CaF_2 (JCPDS No. 99-0051) marked in purple in the diffraction peaks coincided with the formation of CaF_2 crystals during the preparation of Fe_3O_4. The results show that the synthesized magnetic particles contain Fe_3O_4 (blue line) and CaF_2 crystal (red line). Herein, CaF_2 was used to control the size of Fe_3O_4 nanoparticles. Under the coating of PSSMA, the presence of Ca^{2+} makes the Fe_3O_4 nanoparticles more uniform and dense during the formation process, and its size has better uniformity and excellent magnetic properties (Jin et al., 2019).

The chemical structure of FMPBs was then determined by FTIR (**Figure 2C** and **Figure S7**). The absorption peaks at 590 cm^{-1} can be assigned to Fe-O vibration. The absorption peak at 1,089 cm^{-1} proves the tensile and asymmetric tensile vibration of Si-O-Si, indicating that the structure of MSN is included in FMPBs. The absorption peak at 1,500 cm^{-1} proves that the -C=C- was contained in FMPBs. The broad absorption peak at the range of 3,200–3,600 cm^{-1} is the N-H stretching vibration peak, proving the existence of PDA molecules in FMPBs (Li et al., 2018; Maziukiewicz et al., 2019). The absorption peak of 1,100 cm^{-1} is regarded as the deformation vibration peak of -OH. The absorption peak at 1,530 cm^{-1} can be regarded as the deformation vibration peak of (-NH-) in amide II, whereas the absorption peak at 1,640 cm^{-1} is considered as the vibration peak of $-NH_2$) in amide I. The aforementioned several vibration peaks can confirm the existence of BSA molecules in FMPBs. We then used TGA to further monitor the FMPBs surface modification (**Figure 2D**). According to the TGA curve,

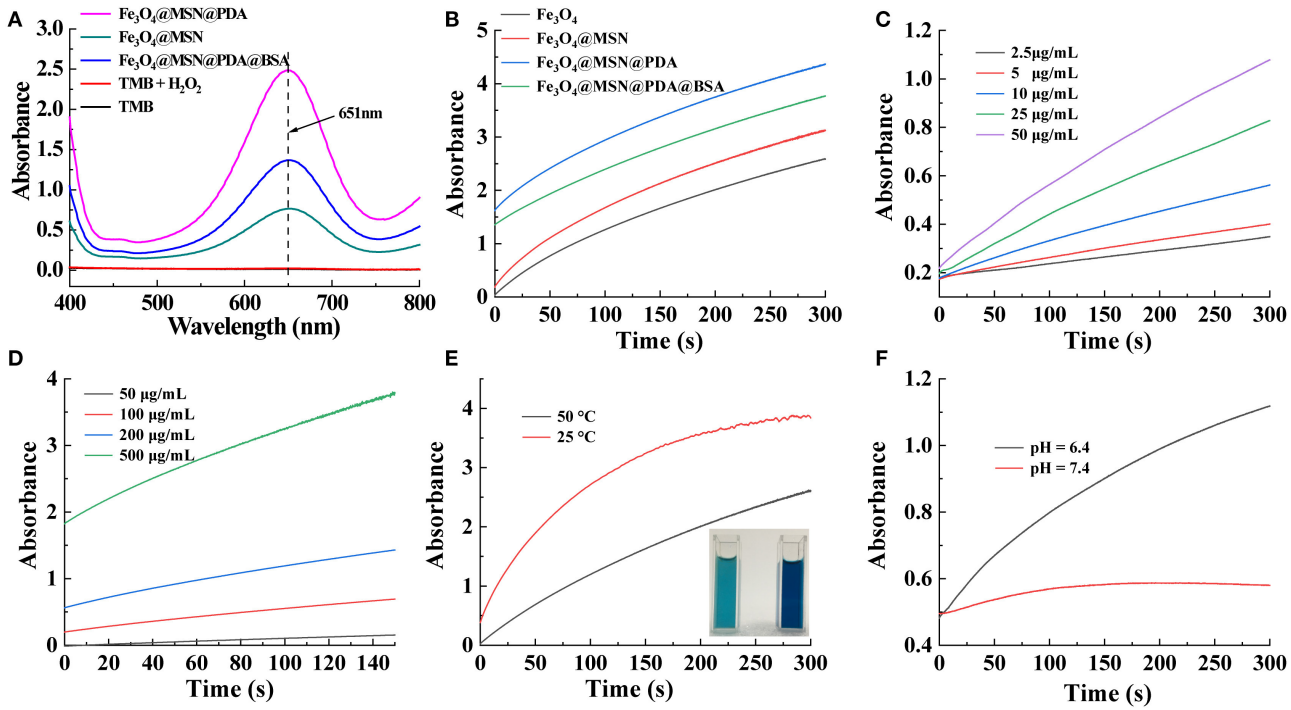

FIGURE 3 | (A) UV-vis spectra of the different solution without and with the addition of H_2O_2; **(B)** time-dependent absorbance of TMB/H_2O_2 solution with Fe_3O_4, Fe_3O_4@MSN, Fe_3O_4@MSN@PDA, and FMPBs, respectively; **(C)** time and H_2O_2 concentration-dependent absorbance of FMPBs/TMB solution; **(D)** time-dependent absorbance of FMPBs/TMB/H_2O_2 solution with different FMPB concentrations; **(E)** time-dependent absorbance of FMPBs/TMB/H_2O_2 solution at the temperature of 25° and 50°C at 651 nm; **(F)** time-dependent absorbance of FMPBs/TMB/H_2O_2 solution at different pH at 651 nm.

the weight loss of FMPBs gradually increased from 40° to 800°C, which was significantly different from Fe_3O_4@MSN and Fe_3O_4@MSN@PDA. After calculation, the mass percentages of the PDA and BSA layers in FMPBs are 5 and 13%, respectively. **Figure 2E** shows the adsorption–desorption isotherm curve and pore size distribution of FMPBs measured by BET. The specific surface area and total pore volume of FMPBs were calculated as 16.7108 m^2/g and 0.057918 cm^3/g, respectively, and the pore size is about 4.0 nm. The results show that the mesoporous structure of MSN in FMPBs was not significantly changed after being coated with PDA and BSA. FMPBs have good colloidal stability in water, PBS, and DMEM (1 mg/mL, **Figure 2F**) and exhibit the typical Tyndall effect in the above solutions (**Figure S8**). Moreover, it is proved that FMPBs can keep stable in water for a long time. The above experiments fully prove that the synthesized FMPBs have good magnetic properties and dispersibility, which provide a reliable guarantee for the long-term tumor treatment.

Fenton Reaction Induced ·OH Generation

Different from normal cells, tumor cells are rich in hydrogen ions and H_2O_2 (Wu et al., 2019). This specificity in the TME can play an important role in the CDT of tumors. As shown in **Figure 3A**, because the synthesized Fe_3O_4 contains Fe^{2+}, the Fenton reaction catalyzed by it can produce a large amount of cytotoxic ·OH. The solution will change from colorless to blue because ·OH can have a significant color reaction with TMB (Wu et al., 2019). The solution after the reaction has a maximum absorption peak at 651 nm, further proving the formation of ·OH in the Fenton reaction (Dong et al., 2019; Wu et al., 2019). However, without of Fe_3O_4, no absorption peak was detected of H_2O_2 and TMB mixed solution. Owing to the reducibility of the amino group, the PDA could prevent the oxidization of Fe_3O_4 and thus support the long-term Fenton reactions (Zeng et al., 2018). Therefore, after adding 1 mg/mL of Fe_3O_4@MSN, Fe_3O_4@MSN@PDA, and FMPBs to the solution for 1 min, the absorbance of Fe_3O_4@MSN@PDA was the largest (**Figure 3A**). In addition, at the same material concentration, the Fenton reaction rate of the material coated with PDA is greater than that without the PDA coating (**Figure 3B**). This further proves the role of PDA in promoting the Fenton response. We also examined the influence of H_2O_2 on the Fenton reaction (**Figure 3C**). As the H_2O_2 concentration increases, the rate of Fenton reaction also increases. Further, with the increase of FMPB concentration, the Fenton reaction rate is faster (**Figure 3D**). Besides, the temperature and the acidic environment simulating the TME environment can also promote the production of ·OH. As shown in **Figure 3E**, the absorbance of FMPBs/TMB/H_2O_2 solution at 651 nm at 50°C increases faster than 25°C. The inserted photograph also proves that the higher temperature solution is darker in its color. Similarly, the absorbance value of the solution increases faster in an acidic environment with a pH of 6.4 (**Figure 3F**). All of these

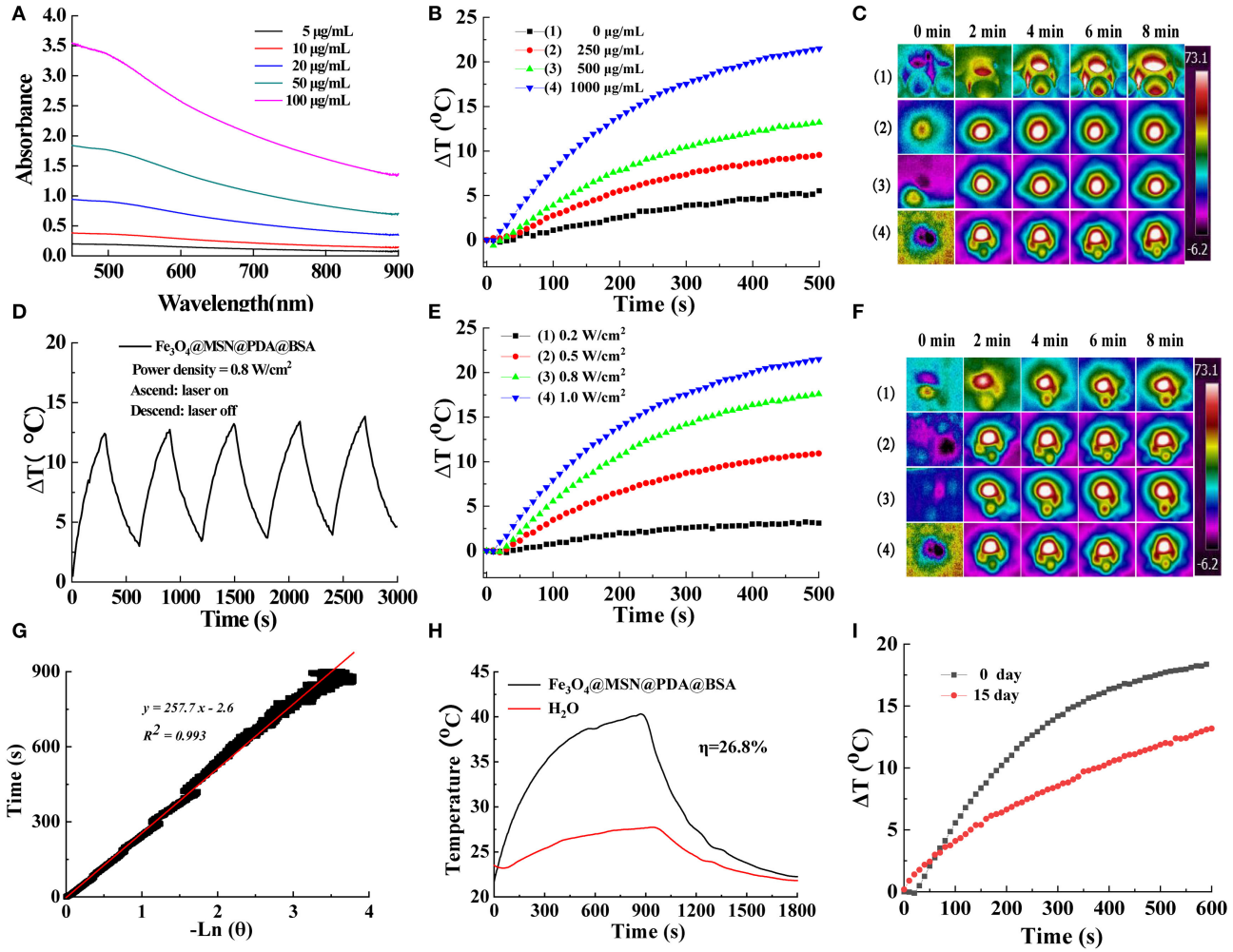

FIGURE 4 | (A) UV-Vis-NIR spectra of FMPBs with different concentrations; **(B)** the concentration-dependent temperature curve of FMPBs dispersion during the irradiation of 808-nm laser for 500 s (power density: 1 W/cm^2); **(C)** corresponding thermal imaging of **(B)**; **(D)** recycling heating profiles of FMPBs; **(E)** power density-dependent temperature curve of 1 mg/mL FMPBs during 500 s of 808-nm laser irradiation; **(F)** corresponding thermal imaging of **(E)**; **(G)** time constant of FMPBs heat transfer under laser irradiation; **(H)** steady-state heating curves of FMPBs and distilled water; **(I)** photothermal conversion profiles of FMPBs dispersed in water after 15 days.

experiments show that the synthesized FMPBs have a good effect in the Fenton reaction and provide good prospects for the TME-specific CDT of tumors.

Photothermal Conversion Performance

Many studies have shown that PDA with good biocompatibility and adhesion can effectively absorb NIR lasers (Maziukiewicz et al., 2019; Tiwari et al., 2019) and efficiently transform light into heat (Liu et al., 2014; Lin et al., 2018; Chen et al., 2019). Therefore, we studied the light absorption behavior of FMPBs to determine their photothermal conversion ability for PTT of tumors (Maziukiewicz et al., 2019). In the NIR region, FMPBs show absorption of light, and the absorption increases with increasing material concentration (**Figure 4A**). To study the photothermal properties of FMPBs, we select 808-nm laser to irradiate FMPBs with different concentrations. It was found that the heating rate of the solution increased as the concentration of the FMPBs solution increased. When the concentration of FMPBs is 0.25, 0.5, and 1 mg/mL respectively, the temperature of nanomaterials increases rapidly at 10°, 12.5°, and 22°C under laser irradiation in 500 s (**Figure 4B**). However, when the material concentration drops to 0, the temperature change is not obvious. We then collected the temperature corresponding photographs of the infrared thermal image, which further provide the evidence of the temperature change of FMPBs (**Figure 4C**). When the concentration of FMPBs in the solution is 1 mg/mL, the ΔT was 3°, 10°, 17°, and 23°C when the laser intensity was 0.2, 0.5, 0.8, and 1.0 W/cm^2, respectively (**Figure 4E**). **Figure 4F** further provides evidence of temperature changes. We further investigated the photothermal stability of FMPBs. After five NIR laser on/off cycles, there is no significant difference in ΔT, which proves that FMPBs have a good photothermal stability

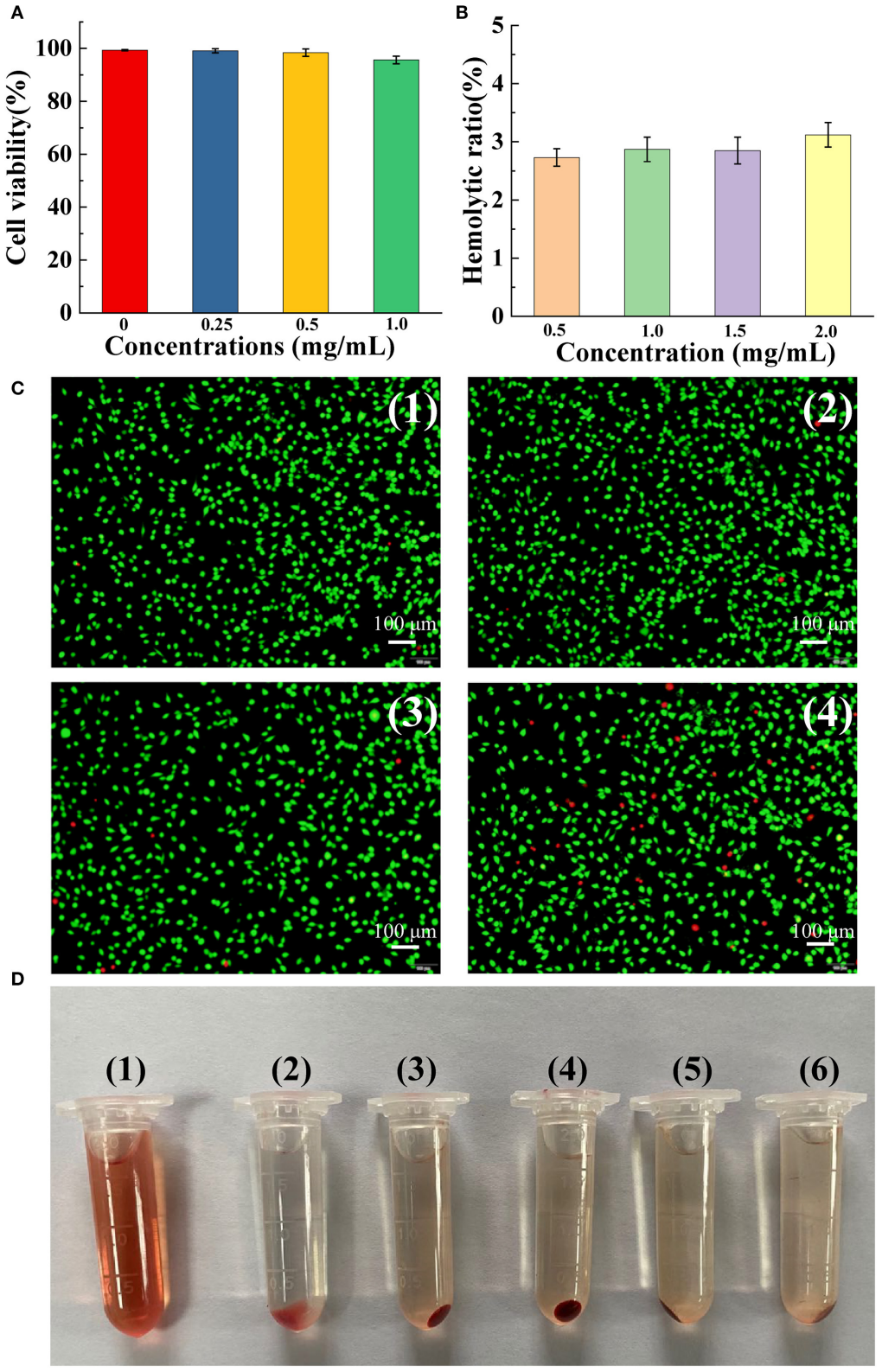

FIGURE 5 | (A) Cell viability after incubating HT29 cells with different concentrations of FMPBs for 48 h; **(B)** hemolytic ratio of FMPBs with different concentrations; **(C)** the staining morphology of HT29 cells treated with different concentrations of FMPBs, corresponding to **(A)**; **(D)** digital images of centrifuged mRBCs incubated with different concentrations of FMPBs: (1) water, (2) PBS, (3) 0.5 mg/mL, (4) 1 mg/mL, (5) 1.5 mg/mL, and (6) 2 mg/mL.

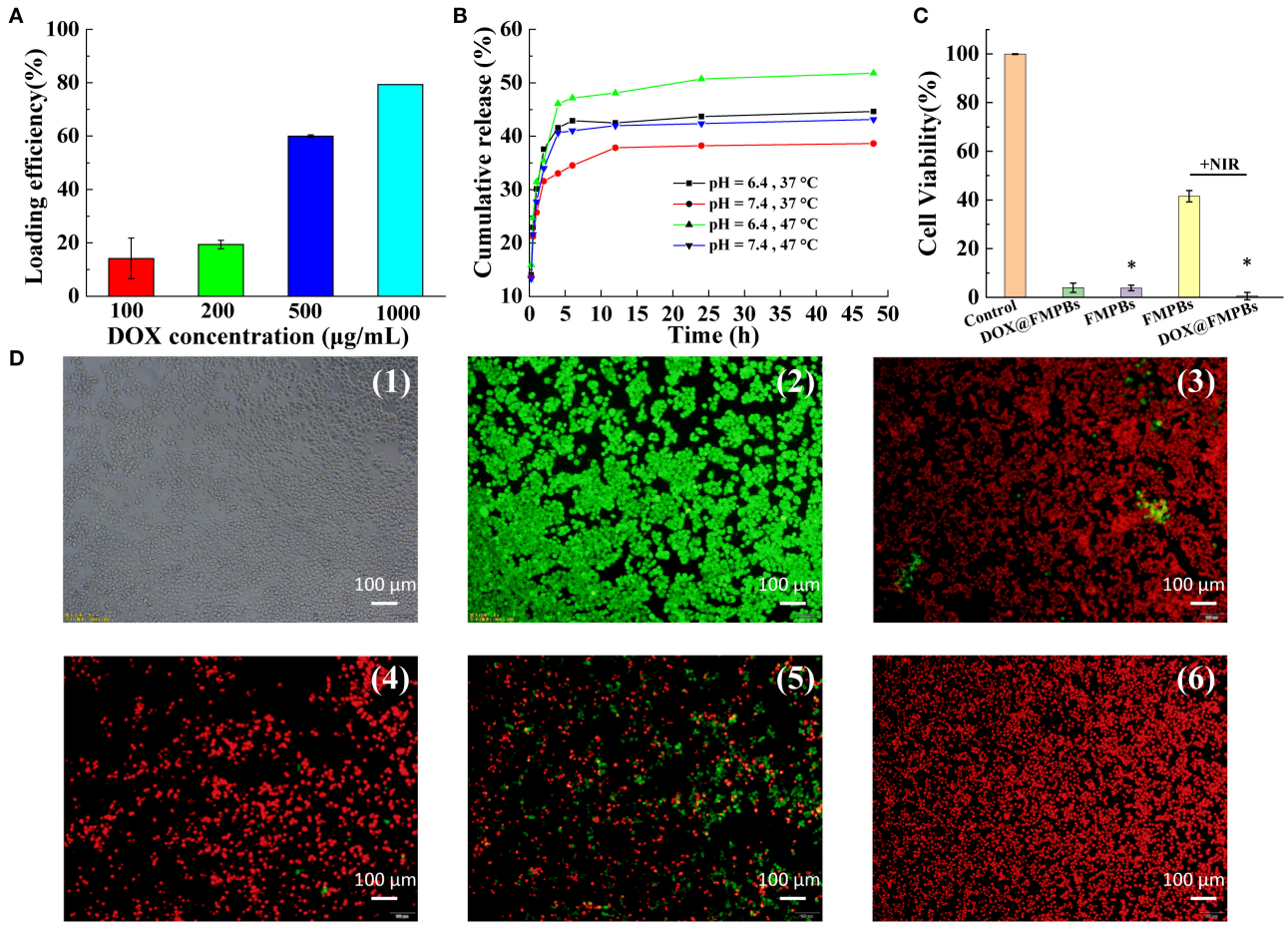

FIGURE 6 | (A) Drug loading efficiency of 1 mg/mL FMPBs at different DOX concentrations; **(B)** *in vitro* drug DOX release curve of FMPBs in buffer solutions with different temperature/pH; **(C)** cell viability of HT29 cells after different therapy (* with H_2O_2 in DMEM); **(D)** digital images of live or dead HT29 cells corresponding to **(C)**: (1 and 2) control, (3) DOX@FMPBs, (4) FMPBs + H_2O_2, (5) FMPBs + NIR, (6) DOX@FMPBs + H_2O_2 + NIR.

(**Figure 4D**). Using 808-nm laser with a power density of 0.8 W/cm^2, the heating transfer time was calculated to be 257.7 s (**Figure 4G**), and the photothermal conversion efficiency was 26.8% (**Figure 4H**). Interestingly, the temperature of FMPBs stored at room temperature for 15 days with low-power laser (0.8 W/cm^2) irradiation still increased by 13°C within 10 min, showing that the material still has good photothermal efficiency after being left for a long time (**Figure 4I**).

In vitro Cytocompatibility Examination and Hemocompatibility

We investigated the biocompatibility of FMPBs. As shown in **Figure 5A**, HT29 was incubated with 0.25 mg/mL FMPBs for 48 h, and its cell viability was 99.12% ± 0.79%. When the concentration of FMPBs increased to 1 mg/mL, the cell viability reached 95.65 ± 1.44%. **Figure 5C** is the photograph of cell morphology after coincubation corroborating the cell viability assay, which indicates that FMPBs have good biocompatibility. Then, the hemolysis experiment was performed to further evaluate the safety of FMPBs in the clinical application. In this experiment, the hemolysis rate of mRBCs treated with water and PBS was set as 100 and 0%, respectively. As can be seen from the **Figure 5B**, with different concentrations of FMPBs, the HP is 2.73 ± 0.15%, 2.87 ± 0.21%, 2.85 ± 0.23%, and 3.12 ± 0.21% when FMPB concentrations are 0.5, 1.0, 1.5, and 2.0 mg/mL, respectively. The result of HPs is all less than 5%, indicating that the FMPBs have good blood compatibility. The mRBCs after the centrifugation (**Figure 5D**) further prove the above conclusion.

Drug Loading and Release

The porous structure of FMPBs can be used to encapsulate various drug molecules, such as DOX. By dispersing FMPBs and DOX in water, this simple method also easily loads drug molecules into the pores of the material. The drug loading efficiency of nanoparticles was studied. When the drug concentration increased from 0.1 to 1 mg/mL, the loading efficiency of DOX increased from 14.17 ± 7.59% to 79.31 ± 0.003% (**Figure 6A**). Meanwhile, the drug loading percentage was calculated. As can be seen from **Figure S9**, as the DOX concentration continuously increased from 100 μg/mL to 1

mg/mL, the drug loading percentage increased from 1.28 ± 0.006% to 39.65 ± 1.56%. According to the results of the above experiments, 1 mg/mL DOX and 1 mg/mL FMPBs were selected to achieve the optimal loading concentration of nanoparticles.

In the study of the pH and temperature-responsive drug release, it was found that the rate of drug release in acidic solutions (pH 6.4) is greater than that in neutral solutions (pH 7.4, **Figure 6B**). Similarly, the rate of drug release in a solution with a temperature of 47°C is greater than a temperature of 37°C, and the drug release rate increases significantly to 51.8 ± 0.1% at 47°C. In the normal cell environment (pH 7.4, $T = 37°C$), the percentage of DOX released was 36 ± 1.5% (48 h), whereas the percentage of DOX released in the acidic environment was 44 ± 1.4%. The pH response of the FMPB experiment can be considered to the better solubility of the drug in an acidic environment. The temperature response is because the higher temperature increases the thermal motion of the DOX molecule. The DOX release kinetics that relies on the NIR/pH makes FMPBs provide it with a good opportunity to enhance tumor chemotherapy.

In vitro Tumor Therapy

To investigate the *in vitro* tumor therapy of FMPBs, we validated the influence of DOX@FMPBs on the viability of HT29 cells *in vitro* (**Figures 6C,D**). To mimic the endogenous redox and acid nature of TME, H_2O_2 (the final concentration of 10 mM) and HCl (the final pH of 6.4) were added in the DMEM. The concentration of FMPBs was 0.25 mg/mL in all the experiments. As can be seen from **Figure 6C**, the viability of HT29 cells treated with DOX@FMPBs decreased to 3.95 ± 1.89% after 24 h, indicating that DOX has released from FMPBs *in vitro*. After incubating with FMPBs and H_2O_2, the viability of HT29 cells decreased to 3.84 ± 1.14% after 24 h, showing that the FMPBs have reacted with H_2O_2 and produced ·OH to kill tumor cells. With laser irradiation (1 W/cm^2, 5 min), the viability of HT29 cells was 41.53 ± 2.37%, while combined with CDT, PTT, and chemotherapy, all of the HT29 cells had been killed. **Figure 6D** further supports the cell-killing outcome, where the living cells showing green fluorescence and dead cells are red. These experiments indicate that the FMPBs have an obvious *in vitro* tumor CDT, PTT, and chemotherapy capability.

CONCLUSIONS

In summary, FMPB nanomaterials with high biocompatibility and good magnetic properties were synthesized by a layer-by-layer coating of Fe_3O_4. It was found that FMPBs gave a photothermal efficiency of 26.8% and a drug loading efficiency of 79.31 ± 0.003%. PDA was found to play a key role in the entire nanoparticle formation. The high photothermal capability of the nanoparticles not only achieves the heat-induced release by irradiating drug-loaded FMPBs, but also kills tumor cells by increasing the temperature. Meanwhile, the reducibility of the PDA can be utilized to reduce the Fe^{3+} in the Fenton reaction to Fe^{2+}. The produced Fe^{2+} can react with H_2O_2 in TME and release ·OH to kill tumor cells. Therefore, the structural feature of MSN, the photothermal and the reducibility characteristics of PDA, and the biocompatibility of BSA are integrated into the one nanomaterial, which is anticipated to further promote the development of the precise cancer treatment.

DATA AVAILABILITY STATEMENT

The raw data supporting the conclusions of this article will be made available by the authors, without undue reservation, to any qualified researcher.

AUTHOR CONTRIBUTIONS

CJ designed and completed all tests and wrote this paper. HW completed the biocompatibility and hemocompatibility tests. KL and WH collected the data. MH and SW make revisions to the paper and approve the final paper to be published.

FUNDING

Science and Technology Commission of Shanghai Municipality for the financial support under grant number 14440502300.

ACKNOWLEDGMENTS

The authors thank the foundation of Hujiang under grant number D15011. This work was also financially supported by National Science Foundation of China (Grant No. 51702214), the Key Program for Basic Research of Shanghai (19JC1415600), and Shanghai Rising-Star Program (20QA1407200).

SUPPLEMENTARY MATERIAL

The Supplementary Material for this article can be found online at: https://www.frontiersin.org/articles/10.3389/fchem.2020.567652/full#supplementary-material

REFERENCES

Barua, S., and Mitragotri, S. (2014). Challenges associated with penetration of nanoparticles across cell and tissue barriers: a review of current status and future prospects. *Nano Today* 9, 223–243. doi: 10.1016/j.nantod.2014.04.008

Bose, R. J., Lee, S. H., and Park, H. (2016). Biofunctionalized nanoparticles: an emerging drug delivery platform for various disease treatments. *Drug Discov Today* 21, 1303–1312. doi: 10.1016/j.drudis.2016.06.005

Bulbake, U., Doppalapudi, S., Kommineni, N., and Khan, W. (2017). Liposomal formulations in clinical use: an updated review. *Pharmaceutics* 9:12. doi: 10.3390/pharmaceutics9020012

Chen, Y., Zhao, J., Wang, S., Zhang, Z., Zhang, J., Wang, Y., et al. (2019). Photothermal composite nanomaterials for multimodal tumor therapy

under MRI guidance. *Chem. Select.* 4, 11156–11164. doi: 10.1002/slct.201903481

Dai, Y., Yang, D., Yu, D., Cao, C., Wang, Q., Xie, S., et al. (2017). Mussel-inspired polydopamine-coated lanthanide nanoparticles for NIR-II/CT dual imaging and photothermal therapy. *ACS Appl. Mater. Interf.* 9, 26674–26683. doi: 10.1021/acsami.7b06109

Dong, Z., Feng, L., Chao, Y., Hao, Y., Chen, M., Gong, F., et al. (2019). Amplification of tumor oxidative stresses with liposomal fenton catalyst and glutathione inhibitor for enhanced cancer chemotherapy and radiotherapy. *Nano Lett.* 19, 805–815. doi: 10.1021/acs.nanolett.8b03905

Du, B., Ma, C., Ding, G., Han, X., Li, D., Wang, E., et al. (2017). Cooperative strategies for enhancing performance of photothermal therapy (PTT) agent: optimizing its photothermal conversion and cell internalization ability. *Small* 13:1603275. doi: 10.1002/smll.201603275

Feng, L., Gai, S., Dai, Y., He, F., Sun, C., Yang, P., et al. (2018a). Controllable generation of free radicals from multifunctional heat-responsive nanoplatform for targeted cancer therapy. *Chem. Mater.* 30, 526–539. doi: 10.1021/acs.chemmater.7b04841

Feng, L., Xie, R., Wang, C., Gai, S., He, F., Yang, D., et al. (2018b). Magnetic targeting, tumor microenvironment-responsive intelligent nanocatalysts for enhanced tumor ablation. *ACS Nano* 12, 11000–11012. doi: 10.1021/acsnano.8b05042

Gao, J., Ran, X., Shi, C., Cheng, H., Cheng, T., and Su, Y. (2013). One-step solvothermal synthesis of highly water-soluble, negatively charged superparamagnetic Fe3O4 colloidal nanocrystal clusters. *Nanoscale* 5, 7026–7033. doi: 10.1039/c3nr00931a

Gulzar, A., Xu, J., Yang, D., Xu, L., He, F., Gai, S., et al. (2018). Nano-graphene oxide-UCNP-Ce6 covalently constructed nanocomposites for NIR-mediated bioimaging and PTT/PDT combinatorial therapy. *Dalton Trans* 47, 3931–3939. doi: 10.1039/C7DT04141A

Hu, H., Yu, B., Ye, Q., Gu, Y., and Zhou, F. (2010). Modification of carbon nanotubes with a nanothin polydopamine layer and polydimethylamino-ethyl methacrylate brushes. *Carbon* 48, 2347–2353. doi: 10.1016/j.carbon.2010.03.014

Huang, M., Liu, L., Wang, S., Zhu, H., Wu, D., Yu, Z., et al. (2017). Dendritic mesoporous silica nanospheres synthesized by a novel dual-templating micelle system for the preparation of functional nanomaterials. *Langmuir* 33, 519–526. doi: 10.1021/acs.langmuir.6b03282

Huo, M., Wang, L., Chen, Y., and Shi, J. (2017). Tumor-selective catalytic nanomedicine by nanocatalyst delivery. *Nat. Commun.* 8:357. doi: 10.1038/s41467-017-00424-8

Jahanban-Esfahlan, A., Panahi-Azar, V., and Sajedi, S. (2015). Spectroscopic and molecular docking studies on the interaction between N-acetyl cysteine and bovine serum albumin. *Biopolymers* 103, 638–645. doi: 10.1002/bip.22697

Jia, H. Z., Zhang, W., Zhu, J. Y., Yang, B., Chen, S., Chen, G., et al. (2015). Hyperbranched-hyperbranched polymeric nanoassembly to mediate controllable co-delivery of siRNA and drug for synergistic tumor therapy. *J. Control Release* 216, 9–17. doi: 10.1016/j.jconrel.2015.08.006

Jin, Q., Liu, L., Zheng, Y., Wang, S., and Huang, M. (2019). Synthesis, characterization, and luminescence properties of BiVO4:Eu3+ embedded Fe3O4@mSiO2 nanoparticles. *J. Luminesci.* 215:116677. doi: 10.1016/j.jlumin.2019.116677

Li, M., Sun, X., Zhang, N., Wang, W., Yang, Y., Jia, H., et al. (2018). NIR-activated polydopamine-coated carrier-free "Nanobomb" for *in situ* on-demand drug release. *Adv Sci.* 5;1800155. doi: 10.1002/advs.201800155

Lin, L. S., Song, J., Song, L., Ke, K., Liu, Y., Zhou, Z., et al. (2018). Simultaneous fenton-like ion delivery and glutathione depletion by MnO2 -based nanoagent to enhance chemodynamic therapy. *Angew. Chem. Int. Ed. Engl.* 57, 4902–4906. doi: 10.1002/anie.201712027

Liu, Y., Ai, K., and Lu, L. (2014). Polydopamine and its derivative materials: synthesis and promising applications in energy, environmental, and biomedical fields. *Chem. Rev.* 114, 5057–5115. doi: 10.1021/cr400407a

Maziukiewicz, D., Grzeskowiak, B. F., Coy, E., Jurga, S., and Mrowczynski, R. (2019). NDs@PDA@ICG conjugates for photothermal therapy of glioblastoma multiforme. *Biomimetics* 4:3. doi: 10.3390/biomimetics4010003

Qin, S. Y., Zhang, A. Q., Cheng, S. X., Rong, L., and Zhang, X. Z. (2017). Drug self-delivery systems for cancer therapy. *Biomaterials* 112, 234–247. doi: 10.1016/j.biomaterials.2016.10.016

Siegel, R. L., Miller, K. D., and Jemal, A. (2016). Cancer statistics, 2016. *CA Cancer J. Clin.* 66, 7–30. doi: 10.3322/caac.21332

Song, X., Liang, C., Feng, L., Yang, K., and Liu, Z. (2017). Iodine-131-labeled, transferrin-capped polypyrrole nanoparticles for tumor-targeted synergistic photothermal-radioisotope therapy. *Biomater. Sci.* 5, 1828–1835. doi: 10.1039/C7BM00409E

Tang, L., and Cheng, J. (2013). Nonporous silica nanoparticles for nanomedicine application. *Nano Today* 8, 290–312. doi: 10.1016/j.nantod.2013.04.007

Tiwari, A. P., Bhattarai, D. P., Maharjan, B., Ko, S. W., Kim, H. Y., Park, C. H., et al. (2019). Polydopamine-based implantable multifunctional nanocarpet for highly efficient photothermal-chemo therapy. *Sci. Rep.* 9:2943. doi: 10.1038/s41598-019-39457-y

Tran, A. V., Shim, K., Vo Thi, T. T., Kook, J. K., An, S. S. A., and Lee, S. W. (2018). Targeted and controlled drug delivery by multifunctional mesoporous silica nanoparticles with internal fluorescent conjugates and external polydopamine and graphene oxide layers. *Acta Biomater.* 74, 397–413. doi: 10.1016/j.actbio.2018.05.022

Wang, S., Li, K., Chen, Y., Chen, H., Ma, M., Feng, J., et al. (2015). Biocompatible PEGylated MoS2 nanosheets: controllable bottom-up synthesis and highly efficient photothermal regression of tumor. *Biomaterials* 39, 206–217. doi: 10.1016/j.biomaterials.2014.11.009

Wang, S., Yang, X., Zhou, L., Li, J., and Chen, H. (2020). 2D nanostructures beyond graphene: preparation, biocompatibility and biodegradation behaviors. *J. Mater. Chem. B* 8, 2974–2989. doi: 10.1039/C9TB02845E

Wang, S., Zhou, L., Zheng, Y., Li, L., Wu, C., Yang, H., et al. (2019). Synthesis and biocompatibility of two-dimensional biomaterials. *Colloids Surf. Physicochem. Eng. Aspects* 583:124004. doi: 10.1016/j.colsurfa.2019.124004

Wang, W., Jiang, Y., Liao, Y., Tian, M., Zou, H., and Zhang, L. (2011). Fabrication of silver-coated silica microspheres through mussel-inspired surface functionalization. *J. Colloid Interface Sci.* 358, 567–574. doi: 10.1016/j.jcis.2011.03.023

Wu, C., Wang, S., Zhao, J., Liu, Y., Zheng, Y., Luo, Y., et al. (2019). Biodegradable Fe(III)@WS_2 -PVP nanocapsules for redox Reaction and TME-Enhanced nanocatalytic, photothermal, and chemotherapy. *Adv. Funct. Mater.* 29:1901722. doi: 10.1002/adfm.201901722

Xu, C., Chen, F., Valdovinos, H. F., Jiang, D., Goel, S., Yu, B., et al. (2018). Bacteria-like mesoporous silica-coated gold nanorods for positron emission tomography and photoacoustic imaging-guided chemo-photothermal combined therapy. *Biomaterials* 165, 56–65. doi: 10.1016/j.biomaterials.2018.02.043

Xu, Y., Zhao, J., Zhang, Z., Zhang, J., Huang, M., Wang, S., et al. (2020). Preparation of electrospray ALG/PDA-PVP nanocomposites and their application in cancer therapy. *Soft. Matter.* 16, 132–141. doi: 10.1039/C9SM01584A

Xue, T., Xu, C., Wang, Y., Wang, Y., Tian, H., and Zhang, Y. (2019). Doxorubicin-loaded nanoscale metal-organic framework for tumor-targeting combined chemotherapy and chemodynamic therapy. *Biomater Sci.* 7, 4615–4623. doi: 10.1039/C9BM01044K

Zeng, X., Luo, M., Liu, G., Wang, X., Tao, W., Lin, Y., et al. (2018). Polydopamine-modified black phosphorous nanocapsule with enhanced stability and photothermal performance for tumor multimodal treatments. *Adv Sci.* 5:1800510. doi: 10.1002/advs.201800510

Zhao, J., Xie, P., Ye, C., Wu, C., Han, W., Huang, M., et al. (2018). Outside-in synthesis of mesoporous silica/molybdenum disulfide nanoparticles for antitumor application. *Chem. Eng. J.* 351, 157–168. doi: 10.1016/j.cej.2018.06.101

Zhou, L., Zhao, J., Chen, Y., Zheng, Y., Li, J., Zhao, J., et al. (2020). MoS2-ALG-Fe/GOx hydrogel with Fenton catalytic activity for combined cancer photothermal, starvation, and chemodynamic therapy. *Colloids Surf. Biointerf.* 195, 111243–111243. doi: 10.1016/j.colsurfb.2020.111243

Zhu, H., Tao, J., Wang, W., Zhou, Y., Li, P., Li, Z., et al. (2013). Magnetic, fluorescent, and thermo-responsive Fe(3)O(4)/rare earth incorporated

poly(St-NIPAM) core-shell colloidal nanoparticles in multimodal optical/magnetic resonance imaging probes. *Biomaterials* 34, 2296–2306. doi: 10.1016/j.biomaterials.2012.11.056

Conflict of Interest: The authors declare that the research was conducted in the absence of any commercial or financial relationships that could be construed as a potential conflict of interest.

frontiers in Nanotechnology

ORIGINAL RESEARCH
published: 26 November 2020
doi: 10.3389/fnano.2020.584233

Proof of Concept Study: Mesoporous Silica Nanoparticles, From Synthesis to Active Specific Immunotherapy

Stephanie Seré [1], Ulrique Vounckx [2], Jin Won Seo [3], Ilse Lenaerts [4], Stefaan Van Gool [5] and Jean-Pierre Locquet [1]**

[1] Functional Nanosystems, Department of Physics and Astronomy, Katholieke Universiteit Leuven, Leuven, Belgium, [2] Design and Synthesis of Inorganic Materials, Department of Chemistry, Hasselt University, Hasselt, Belgium, [3] Functional Nanosystems, Department of Materials Engineering, Katholieke Universiteit Leuven, Leuven, Belgium, [4] TRANSfarm, Science Engineering and Technology Group, Katholieke Universiteit Leuven, Leuven, Belgium, [5] Translational Oncology, Immunologisch Onkologisches Zentrum Köln, Köln, Germany

OPEN ACCESS

Edited by:
Jianhua Zhang, Tianjin University, China

Reviewed by:
Timothy John Mahony, The University of Queensland, Australia
Ajeet Kaushik, Florida Polytechnic University, United States

***Correspondence:**
Stephanie Seré
stephanie.sere@kuleuven.be
Jean-Pierre Locquet
jeanpierre.locquet@kuleuven.be

Specialty section:
This article was submitted to Biomedical Nanotechnology, a section of the journal Frontiers in Nanotechnology

Received: *16 July 2020*
Accepted: *21 October 2020*
Published: *26 November 2020*

Citation:
Seré S, Vounckx U, Seo JW, Lenaerts I, Van Gool S and Locquet J-P (2020) Proof of Concept Study: Mesoporous Silica Nanoparticles, From Synthesis to Active Specific Immunotherapy. Front. Nanotechnol. 2:584233. doi: 10.3389/fnano.2020.584233

Nanomaterials are increasingly valued tools in drug delivery research as they offer enhanced stability, controlled release and more effective drug encapsulation. Though yet to be introduced in clinical trial, mesoporous silica nanoparticles are promising delivery systems, due to their high chemical and mechanical stability while remaining biodegradable. This work provides proof of concept for particle based vaccines as cost-effective alternatives for dendritic cell immunotherapy. Synthesis and surface chemistry of the nanoparticles are optimized for protein conjugation and nanoparticles are characterized for their physicochemical properties and biodegradation. Ovalbumin is used as a model protein to load nanoparticles to produce a nanovaccine. The vaccine is tested *in vitro* on dendritic cultures to verify particle and vaccine uptake, toxicity, maturation effects and explicitly ovalbumin cross-presentation on MHC class I molecules. The optimized synthesis protocol renders reproducible mesoporous silica nanoparticles, resistant against agglomeration, within the required size range and have carboxylic surface functionalization necessary for protein conjugation. They are biodegradable over a time span of 1 week. This period is adjustable by changing synthesis parameters. UV sterilization of the particles does not induce quality loss, nor does it have toxic effects on cells. Treatment with mesoporous silica nanoparticles increases expression of MHC and costimulatory molecules of dendritic cells, indicating an adjuvant effect of nanoparticles on the adaptive immune system. Nanovaccine uptake and cross-presentation of ovalbumin are observed and the latter is increased when delivered by nanoparticles as compared to control conditions. This confirms the large potential of mesoporous silica nanoparticle based vaccines to replace dendritic-based active specific immunotherapy, offering a more standardized production process and higher efficacy.

Keywords: nanoparticles, characterization, biodegradation, immunotherapy, dendritic cells, cross-presentation

1. INTRODUCTION

Cancer is a leading cause of morbidity and mortality with ∼18 million new cases and 9.6 million cancer-related deaths worldwide in 2018. The number of new cases is expected to rise globally by 70% over the next decade according to the world health organization. Immunogenic tumors, such as breast and prostate cancer are among the leading cancer types in terms of the number of new cases, with 2.1 and 1.3 million diagnoses in 2018, respectively (IARC, 2018). Additionally, cancer is known to be a costly illness to the patient and the overall health care system.

Over the past decades, the role of the immune system in the development and maintenance of tumors was unraveled (Van Gool, 2015). On this basis, cancer immunotherapy emerged as an innovative treatment for immunogenic tumors. It intents to activate or stimulate components of the immune system against the tumor, while minimizing off-target effects as compared to agents that directly kill cancer cells, such as chemotherapy. A plethora of immunotherapeutic approaches is available, but the general goal of immunotherapy is to destroy remaining cancer cells and prevent tumor regrowth (Van Gool, 2015; Riley et al., 2019). One particularly promising approach is active specific immunotherapy based on autologous dendritic cells (DCs) loaded with autologous tumor lysate. DC vaccination is nowadays combined with standard treatment in Phase II and Phase III clinical trials for the treatment of immunogenic tumors, such as prostate cancer, ovarian cancer, glioblastoma, among others. It was demonstrated that these vaccines are safe, elicit an anti-tumor immune response and control tumor growth (Van Gool and De Vleeschouwer, 2012; Dejaegher et al., 2014; Galluzzi et al., 2014; Makkouk and Weiner, 2015). Unfortunately, these responses did not significantly improve subsequent clinical outcomes. Reintroducing DCs from the *ex vivo* cell culture into the immunosuppressive environment of the patient probably affects their viability and functionality (Le Gall et al., 2018). Therefore, an effort should be made to increase the efficacy of the vaccine to obtain higher long term survival rates. Moreover, the small-scale production process of DC-based vaccines is expensive, with an estimated cost of 20,500 euros per patient (Van de Velde et al., 2014; Le Gall et al., 2018). One solution is the development of an off-the-shelf, universal drug delivery system (DDS) that carries tumor lysate and immunomodulatory agents to target DCs *in vivo*.

The development of DDSs is a research field of all times. The need for more efficient encapsulation and controlled-release technologies increased, due to the development of new drugs often with poorer stability in biological environments, higher dose sensitivities and larger molecular sizes (Barbé et al., 2004). In the drug delivery research field, nanoparticles (NPs) have been a hot topic for almost 20 years due to their quantum mechanical properties, high surface to volume ratio and therefore relatively large functional surface to bind and carry drugs or probes (De Jong and Brom, 2008). NPs come in all shapes and sizes, but not all of them are suitable for (bio)medical applications. Specifically considering drug delivery, biocompatibility or biodegradability of the NPs is required to release their cargo at the targeted site and reduce or eliminate potential risks. The majority of research on NP-based DDSs focuses therefore mostly on liposomes, micelles and polymeric particles. The NP-based DDS can be specifically chosen and optimized depending on the drug, route of administration and desired pharmacokinetics. Liposomes consist of a lipid bilayer, which is also an important component of the cell membrane. Therefore, research on this type of particles began and developed very early (Delves, 1998). Micelles offer a relatively simple synthesis procedure, as they are formed through self assembly of amphiphilic molecules at a critical micelle concentration (Marasini et al., 2017; Mitra et al., 2017). Liposomes and micelles gained large interest as DDS because they enable encapsulation and delivery of hydrophilic and hydrophobic agents, increasing the bioavailability of these agents. Less favorable properties of these DDS include limited shelf life and administration route due to poor chemical and mechanical stability. In addition, designing these types of particles is more difficult (Barbé et al., 2004). Polymeric particles, partially overcome these limitations and can be categorized in natural and synthetic polymeric NPs. Potential antigenicity and poor batch-to-batch reproducibility are an impediment to the use of natural polymeric NPs (Reverchon et al., 2012; Andronescu and Grumezscu, 2017). On the other hand, synthetic polymers release acidic byproducts during degradation, raising a toxicity issue (Liechty et al., 2010). In comparison to other types of NPs, mesoporous silica nanoparticles (MSNPs) show large potential. Silica is already an additive in medical formulations. In addition, these particles offer biocompatibility and biodegradability, relatively high chemical and mechanical stability, a variety of surface functionalization due to abundant silanol groups and a simple synthesis procedure which can easily be upscaled to industrial applications (Seré et al., 2018).

In this work, proof of concept is provided for the use of biodegradable MSNPs as a carrier of (tumor)proteins as an alternative for DC immunotherapy. We report the relatively simple one pot synthesis of carboxylic functionalized MSNPs. In a first stage, the synthesis procedure is reassessed and optimized. The effect of the washing alcohol on the functional groups, the optimal amount of carboxylation and the optimal silica precursor were studied by complete characterization and biodegradation. From these studies, the optimal synthesis procedure was determined significantly lowering the cost of the vaccine production. The selected particles were then conjugated with proteins and used for *in vitro* stimulation of DCs. Besides being a good cost-effective alternative, another strong feature of this NP-based vaccine is the ability to load the particles with immunomodulatory agents to amplify the immune stimulating effects and increase the efficacy of the vaccine.

2. EXPERIMENTAL SECTION

2.1. MSNP Synthesis and Characterization

This work is a refinement of our previously reported MSNP synthesis procedure (Seré et al., 2018). Therefore, the influence of different silica precursors and dialysis alcohols was assessed, and NPs with different functional groups were produced as a

TABLE 1 | MSNPs examined in this work.

Sample	Functional groups	Precursor	Alcohol
MSNP-OH	None	TEOS	TBA
MSNP-NH_2	Amine	TEOS	TBA
MSNP-COOH-l	Carboxyl 0.075 mmol	TEOS	TBA
MSNP-COOH-m	Carboxyl 0.15 mmol	TEOS	TBA
MSNP-COOH-h	Carboxyl 0.30 mmol	TEOS	TBA
MSNP-OH*	None	TPOS	TBA
MSNP-COOH*	Carboxyl 0.15 mmol	TPOS	TBA
MSNP-COOH**	Carboxyl 0.15 mmol	TEOS	EtOH

*refers to the type of silica precursor used. Samples with * were produced using TPOS in stead of TEOS. **represents particles washed with ethanol in stead of tert-butyl alcohol.

reference for characterization. **Table 1** lists the examined particles in this work.

First, 0.5 g hexadecyltrimethylammonium bromide (CTAB, *acros organics*) and 0.4 g triethanolamine (TEA, *acros organics*) were dissolved in 60 mL ultrapure water. The solution was heated to 80°C and 2.75 mmol tetraethoxysilane (TEOS, *Sigma-Aldrich*) or tetrapropyl orthosilicate (TPOS, *Sigma-Aldrich*) was added while continuously stirring. Next, the mixture was stirred for 24 h to achieve a colloidal state. The NPs were either functionalized with amine or carboxylic surface functionalization, or they were washed without further surface modifications. The carboxylic surface functionalization was performed adding 0.13 mmol extra silica precursor (TEOS or TPOS) and 0.15 mmol carboxyethylsilanetriol (CES, *Gelest*) in case of standard (medium) carboxylation, denoted as MSNP-COOH or MSNP-COOH-m. In this work, the amount of CES was varied. Particles with a low amount of CES (0.075 mmol) or high amount (0.30 mmol) are denoted as MSNP-COOH-l and MSNP-COOH-h, respectively. CES provides the desired functionalization and additional silica precursor stabilizes the incorporation of carboxyl groups on the particle surface. The structural differences between CES and TEOS/TPOS causes faster hydrolysis and condensation of CES on the particle surface, resulting in an unstable surface chemistry. Therefore, CES was added 20 min after the silica precursor in order to have both substances condensate on the NP core simultaneously. Amine functionalized particles were produced by adding 0.13 mmol silica precursor and 0.13 mmol (3-aminopropyl) triethoxysilane (APTES, *Sigma-Aldrich*). For both functionalization types, the mixture was stirred for another 24 h at 80°C. After NP synthesis, the CTAB template was removed by dialysis (dialysis tubing membrane 14 kDa molecular weight cut off (MWCO), *Sigma-Aldrich*) of the NPs in 250 mL ultrapure water, 280 mL tert-butyl alcohol (TBA), or 280 mL ethanol (MSNP-COOH**) and 2.5 M aqueous acetic acid solution (*Sigma-Aldrich*) whilst vigorously stirring. Two different washing alcohols were tested to verify their influence on the carboxylic surface functionalization in acidic conditions. This mixture was refreshed five times after 12 h, afterwards replaced by ultrapure water and refreshed another five times until a neutral pH was reached.

The NP concentration was determined by centrifuging 1 mL MSNP solution for 10 min at 12,000 rcf to precipitate the particles. The sample was frozen and defrosted to destabilize the remaining particles in solution, and centrifuged again. Afterwards, the supernatant was removed and the precipitate was freeze dried under vacuum for 2 days (Alpha 1–4 LSC, *Martin Christ*). The dry particles were weighed to determine the concentration per milliliter.

Finally the MSNPs were fully characterized by a variety of techniques. The surface chemistry was determined with thermogravimetric analysis (TGA, STA 449 F1 *Netzsch*), Fourier transform infrared spectroscopy (FTIR, FTIR spectrometer Vertex 80v *Bruker*) and zeta potential (WALLIS zeta potential analyzer, *Cordouan Technologies*) measurements in function of the pH of the solution. Transmission electron microscopy (TEM, ARM200F *JEOL*) was performed at 200 keV after drying 10 μL of NP solution on a holey carbon-coated copper grid (*Agar Scientific*) under ambient conditions. The images were afterwards analyzed with ImageJ (Schneider et al., 2012), at least 100 NPs were taken into account to determine the core diameter.

2.2. Biodegradation of MSNPs and Spectrophotometric Determination of Silicate With Molybdenum Blue

The biodegradation procedure and analysis were based on our previous work (Seré et al., 2018). In order to verify the degradation of particles in the administration fluid for patients, the degradability was examined in saline solution in stead of PBS. The set-up remained similar, 6 mL of NPs was transferred to a dialysis membrane (dialysis tubing membrane 7 kDa MWCO, *Sigma-Aldrich*) and dialyzed against 100 mL 0.9% sodium chloride. In the first stage of degradation, a sample was taken every hour and the saline solution was refreshed to prevent concentration built-up of silicates [$Si(OH)_4$]. Gradually the time intervals prolonged as the degradation speed has been shown to decrease with increasing time (Seré et al., 2018).

The spectrophotometric determination of the amount of silicates and subsequent analysis was performed as described earlier (Seré et al., 2018).

2.3. Conjugation of MSNP With OVA and FITC

To prepare the nanovaccine, carboxylic functionalized MSNPs (MSNP-COOH) underwent standard carbodiimide cross linking chemistry using N-hydroxysulfosuccinimide (sulfo-NHS, *Thermo Fisher*) and N-(3-Dimethylaminopropyl)-N-ethylcarbodiimide hydrochloric acid (EDC, *Sigma-Aldrich*). For this, an activation mixture of 50 mM buffer 2-(N-morpholino)ethanesulfonic acid sodium salt (MES, *Sigma-Aldrich*), 50 mM sulfo-NHS and 25 mM EDC was prepared in ultrapure water. After adding the particles to the activation mixture at an end concentration of 1 mg/mL, they were left to react on a rotary wheel for 10–15 min. Next, 2 mg/mL OVA (*Sigma-Aldrich*) was added, and the mixture was left to react for 1 h while rotating. The conjugated particles (MSNP-COOH-OVA) were either immediately added to a DC culture, or ultrafiltrated (vivaspin 2 10000 MWCO PES VS0201, *VWR*) in case they were stored overnight to separate the

activation mixture from the nanovaccine. The vivaspin filtration membranes were washed 3 times before use with 2 mL ultrapure water and centrifugation at 1,000 g for 3 min. After filtration, the MSNP-COOH-OVA residue was recovered by resuspension in 1 mL ultrapure water and reverse spinning it into the recovery cap. Finally, the vaccine was administered to DCs at a concentration of 100 μg MSNPs and 200 μg OVA per million cells.

The NP uptake by DCs was investigated by labeling the MSNPs with 5-(aminoacetamido)fluorescein (fluoresceinyl glycine amide) (FITC, *Thermo Fisher*) using the same sulfo-NHS, EDC chemistry. FITC was added after activation of the carboxyl groups at a concentration of 0.25 mM and left on the rotary wheel for 1 h. Afterwards, the excess of FITC was separated from the labeled MSNPs (MSNP-COOH-FITC) using ultrafiltration as discussed in previous paragraph.

2.4. DC Generation and Culturing

The generation and maintenance of bone marrow derived DCs were based on the protocol of Belmans et al. (2017). First, DC culture medium was prepared using RPMI-1640 medium (*Thermo Fisher*), 10% FCS (*Thermo Fisher*), L-glutamine (*Thermo Fisher*), pen/strep (*Thermo Fisher*), 50 μM β-mercaptoethanol (*Sigma*), and 20 ng/mL granulocyte-macrophage colony-stimulating factor (GM-CSF, *Peprotech*). Bone marrow was collected from the femur and tibia of 8–10 weeks old female C57BL/6J mice (*envigo*). The bone marrow was flushed with PBS, the progenitor cells were counted (ABX Micros 60, *Horiba*) and finally cultured at one million cells per mL DC medium. The medium was refreshed on the third and fifth day of the culture. On the sixth and seventh day, the cells were prepared for confocal microscopy and flow cytometry, respectively.

2.5. Confocal Microscopy Staining

On the sixth day of the culture, immature DCs (iDCs) were collected, counted, and seeded onto coverslips. After 24 h of incubation, on day 7, DCs were treated with MSNP-COOH-FITC. Both iDCs (untreated) and mature DCs (mDCs) were used as control groups. The latter were treated with 1 μg/mL Escherichia coli lipopolysaccharide (LPS, *Sigma-Aldrich*). The cells were incubated for another 24 h before staining. They were then washed three times with PBS and incubated at 4°C for 10 min with fragment, crystallizable receptor blocker (FC-block, Anti-Mouse CD16/CD32 clone 93, *ebioscience*). Subsequently, the cells were further incubated at 4°C for 30 min while stained for MHC class I (H-2Kb-PE-Cy7 clone AF6-88.5.5.3, *ebioscience*). DCs underwent another washing procedure with PBS, were then fixed for 20 min at room temperature, followed by a final wash. Confocal microscopy images were analyzed using Fiji after recording on a Zeiss LSM 880—Airyscan (Cell and Tissue Imaging Cluster, KU Leuven) (Schindelin et al., 2012).

2.6. Flow Cytometry Staining

On the seventh day of the culture, DCs were treated with MSNPs, OVA, or MSNP-COOH-OVA. After 90 min incubation at 37°C, treated DCs were matured with LPS. iDCs and mDCs were used as control groups. After 24 h, the cells were collected and stained. The flow cytometry panel was based on the work of Baert et al. (2016) CD11c is typically highly expressed by DCs, an anti-CD11C mAb was therefore used to distinguish DCs from other cells in our samples. Fixable Viability Dye (FVD eFluor 506) was used to exclude dead cells from the data sets. This dye penetrates the compromised cell membranes of dead DCs and reacts with intracellular proteins. Costimulary molecules (CD40, CD86, CD80) and MHC class I and II molecules were stained as maturation markers. In addition, cells were stained for SIINFEKL/H-2Kb interaction. This mAb marked cross-presentation of the $OVA_{257-264}$ octapeptide SIINFEKL on MHC class I molecules. The used clones are listed in **Table 2**. Finally, flow cytometry was performed using a LSR Fortessa Analyzer (*BD Biosciences*) and analyzed with FlowJo software (*Tree Star*). The gating strategy is included in the **Supplementary Figure 2**.

TABLE 2 | Murine DC antibodies used in this work.

Antigen	Fluorochrome	Clone	Supplier
CD11c	Allophycocyanin	N418	eBioscience
CD80	PE-Cy7	16-10A1	eBiosciene
CD86	PE-Cy7	GL1	BD Bioscience
MHC-I (H-2Kb)	PE-Cy7	AF6-88.5.5.3	eBioscience
MHC-II (I-A/I-E)	PE-Cy7	M5/114.15.2	eBioscience
CD40	PE-Cy7	3/23	BioLegend
SIINFEKL/H-2Kb	PE	eBio25-D1.16	eBioscience

3. RESULTS AND DISCUSSION

3.1. MSNP Characterization and Optimization

A limited number of attempts have been made to produce carboxyl functionalized MSNPs in a one-pot process (Han et al., 2007; Kozlova and Kirik, 2010; Gu et al., 2013). Most groups report a complex post-synthesis process consisting of multiple steps (Yang et al., 2003; Chen et al., 2011; Han et al., 2011; Soo et al., 2019). To obtain a cost-effective alternative, we developed a simple one-pot wet chemistry process which is scalable to produce industrial quantities. The optimization of the protocol consisted of complete characterization, followed by improvements of experimental parameters, such as washing alcohol, functionalization precursor, and silica precursor.

3.1.1. Effect of the Washing Alcohol

In a first stage, the influence of the washing alcohol on carboxylic surface functionalization in acidic conditions was assessed. In previous work, ethanol was used to remove the structure directing agent (Yamada et al., 2012; Seré et al., 2018). Inefficient protein conjugation with these particles suggested Fischer esterification of the carboxyl groups when the template was removed with ethanol (Master Organic Chemistry LLC, 2020). To prevent this reaction, NPs were washed with TBA instead. TBA offers more steric hindrance, inhibiting the electrophilic carbon of the carboxylic acid to attack the alcohol. It is therefore less reactive than ethanol. Functionalization of these particles was first assessed with FTIR represented in **Figure 1**. Non-functionalized particles (MSNP-OH, blue curve)

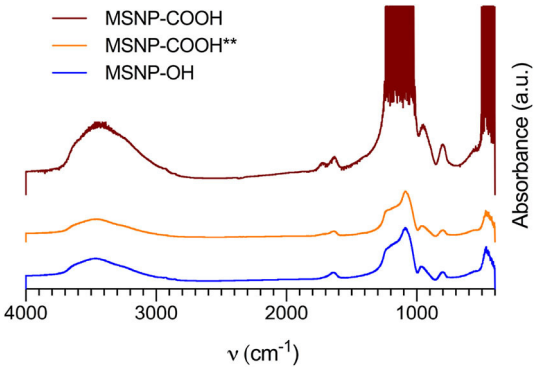

FIGURE 1 | FTIR spectra of non-functionalized MSNPs (MSNP-OH, blue), and carboxy-MSNPs washed with TBA (MSNP-COOH, red) or ethanol (MSNP-COOH**, orange). The characteristic absorption bands for carboxylic functionalization are visible in the TBA washed samples, to a lesser extend in the ethanol washed samples. Non functionalized particles did not show these characteristic bands.

show absorption bands at 480 cm^{-1} corresponding to O–Si–O bending, 800 cm^{-1} for Si-O bending, 950 cm^{-1} for SiO-H bending, in the range of 1,000–1,200 cm^{-1} for Si–O–Si stretching and a broad band around 3,500 cm^{-1} for SiO–H stretching. The band at 1,640 cm^{-1} is probably due to scissor bending vibrations of molecular water. Coating the particle surface with carboxyl groups, introduces additional bands at 1,720 cm^{-1} corresponding with the C=O stretch and 1,420 cm^{-1} which corresponds to the C–O stretch. The latter band is slightly visible in the FTIR spectrum of TBA washed particles (MSNP-COOH, red curve in **Figure 1**), but not present for ethanol washed particles (MSNP-COOH**, orange). Other infrared absorption bands characteristic for carboxyl groups, such as the O–H and C–H stretching band at 3,500 cm^{-1} and the O–H bending at 950 cm^{-1}, overlap with the spectrum for non-functionalized particles.

In essence, the FTIR spectra gave a first indication of successful carboxylic functionalization of MSNPs, especially for TBA washed MSNPs. The distinctive absorption bands for carboxyl groups are less abundant for ethanol washed particles, confirming the Fisher esterification hypothesis. It was therefore decided to use TBA during template removal.

SAXS and TEM analysis confirmed the mesoporous structure (**Supplementary Figure 1** and **Figure 5**). Zeta potential and TGA were performed for aforementioned samples and amine functionalized particles (MSNP-NH_2) in order to assess the grafted functional groups. **Figure 2A**, shows the zeta potential as a function of pH for MSNPs with different surface functionalization. The shape of the curve confirms successful carboxylic surface functionalization. As a reference, the isoelectric point (IEP) is considered. Non-functionalized MSNPs have an IEP at a pH value of 3.5. This value shifts to 6.7 for MSNP-NH_2, due to the change of surface charge. MSNP-COOH show no IEP as the zeta potential of these samples is negative over the complete pH range, confirming efficient carboxylic surface functionalization. Following the same reasoning, the shift of MSNP-COOH toward lower zeta potential values in the higher pH range suggests more carboxyl groups as compared to ethanol washed particles (MSNP-COOH**).

TGA decomposition profiles give a quantitative indication of the functional groups and were normalized to the weight of dry samples. This weight was set at 150°C, after removal of impurities and adsorbed moisture (Musso et al., 2015). Three regions can be observed for samples with functional groups and each can be ascribed to a certain surface chemistry (Gallas et al., 2009; Kozlova and Kirik, 2010; Musso et al., 2015). The first region from 150 to 370°C for carboxylated MSNPs and from 150 to 500°C for MSNP-NH_2, is attributed to the loss of silanol groups. The decomposition profile of carboxylated MSNPs shows a plateau before going into the second region ranging from 440 to 700°C. This steep decline is ascribed to the carboxylic surface functionalization. Amine functionalized MSNPs show a steep slope in the range from 500 to 700°C, representing amine functionalization. The gradual weight loss when increasing the temperature beyond 700°C is ascribed to further dehyroxylation. The TGA curves in **Figure 2B** demonstrate that the particles are grafted with carboxyl groups. The curves of carboxylated MSNP coincide for both washing methods in the first region, indicating an equal amount of silanol groups. In the second region, which represents the carboxylic surface functionalization, the TBA washed particles (MSNP-COOH) show slightly more weight-loss than ethanol washed particles (MSNP-COOH**). This confirms a higher amount of carboxyl groups, supporting the esterification hypothesis for ethanol washed particles.

The particles were degraded in 0.9% NaCl solution and molybdenum blue chemistry was used to assess the degradation kinetics shown in **Figure 3**. The results indicate that degradation occurs fastest for amine functionalized particles (green curve), followed by non-functionalized (blue curve) and carboxylated particles (orange and red curve). It has been shown that the negatively charged ions of a medium are the main mediators for particle degradation (Seré et al., 2018). The fast degradation for amine functionalized MSNPs can therefore be ascribed to the attractive electrostatic interactions between the degrading ions and the positively charged particles. Both silanol groups of non-functionalized particles as well as carboxyl groups of carboxy-MSNP, repel the negative ions. Due to the larger negative potential of carboxylated MSNPs, repulsion is higher and degradation therefore slower as compared to non-functionalized particles. As for the particles produced with different template removing alcohols, TBA washed particles (MSNP-COOH, red curve) degrade slower than ethanol washed particles (MSNP-COOH**, orange curve). Data in **Figure 2A** show that ethanol washed particles have lower absolute zeta potential values, suggesting a decreased ability to repel the degrading ions and resulting in faster degradation.

Based on these results, we conclude that the washing procedure has an impact on the surface functionalization. In addition, TBA washed particles degrade slightly slower, increasing their availability for DCs. We therefore selected TBA as the better washing alcohol for further NP production in this work.

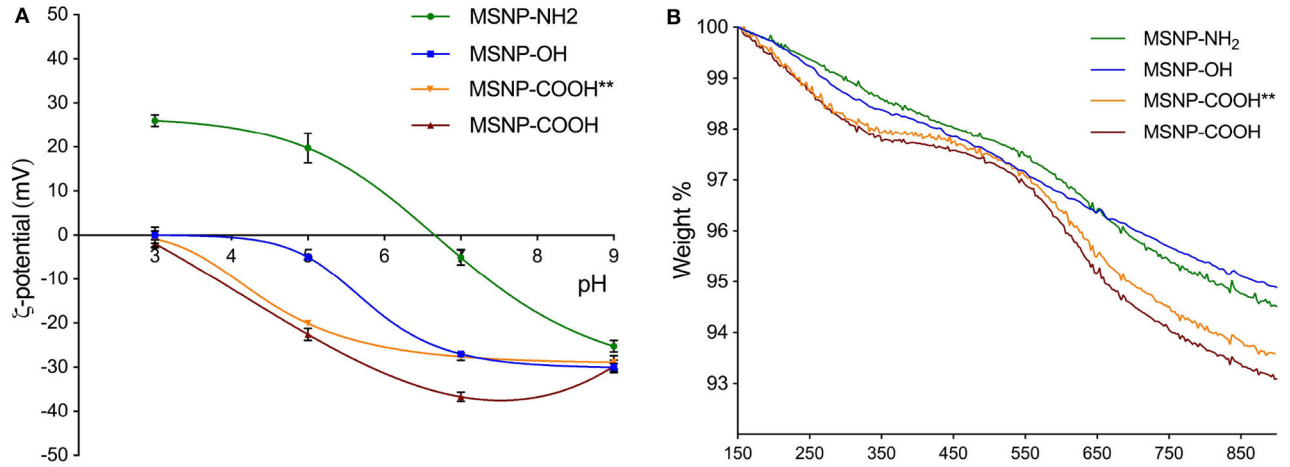

FIGURE 2 | (A) Zeta potential as a function of pH for MSNP-OH (blue), MSNP-NH_2 (green), MSNP-COOH (red), and MSNP-COOH** (orange). The first IEP occurs for MSNP-OH in the lower pH region, followed by MSNP-NH_2 in at high pH values. MSNP-COOH have a negative potential over the complete pH range and therefore do not show an IEP. The shift of the curve offers a first indication of the surface functionalization. **(B)** TGA decomposition profiles for MSNP-OH (blue), MSNP-NH_2 (green), MSNP-COOH (red), and MSNP-COOH**(orange). The first temperature window of the decomposition curves is attributed to the loss of silanol groups, followed by the range characteristic for the functional groups. These are 440–700 and 500–700°C for MSNP-COOH and MSNP-NH_2, respectively.

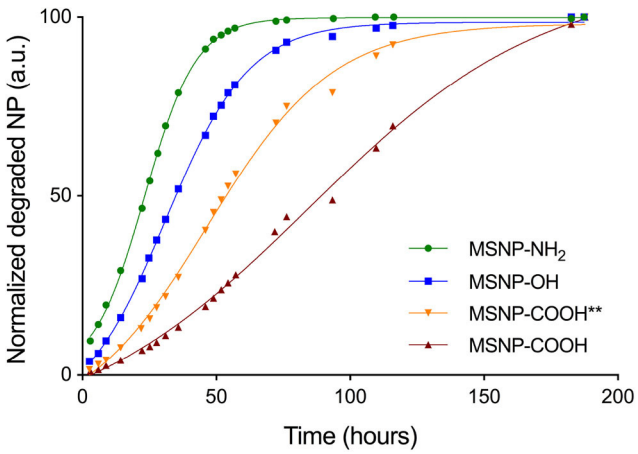

FIGURE 3 | Degradation kinetics for MSNP-OH (blue), MSNP-NH_2 (green), MSNP-COOH (red), and MSNP-COOH** (orange). Fast degradation of MSNP-NH_2 is due to the attractive electrostatic interaction of the particle with the degrading ions. MSNP-OH and carboxy-MSNP both repel the negatively charged ions of the solution. However, carboxy-MSNP have a larger negative potential and will therefore degrade slower. Finally, the zeta potential is more negative for TBA washed carboxy-MSNPs (MSNP-COOH), as compared to ethanol washed carboxy-MSNPs (MSNP-COOH**), causing slower degradation of MSNP-COOH.

3.1.2. Optimal Carboxylation

After improving the washing procedure, the optimal amount of CES for carboxylation was determined. Carboxylic surface functionalization of mesoporous silica materials using the CES precursor, has mainly received attention in the catalytic research field where SBA-15 sieves are functionalized (Han et al., 2007; Tsai et al., 2009). In addition, it is also used for carboxylic mesoporous silica coating of superparamagnetic iron oxide NPs (Sharifi et al., 2013). Other groups produced MSNP-COOH by producing 5-(Triethoxysilyl)pentanoic acid and incorporating it in a one-pot synthesis. The silica end of this carboxyl precursor resembles the TEOS structure more closely but requires another synthesis step (Feinle et al., 2017). Keeping the industrial scaling and costs in mind, water soluble CES was used in this work. Traditional co-condensation might cause the formation of additional silica entities in the solution, especially when higher amounts are used. Earlier research could therefore only implement trace amounts of CES (Gu et al., 2013; Sharifi et al., 2013). Since this work improved the functionalization route, the optimal carboxylation was investigated.

MSNP-COOH samples were produced following the standard protocol and using TBA to remove the CTAB template. The samples were denoted as MSNP-COOH-l, MSNP-COOH-m, and MSNP-COOH-h as the amount of CES was varied 0.075, 0.150, and 0.300 mmol, respectively. **Figure 4A** represents zeta potential measurements. Incorporating more carboxyl groups on the particle surface, increases inter-particle repulsion in the higher pH range (Duffy and Hill, 2011). It results in a higher zeta potential and more stable NPs. MSNP-COOH-h samples in **Figure 4A** (triangle full line) do not follow this expected trend. The progression of the zeta potential curve deviates, suggesting saturation of the NP surface when higher amounts of CES are used during synthesis.

The amount of grafted carboxyl groups was estimated with TGA. The normalized decomposition profiles are illustrated in **Figure 4B** and associated results in **Table 3**. The first temperature region from 150 to 370°C, represents the mass loss due to silanol groups. MSNP-COOH-l show more mass loss in this window as compared to the other two samples. The mass loss due to silanol groups of MSNP-COOH-m and MSNP-COOH-h samples is equal. This suggests an unsaturated particle surface

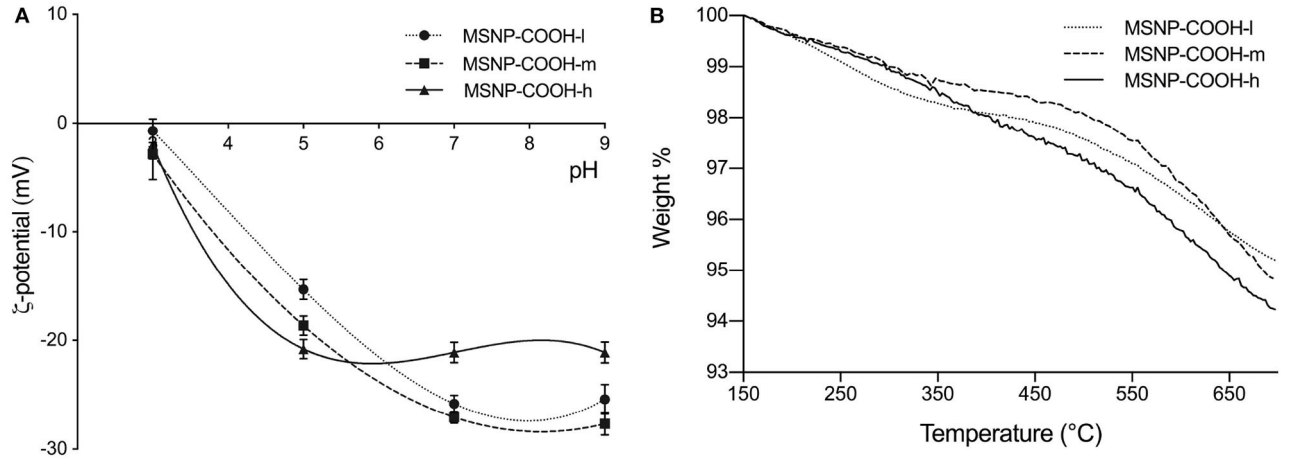

FIGURE 4 | (A) Zeta potential as a function of pH for MSNP-COOH-l, MSNP-COOH-m, and MSNP-COOH-h. NPs are expected to be more stable in the higher pH range, when more carboxyl groups are incorporated. MSNP-COOH-h do not follow this trend, suggesting surface saturation. **(B)** TGA decomposition profiles of MSNP-COOH-l, MSNP-COOH-m, and MSNP-COOH-h. MSNP-COOH-l show more mass loss in the silanol range, as compared to the other two samples. Mass loss in thisl region is equal for MSNP-COOH-m and MSNP-COOH-h. MSNP-COOH-m and MSNP-COOH-h show equal mass loss in the COOH characteristic window. Low amount of CES during synthesis renders particles with unsaturated surface. Saturation of the surface occurs (MSNP-COOH-m), and therefore no increase in functional groups occurs when even more CES is used (MSNP-COOH-h).

TABLE 3 | TGA decomposition of carboxy-MSNPS.

Sample	Weight loss silanol (150–370°C) (%)	Weight loss carboxyl (440–700°C) (%)
MSNP-COOH-l	1.4	2.6
MSNP-COOH-m	1.0	3.6
MSNP-COOH-h	1.0	3.6

when functionalized with 0.075 mmol CES; while adding 0.15 mmol CES or more, decreases the amount of silanol groups to a constant value, indicating particle saturation. The same trend is observed in the temperature range ascribed to the weight loss of carboxyl groups from 440 to 700°C. The amount of carboxyl groups is lower when a low amount of CES (0.075 mmol) is used. On the other hand, amount of grafted carboxyl groups is the same for both 0.15 and 0.30 mmol CES. An equal amount of carboxyl groups suggests saturation of the NP surface, which occurs due to steric hindrance of the carboxyl groups. Adding more CES results therefore in the same amount of carboxylic surface functionalization.

Particles functionalized with 0.15 mmol CES were considered to be optimal for protein loading, as this amount seems to saturate the particle surface.

3.1.3. Optimal Silica Precursor

Finally, in search of the optimal particle, two different silica precursors were examined. TEOS is a well-known and widely used precursor, a standard in the synthesis of silica NP synthesis (Rahman and Padavettan, 2012; Wu et al., 2013; Liberman et al., 2014; Zulfiqar et al., 2016). TPOS is known to render slightly larger particles and larger size distribution due to a lower hydrolysis rate during synthesis (Yamada et al., 2012). The size of TPOS based NPs would still be suitable for passive targeting of DCs (Yamada et al., 2012). Large particulate systems are mainly taken up by DCs, then transferred toward the lymph nodes where they stimulate the $CD8^+$ T-cells. By contrast, smaller particles are taken up by macrophages in the skin which are considered to be tissue resident (Manolova et al., 2008). We therefore aim to produce MSNPs between 20 and 50 nm in this work. In addition, the system's diameter increases with 300–500 nm by coating the MSNPs with tumor proteins to produce the nanovaccine. Therefore, NP monodispersity is not required, as the conjugation of peptides and proteins causes polydispersity of the final product. Our hypothesis is that slower hydrolysis during synthesis could result in more stable particles with regard to biodegradation, arousing interest in TPOS based particles.

TEOS or TPOS silica precursor (2.75 mmol) were used during synthesis and both non-functionalized and carboxy-MSNP were produced for further characterization. **Figures 5**, **6** show typical TEM images and the size distribution of carboxy-MSNP produced with TEOS (MSNP-COOH) and TPOS (MSNP-COOH*), respectively. As expected, TPOS based particles are larger with an average core diameter of (48 ± 8) nm. The TEOS precursor rendered smaller particles with an average diameter of (29 ± 4) nm. In addition, the size distribution of TPOS based particles is larger.

The MSNPs were characterized using zeta potential, TGA, and biodegradation experiments. Zeta potential and TGA data were comparable for TEOS and TPOS based nanoparticles, for both non-functionalized as well as carboxy-MSNP (data not shown). Thus, the silica precursor does not influence the electrochemical stability of the particles in solution, nor does it affect the surface chemistry. Biodegradation experiments were performed in 0.9% sodium chloride and results are shown

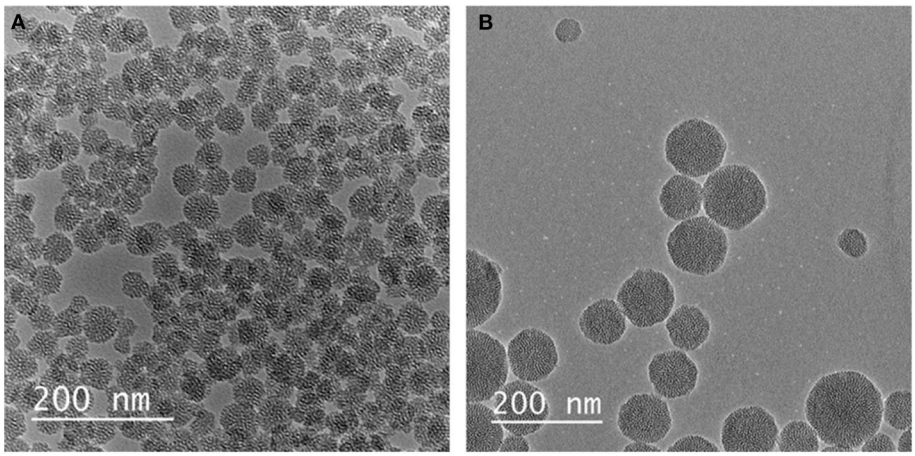

FIGURE 5 | Representative TEM images of **(A)** MSNP-COOH and **(B)** MSNP-COOH*.

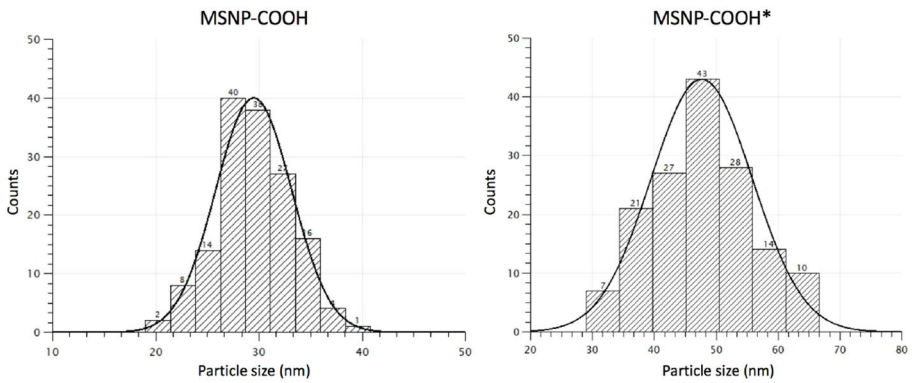

FIGURE 6 | Size distribution MSNP-COOH (TBA washed) and MSNP-COOH* (ethanol washed) based on TEM measurements. The size distribution is narrower when CTAB templates are washed with TBA during synthesis.

in **Figure 7**. All MSNPs degraded in saline solution. The degradation behavior of non-functionalized and carboxylated MSNPs is in line with aforementioned conclusions. Particles with carboxylic surface chemistry degrade slower due to the repulsive interaction with the degrading ions in the medium. In contrast to our expectations, TEOS based particles degrade slower than particles synthesized with TPOS comparing particles with identical functionalization. The degradation curves follow the same course, but are shifted when TEOS is used for core synthesis. At a degradation of 50%, the curve is shifted for 12 and 18 h in case of non-functionalized and carboxylated MSNPs, respectively. The effect of the silica precursor is in contrast to what is expected from the study of Yamada et al. (2012). Probably, the synthesis route used in this work, affects the pore and particle size and hence the biodegradability. Slower degradation implies more chance of DCs to take up the nanovaccine in the human body.

The optimal particles for this work were MSNP-COOH, synthesized with a TEOS precursor, functionalized with 0.15 mmol CES and washed with TBA.

3.2. *In vitro* Assessment of MSNPs and the Nanovaccine

3.2.1. Dose-Response Relationship Between MSNPs and DCs

The first *in vitro* steps were taken by determining the optimal MSNP dose to treat and analyze DCs. The dose response relationship between MSNPs and the viability of DCs is shown in **Figure 8A**. The graph was established by culturing DCs and exposing them to MSNPs. After flow cytometry acquisition, the viability was determined using an adjustment of the general gating strategy in **Supplementary Figure 2**. Single cell selection (**Supplementary Figures 1A,B**) was followed by extracting the $CD11c^{+}$, FVD^{-} populations in a single gate as represented in **Figure 8B**. Control conditions were taken into account with iDCs (untreated) and mDCs (LPS stimulated). The test conditions consisted of DCs incubated with: 50, 100, 200, and 400 μg MSNPs per million DCs. Each NP treated DC culture received an LPS stimulation signal 90 min after the particles were introduced. Data were pooled from two experiments containing five cultures per condition.

The main factors affecting NP cytotoxicity are surface functionalization, size, and concentration. Although MSNPs are known to be biocompatible and biodegradable, their cytotoxicity significantly increased when their concentration increased as shown in **Figure 8**. Anova pairwise comparison was used to determine statistical significance, using iDC and mDC as control conditions. No significant difference was observed when DCs were treated with 50 or 100 μg MSNPs per million DCs. Increasing the quantity of MSNPs significantly decreased DC viability (***$p \leq 0.001$). The threshold toward cytotoxicity for the NPs in this work was set at 100 μg per million DCs and was therefore used as standard for loading DCs. In addition, the viability of DCs treated with 50 or 100 μg MSNPs was significantly higher than DCs treated with higher NP doses (not indicated on graph).

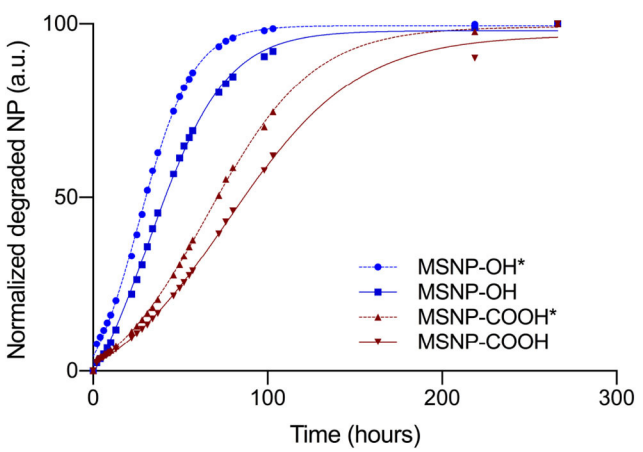

FIGURE 7 | Degradation behavior of non-functionalized and carboxy-MSNP, produced with TEOS and TPOS (*). The shape of the degradation curve is the same for particles with identical functionalization, regardless the silica precursor used during synthesis. Curves shifts to the right for TEOS based particles, indicating slower degradation.

3.2.2. MSNP and Nanovaccine Uptake by DCs

The uptake of particles and nanovaccine by DCs was examined using confocal microscopy. First, DCs were incubated with labeled MSNPs (MSNP-FITC), stimulated with LPS and stained for MHC class I molecules. To gain a better insight in the uptake process, half of the cells were incubated at 4°C and the other half at normal physiological temperatures, i.e., 37°C. The results are illustrated in **Figure 9**. **Figures 9A,B** show images of MSNP treated DCs, incubated at 37°C. The green signal was attributed to the FITC labeled MSNPs, the red signal to PE-Cy7 labeled MHC class I molecules. Since MHC class I molecules are membrane molecules, they visualize the cells' exterior. The green signal of MSNPs is concentrated inside the red MHC signal. No particles were observed being attached to the cell surface, indicating cellular uptake of the MSNPs. In addition, **Figures 9C,D**, display the uptake mechanism since these cells were incubated at different temperatures. It is known that cell metabolism shuts down at 4°C (**Figure 9C**) (De Vleeschouwer et al., 2005; Belmans et al., 2017). The absence of the green MSNP signal, stipulated no particle uptake by DCs. Incubation at 37°C on the other hand, did show particle uptake within the same experiment (**Figure 9D**). In conclusion this demonstrated that particle internalization is an active process (ATP dependent) and not merely NPs penetrating the membrane of DCs. This was an indication of endocytosis, meaning that particles and transported proteins enter the cross-presentation pathway.

Nanovaccine uptake, or at least the internalization of the transported tumor proteins, is of great importance to induce an anti-tumor immune response. To determine protein uptake

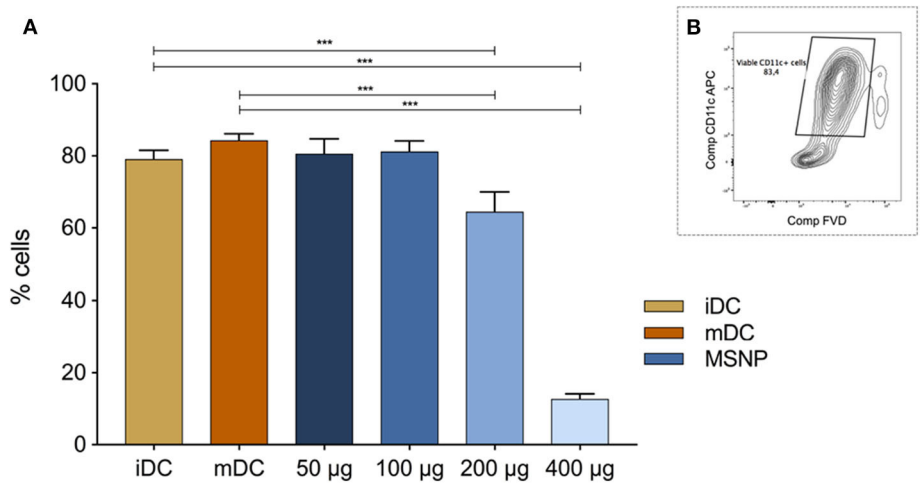

FIGURE 8 | (A) Shows the effect of various doses of MSNPs on the DC viability. iDC and mDC are the control conditions. Blue represents the viability of MSNP treated DCs. The doses included (from dark to light blue) 50, 100, 200, and 400 μg NPs per million DCs. **(B)** Pictures the gating strategy to select viable (FVD^-) DCs ($CD11c^+$). Anova multiple comparison was used to determine significance. The viability of DCs decreased significantly when incubated with 200 or 400 μg MSNPs per million DCs. *$p \leq 0.1$, **$p \leq 0.01$, and ***$p \leq 0.001$ are refers to statistical significance of the data.

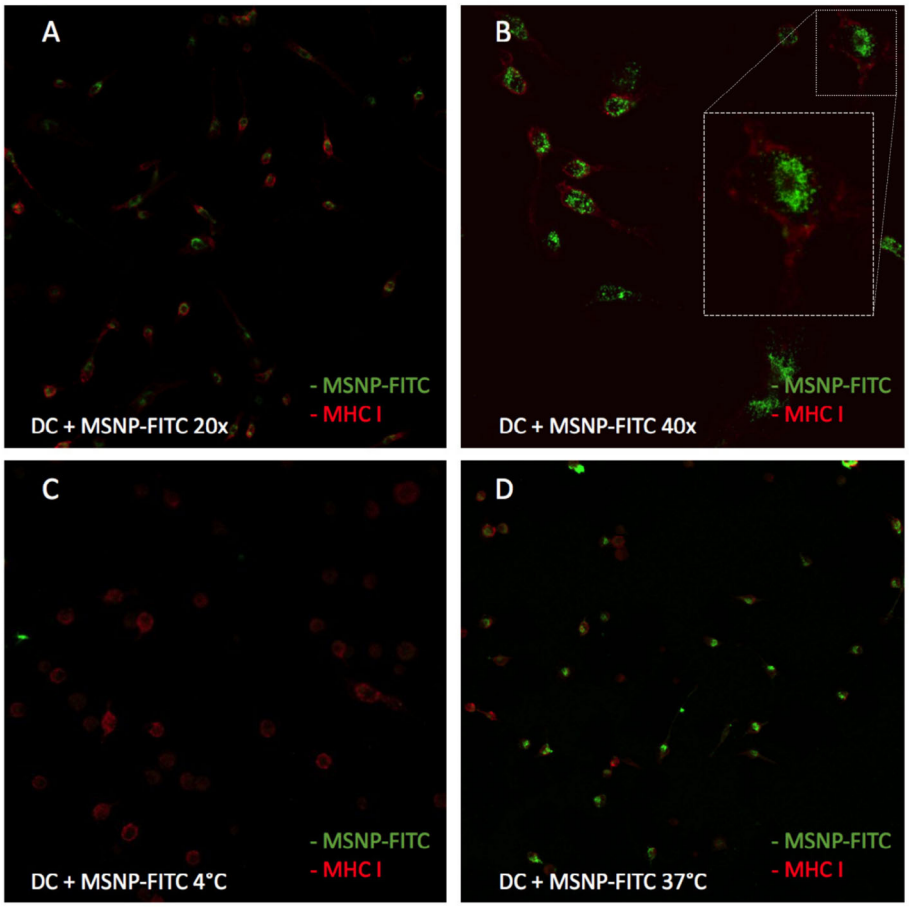

FIGURE 9 | Uptake of MSNPs by DCs. The red signal represents MHC class I molecules at the cell surface. The green signal represents the FITC label on the MSNPs. **(A,B)** Demonstrate NP uptake by DCs as the red signal of the cells' exterior encircles the green signal of the MSNPs. **(C,D)** Show the uptake of NPs when cells are incubated at 37 and 4°C, respectively. When cells are incubated at 4°C, the cell metabolism in shut down. A lack of green signal in **(C)**, represents no particle uptake. Therefore, the uptake is a determined to be an active process.

by DCs after treatment with the nanovaccine, MSNPs were loaded with OVA, Alexa Fluor 488 conjugates (OVA-Alexa). The same incubation and staining process was followed as for particle uptake. Confocal microscopy images confirmed uptake of OVA-Alexa, as shown in **Figure 10**. The green OVA signal is observed within the red MHC signal. Moreover, a yellow overlay of the green OVA signal and the red MHC class I signal was observed for several cells. This was a first suggestion of cross-presentation of OVA by DCs. The cross-presentation was quantitatively determined with flow cytometry.

3.2.3. Nanovaccine Effect on DCs and Cross-Presentation

In a first stage of these experiments, the effect of MSNPs on DCs was investigated by incubating the cells with as-synthesized and UV-sterilized particles. The effect of the nanovaccine was tested as well by incubating the cells with MSNP-OVA. The viability and maturation effect on the DCs were examined with flow cytometry. No significant difference was observed between the viability of treated DCs and control conditions iDC and mDC (data not shown). In addition, the sterilized particles were characterized and no changes were observed before or after sterilization. These results imply that the sterilization step can be included for further application as it does not negatively affect DCs, nor does it affect the quality of the NPs.

After demonstrating particle and vaccine uptake, the maturation effect of the treatment on DCs was examined. **Figure 11** shows the expression levels of the most important maturation markers of these cells, which include CD86, IA/IE, and CD40. MHC class I and CD80 expression levels were excluded from the data as these levels were high and comparable for all samples. The complete data can be found in the **Supplementary Figure 3**. The results were obtained by pooling data of six experiments with three cultures per condition per experiment.

iDCs showed low expression levels for the maturation markers, as expected (**Figure 11**, yellow). The immature state is typically specialized in sampling its environment *in vivo*. Increased expression of costimulatory molecules and MHC only takes place once pathogens are encountered and stimulation occurs. mDCs thus represented the positive control group for

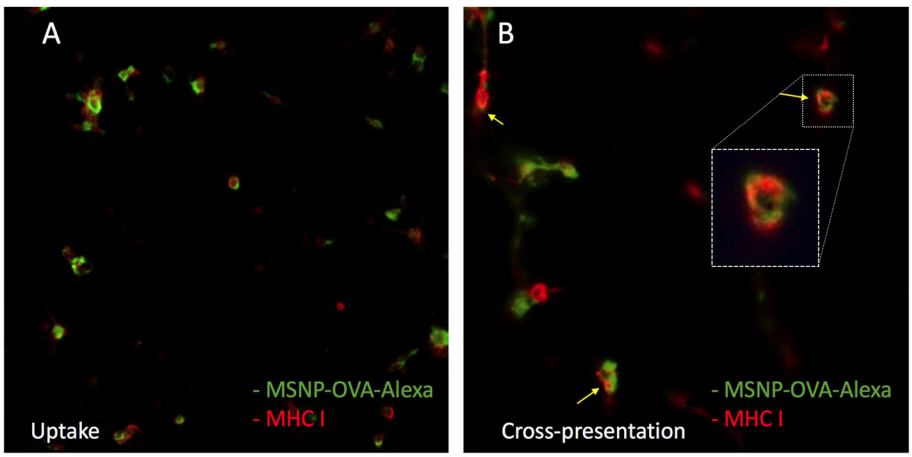

FIGURE 10 | Uptake of the model nanovaccine by DCs. The red signal represents MHC class I molecules at the cell surface. The green signal represents the alexa 488 labeled OVA. **(A)** Confirms nanovaccine uptake. **(B)** Shows a yellow overlay of the green and red signal, indicating cross presentation of OVA on MHC class I molecules.

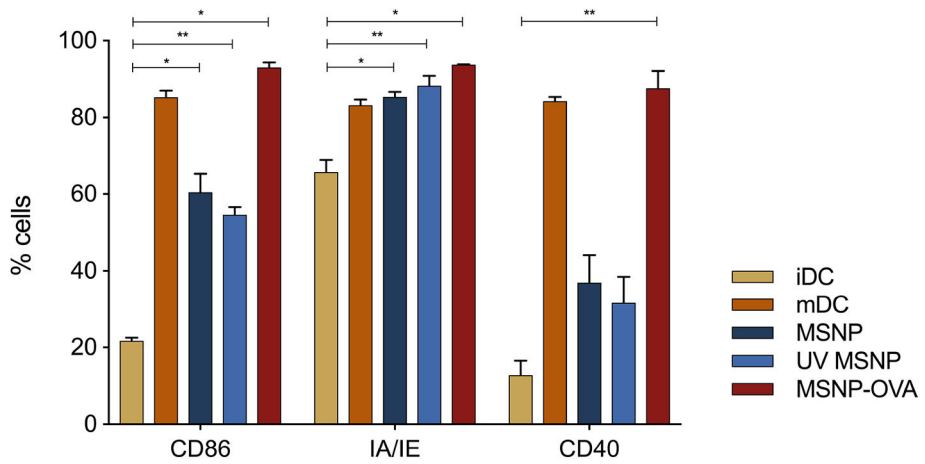

FIGURE 11 | Mean maturation expression levels of DCs are shown. iDCs and mDCs are control conditions, represented in yellow and orange, respectively. The expression levels of costimulatory and MHC molecules are clearly higher for mDCs. DCs treated with MSNPs (as-synthesized and UV sterilized), are represented in blue. No significant difference between DCs treated with sterilized and non-sterilized particles was observed. MSNP treated DCs show elevated expression levels of costimulatory and MHC molecules as compared to iDCs. Albeit the expression was not as high as mature DCs, indicating rather moderate maturation effect of MSNPs. The expression levels of DCs treated with the nanovaccine and stimulated with LPS are shown in red and are significantly higher than MSNP treated DCs and iDCs. $*p \leq 0.1$ and $**p \leq 0.01$ are refers to statistical significance of the data.

the maturation effect (**Figure 11**, orange). The expression levels of the shown markers was significantly higher for mDCs (Anova Dunnett's multiple comparisons test ($**p \leq 0.01$), not indicated on the graph). DCs treated with particles alone (**Figure 11**, blue) did not receive a maturation trigger, in order to assess the effect of MSNPs. These DCs showed significantly increased expression levels of CD86 and MHC class II as compared to iDCs ($*p \leq 0.1$ for MSNP and $**p \leq 0.01$ for UV MSNP). In addition, higher expression of CD40 was observed. However, the expression levels of maturation markers were still lower than those of mDCs. These results were significant for CD40 ($*p \leq 0.1$) and CD86 ($*p \leq 0.1$ for MSNP and $***p \leq 0.001$ for UV MSNP). We concluded that MSNPs have a moderate adjuvant effect on DCs and thus possibly the adaptive immune system. Incorporating immunomodulatory agents, such as TLR ligands (R848), on the particle surface could increase the stimulating effect further. In addition, DCs treated with MSNPs and UV sterilized MSNPs exhibited comparable expression levels of costimulatory and MHC molecules. As expected, DCs treated with the nanovaccine exhibited similar expression levels of MHC and costimulatory molecules as compared to mDCs (**Figure 11**, red, no significant difference). Both conditions were stimulated with LPS. The expression levels of DCs treated with the nanovaccine seemed even higher, which was possibly associated with the accumulative effect of LPS and NPs. MSNPs caused moderate maturation, which is further increased by LPS. These results indicated the adjuvant effect of MSNPs on DCs. which was a first suggestion of DCs being able to communicate the protein information delivered by NPs to the T-cells of the immune system.

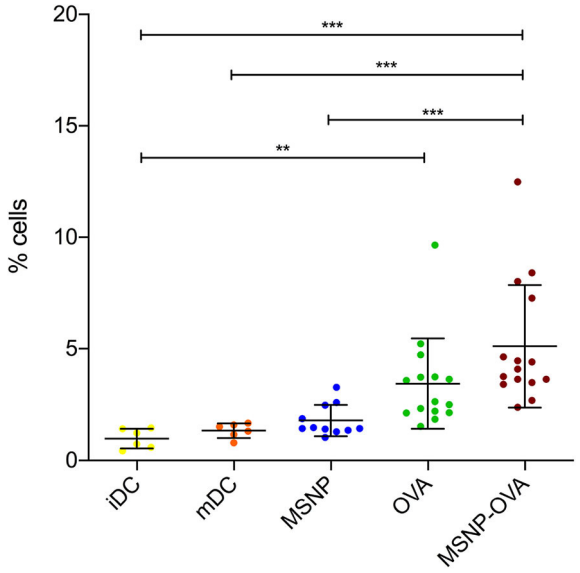

FIGURE 12 | Cross-presentation of the SIINFEKL peptide on MHC class I. iDCs and mDCs are control conditions, represented in yellow and orange, respectively. DCs treated with MSNPs, OVA and the model nanovaccine (MSNP-OVA) are represented in blue, green, and red, respectively. DCs treated with nanovaccine cross-presented the OVA antigen in higher levels. $^{*}p \leq 0.1$, $^{**}p \leq 0.01$, and $^{***}p \leq 0.001$ are refers to statistical significance of the data.

In order to investigate the cross-presentation of OVA on MHC class I molecules, DCs were loaded with the nanovaccine and cells were stained for flow cytometry with SIINFEKL-PE. This antibody stains the combination of the SIINFEKL peptide and MHC class I, and is therefore a quantitative indication of the cross-presentation of MSNP delivered OVA. The data and statistical analysis can be found in the **Supplementary Figures 4, 5** and **Supplementary Tables 1, 2**, results are shown in **Figure 12**. Data of four experiments were pooled, each experiment consisted of three to five groups per condition. Tukey HSD all pairwise comparison implicated significant differences between the cross-presentation of all negative control groups (i.e., iDC, mDC, and MSNP treated DCs) and DCs treated with the model nanovaccine ($^{***}p \leq 0.001$). In addition, cross-presentation of OVA on MHC class I by iDCs was significantly lower than OVA treated DCs ($^{**}p \leq 0.01$). A clear tendency toward higher cross-presentation was perceived when cells were treated with the nanovaccine. This indicated that DCs should be able to stimulate the CTLs of the immune system to specifically attack the tumor.

4. CONCLUSION

The MSNP synthesis and functionalization reported in this work consist of a one pot wet chemistry process which can easily be up-scaled to industrial production. The synthesis and functionalization, were optimized by assessing different silica precursors and different amounts of surface functionalization. These small manipulations during synthesis enable modification of physicochemical properties of the particles. MSNPs were produced within the desired size range (20–50 nm) for passive targeting of DCs after producing the nanovaccine. Characterization confirmed carboxylic surface functionalization necessary for subsequent protein conjugation. The developed MSNPs are resistant against agglomeration at experimental and physiological pH. In addition, they have shown to be biodegradable over a time span of 1 week, which is sufficiently long for DCs to take up the nanovaccine. This period was adjustable by varying the functionalization and silica precursor during synthesis. TEOS based MSNPs were found to be smaller but more resistant against biodegradation in comparison to TPOS based particles. Therefore, TEOS was preferred in further experiments. The optimal amount of carboxylic surface functionalization was reached using 0.15 mmol CES during NP synthesis.

NPs and the nanovaccine were taken up by DCs and this was found to be an active physiological process. Overlay of the MHC-I and OVA signal suggested the ability of DCs to cross-present proteins delivered by MSNPs. UV sterilization of the MSNPs did not induce any decrease in particle quality, nor did it have toxic effects on DC cultures. Treatment with MSNPs increased expression levels of MHC and costimulatory molecules of DCs in culture, indicating an adjuvant effect of the particles on DCs and possibly the adaptive immune system. Finally, cross-presentation was examined quantitatively with flow cytometry. Compared to control conditions, increased cross-presentation of OVA was observed when DCs were treated with the nanovaccine. These preliminary results confirm the large potential of MSNP based nanovaccines as a replacement of the expensive DC-based vaccines for active specific immunotherapy, offering a more standardized production process and possibly higher efficacy.

DATA AVAILABILITY STATEMENT

The raw data supporting the conclusions of this article will be made available by the authors, without undue reservation.

ETHICS STATEMENT

The animal study was reviewed and approved by Animal Ethics Committee KU Leuven.

AUTHOR CONTRIBUTIONS

The work in this article was part of the research activities of SS, in the framework of her doctoral dissertation. UV and SS collaborated and contributed equally. The research was performed in the group of J-PL and JS. SV and IL closely mentored the study and provided important input throughout the different phases of this work. All authors contributed to the article and approved the submitted version.

FUNDING

SS extends her gratitude to the Research Foundation-Flanders (Grant No. 1S52016N) for the Ph.D. scholarship.

JS acknowledges the Hercules Stichting (Project AKUL/13/19), funding the TEM. Finally, we want to acknowledge the Olivia Fund for their financial support.

ACKNOWLEDGMENTS

SS would like to extensively thank the research group of An Coosemans for making their lab and tools available, and for the excellent cooperation. Finally, we thank Carmen Bartic and Olivier Deschaume for the use of the spectrophotometer.

SUPPLEMENTARY MATERIAL

The Supplementary Material for this article can be found online at: https://www.frontiersin.org/articles/10.3389/fnano.2020.584233/full#supplementary-material

REFERENCES

Andronescu, E., and Grumezscu, A. M. (Eds.). (2017). *Nanostructures for Oral Medicine*. Elsevier.

Baert, T., Garg, A. D., Vindevogel, E., Van Hoylandt, A., Verbist, G., Agonistinis, P., et al. (2016). *In vitro* generation of murine dendritic cells for cancer immunotherapy: an optimized protocol. *Anticancer Res.* 36, 5793–5802. doi: 10.21873/anticanres.11163

Barbé, C., Bartlett, J., Kong, L., Finnie, K., Lin, H. Q., Larkin, M., et al. (2004). Silica particles: a novel drug-delivery system. *J. Adv. Mater.* 16, 1959–1966. doi: 10.1002/adma.200400771

Belmans, J., Van Woensel, M., Creyns, B., Dejaegher, J., Bullens, D., and Van Gool, S. (2017). Immunotherapy with subcutaneous immunogenic autologous tumor lysate increases muring glioblastoma survival. *Sci. Rep.* 7:13902. doi: 10.1038/s41598-017-12584-0

Chen, C., Pu, F., Huang, Z., Liu, Z., Ren, J., and Qu, X. (2011). Stimuli-responsive controlled-release system using quadruplex DNA-capped silica nanocontainers. *Nucleic Acids Res.* 39, 1638–1644. doi: 10.1093/nar/gkq893

De Jong, W. H., and Brom, P. J. A. (2008). Drug delivery and nanoparticles: applications and hazards. *Int. J. Nanomed.* 3, 133–149. doi: 10.2147/IJN.S596

De Vleeschouwer, S., Arredouani, M., Adé, M., Cadot, P., Vermassen, E., Ceuppens, J. L., et al. (2005). Uptake and presentation of malignant glioma tumor cell lysates by monocyte-derived dendritic cells. *Cancer Immunol. Immunother.* 54, 372–382. doi: 10.1007/s00262-004-0615-8

Dejaegher, J., Van Gool, S., and De Vleeschouwer, S. (2014). Dendritic cell vaccination for glioblastoma multiforme: review with focus on predictive factors for treatment response. *J. Immunotargets Ther.* 3, 55–66. doi: 10.2147/ITT.S40121

Delves, P. J. (Ed.). (1998). *Encyclopedia of Immunology, 2nd Edn.* Elsevier.

Duffy, J., and Hill, A. (2011). *Suspension Stability: Why Particle Size, Zeta Potential and Rheology Are Important*. Malvern: Malvern Instruments Ltd.

Feinle, A., Leichtfried, F., Straber, S., and Husing, N. (2017). Carboxylic acid-functionalized porous silica particles by a co-condensation approach. *J. Sol-Gel Sci. Technol.* 81, 138–146. doi: 10.1007/s10971-016-4090-4

Gallas, J. P., Goupil, J. M., Vimont, A., Lavalley, J. C., Gil, B., Gilson, J. P., et al. (2009). Quantification of water and silanol species on various silicas by coupling IR spectroscopy and *in-situ* thermogravimetry. *Langmuir* 25, 5825–5834. doi: 10.1021/la802688w

Galluzzi, L., Vacchelli, E., Bravo-San Pedro, J.-M., Buque, A., Senovilla, L., Baracco, E. E., et al. (2014). Classification of current anticancer immunotherapies. *Oncotarget* 5, 12472–12508. doi: 10.18632/oncotarget.2998

Gu, J., Liu, J., Li, Y., Zhao, W., and Shi, J. (2013). One-pot synthesis of mesoporous silica nanocarriers with tunable particle sizes and pendent carboxylic groups for cisplatin delivery. *Langmuir* 29, 403–410. doi: 10.1021/la3036264

Han, L., Sakamoto, Y., Terasaki, O., Lia, Y., and Che, S. (2007). Synthesis of carboxylic group functionalized mesoporous silicas (CFMSS) with various structures. *J. Mater. Chem.* 12, 1216–1221. doi: 10.1039/b615209k

Han, L., Terasaki, O., and Shunai Che, S. (2011). Carboxylic group functionalized ordered mesoporous silicas. *J. Mater. Chem.* 30, 11033–11039. doi: 10.1039/c1jm10561b

IARC (2018). *Latest Global Cancer Data: Cancer Burden Rises to 18.1 Million New Cases and 9.6 Million Cancer Deaths in 2018*. Press release N° 263. IARC.

Kozlova, S. A., and Kirik, S. D. (2010). Post-synthetic activation of silanol covering in the mesostructured silicate materials MCM-41 and SBA-15. *Microporous Mesoporous Mater.* 133, 124–133. doi: 10.1016/j.micromeso.2010.04.024

Le Gall, C. M., Weiden, J., Eggermont, L. J., and Figdor, C. G. (2018). Dendritic cells in cancer immunotherapy. *Nat. Mater.* 17, 472–477. doi: 10.1038/s41563-018-0093-6

Liberman, A., Mendez, N., Trogler, W. C., and Kummel, A. C. (2014). Synthesis and surface functionalization of silica nanoparticles for nanomedicine. *Surf. Sci. Rep.* 69, 132–158. doi: 10.1016/j.surfrep.2014.07.001

Liechty, W. B., Kryscio, D. R., Slaughter, B. V., and Peppas, N. A. (2010). Polymers for durg delivery systems. *Annu. Rev. Chem. Biomol. Eng.* 1, 149–173. doi: 10.1146/annurev-chembioeng-073009-100847

Makkouk, A., and Weiner, G. J. (2015). Cancer immunotherapy and breaking immune tolerance: new approaches to an old challenge. *Cancer Res.* 75, 5–10. doi: 10.1158/0008-5472.CAN-14-2538

Manolova, V., Flace, A., Bauer, M., Schwarz, K., Saudan, P., and Bachmann, M. F. (2008). Nanoparticles target distinct dendritic cell populations according to their size. *Eur. J. Immunol.* 38, 1404–1413. doi: 10.1002/eji.200737984

Marasini, N., Ghaffar, K. A., Skwarczynski, M., and Toth, I. (2017). *Micro and Nanotechnology in Vaccine Development*. Elsevier.

Master Organic Chemistry LLC (2020). *Conversion of Carboxylic Acids to Esters Using Acid and Alcohols (Fischer Esterification)*. Master Organic Chemistry LLC.

Mitra, A. K., Cholkar, K., and Mandal, A. (Eds.). (2017). *Emerging Nanotechnologies for Diagnostics, Drug Delivery and Medical Devices*. Elsevier.

Musso, G. E., Bottinelli, E., Celi, L., Magnacca, G., and Berlier, G. (2015). Influence of surface functionalization on the hydrophilic character of mesoporous silica nanoparticles. *Phys. Chem. Chem. Phys.* 17, 13882–13894. doi: 10.1039/C5CP00552C

Rahman, I. A., and Padavettan, V. (2012). Synthesis of silica nanoparticles by sol-gel: size-dependent properties, surface modification, and applications in silica-polymer nanocomposites–a review. *J. Nanomater.* 2012:132424. doi: 10.1155/2012/132424

Reverchon, E., Baldino, L., Cardea, S., and De Marco, I. (2012). Biodegradable synthetic scaffolds for tendon regeneration. *Muscl. Ligaments Tendons J.* 2, 181–186.

Riley, R. S., June, C. H., Langer, R., and Mitchell, M. J. (2019). Delivery technologies for cancer immunotherapy. *Nat. Rev. Drug Discov.* 18, 175–196. doi: 10.1038/s41573-018-0006-z

Schindelin, J., Arganda-Carreras, I., and Frise, E. (2012). Fiji: an open-source platform for biological-image analysis. *Nat. Methods* 9, 676–682. doi: 10.1038/nmeth.2019

Schneider, C. A., Rasband, W. S., and Eliceiri, K. W. (2012). NIH image to imagej: 25 years of image analysis. *Nat. Methods* 9, 671–675. doi: 10.1038/nmeth.2089

Seré, S., De Roo, B., Vervaele, M., Van Gool, S., Jacobs, S., Seo, J. W., et al. (2018). Altering the biodegradation of mesoporous silica nanoparticles by means of experimental parameters and surface functionalization. *J. Nanomater.* 2018:7390618. doi: 10.1155/2018/7390618

Sharifi, S., Daghighi, S., Motazacker, B., Sanjabi, B., Akbarkhanzadeh, A., Rowshani, S., et al. (2013). Superparamagnetic iron oxide nanoparticles alter expression of obesity and T2D-associated risk genes in human adipocytes. *Sci. Rep.* 3:2173. doi: 10.1038/srep02173

Soo, S., Jung, M. H., Lee, Y.-S., Bae, J.-H., Kim, S.-H., and Ha, C.-S. (2019). Functionalised mesoporous silica nanoparticles with excellent cytotoxicity against various cancer cells for pH-responsive and controlled drug delivery. *Mater. Des.* 184:108187. doi: 10.1016/j.matdes.2019.108187

Tsai, C. T., Pan, Y. C., Ting, C. C., Vetrivel, S., Chiang, A. S. T., Fey, G. T., et al. (2009). A simple one-pot route to mesoporous silicas SBA-15 functionalized

with exceptionally high loadings of pendant carboxylicic acid groups. *Chem. Commun.* 33, 5018–5020. doi: 10.1039/b909680a

Van de Velde, A. L., Anguilie, S., Beutels, P., Dom, S., Cornille, I., Nijs, G., et al. (2014). Cost analysis of immunotherapy using dendritic cells for acurate myeloid leukemia patients. *Blood* 124:1322. doi: 10.1182/blood.V124.21.1322.1322

Van Gool, S. (2015). Brain tumor immunotherapy: what have we learned so far? *Front. Oncol.* 5:98. doi: 10.3389/fonc.2015.00098

Van Gool, S., and De Vleeschouwer, S. (2012). Shoud dendritic cell-based tumor vaccination be incorporated into standard therapy for newly diagnosed glioblastoma patients? *Expert Rev. Neurother.* 12, 1–3. doi: 10.1586/ern.12.107

Wu, S.-H., Mou, C. Y., and Lin, H.-P. (2013). Synthesis of mesoporous silica nanoparticles. *Chem. Soc. Rev.* 42, 3862–3875. doi: 10.1039/c3cs 35405a

Yamada, H., Urata, C., Aoyama, Y., Osada, S., Yamauchi, Y., and Kuroda, K. (2012). Preparation of colloidal mesoporous silica nanoparticles with different diameters and their unique degradation behavior in static aqueous systems. *Chem. Mater.* 24, 1462–1471. doi: 10.1021/cm3001688

Yang, C., Zibrowius, B., and Schüth, F. (2003). A novel synthetic route for negatively charged ordered mesoporous silica SBA-15. *Chem. Commun.* 14, 1772–1773. doi: 10.1039/B304626E

Zulfiqar, U., Subhani, T., and Husain, S. W. (2016). Synthesis and characterization of silica nanoparticles from clay. *J. Asian Ceram. Soc.* 4, 91–96. doi: 10.1016/j.jascer.2015.12.001

Conflict of Interest: The authors declare that the research was conducted in the absence of any commercial or financial relationships that could be construed as a potential conflict of interest.

frontiers in Chemistry

ORIGINAL RESEARCH
published: 20 January 2021
doi: 10.3389/fchem.2020.602941

Stimuli-Responsive, Plasmonic Nanogel for Dual Delivery of Curcumin and Photothermal Therapy for Cancer Treatment

Fadak Howaili[1], Ezgi Özliseli[2], Berrin Küçüktürkmen[2,3], Seyyede Mahboubeh Razavi[4], Majid Sadeghizadeh[1] and Jessica M. Rosenholm[2]**

[1] NanoBiotechnology Department, Faculty of Biological Science, Tarbiat Modares University, Tehran, Iran, [2] Pharmaceutical Sciences Laboratory, Faculty of Science and Engineering, Åbo Akademi University, Turku, Finland, [3] Department of Pharmaceutical Technology Faculty of Pharmacy, Ankara University, Ankara, Turkey, [4] Polymer Reaction Engineering Department, Faculty of Chemical Engineering, Tarbiat Modares University, Tehran, Iran

OPEN ACCESS

Edited by:
Wansong Chen,
Central South University, China

Reviewed by:
Zhongyang Zhang,
Aarhus University, Denmark
Jinggong Liu,
Second Affiliated Hospital of Guangzhou Medical University, China
You Yuanyuan,
Jinan University, China

***Correspondence:**
Jessica M. Rosenholm
jerosenh@abo.fi
Majid Sadeghizadeh
sadeghma@modares.ac.ir

Specialty section:
This article was submitted to Nanoscience, a section of the journal Frontiers in Chemistry

Received: *04 September 2020*
Accepted: *08 December 2020*
Published: *20 January 2021*

Citation:
Howaili F, Özliseli E, Küçüktürkmen B, Razavi SM, Sadeghizadeh M and Rosenholm JM (2021) Stimuli-Responsive, Plasmonic Nanogel for Dual Delivery of Curcumin and Photothermal Therapy for Cancer Treatment. Front. Chem. 8:602941. doi: 10.3389/fchem.2020.602941

Nanogels (Ng) are crosslinked polymer-based hydrogel nanoparticles considered to be next-generation drug delivery systems due to their superior properties, including high drug loading capacity, low toxicity, and stimuli responsiveness. In this study, dually thermo-pH-responsive plasmonic nanogel (AuNP@Ng) was synthesized by grafting poly (N-isopropyl acrylamide) (PNIPAM) to chitosan (CS) in the presence of a chemical crosslinker to serve as a drug carrier system. The nanogel was further incorporated with gold nanoparticles (AuNP) to provide simultaneous drug delivery and photothermal therapy (PTT). Curcumin's (Cur) low water solubility and low bioavailability are the biggest obstacles to effective use of curcumin for anticancer therapy, and these obstacles can be overcome by utilizing an efficient delivery system. Therefore, curcumin was chosen as a model drug to be loaded into the nanogel for enhancing the anticancer efficiency, and further, its therapeutic efficiency was enhanced by PTT of the formulated AuNP@Ng. Thorough characterization of Ng based on CS and PNIPAM was conducted to confirm successful synthesis. Furthermore, photothermal properties and swelling ratio of fabricated nanoparticles were evaluated. Morphology and size measurements of nanogel were determined by transmission electron microscopy (TEM), scanning electron microscopy (SEM) and energy-dispersive X-ray spectroscopy (EDX). Nanogel was found to have a hydrodynamic size of ∼167 nm and exhibited sustained release of curcumin up to 72 h with dual thermo-pH responsive drug release behavior, as examined under different temperature and pH conditions. Cytocompatibility of plasmonic nanogel was evaluated on MDA-MB-231 human breast cancer and non-tumorigenic MCF 10A cell lines, and the findings indicated the nanogel formulation to be cytocompatible. Nanoparticle uptake studies showed high internalization of nanoparticles in cancer cells when compared with non-tumorigenic cells and confocal microscopy further demonstrated that AuNP@Ng were internalized into the MDA-MB-231 cancer cells via endosomal route. *In vitro* cytotoxicity studies revealed dose-dependent and time-dependent drug delivery of curcumin loaded AuNP@Ng/Cur. Furthermore, the developed nanoparticles showed an improved chemotherapy efficacy

when irradiated with near-infrared (NIR) laser (808 nm) *in vitro*. This work revealed that synthesized plasmonic nanogel loaded with curcumin (AuNP@Ng/Cur) can act as stimuli-responsive nanocarriers, having potential for dual therapy i.e., delivery of hydrophobic drug and photothermal therapy.

Keywords: plasmonic nanogel, AuNP, curcumin, stimuli-responsive, photothermal therapy

INTRODUCTION

Breast cancer is the second most common cause of cancer among women worldwide (Bray et al., 2018). Breast cancer treatment usually requires a combination of chemotherapy, radiotherapy, and surgery (Waks and Winer, 2019). However, conventional chemotherapy agents suffer from a lack of aqueous solubility, lack of selectivity, and are subject to multidrug resistance. Nanotherapeutics are rapidly developing to overcome the limitations of traditional drug delivery systems (Dong et al., 2019; He et al., 2020; Liu et al., 2020). Common anticancer drugs damage peripheral tissues and cells other than the targeted tissue, and here, using herbal medicines could be a safer alternative choice to avoid harmful side effects (Pavan et al., 2016; Unlu et al., 2016; Oun et al., 2018). Curcumin is the main component of turmeric, a polyphenol with low molecular weight. *In vivo* studies have shown that curcumin helps to prevent metastatic progression in models of breast cancer and to inhibit cancer cell proliferation and invasion by downregulating the PI3K/Akt signaling pathway (Xu et al., 2014). However, the most significant problems restricting its use in therapy are the poor solubility, instability, rapid metabolism, systemic elimination, and inadequate tissue absorption of curcumin (Kunnumakkara et al., 2017). For instance, the administration of 8 grams of curcumin per day led to only 1.77 μM absorption in the body (Unlu et al., 2016). Thus far, various approaches have been used to overcome curcumin-related issues, some of which are using nanocarriers such as phospholipids, micelles, liposomes, and polymeric nanoparticles (Gatti and Perucca, 1994; Kunwar et al., 2006; Li et al., 2007; Ma et al., 2007; Suresh and Srinivasan, 2007; Takahashi et al., 2009; Bani et al., 2016; Esmatabadi et al., 2018; Farsani et al., 2020). Nanogels are water-soluble crosslinked hydrogel materials that have both hydrogel and nanoparticle properties at the same time, in addition to controlled drug release capability. These carriers thus provide a polymeric nanotechnological approach which has exceptional characteristics such as high drug loading capacity, high stability, responsiveness to a wide variety of environmental stimuli whereby they may shrink or swell in response to pH or temperature change, resulting in the release of the drug under specific conditions. Hence, various bioactive compounds can be encapsulated into nanogels, exceptionally also hydrophobic drugs (Maya et al., 2013). In this context, the use of a responsive polymer for the synthesis of the nanogel is one method of delivering drugs to cancer cells. PNIPAM is a pH and temperature-responsive polymer that can be synthesized via free-radical polymerization. It can be effectively functionalized, making it useful in a range of medical applications. It undergoes a reversible lower critical solution temperature (LCST) around 32°C in water, in which the phase transition from a swollen hydrated state to a shrunken dehydrated state takes place; losing about 90% of its volume(Ormategui et al., 2012). Since PNIPAM expels its liquid content at temperatures close to the human body, several researchers have investigated its potential applications in tissue engineering, biosensors and controlled drug delivery, but its use is limited due to its synthetic nature (Guan and Zhang, 2011). In comparison, the use of chitosan, a natural polymer, enhances the biodegradability and biocompatibility of the synthesized nanogel and improves PNIPAM's LCST by rising it to a drug-release-appropriate temperature at or above body temperature (Oh et al., 2010; Pereira et al., 2015).

AuNP has attracted tremendous as promising PTT agents for the treatment of malignant tumors with impressive localized surface-plasma-resonance (LSPR) properties including absorption in the NIR region, which is essentially required for PTT. Additionally, AuNP is visible in confocal laser scanning microscopy through internal reflection, which provides a tool for tracking the uptake of nanoparticles by cells (Shukla et al., 2005; Murphy et al., 2008; Kim et al., 2015). The present contribution reports the development of stimuli-responsive plasmonic nanogel for combinable curcumin and photothermal therapy, composed of AuNP and PNIPAM-chitosan nanogel. In this work, citrate capped AuNP were synthesized using the Turkevich method and were incorporated into the nanogel in order to introduce imaging and PTT capabilities to the synthesized nanogels (**Figure 1**). Physicochemical properties of developed nanogel including morphology, size, net surface charge (zeta potential), swelling ratio, thermal analysis and size dispersity were characterized. Developed nanogel delivery system not only showed excellent cytocompatibility but could also be utilized as a cellular imaging probe due to the strong light scattering property of incorporated AuNP. Moreover, the chemotherapy, laser-induced PTT therapy efficacy and quantitative cellular uptake of multifunctional AuNP@ Ng were compared by using curcumin as a chemotherapeutic agent and testing single and combined therapy on MDA-MB-231 breast cancer cells and non-tumor cell line MCF 10A. The results showed sustained drug release from nanoparticles and a significant synergistic effect upon combined therapy.

EXPERIMENTAL

Materials

The medium molecular weight chitosan (CS) (190–310 kDa and degree of deacetylation of 75–85%), L-cysteine

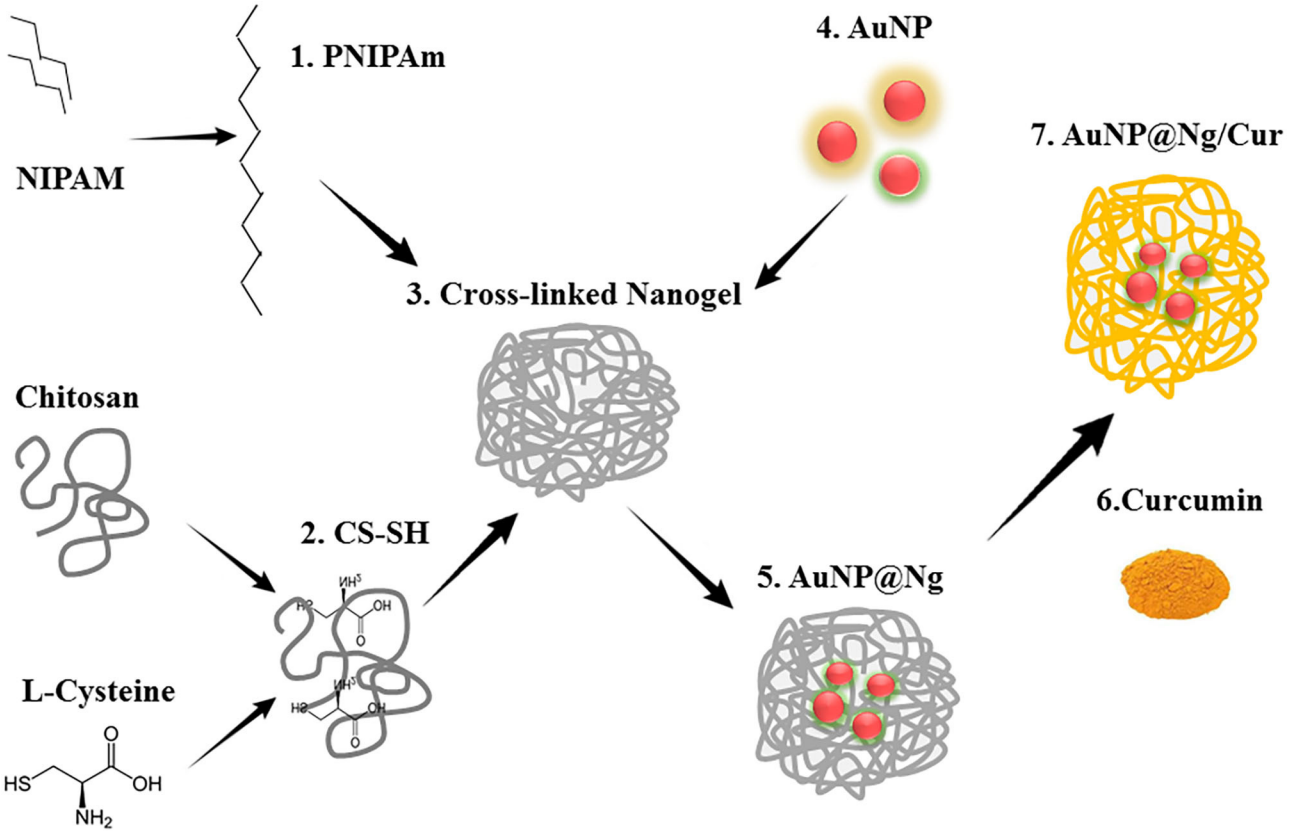

FIGURE 1 | Graphical abstract showing the steps of formation of AuNP@Ng/Cur. Chitosan was thiolated using L-Cysteine, afterwards, it crosslinked to PNIPAM to form the nanogel. The next step was the incorporation of AuNP to nanogel via semi covalent bond of the gold nanoparticle to SH groups in the nanogel. In the end, using the incubation method, the curcumin was loaded to AuNP@Ng.

97%, 1-ethyl-3-(3-dimethylaminopropyl)carbodiimide(EDC) 99%, N-isopropylacrylamide 97%, acetic acid glacial ≥99%, N, N′-methylenebis(acrylamide) (MBA)99%, ammonium persulfate (APS) 98%, hydrochloric acid 37%, gold(III) chloride trihydrate ≥99.9%, sodium citrate dihydrate ≥99%, curcumin powder from Curcuma longa (Turmeric), crystal Violet solution 2.3% (w/v), paraformaldehyde 95% (PFA), hydrocortisone, cholera toxin and insulin all were commercially available and supplied from Sigma-Aldrich Co. Dulbecco's Modified Eagle's Medium (DMEM), Penicillin-Streptomycin, Dulbecco's Phosphate Buffered Saline, Penicillin-Streptomycin(pen/strep) and L-Glutamine were obtained from Lonza. Dil Stain (1,1'-Dioctadecyl-3,3,3',3'-Tetramethylindocarbocyanine Perchlorate ['DiI'; DiIC18(3)], Gibco fetal bovine serum (FBS), Gibco DMEM/F12–Dulbecco's Modified Eagle Medium: Nutrient Mixture F-12, Gibco horse serum and MEM Non-Essential Amino Acids Solution (100X) (NEAA) were purchased from Thermofisher. The epidermal growth factor was purchased from Abcam. AlamarBlue Cell Viability Reagent was obtained from TCI Europe and Vectashield DAPI mounting media from Vector Labs.

Synthesis of AuNP@Ng/Cur

The chitosan was thiolated via attaching L-cysteine to chitosan by the formation of amide bonds to connect the AuNP with Ng, the degree of thiol group modification was measured spectrophotometrically with Ellman's reagent (Schmitz et al., 2008). Subsequently, thiolated Chitosan-PNIPAM Ng were synthesized employing the free radical surfactant-free emulsion polymerization method following the previously described procedure with some desired modification. Briefly, to ionize free -NH_2 group of CS, 500 mg of thiolated CS (4.618 ± 0.25 μmol SH /mg CS) was dissolved in 20 ml acetic acid (1%) solution in a 250 ml three-neck round bottom flask on the heater stirrer under nitrogen atmosphere. After the absolute dissolution of ionized chitosan, 500 mg of NIPAM dissolved in 80 ml of Milli-Q water and 1.7 mg MBA as a crosslinker were added to the reaction, and the temperature was increased gradually to the 80°C. The polymerization was initiated by adding 0.85 ml APS (0.05M in water) as an initiator to the flask after purging with nitrogen for about 30–40 min. The reaction was proceeded for 3 h at 80°C and then terminated by cooling down to room temperature. The obtained samples were filtered with a 1 μm membrane filter and then dialyzed with a dialysis membrane (12,000 Da MWCO)

against Milli-Q water, the water was changed periodically 15 times for 3 days. For long-term storage, nanogel was freeze-dried overnight (Echeverria et al., 2015; Khan et al., 2015).

The Turkevich method was used to synthesize Citrate capped AuNP (Kimling et al., 2006). Subsequently, in order to attach AuNP to nanogel via semi covalent interaction of SH group of Ng and AuNP, 1 ml (5 mg/ml) of synthesized nanogel was added to 5 ml (1 mg/ml) of AuNP suspension and continuously stirred for 2 days at room temperature in the dark. The content was then dialyzed against Milli-Q water overnight using a dialysis membrane (12,000 Da MWCO), and the water was changed at specified intervals (Ding et al., 2009). Curcumin was loaded to the nanogel using the incubation method. Briefly, curcumin (0.25 and 0.5 mg/ml) was dissolved in ethanol with 1 mM concentration and added to the 1 ml AuNP@ nanogel and 1 ml nanogel solution dropwise and at a temperature higher than 32°C under constant stirring in the dark for 24 h. Finally, nanogel was centrifuged by Thermo Scientific™ Sorvall LYNX 4000 Centrifuge at 8,000 rpm for 20 min and lyophilized overnight in Heto CT60e freeze-dryer for storage (Luckanagul et al., 2018).

Characterization of AuNP@Ng/Cur

To analyze the structure of synthesized nanogel, the FTIR spectra of CS, thiolated CS, NIPAM, SH- CS-PNIPAM were obtained using Perkin-Elmer Spectrum Two, scanning from 4,000 to 400 cm^{-1}.

In order to calculate the deswelling ratio of synthesized nanoparticles, the average hydrodynamic size of nanogel and AuNP@Ng was determined at different temperatures and then the deswelling ratio was calculated according to the following equation (Zhao et al., 2019; Agnihotri et al., 2020):

$$Deswelling\ ratio = S_s/S_d \quad (1)$$

Where the S_s is the size of Ng in room temperature and S_d is the size of Ng above LSCT which we measured at 25, 32, 37, 42, and 60°C temperature.

Moreover, polydispersity index (PDI) and zeta potential of nanogel were determined at 25, 32, 37, 42, and 60°C by a Malvern Zeta Sizer ZS (PCS, Malvern Instruments Ltd). The optical properties of AuNP@Ng were obtained by Themo scientific 2000c UV-Vis spectrophotometer using a 1-cm-wide quartz cuvette. TEM was conducted using JEM-1400 Plus TEM following negative staining with uranyl acetate to confirm the size of nanogel as well as the morphology. TEM images were illustrated using Fiji Image J software.

Using a field-emission SEM (FESEM) TeScan-Mira III model, 10 times diluted AuNP@Ng/Cur nanoparticles were sputter-coated with gold after dropping it on the grid to achieve more homogeneous and transparent images. SEM and Elemental analysis for AuNP@Ng/Cur was acquired by EDX X-ray detector of SEM (Thermo Scientific LEO Gemini 1530 model (using uncoated sample.

The thermal analysis of synthesized AuNP@Ng/Cur, AuNP, and control (nanogel) were characterized by measuring the temperature at different time points of 0, 3, 5, 7, and 10 at two different concentrations of 2.5 and 5 μg/ml under NIR exposure(Fu et al., 2018). Using thermal camera GUIDE B from Sensmart, the thermal image and measured temperature were obtained and the temperature change (ΔT) was determined using the following equation (Fu et al., 2018):

$$\Delta T = T_2 - T_1 \quad (2)$$

ΔT is the temperature difference between two heating times. T_2 is the temperature measured for one nanoparticle at one-time point and T_1 is the temperature measured for control at the same time point.

Encapsulation Efficiency (EE%) and Drug Loading (DL%)

The EE% of AuNP@Ng/Cur was determined by measuring the amount of curcumin indirectly from the supernatant. Briefly, Curcumin (0.25 and 0.5 mg/ml) was dissolved in ethanol and then added to both 1 ml Ng and 1 ml AuNP@Ng and stirred for 24 h at room temperature by protecting from light. The following day, nanogel was centrifuged at 3,000 rpm for 5 min. The supernatant was collected, and the amount of excessive curcumin was estimated by using Thermo scientific 2000c UV-Vis spectrophotometer at 450 nm. The EE% and gDL% were calculated using the following equations (Equations 3, 4) (Sarika et al., 2016; Luckanagul et al., 2018).

$$EE\% = \frac{Total\ amount\ of\ \ feeding\ curcumin - free\ curcumin}{Total\ amount\ of\ curcumin} * 100 \quad (3)$$

$$DL\% = \frac{Total\ amount\ of\ feeding\ curcumin\ \ - Free\ curcumin}{Weight\ of\ nanogel} * 100 \quad (4)$$

In vitro Curcumin Release

In vitro curcumin release from nanogel and AuNP@Ng was carried out in a shaker incubator in phosphate-buffered saline containing Tween 80 (0.5% w/v) in two different pH values (pH 7.4 and pH 5.5) and two different temperatures (25 and 37°C) ($n = 3$) for 72 h. Samples were collected (1 ml) at defined time intervals and centrifuged at 13,000 rpm for 8 min. The absorption intensity of the diluted supernatant in DMSO was measured at 450 nm(Sarika and Nirmala, 2016).

Cell Studies

Cell Culture and Maintenance

Human triple-negative breast cancer cell line MDA-MB-231 was cultured with Dulbecco's modified Eagle's medium (DMEM) supplemented with 10% heat-inactivated fetal bovine serum (FBS), 2 mM L-glutamine, 0.1 mM MEM Non-Essential Amino Acids (NEAA), 100 IU/ml penicillin and 100 ug/ml of Streptomycin at 37°C with 5% CO_2. Cells were passaged when they reached 80–90% confluency. Human breast epithelial cell line MCF10A was cultured with Dulbecco's Modified Eagle Medium: Nutrient Mixture F-12 (DMEM/F12) supplemented with 5% heat-inactivated horse serum, 100 IU/ml penicillin and 100 ug/ml of Streptomycin, 20 ng/ml Epidermal Growth Factor, 0.5 mg/ml hydrocortisone, 10 μg/ml insulin and 100 ng/ml cholera toxin.

Cytotoxicity and Chemo-Photothermal Efficacy of AuNP@Ng/Cur Nanoparticles

Alamar Blue cell proliferation assay was carried out to investigate the cytocompatibility of AuNP@Ng and AuNP@Ng/Cur nanoparticles. Briefly, MDA-MB-231 cells (5×10^3 cells/cm^2) and MCF10A cells (7.5×10^3 cells/cm^2) were cultured in a 96-well plate overnight and cell media was replaced with pre-warmed fresh media containing AuNP@Ng (30-60-120 μg/ml) with the corresponding concentrations of AuNP(5-10-20 μg/ml), and nanogel (25-50-100 μg/ml) individually ($n = 4$). Cytotoxicity of nanoparticles was evaluated after 24 and 48 h incubation. Subsequently, the Alamar Blue reagent was added to each well (10% final concentration) as suggested by the manufacturer and incubated at 37°C for 4 h to allow resazurin to undergo metabolic reaction. Fluorescence intensity of reduced form of resazurin was measured spectrophotometrically at 570 nm excitation and 580–600 nm as emission wavelength (Wu et al., 2011; Osterman et al., 2016; Tang et al., 2020) by using Thermo Scientific Varioskan Flash multi-plate reader. The percentage of cell proliferation was reported relative to untreated cells (100% viability) according the following equation using relative fluorescence units (RFU) (Eilenberger et al., 2018):

$$Cell\ viability\ \% = \frac{Experimental\ RFU\ with\ chemical\ compound - background\ RFU}{Untreated\ cell\ control\ RFU\ value - background\ RFU} * 100 \quad (5)$$

The data in each time point were normalized by their corresponding control. A similar procedure was followed to determine the cytotoxicity of AuNP@Ng/Cur. Cells were incubated with the cell media suspension of free curcumin, AuNP@Ng and AuNP@Ng/Cur containing 10, 25, 50, and 100 μg/ml curcumin for 24 and 48 h ($n = 4$). At designated time intervals, Alamar Blue reagent was added to suspension, and fluorescence was measured after 4 h incubation. The autofluorescence of curcumin was subtracted from the acquired measurements.

For photothermal and curcumin-photothermal treatment, the MDA-MB-231 cells were incubated with AuNP, AuNP@Ng, AuNP@Ng/Cur containing 5 μg/ml and 2.5 μg/ml AuNP for 24 h. Following day, the MDA-MB-231 cells were exposed to 2.19 W/cm2, 808 nm NIR laser for 10 min by an ∼6 mm focused spot size, and cell viability was determined by Alamar Blue assay described as previously (Yang et al., 2017; Ong et al., 2019; Park et al., 2019). In parallel, cells were stained with crystal violet after NIR laser treatment to demonstrate the effect of chemo-photothermal treatment on MDA-MB-231 cells visually. Cell media was discarded, and the cells were washed 2 times with 300 μl of PBS, following with the fixation using 200 μl of 4% PFA for 7 min at RT. Finally, the fixed cells were stained with 200 μl crystal violet stain (0.1% in 20% methanol) for 5 min and subsequently washed twice with 300 μl Milli-Q water to remove the excess dye and left to dry. Cell images were acquired by Thermo Fisher EVOS XL Core Cell Imaging System (Palmieri et al., 2015).

Cellular Uptake Study of AuNP and AuNP@Ng by Flow Cytometry and Confocal Microscopy

Cellular internalization of AuNP, AuNP@Ng, and Ng was investigated for cancer cell line MDA-MB-231 and non-tumorigenic cell line MCF10A by using flow cytometry. In brief, MDA-MB-231 and MCF10A cells were seeded in the 12-well plates for overnight attachment with the concentration of (60×10^3 cells/cm^2) and (90×10^3 cells/cm^2), respectively. One day later, the cell media was substituted by fresh media containing AuNP (20 μg/ml), nanogel (100 μg/ml), and AuNP@Ng (120 μg/ml) and incubated at 37°C, 5% CO_2 for 24 h ($n = 3$). Afterwards, cells were harvested with trypsinization, washed twice with ice cold PBS and resuspended in 250 μl of PBS, kept on ice until analysis (Bansal et al., 2020). Mean fluorescence intensity was recorded by using a 561 nm excitation laser and the emission was collected by using RFP 582/15 band pass filter with LSRFortessa (BD Sciences, San Diego, CA, USA). The analyzer was set to record 10,000 events per sample. Flowing Software (Open source software, Turku Center for Biotechnology, Finland) was used for data analysis and WinList 9.0 was used for the visualization of the overlay histograms.

For confocal microscopy, MDA-MB-231 cells were seeded on autoclaved coverslips (19ø) at the density of 16×10^3 cells/cm^2 in 12-well cell culture plates to examine the cellular uptake of AuNP@Ng and Au@Ng/Cur and incubated for 24 h at 37°C. Following day, cells were treated with AuNP, nanogel, AuNP@Ng, and AuNP@Ng/Cur with the concentration range of 2.5–5 μg/ml AuNP, by replacing fresh media containing nanoparticles. After 24 h incubation, cells were rinsed with PBS, and the cell membrane was stained by incubating cells with 1 ml fresh cell media containing 1 μg/ml of DiI hydrophobic dye for 10 min at 37°C. Stained cells were fixed with 4% PFA for 10 min at room temperature, washed thrice with PBS followed by a final washing with MiliQ water. Coverslips were mounted with VECTASHIELD mounting medium and cellular uptake of nanoparticles was imaged by Leica TCS SP5 confocal microscopy. AuNP were detected by reflection imaging by using 488 nm excitation, 481–493 nm emission, and DiI cell membrane dye was detected with 561 nm excitation, 563–612 nm emission wavelength. Images were illustrated using Fiji Image J software (Liu et al., 2015; Senthilkumar et al., 2015).

Statistical Analysis

Statistical analysis was carried out using two-way ANOVA accompanied by Tukey's multiple comparisons test and two-tailed Student's *t*-test in GraphPad Prism 6 software. The collected data is presented in terms of "mean ± standard deviation" values. If the $p < 0.05$, differences are considered statistically significant.

RESULTS AND DISCUSSION

Synthesis and Characterization of Nanogel, AuNP@Ng and AuNP @Ng/Cur

In this study, thermo-responsive plasmonic nanogel was synthesized in order to increase the solubility of curcumin and prevent its rapid degradation metabolism. AuNP were incorporated into the nanogel to add PTT features to the product by thiolating the chitosan using L-cysteine, and the amount of free thiol group on chitosan was quantified using Ellman's reagent. As shown in **Table 1**, by increasing the EDC amount from 150 to 200 mM, the ratio of thiol group on the CS backbone increased from 4.618 ± 0.25 to 9.247 ± 0.381 μmol/mg. Afterward, NIPAM was grafted to thiolated chitosan and crosslinked using MBA. NIPAM/MBA was polymerized by a free radical surfactant-free emulsion polymerization method to form CS-based Ng. For this purpose, PNIPAM and MBA were grafted to CS by the formation of an amide bond between the free -NH_2 group of chitosan and the carboxyl group of NIPAM as well as by free-radical generated onto the CS (Wu et al., 2018). Polymer networks have been formed using MBA as a crosslinker during polymerization. AuNP were then synthesized by the Turkevich process, and incorporated by the semi-covalent bond of -SH groups in the thiolated CS into the nanogel. Finally, curcumin was loaded at a temperature higher than LCST using the incubation method to facilitate the hydrophobic interaction between curcumin and nanogel, which can be clarified based on the phase change from hydrophilic to hydrophilic PNIPAM (Asghar et al., 2017; García-Peñas et al., 2019).

FTIR spectroscopy was used to demonstrate the presence of different functional groups in the nanogel system. The FTIR spectra of pure NIPAM, chitosan, thiolated chitosan, and nanogel are demonstrated in **Figure 2A**, The spectrum of thiolated-CS showed deformation of the –NH- stretching signal at 3225 cm^1 compared to chitosan spectra [**Figure 2A(a,b)**], which confirm the formation of (C-NH) amide bond by attachment of amine groups of chitosan to carboxyl groups of L-cysteine. Moreover, the amine groups of chitosan have sharp peaks in the wavelength between 1,450 and 1,650, and these peaks get weaker after thiolation with the L-cysteine as a result of the formation of amide bonds (Esquivel et al., 2015). In NIPAM spectrum, peaks around 3,280, 1,622, and 1,414 cm^{-1} are assigned to C-H, C=C and CH_2 = respectively, characteristic of vinyl monomer (**Figure 2A**). Compared to NIPAM and thiolated chitosan spectra, the CS-PNIPAM spectrum showed some new signals and many others either disappeared or deformed. As shown in **Figure 2A**, the FTIR spectrum of pure NIPAM has peaks characterizing double bonds, but the FTIR spectrum of nanogel did not show any characteristic peak of the double bond in the range of 1,600–1,650 cm^{-1} (C=C aliphatic and aromatic) and 610–990 cm^{-1} (stretching mode of vinyl double bonds). Similarly, no characteristic peaks of cis-trans and substituted groups with double bonds (700–900 cm^{-1}) or a peak for =C-H could be found. Furthermore, the broad and intense peak near 3,292 cm^{-1} suggests N-H stretching in the spectrum of Ng. This peak showed hydrogen bonding due to the presence of water of hydration attached to the polymer and confirmed gel formation. Thus, our FTIR spectrum results suggest successful CS-PNIPAM polymerization and nanogel formation (**Figure 2A**; Kim et al., 2005; Shah et al., 2013; Esquivel et al., 2015; Khan et al., 2015).

The interaction of AuNP [**Figure 2C(a)**] with Ng [**Figure 2C(b)**] and curcumin loading in AuNP@Ng [**Figure 2C(d)**] was further investigated with UV-spectroscopy. As shown in **Figure 2B(a)** peak at 522 nm can be ascribed to the plasmon resonance effect of the AuNP. After the interaction of AuNP with nanogel, the AuNP peak had a lower absorbance value and showed a redshift in wavelength; this shift in the plasmon resonance effect of the AuNP confirms the interaction of AuNP with Ng and formation of AuNP@Ng (Park et al., 2018). The UV-VIS spectroscopy was also employed to confirm the curcumin loading of AuNP@Ng. As shown in **Figure 2B**, there is a peak at 450 nm in addition to the AuNP peak in the spectrum of AuNP@Ng/Cur, which indicated the encapsulation of curcumin by the nanogel. The difference in the intensity of peaks is due to the difference in concentration of AuNP and curcumin in AuNP@Ng and AuNP@Ng/Cur samples compared to bare curcumin and AuNP (Alam et al., 2012).

Formulated AuNP@Ng were characterized in terms of dynamic light scattering (DLS) analysis, to determine the average hydrodynamic diameter, polydispersity index (PDI), and zeta potential (ZP). The hydrodynamic diameter, PDI, and ZP of bare AuNP were 22.24 nm, 0.305, and −31.1 mV, respectively. Besides, DLS results showed a larger average particle size for AuNP@Ng (215.16 ± 5.78 nm) compared to the bare nanogel (166.8 ± 0.60 nm) (**Table 2**). The results could be explained with the size of nanogel depending on how many AuNP could attach to the CS-SH in the cross-linked nanogel, resulting in a reduction of monodispersity. The size of plasmonic nanogel after curcumin loading was found to be 226 ± 1.49 nm, and it was seen that curcumin loading did not significantly change the nanoparticle size. This result may be due to the high loading capacity of the plasmonic nanogel attributed to its softness and flexibility, where curcumin can be trapped easily (Karg et al., 2019). Changes in the size and swelling ratio of nanoparticles under different environmental conditions may have an impact on the controlled release of drugs. Therefore, to observe the thermal response

TABLE 1 | Characterization of thiolated CS using Ellman's reagent.

CS-SH	CS solution (12.5 mg/ml)	EDC (mM)	L-cystiene(mg)	Total thiol groups (μmol/mg CS) ±SD	Free thiol group (umol/mg) ±SD
1	0.5 ml	150	62	4.618 ± 0.25	0.967 ± 0.013
2	0.5 ml	200	62	9.247 ± 0.381	2.289 ± 0.062

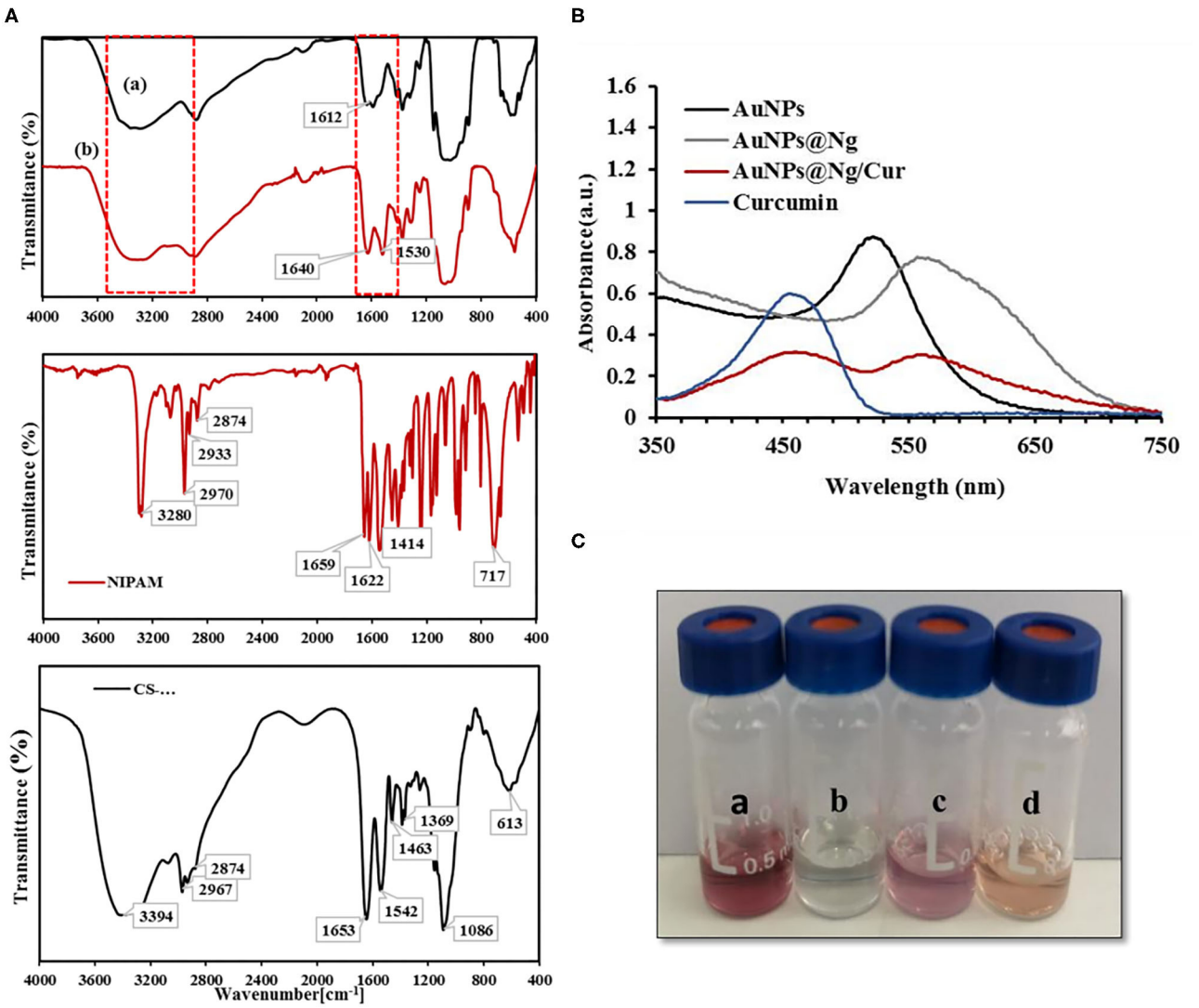

FIGURE 2 | FT-IR spectra of chitosan **(a)**, thiolated chitosan **(b)**, pure NIPAM and Ng. **(A)** UV-VIS spectrum of AuNP, Curcumin, AuNP@Ng, and AuNP@Ng/Cur **(B)**. Physical appearance of AuNP **(a)**, Ng **(b)**, AuNP@Ng **(c)**, and AuNP@Ng/Cur **(d) (C)**.

behavior of synthesized nanoparticles, DLS measurements were applied. For this reason, the size of nanogel and AuNP@Ng was measured at different temperatures: 25, 32, 37, 42, and 60°C and the deswelling ratio was calculated according to Equation 1. As shown in **Figure 3B**, by increasing the temperature to 37°C the size of AuNP@Ng and nanogel were significantly reduced ($P < 0.0001$), and this reduction continued slightly above 37°C. Accordingly, as shown in **Figure 3A**, the deswelling ratio significantly increased ($P < 0.0001$). This change in size demonstrated the thermo-responsive behavior of synthesized nanogel due to the low critical solution temperature property of PNIPAM, which makes the nanogel collapse in temperatures higher than LCST. The LCST of PNIPAM is 32°C, but the use of chitosan increased the LCST of PNIPAm to 37°C, making the drug delivery system more suitable for drug release at body temperature (Ashraf et al., 2016). Thermally-induced color change from transparent to milky was observed by increasing the temperature of Ng as a result of phase transition from swollen state to shrunk state (**Figure 3B**; Christau et al., 2016).

TABLE 2 | Average size, PDI, and Zeta potential of AuNP, Ng, AuNP@Ng, and AuNP@Ng/Cur determined using DLS and TEM.

Nanoparticle	TEM size (nm)	DLS size (nm)	PDI	Zeta potential (mV)
AuNP	19.57 ± 1.22	22.24 ± 0.131	0.051	−31.1
Ng	167.81 ± 4.74	166.8 ± 0.60	0.195	3.97
AuNP@Ng	197.94 ± 2.33	215.16 ± 5.78	0.228	0.655
AuNP @Ng/Cur	214.77 ± 4.28	226 ± 1.49	0.354	0.676

Zeta potential is one of the most crucial parameters in colloidal systems that affect the fate of nanoparticles in

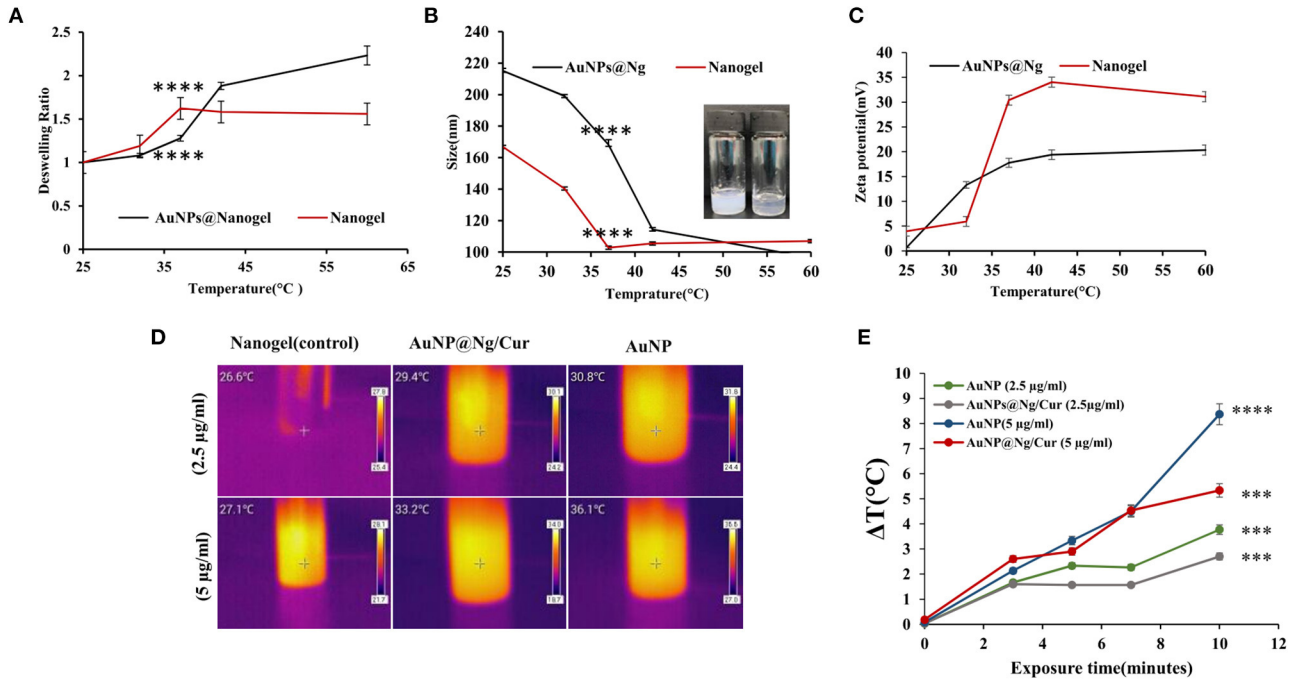

FIGURE 3 | Deswelling ratio of Nanogel and AuNP@Ng at different temperatures. **(A)** The average sizes of the Ng and AuNP@Ng at different temperatures (25–60°C) measured by DLS, physical appearance of Ng at different temperatures of 25 and 42°C. **(B)** Zeta potential of AuNP@Ng and Ng at different temperatures. **(C)** Thermal images of Ng, AuNP and AuNP@Ng/Cur in two different concentrations after 10 min exposure of NIR irradiation. **(D)** ΔT(°C) of AuNP and AuNP@Ng/Cur solutions at different time points after NIR irradiation. **(E)** Two-way ANOVA followed by Tukey's multiple comparisons test was performed to investigate the significant difference (****$p < 0.0001$; ***$p < 0.0001$–0.001).

drug delivery, cellular uptake, and drug interactions with the surrounding environment (Honary and Zahir, 2013). In this study, the zeta potential measurement of AuNP@Ng at different temperatures showed a considerable increase from 0.665 mV at 25°C to 17.76 ± 0.64 mV at 37°C, still gradually increasing to 20.33 ± 0.305 mV at 60°C. Nanogel has a more abrupt change in zeta potential compared to AuNP@Ng at 37°C. This data supports the shrinkage of the nanogel by increasing the temperature, which is due to the placement of positively charged isopropyl groups of polymer on the surface of nanogel in temperatures higher than LCST (**Figure 3C**; Utashiro et al., 2017).

The presence of AuNP incorporated in the nanogel improves the therapeutic effect of the formulation by means of AuNP's surface plasmon resonance property generating heat after exposure to NIR irradiation. In order to demonstrate the photothermal activity of synthesized nanoparticles, nanogel, AuNP, and AuNP@Ng/Cur thermal analysis after exposure of 808 nm NIR laser were assessed at different time points. According to statistical analysis, calculated ΔT according to Equation 1 at different time points of 0, 3, 5, 7, and 10 min showed significant time and dose dependent differences in comparison with the control samples ($P < 0.001$). Both AuNP@Ng/Cur and AuNP samples, respectively, exhibited 5.1 and 8.4°C temperature raise compared with control (**Figure 3E**; Fu et al., 2018). The thermal images show the temperature change of samples after 10 min of exposure of NIR radiation for two different concentration of AuNP, nanogel, and AuNP@Ng/Cur (**Figure 3D**).

According to TEM analysis, AuNP (**Figure 4A**), nanogel (**Figure 4B**), AuNP@Ng (**Figure 4C**), and AuNP@Ng/Cur (**Figure 4D**) were found to be of spherical shape, showing an excellent monodispersity with a corresponding hydrodynamic size of 19.57 ± 1.22, 167.81 ± 4.74, 197.94 ± 2.33, and 214.77 ± 4.28 nm, respectively (**Table 2**). The hydrodynamic size of the nanoparticles obtained by TEM analysis was found smaller compared to the diameter obtained by the DLS method, which is expected due to the difference in the operating principles of these two measurement methods (Kaasalainen et al., 2017). Attributed to the impact of the dispersant on the hydrodynamic diameter of the nanogel, it is predicted that the values obtained from DLS would be slightly higher than TEM, which reveals the solid state size of Ng upon TEM imaging (Zhao et al., 2011).

Due to the impact of drying on the nanogel network structure, FESEM and SEM imaging showed distributed spherical AuNP@Ng/Cur with some heterogeneous nanoparticles (**Figures 4E,F**) (Sidhu et al., 2019). The AuNP@Ng/Cur elemental analysis (EDX) (**Figure 4G**) showed a high content of carbon, nitrogen, and oxygen elements corresponding to chitosan, PNIPAm, and curcumin in the nanogel structure,

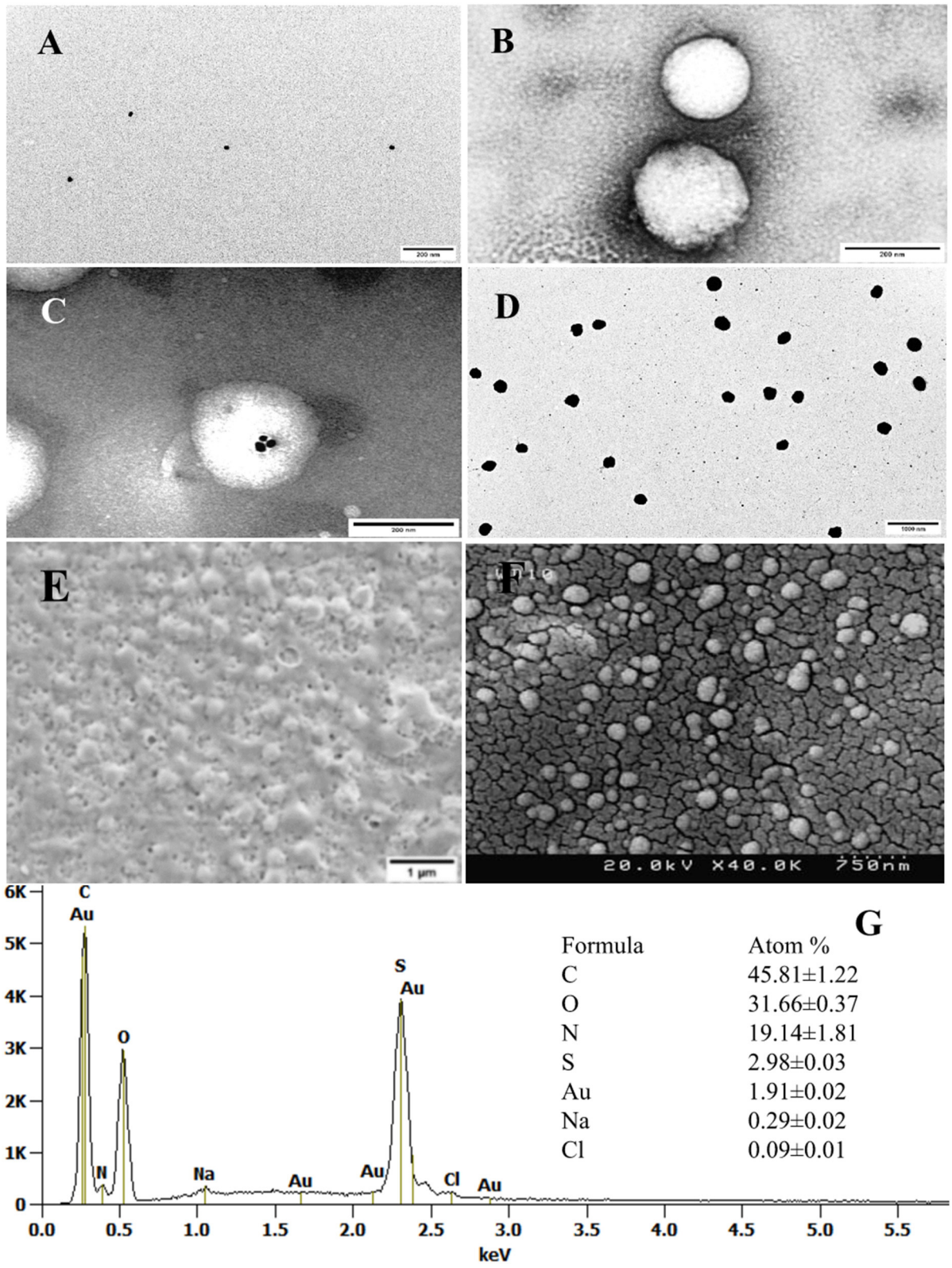

FIGURE 4 | Electron micrograph and analysis. TEM images of the AuNP **(A),** Negatively stained Ng **(B)**, and AuNP@ Ng with uranyl acetate (scale bar 200 nm) **(C)** AuNP@ Ng loaded with Curcumin without being negatively stained (scale bar 1000 nm) **(D).** Untreated SEM image of AuNP@Ng/Cur (scale bar 1μm) **(E)**. Gold sputter-coated AuNP@Ng/Cur FESEM image (scale bar 750 nm) **(F)**. EDX spectrum and quantitative atom% information of AuNP@Ng/Cur **(G)**.

TABLE 3 | DD% and EE% of nanogel before and after conjugation with AuNP.

Nanoparticle	Concentration of curcumin (mg/ml)	DL (%) ± SD	EE (%) ± SD
Ng	0.25	4.7 ± 0.57%	69.03 ± 1.39%
Ng	0.5	8.04 ± 0.25%	90.03 ± 1.01%
AuNP @Ng	0.25	9.2 ± 0.43%	84 ± 1.62%
AuNP @Ng	0.5	17.01 ± 0.33%	92 ± 0.98%

Moreover, the presence of sulfur and gold in the elemental analysis verified the synthesis of thiolated chitosan and existence of AuNP in the structure of AuNP@Ng/Cur (Sidhu et al., 2019).

Curcumin Loading and Encapsulation Efficiency in AuNP@Ng

Curcumin is classified as a Biopharmaceutics Classification System (BCS) Class IV substance and thus, exhibits both poor solubility and permeability (Wang et al., 2017). Consequently, low bioavailability, low solubility in water, and rapid metabolism of curcumin lead to profound problems in inducing an anti-cancer effect. Here, using a plasmonic nanogel as a drug delivery system could protect curcumin from rapid metabolism inside the body and could circumvent any solubility and permeability issues, since these would be determined by the carrier. The higher the drug loading and EE% of a carrier, along with low premature drug loss would overall result in a more significant impact. It has been reported that polymeric Ng have promising potential as drug delivery carriers in terms of drug loading capacity, biocompatibility, and thermal responsivity (Liechty and Peppas, 2012). It is expected that the interaction between nanogel and curcumin is hydrophobic due to the interaction between curcumin and PNIPAM (Asghar et al., 2017). The curcumin loading capacity and EE% of nanogel were measured spectrophotometrically and calculated before and after conjugation with AuNP with two different concentrations of curcumin (0.25 and 0.5 mg/ml). The highest DL% (17%) and EE% (92%) were found with AuNP@Ng formulation at a concentration of 0.5 mg/ml curcumin (**Table 3**). The higher EE% and DL% of AuNP@Ng compared to nanogel is probably related to the ability of curcumin to conjugate to AuNP (Luckanagul et al., 2018). Moreover, it has been observed that the conjugation efficiency of curcumin to AuNP increases with respect to time (Mahalunkar et al., 2019). In this study, it was thought that the 24-h mixing time after adding curcumin to the formulation also increased the conjugation of curcumin to gold nanoparticles. Ng, on the other hand, have the ability to trap drugs due to the presence of an internal network structure(Ghorbani et al., 2016; Vashist et al., 2018). Therefore, it was thought that higher loading capacity was obtained in the AuNPs@Ng formulation with the combination of these two methods. Furthermore, as mentioned, UV-VIS absorption of AuNP@Ng/Cur confirmed the encapsulation of curcumin by the nanogel, as it exhibited a peak at 450 nm wavelength in addition to the AuNP peak, which indicates the presence of curcumin (Alam et al., 2012).

Thermo-pH-Responsive Curcumin Release From AuNP@Ng

One of the major benefits of nanogels is its thermo-responsive property that enables controlled drug release in the cellular environment with an on-off trigger mechanism. In order to evaluate the thermo-pH sensitivity of nanogel, the *in vitro* release of curcumin from Ng and AuNP@Ng was carried out at two different temperatures of 25 and 37°C under pH conditions of 5.5 and 7.4 in a dissolution medium containing tween 20 to provide sink conditions in the release environment (Shahani and Panyam, 2011; Ching et al., 2019). According to statistical analysis, there are significant differences in drug release between the 4 different conditions of 37°C pH 5.5, 37°C pH 7.4, 25°C pH 5.5, and 25°C pH 7.4 for nanogel and AuNP@Ng ($^{****}P < 0.0001$). The release profiles of curcumin from the Ng and AuNP@Ng shown in **Figure 5**, demonstrated no burst release, which indicated that curcumin was not adsorbed to the nanogel surface and was entirely encapsulated in the nanogel structure. Higher curcumin release was observed at acidic pH compared to the release at physiological pH. Drug release reached equilibrium at 80% after 72 h for both nanogel and AuNP@Ng formulations at 37°C and acidic pH. Only 20% of the drug was released from AuNP@Ng within 72 h at 25°C and pH 7.4. The low critical solution temperature (LCST) properties of PNIPAM cause an extraordinary shrinkage, leading to curcumin release at temperatures higher than LCST; whereby the drug release only depends on free diffusion resulting in lower drug release. The significant size transition measured by DLS confirmed the gradual shrinkage of nanogel in temperatures above LCST (**Figure 3B**; Kim et al., 2019). Thus, using chitosan in this formulation not only improved the LCST properties of nanogel by increasing it to the body temperature, but also, the pK_a value of linear chitosan chains make the nanogel pH-responsive and this leads to the rupture of the Ng under acidic conditions, followed by curcumin release (Pujana et al., 2012). Since the tumor cells have an acidic environment, curcumin-loaded Ng appear to be advantageous to deliver the encapsulated drug to tumor cells (Swietach et al., 2014). Hyperthermia generated by Au nanoparticles under NIR irradiation can stimulate drug release from particles after cellular uptake and could effectively reverse drug resistance of tumor cells, which highly enhanced the killing effects of chemotherapeutics and promoted cell apoptosis (Li et al., 2019; Gao et al., 2020).

Cellular Viability of AuNP@Ng/Cur

Cell viability of the nanoparticles was investigated in terms of the effect on the cell proliferation by Alamar Blue assay. MDA-MB-231 and MCF10A cells were treated with different concentrations of AuNP@Ng and the corresponding concentrations of individual AuNP and Ng for 24 and 48 h, as shown in **Figure 6**, The performed statistical analysis for both MDA-MB-231 and MCF 10A cells treated with nanoparticles using two-way ANOVA revealed no significant difference in cell viability between two time points ($p > 0.05$). According to Tukey's multiple comparisons test, there is significant differences

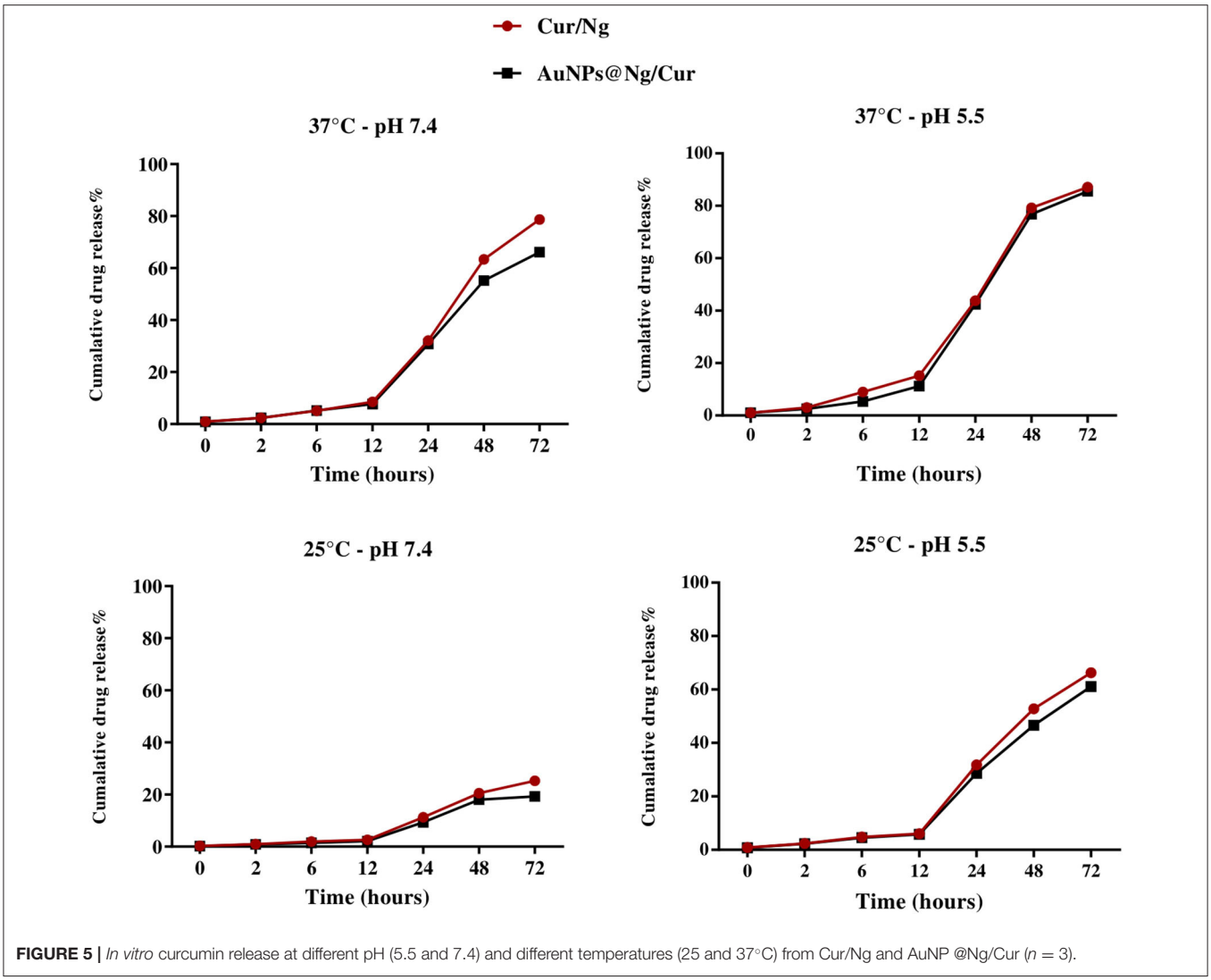

FIGURE 5 | *In vitro* curcumin release at different pH (5.5 and 7.4) and different temperatures (25 and 37°C) from Cur/Ng and AuNP @Ng/Cur ($n = 3$).

in cell viability of MCF10A cells in sample treated with AuNP@Ng 120 μg/ml in 24 h in comparison with control sample ($^{*}p < 0.01$). Same statistical analysis for MDA-MB-231 cells, showed significant difference in cell viability for samples treated with nanogel 100 μg/ml and AuNP@Ng 120 μg/ml in 24 h in comparison with control sample (respectively, $^{*}p < 0.01$ and $^{**}p < 0.001$). Moreover, there are significant differences in increasing the cell viability of MDA-MB-231 cells for samples treated with Ng 50 μg/ml, Ng 100 μg/ml, 60 μg/ml AuNP@Ng, and 120 μg/ml AuNP@Ng after 48 h in comparison with control sample (respectively, $^{*}p < 0.01$; $^{**}p < 0.01$; $^{**}p < 0.01$; $^{***}p < 0.001$). These findings show that nanoparticle treated MDA-MB-231 and MCF10A cells exhibited slightly higher viability in comparison to control cells (100%). These results suggest that AuNP may have a promoting effect on cell proliferation of MDA-MB-231 and MCF10A cells at low concentrations (Gao et al., 2020). Thus, these results indicated that AuNP@Ng nanocarriers are safe for *in vitro* applications where the concentration is below 120 μg/ml.

Intracellular Uptake of AuNP@Ng and AuNP@Ng/Cur Nanoparticles

Following the cellular viability, cellular internalization quantification of the AuNP@Ng nanocarriers was investigated by employing the AuNP detection by flow cytometry. The incubation duration was fixed to 24 h as most of the doubling time of mammalian cell lines are longer than 24 h, and thus cell proliferation effects such as dilution of intracellular nanoparticles due to cell cycling would be eliminated (Shin et al., 2020). Traditionally, AuNPs are detected by the side scattering mode with 488 nm laser illumination (SSC channel). However, this mode of action was found to be not sensitive enough for our application, presumably due to detection range not being close to the SPR peak of AuNPs, and the difference being insignificant due to the small AuNPs particle size and low particle concentration. The other proposed method(Wu et al., 2019) was employing the SPR phenomena of AuNP which gives peak in the 510-550 nm range, and the aggregation of AuNP inside the cells causes a red shift in the SPR peak(Liu et al.,

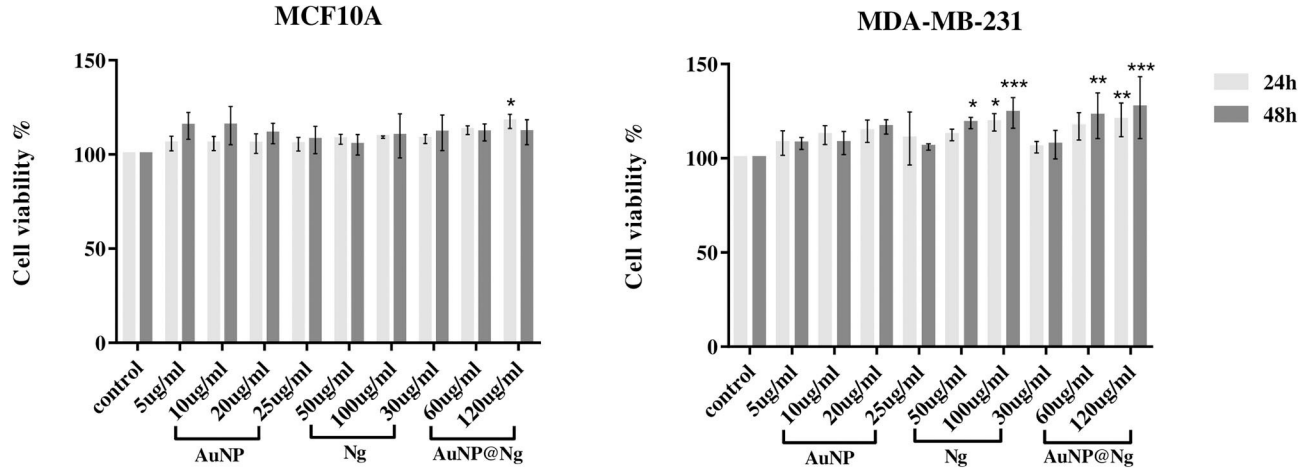

FIGURE 6 | Cellular viability of MDA-MB-231 and MCF-10A cells treated with Ng (25, 50, and 100 μg/ml), AuNP (5, 10, and 20 μg/ml), and AuNP@Ng (30, 60, and 120 μg/ml) nanoparticles after 24 and 48 h treatment. Data are presented as the mean ± standard deviation (SD) ($n = 4$). Two-way ANOVA followed by Tukey's multiple comparisons test was performed to investigate the significant difference (***$p < 0.0001$-0.001; **$p < 0.001$-0.01; *$p < 0.01$).

2017). Therefore, this mode of action is more sensitive to detect the scattered light in a flow cytometer. When the excitation laser 561 nm and corresponding 582/15 band pass filter (RFP filter) was used, MDA-MB-231 cells that internalized AuNP containing nanoparticles showed significant difference in flow cytometry intensity (FCM) (respectively, $^{**}p < 0.001$ and $^{*}p < 0.01$) (**Figure 7A**). Both AuNP and AuNP@Ng showed similar results, whereas the signal intensity of Ng internalized cells was similar to the untreated cells suggesting that the signal is specific to AuNPs, and nanogel-AuNP conjugation does not alter the detection of AuNPs. However, no significant difference was observed for MCF 10A non-tumorigenic cell line ($p > 0.05$). This could be attributed to the slower metabolism of non-tumorigenic cell lines compared with cancer cells (Zancan et al., 2010), resulting with the internalized nanoparticle concentration being below detection range. Additionally, **Figure 7B**, demonstrated that following AuNP or AuNP@Ng nanoparticle treatment, histograms on RFP channel shifted to larger intensities, whereas Ng nanoparticle treatment showed no histogram shift, suggesting the FCM intensity detection was specific to AuNPs. To verify the presence and location of the nanoparticles inside the cells, AuNP, AuNP@Ng treated cells were imaged with confocal microscopy after 24 h incubation. AuNP were detected by using reflection imaging due to its extraordinary efficiency of light absorption and emission. The cell membrane was stained with carbocyanine dye DiI in order to explore the cellular internalization pattern of nanoparticles, as DiI dye stains entire lipid components of the cell (Jensen and Berg, 2016). The scattered light signals of AuNP were bright enough to be distinguished from cellular autofluorescence (**Figure 7C**) when the reflection imaging settings were optimized for image acquisition. Nanoparticles were efficiently internalized by MDA-MB-231 cells and localized in the cytoplasm as aggregates suggesting their endosomal entrapment (Kim et al., 2015). Acquired images suggested dose-dependent internalization with the observations of higher concentration of AuNP and AuNP@Ng, resulting in denser aggregations inside the cells. Recently, it was reported that gelatin/protein Ng serve as reducing and stabilizing agents for the AuNP by allowing for nucleation in a gel network that exhibits colloidal stability (Chen et al., 2019). Our results showed similar results in confocal microscopy, AuNP@Ng showed more dispersed aggregates compared with densely packed AuNP.

Curcumin Delivery and PTT Efficiency Evaluations of AuNP, AuNP@Ng, and AuNP@Ng/Cur Against MDA-MB-231 Cells

The potential anticancer ability of AuNP@Ng/Cur was evaluated by using MDA-MB-231 and MCF10A cells directly comparing its time and dose-dependent efficacy to free curcumin performed by Alamar Blue cell proliferation assay. According to obtained statistical analysis using two-way ANOVA followed by Tukey's multiple comparisons test for MDA-MB-231 and MCF10A cells, there are significant dose dependant decrease in cell viability for both samples treated with curcumin and AuNP@Ng/Cur in comparison with samples treated with 10 μg/ml concentration of curcumin for both time points **Figure 8A** ($p < 0.05$). Therefore, these findings demonstrate the inhibition of the proliferation of cells at the tested concentrations, which increase by increasing the concentration of the treatments (Zancan et al., 2010). For both MDA-MB-231 and MCF10A cells there are time dependent significant differences in cell viability for samples treated with 100 μg/ml ($p < 0.05$). AuNP@NG/Cur nanoparticles had lower proliferation inhibition efficiency when compared with free curcumin. These results suggested nanogels having stimuli-responsive and sustained drug release profile and requiring a longer period for drug release in comparison with the immediate access of free curcumin for cells (Sultana et al., 2013). According to **Figure 5**, ∼75% of the drug was released after 48 h. This sustained-release pattern might be the reason for

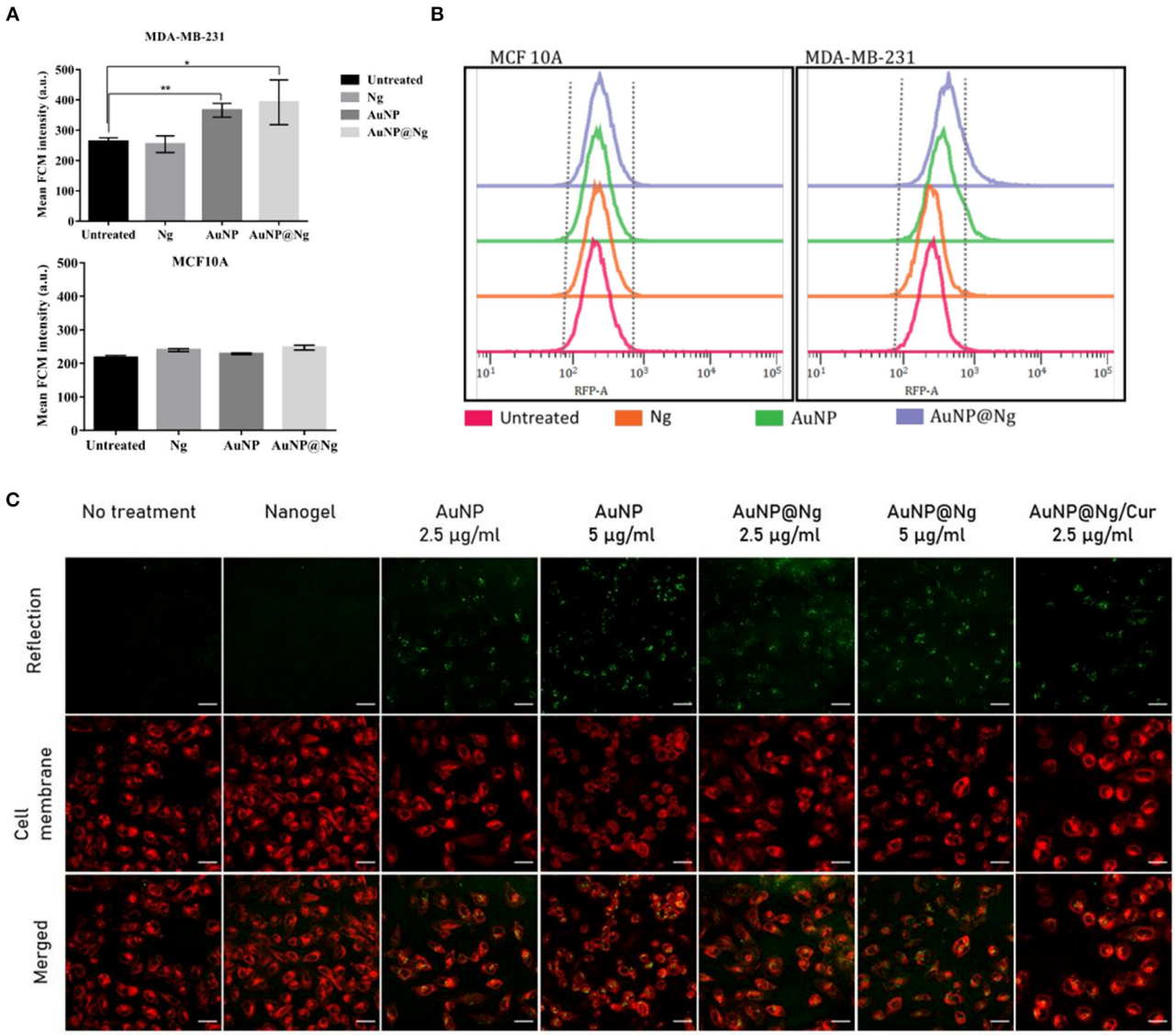

FIGURE 7 | Cellular uptake study of nanoparticles Quantification of cellular uptake by flow cytometry after 24-h incubation of Ng, AuNP, and AuNP@Ng with MDA-MB-231 breast cancer cell line and non-tumorigenic MCF 10A cell line. Significant differences were observed in cellular uptake of nanoparticles in the statistical analysis using the two-tailed Student *t*-test (**$p < 0.0001$–0.001; *$p < 0.001$–0.01) by MDA-MB-231 cells when treated with AuNP and AuNP@Ng compared to untreated samples **(A)**. AuNP intensity histograms detected by RFP filter representing Ng, AuNP, and AuNP@Ng cellular internalization in MDA-MB-231 and MCF 10A cells **(B).** Confocal microscopy images of MDA-MB-231 cells incubated with AuNP (2.5 and 5 µg/ml), AuNP@Ng (2.5 and 5 µg/ml), and AuNP@Ng/Cur for 24 h. AuNP are acquired with reflection imaging (green), the cell membrane was stained with carbocyanine dye DiI (red). The scale bar is 30 µm **(C)**.

the lower inhibition in cell proliferation in the sample treated with AuNP@Ng/Cur.

In addition to curcumin delivery, the photothermal therapeutic effect of AuNP@Ng/Cur against MDA-MB-231 cells was evaluated by applying NIR irradiation after incubating cells with AuNP@Ng/Cur containing 2.5 and 5 µg/ml AuNP. After 24 h of incubation, cells were exposed to NIR irradiation for 10 min. AuNP represent LPSR, which has the ability in absorbing NIR light and converting it to heat. This heat generation causes the shrinkage of nanogel and curcumin release by triggering the thermoresponsive properties of synthesized AuNP@Ng/Cur nanoparticles (Vines et al., 2019). The Alamar blue assay and crystal violet staining after PTT indicated that AuNP, AuNP@Ng, and AuNP@Ng/Cur could significantly decrease the cell viability of MDA-MB-231 cells compared to the control cells with no NIR laser exposure, which were viable after irradiation NIR laser ($p < 0.05$). These results clearly showed the significant photothermal ability of the synthesized nanoparticles against MDA-MB-231 cells when treated with AuNP@Ng/Cur, in addition to increased concentration of AuNP

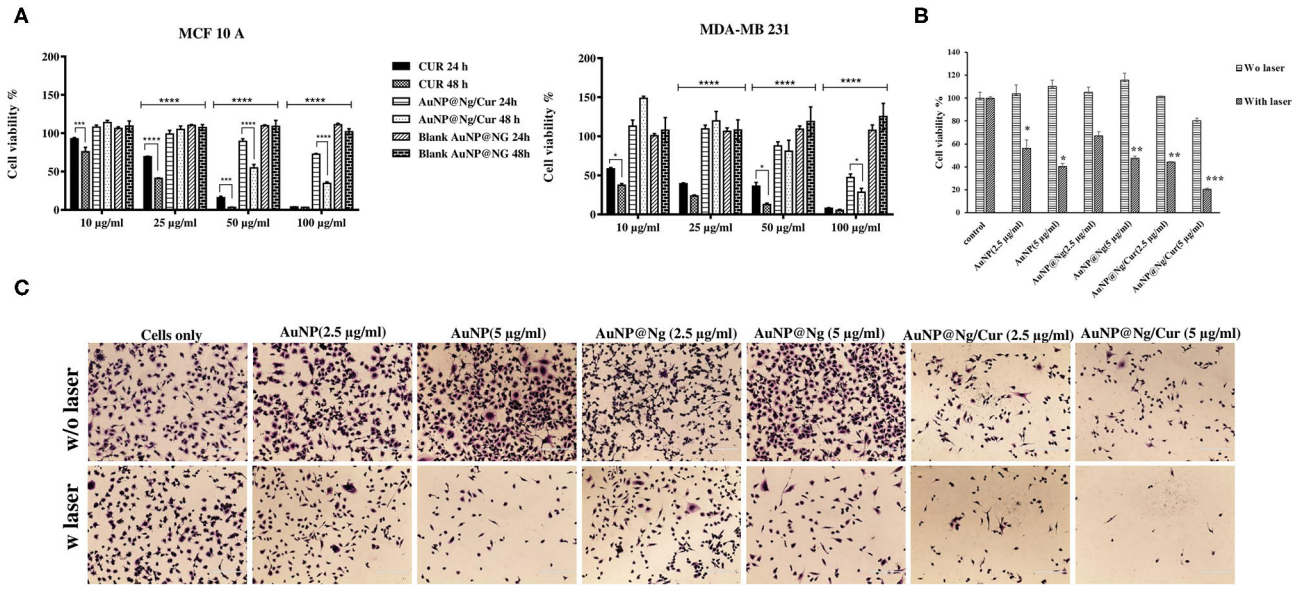

FIGURE 8 | Cytotoxicity of free curcumin and AuNP@Ng/Cur incubated with MDA-MB-231 and MCF-10A cells for 24 and 48 h. Data are presented as the mean ± standard deviation (SD) Two-way ANOVA followed by Tukey's multiple comparisons test was performed to investigate the significant difference (****$p < 0.0001$; ***$p <$ 0.0001–0.001; **$p <$ 0.001–0.01; *$p <$ 0.01) **(A)**. Cell viability of MDA-MB-231 cells treated with AuNP, AuNP@Ng, and AuNP@Ng/Cur after exposure to NIR laser **(B)**. Crystal violates -stained MDA-MB-231 cells treated with AuNP (2.5–5 µg/ml), AuNP@Ng (2.5–5 µg/ml), and AuNP@Ng/Cur (2.5–5 µg/ml) after laser exposure for 10 min (Scale bar is 200 µm) **(C)**.

in AuNP@Ng/Cur and AuNP@Ng being able to remarkably increase the photothermal efficiency of AuNP@Ng/Cur (**Figures 8B**,**C**) ($p < 0.05$). Although drug loaded AuNP@Ng nanoparticles showed less anticancer efficiency, our novel dual therapy nanoparticle system constitutes a potential delivery approach with overall advantages of Ng being cytocompatible and containing AuNP for PTT and enhancing the solubility of poorly water-soluble drugs.

CONCLUSION

Plasmonic nanogels are of interest to a range of medical fields, including hydrophobic drug delivery and bioimaging, due to their high biocompatibility, biodegradability, and stimuli responsivity. To date, various nanogels have been synthesized using different synthetic methods. Although there is considerable progress in the success of nanogels, in practice they suffer from multiple dilemmas such as high toxicity, burst release, and poor diagnostic sensitivity. Therefore, in this study, biocompatible, stimuli-responsive plasmonic nanogel was successfully synthesized in the presence of an MBA crosslinker with free radical surfactant-free emulsion polymerization method by grafting PNIPAM to thiolated chitosan. Having isopropyl hydrophobic groups rendered the AuNP@Ng an appropriate nanocarrier for a wide range of anticancer drugs with low solubility. Sustained curcumin release pattern by AuNP@Ng was achieved for 72 h. Our developed AuNP@Ng/Cur nanoparticles conveniently overcame the cellular barrier and entered the MDA-MB-231 cells, which was observed through confocal microscopy. The pH-thermoresponsive plasmonic nanogel was found to have efficient toxicity against MDA-MB-231 cells, which increased with the combination of photothermal therapy. Thus, it can be suggested that AuNP@Ng could be introduced as a biocompatible multifunctional nanocarrier for the dual delivery of curcumin and photothermal therapy.

DATA AVAILABILITY STATEMENT

The original contributions presented in the study are included in the article/supplementary materials, further inquiries can be directed to the corresponding author/s.

AUTHOR CONTRIBUTIONS

FH: investigation, conceptualization, methodology, data analysis, writing—original draft, and writing—review and editing. EÖ: investigation, methodology, data analysis and writing—original draft, and writing—review and editing. BK: methodology and writing—review and editing. SR: methodology. MS: supervision, investigation, validation, and funding acquisition and editing. JR: supervision, validation, funding acquisition, and writing—review and editing. All authors contributed to the article and approved the submitted version.

ACKNOWLEDGMENTS

We acknowledge financial support from Tarbiat Modarres University, Tehran, Iran and the Academy of Finland (project# 309374). We would like to thank Dr. Mahdi Abdollahi, Associate professor of Polymer Reaction Engineering at Tarbiat Modares University for his expert advice on nanogel synthesis and characterization. EÖ thankfully acknowledges the Doctoral Network of Molecular Biosciences at Åbo Akademi University and Magnus Ehrnrooth Foundation for financial support. The APC-pool at ÅAU is acknowledged for providing funding for the APC-fees.

REFERENCES

Agnihotri, P., Raj, R., Kumar, D., and Dan, A. (2020). Short oligo (ethylene glycol) chain incorporated thermoresponsive microgels: from structural analysis to modulation of solution properties. *Soft Matter* 16, 7845–7859. doi: 10.1039/D0SM01187H

Alam, S., Panda, J. J., and Chauhan, V. S. (2012). Novel dipeptide nanoparticles for effective curcumin delivery. *Int. J. Nanomed.* 7:4207. doi: 10.2147/IJN.S33015

Asghar, K., Qasim, M., Dharmapuri, G., and Das, D. (2017). Investigation on a smart nanocarrier with a mesoporous magnetic core and thermo-responsive shell for co-delivery of doxorubicin and curcumin: a new approach towards combination therapy of cancer. *RSC Adv.* 7, 28802–28818. doi: 10.1039/C7RA03735J

Ashraf, S., Park, H.-K., Park, H., and Lee, S.-H. (2016). Snapshot of phase transition in thermoresponsive hydrogel PNIPAM: role in drug delivery and tissue engineering. *Macromol Res.* 24, 297–304. doi: 10.1007/s13233-016-4052-2

Bani, F., Adeli, M., Movahedi, S., and Sadeghizadeh, M. (2016). Graphene–polyglycerol–curcumin hybrid as a near-infrared (NIR) laser stimuli-responsive system for chemo-photothermal cancer therapy. *RSC Adv.* 6, 61141–61149. doi: 10.1039/C6RA05917A

Bansal, K. K., Özliseli, E., Saraogi, G. K., and Rosenholm, J. M. (2020). Assessment of intracellular delivery potential of novel sustainable poly (δ-decalactone)-based micelles. *Pharmaceutics* 12:726. doi: 10.3390/pharmaceutics12080726

Bray, F., Ferlay, J., Soerjomataram, I., Siegel, R. L., Torre, L. A., and Jemal, A. (2018). Global cancer statistics 2018: GLOBOCAN estimates of incidence and mortality worldwide for 36 cancers in 185 countries. *CA Cancer J. Clin.* 68, 394–424. doi: 10.3322/caac.21492

Chen, I.-H., Chen, Y.-F., Liou, J.-H., Lai, J.-T., Hsu, C.-C., Wang, N.-Y., et al. (2019). Green synthesis of gold nanoparticle/gelatin/protein nanogels with enhanced bioluminescence/biofluorescence. *Mater. Sci. Eng. C* 105:110101. doi: 10.1016/j.msec.2019.110101

Ching, Y. C., Gunathilake, T. M. S., Chuah, C. H., Ching, K. Y., Singh, R., and Liou, N.-S. (2019). Curcumin/Tween 20-incorporated cellulose nanoparticles with enhanced curcumin solubility for nano-drug delivery: characterization and *in vitro* evaluation. *Cellulose* 26, 5467–5481. doi: 10.1007/s10570-019-02445-6

Christau, S., Möller, T., Brose, F., Genzer, J., Soltwedel, O., and von Klitzing, R. (2016). Effect of gold nanoparticle hydrophobicity on thermally induced color change of PNIPAM brush/gold nanoparticle hybrids. *Polymer* 98, 454–463. doi: 10.1016/j.polymer.2016.03.088

Ding, Y., Gu, G., Xia, X.-H., and Huo, Q. (2009). Cysteine-grafted chitosan-mediated gold nanoparticle assembly: from nanochains to microcubes. *J. Mater. Chem.* 19, 795–799. doi: 10.1039/b816886e

Dong, P., Rakesh, K., Manukumar, H., Mohammed, Y. H. E., Karthik, C., Sumathi, S., et al. (2019). Innovative nano-carriers in anticancer drug delivery-a comprehensive review. *Bioorg. Chem.* 85, 325–336. doi: 10.1016/j.bioorg.2019.01.019

Echeverria, C., Soares, P., Robalo, A., Pereira, L., Novo, C. M., Ferreira, I., et al. (2015). One-pot synthesis of dual-stimuli responsive hybrid PNIPAAm-chitosan microgels. *Mater. Des.* 86, 745–751. doi: 10.1016/j.matdes.2015.07.170

Eilenberger, C., Kratz, S. R. A., Rothbauer, M., Ehmoser, E.-K., Ertl, P., and Küpc,ü, S. (2018). Optimized alamarBlue assay protocol for drug dose-response determination of 3D tumor spheroids. *MethodsX* 5, 781–787. doi: 10.1016/j.mex.2018.07.011

Esmatabadi, M. J. D., Motamedrad, M., and Sadeghizadeh, M. (2018). Down-regulation of lncRNA, GAS5 decreases chemotherapeutic effect of dendrosomal curcumin (DNC) in breast cancer cells. *Phytomedicine* 42, 56–65. doi: 10.1016/j.phymed.2018.03.022

Esquivel, R., Juárez, J., Almada, M., Ibarra, J., and Valdez, M. A. (2015). Synthesis and characterization of new thiolated chitosan nanoparticles obtained by ionic gelation method. *Int. J. Polym. Sci.* 2015:502058. doi: 10.1155/2015/502058

Farsani, S. S. M., Sadeghizadeh, M., Gholampour, M. A., Safari, Z., and Najafi, F. (2020). Nanocurcumin as a novel stimulator of megakaryopoiesis that ameliorates chemotherapy-induced thrombocytopenia in mice. *Life Sci.* 256:117840. doi: 10.1016/j.lfs.2020.117840

Fu, Y., Feng, Q., Shen, Y., Chen, M., Xu, C., Cheng, Y., et al. (2018). A feasible strategy for self-assembly of gold nanoparticles via dithiol-PEG for photothermal therapy of cancers. *RSC Adv.* 8, 6120–6124. doi: 10.1039/C7RA12735A

Gao, J., Wang, F., Wang, S., Liu, L., Liu, K., Ye, Y., et al. (2020). Hyperthermia-triggered on-demand biomimetic nanocarriers for synergetic photothermal and chemotherapy. *Adv. Sci.* 7:1903642. doi: 10.1002/advs.202070060

García-Peñas, A., Biswas, C. S., Liang, W., Wang, Y., Yang, P., and Stadler, F. J. (2019). Effect of hydrophobic interactions on lower critical solution temperature for poly (N-isopropylacrylamide-co-dopamine Methacrylamide) copolymers. *Polymers* 11:991. doi: 10.3390/polym11060991

Gatti, G., and Perucca, E. (1994). Plasma concentrations of free and conjugated silybin after oral intake of a silybin-phosphatidylcholine complex (silipide) in healthy volunteers. *Int. J. Clin. Pharmacol. Ther.* 32, 614–617.

Ghorbani, M., Hamishehkar, H., Arsalani, N., and Entezami, A. A. (2016). A novel dual-responsive core-crosslinked magnetic-gold nanogel for triggered drug release. *Mater. Sci. Eng. C,* 68, 436–444. doi: 10.1016/j.msec.2016.06.007

Guan, Y., and Zhang, Y. (2011). PNIPAM microgels for biomedical applications: from dispersed particles to 3D assemblies. *Soft Matter* 7, 6375–6384. doi: 10.1039/c0sm01541e

He, L., Huang, G., Liu, H., Sang, C., Liu, X., and Chen, T. (2020). Highly bioactive zeolitic imidazolate framework-8–capped nanotherapeutics for efficient reversal of reperfusion-induced injury in ischemic stroke. *Science Adv.* 6:eaay9751. doi: 10.1126/sciadv.aay9751

Honary, S., and Zahir, F. (2013). Effect of zeta potential on the properties of nano-drug delivery systems-a review (Part 1). *Trop. J. Pharm. Res.* 12, 255–264. doi: 10.4314/tjpr.v12i2.19

Jensen, K. H., and Berg, R. W. (2016). CLARITY-compatible lipophilic dyes for electrode marking and neuronal tracing. *Sci. Rep.* 6:32674. doi: 10.1038/srep32674

Kaasalainen, M., Aseyev, V., von Haartman, E., Karaman, D. S., Mäkil,ä, E., Tenhu, H., et al. (2017). Size, stability, and porosity of mesoporous nanoparticles characterized with light scattering. *Nanoscale Res. Let.* 12:74. doi: 10.1186/s11671-017-1853-y

Karg, M., Pich, A., Hellweg, T., Hoare, T., Lyon, L. A., Crassous, J., et al. (2019). Nanogels and microgels: from model colloids to applications, recent developments, and future trends. *Langmuir* 35, 6231–6255. doi: 10.1021/acs.langmuir.8b04304

Khan, A., Othman, M. B. H., Chang, B. P., and Akil, H. M. (2015). Preparation, physicochemical and stability studies of chitosan-PNIPAM based responsive microgels under various pH and temperature conditions. *Iran. Polymer J.* 24, 317–328. doi: 10.1007/s13726-015-0324-5

Kim, C. S., Li, X., Jiang, Y., Yan, B., Tonga, G. Y., Ray, M., et al. (2015). Cellular imaging of endosome entrapped small gold nanoparticles. *MethodsX,* 2, 306–315. doi: 10.1016/j.mex.2015.06.001

Kim, M. H., Kim, J.-C., Lee, H. Y., Dai Kim, J., and Yang, J. H. (2005). Release property of temperature-sensitive alginate beads containing poly (N-isopropylacrylamide). *Colloids Surf B Biointerfaces* 46, 57–61. doi: 10.1016/j.colsurfb.2005.09.002

Kim, Y. K., Kim, E.-J., Lim, J. H., Cho, H. K., Hong, W. J., Jeon, H. H., et al. (2019). Dual stimuli-triggered nanogels in response to temperature and pH changes for controlled drug release. *Nanoscale Res. Lett.* 14, 1–9. doi: 10.1186/s11671-019-2909-y

Kimling, J., Maier, M., Okenve, B., Kotaidis, V., Ballot, H., and Plech, A. (2006). Turkevich method for gold nanoparticle synthesis revisited. *J. Phys. Chem. B* 110, 15700–15707. doi: 10.1021/jp061667w

Kunnumakkara, A. B., Bordoloi, D., Harsha, C., Banik, K., Gupta, S. C., and Aggarwal, B. B. (2017). Curcumin mediates anticancer effects by modulating multiple cell signaling pathways. *Clin. Sci.* 131, 1781–1799. doi: 10.1042/CS20160935

Kunwar, A., Barik, A., Pandey, R., and Priyadarsini, K. I. (2006). Transport of liposomal and albumin loaded curcumin to living cells: an absorption and fluorescence spectroscopic study. *Biochim Biophys Acta Gen Subjects* 1760, 1513–1520. doi: 10.1016/j.bbagen.2006.06.012

Li, B., Xu, Q., Li, X., Zhang, P., Zhao, X., and Wang, Y. (2019). Redox-responsive hyaluronic acid nanogels for hyperthermia-assisted chemotherapy to overcome multidrug resistance. *Carbohydr. Polym.* 203, 378–385. doi: 10.1016/j.carbpol.2018.09.076

Li, L., Ahmed, B., Mehta, K., and Kurzrock, R. (2007). Liposomal curcumin with and without oxaliplatin: effects on cell growth, apoptosis, and angiogenesis in colorectal cancer. *Mol. Cancer Ther.* 6, 1276–1282. doi: 10.1158/1535-7163.MCT-06-0556

Liechty, W. B., and Peppas, N. A. (2012). Expert opinion: responsive polymer nanoparticles in cancer therapy. *Eur. J. Pharm. Biopharm.* 80, 241–246. doi: 10.1016/j.ejpb.2011.08.004

Liu, G., Li, Q., Ni, W., Zhang, N., Zheng, X., Wang, Y., et al. (2015). Cytotoxicity of various types of gold-mesoporous silica nanoparticles in human breast cancer cells. *Int. J. Nanomedicine* 10:6075. doi: 10.2147/IJN.S90887

Liu, J., Li, Y., Chen, S., Lin, Y., Lai, H., Chen, B., et al. (2020). Biomedical application of reactive oxygen species–responsive nanocarriers in cancer, inflammation, and neurodegenerative diseases. *Front. Chem.* 8:838. doi: 10.3389/fchem.2020.00838

Liu, M., Li, Q., Liang, L., Li, J., Wang, K., Li, J., et al. (2017). Real-time visualization of clustering and intracellular transport of gold nanoparticles by correlative imaging. *Nat. Commun.* 8:15646. doi: 10.1038/ncomms15646

Luckanagul, J. A., Pitakchatwong, C., Bhuket, P. R. N., Muangnoi, C., Rojsitthisak, P., Chirachanchai, S., et al. (2018). Chitosan-based polymer hybrids for thermo-responsive nanogel delivery of curcumin. *Carbohydr. Polym.* 181, 1119–1127. doi: 10.1016/j.carbpol.2017.11.027

Ma, Z., Shayeganpour, A., Brocks, D. R., Lavasanifar, A., and Samuel, J. (2007). High-performance liquid chromatography analysis of curcumin in rat plasma: application to pharmacokinetics of polymeric micellar formulation of curcumin. *Biomed. Chromatogr.* 21, 546–552. doi: 10.1002/bmc.795

Mahalunkar, S., Yadav, A. S., Gorain, M., Pawar, V., Braathen, R., Weiss, S., et al. (2019). Functional design of pH-responsive folate-targeted polymer-coated gold nanoparticles for drug delivery and *in vivo* therapy in breast cancer. *Int. J. Nanomedicine* 14:8285. doi: 10.2147/IJN.S215142

Maya, S., Sarmento, B., Nair, A., Rejinold, N. S., Nair, S. V., and Jayakumar, R. (2013). Smart stimuli sensitive nanogels in cancer drug delivery and imaging: a review. *Curr. Pharm. Des.* 19, 7203–7218. doi: 10.2174/13816128194131219124142

Murphy, C. J., Gole, A. M., Stone, J. W., Sisco, P. N., Alkilany, A. M., Goldsmith, E. C., et al. (2008). Gold nanoparticles in biology: beyond toxicity to cellular imaging. *Acc. Chem. Res.* 41, 1721–1730. doi: 10.1021/ar800035u

Oh, N. M., Oh, K. T., Baik, H. J., Lee, B. R., Lee, A. H., Youn, Y. S., et al. (2010). A self-organized 3-diethylaminopropyl-bearing glycol chitosan nanogel for tumor acidic pH targeting: *in vitro* evaluation. *Colloids Surf. B Biointerfaces* 78, 120–126. doi: 10.1016/j.colsurfb.2010.02.023

Ong, C., Cha, B. G., and Kim, J. (2019). Mesoporous silica nanoparticles doped with gold nanoparticles for combined cancer immunotherapy and photothermal therapy. *ACS Appl. Bio Mater.* 2, 3630–3638. doi: 10.1021/acsabm.9b00483

Ormategui, N., Zhang, S., Loinaz, I., Brydson, R., Nelson, A., and Vakurov, A. (2012). Interaction of poly (N-isopropylacrylamide)(pNIPAM) based nanoparticles and their linear polymer precursor with phospholipid membrane models. *Bioelectrochemistry* 87, 211–219. doi: 10.1016/j.bioelechem.2011.12.006

Osterman, C. J. D., Gonda, A., Stiff, T., Sigaran, U., Valenzuela, M. M. A., Bennit, H. R. F., et al. (2016). Curcumin induces pancreatic adenocarcinoma cell death via reduction of the inhibitors of apoptosis. *Pancreas* 45:101. doi: 10.1097/MPA.0000000000000411

Oun, R., Moussa, Y. E., and Wheate, N. J. (2018). The side effects of platinum-based chemotherapy drugs: a review for chemists. *Dalton Trans.* 47, 6645–6653. doi: 10.1039/C8DT00838H

Palmieri, D., Richmond, T., Piovan, C., Sheetz, T., Zanesi, N., Troise, F., et al. (2015). Human anti-nucleolin recombinant immunoagent for cancer therapy. *Proc. Natl. Acad. Sci. U.S.A.* 112, 9418–9423. doi: 10.1073/pnas.1507087112

Park, H. H., Srisombat, L.-,o., Jamison, A. C., Liu, T., Marquez, M. D., Park, H., et al. (2018). Temperature-responsive hydrogel-coated gold nanoshells. *Gels* 4:28. doi: 10.3390/gels4020028

Park, S., Lee, W. J., Park, S., Choi, D., Kim, S., and Park, N. (2019). Reversibly pH-responsive gold nanoparticles and their applications for photothermal cancer therapy. *Sci. Rep.* 9:20180. doi: 10.1038/s41598-019-56754-8

Pavan, A. R., Silva, G. D. B., d., Jornada, D. H., Chiba, D. E., Fernandes, G. F., et al. (2016). Unraveling the anticancer effect of curcumin and resveratrol. *Nutrients* 8:628. doi: 10.3390/nu8110628

Pereira, P., Pedrosa, S. S., Correia, A., Lima, C. F., Olmedo, M. P., González-Fernández, Á., et al. (2015). Biocompatibility of a self-assembled glycol chitosan nanogel. *Toxicol. Vitro,* 29, 638–646. doi: 10.1016/j.tiv.2014.11.004

Pujana, M. A., Pérez-Álvarez, L., Iturbe, L. C. C., and Katime, I. (2012). Water dispersible pH-responsive chitosan nanogels modified with biocompatible crosslinking-agents. *Polymer* 53, 3107–3116. doi: 10.1016/j.polymer.2012.05.027

Sarika, P., James, N. R., and Raj, D. K. (2016). Preparation, characterization and biological evaluation of curcumin loaded alginate aldehyde–gelatin nanogels. *Mater. Sci. Eng. C* 68, 251–257. doi: 10.1016/j.msec.2016.05.046

Sarika, P., and Nirmala, R. J. (2016). Curcumin loaded gum arabic aldehyde-gelatin nanogels for breast cancer therapy. *Mater. Sci. Eng. C* 65, 331–337. doi: 10.1016/j.msec.2016.04.044

Schmitz, T., Grabovac, V., Palmberger, T. F., Hoffer, M. H., and Bernkop-Schnürch, A. (2008). Synthesis and characterization of a chitosan-N-acetyl cysteine conjugate. *Int. J. Pharm.* 347, 79–85. doi: 10.1016/j.ijpharm.2007.06.040

Senthilkumar, R., Karaman, D. S., Paul, P., Björk, E. M., Odén, M., Eriksson, J. E., et al. (2015). Targeted delivery of a novel anticancer compound anisomelic acid using chitosan-coated porous silica nanorods for enhancing the apoptotic effect. *Biomater. Sci.* 3, 103–111. doi: 10.1039/C4BM00278D

Shah, L. A., Farooqi, Z. H., Naeem, H., Shah, S. M., and Siddiq, M. (2013). Synthesis and characterization of poly (N-isopropylacrylamide) hybrid microgels with different cross-linker contents. *J. Chem. Soc. Pakistan* 35, 1522–1529.

Shahani, K., and Panyam, J. (2011). Highly loaded, sustained-release microparticles of curcumin for chemoprevention. *J. Pharm. Sci.* 100, 2599–2609. doi: 10.1002/jps.22475

Shin, H., Kwak, M., Lee, T. G., and Lee, J. Y. (2020). Quantifying the level of nanoparticle uptake in mammalian cells using flow cytometry. *Nanoscale* 12, 15743–15751. doi: 10.1039/D0NR01627F

Shukla, R., Bansal, V., Chaudhary, M., Basu, A., Bhonde, R. R., and Sastry, M. (2005). Biocompatibility of gold nanoparticles and their endocytotic fate inside the cellular compartment: a microscopic overview. *Langmuir* 21, 10644–10654. doi: 10.1021/la0513712

Sidhu, J. S., Singh, A., Garg, N., Kaur, N., and Singh, N. (2019). Gold conjugated carbon dots nano assembly: FRET paired fluorescence probe for cysteine recognition. *Sensors Actuators B Chem.* 282, 515–522. doi: 10.1016/j.snb.2018.11.105

Sultana, F., Manirujjaman, M., Imran-Ul-Haque, M. A., and Sharmin, S. (2013). An overview of nanogel drug delivery system. *J. Appl. Pharm. Sci.* 3, 95–105. doi: 10.7324/JAPS.2013.38.S15

Suresh, D., and Srinivasan, K. (2007). Studies on the *in vitro* absorption of spice principles–curcumin, capsaicin and piperine in rat intestines. *Food Chem. Toxicol.* 45, 1437–1442. doi: 10.1016/j.fct.2007.02.002

Swietach, P., Vaughan-Jones, R. D., Harris, A. L., and Hulikova, A. (2014). The chemistry, physiology and pathology of pH in cancer. *Philos. Trans. R Soc B Biol. Sci.* 369:20130099. doi: 10.1098/rstb.2013.0099

Takahashi, M., Uechi, S., Takara, K., Asikin, Y., and Wada, K. (2009). Evaluation of an oral carrier system in rats: bioavailability and antioxidant properties of liposome-encapsulated curcumin. *J. Agric. Food Chem.* 57, 9141–9146. doi: 10.1021/jf9013923

Tang, Z., Kong, N., Ouyang, J., Feng, C., Kim, N. Y., Ji, X., et al. (2020). Phosphorus science-oriented design and synthesis of multifunctional nanomaterials for biomedical applications. *Matter* 2, 297–322. doi: 10.1016/j.matt.2019.12.007

Unlu, A., Nayir, E., Kalenderoglu, M. D., Kirca, O., and Ozdogan, M. (2016). Curcumin (Turmeric) and cancer. *J. BUON* 21, 1050–1060.

Utashiro, Y., Takiguchi, M., and Satoh, M. (2017). Zeta potential of PNIPAM microgel particles dispersed in water—effects of charged radical initiators vs. OH– ion adsorption. *Colloid Polymer Sci.* 295, 45–52. doi: 10.1007/s00396-016-3976-6

Vashist, A., Kaushik, A., Vashist, A., Bala, J., Nikkhah-Moshaie, R., Sagar, V., et al. (2018). Nanogels as potential drug nanocarriers for CNS drug delivery. *Drug Discov. Today* 23, 1436–1443. doi: 10.1016/j.drudis.2018.05.018

Vines, J. B., Yoon, J.-H., Ryu, N.-E., Lim, D.-J., and Park, H. (2019). Gold nanoparticles for photothermal cancer therapy. *Front. Chem.* 7:167. doi: 10.3389/fchem.2019.00167

Waks, A. G., and Winer, E. P. (2019). Breast cancer treatment: a review. *JAMA* 321, 288–300. doi: 10.1001/jama.2018.19323

Wang, Y., Wang, C., Zhao, J., Ding, Y., and Li, L. (2017). A cost-effective method to prepare curcumin nanosuspensions with enhanced oral bioavailability. *J. Colloid Interface Sci.* 485, 91–98. doi: 10.1016/j.jcis.2016.09.003

Wu, S.-W., Liu, X., Miller, I. I., A. L., Cheng, Y.-S., Yeh, M.-L., et al. (2018). Strengthening injectable thermo-sensitive NIPAAm-g-chitosan hydrogels using chemical cross-linking of disulfide bonds as scaffolds for tissue engineering. *Carbohydr. Polym.* 192, 308–316. doi: 10.1016/j.carbpol.2018.03.047

Wu, W., Shen, J., Banerjee, P., and Zhou, S. (2011). Water-dispersible multifunctional hybrid nanogels for combined curcumin and photothermal therapy. *Biomaterials* 32, 598–609. doi: 10.1016/j.biomaterials.2010.08.112

Wu, Y., Ali, M. R., Dansby, K., and El-Sayed, M. A. (2019). Improving the flow cytometry-based detection of the cellular uptake of gold nanoparticles. *Anal. Chem.* 91, 14261–14267. doi: 10.1021/acs.analchem.9b02248

Xu, X., Qin, J., and Liu, W. (2014). Curcumin inhibits the invasion of thyroid cancer cells via down-regulation of PI3K/Akt signaling pathway. *Gene* 546, 226–232. doi: 10.1016/j.gene.2014.06.006

Yang, Y., Lin, Y., Di, D., Zhang, X., Wang, D., Zhao, Q., et al. (2017). Gold nanoparticle-gated mesoporous silica as redox-triggered drug delivery for chemo-photothermal synergistic therapy. *J. Colloid Interface Sci.* 508, 323–331. doi: 10.1016/j.jcis.2017.08.050

Zancan, P., Sola-Penna, M., Furtado, C. M., and Da Silva, D. (2010). Differential expression of phosphofructokinase-1 isoforms correlates with the glycolytic efficiency of breast cancer cells. *Mol. Genet. Metab.* 100, 372–378. doi: 10.1016/j.ymgme.2010.04.006

Zhao, X.-q., Wang, T.-x., Liu, W., Wang, C.-d., Wang, D., Shang, T., et al. (2011). Multifunctional Au@ IPN-pNIPAAm nanogels for cancer cell imaging and combined chemo-photothermal treatment. *J. Mater. Chem.* 21, 7240–7247. doi: 10.1039/c1jm10277j

Zhao, Y., Ju, X.-J., Zhang, L.-P., Wang, W., Faraj, Y., Zou, L.-B., et al. (2019). Transparent thermo-responsive poly (N-isopropylacrylamide)-l-poly (ethylene glycol) acrylamide conetwork hydrogels with rapid deswelling response. *N J. Chem.* 43, 9507–9515. doi: 10.1039/C9NJ01545K

Conflict of Interest: The authors declare that the research was conducted in the absence of any commercial or financial relationships that could be construed as a potential conflict of interest.

frontiers in Chemistry

ORIGINAL RESEARCH
published: 16 March 2021
doi: 10.3389/fchem.2021.522708

Zirconia Nanoparticles Induce HeLa Cell Death Through Mitochondrial Apoptosis and Autophagy Pathways Mediated by ROS

Yinghui Shang[1], Qinghai Wang[2], Jian Li[1], Haiting Liu[1], Qiangqiang Zhao[1], Xueyuan Huang[1], Hang Dong[1], Wansong Chen[3], Rong Gui[1] and Xinmin Nie[4]**

[1]Department of Blood Transfusion, The Third Xiangya Hospital, Central South University, Changsha, China, [2]Department of Cardiology, The Second Hospital of Shandong University, Jinan, China, [3]College of Chemistry and Chemical Engineering, Central South University, Changsha, China, [4]Clinical Laboratory of the Third Xiangya Hospital, Central South University, Changsha, China

Zirconia nanoparticles (ZrO_2 NPs) are commonly used in the field of biomedical materials, but their antitumor activity and mechanism is unclear. Herein, we evaluated the anti-tumor activity of ZrO_2 NPs and explored the anti-tumor mechanism. The results of *in vitro* and *in vivo* experiments showed that the level of intracellular reactive oxygen species (ROS) in HeLa cells was elevated after ZrO_2 NPs treatment. Transmission electron microscopy (TEM) showed that after treatment with ZrO_2 NPs, the mitochondria of HeLa cells were swollen, accompanied with the induction of autophagic vacuoles. In addition, flow cytometry analysis showed that the apoptotic rate of HeLa cells increased significantly by Annexin staining after treatment with ZrO_2 NPs, and the mitochondrial membrane potential (MMP) was reduced significantly. The proliferation of HeLa cells decreased as indicated by reduced Ki-67 labeling. In contrast, TUNEL-positive cells in tumor tissues increased after treatment with ZrO_2 NPs, which is accompanied by increased expression of mitochondrial apoptotic proteins including Bax, Caspase-3, Caspase-9, and Cytochrome C (Cyt C) and increased expression of autophagy-related proteins including Atg5, Atg12, Beclin-1, and LC3-II. Treating HeLa cells with N-acetyl-L-cysteine (NAC) significantly reduced ROS, rate of apoptosis, MMP, and *in vivo* anti-tumor activity. In addition, apoptosis- and autophagy-related protein expressions were also suppressed. Based on these observations, we conclude that ZrO_2 NPs induce HeLa cell death through ROS mediated mitochondrial apoptosis and autophagy.

Keywords: anticancer, reactive oxygen species, autophagy, apoptosis, zirconia

OPEN ACCESS

Edited by:
Andreas Rosenkranz, University of Chile, Chile

Reviewed by:
Zhiqing Pang, Fudan University, China
Shusheng Tang, China Agricultural University, China
Maibelin Rosales Vera, University of Chile, Chile

****Correspondence:***
Rong Gui
aguirong@163.com
Xinmin Nie
niexinmin7440@sina.com

Specialty section:
This article was submitted to Nanoscience, a section of the journal Frontiers in Chemistry

Received: *24 December 2019*
Accepted: *01 February 2021*
Published: *16 March 2021*

Citation:
Shang Y, Wang Q, Li J, Liu H, Zhao Q, Huang X, Dong H, Chen W, Gui R and Nie X (2021) Zirconia Nanoparticles Induce HeLa Cell Death Through Mitochondrial Apoptosis and Autophagy Pathways Mediated by ROS. Front. Chem. 9:522708. doi: 10.3389/fchem.2021.522708

INTRODUCTION

ZrO_2 NPs are the main raw material for synthetic casting sand, refractory and porcelain. In addition, they are common biomedical materials used for biosensors, implants, joints and oral prosthesis replacement (Lohbauer, et al., 2010; Qeblawi, et al., 2010). However, their anti-tumor activity is rarely reported. Reduced graphene oxide modified by ZrO_2 NPs are used for highly sensitive electrochemical sensors for anticancer drugs (Venu, et al., 2018). Iron-manganese-doped sulfated zirconia nanoparticles have been shown to induce HepG2 and MDA-MB-231 cell death, while they are less effective at killing normal Chang cells and HUVECs (Al-Fahdawi, et al., 2015). Sulphated

zirconia nanoparticles have significant cytotoxic effects on colon cancer HT29 cells (Mftah, et al., 2015). Synthetic ZrO_2 NPs can play a role in biomedical applications through the production of ROS and antioxidant activities (Balaji, et al., 2017), but the detailed mechanism has not been explored. Based on this, we investigated the anti-tumor activity and anti-tumor mechanism of zirconia nanoparticles using *in vivo* and *in vitro* experiments.

ROS are molecules or ions composed of oxygen containing single unpaired electrons, including hydroxyl radicals, superoxides, and hydrogen peroxide, etc (Chen and Gibson, 2008). They play important roles in cell apoptosis and autophagy (Araveti and Srivastava, 2019; Wang, et al., 2019; Ye et al., 2019). Mitochondria are the main organelles for ROS production (Addabbo, et al., 2009). Although autophagy is the protective response of living organisms to various adverse stress conditions during evolution, excessive autophagy is another way for anti-tumor drugs to induce tumor cell death (Kroemer and Levine, 2008). Overproduction of ROS can promote autophagy (Chen and Gibson, 2008). Based on the close relationship between ROS and apoptosis and autophagy, in this study, we investigated the anti-tumor mechanism of ZrO_2 NPs focusing ROS generation, apoptosis and autophagy induction.

MATERIALS AND METHODS

Materials

Zirconia nanoparticle (XF101) was purchased from XFNANO Materials Tech Co., Ltd. (China). NAC was purchased from Sigma Aldrich (United States). MTT cell proliferation and cytotoxicity assay kit was purchased from Beyotime Biotechnology. Rhodamine 123 (Rh123) was obtained from Yeasen Biotechnology (China). Annexin V-FITC/PI Apoptosis Detection Kit, MMP Detection Kit (JC-1), and ROS Assay Kit were purchased from KeyGEN BioTECH (China). BCA Protein Assay Kit was purchased from Solarbio science and technology Co., Ltd. (China). DMEM-HG (high glucose), fetal bovine serum (FBS), and trypsin were purchased from Life Technologies (United States). BBoxiProbe® superoxide anion detection kit, Singlet oxygen detection kit were from Shanghai Bestbio Biotechnology Co., Ltd. (China). Hydroxyl radical *in situ* fluorescence staining kit was from Shanghai Haling Biological Technology Co., Ltd. (China). One Step TUNEL Apoptosis Assay Kit, Ki-67 cell proliferation Detection Kit (IHC), DAPI and hematoxylin and eosin (HE) were purchased from Servicebio Tech Co., Ltd. (China). Anti-Bax, anti-Bcl-2, anti-Caspase-9, anti-Caspase-3, anti-Cytochrome C, anti-LC3, anti-Atg12, anti-Atg5, anti-Beclin-1, anti-β-actin antibodies, and horseradish peroxidase (HRP) goat anti-mouse and goat anti-rabbit IgG secondary antibodies were produced by Proteintech (United States).

Cell Culture

Human cervical cancer HeLa cells were prepared in the laboratory and cultured with DMEM-HG, containing 10% fetal bovine serum at 37°C, in 5% CO_2 and saturated humidity condition.

Cell Viability and Mitochondrial Metabolic Activity Detected by MTT Cell Proliferation and Cytotoxicity Assay

HeLa cells growing in log phase were collected and inoculated in 96-well plate (2×10^3/well). After 24 h, confluent cells were divided into control group, NAC (160 μg/ml) group, ZrO_2 NPs (100 μg/ml) + NAC (160 μg/ml) group, ZrO_2 NPs (50 μg/ml) group, and ZrO_2 NPs (100 μg/ml) group, respectively. After 24 h, 10 μL MTT solution was added to each well and the plate was incubated for 4 h. 100 μl Formazan solution was added to each well and the plate was incubated for additional 4 h. The absorbance (A) at 570 nm was detected by an EnSpire 2300 Multilabel Plate Reader. Cell viability (%) = (1 − average A value of ZrO2 NPs group/average A value of negative control group) × 100%. The experiment was performed in triplicates.

Preparation of Samples for TEM

After being treated with fresh medium, ZrO_2 NPs (100 μg/ml) + NAC (160 μg/ml), ZrO_2 NPs (50 μg/ml), or ZrO_2 NPs (100 μg/ml) for 24 h, respectively, HeLa cells were collected by trypsin digestion, washed with PBS and centrifuged at 1,000 rpm for 5 min. PBS wash was repeated three times. Cell clumps (about 1–2 mm^3) were fixed in 3% glutaraldehyde at 4°C for 2 h, after being washed with PBS, and then fixed with 1% osmic acid for 2 h. After dehydration with ethanol and acetone, cells were embedded with Epon821 and followed by polymerization. Cell clumps were sliced by an ultra-thin slicing machine, counterstained with oil and citric lead acetate, and then observed under TEM (GEM-100-CX II, JEO, Japan) and pictures were taken.

Apoptosis Assay by Annexin V-FITC/PI Double Staining

HeLa cells were inoculated into culture bottles, treated with fresh medium, ZrO_2 NPs (100 μg/ml) + NAC (160 μg/ml), ZrO_2 NPs (50 μg/ml), or ZrO_2 NPs (100 μg/ml), respectively. After 24 h, cells were digested with Trypsin that did not contain EDTA, collected, washed with pre-cooled PBS twice, and centrifuged (2000 rpm, 5 min) at 4°C. 1–5 × 10^5 cells were collected. PBS was discarded, and 100 μl 1x Binding Buffer was added to re-suspend the cells. 5 μl Annexin V-FITC and 10 μl PI Staining Solution was added and mixed gently. The cells were incubated in dark at room temperature for 10–15 min. 400 μl 1x Binding Buffer was added, and the cells were suspended. The samples were subjected to FCM (BectonDickinson-LSR, United States) within 1 h.

MMP Assay

HeLa cells were inoculated into culture bottles, treated with fresh medium, ZrO_2 NPs (100 μg/ml) + NAC (160 μg/ml), ZrO_2 NPs (50 μg/ml), or ZrO_2 NPs (100 μg/ml), respectively. After 24 h, cells were collected, washed, and suspended with 500 μl PBS. 500 μl Rhodamine 123 (10 mg/L) was added to each cell suspension. After incubation at 37°C for 30 min, cells were washed with PBS three times, and suspended with PBS. FCM (BectonDickinson-LSR, United States) was used to detect the

MMP of HeLa cells. The excitation wavelength is 488 nm and the emission wavelength is 525 nm.

Reactive Oxygen Species Detection

HeLa cells were inoculated into culture bottles, treated with fresh medium, ZrO_2 NPs (100 μg/ml) + NAC (160 μg/ml), ZrO_2 NPs (50 μg/ml), or ZrO_2 NPs (100 μg/ml), respectively. Cells were collected after 24 h and washed with PBS three times. The cells were collected and suspended in DCFH-DA (10 mmol/L) with a cell concentration of 1–20 × 10^6/ml, and incubated at 37°C for 20 min. The cells were washed three times with serum-free cell culture medium to fully remove DCFH-DA, and cellular ROS level was detected by FCM (BectonDickinson-LSR, United States).

Superoxide Anion, Singlet Oxygen, and Hydroxyl Radical Detection

To further explore which kinds of ROS were generated by ZrO_2 NPs, we detected the superoxide anion, singlet oxygen, and hydroxyl radicals in HeLa cells after treated with ZrO_2 NPs.

Superoxide Anion in HeLa Cells Detected by Superoxide Anion Detection Kit After Treated With ZrO_2 NPs

The 100 fold diluted probe was added to serum-free cell culture medium, and the cells were incubated at 37°C for 2 h in dark, washed twice with PBS, observed and photographed under fluorescence microscope (ECLIPSE TE2000-U, Nikon, Japan, excitation wavelength: 518 nm, emission wavelength: 606 nm).

Singlet Oxygen in HeLa Cells Detected by Singlet Oxygen Detection Kit After Treatment With ZrO_2 NPs

The 100 fold diluted singlet oxygen R probe was added to serum-free cell culture medium, and the cells were incubated at 37°C for 2 h in the dark, washed twice with PBS, and observed and photographed under fluorescence microscope (ECLIPSE TE2000-U, Nikon, Japan, excitation wavelength: 488 nm, emission wavelength: 526 nm).

Hydroxyl Radicals in HeLa Cells Were Detected by Hydroxyl Radical *In Situ* Fluorescence Staining Kit After Treated With ZrO_2 NPs

The cell medium was discarded and 500 μl of Reagent A added. Cleaning agent (Reagent A) was disposed of, then 500 μl of Reagent B and Reagent C were added, then incubated with cells at 37°C in cell incubator for 30 min. The staining agent was discarded, and 500 μl of preheated Reagent D was added at 37°C and observed and photographed with inverted fluorescence microscope (ECLIPSE TE2000-U, Nikon, Japan, excitation wavelength: 499 nm, emission wavelength: 515 nm).

Establishment of Xenograft Animal Model

Female BALB/c nude mice aged 6 weeks (about 20 g) were purchased from Hunan Slake Jingda Laboratory animal Co. Ltd. Xenograft tumor models of nude mice were prepared by subcutaneous inoculation of HeLa cells at 1 × 10^7/100 μl.

Anticancer Effect of ZrO_2 NPs on Nude Mice With Transplanted Tumor

Day 1 was defined when tumor volume reaches 100 mm^3. Female BALB/c nude mice were randomly divided into four groups with five in each group. PBS, ZrO_2 NPs (50 mg/Kg/d) + NAC (80 mg/Kg/d), ZrO2 NPs (25 mg/Kg/d), and ZrO2 NPs (50 mg/Kg/d) was injected into the tail vein in 100 μl daily for four consecutive days. Tumor volume and body weight were measured every 4 days. On the 20th day, mice were anesthetized and sacrificed. Whole blood, tumor, and tissues (heart, liver, spleen, lung, and kidney) were collected. Whole blood was collected with EDTA anticoagulation, and analyzed on BC-5390 (Mindray, China). Whole blood samples were centrifuged at 3,000 rpm for 10 min, and the serum enzymatic indexes were detected by automatic biochemical analyzer (7100, HITACHI, Japan) and immune analyzer (Cobas 6000 e601, ROCHE, United States). All the organs and tumor tissues were either fixed with 4% paraformaldehyde or stored in −80°C until use. Frozen tissue sections were prepared for immunofluorescence staining and Western Blotting. Fixed tissues were embedded in paraffin and made into tissue sections for HE staining, immunofluorescence and immunohistochemical staining.

Immunohistochemistry and Immunofluorescence Staining

Ki-67 Assay

Paraffin-embedded tumor sections were dewaxed and antigen repaired in the antigen repair solution. Slices were heated to 95°C for 20 min, then slowly cooled to 65°C, and placed in the elution buffer for 5 min. The slices were incubated with peroxidase blocker, rinsed with elution buffer for 5 min, incubated with primary antibody for 20 min, washed with elution buffer, incubated with secondary antibody for 20 min, and flushed with elution buffer. Then DAB was applied for color rendering. The slices were rinsed with tap water, stained with hematoxylin, and then rinsed in 70% alcohol, 80% alcohol, 90% alcohol, 100% alcohol, and 100% alcohol for 2 min, respectively. The slices were vitrified by dimethylbenzene. The slices were sealed with neutral gum, observed and photographed under a light microscope.

TUNEL, MMP and ROS Assay

Frozen sections of tumor tissues were used to detect the apoptosis according to the instructions of One Step TUNEL Apoptosis Assay Kit. The cells were fixed for 30–60 min with 4% paraformaldehyde. The slices were washed with PBS twice for 10 min each time, incubated in PBS containing 0.5% Triton X-100 at room temperature for 5 min, washed twice with PBS, incubated with 50 μl TUNEL test solution at 37°C in the dark for 60 min, and washed with PBS three times. The nuclei were counterstained with DAPI. The slices were sealed with anti-fluorescence quenching solution.

Frozen sections of tumor tissue were incubated with JC-1 staining solution at 37°C for 20 min, washed with JC-1 staining buffer twice. The nuclei were counterstained with DAPI.

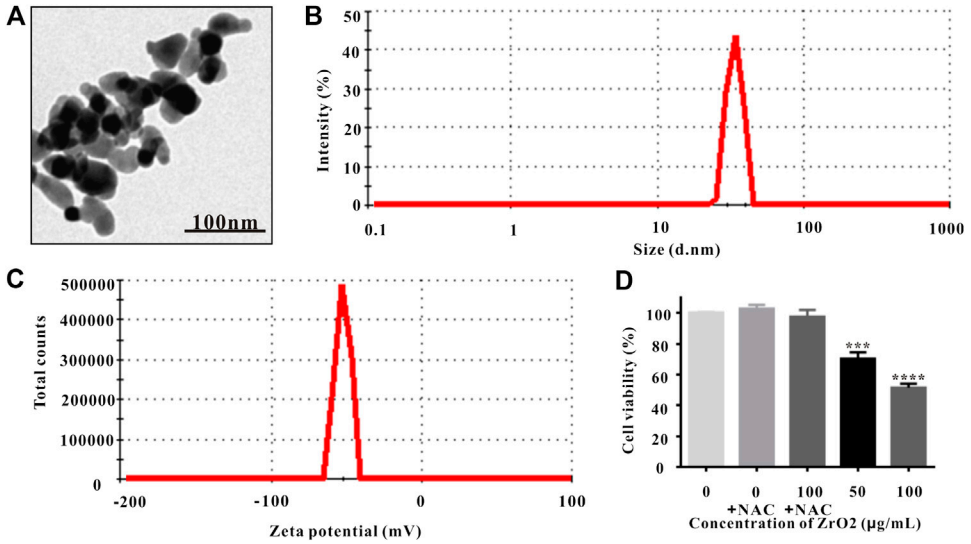

FIGURE 1 | Characterization of ZrO_2 NPs. **(A)** TEM image of ZrO_2 NPs. Scale bar: 100 nm. **(B)** The particle size of ZrO_2 NPs. **(C)** Zeta potential of ZrO_2 NPs. **(D)** HeLa cell viability upon administration of NAC, ZrO_2 NPs, and ZrO_2 NPs + NAC for 24 h, respectively. Data are mean ± SD ($n = 3$). Compared to the control group: $^{***}p < 0.001$, and $^{****}p < 0.0001$.

Frozen tissue slices were incubated in DCFH-DA (10 mmol/L) at 37°C for 20 min and washed three times with PBS to fully remove DCFH-DA. The nuclei were counterstained with DAPI. All the tissue sections were observed and photographed under fluorescence microscope (ECLIPSE TE2000-U, Nikon, Japan).

Western Blot Detection of Apoptosis and Autophagy-Related Proteins

The cryopreserved tumor tissues were blended with cell lysis solution for 40 min, centrifugated (13,000 rpm, 20 min) at 4°C, and supernatant was taken for protein quantification with BCA Protein Assay Kit. Protein samples were separated by 80 V electrophoresis and transferred to nitrocellulose membrane. Sealed membrane protein was blotted with Tris Buffered Saline Tween (TBST) buffer containing 5% skim milk at room temperature for 1 h, and then blotted at room temperature for 1 h with anti-Bax, anti-Bcl-2, anti-Caspase-3, anti-Caspase-9, anti-Cytochrome C, anti-Beclin-1, anti-LC3, anti-Atg5, anti-Atg12, and anti-β-actin antibody, respectively. Membranes were washed with TBST three times, 10 min each, and then incubated with horseradish peroxidase (HRP)-labeled goat anti-mouse or goat anti-rabbit IgG secondary antibody at room temperature for 1 h. Membranes were washed with TBST three times, 10 min each, reacted with enhanced chemical illuminant (ECL), and developed by exposure on X film.

Image and Statistical Analysis

SPSS 20.0 software was used for statistical analysis, and GraphPad Prism plot was used to plot the data. Data was expressed as mean ± standard deviation. ANOVA was used to evaluate the differences between groups, and Tukey's post-test was conducted. $^{*}p < 0.05$, $^{**}p < 0.01$, $^{***}p < 0.001$, and $^{****}p < 0.0001$.

RESULTS AND DISCUSSION

Characterization of Zirconia Nanoparticles

Observed under TEM, ZrO_2 NPs were monodispersed with diameters averaging about 25 nm (**Figure 1A**), which were larger than the previous reported green synthesized Nanozirconia (of ~9–11 nm) using leaf extract of *Eucalyptus globulus* (*E. globulus*) (Balaji, et al., 2017). Based on dynamic light scattering (DLS) data (**Figure 1B**), ZrO_2 NPs averaged 25 nm in size, which was consistent with the data of TEM. Zeta potential is related to colloid stability of nanoparticle-dispersions, and Zeta potential values of ±0–10, ±10–20, and ±20–30 mV and >±30 mV are classified as highly unstable, relatively stable, moderately stable and highly stable (Bhattacharjee, 2016). Nanoparticles with low Zeta potential are easy to agglomerate (Hanaor et al., 2012). ZrO_2 NPs had Zeta potential values of −51.5 ± 3.1 mV (**Figure 1C**), which was higher than the reported green synthesized Nano zirconia (−45.5 mV) (Balaji et al., 2017). Besides, Zeta potentials of ZrO_2 NPs over 180 days did not change significantly (**Supplementary Figure S1**). Taking all these into account, ZrO_2 NPs exhibit higher colloid stability and anti-agglomeration tendency. The X-Ray Diffraction (XRD) pattern indicates that the fitting line is relatively flat and the fitting is very good (**Supplementary Figure S2A**), and the crystallinity of ZrO_2 NPs is 99.3% (**Supplementary Figure S2B**).

Cell Viability and Mitochondrial Metabolic Activity of HeLa Cell Growth

MTT assay is widely used to assess cell viability, and the involvement of mitochondrial metabolic activity in MTT

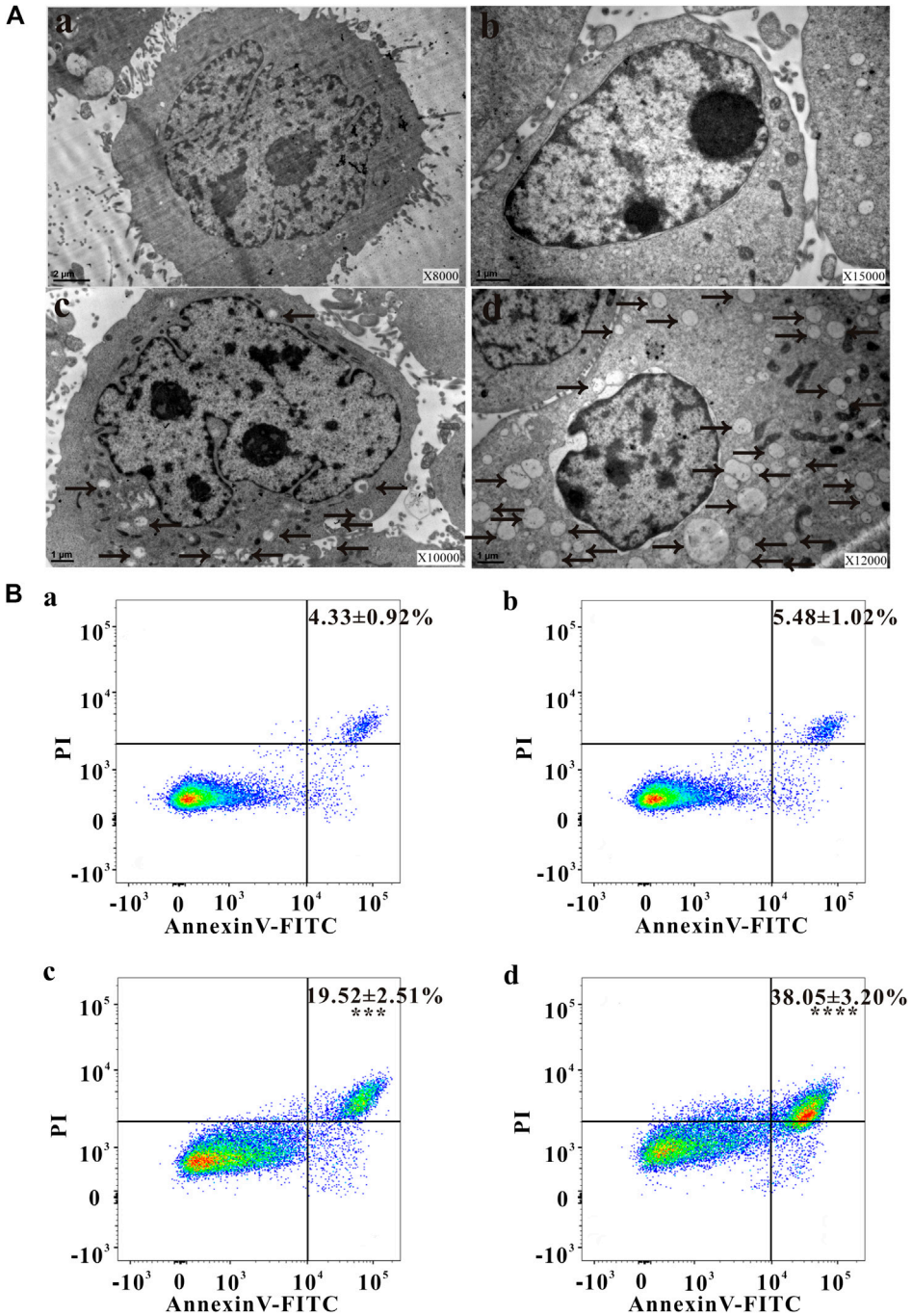

FIGURE 2 | Changes of ultrastructure, apoptosis ratio, MMP and ROS level of HeLa cells. **(A)** The ultrastructural changes of HeLa cells after treatment with ZrO_2 NPs, and ZrO_2 NPs + NAC for 24 h, respectively. **(B)** Apoptosis ratio of HeLa cells after treatement with ZrO_2 NPs and ZrO_2 NPs + NAC detected by Flow Cytometer. a: Control; b: ZrO_2 NPs (100 μg/ml) + NAC (160 μg/ml); c: ZrO_2 NPs (50 μg/ml); d: ZrO_2 NPs (100 μg/ml). Data are presented as the mean ± SD (n = 3). Compared to the control group: ***$p < 0.001$ and ****$p < 0.0001$.

reduction has been confirmed (Berridge and Tan, 1993). NAC, the ROS scavenger, was utilized to suppress ROS accumulation (Singh, et al., 2005; Kim, et al., 2006). MTT assay showed that NAC did not inhibit the viability and mitochondrial metabolic activity of HeLa cells, but the cell viability and mitochondrial metabolic activity of HeLa cells was significantly inhibited (**Figure 1D**). Treating with ZrO_2 NPs together with NAC did not show obvious inhibitory effect (**Figure 1D**), indicating NAC

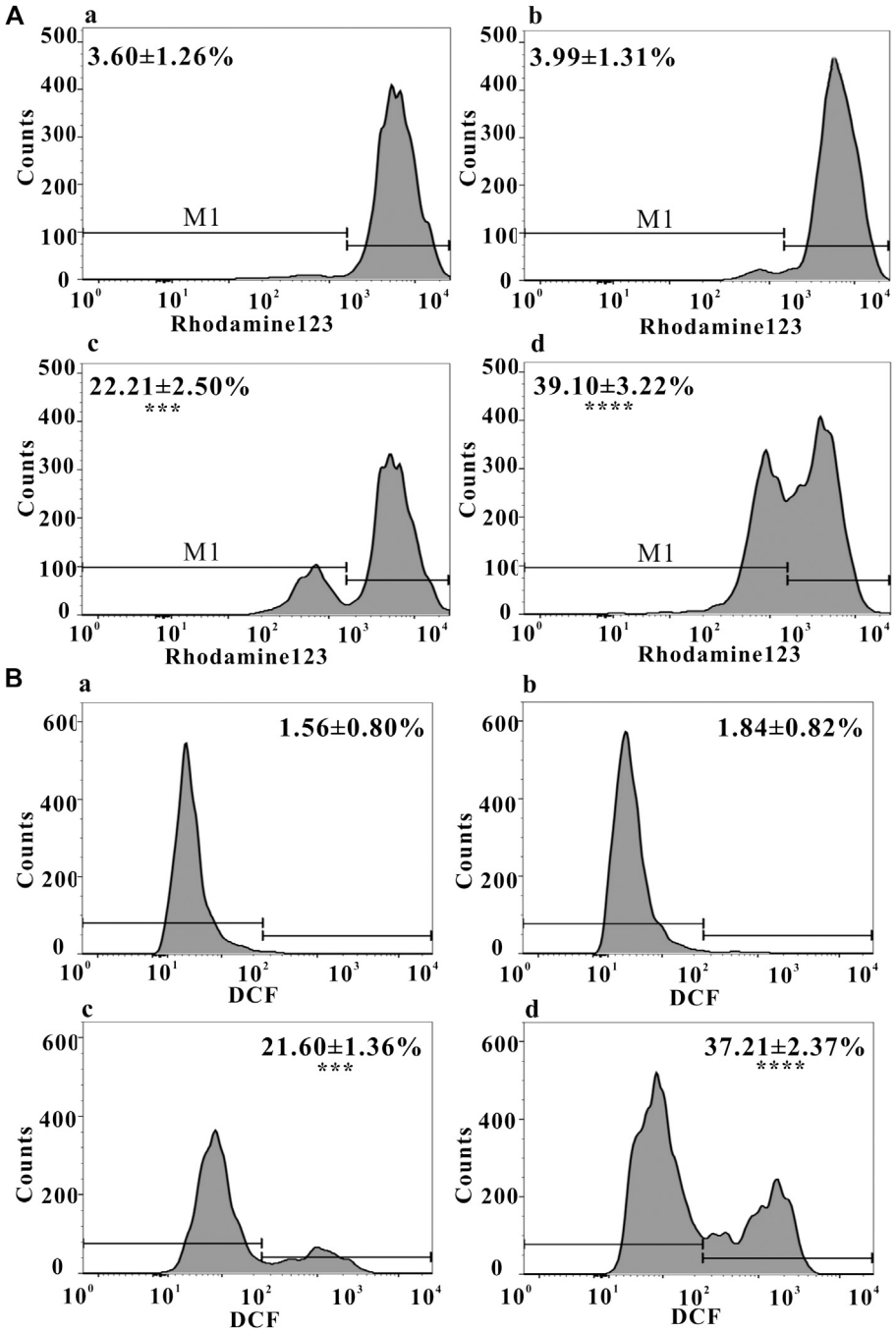

FIGURE 3 | (A) MMP of HeLa cells after treatment with ZrO_2 NPs and ZrO_2 NPs + NAC detected by Flow Cytometer. **(B)** ROS level of HeLa cells after treatment with ZrO_2 NPs and ZrO_2 NPs + NAC detected by Flow Cytometer. a: Control; b: ZrO_2 NPs (100 μg/ml) + NAC (160 μg/ml); c: ZrO_2 NPs (50 μg/ml); d: ZrO_2 NPs (100 μg/ml). Data are presented as the mean ± SD (n = 3). Compared to the control group: ***p < 0.001 and ****p < 0.0001.

could counter the cytotoxicity induced by ZrO_2 NPs and ZrO_2 NPs could inhibit the growth of HeLa cells through ROS production.

Ultrastructure Changes of HeLa Cells Observed Under TEM

Autophagy has been involved in pathological conditions such as cancer and inflammatory diseases (Choi, et al., 2013). Promotion of autophagy has been a potent therapeutic target in human diseases, including tumor (Yoshii and Mizushima, 2017). As shown in **Figures 2Aa,Ab**, no autophagic vacuoles were found in the cytoplasm of HeLa cells, but lots of autophagosomes (black arrows) were present in the apoptotic cells (**Figures 2Ac,Ad**), indicating NAC inhibited the autophagy induced by ZrO_2 NPs. Apoptotic cell death is an important mechanism of anti - tumor therapy and most anticancer drugs exploit apoptotic signaling

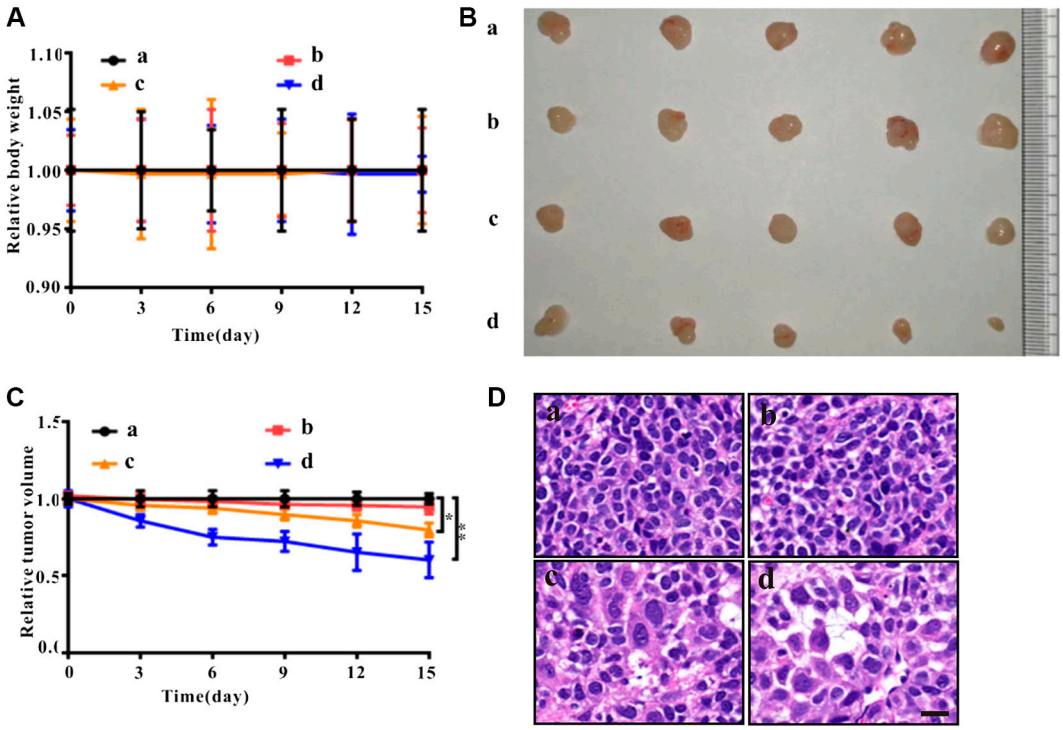

FIGURE 4 | Anticancer effects of ZrO_2 NPs and ZrO_2 NPs + NAC on HeLa bearing BALB/c nude mice. **(A)** The change of body weight after treated with ZrO_2 NPs and ZrO_2 NPs + NAC. **(B)** The representative picture of tumors. **(C)** The change of tumor volume after treated with ZrO_2 NPs and ZrO_2 NPs + NAC. **(D)** The representative cell morphology of tumor tissues after treated with ZrO_2 NPs and ZrO_2 NPs + NAC, and HE staining. Scale bar: 20 μm. a: Control; b: ZrO_2 NPs (50 mg/Kg/d) + NAC (80 mg/Kg/d); c: ZrO_2 NPs (25 mg/Kg/d); d: ZrO_2 NPs (50 mg/Kg/d). Data are presented as the mean ± SD (n = 3). Compared to the control group: ***p < 0.001 and ****p < 0.0001.

pathways to induce cancer cell death (Pistritto et al., 2016). TEM images also showed that autophagy was associated with apoptosis. The membrane of HeLa cell in the control group was intact, while the nuclei, nuclear membrane and nucleoli were clearly visible (**Figure 2Aa**). After ZrO_2 NPs treatment, cells appeared wrinkled while the chromatin became dense and gathered under the nuclear membrane. The mitochondria were swollen and expanded, but the cell membrane was still intact indicating apoptosis (**Figures 2Ac,Ad**). After ZrO_2 NPs plus NAC treatment, the swelling and enlargement of mitochondria in the cells was not obvious, suggesting that NAC inhibited the apoptosis induced by ZrO_2 NPs (**Figure 2Ab**).

Cell Apoptosis Rate, MMP Changes, and ROS Levels Detected by FCM

Escaping from apoptosis is a hallmark of cancer and promoting apoptosis is an interesting therapeutic strategy (Pistritto, et al., 2016). The percentage of apoptotic cells in the control group was low (4.33 ± 0.92%), but apoptosis increased after cells were treated with ZrO_2 NPs (100 μg/ml), reaching 38.05 ± 3.20%. After ZrO_2 NPs plus NAC treatment, the percentage of apoptotic cells was significantly lower than that in the ZrO_2 NPs group, showing that NAC inhibited apoptosis induced by ZrO_2 NPs (**Figure 2B**).

Mitochondrial function, a key indicator of cell apoptosis, can be assessed by monitoring changes in MMP (Sakamuru, et al., 2016). MMP reflects the functional status of the mitochondrion (Zhang, et al., 2015a), and a decrease in MMP is linked to apoptosis (Lemasters, et al., 2002). As shown in **Figure 3A**, after treating with ZrO_2 NPs + NAC for 24 h, the proportion of HeLa cells with weak fluorescence (M1 channel) was 3.99 ± 1.31%, which was close to that in the control group (3.60 ± 1.26%). The proportion of cells with weak fluorescence (M1 channel) in the ZrO_2 NPs (100 μg/ml) groups increased significantly, reaching 39.10 ± 3.22%. This result suggested that ZrO_2 NPs decreased the binding ability of mitochondria to Rhodamine 123, resulting in a decrease of fluorescent dyes entering cells and an increase of the percentage of cells with weak fluorescence, and a decrease of MMP, while NAC could significantly inhibit this effect.

Mitochondria and potentially mitochondrial ROS play an important role in regulating apoptosis (Bender and Martinou, 2013) and autophagy (Chen et al., 2009). As shown in **Figure 3B**, the proportion of DCF-positive cells was 1.56 ± 0.80% in the control group, 1.84 ± 0.82% in the ZrO_2 NPs + NAC group, 21.60 ± 1.36% and 37.21 ± 2.37% in the ZrO_2 NPs 50 and 100μg/ml groups, respectively, suggesting that ZrO_2 NPs promote ROS production in HeLa cells, while NAC

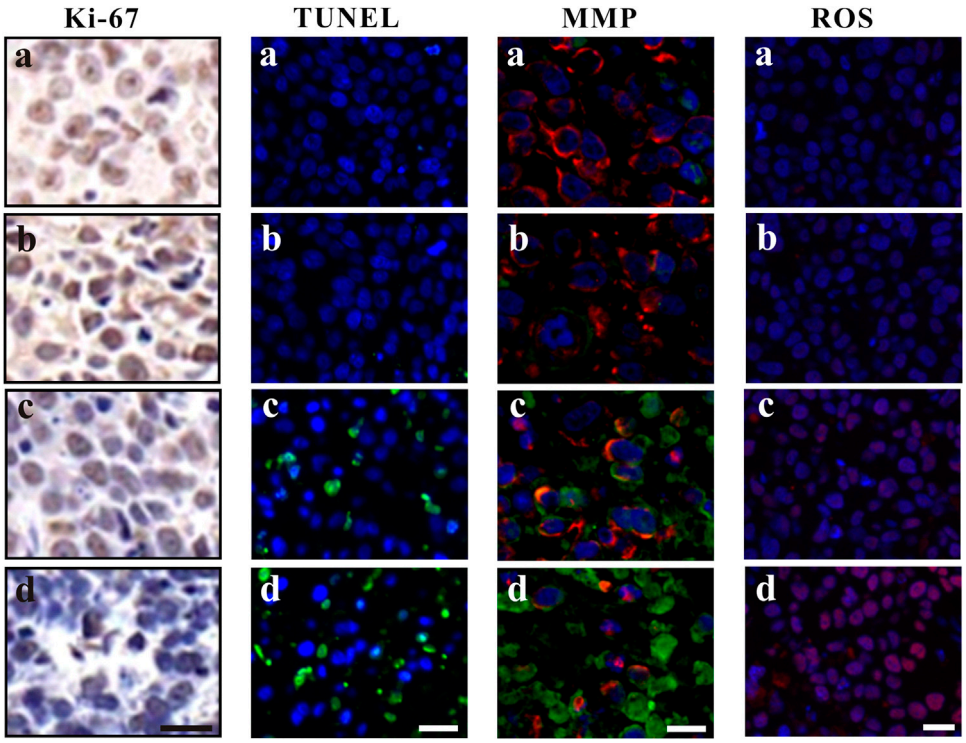

FIGURE 5 | Ki-67 assay, TUNEL assay, MMP assessment and ROS analysis of tumor tissues at 20th day after the intravenous injection of ZrO_2 NPs and ZrO_2 NPs + NAC. a: Control; b: ZrO_2 NPs (50 mg/Kg/d) + NAC (80 mg/Kg/d); c: ZrO_2 NPs (25 mg/Kg/d); d: ZrO_2 NPs (50 mg/Kg/d). Scale bar: 20 μm.

significantly inhibits ROS production induced by ZrO_2 NPs. ROS generation by ZrO_2 NPs is likely caused a decrease in $n \rightarrow \pi^*$ transition intensity due to the transfer of electron from oxygen atom present in ZrO_2 NPs (Balaji, et al., 2017). Further, ZrO_2 NPs may inhibit the scavenging of free radicals (Balaji, et al., 2017).

Generation of Superoxide Anion, Singlet Oxygen, and Hydroxyl Radicals After Treated With Zirconia Nanoparticles

Superoxide Anion Assay

The Bestbio ® BBoxiProbe® superoxide anion detection kit is a superoxide anion detection kit that utilizes the BBoxiProbe® O88 superoxide anion specific fluorescent probe. BBoxiProbe ® O88 can enter the cell freely through the living cell membrane and is oxidized by the intracellular superoxide anion to produce red fluorescence products. According to the production of red fluorescence in living cells, the amount and change of cell superoxide anion content can be determined. Superoxide anion was transformed from an oxygen molecule which accepted an electron. Repeated such reactions lead to an excess of superoxide anions, resulting in cytotoxicity (Sun, et al., 2020). After treatment with ZrO_2 NPs, red fluorescence in HeLa cells enhanced (**Supplementary Figure S3A**), indicating generation of superoxide anion to induce cell death.

Singlet Oxygen Assay

Singlet oxygen specific fluorescent probe *R* in Singlet oxygen detection kit was used to detect singlet oxygen. Singlet oxygen probe *R* is a synthetic phenylanthracene fluorescent probe, which can freely enter cells, react with singlet oxygen in cells, and be oxidized to produce green fluorescent substances. The intensity of green fluorescence is proportional to the level of singlet oxygen in cells, and the changes of singlet oxygen in cells can be known by detecting green fluorescence. O_2 derivatives (such as singlet oxygen and hydroxyl radical), owing to their redox potential, can promote cell death (Bubici, et al., 2006). After being treated with ZrO_2 NPs, green fluorescence in HeLa cells was enhanced (**Supplementary Figure S3B**), indicating that ZrO_2 NPs increased the generation of singlet oxygen to induce HeLa cells death.

Hydroxyl Radical Assay

Hydroxyphenyl fluorescein (HPF) is a kind of dye that passes through cell membrane freely. Once it reacts with hydroxyl radicals, it generates o-dearylation and fluorescein. These results proved the existence of hydroxyl radical reactive oxygen group in cells. Enhanced green fluorescence indicates high hydroxyl radical content. Excess hydroxyl radical (OH) can promote oxidation and stimulate lipid peroxidation (Polyakov, et al., 2018), damage DNA and protein, and promote the apoptosis of cancer cells (Lin

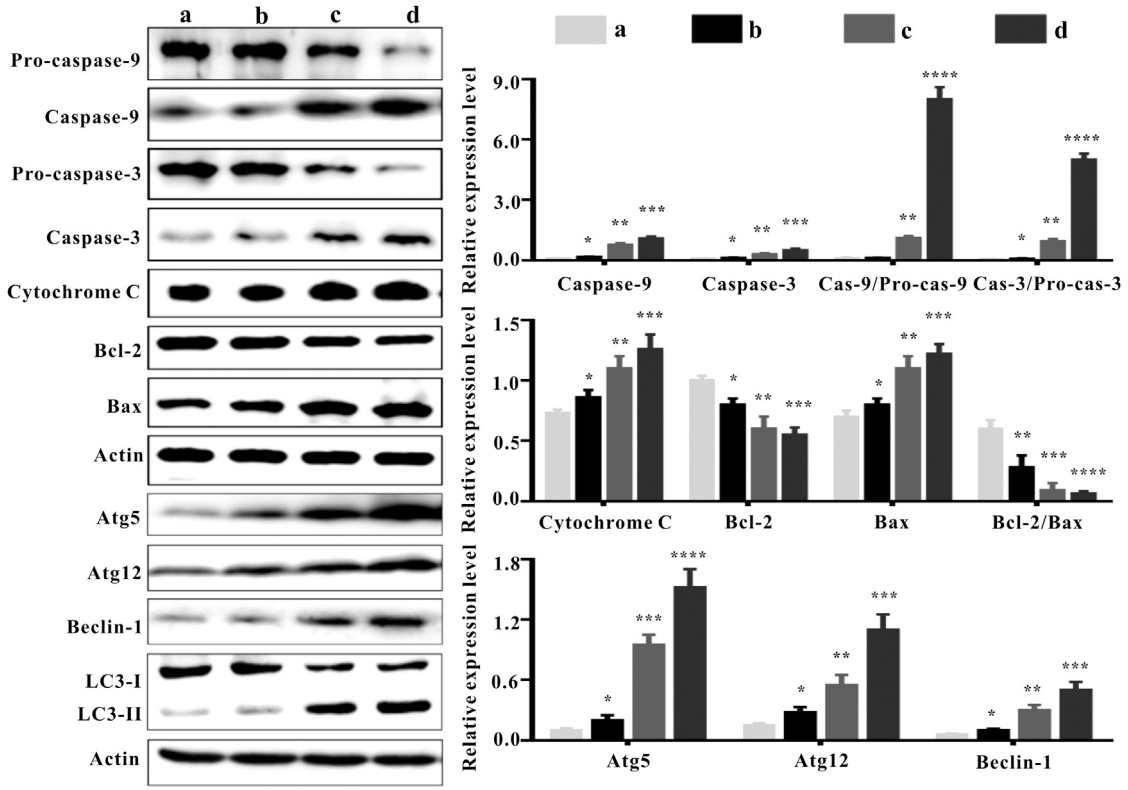

FIGURE 6 | Apoptosis and autophagy-associated protein expressions in tumor tissues at the 20th day after intravenous injection of ZrO_2 NPs and ZrO_2 NPs + NAC. a: Control; b: ZrO_2 NPs (50 mg/Kg/d) + NAC (80 mg/Kg/d); c: ZrO_2 NPs (25 mg/Kg/d); d: ZrO_2 NPs (50 mg/Kg/d). Data are presented as the mean ± SD (n = 3). Compared to the control group: $^{*}p < 0.05$, $^{**}p < 0.01$, $^{***}p < 0.001$, and $^{****}p < 0.0001$.

et al., 2018). After being treated with ZrO_2 NPs, green fluorescence in HeLa cells was enhanced (**Supplementary Figure S3C**), indicating that ZrO_2 NPs can promote the generation of hydroxyl radical, which may play an important role in inducing HeLa cells apoptosis.

Antitumor Effect of Zirconia Nanoparticles *in vivo*

As shown in **Figure 4A**, compared to the control group, there was no significant change in body weight of nude mice treated with ZrO_2 NPs and ZrO_2 NPs + NAC. As shown in **Figures 4B,C**, compared to the control group, tumor volume decreased after ZrO_2 NPs treatment, suggesting that ZrO_2 NPs inhibit tumor growth. However, ZrO_2 NPs plus NAC treatment did not further decrease tumor volume. After HE staining, tumor tissue sections (**Figure 4D**) showed tumor cells were thriving in the control group and the ZrO_2 NPs + NAC group. After ZrO_2 NPs treatment, necrotic HeLa cells increased, suggesting that ZrO_2 NPs inhibit HeLa cell growth while NAC counteracts the inhibition effect induced by ZrO_2 NPs.

Immunohistochemistry and Immunofluorescence Staining of Tumor Sections

Ki-67 Immunohistochemistry and TUNEL Immunofluorescence Assays

Ki-67, a nuclear and nucleolar protein, is associated with cell proliferation (Campelo, et al., 2015). As shown in **Figure 5**, compared to the control group, Ki-67-positive (brown) cells decreased after ZrO_2 NPs treatment, while the decrease of Ki-67 labeling was not apparent in the ZrO_2 NPs + NAC group suggesting that ZrO_2 NPs could inhibit HeLa cell proliferation, and NAC could counter the inhibitory effect induced by ZrO_2 NPs. TUNEL assay has been designed to detect apoptotic cells that undergo extensive DNA degradation during the late stages of apoptosis, which is based on the ability of TdT to label blunt ends of double-stranded DNA breaks independent of a template (Kyrylkova, et al., 2012). As shown in **Figure 5**, compared to the control group, TUNEL-positive (green fluorescent) cells increased after ZrO_2 NPs treatment, but no obvious change was detected in the ZrO_2 NPs + NAC group, suggesting that ZrO_2 NPs induce apoptosis of HeLa cells and that NAC reverses the apoptosis induced by ZrO_2 NPs.

TABLE 1 | The blood cell counts, the enzyme level and myocardial enzyme spectrum analysis of tumor bearing mice after treated with ZrO_2 NPs, or ZrO_2 NPs + NAC.

	Control	ZrO_2 NPs (50 mg/kg/d) + NAC (80 mg/Kg/d)	ZrO_2 NPs (25 mg/kg/d)	ZrO_2 NPs (50 mg/kg/d)
Blood cell count				
WBC(10^9/L)	7.5 ± 0.4	7.3 ± 0.7	7.5 ± 0.4	7.6 ± 0.4
RBC(10^{12}/L)	11.2 ± 1.3	11.3 ± 1.1	11.2 ± 0.7	11.3 ± 1.0
HGB(g/dl)	14.6 ± 0.4	14.7 ± 0.3	14.5 ± 0.5	14.4 ± 0.6
HCT(%)	49.0 ± 1.4	49.2 ± 0.3	48.8 ± 1.1	48.7 ± 0.3
PLT(10^{11}/L)	8.6 ± 0.3	8.4 ± 0.5	8.4 ± 0.6	8.3 ± 0.7
Serum enzyme level				
ALT(U/L)	9.6 ± 0.3	9.6 ± 0.4	9.7 ± 0.5	9.8 ± 0.6
AST(U/L)	47.6 ± 2.3	47.7 ± 2.1	48.5 ± 2.5	48.8 ± 2.6
BUN(mmol/L)	2.0 ± 0.2	2.0 ± 0.3	2.2 ± 0.2	2.3 ± 0.3
Cr(μmol/L)	6.6 ± 0.3	6.6 ± 0.4	6.7 ± 0.3	6.8 ± 0.3
Myocardial enzyme spectrum				
TNT-HS(pg/ml)	47.5 ± 3.4	47.4 ± 3.8	47.9 ± 3.1	48.2 ± 3.2
CK(U/L)	3742.0 ± 120.2	3745.3 ± 122.8	3775.4 ± 131.9	3790.3 ± 147.2
LDH-L(U/L)	7695.2 ± 120.2	7699.5 ± 122.3	7695.4 ± 111.8	7709.3 ± 120.4
CK-MB(U/L)	3780.5 ± 76.1	3782.5 ± 101.2	3792.3 ± 104.0	3809.9 ± 112.5
Myo(ng/ml)	73.4 ± 2.8	73.5 ± 3.2	73.7 ± 3.4	73.9 ± 3.5

Data are mean ± SD (n = 3).

MMP and ROS Immunofluorescence Staining

The decrease of MMP is the direct consequence of the imbalance between pro-apoptosis factor and anti-apoptosis factor, which leads to altered mitochondrial permeability and triggers an early and subsequent intracellular event in apoptosis (Cetindere, et al., 2010; Indran, et al., 2011). The lipophilic cation JC-1 has been used as a specific dye for measuring MMP (De Biasi, et al., 2015). As shown in **Figure 5**, cells of tumor tissue sections in the control group and ZrO_2 NPs + NAC group showed robust staining with JC-1, indicating active proliferation. However, cells in the ZrO_2 NPs group had a significant decrease of MMP as indicated by the increase of green fluorescent cells, suggesting that ZrO_2 NPs result in MMP reduction in HeLa cells. ROS formation has long been found to play a vital role in mediating apoptosis (Pierce, et al., 1991). As shown in **Figure 5**, DCFH-DA intensity was much stronger in tumor cells treated with ZrO_2 NPs than that of the control group and ZrO_2 NPs + NAC group, and the intensity increases as the dose of ZrO_2 NPs increases, suggesting that ZrO_2 NPs induce tumor cells to produce ROS while NAC could inhibit the ROS production induced by ZrO_2 NPs.

Changes in Apoptosis and Autophagy-Associated Proteins Expression

The balance between Bcl-2 family members which include anti-apoptotic proteins (such as Bcl-2) and pro-apoptotic proteins (such as Bax) determine the fate of a cell (Adams and Cory, 2007). Bcl-2 expression was down-regulated in the ZrO_2 NPs groups (25 mg/Kg/d, 50 mg/Kg/d) (**Figure 6**), suggesting that ZrO_2 NPs could promote apoptosis in HeLa cells. Compared to the ZrO_2 NPs (50 mg/Kg/d) group, there was relatively milder up-regulation of Bax and the down-regulation of Bcl-2 in the ZrO_2 NPs + NAC group.

The family of proteases known as the caspases play a key role in apoptosis (Li and Yuan, 2008). Caspases are central to apoptosis as they include both the initiators which are primarily responsible for the beginning of the apoptotic pathway (such as Caspase-2, -8, -9, and -10) and the executors which are responsible for the definite cleavage of cellular components (such as Caspase-3, -6 and -7) (Thornberry and Lazebnik, 1998; Lakhani et al., 2006). ZrO_2 NPs could down-regulate the expressions of Pro-caspase-9 and Pro-caspase-3. However, the expressions of Caspase-9 and Caspase-3 were up-regulated by ZrO_2 NPs, suggesting that Caspase-9 and Caspase-3 are activated. Compared to the ZrO_2 NPs (50 mg/Kg/d) group, there was a milder up-regulation of Pro-caspase-9 and Pro-caspase-3 and a milder down-regulation of Caspase-9 and Caspase-3 in the ZrO_2 NPs + NAC group, indicating that ZrO_2 NPs promote apoptosis and NAC inhibits the apoptosis induced by ZrO_2 NPs.

Translocation of Bax into mitochondria, which initiates the mitochondrial apoptosis pathway and causes the release of Cyt C from the mitochondria (Guo, et al., 2012) prompts the binding of Apaf-1 to Caspase-9, thus activating Caspase-9 (Brentnall et al., 2013) and inducing subsequent cell death (Jiang and Wang, 2004). Compared to the control group, cytoplasmic Cyt C expression was significantly increased by ZrO_2 NPs, while the up-regulation of Cyt C in the ZrO_2 NPs + NAC group was relatively weak. Taken together, these results suggest that NAC inhibits the mitochondria mediated apoptosis induced by ZrO_2 NPs.

ROS are involved in the regulation of a variety of biological processes (Galadari et al., 2017). Increased ROS in cancer cells may eliminate cancer cells via activating various ROS-induced cell death pathways including autophagy (Chen et al., 2017). In addition to apoptosis, autophagy is also a mode of programmed cell death (Liu and Levine, 2015). LC3-II transforming from LC3-I, a hallmark of autophagy (Rabinowitz and White, 2010), participates in autolysosome formation (Boya et al., 2013). As

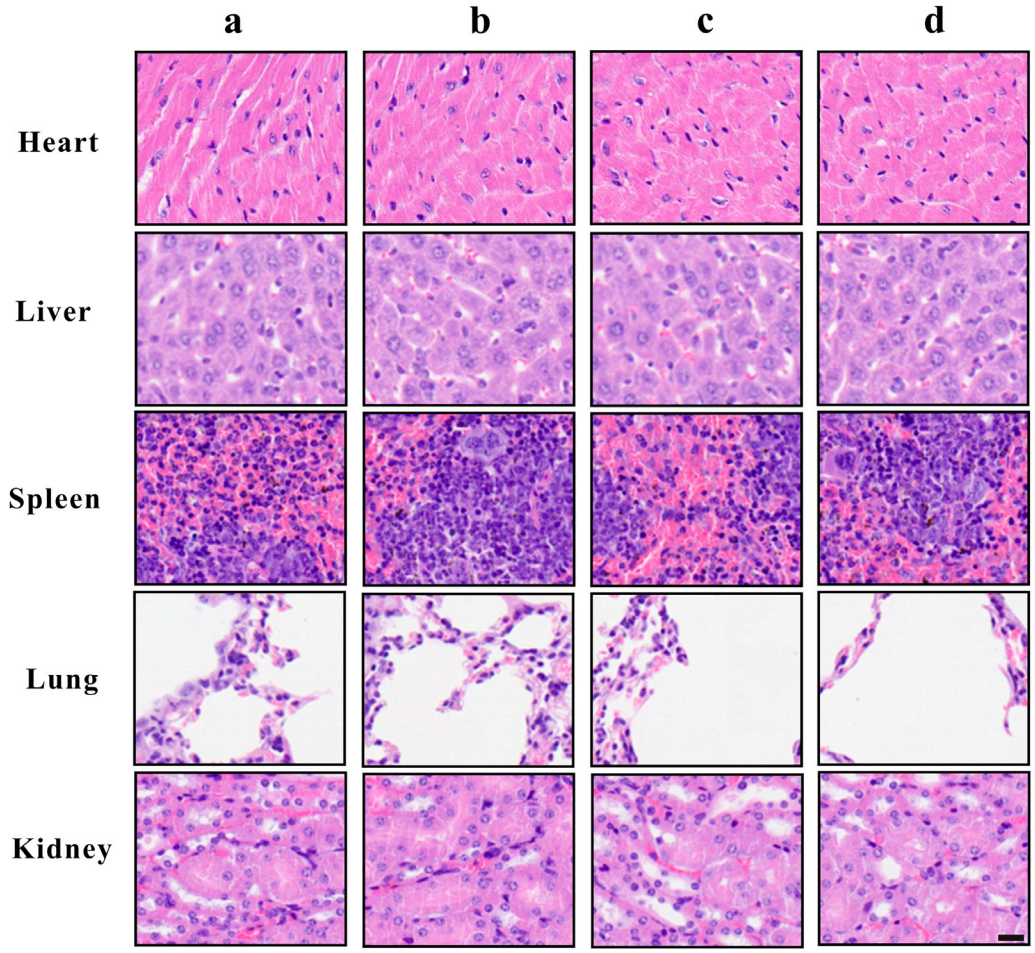

FIGURE 7 | Tissue morphology of heart, liver, spleen, lung, and kidney after ZrO_2 NPs or ZrO_2 NPs + NAC treatment, and HE staining. a: Control; b: ZrO_2 NPs (50 mg/Kg/d) + NAC (80 mg/Kg/d); c: ZrO_2 NPs (25 mg/Kg/d); d: ZrO_2 NPs (50 mg/Kg/d). Scale bar: 20 μm.

shown in **Figure 6**, ZrO_2 NPs decreased LC3-I expression in HeLa cells but increased LC3-II expression, indicating that LC3-I was transformed into LC3-II after ZrO_2 NPs treatment. In addition, NAC reversed the changes observed with ZrO_2 NPs treatment by restoring the expression levels of LC3-I and LC3-II to close to those in the control group.

Recent studies suggest that autophagy plays a dual role in determining cell fate. It either functions as a survival mechanism or induce programmed cell death under different cellular stresses (Zhang et al., 2015b). *ATG 5* is a major autophagy gene required for autophagosome synthesis (Mizushima, 2007). Beclin-1 governs autophagosome formation and recruits other autophagy proteins to the pre-autophagosomal membrane (Kihara, et al., 2001). During the expansion of autophagosome membranes, Atg7 activates Atg12 which is transferred to Atg10 and covalently linked to Atg5 (Kihara, et al., 2001). ZrO_2 NPs could up-regulate autophagy-related proteins, including Atg5, Atg12, and Beclin-1, while NAC inhibited the up-regulation of their expressions in the ZrO_2 NPs + NAC group. These results suggest that ZrO_2 NPs promote autophagy in HeLa cells by activating ATGs and upregulating the expression of autophagy related proteins, while NAC inhibits the effect induced by ZrO_2 NPs.

Complete Blood Count, Serum Enzyme Levels and Tissue Images

To assess the hematologic toxicity of ZrO_2 NPs, CBC analysis was conducted. In mice treated with ZrO_2 NPs, CBC analysis showed that the counts of white blood cell (WBC), red blood cell (RBC) and platelets (PLT) were all in the normal range. To assess the effect of ZrO_2 NPs on visceral organ function, serum enzyme assays and histological assays were performed. As shown in **Table 1**, liver function indicators (alanine transaminase (ALT), aspartate amino-transferase (AST)) did not increase. Renal function indicators (blood urea nitrogen (BUN) and creatinine (Cr)) were not elevated either. Further, ZrO_2 NPs did not alter cardiac toxicity indexes (lactate dehydrogenase (LDH), hypersensitive troponin T (TNT - HS), creatine kinase (CK), creatine kinase-MB (CK - MB) and myoglobin (Myo)) levels (**Table 1**). On day 20 after treatment, nude mice vital tissue and organ specimens were

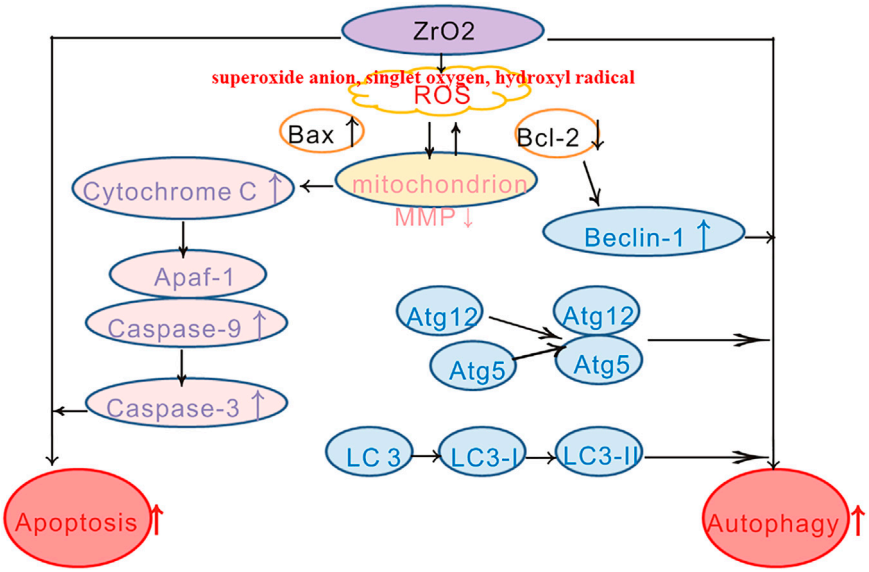

SCHEME 1 | Schematic diagram of HeLa cell death induced by ZrO_2 NPs through mitochondrial apoptosis and autophagy pathway mediated by ROS.

sectioned and stained with HE. No significant abnormalities were found in the heart, liver, spleen, lung, and kidney (**Figure 7**). These results suggest that ZrO_2 NPs do not cause significant myelosuppression and toxicity to the heart, liver, spleen, lungs, and kidneys. In summary, ZrO_2 NPs have no apparent systemic toxic effects.

CONCLUSION

ZrO_2 nanoparticles treatment results in swollen mitochondria, increased apoptosis rate, decreased MMP, reduced Ki-67 labeling and increased TUNEL-positive cells, increased expression of mitochondrial apoptotic proteins (Bax, Caspase-3, Caspase-9, and Cyt C). Besides, autophagic vacuoles, increased expression of autophagy-related proteins (Atg5, Atg12, Beclin-1, and LC3-II) can also be detected. To conclude, ZrO_2 nanoparticles induce HeLa cell death through apoptosis and autophagy pathways. NAC, a ROS-reducing agent, significantly reduced the rate of apoptosis, MMP, and *in vivo* anti-tumor activity. Based on these observations, we conclude that ZrO_2 NPs could induce tumor cells death via apoptosis and autophagy, which is mediated by ROS (**Scheme 1**).

DATA AVAILABILITY STATEMENT

The raw data supporting the conclusions of this article will be made available by the authors, without undue reservation, to any qualified researcher.

ETHICS STATEMENT

The animal study was reviewed and approved by the Ethics committee of the Third Xiangya Hospital of Central South University.

AUTHOR CONTRIBUTIONS

The manuscript was written through contributions of all authors. All authors have given approval to the final version of the manuscript.

FUNDING

This work was supported by the National Natural Science Foundation of China (No. 81971748), National Natural Science Foundation of China (No. 81600461), National Natural Science Foundation of China (No. 81602801), and the Graduate Self-Exploration and Innovation Project of Central South University of China under Grant (No. 2019zzts363).

SUPPLEMENTARY MATERIAL

The Supplementary Material for this article can be found online at: https://www.frontiersin.org/articles/10.3389/fchem.2021.522708/full#supplementary-material.

REFERENCES

Adams, J. M., and Cory, S. (2007). The Bcl-2 apoptotic switch in cancer development and therapy. *Oncogene* 26 (9), 1324–1337. doi:10.1038/sj.onc.1210220

Addabbo, F., Montagnani, M., and Goligorsky, M. S. (2009). Mitochondria and reactive oxygen species. *Hypertension* 53 (6), 885–892. doi:10.1161/hypertensionaha.109.130054

Al-Fahdawi, M. Q., Rasedee, A., Al-Qubaisi, M. S., Alhassan, F. H., Rosli, R., et al. (2015). Cytotoxicity and physicochemical characterization of iron-manganese-doped sulfated zirconia nanoparticles. *Int. J. Nanomedicine* 10, 5739–5750. doi:10.2147/IJN.S82586

Araveti, P. B., and Srivastava, A. (2019). Curcumin induced oxidative stress causes autophagy and apoptosis in bovine leucocytes transformed by *Theileria annulata*. *Cell Death Discov.* 5, 100. doi:10.1038/s41420-019-0180-8

Balaji, S., Mandal, B. K., Ranjan, S., Dasgupta, N., and Chidambaram, R. (2017). Nano-zirconia - evaluation of its antioxidant and anticancer activity. *J. Photochem. Photobiol. B.* 170, 125–133. doi:10.1016/j.jphotobiol.2017.04.004

Bender, T., and Martinou, J. C. (2013). Where killers meet--permeabilization of the outer mitochondrial membrane during apoptosis. *Cold Spring Harb. Perspect. Biol.* 5 (1), a011106. doi:10.1101/cshperspect.a011106

Berridge, M. V., and Tan, A. S. (1993). Characterization of the cellular reduction of 3-(4,5-dimethylthiazol-2-yl)-2,5-diphenyltetrazolium bromide (MTT): Subcellular localization, substrate dependence, and involvement of mitochondrial electron transport in MTT reduction. *Arch. Biochem. Biophys.* 303 (2), 474–482. doi:10.1006/abbi.1993.1311

Bhattacharjee, S. (2016). DLS and zeta potential - What they are and what they are not?. *J. Controlled Release* 235, 337–351. doi:10.1016/j.jconrel.2016.06.017

Boya, P., Reggiori, F., and Codogno, P. (2013). Emerging regulation and functions of autophagy. *Nat. Cell Biol.* 15 (7), 713–720. doi:10.1038/ncb2788

Brentnall, M., Rodriguez-Menocal, L., De Guevara, R. L., Cepero, E., and Boise, L. H. (2013). Caspase-9, caspase-3 and caspase-7 have distinct roles during intrinsic apoptosis. *BMC Cell Biol.* 14, 32. doi:10.1186/1471-2121-14-32

Bubici, C., Papa, S., Dean, K., and Franzoso, G. (2006). Mutual cross-talk between reactive oxygen species and nuclear factor-kappa B: molecular basis and biological significance. *Oncogene* 25 (51), 6731–6748. doi:10.1038/sj.onc.1209936

Campelo, A. P., Campelo, M. W., Brito, G. A., Jamacaru, F. V., Leitao, R. F., et al. (2015). Oil mixes omega 9, 6 and 3, enriched with seaweed, promoted reduction of thermal burned modulating NF-kB and Ki-67. *Acta Cir. Bras.* 30 (6), 430–438. doi:10.1590/s0102-865020150060000009

Cetindere, T., Nambiar, S., Santourlidis, S., Essmann, F., and Hassan, M. (2010). Induction of indoleamine 2, 3-dioxygenase by death receptor activation contributes to apoptosis of melanoma cells via mitochondrial damage-dependent ROS accumulation. *Cell Signal.* 22 (2), 197–211. doi:10.1016/j.cellsig.2009.09.013

Chen, Y., and Gibson, S. B. (2008). Is mitochondrial generation of reactive oxygen species a trigger for autophagy?. *Autophagy* 4 (2), 246–248. doi:10.4161/auto.5432

Chen, Y., Azad, M. B., and Gibson, S. B. (2009). Superoxide is the major reactive oxygen species regulating autophagy. *Cell Death Differ.* 16 (7), 1040–1052. doi:10.1038/cdd.2009.49

Chen, Y. F., Liu, H., Luo, X. J., Zhao, Z., Zou, Z. Y., et al. (2017). The roles of reactive oxygen species (ROS) and autophagy in the survival and death of leukemia cells. *Crit. Rev. Oncol. Hematol.* 112, 21–30. doi:10.1016/j.critrevonc.2017.02.004

Choi, A. M., Ryter, S. W., and Levine, B. (2013). Autophagy in human health and disease. *N. Engl. J. Med.* 368 (19), 1845–1846. doi:10.1056/nejmra1205406

De Biasi, S., Gibellini, L., and Cossarizza, A. (2015). Uncompensated polychromatic analysis of mitochondrial membrane potential using JC-1 and multilaser excitation. *Curr. Protoc. Cytom* 72, 7 32 1–7.32.11. doi:10.1002/0471142956.cy0732s72

Galadari, S., Rahman, A., Pallichankandy, S., and Thayyullathil, F. (2017). Reactive oxygen species and cancer paradox: to promote or to suppress?. *Free Radic. Biol. Med.* 104, 144–164. doi:10.1016/j.freeradbiomed.2017.01.004

Guo, B., Yang, M., Liang, D., Yang, L., Cao, J., et al. (2012). Cell apoptosis induced by zinc deficiency in osteoblastic MC3T3-E1 cells via a mitochondrial-mediated pathway. *Mol. Cell Biochem.* 361 (1-2), 209–216. doi:10.1007/s11010-011-1105-x

Hanaor, D., MicHeLazzi, M., Leonelli, C., and Sorrell, C. C. (2012). The effects of carboxylic acids on the aqueous dispersion and electrophoretic deposition of ZrO2. *J. Eur. Ceram. Soc.* 32 (1), 235–244. doi:10.1016/j.jeurceramsoc.2011.08.015

Indran, I. R., Tufo, G., Pervaiz, S., and Brenner, C. (2011). Recent advances in apoptosis, mitochondria and drug resistance in cancer cells. *Biochim. Biophys. Acta* 1807 (6), 735–745. doi:10.1016/j.bbabio.2011.03.010

Jiang, X., and Wang, X. (2004). CytochromeC-mediated apoptosis. *Annu. Rev. Biochem.* 73, 87–106. doi:10.1146/annurev.biochem.73.011303.073706

Kihara, A., Kabeya, Y., Ohsumi, Y., and Yoshimori, T. (2001). Beclin-phosphatidylinositol 3-kinase complex functions at the trans -Golgi network. *EMBO Rep.* 2 (4), 330–335. doi:10.1093/embo-reports/kve061

Kim, H., Kim, E. H., Eom, Y. W., Kim, W.-H., Kwon, T. K., et al. (2006). Sulforaphane sensitizes tumor necrosis factor-related apoptosis-inducing ligand (TRAIL)-resistant hepatoma cells to TRAIL-induced apoptosis through reactive oxygen species-mediated up-regulation of DR5. *Cancer Res.* 66 (3), 1740–1750. doi:10.1158/0008-5472.can-05-1568

Kroemer, G., and Levine, B. (2008). Autophagic cell death: the story of a misnomer. *Nat. Rev. Mol. Cell Biol.* 9 (12), 1004–1010. doi:10.1038/nrm2529

Kyrylkova, K., Kyryachenko, S., Leid, M., and Kioussi, C. (2012). Detection of apoptosis by TUNEL assay. *Methods Mol. Biol.* 887, 41–47. doi:10.1007/978-1-61779-860-3_5

Lakhani, S. A., Masud, A., Kuida, K., Porter, G. A., Jr., Booth, C. J., Mehal, W. Z., et al. (2006). Caspases 3 and 7: key mediators of mitochondrial events of apoptosis. *Science* 311 (5762), 847–851. doi:10.1126/science.1115035

Lemasters, J. J., Qian, T., He, L., Kim, J. S., Elmore, S. P., et al. (2002). Role of mitochondrial inner membrane permeabilization in necrotic cell death, apoptosis, and autophagy. *Antioxid. Redox Signal.* 4 (5), 769–781. doi:10.1089/152308602760598918

Li, J., and Yuan, J. (2008). Caspases in apoptosis and beyond. *Oncogene* 27 (48), 6194–6206. doi:10.1038/onc.2008.297

Lin, L. S., Song, J., Song, L., Ke, K., Liu, Y., et al. (2018). Simultaneous fenton-like ion delivery and glutathione depletion by MnO2 -based nanoagent to enhance chemodynamic therapy. *Angew. Chem. Int. Ed.* 57 (18), 4902–4906. doi:10.1002/anie.201712027

Liu, Y., and Levine, B. (2015). Autosis and autophagic cell death: The dark side of autophagy. *Cell Death Differ.* 22 (3), 367–376. doi:10.1038/cdd.2014.143

Lohbauer, U., Wagner, A., Belli, R., Stoetzel, C., Hilpert, A., et al. (2010). Zirconia nanoparticles prepared by laser vaporization as fillers for dental adhesives. *Acta Biomater.* 6 (12), 4539–4546. doi:10.1016/j.actbio.2010.07.002

Mftah, A., Alhassan, F. H., Al-Qubaisi, M. S., El Zowalaty, M. E., Webster, T. J., et al. (2015). Physicochemical properties, cytotoxicity, and antimicrobial activity of sulphated zirconia nanoparticles. *Int. J. Nanomedicine* 10, 765–774. doi:10.2147/IJN.S66058

Mizushima, N. (2007). Autophagy: Process and function. *Genes Dev.* 21 (22), 2861–2873. doi:10.1101/gad.1599207

Pierce, G. B., Parchment, R. E., and Lewellyn, A. L. (1991). Hydrogen peroxide as a mediator of programmed cell death in the blastocyst. *Differentiation* 46 (3), 181–186. doi:10.1111/j.1432-0436.1991.tb00880.x

Pistritto, G., Trisciuoglio, D., Ceci, C., Garufi, A., and D'Orazi, G. (2016). Apoptosis as anticancer mechanism: function and dysfunction of its modulators and targeted therapeutic strategies. *Aging (Albany, NY)* 8 (4), 603–619. doi:10.18632/aging.100934

Polyakov, N., Leshina, T., Fedenok, L., Slepneva, I., Kirilyuk, I., et al. (2018). Redox-active quinone cHeLators: Properties, mechanisms of action, cell delivery, and cell toxicity. *Antioxid. Redox Signal.* 28 (15), 1394–1403. doi:10.1089/ars.2017.7406

Qeblawi, D. M., Munoz, C. A., Brewer, J. D., and Monaco, E. A. (2010). The effect of zirconia surface treatment on flexural strength and shear bond strength to a resin cement. *J. Prosthet. Dent.* 103 (4), 210–220. doi:10.1016/s0022-3913(10)60033-9

Rabinowitz, J. D., and White, E. (2010). Autophagy and metabolism. *Science* 330 (6009), 1344–1348. doi:10.1126/science.1193497

Sakamuru, S., Attene-Ramos, M. S., and Xia, M. (2016). Mitochondrial membrane potential assay. *J. Biol. Chem.* 1473, 17–22. doi:10.1007/978-1-4939-6346-1_2

Singh, S. V., Srivastava, S. K., Choi, S., Lew, K. L., Antosiewicz, J., et al. (2005). Sulforaphane-induced cell death in human prostate cancer cells is initiated by reactive oxygen species. *J. Biol. Chem.* 280 (20), 19911–19924. doi:10.1074/jbc.m412443200

Sun, J., Patel, C. B., Jang, T., Merchant, M., Chen, C., et al. (2020). High levels of ubidecarenone (oxidized CoQ10) delivered using a drug-lipid conjugate nanodispersion (BPM31510) differentially affect redox status and growth in malignant glioma versus non-tumor cells. *Sci. Rep.* 10 (1), 13899. doi:10.1038/s41598-020-70969-0

Thornberry, N. A., and Lazebnik, Y. (1998). Caspases: enemies within. *Science* 281 (5381), 1312–1316. doi:10.1126/science.281.5381.1312

Venu, M., Venkateswarlu, S.-D., Reddy, Y. V. M., Seshadri Reddy, A., Gupta, V. K., et al. (2018). Highly sensitive electrochemical sensor for anticancer drug by a zirconia nanoparticle-decorated reduced graphene oxide nanocomposite. *Toxicol. Applied Pharmacol.* 379 (11), 14597–14605. doi:10.1021/acsomega.8b02129

Wang, P., Zhang, S. D., Jiao, J., Wang, W., Yu, L., et al. (2019). ROS -mediated p53 activation by juglone enhances apoptosis and autophagy *in vivo* and *in vitro*. *Toxicol. Appl. Pharmacol.*, 114647. doi:10.1016/j.taap.2019.114647

Ye, J., Xue, M., Liu, Y., Zhu, S., Li, Y., et al. (2019). Diosbulbin B-induced mitochondria-dependent apoptosis in L-02 hepatocytes is regulated by reactive oxygen species-mediated autophagy. *Front. Pharmacol.* 10, 676. doi:10.3389/fphar.2019.00676

Yoshii, S. R., and Mizushima, N. (2017). Monitoring and measuring autophagy. *Int. J. Mol. Sci.* 18 (9), 1865. doi:10.3390/ijms18091865

Zhang, B. B., Wang, D. G., Guo, F. F., and Xuan, C. (2015a). Mitochondrial membrane potential and reactive oxygen species in cancer stem cells. *Fam. Cancer* 14(1), 19–23. doi:10.1007/s10689-014-9757-9

Zhang, D., Tang, B., Xie, X., Xiao, Y. F., Yang, S. M., et al. (2015b). The interplay between DNA repair and autophagy in cancer therapy. *Cancer Biol. Ther.* 16 (7), 1005–1013. doi:10.1080/15384047.2015.1046022

Conflict of Interest: The authors declare that the research was conducted in the absence of any commercial or financial relationships that could be construed as a potential conflict of interest.

Advantages of publishing in Frontiers

OPEN ACCESS
Articles are free to read for greatest visibility and readership

FAST PUBLICATION
Around 90 days from submission to decision

HIGH QUALITY PEER-REVIEW
Rigorous, collaborative, and constructive peer-review

TRANSPARENT PEER-REVIEW
Editors and reviewers acknowledged by name on published articles

Frontiers
Avenue du Tribunal-Fédéral 34
1005 Lausanne | Switzerland

Visit us: www.frontiersin.org
Contact us: frontiersin.org/about/contact

REPRODUCIBILITY OF RESEARCH
Support open data and methods to enhance research reproducibility

DIGITAL PUBLISHING
Articles designed for optimal readership across devices

FOLLOW US
@frontiersin

IMPACT METRICS
Advanced article metrics track visibility across digital media

EXTENSIVE PROMOTION
Marketing and promotion of impactful research

LOOP RESEARCH NETWORK
Our network increases your article's readership